

Biophysics for the Life Sciences

Norma M. Allewell  
Linda O. Narhi  
Ivan Rayment *Editors*

# Molecular Biophysics for the Life Sciences

 Springer

# Biophysics for the Life Sciences

*Series Editor*

Norma M. Allewell

For further volumes:

<http://www.springer.com/series/10230>



Norma M. Allewell • Linda O. Narhi  
Ivan Rayment  
Editors

# Molecular Biophysics for the Life Sciences

 Springer



*Editors*

Norma M. Allewell  
Department of Cell Biology  
and Molecular Genetics  
University of Maryland  
College Park, MD, USA

Linda O. Narhi  
Research & Development  
Amgen, Inc.  
Thousand Oaks, CA, USA

Ivan Rayment  
Department of Biochemistry  
University of Wisconsin-Madison  
Madison, WI, USA

ISBN 978-1-4614-8547-6      ISBN 978-1-4614-8548-3 (eBook)  
DOI 10.1007/978-1-4614-8548-3  
Springer New York Heidelberg Dordrecht London

Library of Congress Control Number: 2013949607

© Springer Science+Business Media New York 2013

This work is subject to copyright. All rights are reserved by the Publisher, whether the whole or part of the material is concerned, specifically the rights of translation, reprinting, reuse of illustrations, recitation, broadcasting, reproduction on microfilms or in any other physical way, and transmission or information storage and retrieval, electronic adaptation, computer software, or by similar or dissimilar methodology now known or hereafter developed. Exempted from this legal reservation are brief excerpts in connection with reviews or scholarly analysis or material supplied specifically for the purpose of being entered and executed on a computer system, for exclusive use by the purchaser of the work. Duplication of this publication or parts thereof is permitted only under the provisions of the Copyright Law of the Publisher's location, in its current version, and permission for use must always be obtained from Springer. Permissions for use may be obtained through RightsLink at the Copyright Clearance Center. Violations are liable to prosecution under the respective Copyright Law.

The use of general descriptive names, registered names, trademarks, service marks, etc. in this publication does not imply, even in the absence of a specific statement, that such names are exempt from the relevant protective laws and regulations and therefore free for general use.

While the advice and information in this book are believed to be true and accurate at the date of publication, neither the authors nor the editors nor the publisher can accept any legal responsibility for any errors or omissions that may be made. The publisher makes no warranty, express or implied, with respect to the material contained herein.

Printed on acid-free paper

Springer is part of Springer Science+Business Media ([www.springer.com](http://www.springer.com))

# Preface

The scope, accessibility, impact, and relevance of biophysics to many different areas of inquiry have grown tremendously in recent years, driven by major conceptual advances, innovations in instrumentation, and powerful new analytical, computational, genomic, and imaging methods. These advances enable us to visualize the structures and dynamics of proteins and nucleic acids at atomic resolution, observe single molecules in real time, monitor processes within living cells at high resolution, identify and determine the chemical structures of individual molecules in complex biological samples, and define the complex network of interactions that regulate cellular function. Biophysical insights into plant, animal, and human inheritance, development, physiology, health, and disease have driven and will continue to drive many of the major advances in our quality of life. As a result, many people who are not professional biophysicists increasingly have a need to learn about biophysics.

This volume is designed to enable students, scientists trained in other disciplines, clinicians, members of the chemical, pharmaceutical, and biotech industries, intellectual property professionals, and the general public to acquire an understanding of molecular biophysics. In contrast to other areas of biophysics, molecular biophysics focuses on the complex and beautiful macromolecules that encode all genetic information and form the molecular machinery that drives all cellular processes. This volume provides an overview of the development and scope of molecular biophysics and in-depth discussions of the major experimental methods that enable biological macromolecules to be studied at atomic resolution. It also reviews the physical–chemical concepts that are needed to interpret the experimental results and to understand how the structure, dynamics, and physical properties of biological macromolecules enable them to perform their biological functions. Reviews of research on three disparate biomolecular machines—DNA helicases, ATP synthases, and myosin—illustrate how the combination of theory and experiment leads to new insights and new questions.

This volume is a foundational volume in a series entitled *Biophysics for the Life Sciences* which is designed to introduce nonspecialists to major areas of biophysics and to enable established investigators to learn about areas that lie outside their

primary interests. The scope of the series will be broad, encompassing molecular, cellular, and organismal biophysics. The series is intended to be synthetic and to emphasize concepts, rather than comprehensive or didactic. Each volume will consist of up-to-date presentations of research topics and research approaches, including observation, experiment, and computation. When appropriate, the relationship of basic research to translational research, clinical issues, and technology transfer will be considered.

The editors would like to thank all the people who contributed to this volume, including their colleagues and students, and the following topic area experts: Gerald Becker, Clive Bagshaw, Christine Cremo, Stanley Dunn, Walter Englander, R. Matthew Fesinmeyer, Masa Futai, Michael Geeves, Wouter Hoff, Andreas Holzenburg, Tatyana Igumenova, Yijia Jiang, Miklós Kellermayer, Gerd Kleeman, Ramil Latypov, Juliette Lecomte, Russell Middaugh, Marcia Newcomer, Joseph Phillips, Leszek Poppe, Kevin Raney, Vladimir Razinkov, George Reed, Gina Sosinsky, Stefan Stoll, Jiraj Svitel; John Tesmer, Michael Trakselis, Art van der Est, Stanislav Vitha, Joseph Wedekind, and Julian Whitelegge.

College Park, MD, USA  
Thousand Oaks, CA, USA  
Madison, WI, USA

Norma M. Allewell  
Linda O. Narhi  
Ivan Rayment

## About the Editors

**Dr. Norma M. Allewell** is Professor of Cell Biology and Molecular Genetics, and Affiliate Professor of Chemistry and Biochemistry at the University of Maryland, where she served as Interim Vice President for Research, and Dean of the College of Chemical and Life Sciences for a decade. She also held faculty positions at the University of Minnesota, where she was a department head and vice provost; Wesleyan University, where she was founding chair of the Department of Molecular Biology and Biochemistry; and the Polytechnic Institute of Brooklyn. Dr. Allewell holds a B.Sc. (Hon.) from McMaster University and a Ph.D. in molecular biophysics from Yale University. Her research focuses on protein structure, function, and dynamics, and metabolic regulatory mechanisms and diseases. She has published approximately 150 peer-reviewed papers, edited two books, and contributed several book chapters. She is a Past President of the Biophysical Society a former US representative to the International Union of Pure and Applied Biophysics and a Fellow of the American Association for the Advancement of Science. She is an Associate Editor of the *Journal of Biological Chemistry* and a former Editorial Board Member for *Biopolymers*. She served on the National Academy of Sciences Space Studies Board Committee on Space Biology and Medicine; the Board of Scientific Advisors for the National Center for Biotechnology Information; and the Advisory Committee, Directorate of Biological Sciences, National Science Foundation, as well as numerous review panels for the National Institutes of Health, National Science Foundation, and Howard Hughes Medical Institute. She was a Jefferson Science Fellow at the US State Department in the Bureau of East Asia and the Pacific in 2011–2012.

**Dr. Linda O. Narhi** received her B.Sc. in Chemistry (Honors) from the University of Michigan and her Ph.D. in Biological Chemistry from UCLA. She joined Amgen 26 years ago and has been a member of the R&D, Quality, and Operations groups. She is currently a Scientific Executive Director in the Product Attribute Science group in R&D, where her responsibilities include solution stability assessment of all protein-based therapeutic candidates, developing and implementing predictive

assays for protein stability to process, storage and delivery conditions. She is also responsible for developing and implementing assays to assess biological consequences of product quality attributes, especially protein aggregates. She co-leads the cross functional Immunogenicity Team, developing, adapting, and implementing methods to assess relative immunogenic potential of protein aggregates and other quality attributes, and also co-leads the cross functional antibody engineering team. She is the leader of the Technology Forum Leadership Team, coordinating and leading the technology development efforts in Process and Product development, a department of about 600 scientists in R&D. She is the editor for Galenics, the internal Process and Product Development journal for original research. She is a member of the US Pharmacological Convention expert committee on subvisible particle analysis for Biologics, on the steering committee for the American Association of Pharmaceutical Chemists Focus group on protein aggregates and Biological Consequences, and for the next several years will co-chair the annual meeting on protein higher order structure sponsored by CASSS, an international separation science society. She has published well over 100 articles in peer reviewed journals and authored numerous book chapters on the subjects of protein folding, stability, aggregation, and biotherapeutic development.

**Dr. Ivan Rayment** is Professor of Biochemistry at the University of Wisconsin–Madison, where he holds the Michael G. Rossmann Professorship in Biochemistry. Dr. Rayment received his B.Sc. and Ph.D. in Chemistry from Durham University, England. He has a wide range of interests in structural biology and has made seminal contributions to our understanding of the structural basis of motility, enzyme evolution, cobalamin biosynthesis, and transposition. He has published over 180 peer reviewed papers. He is a Fellow of the American Association for the Advancement of Science and a Fellow of the Biophysical Society.

# Contents

<b>1</b>	<b>Introduction.....</b>	<b>1</b>
	Norma M. Allewell, Linda O. Narhi, and Ivan Rayment	
<b>2</b>	<b>Structural, Physical, and Chemical Principles.....</b>	<b>17</b>
	Norma M. Allewell, Linda O. Narhi, and Ivan Rayment	
<b>Part I The Experimental Tools of Molecular Biophysics</b>		
<b>3</b>	<b>Optical Spectroscopic Methods for the Analysis of Biological Macromolecules .....</b>	<b>33</b>
	Linda O. Narhi, Cynthia H. Li, Ranjini Ramachander, Juraj Svitel, and Yijia Jiang	
<b>4</b>	<b>Diffraction and Scattering by X-Rays and Neutrons.....</b>	<b>91</b>
	Ivan Rayment	
<b>5</b>	<b>Nuclear Magnetic Resonance Spectroscopy .....</b>	<b>113</b>
	Thomas C. Pochapsky and Susan Sondej Pochapsky	
<b>6</b>	<b>Electron Paramagnetic Resonance Spectroscopy .....</b>	<b>175</b>
	John H. Golbeck and Art van der Est	
<b>7</b>	<b>Mass Spectrometry .....</b>	<b>215</b>
	Igor A. Kaltashov and Cedric E. Bobst	
<b>8</b>	<b>Single-Molecule Methods .....</b>	<b>257</b>
	Paul J. Bujalowski, Michael Sherman, and Andres F. Oberhauser	
<b>Part II Biological Macromolecules as Molecular Machines: Three Examples</b>		
<b>9</b>	<b>Helicase Unwinding at the Replication Fork.....</b>	<b>291</b>
	Divya Nandakumar and Smita S. Patel	

<b>10 Rotary Motor ATPases .....</b>	<b>313</b>
Stephan Wilkens	
<b>11 Biophysical Approaches to Understanding the Action of Myosin as a Molecular Machine.....</b>	<b>341</b>
Mihály Kovács and András Málnási-Csizmadia	
 <b>Part III Future Prospects</b>	
<b>12 Future Prospects .....</b>	<b>365</b>
Norma M. Allewell, Igor A. Kaltashov, Linda O. Narhi, and Ivan Rayment	
<b>Index.....</b>	<b>381</b>

# Contributors

**Cedric E. Bobst** Department of Chemistry, University of Massachusetts-Amherst, Amherst, MA, USA

**Paul J. Bujalowski** Department of Biochemistry and Molecular Biology, University of Texas Medical Branch at Galveston, Galveston, TX, USA

**John H. Golbeck** Department of Biochemistry and Molecular Biology, The Pennsylvania State University, University Park, PA, USA

Department of Chemistry, The Pennsylvania State University, University Park, PA, USA

**Yijia Jiang** Research and Development, Amgen Inc., Thousand Oaks, CA, USA

**Igor A. Kaltashov** Department of Chemistry, University of Massachusetts-Amherst, Amherst, MA, USA

**Mihály Kovács** Department of Biochemistry, Eötvös Loránd University-Hungarian Academy of Sciences “Momentum” Motor Enzymology Research Group, Eötvös Loránd University, Budapest, Hungary

**Cynthia H. LI** Research and Development, Amgen Inc., Thousand Oaks, CA, USA

**András Málnási-Csizmadia** Department of Biochemistry, Eötvös Loránd University-Hungarian Academy of Sciences Molecular Biophysics Research Group, Eötvös Loránd University, Budapest, Hungary

**Divya Nandakumar** Department of Biochemistry and Molecular Biology, Robert Wood Johnson Medical School, Rutgers University, Piscataway, NJ, USA



**Andres F. Oberhauser** Department of Biochemistry and Molecular Biology, University of Texas Medical Branch at Galveston, Galveston, TX, USA

Department of Neuroscience and Cell Biology, University of Texas Medical Branch at Galveston, Galveston, TX, USA

Sealy Center for Structural Biology and Molecular Biophysics, University of Texas Medical Branch at Galveston, Galveston, TX, USA

**Smita S. Patel** Department of Biochemistry and Molecular Biology, Robert Wood Johnson Medical School, Rutgers University, Piscataway, NJ, USA

**Susan Sondej Pochapsky** Department of Chemistry and Rosenstiel Basic Medical Sciences Research Institute, Brandeis University, Waltham, MA, USA

**Thomas C. Pochapsky** Department of Chemistry and Rosenstiel Basic Medical Sciences Research Institute, Brandeis University, Waltham, MA, USA

**Ranjini Ramachander** Research and Development, Amgen Inc., Thousand Oaks, CA, USA

**Michael Sherman** Department of Biochemistry and Molecular Biology, University of Texas Medical Branch at Galveston, Galveston, TX, USA

**Juraj Svitel** Research and Development, Amgen Inc., Thousand Oaks, CA, USA

**Art van der Est** Department of Chemistry, Brock University, St. Catharines, ON, Canada

**Stephan Wilkens** Department of Biochemistry and Molecular Biology, SUNY Upstate Medical University, Syracuse, NY, USA

# Chapter 1

## Introduction

Norma M. Allewell, Linda O. Narhi, and Ivan Rayment

**Abstract** This introductory chapter reviews the history and development of biophysics and provides an overview of topics covered in the volume. It introduces the major experimental methods available for studying biological macromolecules (optical spectroscopy, X-ray and neutron diffraction and scattering, electron paramagnetic resonance spectroscopy, nuclear magnetic resonance spectroscopy, mass spectrometry, and single molecule methods). The role of biological macromolecules as molecular machines is discussed, using as examples the three macromolecular machines presented in subsequent chapters: helicases, membrane ATPases, and myosin. The chapter concludes with brief discussions of the role of computation and future prospects in three areas: X-ray and neutron diffraction and scattering, mass spectrometry, and drug and pharmaceutical development.

**Keywords** Biomolecular machines • Diffraction • Electron paramagnetic resonance spectroscopy • Experimental methods • Future prospects • Historical overview • Mass spectrometry • Molecular machines • Optical spectroscopy • Nuclear magnetic resonance spectroscopy • Single molecule methods

---

N.M. Allewell (✉)  
Department of Cell Biology and Molecular Genetics,  
University of Maryland, College Park, MD 20852, USA  
e-mail: allewell@umd.edu

L.O. Narhi  
Research and Development, Amgen, Inc., One Amgen Center Drive,  
Thousand Oaks, CA 91320, USA  
e-mail: lnarhi@amgen.com

I. Rayment  
Department of Biochemistry, University of Wisconsin-Madison,  
433 Babcock Drive, Madison, WI 53706-1544, USA

## 1.1 What Is Biophysics?

Biophysics seeks to define the physical properties of living systems and to understand the relationship between the physical properties of biological molecules, cells, tissues and organs and their biological function. The science of biophysics provides both a conceptual framework and powerful experimental and theoretical tools. Biophysicists use these approaches to work towards an understanding of the physical basis of life at every level—from the physiological and neurological to the cellular and molecular. Examples of the kinds of questions biophysicists ask include the following:

- How do muscles contract?
- How do nerves send signals to the brain?
- How do we see and hear?
- How do we taste and smell chemicals?
- How do plant cells use light to convert carbon dioxide and water to nutrients?
- How do protozoa and sperm swim?
- How do enzymes recognize their substrates and catalyze their conversion to products?
- How do the three-dimensional structures of macromolecules enable them to perform their function?
- What physical forces determine the three-dimensional structures of macromolecules and their assembly to form larger structures, and how does assembly affect function?

Completely answering these questions requires integrating knowledge obtained by scientists from many different disciplines—biochemists, chemists, cell biologists, geneticists, microbiologists, neurobiologists, physiologists, plant biologists, and others. Thus biophysics is inherently interdisciplinary and cross-disciplinary. The experimental tools of physics and chemistry enable visualization of both the structures and dynamics of organs, tissues, cells, and molecules and allow the molecular processes and chemical reactions that underlie biological function to be explored and defined. The conceptual and computational tools of mathematics and computer science are required all along the way—first, to translate the raw experimental data into meaningful information about the process under investigation, and then to develop, refine, and test models of how the process might occur. Usually the initial models are descriptive and qualitative, but as more and better information is obtained, the models can be made increasingly quantitative, enabling them to be tested more rigorously. Importantly, quantitative models incorporate experimentally derived knowledge about the process that generally leads to hypotheses that extend beyond the scope of the original question.

Over the past several decades, groundbreaking advances have increased the scope, impact, and relevance of biophysics tremendously. Fundamental biophysical questions are being addressed at every level of biology. Experimental biophysics continues to generate new challenges and opportunities in the physical sciences, mathematics, and computation, and, in turn, new developments in these fields create new opportunities in experimental biophysics. There are also important interfaces between biophysics and

other rapidly developing interdisciplinary fields, such as bioengineering, genomics, and bioinformatics. Finally, biophysics has much to contribute to biotechnology, drug discovery, and clinical medicine, as well as many other fields.

## 1.2 How Did Biophysics Develop?

The origins of biophysics go back at least as far as Leonardo da Vinci's anatomical and biomechanical studies of the human skeleton, muscles, and heart in the sixteenth century (Fig. 1.1); William Harvey's analysis of blood circulation in the mid-seventeenth century; and Antonie van Leeuwenhoek's observations of cell structure and function in the late seventeenth century (Fig. 1.2). From that time forward, microscopists, anatomists, physiologists, physicians, and others who worked to understand how cells, tissues, and organs function pursued studies that often had a substantial biophysical component. In the mid-nineteenth century, Claude Bernard's investigations of organ function and the mechanisms that enable organisms to maintain a steady state laid the foundations for systems physiology. In the mid-twentieth

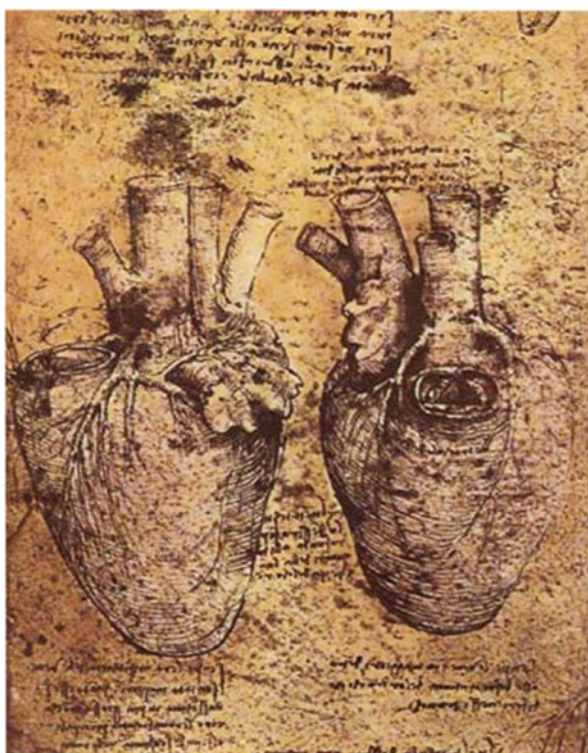


**Fig. 1.1** Leonardo da Vinci's sketch of the heart showing the distribution of the blood vessels. Image provided to Springer Images by BioMed Central



**Fig. 1.2** From a portrait by Van Verkolje of Antonie Leeuwenhoek, a Dutch tradesman who lived in the seventeenth century and developed and built the first microscopes that enabled microorganisms and plant and animal cells to be viewed (Reproduced with permission of the Rijksmuseum)

century, Alan Hodgkin and Andrew Huxley's mathematical reconstruction of the nerve impulse initiated the development of cellular biophysics.

Biophysics did not emerge as a recognized scientific field until the middle of the twentieth century, when a visionary group of atomic physicists turned their attention to the major unsolved problems in biology. Erwin Schrödinger, one of the founders of quantum mechanics, was a member of this group and in 1944 published a series of lectures entitled "What is Life?" that proved to be transformational. In these lectures, Schrödinger defined the central question for physicists (and chemists) entering the new field of biophysics as follows: "How can the events in space and time which take place within the spatial boundaries of a living organism be accounted for by physics and chemistry?" He then went on to argue that "The obvious inability of present day physics and chemistry to account for such events is no reason at all for doubting that they can be accounted for by those sciences."

Soon after the publication of "What is Life?" molecular biophysics emerged as a new scientific discipline with the discovery that the three-dimensional structures of biological macromolecules could be determined by X-ray diffraction. This discovery enabled the hard won gains of several generations of biochemists who had worked to define the chemical structures and biological functions of biological molecules to be taken to a new level. The success of Dorothy Crowfoot Hodgkin (Fig. 1.3) in determining the three-dimensional structures of cholesterol, penicillin, and Vitamin B<sub>12</sub> was a ground breaking example. Building on the experimental work of Maurice Wilkins and Rosalind Franklin, James Watson and Francis Crick (Fig. 1.4) proposed in 1953 that DNA had a double helical structure that enabled it to encode genetic information. A full history of the science that paved the way for this discovery can be found in [1]. At the same time, Max Perutz began to develop



**Fig. 1.3** Dorothy Crowfoot Hodgkin was awarded the Nobel Prize in Chemistry in 1964 for her discoveries, through the use of X-ray diffraction, of the structures of biologically important molecules, including penicillin, vitamin B-12 and the protein hormone insulin (1969). Her achievements included not only these structure determinations and the scientific insight they provided but also the development of methods that made such structure determinations possible (Reproduced with permission of the Royal Society)

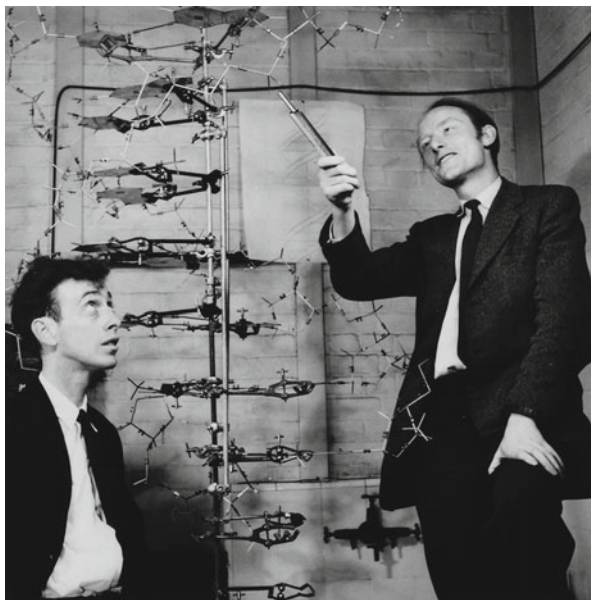


**Fig. 1.4** James Watson and Francis Crick shown with their model of the DNA double helix. Together with Maurice Wilkins, they received the Nobel Prize in 1962 for “their discoveries concerning the molecular structure of nucleic acids and its significance for information transfer in living material.” Research on the crystal structure of DNA by Rosalind Franklin in Maurice Wilkins’ laboratory was critical to the development of this model (Reproduced with permission of Photo Researchers, Inc.)





**Fig. 1.5** Linus Pauling, Max Delbrück and Max Perutz in 1962. All three won Nobel Prizes: Linus Pauling for his research into the nature of the chemical bond and its application to the elucidation of the structure of complex substances; Max Delbrück, with Alfred Hershey and Salvador Luria, for their discoveries concerning the replication mechanism and the genetic structure of viruses; and Max Perutz, with John Kendrew, for their studies of the structures of globular proteins (Reproduced with permission of Oregon State University Libraries)

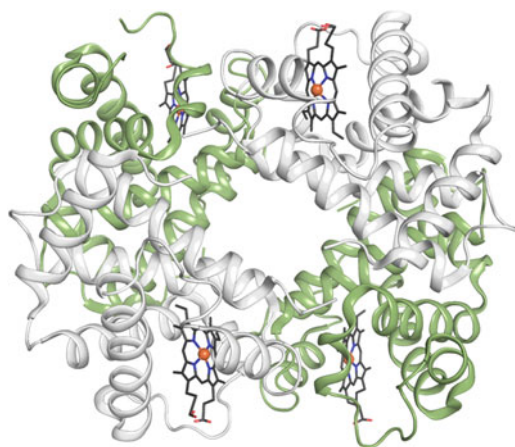


**Fig. 1.6** The fold of the polypeptide backbone of the four subunits in human deoxyhemoglobin at 1.74 Å resolution, as reported by Fermi and Perutz. The  $\alpha$ -chains are colored in *white* and the  $\beta$ -chains are depicted in *green*. The four heme groups that bind oxygen are shown in *black*, with the central iron ion in *red*. Nitrogen atoms of histidine side chains that interact with the iron ion are shown in *blue* (PDB accession number 4HHP)

experimental and computational methods for visualizing the three-dimensional structures of proteins at atomic resolution (Fig. 1.5). By 1959, Perutz was able to report the three-dimensional structure of hemoglobin, the major carrier for oxygen in the blood (Fig. 1.6), and shortly thereafter, John Kendrew and colleagues determined the structure of myoglobin, which sequesters oxygen in tissues. Since that

time, more than 80,000 protein structures have been reported. The relationship between the structures of proteins and nucleic acids and their function is discussed in detail in [2–5].

Schrödinger and his fellow physicists recognized that understanding how genetic information was stored and transmitted from one generation to the next is as important as understanding the structure and physical properties of macromolecules. Another member of this group, Max Delbrück (Fig. 1.5), played a critical role by arguing successfully that bacterial viruses provide the best opportunity to understand the flow of genetic information in living systems, because they are among the simplest organisms. The work of Delbrück, his colleagues, and their successors laid the foundations for a second new scientific discipline, molecular biology, based on the successful elucidation of the genetic code. Over the next 6 decades, the interaction and weaving together of molecular biology and molecular biophysics have led to a rich succession of dazzling scientific discoveries, many of which have been honored with Nobel Prizes [6–12].

### 1.3 The Experimental Tools of Molecular Biophysics

While all the molecules of the cell play a role in its function, molecular biophysics is particularly focused on macromolecules, large molecules with molecular weights in the tens to hundreds of thousand Daltons. Macromolecules consist of small monomeric units linked together to form large polymers. Often single polymers assemble to form larger multimeric units, called macromolecular assemblies. The best known and most intensively studied biological macromolecules are nucleic acids and proteins, both of which are critically important to the functioning of living systems. Nucleic acids encode the genetic information of the cell, and act as templates for the synthesis of proteins, while proteins are the molecular machines that enable most functions of the cell to be carried out.

As is the case throughout science, advances in biophysics are built on observation and measurement. Because molecules and cells are much too small to be seen with the naked eye, molecular and cellular biophysicists depend upon various kinds of scientific instrumentation that gather different kinds of information. The physical properties of molecules that molecular biophysicists are most interested in are their three-dimensional structures and dynamics and their energetic, electrical, magnetic, and mechanical properties. This volume describes the major experimental approaches that are currently used to probe and analyze the structural, dynamic, and physical properties of biological macromolecules at atomic resolution. The next section presents a brief survey of these methods, with many interesting and important features of each approach deferred for discussion in subsequent chapters. The last three chapters of the volume present three examples of how experimental results obtained by a variety of approaches can be integrated and used to develop a comprehensive understanding of how proteins function as molecular machines.



### 1.3.1 *Absorption, Circular Dichroic, and Fluorescent Spectroscopy*

Several forms of *absorption spectroscopy*, discussed in Chap. 3, monitor the absorption of ultraviolet, visible, and infrared light by biological molecules. The intrinsic chromophores of DNA are the nucleotide bases, while in proteins both the peptide backbone and the aromatic amino acids have specific absorbances that can be exploited to provide information about the structure of the molecules. Most forms of absorption spectroscopy do not have the resolution required to acquire highly detailed structural information. They are, however, invaluable in characterizing larger elements of molecular structure and monitoring structural changes and chemical processes. In addition, attachment of specific chemical groups that have unique spectral properties (external chromophores) may allow higher resolution information to be obtained.

*Circular dichroic spectroscopy* measures the difference in absorption of left- and right-handed circularly polarized light and is often used to probe the overall structure of chiral macromolecules. In proteins, different types of secondary structure have specific signals in the far ultraviolet region, while the aromatic amino acids and disulfide bonds have signals in the near ultraviolet region that can be used to follow changes in tertiary structure.

*Fluorescence spectroscopy* monitors the emission of light from chemical groups that are also able to absorb light of a shorter wavelength. Fluorescence spectroscopy has more specificity and resolution than absorption spectroscopy, but decreased signal strength relative to absorption spectroscopy because fewer chemical groups are fluorescent. The specificity of fluorescence spectroscopy has made it possible to develop *molecular rulers* that measure the distance between two different fluorescent groups attached to a biological macromolecule. When the two groups are appropriately matched, fluorescent energy will be transferred between them. The efficiency of energy transfer depends upon the distance between the two molecules, and so measuring the efficiency of transfer enables the distance to be determined at high resolution. Changes in the efficiency of energy transfer with time also allow fluctuations in molecular structure to be monitored and analyzed.

In common with most spectroscopic methods, optical spectroscopy provides the average for the total population, but cannot differentiate between subpopulations. Thus large changes in the magnitude of the signal could stem from small uniform changes across the entire molecular population in the test samples, or could result from large changes in structure that occur in only a fraction of the population.

### 1.3.2 *Atomic-Level Structural Methods*

Only two experimental approaches, both developed by physicists, enable the structures of macromolecules to be determined at atomic resolution. *X-ray crystallography*, discussed in Chap. 4, depends upon the diffraction of X-rays by crystals of the molecule being studied. Since the structures determined by X-crystallography

are derived from molecules in a crystal, the information that they provide about the flexibility and dynamics of the molecule may not reflect the full flexibility and dynamics of the molecule in solution.

The second approach, *nuclear magnetic resonance spectroscopy*—often abbreviated NMR—is discussed in Chap. 5. NMR exploits the fact that many of the atoms in biological molecules have nuclear spins that align with an externally applied electric field. When a radio frequency pulse is applied, the alignment changes, and the change in alignment can be measured. The response of individual nuclei to the radio frequency pulse depends upon the location of other nuclei. Mathematical analysis of the response of the nuclear spins of different kinds of atoms in the molecule to various pulses enables the three-dimensional structure of the molecule to be deduced.

In contrast to X-ray crystallography, most structures determined by NMR are derived from molecules in solution and so provide more information about the dynamical properties of the molecule. However, there is an upper limit on the molecular weight of molecules that can be studied by NMR (currently in the range of 60,000 Da), whereas in principle there is no limit on the molecular weights of molecules that can be studied by X-ray crystallography, provided they can be crystallized.

Although only X-crystallography and NMR allow the structure of the entire molecule to be defined at atomic resolution, several other approaches provide atomic resolution information about specific elements of the structure. *Electron paramagnetic resonance spectroscopy*—often abbreviated EPR—is discussed in Chap. 6. EPR spectroscopy depends upon the magnetic dipole moments of metal ions or free radicals that, like nuclear spins, align with magnetic fields and change their alignment when a microwave pulse is applied. EPR is often used to obtain atomic-level information about metal centers in macromolecules, many of which are proteins—for example, chlorophyll and iron containing proteins.

### 1.3.3 Mass Spectrometry

*Mass spectrometry*, discussed in Chap. 7, is a versatile and evolving technology that has several different modes and many different applications in both the physical and life sciences. In all mass spectrometry experiments, molecules are broken into charged fragments, either by collisions with other molecules or by fast moving electrons. The fragments are then separated and analyzed. Mass spectrometry is routinely used to sequence biopolymers and is also a powerful tool for analyzing interactions between molecules and structural fluctuations within molecules.

### 1.3.4 Single Molecule Methods

As powerful as they are, all of the methods discussed above have a major limitation; they monitor only the average structures and behaviors of an enormous ensemble of molecules whose behavior is not synchronized, as discussed above. As a result, many

details of molecular structure and behavior that are essential to function cannot be explored. However, advances in recent decades have led to the development of five methods, briefly described below, for studying the structure and behavior of single molecules. These single molecule methods make use of different physical phenomena, provide different kinds of information, and have different advantages and disadvantages. They are discussed in detail in Chap. 8 and in another volume in this series [13].

Three of these methods provide structural information that cannot be obtained by X-ray crystallography or NMR. *Cryo-electron microscopy* (electron microscopy carried out at very low temperatures) is often used to provide medium resolution structures of very large molecular assemblies that cannot be crystallized and studied by X-ray crystallography. It has the advantage over classical electron microscopy in not requiring fixatives that may distort the structure. *Atomic Force Microscopy* (AFM) uses a microprobe to map the surfaces of individual molecules deposited on a solid support—for example DNA molecules on a glass plate. *Total Internal Reflectance Microscopy* (TIRFM), like AFM, is designed to study the structure of surfaces. However, the two microscopes are based on different physical principles and are used to study different phenomena. In TIRFM experiments, the sample is deposited at a glass–liquid interface and the fluorescence generated by light totally internally reflected from the glass–liquid interface is monitored. This method has been particularly useful in studying the structure of cell membranes in living cells.

The two remaining single molecule methods provide dynamic, as well as structural information. *Molecular tweezers* measure the response of a molecule to an imposed force, either optical or magnetic, and provide information about molecular elasticity and internal motions. This method has been particularly important in studying molecular motors; for example, muscle and cellular actin and myosin (discussed in Chap. 11). *Single Molecule Fluorescence Resonance Energy Transfer* (FRET) makes use of the strategy described above for molecular rulers—monitoring the transfer of light energy absorbed by one chromophore at a given wavelength to a second chromophore which fluoresces at a longer wavelength. However, while molecular rulers were originally used to study the average distance between the two chromophores in an ensemble of molecules, FRET can now be carried out with single molecules, rather than an ensemble, enabling the dynamics of single molecules to be studied over time.

## 1.4 The Role of Computation in Biophysics

The high resolution methods of molecular biophysics generate huge amounts of raw data that can only be collected, stored, analyzed, and interpreted with the aid of powerful computers and a variety of sophisticated mathematical tools. Advances in mathematical theory and computing power have driven many advances in molecular biophysics. Examples include the introduction of computer graphics to model molecular structure in the 1970s and the use of molecular dynamics techniques to simulate intramolecular motion in the 1980s. The need for computational power has increased dramatically with the advent of genomic and proteomic approaches, bioinformatics,

and powerful new cell imaging methods. These advances have opened new frontiers in terms of understanding how macromolecules function in a cellular context. A full treatment of computational biophysics is beyond the scope of this volume.

## 1.5 Biological Macromolecules as Molecular Machines

One of the most fundamental and important insights to emerge from more than a half century of biophysical investigations of biological macromolecules is that they are the molecular machines that perform the essential functions of the cell. Like the machines developed during the industrial revolution, they consume energy, have moving parts, and do work. Like the engines and motors of everyday life, the levels of their activity can be regulated to adjust to changes in external conditions. In addition, like the machines of the twenty-first century, biomolecular machines store information that directs and modulates their function; however, these molecular machines have dimensions of nanometers rather than meters.

Most of the molecular machines of the cell are proteins that perform a multitude of functions. Some are motor proteins that have the ability to move along fibers and surfaces within the cell. For example, the movement of myosin molecules along an actin fiber drives muscle contraction (Fig. 1.7). Most non-muscle cells also contain other forms of actin and myosin, as well as other motor proteins that are responsible for cell motility, the mechanics of cell division, and transport of materials within cells; for example, dynein and kinesin.

Enzymes, the proteins that catalyze chemical reactions in cells, are another class of molecular machines, analogous to the machines that convert raw materials into products in industrial factories. Every cell has hundreds of different enzymes that act on different substrates to convert them into products needed by the cell. Among

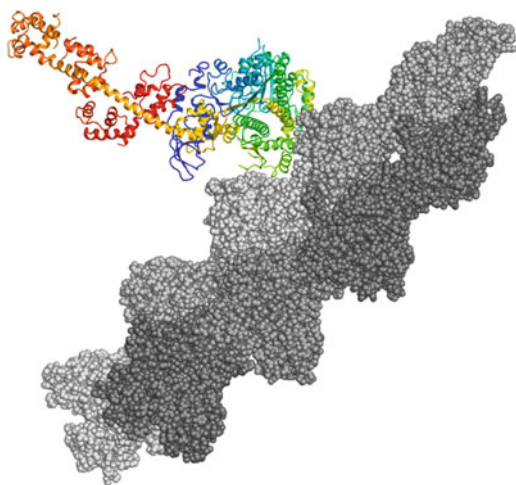


**Fig. 1.7** Molecular model of subfragment-1 of chicken myosin docked onto actin (PDB accession number 2MYS for myosin)

the best known and most widely studied are the enzymes of metabolism, which break the molecules in food into smaller molecules, many of which are used to synthesize molecules needed by the organism. Other enzymes are involved in cell signaling pathways, cell death, and the synthesis of macromolecules such as DNA, RNA, and proteins.

Both the plasma membrane that encloses the cell and intracellular membranes that form compartments within cells have membrane proteins imbedded in or attached to them. These membrane proteins perform several different functions. Some control movement of ions or molecules across membranes. Others are components of signaling pathways that transfer signals from one side of the membrane to the other and modulate the action of signaling pathways within cells. Some cell membrane enzymes are part of the immune system, and act to neutralize toxic molecules or pathogens.

While proteins frequently function autonomously as molecular machines, they also assemble with other types of macromolecules to form more complex structures with novel properties. One of the best-known examples is the ribosome, a huge molecular machine that plays a central role in the synthesis of proteins from an m-RNA template. Eukaryotic ribosomes have a diameter of 25–30 nm and are made up of two subunits. Each ribosome consists of one RNA molecule per subunit and a total of more than 80 protein molecules. Ribosome structure and function are discussed in detail in another volume in this series [14].

To understand how biomacromolecules function as molecular machines, their structures, interactions with other molecules, and physical properties must be explored and defined experimentally, using the experimental approaches described above and others that lie outside the scope of this volume. This information enables the development of models that predict how the molecule functions. The fidelity with which the model predicts the behavior of the molecule can then be evaluated in additional experiments. When sufficient information is available, a quantitative model with defined physical and chemical parameters can be constructed and used to simulate mathematically the properties of the actual biomacromolecule. A successful mathematical model must not only account for the original experimental data but must also provide predictions that can be validated. The predictive quality is a measure of the fundamental understanding embodied in the model. The physical chemical concepts that enable quantitative models to be developed are reviewed in Chap. 2. Repeated cycles of experiment, modeling, and testing the model against additional experiments, often by multiple teams of investigators, lead to an increasingly detailed and accurate understanding of how the molecular machine functions in the cell.

## 1.6 Examples of Molecular Machines

To illustrate these principles, Chaps. 9–11 focus on three families of biomolecular machines and demonstrate how results obtained with several different research approaches have led to our current understanding of how these biomolecular

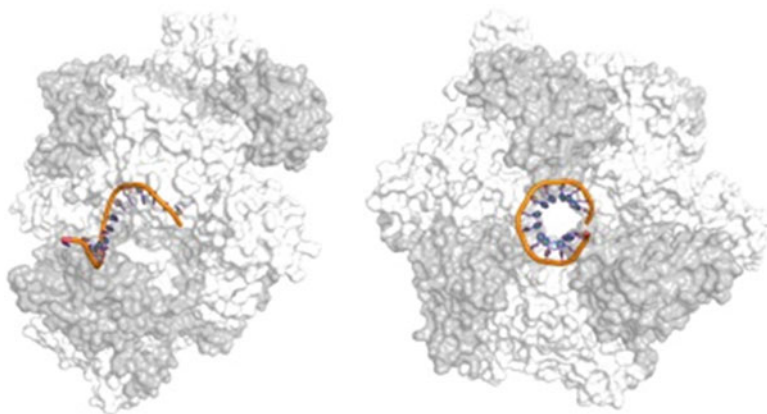


**Fig. 1.8** Structure of DnaB hexameric helicase (shown in *gray*) with a bound molecule of single stranded DNA, shown in *brown* (PDB accession number 4ESV)

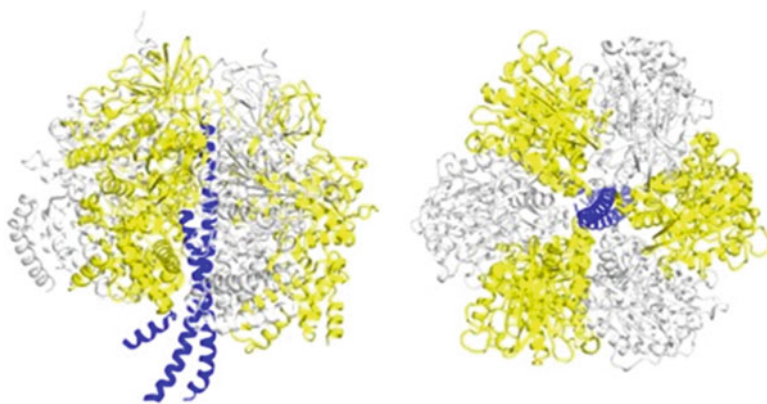


**Fig. 1.9** Structure of bovine mitochondrial F1 ATPase. The native protein is a hexamer with six subunits, three of which are shown in *gray* and three in *yellow*. The *blue* helices correspond to part of the  $\gamma$ -subunit which connects the membrane embedded rotary motor to the catalytic core (PDB accession number 1E1R)

machines work and their roles in disease. Chapter 9 focuses on enzymes called helicases that partially unwind the double helix of the DNA molecule, enabling it to replicate. Figure 1.8 shows an example. Membrane bound transport ATPases, enzymes that use the chemical energy made available by hydrolyzing ATP (adenosine triphosphate) to transport molecules across cell membranes, are the subject of Chap. 10. Figure 1.9 shows the structure of one membrane ATPase. Chapter 11 discusses the myosin family of motor proteins that are involved in both muscle contraction and cellular motility and transport. The structure of part of the actin-myosin complex is shown in Fig. 1.7.

## 1.7 Future Prospects

While biophysics has had a brilliant past, the future appears even brighter. Investments in instrument development have streamlined experiments, making them much less arduous, and the development of molecular biology and recombinant DNA technology has greatly increased the ease with which molecules can be identified, isolated, and manipulated. Genomics has opened a path for studying not only the major macromolecules of the cell but also molecules never before identified. Proteomics provides new approaches for studying the macromolecular interactions that are so critical to cell function, and the development of cell biology enables the linkages between molecular and cellular structure and function to be explored in detail. Ever increasing computational power supports all of these endeavors and enables the development of massive databases that can be mined for new correlations and insights.

As our understanding has grown, the relevance and importance of biophysics to solving real world problems in medicine, industry, agriculture, forensics, and many other fields have become increasingly clear. In addition to pushing back frontiers within the discipline, there is now a pressing need and responsibility to communicate the contributions that biophysics can make not only to other areas of science but also to other fields. Fortunately, the clarity of the fundamental principles that have emerged as a result of decades of dedicated work by highly trained physical scientists and mathematicians makes them highly accessible to professionals in other fields and to the general public.

*Future Prospects*, the final chapter of this volume (Chap. 12), focuses on the future of molecular biophysics and three of the major technologies discussed in this volume—X-ray diffraction and neutron scattering, mass spectrometry, and protein therapeutics. As always, new and advancing technologies and the development of new interdisciplinary foci are among the major drivers. The chapter concludes with a discussion of the opportunities and challenges of translating biophysical discoveries into solutions to real-world problems, as illustrated in drug and pharmaceutical development.

## 1.8 Other Volumes in this Series

This book is a foundational volume for the series *Biophysics for the Life Sciences*, published by Springer, a series intended for students and professionals from other fields. Other volumes in this series deal with specific areas of molecular or cellular biophysics. Volumes in print focus on translational control of gene expression, single molecule studies of proteins, therapeutic protein development, and RNA folding [13–16].



## References

1. Olby RC (1974) The path to the double helix: the discovery of DNA. Dover, Mineola, NY
2. Goodsell DS (2009) The machinery of life. Springer, New York
3. Cantor CR, Schimmel PR (1980) Biophysical chemistry. Part I. The conformation of biological macromolecules. Freeman, San Francisco
4. Cantor CR, Schimmel PR (1980) Biophysical chemistry. Part II. Techniques for the study of biological macromolecules. Freeman, San Francisco
5. Cantor CR, Schimmel PR (1980) Biophysical chemistry. Part III. The behavior of biological macromolecules. Freeman, San Francisco
6. Perutz MF (1964) X-ray analysis of hemoglobin. Nobel lectures, chemistry 1942–1962. Elsevier, Amsterdam
7. Huxley AF (1972) The quantitative analysis of excitation and conduction in nerve. Nobel lectures, physiology and medicine, 1963–1970. Elsevier, Amsterdam
8. Watson JD (1964) The involvement of RNA in the synthesis of proteins. Nobel lectures, physiology and medicine, 1942–1962. Elsevier, Amsterdam
9. Crick F (1964) On the genetic code. Nobel lectures, physiology and medicine, 1942–1962. Elsevier, Amsterdam
10. Hodgkin DC (1972) The X-ray analysis of complicated molecules. Nobel Lectures, chemistry, 1963–1970. Elsevier, Amsterdam
11. Delbrück M (1970) A physicist's renewed look at biology, twenty years later. Nobel lectures, physiology and medicine, 1963–1970. Elsevier, Amsterdam
12. Wuthrich K (2003) NMR studies of structure and function of biological molecules. In: Frangsmyr T (ed) The Nobel prizes, 2002. Nobel Foundation, Stockholm
13. Oberhauser AF (2012) Single-molecular studies of proteins. Springer, New York
14. Dinman JD (2012) Biophysical approaches to translational control of gene expression. Springer, New York
15. Narhi LO (2013) Biophysics for therapeutic protein development. Springer, New York
16. Russell R (2013) Biophysics of RNA folding. Springer, New York



## Chapter 2

# Structural, Physical, and Chemical Principles

Norma M. Allewell, Linda O. Narhi, and Ivan Rayment

**Abstract** This chapter introduces the structural, physical, and chemical foundations of molecular biophysics. The section on structure describes the major molecular components of the cell (water, metabolites, and macromolecules) and discusses the three-dimensional macromolecular structure, folding, and assembly of macromolecules. The section on molecular thermodynamics and kinetics includes energies, equilibria, and rate constants. These concepts are applied to protein folding and aggregation and illustrated with examples relevant to the development of protein pharmaceuticals. The chapter closes with a discussion of the interplay between molecular structure and energetics and biological function.

**Keywords** Biomolecular structure • Protein folding • Macromolecular assembly • Thermodynamics • Energetics • Kinetics • Free energy • Equilibrium constant • Rate constant • Protein aggregation • Protein pharmaceuticals • Structure-function relationships

Investigating and understanding biophysical properties and structural problems in the life sciences requires integrating structural, physical, and chemical information. In acquiring and interpreting this information, biophysicists rely heavily on the theoretical frameworks and experimental approaches of physics and chemistry.

---

N.M. Allewell (✉)  
Department of Cell Biology and Molecular Genetics,  
University of Maryland, College Park, MD 20852, USA  
e-mail: allewell@umd.edu

L.O. Narhi  
Research and Development, Amgen, Inc., One Amgen Center Drive,  
Thousand Oaks, CA 91320, USA  
e-mail: lnarhi@amgen.com

I. Rayment  
Department of Biochemistry, University of Wisconsin-Madison,  
433 Babcock Drive, Madison, WI 53706-1544, USA

Fully exploring the breadth and depth of these disciplines is far beyond the scope of this volume. The goal of this chapter is simply to provide nonspecialists with the core vocabulary and background in principles and concepts that will be needed to utilize subsequent chapters in this volume and other volumes in this series. Some widely used textbooks are listed in the references [1–6].

## 2.1 The Molecules of the Cell

The major chemical components of the cell fall into a few major categories—water ions, metabolites, lipids, and macromolecules. Most molecules in the cell contain at most six different atoms, including carbon, hydrogen, nitrogen, oxygen, phosphorus, and sulfur. *Water* is the most abundant molecule in the cell and exerts profound effects on the physicochemical properties and biological function of all other molecules. The most abundant *ions* in a typical mammalian cell, listed in order of their intracellular concentrations are potassium, bicarbonate, sodium, and chloride, followed by magnesium and calcium, which, although present in much lower concentrations, have critically important biological functions. *Metabolites* are small molecules, produced by partially digesting foods. Depending upon the needs of the cell, these are either broken down completely to produce carbon dioxide, water, and ammonia, or used to synthesize other small molecules or macromolecules that are required by the organism. One class of metabolites that is particularly important is *lipids*, oily molecules of intermediate size, generally in the range of a few hundred Daltons, that have several roles in the cell. Two of the most important roles are serving as major components of all cell membranes and as major reserves of chemical energy.

The macromolecules of the cell, with molecular weights in the range of several thousand to millions of Daltons are formed by linking together small molecules, often called building blocks, to form polymers. *Proteins* are formed by linking twenty different amino acids together in a sequence specific to a given protein to form a linear polymer (Fig. 2.1). The corresponding building blocks for the nucleic acids, *DNA* (*deoxyribonucleic acid*) and *RNA* (*ribonucleic acid*), are four nucleotides, each of which has three elements—an aromatic base, characteristic of a given nucleotide; a sugar; and a phosphate group (Fig. 2.2). Three of the four bases in RNA and DNA are identical, while the fourth differs by one functional group. The sugar groups in DNA and RNA also differ by one functional group. Although these chemical differences between DNA and RNA may appear minor, they have major biological consequences. *Polysaccharides* are formed by linking together many sugar groups from a defined set of molecules, often in a branched structure (Fig. 2.3). Glycogen, a polymer of glucose, is, together with the lipids mentioned above, a major reservoir of chemical energy in the cell.

Different kinds of molecules also combine to increase the chemical and biological repertoire of the cell. For example, *glycolipids* have both lipid and sugar components, while *glycoproteins* have both protein and sugar components (Fig. 2.4).

**Fig. 2.1** Proteins are linear condensation polymers of amino acids. The amino acids are connected by amide linkages or “peptide bonds.” The structure and function of the protein is governed by the sequence of amino acids in the polypeptide chain

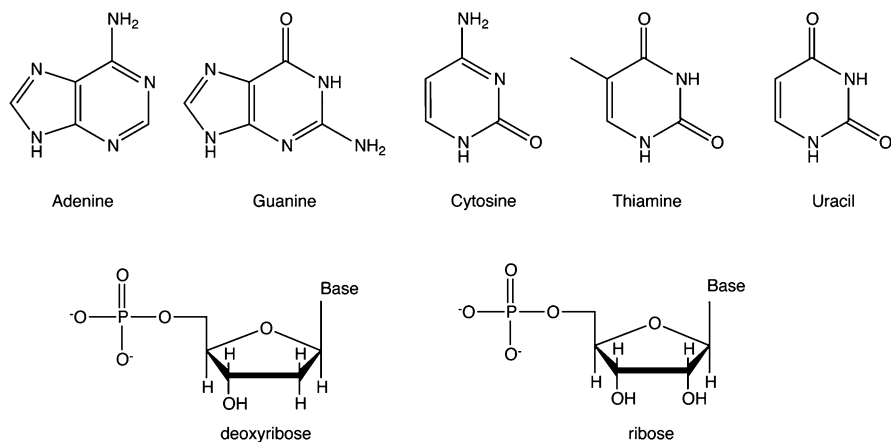
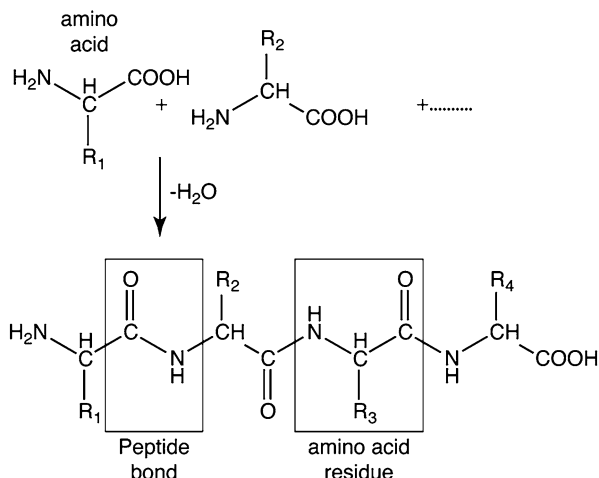


**Fig. 2.2** Building blocks of DNA and RNA. DNA and RNA both utilize four bases to convey genetic information. Three of these are in common, but differ in the incorporation of thiamine in DNA and uracil into RNA. In addition, the sugar in DNA is deoxyribose, while the sugar in RNA is ribose

## 2.2 The Importance of Three-Dimensional Structure

While the chemical properties of small molecules can be inferred from their covalent chemical structure alone, the physical, chemical, and biological properties of biological macromolecules depend not only on their covalent chemical structure but also on the three-dimensional shape (conformation) that they assume within the cell. The double helical structure of DNA, first proposed by Watson and Crick, is an outstanding example (Fig. 2.5). As many readers will be aware, the double helix consists of two DNA

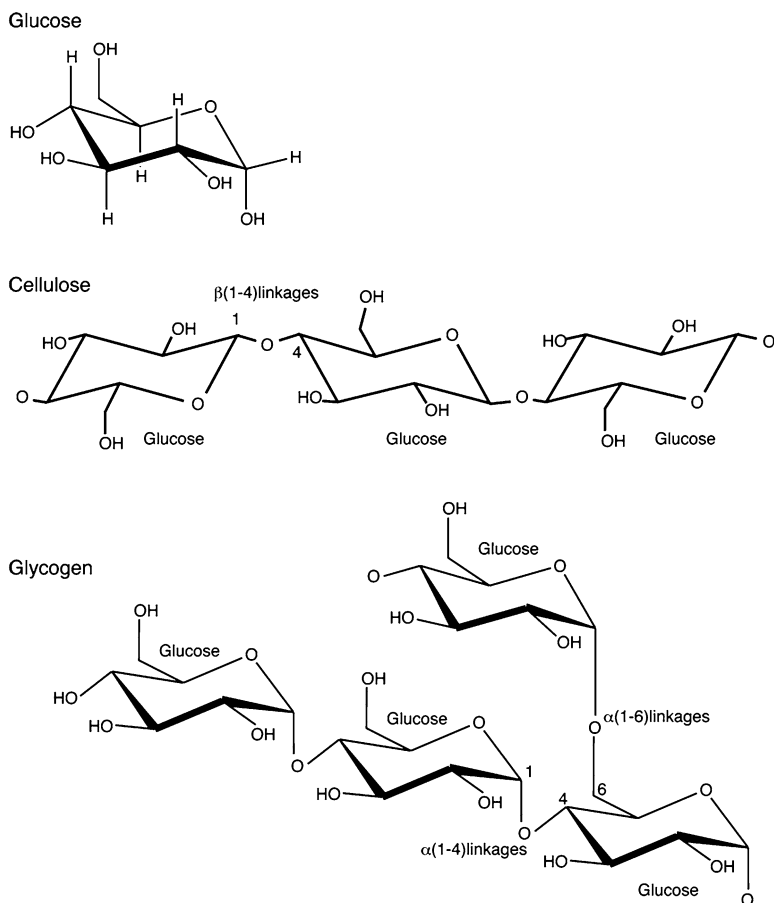


**Fig. 2.3** Carbohydrates are the most abundant macromolecules in the biosphere. These form the basis for polysaccharides which consist of polymers of sugar moieties. An immense variety of building blocks are available that lead to linear or branched chains

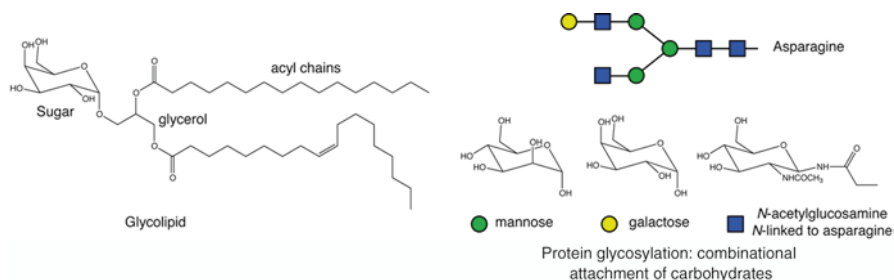


**Fig. 2.4** Complex biological molecules are constructed from small building blocks. Carbohydrates, lipids, and proteins are frequently combined to create larger macromolecules. This combinatorial approach dramatically increases the biological functions that can be accomplished with a small number of chemical templates. Glycolipids are key components of membranes whereas glycosylation of proteins creates a population of proteins with differing characteristics

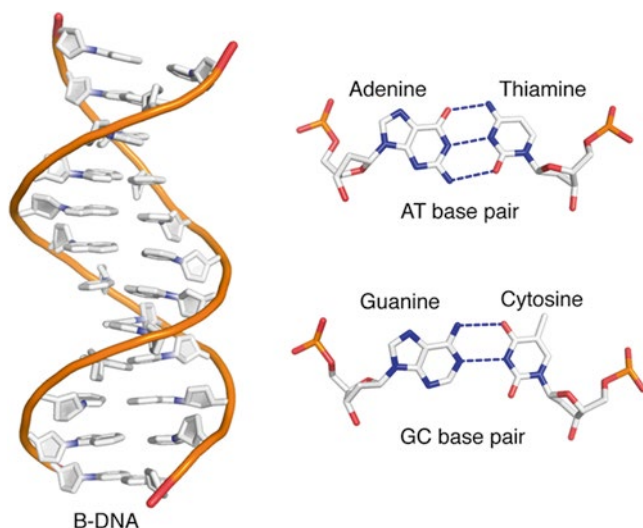


**Fig. 2.5** Three-dimensional structure of DNA. B-DNA forms a double helix whose conformation is dictated in part by hydrogen bonds between complementary pairs of bases (RCSB accession number 1D29)

molecules, held together by noncovalent interactions. This structure is integral to the transmission of genetic information within cells and to the next generation.

Most proteins have complex three-dimensional structures that form as a result of the folding of the chain of linked amino acids in the protein. The way in which the protein folds is determined by noncovalent interactions between the chemical groups in the protein including the peptide backbone and the side chains of the amino acids, as well as by the interaction of the protein with molecules and ions in the environment. The folded protein has a unique structure resulting in specific surface properties that enable the protein to recognize and interact selectively with specific molecules within the cell (Fig. 2.6). Examples include the interactions of enzymes with substrates, actin with myosin, and antibodies with antigens.

The three-dimensional structures of RNA share similarities with both DNA and proteins. In contrast to DNA, most RNA molecules are single stranded. However, turns or hairpin bends in the polynucleotide strand enable short double helical segments to form, similar to those found in DNA (Fig. 2.5). In addition, other bends result in the overall structure of the molecule being fairly compact, as most protein molecules are. The three-dimensional structures of RNA molecules sometimes enable them to bind cognate molecules selectively and specifically and to catalyze chemical reactions, just as proteins do.

The three-dimensional structures of the other macromolecules of the cell tend to be less well defined than those of the proteins and nucleic acids, because molecular recognition is not one of their major functions. For example, glycogen exists in disordered granules in cells and fats exist as lipid droplets. On the other hand, their characteristic chemical features enable them to be recognized by the proteins with which they interact.

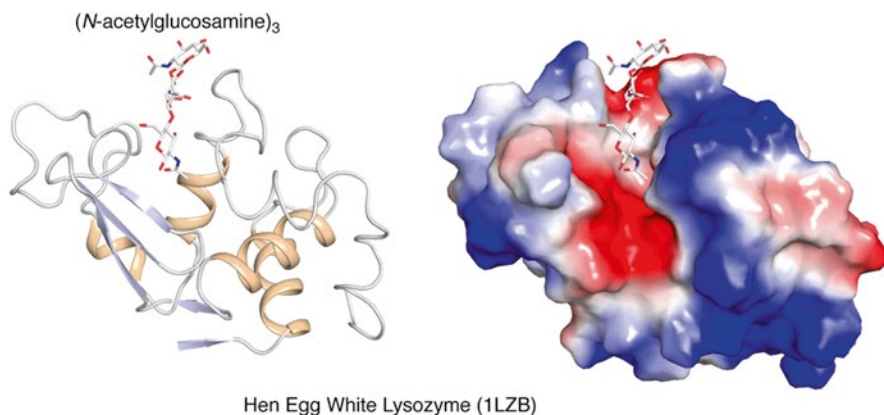


**Fig. 2.6** Proteins adopt structures that are complementary to their ligands. To a first approximation most proteins adopt a unique fold that is essential for function. Furthermore, all proteins have a function and hence interact with some other component of the biological milieu. In this case the binding site and the ligand exhibit complementarity as seen here for the binding of (N-acetylglucosamine)<sub>3</sub> to hen egg white lysozyme (RCSB accession number 1LZB). The cartoon ribbon representation (*left*) reveals the path of the polypeptide chain and major secondary structural features that define the fold. The electrostatic surface (*right*) shows the magnitude and nature of the active site cleft. Positive and negative potential are depicted in blue and red respectively

The structures of macromolecules are not rigid, and cannot be defined by a single set of coordinates, because the forces that shape the three-dimensional structures are weak. The flexibility of biological molecules is essential to their biological function for two reasons. First, it enables the molecules to function as macromolecular machines, and, secondly, it enables the molecules and hence the cell and the organism to respond to their environment. The degree of flexibility spans a wide range, depending on the number and configuration of the intra- and intermolecular interactions that maintain the structure, as well as external conditions. In conditions similar to those that exist in the cell, most DNA and protein molecules are quite stable, completely unwinding or unfolding in solution only when the temperature is raised or chemicals that disrupt the native structure are introduced. At the same time, because the intramolecular forces are weak, macromolecular structures are in constant motion. Generally these rapid structural fluctuations are integrally related to function. The frequency and scale of the fluctuations span a wide range, with the structure of RNA generally being more fluid than that of double-stranded DNA and proteins.

## 2.3 Macromolecular Folding and Assembly

Biological macromolecules have a remarkable ability to self-assemble. The same forces that drive individual macromolecules to assume their three-dimensional structures also allow macromolecules to assemble into larger structures. For example,

proteins interact with DNA to form chromatin and with RNA to form ribosomes. Lipids assemble into bilayers studded with membrane proteins in the cell membrane and in the intracellular membranes that form the boundaries of cellular organelles such as mitochondria. Proteins assemble with other proteins to form multisubunit enzymes, the cytoskeleton of the cell, muscle fibers, virus capsules, and many other specialized structures.

To understand the forces that drive both the folding and assembly of macromolecules, we need to delve a little deeper into the chemical structures of their macromolecular components. The kinds of noncovalent interactions that can occur are limited in number because most biological molecules contain only six elements: carbon, hydrogen, nitrogen, oxygen, sulphur, and phosphorus. *Hydrogen bonds* form when two electronegative atoms (N or O) interact with each other by sharing a single hydrogen atom. As an example, hydrogen bonds between complementary bases link the two strands of the DNA double helix. *Hydrophobic interactions* form when nonpolar groups, made up solely of carbon and hydrogen atoms, cluster to shield themselves from water, in the same way that oil forms droplets in water. *Ionic bonds* involve interactions between oppositely charged groups—for example, negatively charged phosphate groups and positively charged amino groups. *Stacking interactions* occur between aromatic rings—for example, between the bases of nucleic acids.

When individual macromolecules fold or macromolecules assemble to form a larger structure, they do so in a way that maximizes these interactions. For example, the double helical structure of DNA maximizes the number of hydrogen bonds and stacking interactions that form, as shown in Fig. 2.5. Similarly, the helices and pleated sheets of proteins are rich in hydrogen bonds, while hydrophobic groups tend to cluster in the interior of proteins where they are shielded from water. When charged groups occur in the interior of proteins, groups with opposite charges are almost always paired in ionic bonds (salt bridges).

The surfaces that come together when macromolecules assemble together to form larger structures tend to have complementary charged or nonpolar surfaces. Thus a positively charged region on one surface will be matched by a negatively charged region on the opposing surface, while nonpolar, hydrophobic regions will be positioned so that they come together when the two surfaces meet.

The weak forces that hold macromolecular assemblies together allow some to act as molecular switches that change the way they assemble when the external environment changes. Since structure is so tightly coupled to function, any change in structure will most likely also result in a change in function that enables the organism to respond to change in its external environment. One of the first molecular switches to be discovered was hemoglobin, the protein that binds oxygen in the lung and releases it in the tissues. In the high oxygen environment of the lungs, the four subunits of hemoglobin assemble in one mode that binds oxygen strongly. In the low oxygen environment of the tissues, the subunits assemble in a different mode that binds oxygen weakly, allowing it to be released into the tissues. Molecular switches are now recognized to be ubiquitous and to play major roles in both health and disease.

## 2.4 Thermodynamic and Kinetic Principles

Knowing the structure of a macromolecule is only the first step in understanding the physical basis of its function. Advancing to the next level requires defining the cellular processes in which the macromolecule participates in chemical terms. This includes not only identifying all of the reactants, intermediates, and products but also defining the thermodynamic and kinetic features of each step of the process, that is, the differences in energy between reactants and products (thermodynamics) and the rates of both the forward and reverse reactions (kinetics). When these quantities are defined, the amounts of reactant and product that will be present under different conditions and the overall rate at which reactant will be converted to product under different conditions can be predicted.

### 2.4.1 *Energies, Equilibrium Constants, and Rates*

Since molecular biophysics emphasizes reactions carried out in solution, generally at constant temperature and pressure, the three thermodynamic parameters of greatest interest are often the Gibbs free energy (named after the great nineteenth century mathematician and physical chemist Willard Gibbs), enthalpy, and entropy.

When a chemical reaction occurs, the heat released or absorbed corresponds to the difference in the enthalpy of products and reactants. The difference in the degree of disorder of products and reactants corresponds to the change in the entropy of the reaction. The change in Gibbs free energy ( $\Delta G$ ) in the reaction is related to the changes in enthalpy ( $\Delta H$ ) and entropy ( $\Delta S$ ) as described by the following equation:

$$\Delta G = \Delta H - T\Delta S \quad (2.1)$$

The sign of the change in the free energy of a reaction indicates whether a reaction is spontaneous or occurs only with the input of external energy. A negative change in free energy corresponds to a spontaneous reaction that does not need to be driven by the input of energy. Conversely a reaction with a positive change in free energy will not occur without the input of energy.

The sign of the enthalpy change indicates whether heat is released or absorbed in a reaction. A negative change in enthalpy indicates that the reaction results in the release of heat. As the equation indicates, a negative change in enthalpy contributes to a more negative free energy, and thus makes the reaction more favorable.

A negative change in entropy indicates that the products are more ordered than the reactants, and also results in a more positive change in free energy. Thus any increases in order make a reaction less favorable.

Many chemical reactions are readily reversible, with reactants and products coexisting. The ratio of the concentration of product to reactant defines the equilibrium



constant ( $K$ ). In the simplest case, in which  $A$  is the reactant and  $B$  is the product, the equilibrium constant is defined as the ratio of the molar concentrations of  $[B]$  and  $[A]$ :

$$K = [B] / [A] \quad (2.2)$$

Equilibrium constants and standard free energies are related by the equation:

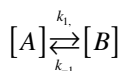
$$\Delta G^\circ = -R T \ln K \quad (2.3)$$

where  $\Delta G^\circ$  is the change in free energy change at standard concentrations of reactants and products and standard temperature and pressure.  $R$  is a universal constant called the gas constant because it is defined by the equation for ideal gases ( $PV = nRT$ , where  $n$  is the number of moles,  $T$  is the ideal gas temperature in degrees Kelvin (K),  $V$  is volume of the system, and  $P$  is pressure.  $R$  has a value of  $8.31 \text{ J K}^{-1} \text{ mol}^{-1}$ . For biochemical reactions in solution, the standard concentration is typically 1 M, the standard temperature is 298.15 K, the standard pressure is 1 atm and  $R$  has a value of  $1.98 \times 10^{-3} \text{ kcal-K}^{-1}\text{-M}^{-1}$ ).

The free energy change at other concentrations of reactants and products is given by

$$\Delta G = \Delta G^\circ + R T \ln [B] / [A] \quad (2.4)$$

While thermodynamics defines the energies of the components of a biophysical system, rate constants define the rates of the reactions that link them. For example, two rate constants define the rates of the interconversion of  $A$  and  $B$ :  $k_1$ , the rate constant for converting  $A$  to  $B$ , and  $k_{-1}$ , the rate constant for converting  $B$  to  $A$ .



In the absence of  $B$ , the rate at which  $A$  is converted to  $B$  is given by  $k_1[A]$ , and, in the absence of  $A$ , the rate at which  $B$  is converted to  $A$  is given by  $k_{-1}[B]$ .

When  $A$  and  $B$  coexist, the net rate of change of  $[A]$  will be the difference in the rates of the forward and reverse reactions:

$$d[A]/dt = k_{-1}[B] - k_1[A]$$

When  $d[A]/dt = 0$ ,  $k_{-1}[B] = k_1[A]$

However,  $K$ , the equilibrium constant for the reaction, equals  $[B]/[A]$  and

$$K = k_1 / k_{-1} \quad (2.5)$$

## 2.5 An Example: The Energetics of Protein Folding

To illustrate how thermodynamics and kinetics are helpful in understanding the behavior of macromolecules, let's consider the case of protein folding. This simplest reaction pathway can be represented as



where U is the unfolded protein, F is the folded protein,  $k_1$  is the rate constant for folding, and  $k_{-1}$  is the rate constant for unfolding. The rate constants for this equation have units of seconds<sup>-1</sup>.

The equilibrium constant for the folding reaction will be given by

$$K = [F]/[U]$$

where the fraction indicates the ratio of the concentrations of folded and unfolded protein. Often this ratio can be determined experimentally.

Let's suppose that this ratio is 1,000, meaning that there are 1,000 times as many folded protein molecules in solution under the conditions of the experiment as there are unfolded molecules. Then the value of the equilibrium constant under those conditions will also be 1,000.

With the equilibrium constant known, the value of the change in free energy can also be calculated, using the following values:

$$R = 1.98 \times 10^{-3} \text{ kcal-K}^{-1}\text{-M}^{-1}$$

$$T = 298 \text{ K}$$

$$K = 1,000; \log K = 3; \ln K = 2.303(\log K)$$

$$\Delta G^\circ = -RT \ln K = -(1.98 \times 10^{-3})(298)(2.303)(3) = -4.08 \text{ kcal/M}$$

As expected, the change in the standard free energy is negative, since protein folding is a spontaneous reaction.

With the standard free energy change known, the next question is, what are the values for the changes in enthalpy and entropy? Does folding a protein consume or release heat? Does the system (which includes both the protein and the solvent in which it is dissolved) become more ordered or disordered when the protein folds?

Enthalpy changes for temperature-induced chemical changes can often be determined experimentally using instruments called scanning calorimeters, in which a solution is gradually heated, and the heat lost or gained by thermally induced processes is measured. Calorimeters can readily be used to study protein unfolding, since most proteins unfold when they are heated. Let's suppose that the molar enthalpy change for unfolding the protein is 10 kcal mol<sup>-1</sup>, indicating that 10 kcal of heat are absorbed when one mole of protein unfolds. Since folding is the reverse of unfolding, 10 kcal of heat will be released when one mole of protein folds, and the enthalpy change for folding is -10 kcal mol<sup>-1</sup>.

Next, let's insert the values for the standard free energy and enthalpy into the Gibbs equation:

$$\begin{aligned}\Delta G^\circ &= \Delta H^\circ - T\Delta S^\circ \\ \Delta S^\circ &= -1/T(\Delta G^\circ - \Delta H^\circ) \\ &= -1/298(-4.08 + 10) \\ &= -19.9 \text{ cal/K/M}\end{aligned}$$

The negative entropy change indicates that, in this case, protein folding results in a decrease in the entropy of the system (protein plus solution), or an increase in order. The most likely contributors to the increase in order are the folding of the protein and the ordering of solvent and ions around the folded protein.

## 2.6 Applications to Protein Pharmaceuticals

The above reaction and equations represent the simplest case of protein folding, and the most common situation *in vivo*. Kinetic and thermodynamic theory encompasses many other scenarios and many other questions. As the complexity of the reaction under study increases, the equations become more complex. However, the principles remain the same. More complex situations involving not only equilibrium unfolding but also the formation of intermediate states and irreversible interactions also occur, both *in vivo* and *in vitro*. A common unfolding intermediate that is seen for many proteins under mildly denaturing conditions is the “molten globule” state, first defined by Wada and Ohgushi in 1983 [7]. A molten globule is defined as an intermediate state, which has lost its native tertiary structure and has increased surface hydrophobicity, but retains native secondary structure. Depending on the conditions involved formation of this intermediate can be a reversible reaction with the native structure, or can irreversibly associate resulting in larger aggregated species.

Another example of complex protein folding, unfolding, and self-association reactions occurring *in vivo* is the formation of amyloid fibers. This irreversible structure is characterized by formation of intermolecular beta sheet secondary structure (regardless of the native secondary structure of the monomer), and is defined by the  $\sim 4.7 \text{ \AA}$  and  $10 \text{ \AA}$  signatures of the cross- $\beta$  diffraction pattern. Amyloid formation is initiated by a nucleation event believed to start with an unfolded intermediate species that results in a lag phase prior to formation of the protein aggregate [8]. This phenomenon was originally thought to occur for only a few specific proteins, but it has subsequently been demonstrated to occur for most proteins under some conditions. Amyloid formation has been implicated in several diseases, including Alzheimer's disease.

The unfolding of multi-domain proteins, such as the monoclonal antibodies commonly used as protein therapeutics, is even more complex, with multiple intermediates and irreversible aggregated species. The formation of intermediates is usually

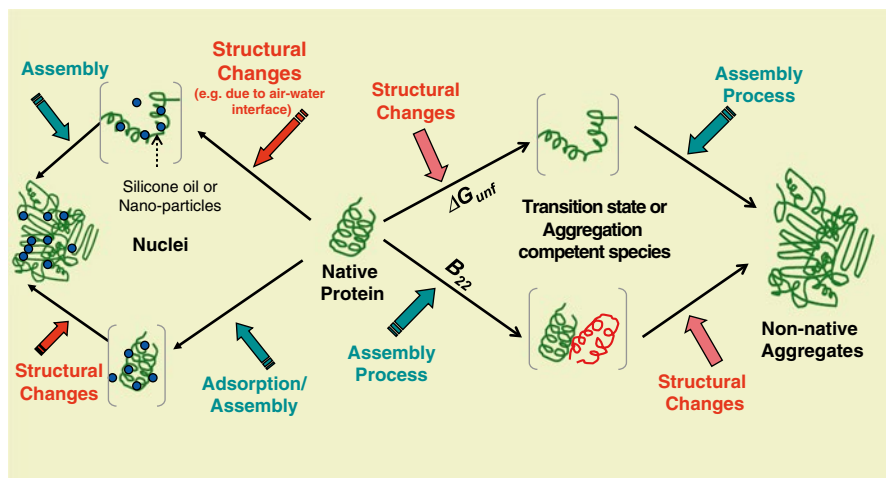


**Fig. 2.7** Schematic of potential protein unfolding reactions

reversible, followed by irreversible self-association. Unfolding of a multi-domain protein can be cooperative with all domains unfolding together, in which case it can be modeled as a single domain. Alternatively each domain can unfold independently, resulting in multiple intermediates with different combinations of folded and unfolded domains. The multistep unfolding and aggregation of proteins is a process that can be described by the Lumry–Eyring framework [9, 10]. Each state of the protein has a different free energy of activation, and also a different colloidal stability (propensity for self-association under the conditions of the surrounding solution or environment). The rate limiting step is the one with the highest energy barrier.

As proteins are isolated and studied, the types of solution conditions they are exposed to also increases, many of which can have deleterious effects on the native state of the protein. The complexity of protein folding, unfolding, and self-association is indicated in Fig. 2.7, a result of the work described in [9, 10] and others.

Subsequent chapters will further develop these principles and provide examples of their application to specific biophysical phenomena.

## 2.7 Relating Structure, Energetics, and Function

Over millions of years, the structures of biological macromolecules have evolved to optimize their ability to perform their specific biological functions. As a result, the structure, physical properties, and function of biological macromolecules are intimately related, and understanding these relationships is key to understanding how biological macromolecules function as molecular machines in living cells.

As we explore these relationships, the kinds of questions molecular biophysicists ask include the following:

1. What is the relationship between the chemical structure of the macromolecule and its three-dimensional structure?
2. What does the three-dimensional structure of the macromolecule predict about its physical and chemical properties and its biological function?
3. How many different three-dimensional structures (states) can the macromolecule assume?
4. What is the equilibrium distribution of the macromolecule between these different states? Which, if any, represent irreversible reactions?
5. How rapidly do the states interconvert?
6. How does this distribution of states change when the macromolecule interacts with other molecules or ions in the cell?
7. How do the functional properties of the different states differ?
8. How do these differences enable the macromolecule to perform its biological function? When do they impede this function?

In answering these questions, contemporary biophysics makes use of a set of sophisticated physical and chemical experimental approaches and instrumentation that was introduced in Chap. 1, and will be the subject of several subsequent chapters. These studies are enriched immensely when the powerful approaches of molecular biology are used to examine the effects of systematically modifying chemical structure, and computational tools are used for in depth analysis and modeling. Chapters 9–11 will illustrate how physical, chemical, molecular biological, and computational tools can be used in combination to develop a complete understanding of three very different biomolecular machines in terms of their structure, energetics, and function. The three classes of molecules to be examined are helicases, proteins that unwrap the DNA double helix to allow DNA replication; membrane ATPases, which convert electrical energy into chemical energy; and a molecular motor (myosin). Despite the very different biological functions of these molecules, all three operate according to very similar physicochemical principles, and hence the strategies used to investigate their functional mechanisms follow a common biophysical theme.

## References

1. Atkins P, de Paula J (2009) Atkins' Physical Chemistry, 9th edn. Oxford University Press, Oxford
2. Berg JM, Tymoczko JL, Stryer L (2006) Biochemistry, 6th edn. WH Freeman and Company, New York
3. Nelson DL, Cox MM (2008) Lehninger's Principles of Biochemistry, 5th edn. WH Freeman and Company, New York
4. Alberts B, Johnson A, Lewis J, Raff M, Roberts K, Walker P (2008) Molecular Biology of the Cell. Garland Science, Taylor and Francis, New York

5. McQuarrie DA, Smith JD (1997) *Physical Chemistry: a Molecular Approach*. University Science, Sausalito, CA
6. Atkins P, de Paula J (2005) *Physical Chemistry for the Life Sciences*. WH Freeman and Company, New York
7. Ohgushi M, Wada A (1983) "Molten-globule state": a compact form of globular proteins with mobile side-chains. *FEBS Lett* 164:21–24
8. Goda S, Takano K, Yamagata Y, Nagata R, Akutsu H, Maki S, Namba K, Yutani K (2000) Amyloid protofilament formation of hen egg lysozyme in highly concentrated ethanol solution. *Protein Sci* 9:369–375
9. Chi EY, Krishnan S, Kendrick BS, Chang BS, Carpenter JF, Randolph TW (2003) Physical stability of proteins in aqueous solution: mechanism and driving forces in nonnative protein aggregation. *Pharm Res* 20:1325–1336
10. Chi EY, Krishnan S, Kendrick BS, Chang BS, Carpenter JF, Randolph TW (2003) Roles of conformational stability and colloidal stability in the aggregation of human granulocyte colony stimulation factor. *Protein Sci* 12:903–913

**Part I**  
**The Experimental Tools of Molecular**  
**Biophysics**

# Chapter 3

## Optical Spectroscopic Methods for the Analysis of Biological Macromolecules

Linda O. Narhi, Cynthia H. Li, Ranjini Ramachander,  
Juraj Svitel, and Yijia Jiang

**Abstract** The interaction of light with macromolecules is used in multiple different ways in the life sciences. These interactions can be exploited to learn about the structure, stability, and function of proteins and nucleic acids. In this chapter we cover analysis of macromolecules, primarily at equilibrium, by UV absorbance, circular dichroism, fluorescence, Fourier transform infrared, and Raman spectroscopies, and light scattering. A brief description of the underlying theory and some examples of applications are provided for each technique.

**Keywords** UV absorbance • Fluorescence spectroscopy • Fourier transform infrared (FTIR) spectroscopy • Raman spectroscopy • Circular dichroism • Light scattering • Spectroscopy

### 3.1 Introduction

#### 3.1.1 *Physical Basis of Light Spectroscopy*

The explanation of the nature of light and its interactions with molecules is one of the basic tenets of quantum mechanics. Light is a rapidly oscillating electromagnetic field that can be described as either a wave or a photon. In-depth discussion of the fundamentals of the interactions of light with molecules and applications of these phenomena for the analysis of macromolecules are included in most physics and

---

L.O. Narhi (✉) • C.H. Li • R. Ramachander • J. Svitel • Y. Jiang  
Research and Development, Amgen, Inc., One Amgen Center Drive,  
Thousand Oaks, CA 91320, USA  
e-mail: lnarhi@amgen.com



chemistry textbooks, and in multiple reviews on the subject [1–6]. A brief summary of some of the basic concepts is presented here so that the principles of the different types of analyses discussed in this chapter can be understood. The energy of the photon can be related to frequency or wavelength by the equation below:

$$E = h\nu = \frac{hc}{\lambda} \quad (3.1)$$

This relation between the energy and frequency is called the Planck relation where  $h$  is the Planck constant ( $6.626 \times 10^{-34}$  J/s),  $c$  is the speed of light ( $3 \times 10^8$  m/s),  $\nu$  is the frequency ( $\text{s}^{-1}$ ), and  $\lambda$  is the wavelength (m).

The formation of a molecular bond results in a bonding orbital, which is the lowest energy orbital and is occupied by spin paired electrons, and the formation of an antibonding orbital that is at a higher energy and usually empty. If the molecule has an odd number of electrons one of these electrons will occupy the nonbonding orbital. At any given time the majority of molecules in a population exist in the ground state, with the electrons in the bonding orbital. When the energy of an incident photon is equivalent to the energy gap between the bonding and antibonding electron orbitals, the electron absorbs this photon and temporarily makes the transition from the lower to the higher energy state (from the HOMO or highest occupied molecular orbital to the LUMO, or lowest unoccupied molecular orbital), and the molecule as a whole undergoes a transition from the ground state to the excited state. The electron then returns to the HOMO, and the molecule returns to the ground state, by one of many different pathways including the generation of heat, solvent quenching, and vibrational modes (non-radiative processes), or fluorescence or phosphorescence (radiative processes). These transitions can be further described by the spin state of the electrons; the singlet state where they have opposite spins so that the total spin state of the molecule is 0, or the triplet state, where the electrons have parallel spins and the total spin state is 1. This is often visualized in a Jablonski diagram, shown in Fig. 3.1 [7], and is discussed briefly in Chap. 2 in this volume as well as numerous textbooks [4, 8]. The smaller the energy gap between the HOMO and the LUMO, the longer the wavelength of light that is absorbed. In macromolecules (and other organic molecules) the transition from the  $\pi$  to the  $\pi^*$  orbital is the transition that contributes most to absorbance, though  $\sigma$  to  $\sigma^*$  transitions can occur as well, with the  $n$  to  $\pi^*$  occurring much less frequently. Within each electronic state there are also vibrational and rotational states of the molecule. The distribution of the energy of the electronic excited states across these molecular states results in broadening of the peak of light absorbed from a line spectrum to a distribution, quite often a Lorentzian distribution, as the electrons transition to the LUMO. The peak of emitted light as the molecule returns to the ground state is also broadened.

The excited states of molecules usually have a greater charge separation than the ground state, resulting in a larger dipole moment. Interactions between the molecular dipole and the solvent or surrounding environment can increase or decrease the energy needed to transfer from the HOMO to LUMO states, affecting the

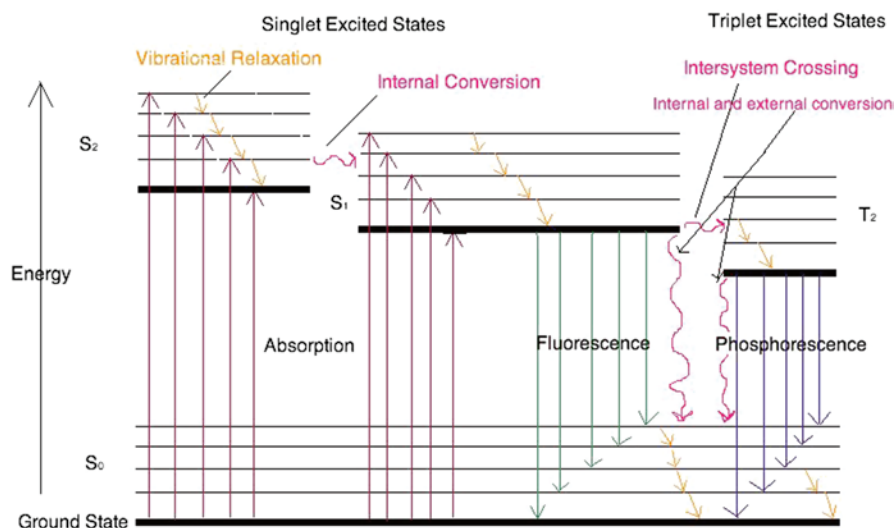


**Fig. 3.1** Jablonski diagram showing absorbance of energy with excitation of the electron to an excited state, with multiple pathways for dissipating the energy as the electron returns to the ground state, including non-radiative (internal conversion, vibrational relaxation) and radiative (fluorescence and phosphorescence) processes (from [1])

wavelength of light absorbed by the molecule as it makes this transition. The intensity of the absorbance is also dependent on the number of double bonds that are connected, or conjugated. This conjugation of the carbon bonds lowers the energy of the  $\pi$  to  $\pi^*$  transition, resulting in an increase in both the wavelength and intensity of the absorbance peak.

The transition dipole moment is the electric dipole moment vector associated with the interaction of the molecule with the electromagnetic radiation (light) to which it is exposed. The direction of the vector determines the polarization of the transition, a principle that is very useful in fluorescence spectroscopy.

In biological macromolecules the chromophores which have absorbance in the visible region are cofactors, including metal containing molecules such as the hemes in cytochromes and hemoglobin, or those like the flavins and carotenoids which have extended  $\pi$  conjugation. The proteins and nucleic acids themselves intrinsically absorb in the ultraviolet and infrared regions of the spectrum. The transition between ground and excited states for these chromophores is influenced by the environment in which they are located, making them sensitive probes of the conformation and stability of the molecules. In proteins, the peptide backbone, the aromatic amino acid side chains, and the disulfide bonds are the primary chromophores (Table 3.1). The peptide backbone absorbs between 170 and 230 nm [8, 9] as a result of two major electron transitions, the  $\pi$  to  $\pi^*$  transition at 190–195 nm and the weaker  $n$  to  $\pi^*$  transition occurring at 210–220 nm. The  $\pi$  to  $\pi^*$  transition of the side chains of the aromatic amino acids is responsible for the signal in the near-UV

**Table 3.1** Electronic transitions of amino acids that contribute to absorbance spectra [8, 9]

Chromophore	Transitions	Wavelengths (nm)
Peptide backbone	$\pi$ to $\pi^*$	190–195
	$n$ to $\pi^*$	210–220
Tryptophan (Trp)	$\pi$ to $\pi^*$	280
		292
Tyrosine (Tyr)	$\pi$ to $\pi^*$	276
		Shoulders at 267, 280
Phenylalanine (Phe)	$\pi$ to $\pi^*$	Triplet, 250–270
Cysteine (Cys)	$\pi$ to $\pi^*$	<260
Histidine (His)	$n$ to $\pi^*$	<260
Nucleic acids	$\pi$ to $\pi^*$	260 (240–275)

region. The indole side chain of tryptophan (Trp) has the most intense signal with a maximum around 280 nm, and a weaker transition at 292 nm. Tyrosine (Tyr) has a weaker absorbance, with its strongest transition occurring at 276 nm and weaker transitions appearing as shoulders at 267 and 280 nm in the absorbance spectrum. Phenylalanine (Phe) has an even weaker absorbance which occurs as a triplet at 250–270 nm due to its vibrational states. Disulfide bonds absorb weakly from about 260 nm and below, and the His imidazole ring has a weak  $n$  to  $\pi^*$  transition which can also contribute to the intensity of the protein absorbance in this part of the spectrum. Ribonucleic acid (RNA) and deoxyribonucleic acid (DNA) both absorb light between 240 and 275 nm, with the maximum around 260 nm originating from the  $\pi$  to  $\pi^*$  transition of the pyrimidine and purine ring systems.

The electron transitions resulting from interactions between these chromophores and light of specific wavelengths are the basis for all the spectroscopic techniques discussed in this chapter. Both the absorbance of light and the emitted energy as the macromolecule relaxes back to its energetic ground state are exploited by different technologies, providing information on the conformation of proteins and nucleic acids and the folding and unfolding of these important molecules.

### 3.1.2 Theory of Light Scattering

Most of the events described above depend on the absorbance of light as the electrons are excited and then return to their ground state. Another important, more complex interaction between light waves and macromolecules results in light scattering. Light scattering occurs when electrons are perturbed by the same frequency as the electric field of the incident wave, creating an induced dipole moment, which becomes a source of electromagnetic radiation emitted at the same frequency but different angle than that of the incident light, or the light passing through the solution without molecular interactions [10–12].

When the size of the scattering molecule is significantly smaller than the wavelength of the incident light, Rayleigh scattering occurs. The scattering for a single, small isotropic particle can be expressed as

$$\frac{I}{I_0} = \frac{8\pi^4 \alpha^2}{r^2 \lambda^4} (1 + \cos^2 \theta) \quad (3.2)$$

where  $I$  is the intensity of scattered light,  $I_0$  is the intensity of the original incident light,  $\alpha$  is the molecular polarizability,  $r$  is the distance between the point of observation and the position of the scattering particle,  $\lambda$  is the wavelength of the incident light, and  $\theta$  is the angle between the incident beam and the direction of observation. In reality, proteins are studied in solutions. For a dilute ideal solution containing concentration  $c$  of particles of molecular weight  $M$ , scattering can be quantified by the Raleigh ratio ( $R_\theta$ ). The advantage of the Rayleigh ratio is that it is independent of the incident light intensity and the distance to the scattered light detector (i.e., independent of  $I_0$  and  $r$ ).

$$R_\theta = KCM \quad (3.3)$$

where  $K$  is a constant

$$K = \frac{2\pi^2 n_0^2 (dn/dc)^2}{\lambda_0^4 N} \quad (3.4)$$

and  $N$  is Avogadro's number,  $n_0$  is the refractive index of the solvent, and  $dn/dc$  is the refractive index increment and  $\lambda_0$  is the wavelength of the light in vacuo. Note that if the refractive indexes of the solvent and of the polymer are equivalent then  $dn/dc$  will be zero and there will be no polarizability and therefore no scattered light. The constant  $K$  depends only on the solvent properties, on  $\lambda$ , and on  $\theta$ .  $K$  is therefore a system constant that is independent of the concentration of the solution and the molecular weight of the polymer.  $M$  is the weight-averaged molecular weight of the solute present; all of the self-associated states present contribute to this based on their fraction of the total weight. This can be used to determine the molecular weight of the protein being analyzed as a function of any solution condition, as long as the protein concentration is low enough to prevent intermolecular interactions between the individual molecules that would affect the scattering behavior.

## 3.2 Chapter Overview

In this chapter we will discuss absorbance, circular dichroism, fluorescence, Fourier transform infrared (FTIR), Raman spectroscopy, and light scattering. Each section begins with a brief overview of supporting theory for the methodology, followed by examples of its application to the analysis of macromolecules, primarily under equilibrium conditions.

### 3.2.1 Light Absorbance

#### 3.2.1.1 Introduction

Most biological macromolecules have absorbance in the ultraviolet region (as described in the introduction to this chapter); several good reviews in this area have been published recently [13, 14], and this is the subject of several text books [1–6].

A typical absorbance spectrum is taken by shining light of varying wavelengths through a solution and recording the intensity of the energy passing through the sample (transmission) or the amount of light blocked by the samples (absorbance) as a function of wavelength. An example of the absorbance spectrum of a protein is shown in Fig. 3.2. According to the Lambert–Beer law (also Beer’s law), the amount of light absorbed is directly proportional to the concentration of the chromophores present:

$$A = \log_{10} \left( \frac{I}{I_0} \right) = kl = \epsilon cl \quad (3.5)$$

where  $A$  is the measured absorbance,  $I_0$  is the original intensity of the light,  $I$  is the intensity of the light transmitted through the sample, and  $l$  is the distance in cm the light travels through the material (i.e., path length);  $k$  is the absorption coefficient, which is determined for each molecule based on Beer’s law;  $c$  is the molar concentration of the chromophores, and  $\epsilon$  (L/mol cm) is the absorbance of a 1 M solution (molar absorptivity) of the chromophores, often referred to as the extinction coefficient.

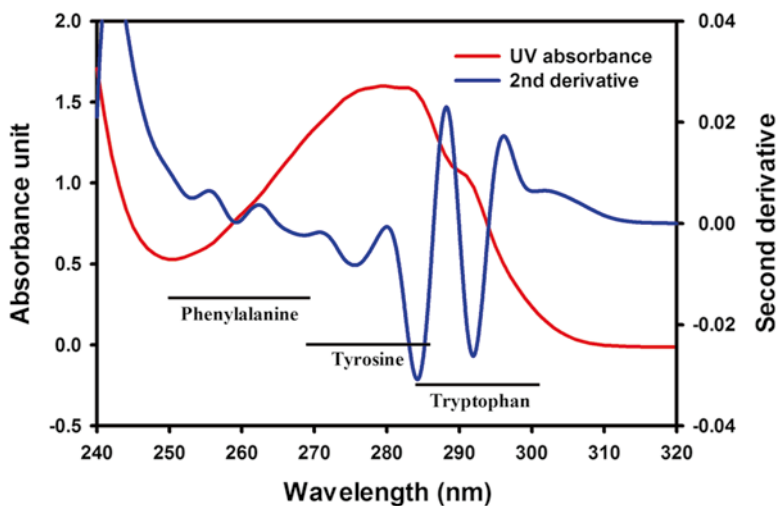


**Fig. 3.2** Absorbance spectrum of anti-streptavidin (*red*) and second derivative spectrum (*blue*). Provided by Feng He, Amgen, Inc.

However, the actual extinction coefficient as well as the wavelength of maximum absorbance can be affected by both the environment of the chromophores in the protein, including interactions with the surrounding amino acid residues, the secondary structure, and the amount of buffer exposure. The buffer solutions commonly used for protein separation and characterization often have absorption that overlaps with that of the peptide bond in the far UV region. Because of these background interferences, absorbance at these wavelengths is often used for detection of proteins in solutions, but not for other analyses. More sensitive analysis of the secondary structure based on peptide bond configurations and interactions with light of these wavelengths can be obtained with FTIR, circular dichroism, and Raman spectroscopies.

The absorbance spectra of proteins between 250 and 300 nm are the result of a combination of the absorbance spectra of the aromatic amino acid chromophores and disulfide bonds, as described in the introduction. The wavelength maximum of the spectrum depends on the specific amino acid composition and the local environment of individual chromophores, which is dependent on the tertiary structure of the protein [8, 15]. Modifications of any of these residues including oxidation and ionization can affect the absorbance spectra of these chromophores, and can also change the local environment in that region of the protein. In addition to the intrinsic chromophores of proteins, cofactors can also contribute to the absorbance of light and often have characteristic spectra in the visible range of the radiative spectrum.

Nucleic acids also absorb in the UV region [8, 15]; the intensity of absorbance is affected by the protonation states of the aromatic rings and by the hydrophobic environment created by the stacking of the bases. Single stranded nucleic acids have much stronger absorbance than double stranded molecules. This feature can be used to monitor the “melting” or loss of structure of the nucleic acids.

The dependence of absorbance on path length allows this type of measurement to be applied across a broad concentration range for all chromophores by the use of cuvettes with the appropriate path length, or the recently developed variable path length spectrometers. As long as the absorbance is greater than the buffer blank and the signal to noise ratio is acceptable, the path length can be increased to allow measurement of low concentration solutions, or decreased to allow analysis of very high concentration solutions.

### 3.2.1.2 Applications

#### Detection

UV absorbance can be used as a sensitive detection method for many macromolecules. For proteins it is commonly used for detecting which fractions contain protein during column chromatography, and it is also used to detect the presence of nucleic acids. The wavelength used can depend on the sensitivity and specificity needed for the specific analysis. Detection in the far UV region is the most sensitive due to the large number of peptide bond chromophores in the molecule and also has the most

interference from buffer components, etc. Monitoring of proteins at 280 nm is used if there is a sufficient amount of protein present to be detected. Though the absorbance of proteins is less at 280 than at 214 nm, there is significantly less interference from buffer components, allowing for better differentiation of the protein signal from the baseline. Interference from particles, including protein aggregates, as well as DNA or RNA if they are present, can confound the quantitation, and a calibration curve is often used here as well. Absorbance in the UV will give relative amounts of protein, for instance in different fractions eluting from a column.

## Concentration Determination

The absorbance of light is one of the oldest, and yet still most reliable, methods for determining the concentration of chromophores. The accuracy of the measurement depends on the accuracy of the extinction coefficient determination. For proteins the theoretical extinction coefficient at 280 nm in water can be determined based on the molar absorptivity ( $\epsilon$ ) of the aromatic amino acids and disulfide bonds present in the molecule, as described by Pace et al. [16]. The extinction coefficient at this wavelength for the free amino acid in water is 5,540 for tryptophan, 1,480 for tyrosine, 125 for the disulfide bonds, and 10 for phenylalanine. The theoretical extinction coefficient of a protein is derived by summing the contributions of all of these species in the protein and dividing the result by the molecular weight of the entire protein. This is usually very close to the actual extinction coefficient of the protein in the aqueous buffers most commonly used for protein characterization. Once the molar extinction coefficient of a protein solution has been determined the concentration of any sample can be measured using the Lambert–Beer law as described above (3.5). This method allows not only quantitation of individual protein samples but also the comparison of properties such as enzyme activity or binding affinity across different protein species or solutions, since they can be normalized for protein concentration.

The absorbance spectra of proteins and nucleic acids overlap between 250 and 280 nm, with proteins having a much weaker molar absorptivity (smaller extinction coefficient). If a sample contains both protein and nucleic acids it is necessary to correct for the DNA contribution before calculating the protein concentration. The reverse is not true because of the much smaller protein contribution at 260 nm relative to that of the nucleic acids. The Warburg–Christian equation uses the ratio of the absorbance at 260 to that at 280 nm ( $A_{260}/A_{280}$ ) to correct for the contribution of nucleic acid to the protein absorbance spectrum in this wavelength range. In water this ratio is 0.57 for pure protein solutions, about 1.8 for pure DNA, and about 2 for solutions of pure RNA [14].

The determination of concentration from the absorbance of a protein at 280 nm can be complicated by light scattering from larger protein aggregates or particles. As described previously, the wavelength maximum for light scattering is dependent on the size of the species responsible for the scattering, extending well into the visible region; however, there can also be contributions as low as 280 nm from this

phenomenon. Consequently light scattering causes an apparent increase in the absorbance of the solution due to the interference of the transmission of light through the sample, and can result in overestimating the concentration of the protein. Removal of the scattering species prior to analysis should be attempted whenever possible. When light scattering is known to occur and the species responsible cannot be removed, approximate corrections can sometimes be made [7].

## Structural Determination

As shown in Fig. 3.2, the typical UV absorbance spectrum of a protein is a broad peak that is made up of the contributions of all of the Trp and Tyr residues as well as the disulfide bonds and Phe in a molecule. It is possible to differentiate these individual contributions with a combination of sensitive detectors and sophisticated lineshape data analysis [7, 17–19]. The underlying contributions of the individual aromatic amino acids can often be differentiated by taking the second or fourth derivative of the absorption spectrum (Fig. 3.2). Changes in the environment of the chromophores can be detected with this type of spectroscopy [20, 21]. While not as sensitive as the near-UV circular dichroism (CD) or fluorescence spectroscopies which are described in the following sections, the relative ease of acquiring this type of data makes it an important component in the toolbox of biophysical techniques for analysis of macromolecules, especially proteins.

## Other Chromophores

The presence of important biological cofactors can also be exploited with light spectroscopy, in this case often in the visible range [21, 22]. Absorbance of the metal containing chromophores is sensitive to the oxidation state of the metal as well as its local environment within the protein, and therefore these characteristics can be used to probe both the ionization state of the metal and the binding affinity to the protein [21, 22]. For instance, for the cytochrome family and other heme-containing molecules, absorbance results in Soret bands, an intense peak in the blue wavelength region of the visible spectrum, that is sensitive to the spin state of the electrons and the oxidation state of the metal. Thus visible spectra have been employed to follow electron flow during the catalytic cycle of cytochrome P-450's and the other cytochromes important for energy metabolism, as well as other metallo-proteins. Changes in the spin state or absorbance of the metal can be used to study the kinetics of ligand binding. The interaction of the flavin, retinoid, and other  $\pi$ -conjugated cofactors with visible light is often necessary for the biological function of the protein as well; for example the initial steps of photosynthesis, or the functioning of the cones and rods in our eyes. The cofactor nicotinamide adenine dinucleotide (NAD) shows a substantial increase in absorbance at 340 nm when converted to NADH, an important reaction in energy metabolism. This change in absorbance intensity has been used extensively in enzyme kinetic studies of systems that utilize this cofactor.



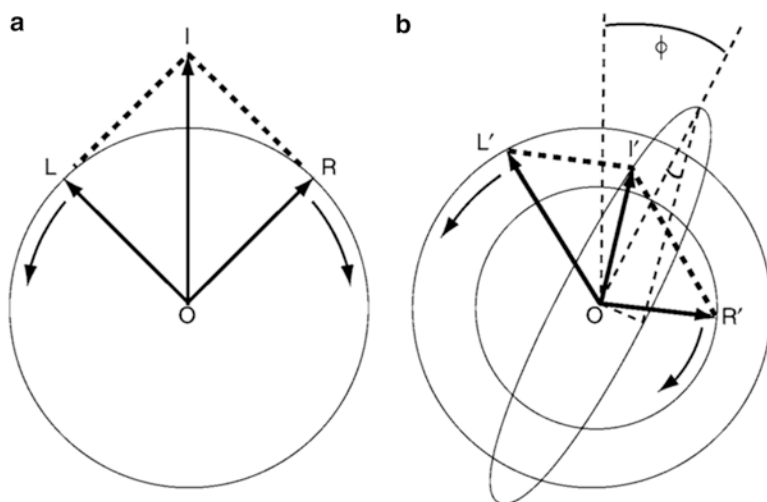


**Fig. 3.3** The relation of ellipticity to the differential absorption of circularly polarized radiation. (a) Plane-polarized radiation is made up of left- and right-handed circularly polarized components, (b) interaction of the radiation with a chiral chromophore leads to unequal absorption

### 3.2.1.3 Concluding Comments on UV Absorbance

UV absorbance is perhaps the simplest interaction of macromolecules with light. It can be used for detection of proteins and DNA, and for determination of the concentration of these species. Changes in the conformation of proteins can be followed by taking the derivatives of the absorbance spectra. It can also be a very useful tool for studying systems with cofactors such as the heme group or conjugated  $\pi$  systems like the flavins. While it is a relatively low resolution technique, its wide availability and ease of use make it perhaps the most frequently used of the light spectroscopy methodologies.

## 3.2.2 Circular Dichroism

### 3.2.2.1 Theory

As described above, the local environment can affect the interactions of chromophores with light, and this can be used to analyze the structure of macromolecules. Circular dichroism (CD), the differential absorption of the left- and right-circularly polarized components of plane-polarized electromagnetic radiation (Fig. 3.3), is frequently used to monitor structural changes.

A CD signal arises when a chromophore is chiral (optically active); a CD spectrum is obtained when circular dichroism is measured as a function of wavelength. Since this methodology is based on absorbance, the chromophores in proteins are

the peptide bonds, aromatic amino acids, disulfide bonds and cofactors discussed in the introduction. Exposure of these chromophores to a chiral field introduces perturbations that increase the optical activity of the molecule. In the far UV region (240–190 nm), the peptide bond absorption can be used to assess the content of regular secondary structural features such as  $\alpha$ -helix and  $\beta$ -sheet. The CD spectrum in the near-UV region (320–260 nm) reflects the environments of the aromatic amino acid side chains and can be used to assess changes in the tertiary structure of the protein. Other nonprotein chromophores such as flavin and heme moieties can give CD signals in the range of 300–700 nm which depend on the environment of the chromophore. DNA in its helical form can also have a CD signal; in this case the signal maximum is around 260 nm.

CD is one of the most sensitive techniques for determining structures and monitoring structural changes of biomolecules, though like all spectroscopic methods it can only determine the average of a molecular population, and cannot provide the high-resolution structural data available from X-ray crystallography or nuclear magnetic resonance (NMR). Because of its convenience and applicability under a wide variety of experimental conditions, CD can be used for many applications, including exploring protein–ligand interactions, assessing conformational changes and studying protein folding. For proteins and peptides, CD data are usually reported in units of mean residue ellipticity (degrees squared  $\times$  centimeters per decimole).

$$[\theta] = \frac{Mr}{10 \times C \times d} \theta_{\text{obs}} \quad (3.6)$$

$[\theta]$ : Mean residue ellipticity (degree  $\text{cm}^2/\text{decimole}$ )

Mr: mean residue weight

C: protein concentration (mg/mL)

d: Path length of the cell (cm)

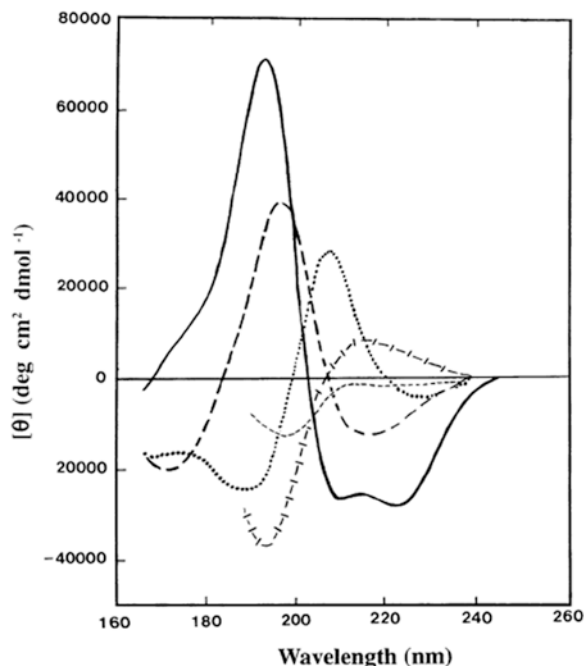
$\theta_{\text{obs}}$ : Ellipticity

### 3.2.2.2 Applications

#### Secondary Structure

In the far UV region (250 nm and below) the CD signal from proteins is the result of multiple electronic transitions arising from energy transfer to all of the peptide bonds. The difference in the hydrogen bonding states of different forms of secondary structure in proteins (e.g.,  $\alpha$ -helix,  $\beta$ -sheet, turn and disordered) results in characteristic CD signals (Fig. 3.4) that can provide information about the amounts and different forms of regular secondary structure [23–32] in the protein under the solution conditions being analyzed. For example,  $\alpha$ -helices have a strong and characteristic CD spectrum with an intense positive band at 192 nm and two negative bands at 208 and 222 nm;  $\beta$ -sheets display a fairly intense positive band at 198 nm and a negative band at 215 nm; turns display a positive band at 205 nm, a very weak negative band at 230 nm and an intense negative band at 195 nm whereas completely

**Fig. 3.4** Far UV CD spectra associated with various types of secondary structure. *Solid line*  $\alpha$ -helix, *long dashed line* antiparallel  $\beta$ -sheet, *dotted line* type I  $\beta$ -turn, *cross dashed line* extended 31-helix or poly (Pro) II helix, *short dashed line* irregular structure. The data are adapted from Kelly et al. [23]



unfolded proteins (random coils) display an intense negative band at 198 nm. In addition, aromatic residues can occasionally contribute to this part of the spectrum; Tyr and Phe can have positive bands near 220 nm, and Trp can also have a negative band at 214 nm. However, in helical proteins these contributions are often masked by the strong negative ellipticity of the alpha-helix. Many additives such as salts and surfactants (excipients) commonly used in protein formulations have absorbance in the region below 200 nm. The increase in the total absorbance of the solution in the presence of excipients leads to a decrease in the signal to noise ratio, and greater experimental variability in this region, making it difficult to detect small differences in the CD signal. When possible spectra should be collected down to 170 nm or below, but in the aqueous buffers most commonly used for DNA and protein solutions the lower limit is usually closer to 200 nm.

There are a number of algorithms that use data from far UV CD spectra to provide an estimation of the secondary structure composition of proteins. Most of these procedures are based on datasets comprised of CD spectra of proteins whose structures have been solved by X-ray crystallography and span the different types of secondary structures [24, 25]. Widely used algorithms include SELCON (self-consistent) [26], VARSLC (variable selection) [27], CDSSTR [28], K2d [29] and CONTIN [30]. An online server DICHROWEB [31, 32] has been developed by the laboratory of Dr. Bonnie Wallace at the University of London, which allows data to be entered and analyzed by various algorithms with a choice of databases to estimate the secondary structure content and the structural family of a protein.

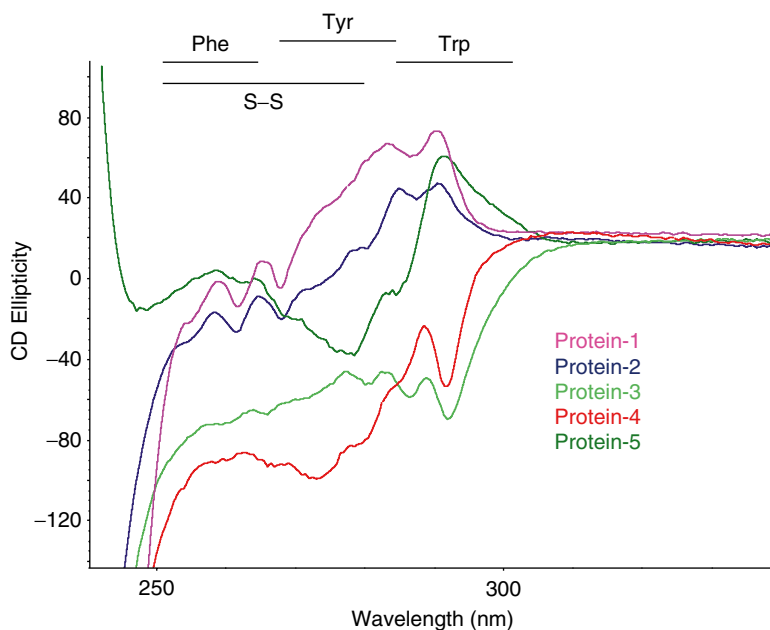


**Fig. 3.5** Near-UV CD spectra of five different proteins

### Tertiary Structure

Proteins also have a CD signal in the 240–340 nm range because of the absorbance of light by the aromatic amino acid side chains and the disulfide bonds in the near-UV region of the spectrum. The intensity and sign (negative or positive) of the CD signal of these residues depends on the asymmetric environment in which they are located, determined by the three-dimensional structure of the protein, and thus providing a fingerprint representative of the tertiary structure of the folded protein [33–36]. Each of the aromatic amino acids has a characteristic CD wavelength profile that corresponds to its absorbance spectrum. Trp has a peak close to 290 nm with fine structure between 285 and 305 nm; Tyr has a peak between 270 and 285 nm, with a maximum at 278 nm and a shoulder at longer wavelengths often obscured by the Trp band; Phe is a triplet between 250 and 265 nm with the strongest peak at 257 nm. Disulfide bonds also absorb in the near-UV region (weak broad absorption bands from 250 to 280 nm), the changes in the dihedral angle of the disulfide bond will result in a change in the intensity of the signal in this region of the spectrum. The actual shape and magnitude of the near-UV CD spectrum of a protein will depend on the protein primary sequence, the number of each type of aromatic amino acids present, their mobility, and the nature of their environment (H-bonding, polarity, and polarizability). Figure 3.5 shows an overlay of near-UV CD spectra of five different proteins. For proteins, the absence of regular structure results in a symmetric environment, and zero CD intensity, while an ordered

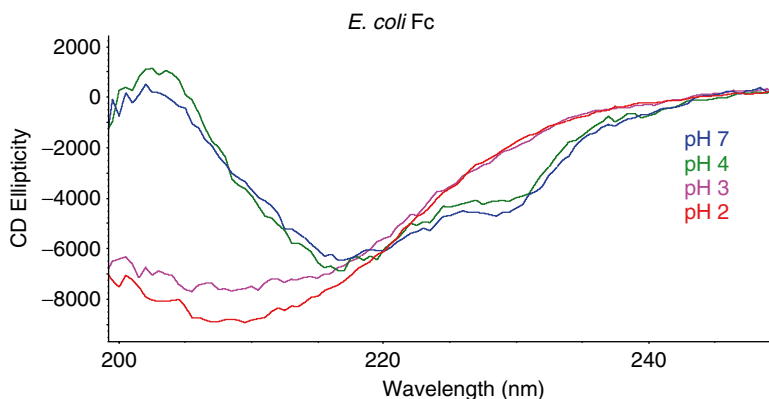


**Fig. 3.6** Far UV CD spectra of the *E. coli*-derived Fc molecules as a function of pH

structure and the resulting local asymmetric environment of the aromatic amino acid residues and disulfide bonds results in a characteristic spectrum. Unlike far-UV CD spectroscopy (170–240 nm), features in the near-UV CD (240–340 nm) spectrum cannot be assigned to any particular three-dimensional structure. Rather, near-UV CD spectra provide information on the nature of the chromophores in the proteins, the interactions of these residues with other amino acids in close proximity, and their interactions with the solvent. This methodology can be used to study unfolding and folding of proteins under specific solution conditions as changes in the spectra reflect changes in the local environment of the chromophores and the degree of solvent exposure, resulting in changes in the “fingerprint.”

### Conformational Changes in Proteins

CD spectra are dependent on the protein conformation, and therefore can be used to monitor changes in the protein structure that are induced by temperature, mutations, pH, denaturants, binding interactions, etc., to follow the kinetics of protein unfolding and to determine the amount and type of secondary structure. As an example, Figs. 3.6 and 3.7 show the far- and near-UV CD spectra, respectively, of the *E. coli*-derived Fc domain as a function of pH (the Fc is the crystallizable fragment of an IgG that contains the CH1 and CH2 constant domains). The data demonstrate that as the pH decreases from pH 7 to pH 2 the far-UV CD spectra of the Fc domain loses the band at 218 nm which is characteristic of  $\beta$ -sheet structure. At the same time the intensity of the near-UV CD signal decreases towards the baseline signal of unfolded protein. The far- and near-UV CD data suggest that as the pH decreases from pH 7 to pH 2, the secondary and tertiary structure of the Fc domain unfold significantly. These data can be used to generate unfolding rates, and identify solution conditions under which the protein unfolds, but cannot provide information on the specific

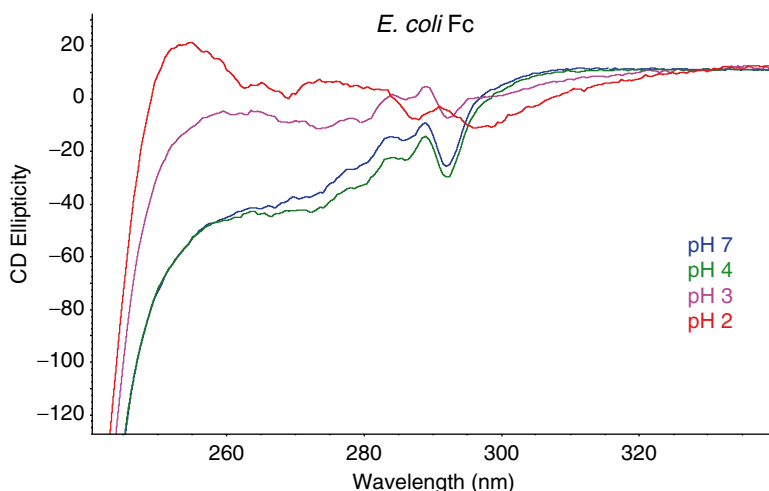


**Fig. 3.7** Near-UV CD spectra of the *E. coli*-derived Fc molecules as a function of pH

region or sequence of the protein involved in the changes being monitored. Mutations or labeling of the protein can be used to provide more information about the primary sequence involved, but this technique can never provide structural information on an atomic level like X-ray crystallography or NMR. Assessing stability to solution conditions is very important as a screening tool during the development of protein therapeutics, and is used to help identify candidates that can survive manufacturing, storage, and delivery conditions.

### DNA Conformation and Conformational Changes

DNA also can adopt different conformations, including the B-family of structures, the A-form, the Z-form, guanine quadruplexes, cytosine quadruplexes, triplexes, and other less-characterized structures. The different forms of DNA give rise to different CD signals [37]. Spectra of the B-DNA forms contain a positive band between 260 and 280 nm and a negative band around 245 nm; the A-DNA form contains a dominant positive band at 260 nm and a negative band at 210 nm; in the Z-DNA form, the base pairs have an opposite orientation with respect to the backbone of the B- and the A-forms, resulting in a spectrum with a negative band at about 290 nm, a positive band around 260 nm and an increasingly negative signal at 205 nm (Fig. 3.8). Therefore CD can be used to study the conformational transitions between different states of DNA, generating a titration curve of changes in DNA structure as a function of various solution conditions. By following the CD titration curve generated, it is possible to distinguish between gradual changes within a single DNA conformation and cooperative isomerization between discrete structural states. This methodology can also be used to follow the kinetics of the appearance of

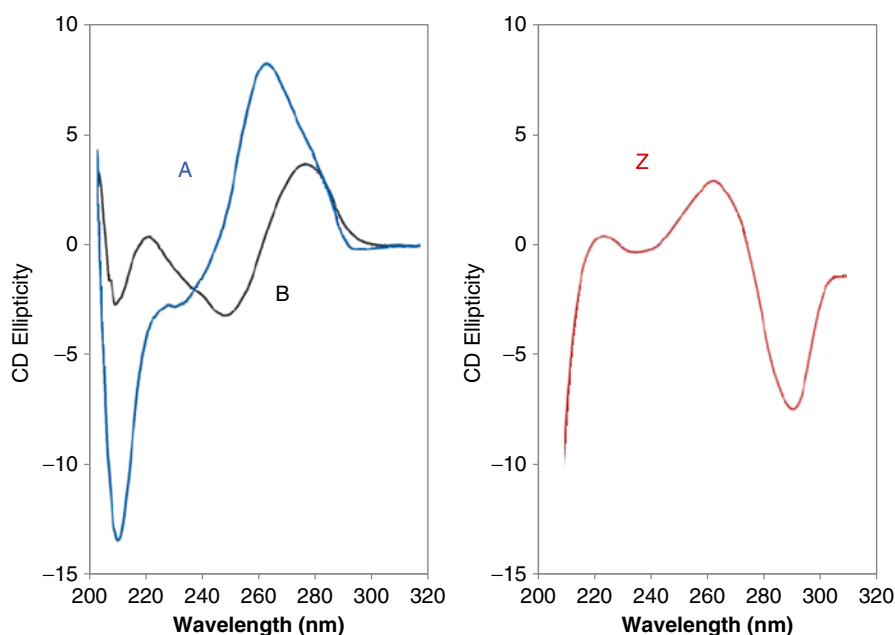


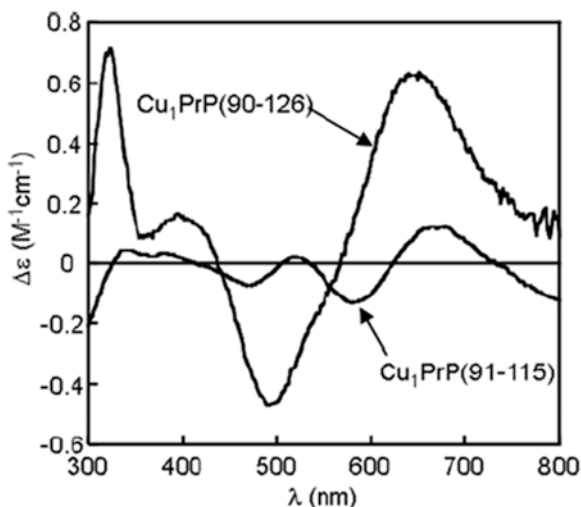
**Fig. 3.8** UV CD spectra of A- and B-forms DNA (*left*) and Z-form DNA (*right*)

particular conformers and to determine their thermodynamic parameters. CD was also used to study DNA and RNA conformations in a receptor-mediated DNA and RNA delivery complex [38]

### Quantitative Comparison of CD Spectrum

Quantitative comparison of CD spectra remains a challenge due to their broad spectral features and the inclusion of positive and negative signals. One method commonly used by researchers in the field is deconvolution of the CD spectra of a protein or DNA to determine contributions of individual structural elements, followed by determination of the percentage of each component in the protein secondary structure or each DNA form. Comparability is then determined by comparing changes in the percentage of each component [28, 39–42]. The accuracy and effectiveness of the deconvolution method is limited due to the overlapping CD signals of the amino acid side chains and conformational features of the different secondary structure elements in a protein, as well as the lack of defined conformational CD features for protein tertiary structure, and the lack of defined characteristic CD features for the various forms of DNA. Therefore, deconvolution of CD spectra is not routinely carried out for protein comparability assessments in the biopharmaceutical industry. In recent publications by several groups, the authors have used

**Fig. 3.9** Comparison of visible CD spectra of CuI PrP-(91–115) and CuI PrP-(90–126). Reproduced with permission, from Klewpatinod et al., 2007, *Biochem. J.*, **404**, 393–402. © The Biochemical Society [48]



software from Thermo, Thermo Electron OMNIC software-QC compare function [43, 44] to compare the entire CD spectra in both the near- and far-UV CD region for protein to systematically qualify a CD method based on its precision and sensitivity [45–47].

## Protein Binding

Visible CD spectroscopy is a very powerful technique for studying metal–protein interactions and can resolve individual d–d electronic transitions as separate bands. A protein or polypeptide in solution has a CD spectrum in the visible region of the radiative spectrum when a metal ion binds to a protein and the complex is in a chiral environment [48]. This can be used to study protein–metal binding, including the pH dependence and stoichiometries of the interactions. As an example, Fig. 3.9 compares the visible CD spectra of 1 mol equivalent of  $\text{Cu}^{2+}$  ions bound at pH 7.8 to two fragments of the prion protein, PrP-(91–115) and the longer fragment, PrP-(90–126) [49]. The significant difference between the visible CD spectra of PrP-(91–115) and PrP-(90–126) reflects differences in the relative affinity of the two  $\text{Cu}^{2+}$  binding sites. Addition of 1 mol of  $\text{Cu}^{2+}$  to PrP-(91–115) at pH 7.8 results in ~70 % of  $\text{Cu}^{2+}$  binding to His 111 and ~30 % to His 96. In contrast, when the longer fragment, PrP-(90–126) is used, ~95 % of the  $\text{Cu}^{2+}$  binds to His 111 and only 5 % to His 96 under the same condition, resulting in a dramatically different visible CD spectrum.

Aromatic side chains are frequently found in ligand-binding sites and often present in regions affected by conformational changes upon binding. When this occurs the near-UV CD spectra of proteins can also be used to probe ligand binding and the resulting changes in protein conformation [50, 51].



### 3.2.2.3 Emerging CD Technology

#### Synchrotron Radiation Circular Dichroism

Synchrotron radiation circular dichroism (SRCD) spectroscopy is a modified version of the CD technique that uses the intense light from a synchrotron source to enable the collection of data at much lower wavelengths than is possible with a conventional CD instrument [52, 53]. For conventional CD instruments with a Xenon (Xe) light source, the intensity of the radiation decreases dramatically below 190–180 nm. N<sub>2</sub> used for purging the sample compartment, the optics, and the H<sub>2</sub>O present in conventional solvents all absorb significantly in this region; this combination of factors makes it almost impossible to collect data below 180 nm. However, estimation of secondary structure content is more reliable and accurate if CD data at 170 nm and below are included; this is possible with SRCD, making secondary structure determination far more accurate. One caveat with this technique is that most of the commonly used buffers for protein therapeutics, and for routine protein analysis, contain buffer components that absorb below 190 nm, and therefore cannot be used in these experiments.

#### Vibrational Circular Dichroism

Vibrational circular dichroism (VCD) extends circular dichroism spectroscopy into the infrared and near infrared ranges (4,000–750 cm<sup>-1</sup>) [54–59], monitoring the molecular vibrational and rotational transitions. Proteins with different secondary structure have characteristic VCD spectra, which vary most for the amide I mode (C=O stretch), but are also easily detectable for the broader amide II and III (very weak) modes (N–H deformation and C–N stretch). This technique complements FTIR, described later in this chapter, but at present is primarily used only by specialist.

#### Concluding Comments on CD

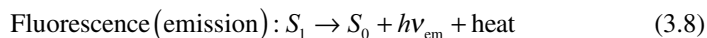
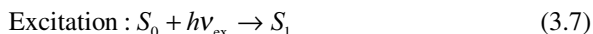
CD spectroscopy is a powerful method for studying the conformational properties of protein and DNA. It can be used to determine the secondary and tertiary structure of proteins and the different types of DNA helices in solution because of its ability to detect, and quantify the proportion of different conformations of these macromolecules. Because CD spectroscopy is sensitive and relatively inexpensive, it has seen widespread use in the life sciences, and is often used by the biopharmaceutical industry as a characterization tool to study the effect on protein conformation of manufacturing processes, formulation compositions and conditions, storage conditions, and delivery systems. Like most spectroscopic techniques, it measures the average overall solution property of the population present in a sample. For example it is impossible to determine whether a 10 % decrease in signal corresponds to 10 %

of the total molecular population with a complete loss of signal while the remaining 90 % retains the native structure, or whether 10 % the entire population has undergone a 10 % change in signal. CD is also unable to determine the structure of the biomolecule at the atomic level and absorption flattening artifacts are common when analyzing membrane protein solutions [60]. However, with recent developments in the quantification of CD spectroscopy more objective numerical methods are being used for comparing the CD spectra over the entire spectral range. By following the titration curve with CD spectra, or the time course of changes in the CD signals, one can study the binding properties of protein or DNA with particular ligands, or the kinetics of unfolding/refolding of these molecules. Thus CD is a very useful technique for higher order structure determination. The applications of CD spectroscopy described here focused on the analysis of systems at equilibrium; even when generating a denaturation curve the system is at equilibrium at each time point. Stopped-flow instruments and laser excitation methods are being developed to follow protein dynamics, and changes in the molecule in ns, but are not in scope for this chapter.

### 3.2.3 Fluorescence

#### 3.2.3.1 Theory

Fluorescence spectroscopy has made important contributions to the study of macromolecules, especially proteins, and has become an invaluable tool in the development of the field of biotechnology. This method is more sensitive than light absorption, but has more limited applications. The most common way to visualize the physical phenomenon of fluorescence is via the Jablonski diagram shown in Fig. 3.1 [7, 61]. Fluorescence can be described by the equation shown below.



where  $h$  is the Planck constant,  $\nu$  is the frequency of light, and  $S_0$  and  $S_1$  are the ground state and excited state of the fluorophore, respectively.

Fluorescence results from the emission of light of a lower energy than that absorbed by the molecule following excitation, due to loss of energy by non-radiative processes. This can occur because absorption occurs faster than the relaxation of vibrational states ( $10^{-15}$  s vs.  $10^{-12}$  s), in other words, the electron transfer from one energy level to another occurs over a much shorter time than the atomic motions of vibration, rotation, etc. No angular momentum is transferred during electron transfer, and the move to a different vibrational state only occurs if the vibrational states align. Thus the molecule in the excited state has the same vibrational states as in the ground state. This is the Franck–Condon principle,

which states that the likelihood of a transition from one vibrational state to another occurring during the transition between electronic states is dependent on the overlap between the two vibrational waveforms. This relaxation of the electron to the lowest vibrational energy level of an excited state without emitting any light is internal conversion.

Once the molecule is at the lowest vibrational energy level of an excited state, there are both non-radiative and radiative processes by which it can release the remainder of the energy and return to the ground state. The phenomenon of fluorescence occurs when the molecule emits a photon during its return to the ground state. In accord with Kasha's rule, emission of light, in this case fluorescence, can only occur from the lowest excited state. The fluorescence "lifetime" is on the order of  $10^{-8}$  s for organic molecules, which is the approximate time the molecule spends in the lowest vibrational energy level of the excited state. Following internal conversion the energy of the emitted photon is lower than that of the photon of the incident light used to excite the molecule; the corresponding shift of the emitted light to a lower frequency (longer wavelength) is called a *Stokes* shift.

Another way a molecule can dissipate energy and return to the ground state is through Förster (fluorescence) resonance energy transfer (FRET) to another fluorophore in physical proximity through dipole–dipole coupling. Energy from the excited state of one fluorophore (the "donor") can be transferred to the excited state of the other fluorophore (the "acceptor"). For this to occur there needs to be significant overlap between the emission spectrum of the donor and the absorption spectrum of the acceptor. There is in fact no transfer of energy by fluorescence or "absorption" that occurs for the acceptor fluorophore, but rather an excited state energy transfer (non-radiative transfer of energy) occurs because of interactions (resonance) between the dipoles of the two fluorophores. The efficiency of the energy transfer is directly related to the distance between the two molecules involved, the spectral overlap of the emission spectrum of the donor molecule and the absorption spectrum of the acceptor molecule, and the overlap in the orientation or direction of the dipole moments of the two molecules [61]. The Förster distance, defined as the distance at which 50 % FRET occurs, is in the range of 20–60 Å for most biological macromolecules. This is given by the following equation:

$$E = \frac{k_{\text{ET}}}{k_f + k_{\text{ET}} + \sum k_i} \quad (3.9)$$

The FRET efficiency ( $E$ ) is the quantum yield of the energy transfer transition,  $k_{\text{ET}}$  is the rate of energy transfer,  $k_f$  is the radiative decay rate, and  $k_i$  are the rate constants of other de-excitation pathways.

$E$  depends on the donor-to-acceptor separation distance  $r$  with an inverse sixth power law because of the dipole–dipole coupling mechanism:

$$E = \frac{1}{1 + (r / R_0)^6} \quad (3.10)$$

with  $R_0$  being the Förster distance for the donor and acceptor pair at which the energy transfer efficiency is 50 %. The Förster distance is dependent on the overlap of the emission spectrum of the donor and the excitation spectrum of the acceptor molecule, and the alignment of the orientation between the dipoles of the two molecules. This is expressed as

$$R_0^6 = 9Q_0 (\ln 10) \kappa^2 J / 128\pi^2 \eta^4 N_A \quad (3.11)$$

where  $Q_0$  is the fluorescence quantum yield of the donor in the absence of the acceptor molecule,  $\kappa^2$  is the dipole orientation factor,  $J$  is the spectral overlap factor,  $\eta$  is the refractive index of the solution, and  $N_A$  is Avogadro's number.

Time-resolved fluorescence spectroscopy is a tool used for monitoring the kinetics of protein folding that exploits intrinsic fluorescence. For proteins containing multiple Trps, this approach can be utilized to monitor the folding of the protein surrounding the individual Trp (by the formation of the correct local environments). In this technique the sample is excited with a pulse of light with a duration that is much shorter than the fluorescence lifetime of the sample, resulting in a population of fluorophores in the excited state. Over time, with fluorescence emission, these excited state molecules will return to the ground state. The time-dependent emission intensity is measured, and in most cases there is an exponential decay of intensity over time. Fitting the exponential decay plot yields the lifetime of the molecule ( $\tau$ ) in the excited state. This is shown by the following equation.

$$F(t) = F_0 e^{(-t/\tau)} \quad (3.12)$$

$\tau$  is the fluorescence lifetime and  $F_0$  is the intensity at time zero.

### 3.2.3.2 Applications

#### Intrinsic Fluorescence

The sources of intrinsic fluorescence in proteins are the aromatic amino acids. In most cases, the indole group in Trp dominates in protein fluorescence, with relatively weaker contributions from Tyr and Phe. Within proteins, FRET can occur between Trp and Tyr due to overlap between the emission spectrum of Trp and the absorbance (or excitation) spectrum of Tyr, if the distance and orientation between the two amino acids in the folded protein allow this to occur. Thus Trp emission is the most frequently observed fluorescence signal in proteins.

The emission of Trp in particular is highly dependent on its local environment, making it a valuable probe for monitoring protein conformational changes. The energy released by the transition from the LUMO to the HOMO is dependent on the interactions between the molecular dipole and the solvent or surrounding environment in the protein, similar to the effect they have on the wavelength of light absorbed in absorbance spectroscopy. Adjusting the wavelength of absorption can

**Table 3.2** Fluorescence attributes of aromatic amino acids in proteins, when present in water at pH 7.0 (adapted from ref. [61])

Amino acid	Excitation wavelength max (nm)	Emission wavelength max (nm)	Quantum yield	Lifetime (ns)
Phenylalanine	260	282	0.02	6.8
Tyrosine	275	304	0.14	3.6
Tryptophan	295	353	0.13	3.1

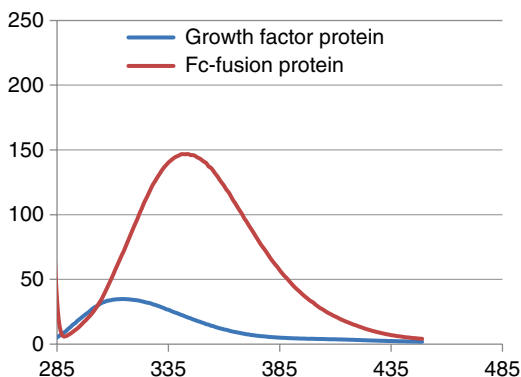
ensure that Trp fluorescence is monitored with minimal contribution from Tyr and Phe. (See Table 3.2 for fluorescence parameters of aromatic amino acids in water.) When excited at 295 nm, >95 % of protein intrinsic fluorescence emission is from Trp and the emission maximum of free or exposed tryptophan in water at pH 7 is about 353 nm. Generally the tryptophan emission in proteins is significantly blue-shifted (towards lower wavelengths) because of the lower polarity of the local environments created by the peptide backbone and the fold of the protein, which protects the fluorophore from the solvent. The amount of solvent exposure of the Trp depends on the hydrophobicity of its local environment in the native protein; as a protein unfolds the solvent exposure typically increases and the wavelength of maximum emission approaches that of fully solvent-exposed Trp (353 nm). This sensitivity to the local environment makes intrinsic fluorescence a potent probe for the degree of folding/unfolding in a protein sample.

## Protein Conformation

The wavelength of maximum fluorescence and the intensity provide information on the environment of the fluorophores and thus the conformation of the protein. The azurins provide an excellent illustration of the effect of environment on Trp fluorescence. The azurin Pae from *Pseudomonas aeruginosa* contains a single tryptophan at position 48, which is in a highly hydrophobic environment in the protein core formed by an eight stranded beta barrel, resulting in an emission maximum at 308 nm [62]. Figure 3.10 illustrates the red and blue shift of the spectra that can occur as a result of different Trp environments present in several different proteins. The figure shows a comparison of the intrinsic fluorescence spectra of growth factor, a protein that contains one buried tryptophan with a maximum at about 310 nm, and an Fc-fusion protein (the IgG1 Fc fused to a receptor domain) that contains over 27 Trps in more solvent-exposed environments resulting in a wavelength maximum at ~340 nm. The width of the fluorescence emission is also a reflection of the number of Trps and the heterogeneity of the environments in which they are located in the folded protein, with broader spectra corresponding to protein with multiple Trp, located in environments with differing polarizability.

Red or blue shifts of the intrinsic fluorescence maximum of a protein can indicate conformational changes such as unfolding and/or aggregation. Upon denaturation of a protein by 6 M guanidine hydrochloride (GdnHCl), the Trp fluorescence shifts to 351 nm, close to the value observed for the individual amino acid in water.

**Fig. 3.10** Intrinsic fluorescence spectra of growth factor protein (*blue*) and Fc-fusion protein (*red*) showing significant differences in their wavelength at maximum fluorescence [85]



The intensity of fluorescence of Trp and Tyr residues is also dependent on the polarity of the solvent environment and nearby residues. The interior hydrophobic environment of proteins inhibits non-radiative processes and promotes high fluorescence quantum yields and therefore higher intensity of fluorescence, while exposure to a polar solvent environment in unfolded proteins results in a lower quantum yield and decreased fluorescence intensity. In this context, Latypov et al. have shown that the emission spectrum of IL-1Ra undergoes a 50 % loss in intensity when denatured by urea [63]. However, in certain instances unfolding increases the fluorescence of the protein; this occurs if the Trp fluorescence is quenched by nearby amino acids in the folded state, in particular nearby disulfide groups, amides and protonated His [64].

The intensity of intrinsic fluorescence of a protein can also be affected by protein concentration and temperature. The linear relationship of protein concentration and fluorescence intensity is limited to very low protein concentrations. As protein concentration increases, the inner filter effect occurs due to the optical density of the protein itself, which will cause decreased fluorescence intensity compared to that in an infinitely diluted solution. The intrinsic fluorescence intensity of a protein decreases with increasing temperature before the onset of an unfolding event due to the quenching effect brought upon by higher temperature.

Conformational changes and kinetics of folding have been extensively investigated for human granulocyte colony stimulating factor (G-CSF) [65–67]. In this case not only does the environment of the Trp residues change with unfolding, but the efficiency of energy transfer from nearby Tyr residues decreases as well. Decreasing the pH from 6 to 2.5 caused a decrease in Trp fluorescence, with a concurrent increase in the intensity of Tyr fluorescence [8]. Native G-CSF has two Trp residues, at positions 58 and 118. Proteins with individual tryptophans mutated by site-directed mutagenesis, showed that Trp 58 was solvent accessible with an emission maximum of 350 nm readily quenched by GdnHCl, while Trp 118 had an emission maximum of 344 nm and required a higher concentration of GdnHCl for quenching [66]. As the protein unfolds changes in the tertiary and secondary structure also increase the distance between a Tyr and Trp 118, decreasing the

efficiency of energy transfer. This results in a decrease in the Trp fluorescence, and an accompanying increase in fluorescence of the Tyr.

The fluorescence lifetime can also provide information on the protein fold and the environment surrounding the Trp. In the case of G-CSF, the kinetics of GdnHCl-induced unfolding and refolding has been studied using time-resolved fluorescence spectroscopy [67]. The decay time for G-CSF in GdnHCl concentrations beyond the equilibrium denaturation transition zone is adequately fit by a single time constant for the unfolding kinetics, while the refolding kinetics required two time constants to adequately fit the behavior, one in the 20–100 ms range and another in the 200–1,000 ms range. Interestingly, this was not due to the presence of the two Trps in the wild-type molecule, as mutagenesis experiments showed that the single Trp containing constructs also exhibited the same refolding behavior. The data in fact supported the generation of an intermediate during the refolding process rather than a cooperative two state reaction. Additional experiments showed that when the starting GdnHCl concentration was below the equilibrium denaturation transition, the refolding kinetics were best represented by two intermediates in the process.

### Fluorescence Quenching

Fluorescence quenching refers to the decrease in fluorescence intensity of a fluorophore that results from the presence of a quencher such as molecular oxygen, acrylamide, etc. Fluorescence quenching can result from multiple pathways including dynamic/collisional and static quenching. Collisional quenching is described by the Stern–Volmer equation:

$$F_0 / F = 1 + K_D [Q] \quad (3.13)$$

$F_0$  and  $F$  are fluorescence intensity in the absence and presence of a quencher,  $K_D$  is the Stern–Volmer constant,  $[Q]$  is the concentration of quencher. For biophysical applications, quenching experiments are mostly used to probe the solvent accessibility of Trp in the folded protein and during protein folding. The larger the  $K_D$ , the more accessible the fluorophores are to the quenchers, indicating greater exposure of these residues to the external solvent. Examples of the applications can be found in multiple publications [68, 69].

### Extrinsic Fluorescence

In addition to the intrinsic fluorophores (the aromatic residues present in proteins), extrinsic fluorophores can expand the application of fluorescence as a tool to study a variety of biochemical phenomena. These fluorophores may be either covalently attached to proteins or bind to proteins in a noncovalent fashion. The amine, sulfhydryl, or His amino acid side chains provide convenient reactive groups for labeling

proteins in a covalent manner. Commonly used fluorophores in this category include dansyl chloride (DNS-Cl) and fluorescein isothiocyanate (FITC) [61]. Attachment of a fluorophore like DNS-Cl is especially useful as this probe absorbs at 350 nm and emits in the 520 nm range and thus does not interfere with the intrinsic fluorescence of proteins. DNS-HCl can be a good probe for fluorescence polarization experiments, a measure of rotational diffusion of a protein because of its short fluorescence lifetime in the unbound state ( $\sim 10$  ns). Fluorescence polarization or anisotropy occurs because fluorophores absorb light in a particular direction, or along a particular vector. The extent that the fluorophore rotates during excitation affects the anisotropy and any process that changes the rotational diffusion of the protein, such as protein–protein or protein–membrane interactions, can be studied by following changes in polarization of the fluorophore. Some examples of this approach using extrinsic fluorescence to study protein–protein association and membrane microenvironments can be found in [70, 71].

The other classes of extrinsic fluorophores are those that bind noncovalently to proteins. One of the most frequently used members of this class is 1-anilidonaphthalene-8-sulfonic acid (ANS). ANS is only weakly fluorescent in water, but fluoresces strongly when bound to protein surfaces. In one of the earliest experiments using this approach, ANS was bound to bovine serum albumin [72]. Interactions between protein and the ANS family of dyes typically increases as a protein unfolds, so increased dye fluorescence in the presence of protein is an indirect measure of protein unfolding. This can be used as a probe for protein folding under different solution conditions, and stresses. Because of this, ANS has become a useful tool for comparing relative stability to pH, temperature, etc., during selection of protein therapeutic candidates for optimal stability [73]. In an example of this type of study, either two or four copies of a non-Fc moiety were attached to the Fc domain of an antibody, creating a series of “2x” or “4x” Fc-constructs. In the case of the 4x Fc-constructs, it was found that one had more than a twofold increase in ANS binding compared to the other two indicating greater exposure of the protein core, and thus decreased conformational stability. This, along with other biophysical data, was used to eliminate this construct from further development. There are two schools of thought regarding the mechanism of action of ANS. One theory is that due to the amphipathic nature of the dye, ANS associates with the nonpolar regions of the macromolecule [61]. However, a recent report studying the binding of ANS to human interleukin-1 receptor antagonist suggests, using two-dimensional NMR data, that ANS was bound in this case to a solvent-exposed positively charged region of the protein. Other related dyes with stronger signals have more recently been developed and applied to protein characterization, including in a high-throughput configuration [73]. In this application a 96 well plate is heated while fluorescence is measured, with samples in the wells differing either in protein or buffer content. The temperature at which unfolding begins correlates with the point where fluorescence of the probe increases, allowing a quick assessment of relative stability between the samples tested.



## Red Edge Excitation of Fluorescence

Another fluorescence method that is used to study protein and membrane dynamics is red edge excitation. A red edge excitation shift of fluorescence is observed when the fluorophores are in an environment that is not fully fluid, such that fluorescence emission becomes dependent on the excitation wavelength. Through the use of different excitation wavelengths, fluorophores in different environments can be monitored to investigate the stability and dynamics of proteins and membranes. Examples of this approach can be found in references from Lakowicz, Chattopadhyay, and Thakkar [69, 74, 75].

## Förster (Fluorescence) Resonance Energy Transfer

FRET can be used to determine the proximity of fluorophores intrinsic to proteins and other molecules. Alternatively molecules can be labeled specifically with fluorophore donor/acceptor pairs and the efficiency of transfer then used to determine the distance between the labeled sites in a folded protein, changes in conformation induced by stress, protein unfolding, etc.

There are several different donor/acceptor pairs like CFP (cyan fluorescent protein; donor; 447 nm) and YFP (yellow fluorescent protein; acceptor; 514 nm), which can be used to probe the distances between the sites where they are attached within a molecule. In general, the assumption is that the transition dipoles of the donor and acceptor are randomly distributed, but that in certain constrained environments, if they are perpendicular to each other, FRET does not occur. An illustrative example of the application of FRET to biological systems can be found in Shih et al. [76]. These authors used FRET to understand the conformational changes that occur in myosin because of ATP hydrolysis. In order to do so, they replaced all the native Cys in *Dictyostelium* myosin-II, and then reintroduced Cys in specific locations on the protein surface, based on the crystal structure. The only Cys that they did not mutate was Cys 655, a highly conserved residue essential for function, which the crystal structure indicates, is completely buried and therefore not accessible to either donor or acceptor dyes during the labeling reaction. The reintroduced Cys were then labeled with donor (Oregon green 488 maleimide) and acceptor (tetramethylrhodamine-5-maleimide) fluorescent dyes. These dyes served as reporters of conformational change based on the efficiency of the FRET, which was indirectly probing changes in the distance separating them. Indeed, they observed that the efficiency of the FRET was in the range of 11–16 % in the absence of nucleotide (donor fluorophore at position 114 or 116, acceptor fluorophore at position 250), while in the presence of Mg-ATP the efficiency of the FRET increased to 32–36 %, and in the presence of Mg-ADP it was increased even further, to 57–61 %. This work supported a long standing theory that there was a 70° conformational change in the light chain region of myosin because of ATP binding. Variants of green fluorescent protein (GFP), such as CFP and YFP, can be used as FRET probes

within living cells. These have been employed in biological systems to understand interactions inside the cell [77, 78], and how the proximity of different proteins changes under different conditions, with the CFP as the donor and the YFP as the acceptor fluorophore.

## Fluorescence Microscopy

Fluorescence microscopy is another technique that utilizes extrinsic fluorescence labeling, in this case in conjunction with an optical microscope which is used to monitor fluorescent emission, following the illumination of a sample with light corresponding to its excitation wavelength. This light is absorbed by the fluorophores (fluorescent tag) and causes them to emit light at a longer, lower energy wavelength, allowing localization of the fluorescent tag within the sample or structure being studied. This fluorescent light can be separated from the surrounding radiation with filters designed for that specific wavelength, so that only the fluorescent molecules are seen. The excitation filters ensure that light of the appropriate wavelengths from the source (e.g., a Xenon arc lamp) illuminate the sample, while an emission filter ensures that light at the fluorescence emission wavelengths is captured while excluding light from other wavelengths. Fluorescence microscopy has been successfully employed in cell biology to image protein distributions and cellular compartments within a cell. For example, 4',6-diamidino-2-phenylindole (DAPI) is a dye that selectively binds to A-T rich regions in DNA, and therefore readily stains nuclei within cells.

Immunofluorescence is another technique used to selectively stain proteins [79, 80]. Direct immunofluorescence uses a single antibody conjugated to a fluorophore to stain the target protein of interest inside cells. Indirect immunofluorescence uses two antibodies; the first IgG is specific to the target while the second is targeted to the constant region of the first (anti-IgG). Each approach has advantages and disadvantages: direct immunofluorescence is more specific and involves fewer steps in the staining procedure, but the number of targets with available primary antibodies directly conjugated to a dye is limited. The indirect immunofluorescent method is more widely applicable because the second labeled antibody recognizes the constant region of a class of primary antibodies, e.g., “rabbit anti-goat” means a fluorescently labeled secondary antibody from the rabbit species that recognizes all antibodies with a goat Fc domain, and can therefore be used to visualize the location of any goat IgG. Applications of this technique are thus only limited by the ability to generate primary antibody to the target protein of interest. Immunofluorescence has been utilized in several studies to stain intracellular distributions of proteins, such as inclusion bodies [80] and regulation of proteins associated with the cell cycle [81].

In addition to monitoring fluorescence of proteins, newer approaches have been developed to monitor protein–protein interactions in living cells. For example, Kim et al. have shown that FRET, bioluminescence resonance energy transfer

(BRET) and fluorescence lifetime imaging microscopy (FLIM) can be adapted for microscopy-based visualization of protein–protein interactions [82]. In this case, they showed that all three methods detected interactions between amyloid precursor protein (APP) and two proteins called APBB1 and APBB2.

### Solid-State Fluorescence

Until recently fluorescence was limited primarily to the analysis of solutions. However, studying proteins in the solid state is useful for protein therapeutics formulated using processes such as lyophilization and spray drying to produce a solid, to circumvent instabilities of the molecule which occur in solution. In these instances, the secondary and tertiary structures of the protein still need to be monitored to determine if the protein is stable during storage in the solid state. While FT-IR is readily available to assess secondary structure ([83] see later section of this chapter), there are significant limitations in utilizing available techniques, such as X-ray diffraction and NMR, to monitor changes in tertiary structure that could affect protein folding and function [84].

Fluorescence spectroscopy offers a convenient approach to monitor changes in the tertiary structure in the solid state. The main limitation of this technique in the past has been interference from scattering of light in the same spectral region as the emission spectrum of the solid. Sharma and Kalonia [84] showed that a front-faced sample holder could be used to obtain intrinsic fluorescence (Trp) spectra in these samples. Their data indicated that the changes in  $\lambda_{\text{max}}$  of different proteins could be correlated with the inherent differences in the tertiary structure. However, they encountered difficulty in quantitatively correlating any changes observed in fluorescence intensity to changes in tertiary structure of the samples.

Recently, Ramachander et al. [85] overcame these difficulties using a Cary-Eclipse solid-state holder. In this case, *N*-acetyl tryptophan amide (NATA) was used to demonstrate reproducibility in measurements, as well as to provide a reference for a “fully-exposed” Trp environment. A significant blue shift (~21 nm) was seen between NATA in the solid state (334 nm) and the reconstituted NATA from the lyophilized formulation (355 nm) indicating a decrease in polarity in the solid-state environment. The Trp emission of one of the proteins tested in the solid state was blue shifted even further (~314 nm). Figure 3.11 illustrates the significant blue shift for the same protein in the solid-state vs. in solution. However, for a given protein, these authors observed that fluorescence intensity, and not wavelength, was a better indicator of stability under accelerated stability conditions. The loss of fluorescence intensity over time at 60 °C was well correlated ( $R^2 = 89\%$ ) with the appearance of the tetramer peak for reconstituted samples as analyzed by Size Exclusion Chromatography SEC, suggesting that the solid-state fluorescence measurements were indeed picking up changes in protein conformation related to aggregation in the solid state (Fig. 3.12).

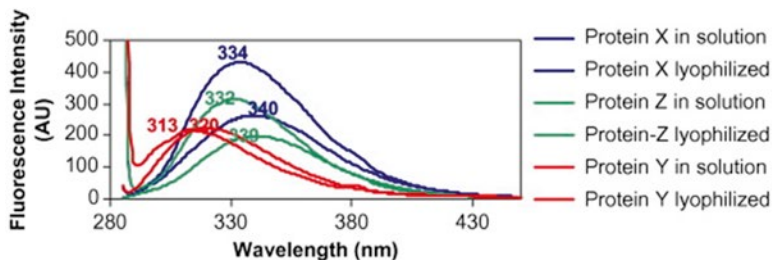


**Fig. 3.11** Comparison of intrinsic fluorescence of protein x, y, and z in solid-state and solution state in their formulation buffers [85]

### Use of Fluorescence Detection in High Performance Liquid Chromatography

Ultraviolet detection has been the standard for protein high performance liquid chromatography (HPLC). However, sometimes the analyte that is being followed may be in such low abundance that it is below the sensitivity (limit of detection) of detection of UV absorbance. In the case of proteins, concentrations in the  $\mu\text{g/mL}$  range cannot be easily detected by UV absorbance and in this instance fluorescence detection, usually by tryptophan fluorescence, is the method of choice. In other examples, fluorescence has been employed to improve selectivity, such as the detection and quantification of the total concentration of free homocysteine in human plasma by Araki and Sako [86]. Another example demonstrating the novel use of fluorescence is the detection of adducts to protein and to DNA, whose levels are typically fairly low in biological samples [87].

### Other Applications

In this section we have focused primarily on applications of fluorescence to study systems or samples in equilibrium. This field is constantly evolving and there are other emerging technologies which have great promise for the future. The use of fluorescence for single molecule analysis is included in Chap. 10. An example of fluorescence correlation spectroscopy, another rapidly expanding application of fluorescence, is included in the chapter on molecular machines. The application of fluorescence to the life sciences is a dynamic, rapidly evolving field.

#### 3.2.3.3 Concluding Comments on the Use of Fluorescence

Fluorescence is a very powerful technique in the life sciences for studying macromolecules and their interactions. Intrinsic fluorescence can be used to monitor protein conformation, stability, and folding/unfolding kinetics. The development of

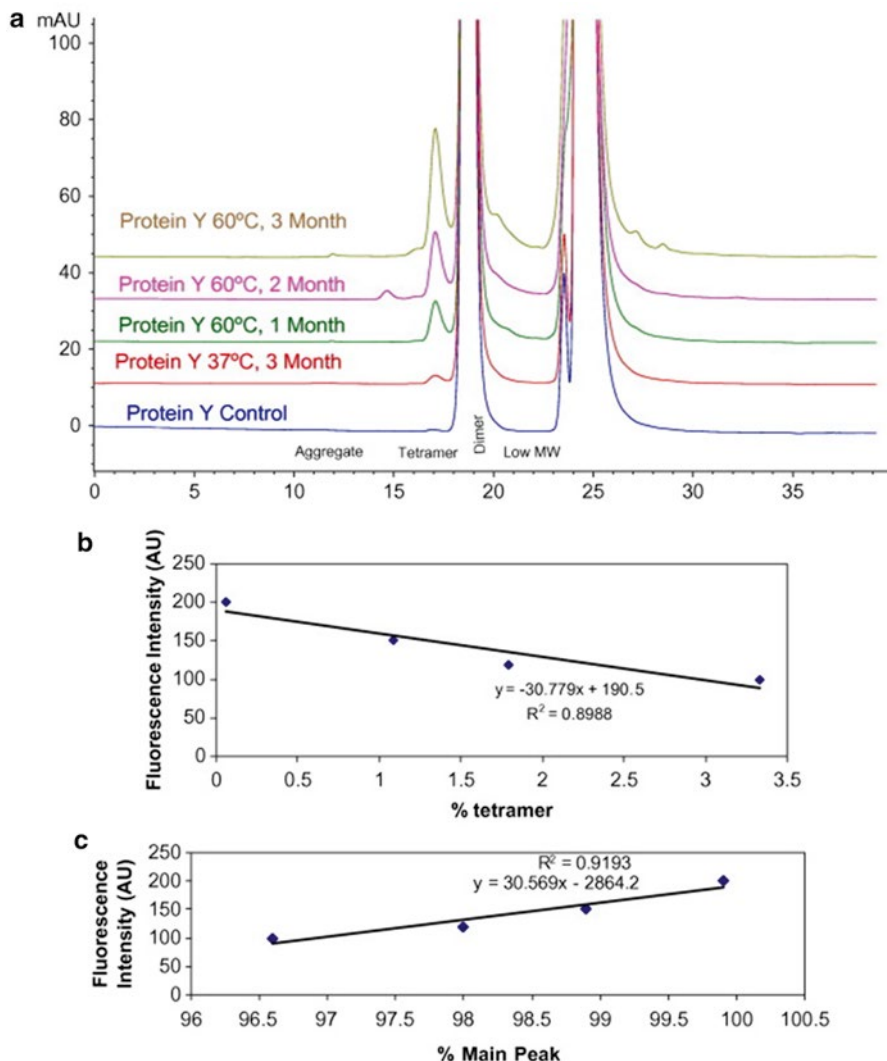
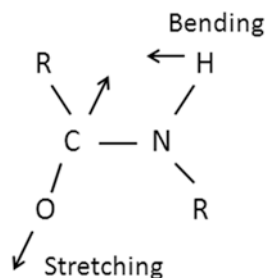


**Fig. 3.12** Formation of HMWS observed by size exclusion chromatography. **(a)** SEC profile following incubation of the lyophilized samples at 60 °C. The SEC technique separates proteins in solution based on their hydrodynamic volume. The larger aggregates and tetramers pass through the column faster and have an earlier retention time than the native Pro Y dimer and lower-molecular-weight species. Excipients and buffer salts in the sample are the last peaks to be observed in the chromatogram. **(b)** Plot of intrinsic fluorescence intensities of protein Y at all time points in the solid state vs. % tetramer observed in SEC. **(c)** Plot of intrinsic fluorescence intensities of protein Y at all time points in the solid state vs. % main peak observed in SEC [85]

**Fig. 3.13** Examples of vibrational modes of the peptide backbone



specific fluorescent dyes that interact with macromolecules expanded the application of fluorescence beyond those proteins where Trp and Tyr were fortuitously located in regions of interest, to all molecules that can be labeled. Incorporation of fluorescent labels has made it possible to interrogate interactions between specific regions of the same protein, or between different proteins and macromolecules that can be labeled. Fluorescent microscopy can be used to visualize the interactions and localization of these molecules at the level of the cell and organelles. For the applications discussed in this section, fluorescence spectroscopy provides information on the average environment of the ensemble of tertiary structures present in the sample being analyzed; the technique can provide even more valuable information about protein structure in conjunction with other spectroscopic techniques such as CD, FTIR, and NMR spectroscopies. The evolution of the technology continues to expand to other conditions and even to the level of individual molecules. When applicable this technique is a powerful biophysical tool for scientists in the life sciences.

### 3.2.4 FTIR

#### 3.2.4.1 Theory

Infrared (IR) spectroscopy measures the wavelength and intensity of the absorption of infrared light by a sample due to transitions in the vibrational state (i.e., stretching or bending of a chemical bond, Fig. 3.13) of a molecule, rather than the transitions of electrons to different energy levels as is the case for UV absorbance, UV CD, and fluorescence spectroscopies described in the previous sections of this chapter. The vibrational frequency and intensity of an IR band depends on the specific chemical bond strength, on the atoms of the molecule, and on a change in the dipole moment of the bond. For proteins, the amide bond of the peptide backbone exhibits characteristic bands in different regions of an FTIR spectrum, designated amide A, B, I, II, III, IV, V, VI, VII bands (Fig. 3.14). The Amide I, II, and III bands are the three major bands of a protein infrared spectrum. The amide I band ( $1,600\text{--}1,700\text{ cm}^{-1}$ ) is mainly associated with the  $\text{C}=\text{O}$  stretching vibration. Different secondary structural

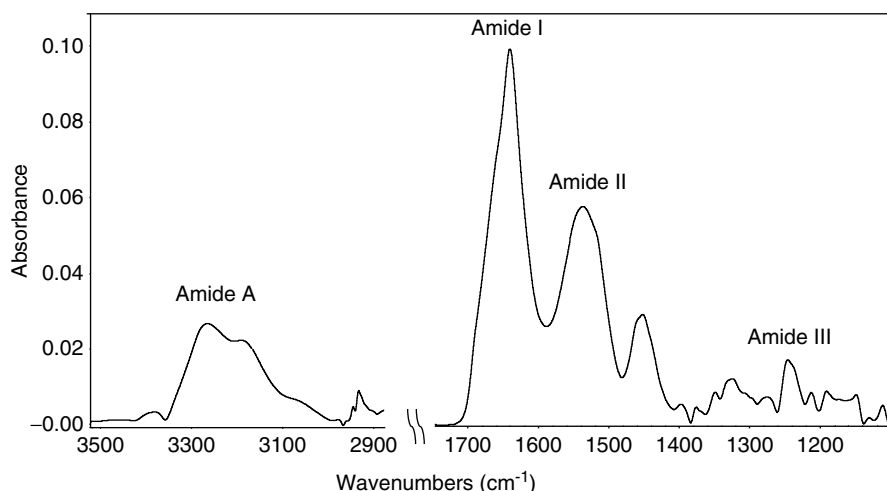


**Fig. 3.14** FTIR spectrum with the different amide regions labeled

features such as  $\alpha$ -helix and  $\beta$ -sheet have characteristic band frequencies and intensities in the amide I band region [88, 89]. The Amide II band ( $1,500\text{--}1,600\text{ cm}^{-1}$ ) results from the combination of N–H bending and C–N stretching vibrations. This band is also conformationally sensitive and has been used in conjunction with hydrogen–deuterium exchange to study changes in protein flexibility and dynamics [90–92]. Amide III bands ( $1,200\text{--}1,350\text{ cm}^{-1}$ ) are predominantly the result of C–N stretching and C–N–H in-plane bending modes, and are sensitive to different secondary structures [93]. The combination of C=O and C–N stretching, C–N–H bending, etc., results in an IR spectrum containing various amide bands that are sensitive indicators of the conformation and dynamics of the macromolecule being studied. FTIR spectroscopy can be used to study changes in the vibrational state of molecules in solution, on a surface, or in the solid state [88–97]. Thus it is a very versatile technique, one of the few that can be used for studying molecular structure of biological molecules regardless of the state of the sample and whether the sample is colored or not.

The Fourier Transform (FT) version of IR spectroscopy allows the use of a continuum light source (such as a Globar) to produce light over a broad range of infrared wavelengths and faster and simultaneous generation of an IR spectrum (intensity vs. frequency) by the use of a Michelson Interferometer [90]. This is done by converting the interferogram generated through measuring the light signals at many discrete positions of the moving mirror to an IR spectrum using Fourier transformation.

Proteins, lipids, and nucleic acids are major components of all living things; FTIR spectroscopy can detect changes in the molecular structures of all three classes of macromolecules, and therefore this technique has been widely used in the life sciences in applications ranging from diagnostics, to assessing cellular responses, to

protein conformational analysis of therapeutic proteins [88–113]. In this chapter we will focus on applications of FTIR to equilibrium measurements of protein structure. Using FTIR for clinical diagnostics is an exciting new and evolving field [106–108], but is beyond the scope of this chapter.

### 3.2.4.2 Applications

#### Protein Secondary Structure Analysis

Over the past 25 years FTIR spectroscopy has been used extensively to analyze protein secondary structure under many different conditions, including in solution [91–105], in the solid-state form [92–94], absorbed on surfaces [97–107], in biodegradable polymers [108], on aluminum oxide [109], and on glass particles [110]. Early applications were limited to solid state or deuterium oxide solutions due to interference from strong IR absorption by water that was difficult to accurately subtract; this was later addressed by the use of very small path length (i.e., <10  $\mu\text{m}$ ) sample cells [91]. Correlation between the secondary structure content of proteins determined from X-ray crystallography (PDB) and the Amide I and III regions of the FTIR spectra identified specific bands that correspond to the different types of secondary structure (such as  $\alpha$ -helices and  $\beta$ -sheets) in aqueous solution [91–93, 98, 99, 113]. The FTIR amide I and III bands have been used to identify the components of the secondary structure of a protein, and to monitor changes in this structure induced by changes in the solution conditions, by stress, upon binding to solid surfaces, and by lyophilization, etc. FTIR is particularly sensitive to the presence of  $\beta$ -sheet secondary structures that generally have very weak signals in the far-UV CD region, making these two methodologies complementary. Until recently a relatively high protein concentration, on the order of 10 mg/mL or higher, was required for FTIR analyses. This has been addressed through the development of newer FTIR instruments with greatly improved signal to noise levels, and the use of an ATR (attenuated total reflectance) accessory [114]. With this combination of improvements undistorted protein structure analysis can be achieved at single digit protein concentrations.

An example of the analysis of protein secondary structure in the solid state is given by Griebenow and Klibanov, who used FTIR spectroscopy in the amide III band region to study changes in protein secondary structure of over a dozen proteins following lyophilization [112]. They found that dehydration reversibly affected the secondary structures while lyophilization increased the  $\beta$ -sheet content and decreased the  $\alpha$ -helix content significantly for all proteins tested. Prestrelski et al. [93] showed that dehydration induced conformational changes in proteins, and that these changes could be inhibited by the inclusion of stabilizers such as sucrose, based on changes in the Amide I region of the protein FTIR spectra. The application of FTIR-ATR to the study of kinetics of protein adsorption and changes in protein secondary structure and orientation upon adsorption to surfaces has been reviewed by Chittur [113]. The utility of using FTIR for protein secondary structure characterization for many



different protein families including enzymes, cytokines/growth factors, and therapeutic proteins is demonstrated by the abundance of publications in this area, a few of which are included in this section.

## **Tertiary Structure**

The IR bands from the aromatic side chains of the amino acids in proteins are especially sensitive conformational changes. FTIR and its difference spectroscopy have been widely used for analysis of protein conformation and to obtain detailed local information around active sites, by monitoring the amide bands [88–102] and the specific functional groups involved [115, 116]. The IR properties of most amino acid side chains have been used to study the mechanism of protein reactions. A comprehensive review by Barth on the infrared absorption of amino acid side chains, a less common use of FTIR, describes how the IR properties of side chains have been determined and used to study changes in protein structures and enzymatic reactions [117].

## **FTIR Difference Spectroscopy**

FTIR difference spectroscopy is a modification of the IR methodology that has proven successful in following the molecular details of protein function and mechanisms of action, due to its selectivity and sensitivity. Applications of FTIR difference spectroscopy have been reviewed extensively by Mäntele, Zscherp, and Barth [118–120]. This technology was originally developed for the investigation of light-induced reactions of photo-reactive proteins. FTIR difference spectroscopy can also be used for the study of redox proteins by the use of electrochemical cells, for the study of many different enzymes by the use of photolabile effector molecules, or as a more general method for the study of buffer and ligand effect by the use of immobilized proteins on ATR crystals.

## **H/D Exchange for Dynamic Structure Analysis**

Hydrogen to deuterium (H/D) exchange occurs quite rapidly for solvent-exposed protons in N–H and O–H bonds when proteins are placed in deuterium oxide,  $^2\text{H}_2\text{O}$ , or  $\text{D}_2\text{O}$  (“heavy water”). H/D exchange can be monitored by mass spectrometry (MS), NMR, and FTIR to study protein conformation and dynamics [121, 122]. H/D exchange in conjunction with MS or NMR can provide information on the regions of the protein polypeptide chain that are in the most flexible parts of the molecules, discussed in other chapters in this volume [123]. The exchange of hydrogen ( $^1\text{H}$ ) to deuterium ( $^2\text{H}$ ) in the protein peptide bonds affects the frequency and intensity of the amide I and II bands of the FTIR spectrum of the molecule. H–D exchange allows the monitoring of the flexibility and dynamics of the protein structure.

FTIR in conjunction with hydrogen deuterium exchange has been used to study protein dynamics and identify the secondary structures that are the most flexible within a protein. Changes in the flexibility of a protein both in solution and in the solid state under different conditions, and as a result of mutations, can also be probed [99, 124–132]. This is achieved by measuring the integrated intensity of the amide I and amide II bands and following the changes in the ratio as a function of time. This complements MS or NMR analyses and can provide conformation-specific information that MS cannot.

An example of the type of information that can be gained using FTIR and H–D exchange can be found in the work by Narhi and colleagues, in their study on the effect of mutations on the propensity of  $\alpha$ -synuclein to aggregate [124]. They showed that the familial Parkinson's disease mutations resulted in more flexible proteins and accelerated  $\alpha$ -synuclein aggregation based on the increase in their H–D exchange rates. FTIR and H–D exchange were used by Baenziger and Méthot [125] to study nicotine acetylcholine receptor. They found that the  $\alpha$ -helical secondary structure in the protein is buried, resistant to exchange, and likely composed of the transmembrane domains. Using FTIR and H–D exchange, Rath et al. showed photoactivation of rhodopsin causes an increase in hydrogen–deuterium exchange rates of buried peptide groups as evidenced by the extent of hydrogen–deuterium exchange of the backbone peptide groups [126]. French and coauthors investigated the influence of trehalose and humidity on the conformation and hydration of spray-dried recombinant human G-CSF and recombinant consensus interferon-alpha (rConIFN) using FTIR and H–D exchange [127]. They revealed that trehalose had a protective effect on the secondary structure of the protein and the stabilization of the proteins at 33 % RH (relative humidity).

Yu et al. also applied FTIR and H–D exchange to study the mechanism of cAMP activation [128]. The authors demonstrated that in contrast to the cAMP-dependent protein kinase, binding of cAMP to Epac does not induce significant changes in overall secondary structure and structural dynamics of the classic intracellular cAMP receptor. Additionally Kamerzell and Middaugh [129] employed two-dimensional correlation FTIR spectroscopy and H–D exchange to monitor the time-dependent structural changes of an IgG1 as a function of pH and revealed coupled immunoglobulin regions of differential flexibility that influence the stability of the antibody. This is only a small sampling of the great potential for applying FTIR and H–D exchange in the life sciences.

### Protein Folding and Stability

The sensitivity of FTIR spectroscopy in analyzing protein structure and dynamics has led to numerous applications in studying protein folding and stability. Fabian and Naumann [130] reviewed the use of stopped-flow FTIR for initiating and monitoring protein folding processes on the millisecond to minute timescale. The unfolding and refolding of ribonuclease A under various conditions such as temperature, pressure, pH, and denaturant has been extensively studied by a number of scientists

using FTIR [100, 131, 132]. FTIR offers the advantage of monitoring the kinetics of different secondary structure components simultaneously, and assessing the order of the events, helping to identify which regions of the protein unfold or fold first. Sethuraman and Belfort [133] used FTIR-ATR in the amide I region to demonstrate that globular proteins, such as hen egg lysozyme in phosphate-buffered saline at room temperature, lose native structural stability and activity when adsorbed onto well-defined homogeneous solid surfaces. The structural loss and change is shown by the transition of  $\alpha$ -helix to turns or random coil followed by a slow  $\alpha$ -helix to  $\beta$ -sheet transition, as evidenced by the changes in the characteristic band frequencies and intensities of these different secondary structure components. Recently, Sharma et al. used FTIR to study thermal and structural stability of adsorbed proteins [134]. They showed that proteins adsorbed to hydrophobic surfaces at low coverage are stabilized relative to the bulk while at larger coverage proteins unfold and form  $\beta$ -sheets. These results demonstrate the utility of the FTIR spectroscopic technique for the characterization of protein folding and stability.

### 3.2.4.3 Data Analysis

Data analysis of FTIR spectra has evolved over the years from a qualitative assessment of the changes in band frequencies and intensities to more complicated mathematical algorithms, especially for the study of changes in protein conformation. Because the protein FTIR spectrum consists of overlapping bands the features are quite broad. Fourier self-deconvolution and derivative methods [89, 98–100, 133] have been used to resolve the contributions of the various types of secondary structure. This allows the estimation and quantification of the changes in the individual components. Fourier self-deconvolution and second derivative algorithms are the most commonly used methods for identifying the presence of different types of protein secondary structure and monitoring changes in the protein secondary structure. Many of the examples described above made use of these methods.

Two-dimensional correlation FTIR spectroscopy is another method that was developed to improve the resolution for detecting spectral and structural changes [135–137]. In the last few years this method has been applied with increasing frequency to studies of protein structure and dynamics as a function of external conditions such as pH, temperature, etc. Kamerzell and Middaugh [129] used two-dimensional correlation FTIR spectroscopy to monitor the time evolution of hydrogen–deuterium exchange of an IgG1 as a function of pH. They observed differential flexibility of various immunoglobulin regions in response to an external perturbation. Sosa and coauthors [138] used the method to study the structure of the protein centrin and its interaction with melittin. The authors showed that two-dimensional correlation FTIR spectroscopy enabled the determination of the increased helicity of melittin, demonstrated that the centrin was stabilized within the complex, and provided a complete molecular description of the formation of the centrin–melittin complex and the dissociation process.

Other mathematical algorithms such as the correlation coefficient, the spectral area of overlap and the derivative correlation function [94, 139–141] have been

developed and/or applied to compare and quantify the overall changes in FTIR spectra as a result of external conditions. D'Antonio and colleagues [46] compared the FT-IR spectra by using several mathematical algorithms including the spectral correlation coefficient, area of overlap, derivative correlation, and a modified area of overlap method. The authors showed that all four algorithms were able to detect significant differences between samples and that the results from all four algorithms were consistent with visual assessments by expert spectroscopists.

#### **3.2.4.4 Concluding Comments on FTIR**

FTIR spectroscopy is a versatile technique that has been used widely in the life sciences for the study of protein structure, dynamics, and stability. The main advantage of FTIR over other spectroscopic techniques such as UV CD and fluorescence is that FTIR can be used to study samples in any form, including liquids, solids, and even gases. The primary weakness of the technique is the need for relatively high protein concentration for the study of protein conformation as compared to other types of analyses. With the continued evolution of both more sensitive instruments and improved mathematical approaches, this technique will continue to see growing applications in the life sciences.

### **3.2.5 Raman**

#### **3.2.5.1 Theory**

Raman spectroscopy measures inelastic scattering, or Raman scattering, of monochromatic light based on interactions of laser light with molecular vibrations, phonons, or other excitations in the system, shifting the energy of the laser photons up or down. The shift in energy gives information about the vibrational modes in the system. Raman scattering is sensitive to the changes of polarizability of the molecule or chemical bond. The polarizability represents the ability of an applied electric field to induce a dipole moment in a molecule or chemical bond without changing the inter-nuclear separation. The intensity and frequency of the Raman scattering are determined by the amount of the induced dipole moment changes and the energy stage of the chemical bond respectively. Therefore this technique can be used to study the vibrational, rotational, and other low-frequency modes of a molecular system. The Raman spectrum of protein or DNA consists of numerous discrete bands representing the normal molecular modes of vibration and serves as a sensitive and selective fingerprint of three-dimensional structure (including secondary and tertiary structures) intermolecular interactions, and dynamics. For a protein molecule, the stretching vibrations of the peptide C=O and C-N bonds yield high Raman intensities because of the large polarizability changes associated with these vibrations. In-plane vibrations of the rings of the aromatic side chains of Trp, Tyr, Phe also produce high intensity Raman bands. Stretching vibrations of C-C, C-N, and C-O bonds will also

**Table 3.3** Raman amide I and amide III band different structure of proteins or polypeptides [142–149]

Molecule	Amide I (cm <sup>-1</sup> )	Amide III (cm <sup>-1</sup> )	Secondary structure
α-Poly-L-alanine	1,655	1,264–1,348	α-Helix
α-Poly-L-glutamate	1,652	1,290	α-Helix
α-Poly-L-lysine	1,645	1,295–1,311	α-Helix
β-Poly-L-alanine	1,669	1,226–1,243	β-Strand
β-Poly-L-glutamate	1,672	1,236	β-Strand
β-Poly-L-lysine	1,670	1,240	β-strand
Poly-L-lysine, pH 4	1,665	1,243–1,248	Irregular
Poly-L-glutamate, pH 11	1,656	1,249	Irregular
Fc	1,670	1,240	β-Strand
α-Helical protein	1,652	1,276–1,327	α-Helix
Protein-2	1,671	1,240	

produce intense Raman bands. Vibrations that involve the displacement of heavy atoms such as sulfur in the C–S stretching modes of methionine (Met) and cysteine (Cys), and the S–S stretching of cystine, the S–H stretching of Cys, and the Zn–S stretching in zinc metallo-proteins are relatively intense as well [142–159].

The correlation between Raman band intensities and frequencies in a protein spectrum to the local environment and structure of the peptide bond or specific side chains are detailed below.

## Peptide Bond

The band shapes and peak positions of the amide I region (1,640–1,680 cm<sup>-1</sup>), which is primarily a carbonyl stretching mode, and the amide III signal (1,230–1,310 cm<sup>-1</sup>), which combines both in-plane C–N–H bending and C–N stretching motions, are very sensitive to changes in the protein secondary structure and are often used as indicators of protein secondary structure integrity. Table 3.3 lists the assigned Raman amide I and amide III bands assigned to the different secondary structure of representative polypeptides and proteins [142–149].

## Tyr

The phenyl ring of Tyr can generate a pair of relatively intense Raman bands at 850 and 830 cm<sup>-1</sup>. The intensity ratio of the Tyr doublet ( $I_{850}/I_{830}$ ) is related to the hydrogen bonding state of the phenolic OH group of this amino acid. When the phenolic OH group is a strong hydrogen-bond donor,  $I_{850}/I_{830}=0.3$ ; when the phenolic OH group is a strong hydrogen-bond acceptor,  $I_{850}/I_{830}=2.5$ ; and when the phenolic OH group functions as both a donor and an acceptor,  $I_{850}/I_{830}=1.25$  [150–152].

## Trp

Trp generates many Raman bands [153–156] which have been correlated to the local environment and geometry of the Trp side chain in proteins. An intense and sharp Raman band in the spectrum between 1,540 and 1,560  $\text{cm}^{-1}$  is the indicator of the absolute value of the side chain torsion angle  $\chi^{2,1}$  ( $\text{C}^{\delta 1}-\text{C}^{\gamma}-\text{C}^{\beta}-\text{C}^{\alpha}$ ). This aromatic amino acid also generates a Fermi doublet with components at 1,360 and 1,340  $\text{cm}^{-1}$ . The intensity ratio of the Fermi doublet ( $I_{1,360}/I_{1,340}$ ) increases with increasing hydrophobicity of the indolyl ring environment and thus serves as an indicator of local hydrophathy. A Raman band near 880  $\text{cm}^{-1}$  is sensitive to indolyl N–H hydrogen-bond donation and shifts to lower frequency with increasing strength of N–H...X hydrogen bonding. An indole ring-breathing vibration of Trp generates an intense band (near 755  $\text{cm}^{-1}$ ) in the Raman spectra of proteins. This band intensity increases with decreasing hydrophobicity of the indolyl ring environment.

## Cys

The Raman band resulting from the Cys sulfhydryl bond (S–H) stretching vibration occurs in the Raman region of 2,500–2,600  $\text{cm}^{-1}$ . The S–H stretching vibrational band is sensitive to the hydrogen-bond interactions of the S–H group; the frequencies of S–H at different H-bonding states are listed in Table 3.4 [157–159]. The intensity of this band is a direct measure of the concentration of cysteinyl S–H in a protein.

## His

In  $\text{D}_2\text{O}$  solution, histidine has a moderately intense Raman band near 1,408  $\text{cm}^{-1}$ , which is assigned to an in-plane vibration of the N-deuterated imidazolium ring [160, 161].

**Table 3.4** Raman S–H frequency and hydrogen bonding states [157–159]

Hydrogen bonding state of S–H group	S–H band frequency ( $\text{cm}^{-1}$ )	S–H band width ( $\text{cm}^{-1}$ )	Examples
No hydrogen bond	2,581–2,589	12–17	Thiols in $\text{CCl}_4$ (dilute solution)
S acceptor	2,590–2,595	12–17	Thiols in $\text{CHCl}_3$
Weak S–H donor	2,575–2,580	20–25	Thiol neat liquids; thiols in thioesters
Moderate S–H donor	2,560–2,575	25–30	Thiols in acetone; crystal structures
Strong S–H donor	2,525–2,560	35–60	Thiols in dimethylacetamide; crystal structures
S–H donor and S acceptor	2,565–2,575	30–40	Thiols in $\text{H}_2\text{O}$

## DNA

For a DNA molecule, different nucleotide conformations and secondary structures will exhibit different characteristic Raman bands. Characteristic carbonyl modes in the 1,600–1,700  $\text{cm}^{-1}$  region reflect differences in base pair hydrogen bonding of the respective GC complexes. The intense Raman lines of the phosphodiester backbone in the 750–850  $\text{cm}^{-1}$  region are the most useful for qualitative identification of B-, Z-, and A-forms of DNA structures.

### 3.2.5.2 Applications

#### Protein Conformation

The Raman spectrum of a protein usually contains signals from a mixture of  $\alpha$ -helix,  $\beta$ -sheet, and random structures, as well as contributions from the aromatic amino acids and Cys as described above. Raman band frequencies and shapes can be used to analyze protein secondary structures, determine side chain conformations, and detect intra- and intermolecular interactions, including the formation of specific complexes and large assemblies and the amount of free S–H. Thus one can obtain information about the secondary structure content of a protein as well as information about the tertiary structure from the same spectrum, obtained under the same conditions. Figure 3.15 shows an FT-Raman spectrum of an *E. coli*-derived Fc domain at pH 7, with most of the characteristic Raman bands labeled.

Raman spectroscopy is very useful for protein secondary structure analysis, complementing the information one gets from FTIR or far UV CD analysis. The Raman spectra of two proteins can have the same peak position but different shapes for the amide I band, due to differences in the percentages of  $\alpha$ -helix,  $\beta$ -sheet, and random structure in the secondary structures of the proteins. This can be determined by deconvolution of the spectra in this region.

Tertiary structure can be probed with Raman spectroscopy by monitoring several amino acid side chain conformations and the environments in which they are located. A number of correlations have been established between Raman band intensities and/or frequencies of Cys, Tyr, Trp, and His residues and the local environments or structures of these specific side chains, as detailed in the theory subsection above, and changes in protein conformation can be monitored by changes in these signals. Raman spectra can be useful for monitoring His H/D exchange dynamics as well as histidine–histidinium equilibria (in  $\text{D}_2\text{O}$ ). A linear correlation between the frequency of the 1,408  $\text{cm}^{-1}$  Raman band and the His side chain conformation has been proposed.

One important aspect of Raman spectroscopy of proteins is the ability to detect free (reduced) Cys. Because the Raman band is specific to the S–H group its intensity is a direct measure of the concentration of cysteinyl S–H sites, and it can be used to determine the H-bonding states and amount of free S–H in a protein, and

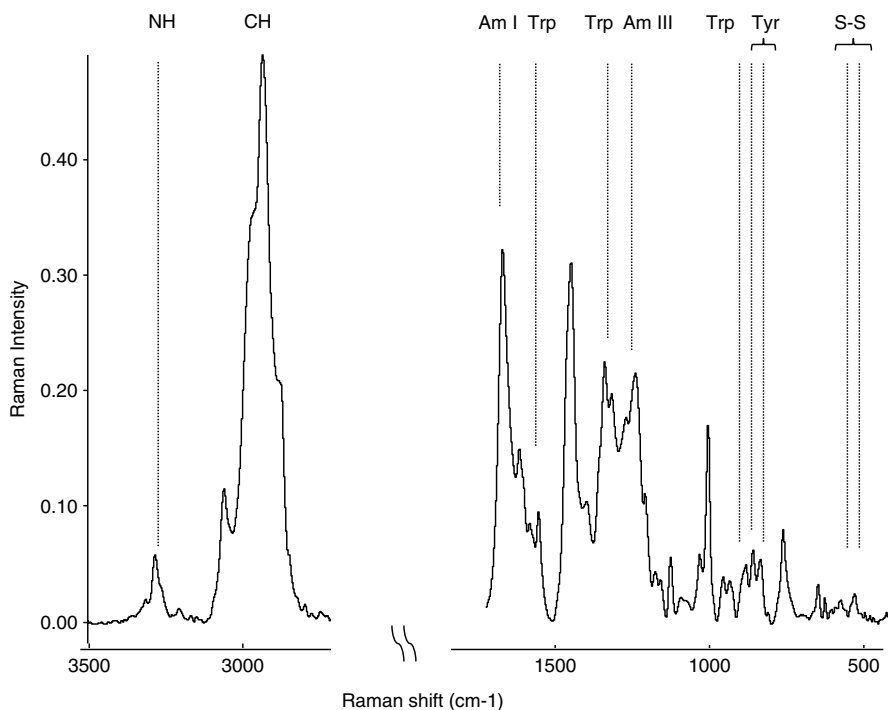


**Fig. 3.15** Raman spectrum of mAb in 400–3,500  $\text{cm}^{-1}$

also to measure the  $\text{pK}_a$  of thiolate titration. This can be very useful in following the oxidation and formation of disulfide bonds.

In Raman difference spectroscopy, a digitally computed spectrum obtained by subtracting one Raman spectrum from another, can be very useful in visualizing the difference in the Raman band shape and/or frequency changes between samples, and in increasing sensitivity in detecting conformational changes in a protein.

## Protein Dynamics

Ultraviolet resonance Raman (UVRR) spectroscopy uses selective excitation in the UV absorption bands of macromolecules to produce spectra of particular chromophoric segments. Resonance excitation has the advantage of selectivity in the transitions being targeted for study, and has become a powerful tool for protein folding studies, via enhancement of the amide vibrations of the polypeptide backbone by the use of deep UV excitation [162, 163]. Dual wavelength UVRR allows both peptide and aromatic spectra to be obtained simultaneously [164]. Due to its sensitivity



and structural selectivity, UVRR spectroscopy can provide unique insight into protein dynamics. Selective excitation ( $\sim 230$  nm) of Trp and Tyr residues can monitor the details of the dynamic flexibility of the tertiary structure of a protein and the structural changes involved. When changes in secondary structure occur, as in protein folding, these can be elucidated via excitation ( $\sim 200$  nm) of the amide backbone. H–D exchange Raman spectroscopy can also be used to study protein flexibility and folding [165–168].

## DNA Conformation

Raman spectroscopy is very useful for DNA structure analysis. A conformationally sensitive guanine mode, which yields Raman bands near 682, 668, or 625  $\text{cm}^{-1}$  in B (C2'-endo, anti), A (C3'-endo, anti), or Z (C3'-endo, syn) structures, respectively, is the most useful for quantitative analysis. In  $\text{D}_2\text{O}$ , the guanine band of Z-DNA is shifted to 615  $\text{cm}^{-1}$ , permitting its detection even in the presence of proteins. These conformationally sensitive Raman bands can be employed to identify the nucleic acid secondary structure within a capsid or nucleoproteins [169, 170].

## Deconvolution of Raman Spectra

Like most spectroscopic techniques, Raman spectroscopy captures the distribution of conformations and thus reflects the average conformation. The most commonly used quantitative analysis method by researchers in the field is the deconvolution of the Raman spectrum of a protein or DNA to the contributions of individual structural elements ( $\alpha$ -helix,  $\beta$ -sheet,  $\beta$ -turn and unordered conformation for a protein or B-, A-, and Z-forms for a DNA) followed by the determination of the percentage of each component in the protein secondary structure or DNA form [171]. This is used primarily for secondary structure determination.

## Raman Microscopy

Raman microscopy is a powerful technique for solid-state analysis of protein pharmaceuticals; it can be applied in situ within glass containers or on the isolated particle samples. The laser beam of a confocal Raman microscope can be focused sharply on small particles (on the order of 20  $\mu\text{m}$  or larger) to obtain high quality Raman spectra. The penetration of visible laser light through glass enables in situ analysis to be performed without any sample manipulation [172, 173]. The characteristic fingerprint of Raman protein spectra allows differentiation between protein product and placebo and between different protein products. Raman microscopy has been used to differentiate drug counterfeits from authentic products and employed in investigations of regulatory nonconformance to quickly confirm the presence and identity of foreign particles in primary glass containers by in situ analysis.

Some applications of Raman spectroscopic analysis for protein pharmaceuticals, solutions and solids, in primary glass containers are described by Wen and colleagues [172]. This included protein gelation, protein product identification, and in situ analysis of residues in primary containers as well as investigating manufacturing incidents during drug product filling operations [172].

### 3.2.5.3 Emerging Raman Technologies

Applications of Raman spectroscopy to the life sciences are rapidly increasing, in part as a result of the rapid evolution of the instrumentation itself. One relatively new innovation is the nondestructive point-and-shoot handheld, lightweight Raman system that is being widely used for rapid raw material and drug product verification. The system enables analysis through sealed packaging to minimize risk of exposure and contamination of the material being tested and its embedded analysis software delivers a PASS/FAIL decision verifying the identity of a sample.

There are a number of advanced types of Raman spectroscopy under development, including surface-enhanced Raman (SERS) where the Raman signals are enhanced when molecules bind to the surface of metal in a variety of morphologies. Tip-enhanced Raman is an alternative to conventional SERS where a modified AFM tip is brought into contact with a sample surface. Polarized Raman spectroscopy can probe information about molecular orientation and symmetry of the bond vibrations, in addition to the general chemical identification which conventional Raman provides. Stimulated Raman is a technique being explored where both the signal Raman beam inducing the inelastic scattering and a pump Raman beam in an optical medium are applied to the samples at the same time.

Raman optical activity (ROA) is a vibrational spectroscopic technique complementary to VCD, similar to the way Raman absorption spectroscopy is complementary to FTIR, and is especially useful in the spectral region between 50 and 1,600  $\text{cm}^{-1}$ . It is considered the technique of choice for determining optical activity for photon energies less than 600  $\text{cm}^{-1}$  [174].

### 3.2.5.4 Concluding Comments on Raman Spectroscopy

The Raman spectrum of a protein contains information on both the secondary and tertiary structure of the molecule. This includes the secondary structure of the protein backbone and the amount of  $\alpha$ -helix,  $\beta$ -sheet and irregular structures present, as well as the state of hydrogen bonding, the conformation and configuration of local environments of side chains, and intermolecular interactions. It can also be used to determine the different helical forms of DNA. This technique is also very useful for studying protein and nucleic acid assemblies. An important advantage of Raman over IR spectroscopy for applications to proteins and their complexes is the virtual transparency of liquid water in this type of spectroscopy. This greatly simplifies the analysis of spectra of aqueous solutions of biomolecules. Another advantage of

Raman spectroscopy is that Raman can be used for samples in different physical states (solutions, suspensions, gels, precipitates, fibers, single crystals, amorphous solids, etc.). However, in general, the Raman instrument is more complex than the FTIR instrument, and it is more problematic to compare quantitatively the scattering intensities of Raman bands, whereas IR absorbance intensities are governed by Beer's Law. The Raman signal is also typically weaker than the corresponding IR signal of the same sample, meaning that higher concentrations of the macromolecule being analyzed are required.

### **3.2.6 *Light Scattering***

#### **3.2.6.1 Theory**

In addition to absorption and emission, light scattering is another, more complex, interaction between light and macromolecules, as described in the theory section of this chapter. There are two common types of light scattering analyses that are used in the life sciences: static light scattering and dynamic light scattering (DLS).

In static light scattering a high intensity monochromatic light, most often a laser, of appropriate wavelength is passed through a solution of interest and the resulting time-averaged scattered light intensity is collected at multiple different angles. This technique is commonly known as multiple angle light scattering (MALS); or more recently as multiple angle laser light scattering (MALLS) with a laser used as the light source. In order to detect the scattered light at multiple different angles the wavelength of light should be at least 50 times greater than the macromolecular species (usually protein) doing the scattering. To this end laser light of 690 nm is typically used for MALS/MALLS experiments. When the particles are closer in size to the incident wavelength the interactions between light and the particles become more complex, with forward scattering being the most significant component of the scattered light, an event also referred to as Mie scattering. Because of this phenomenon a few large particles can skew the results and make the size or hydrodynamic radius of the solution appear to be larger than it is. SLS can be used to determine the molecular weight of the protein being analyzed as a function of solution condition, as long as the concentration is low enough to prevent intermolecular interaction that could affect the scattering behavior.

DLS, also referred to as quasi elastic light scattering (QELS), measures the fluctuations in the intensity of scattered light from a collection of molecules in the sample as a function of time. This fluctuation in intensity is caused by the constant motion of the molecules in solution due to Brownian motion and intermolecular interactions. It is used to calculate the average size of the molecules, including their hydration shells, doing the scattering; in other words the hydrodynamic radius. Most modern instruments use autocorrelation analysis of the light fluctuations

where the intensity at any time is compared to the intensity at time + time interval  $\tau$ . The autocorrelation function is then defined as

$$g^{(2)}(\tau) = 1 + ce^{-2h^2 D \tau} \quad (3.14)$$

where  $\tau$  is the time interval of the measurement,  $D$  is the translational diffusion coefficient,  $h = 4\pi n \lambda^{-1} \sin(\theta/2)$  where  $\theta$  is scattering angle and  $n$  is the refractive index. The autocorrelation data is analyzed using various mathematical methods including the cumulant method, the CONTIN algorithm or the maximum entropy method. The cumulant analysis method is currently defined in the ISO standards and is included with the instruments by major manufacturers. The primary result of a DLS experiment is the averaged diffusion coefficient  $D$ . From the diffusion coefficient the size of a molecule, defined by the hydrodynamic radius  $r_h$ , can be calculated and with some further assumptions the molar mass can be estimated. For the diffusion of spherical particles the Stokes–Einstein equation can be used to calculate hydrodynamic radius from the diffusion coefficient

$$D = \frac{kT}{f} = \frac{kT}{6\pi\eta r_h} \quad (3.15)$$

where  $k$  is the Boltzmann constant,  $T$  is the absolute temperature,  $\eta$  is the solution viscosity, and the frictional coefficient  $f$  is defined by the Stokes Equation as  $f = 6\pi\eta r_h$ . Application of these principles to macromolecular analysis is detailed below.

### 3.2.6.2 Applications

#### Static Light Scattering

The primary application of static light scattering is in the determination of the molecular weight of the macromolecules in a relatively dilute solution of interest, in order to avoid non-ideality [175]. High-throughput light scattering techniques are preferred in formulation development [176] in order to rapidly compare multiple formulation candidates. Static light scattering can be used to determine the molecular weight of species eluting from chromatography columns. In this application a light scattering detector is coupled with a concentration detector, most commonly a UV absorbance and/or refractive index detector [59, 177]. This technique has become a very important tool to characterize the components of drug products, and other macromolecular samples. An example of a typical SEC analysis of multiple oligomeric species is illustrated in Fig. 3.16.

Characterization of eluting species by this SLS has also proven to be a useful tool in situations where the kinetics of aggregation or heterogeneous protein interactions

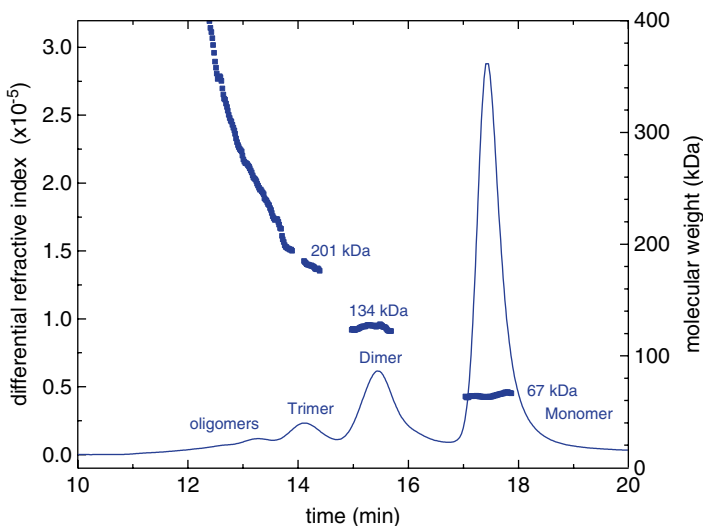


**Fig. 3.16** Size exclusion chromatography of heat-stressed human serum albumin, with the molecular weights as determined using MALLS show above each peak

are being studied, or where ligand binding is present. In these experiments different proteins of interest are mixed in varying ratios, and changes in the molecular weight of the eluting species are analyzed.

Weaker types of protein self-association can also be studied using static light scattering. If attractive or repulsive forces between molecules occur results in thermodynamic non-ideality, then the equation  $R_0 = KMc$  can be modified to account for non-ideality

$$\frac{KC}{R_0} = \frac{1}{M} + 2Bc \quad (3.16)$$

where  $B$  is the second virial coefficient, a measure of protein non-ideality. The absolute value of  $B$  represents the strength of the interaction; a negative value indicates attraction and a positive value indicates repulsion. The second virial coefficient is typically determined by measuring the light scattering intensity of a series of dilutions; the maximum concentration must be in the concentration range where significant protein non-ideality is present.

### Dynamic Light Scattering

DLS is most frequently used to determine size distribution of macromolecules and to study protein aggregation in solution [178, 179]. A typical hydrodynamic radius determination by DLS is presented in Fig. 3.17.

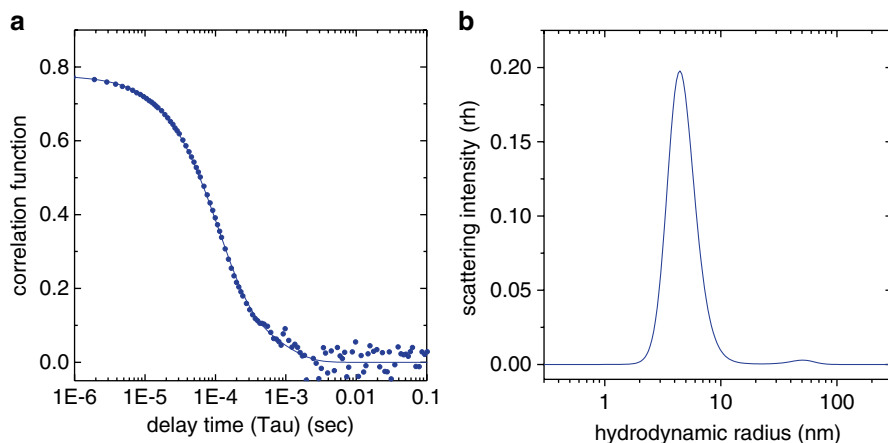


**Fig. 3.17** Determination of the hydrodynamic radius of an IgG. (a) Autocorrelation function fitting, (b) hydrodynamic radius distribution, the  $r_h$  of the monomer was determined to be 5.3 nm

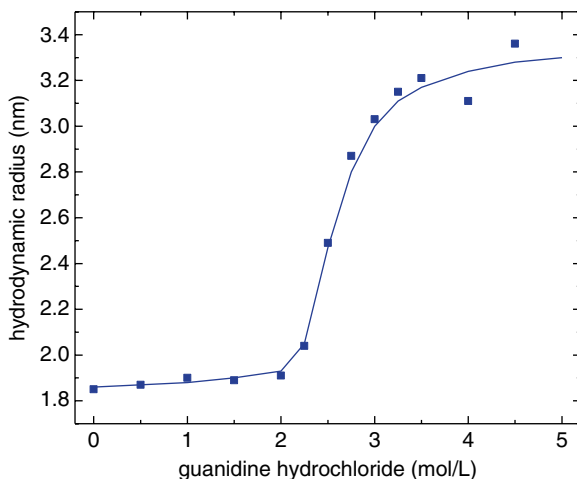
This technique is attractive as it can cover a large size range, requires very little material, is nondestructive, and can be conducted in a high throughput configuration. DLS is increasingly being implemented during protein development as a powerful tool in studies on the effect of solution conditions, formulation components, stress, and forced degradation studies on the size and self-association status of the protein. The results are used to inform candidate selection, and process and formulation conditions [180].

Since DLS measures the hydrodynamic radius, it is sensitive to changes in shape as well as size. This can be used to follow perturbations in the protein structure, changes in conformation and unfolding. An example of changes in hydrodynamic radius due to protein unfolding is shown in Fig. 3.18.

Information on the homogeneity, or polydispersity, of a sample can also be obtained from DLS measurements. A polydisperse solution will result in a multi-exponential decay in the autocorrelation function. An increase in the polydispersity even though a single molecular weight is detected suggests either the presence of small amounts of larger species, or the presence of other differently shaped molecules (most likely from unfolding and structural perturbations) with the same molecular weight. The sensitivity of this method increases with size and DLS is therefore capable of detecting the presence of extremely small amounts of particles in the submicron range which are often difficult to detect by other techniques. The practical upper limit for DLS measurements is approximately 1  $\mu\text{m}$ , for larger particles other techniques, such as light obscuration must be used.

DLS can also be used to study the weak self-associations of macromolecules, by probing the effect of protein concentration on the diffusion coefficient. When interactions are occurring the solution will show nonideal behavior, and the diffusion coefficient measured ( $D_m$ ) will change with protein concentration until it is

**Fig. 3.18** Unfolding of cytochrome *c* in the presence of denaturing agent measured by DLS, monitoring the increase in hydrodynamic radius



equivalent to the self-diffusion coefficient of the monomeric species ( $D_0$ ) at very dilute concentrations. This dependence on protein concentration can be represented as

$$D_m = \frac{D_0}{1 + k_D c} \quad (3.17)$$

$k_D$  can be determined from measurements of the diffusion coefficient in a series of protein dilutions, and is a measure of protein–protein interaction. A negative  $k_D$  signifies attraction and association between molecules while a positive  $k_D$  represents repulsion. This type of analysis can be used to assess the effects of different solution conditions on the association behavior of a molecule. DLS experiments can be performed at protein concentrations up to several mg/mL.

### Other Applications of Light Scattering

Static light scattering measures the apparent molecular weight of the molecule while DLS measures the hydrodynamic radius. Combining these two techniques allows one to probe the shape and the openness or density of the protein or protein aggregates being analyzed. Discrepancies between the determined molecular weight of the molecule being studied (modeled as a sphere) by SLS and the size obtained with DLS can be used as an indication of irregular or elongated shape. For more accurate shape determination analytical ultracentrifugation should be considered; this is a complementary technique that can be used over a wide range of concentrations.

One practical application of light scattering for the study of macromolecules is the use of turbidity to follow protein aggregation. There are two different methods to measure turbidity: determination of the light loss of the transmitted beam

(scatter coefficient) or determination of the intensity of the scattered light. The scatter coefficient represents the total scattered light that has been withdrawn from the incident beam, while the scatter intensity corresponds to how much scattered light has been deflected at a given angle. Measurements of the scattering intensity can only be performed at lower concentrations due to multiple scattering, while transmission measurements can be used at higher protein concentrations. Another limit for turbidity measurements is that they can only be performed at wavelengths where the chromophores in the macromolecules do not absorb or absorb minimally; the visible range is therefore most suitable but turbidity studies can be also performed in the near-UV region (320–400 nm). Changes in the signal at 600 nm can be used to detect the beginning of aggregation which is often employed in accelerated stress studies to assess stability of a given molecule as a function of storage or handling conditions. Turbidity measurements can be easily performed in a high-throughput experimental setup and is suitable for the measurement of aggregation kinetics, to assess relative stability to heat, pH, or any type of accelerated degradation study to predict relative stability of proteins under targeted conditions.

### **Other Techniques**

There are several other more specialized applications of light spectroscopy in the life science, such as reflectance difference spectroscopy, small angle X-ray scattering, Raman scattering. More detailed discussions of these types of applications can be found in several reviews and books published recently [9, 10].

#### **3.2.6.3 Concluding Comments on Light Scattering**

Both static and dynamic light scattering provide information on size distribution and hydrodynamic shape that cannot be obtained by other spectroscopic techniques. They are qualitative rather than quantitative techniques that are most commonly used to assess the effect of different solution conditions and stress on the proteins being studied. SLS can be used in conjunction with separation methods to identify the molecular weight of the species eluting, and they can both be used to understand macromolecular self-association.

## **3.3 Chapter Summary**

This chapter illustrated the many different ways that the interactions of light photons with macromolecules can be used to gain information on the structure, stability, interactions, and other properties of proteins and nucleic acids. Each of these techniques has strengths and weaknesses, but together they make a potent tool box which can be used to increase our understanding of the behavior of macromolecules



throughout the life sciences. The biophysicist can select the appropriate methodology for the questions being addressed, based on the amount of sample and time available. Most of the currently commercially available instruments are designed to perform one type of spectrophotometric technique. More advanced instrumentation already combines more techniques, e.g., absorbance and fluorescence, or static light scattering with dynamic light scattering. Wyatt Corporation, a leading manufacturer in the field of light scattering instruments, integrated SLS, DLS, and the measurement of zeta potential and electrophoretic mobility into one instrument and refers to this solution as “Massively Parallel Phase Analysis Light Scattering.” The trend of the future appears to be integrating multiple spectrometric techniques into one instrument allowing synthesis of data from multiple techniques into an “abstract picture of protein behavior.”

## References

1. Atkins P, de Paula J (2009) *Atkin's Physical chemistry*, 9th edn. Oxford University Press, Oxford
2. Berg JM, Tymoczko JL, Stryer L (2006) *Biochemistry*, 6th edn. W H Freeman and Company, New York, NY
3. Nelson DL, Cox MM (2008) *Lehninger's Principles of biochemistry*, 5th edn. W H Freeman and Company, New York, NY
4. Alberts B, Johnson A, Lewis J, Raff M, Roberts K, Walker P (2007) *Molecular biology of the cell*, 5th edn. Garland Science, Taylor and Francis Group, New York, NY
5. McQuarrie DA, Smith JD (1997) *Physical chemistry: a molecular approach*. University Science, Sausalito, CA
6. Atkins P, De Paula J (2005) *Physical chemistry for the life sciences*. W H Freeman and Company, New York, NY
7. Larsen D (2011) Electronic spectroscopy. <http://chemwiki.ucdavis.edu>
8. Wetlaufer DB (1962) Ultraviolet spectra of proteins and amino acids. *Adv Protein Chem* 17:303–390
9. Schmid F-X (2001) Biological macromolecules: UV-visible spectrophotometry in encyclopedia of life sciences. Macmillan, London, pp 1–4. <http://www.els.net>
10. Kerekr M (1969) *The scattering of light and other electromagnetic radiation*. Academic, New York, NY
11. van Holde KE, Johnson WC, Ho PS (2006) Chapter 7: Scattering from solutions of macromolecules. In: van Holde KE, Johnson WC, Ho PS (eds) *Principles of physical biochemistry*, 2nd edn. Pearson Prentice Hall, Upper Saddle River, NJ
12. Demeester J, De Smedt S, Sanders NN, Hausstraete J (2005) Chapter 7: Light scattering, In: Jiskoot W, Crommelin D (eds) *Methods for structural analysis of protein pharmaceuticals*. AAPS, Arlington, VA
13. Kueltozo LA, Middaugh CR (2005) Ultraviolet absorption spectroscopy in methods for structural analysis of protein pharmaceuticals. AAPS, Arlington, VA
14. Mach H, Middaugh RC (2010) Ultraviolet spectroscopy as a tool in therapeutic protein development. *J Pharm Sci* 100:1214–1227
15. Omura T, Sato R (1964) The carbon monoxide-binding pigment of liver microsomes: I. Evidence for its hemoprotein nature. *J Biol Chem* 239:2370–2378
16. Pace CN, Vajdos F, Fee L, Grimsley G, Gray T (1995) How to measure and predict the molar absorption coefficient of a protein. *Protein Sci* 4:2411–2423

17. Burke CJ, Sanyal G, Bruner MW, Ryan JA, LaFemina RL, Robins HL, Zeff AS, Middaugh CR, Cordingley MG (1992) Structural implications of spectroscopic characterization of a putative zinc finger peptide from HIV-1 integrase. *J Biol Chem* 267(14):9639–9644
18. Narhi LO, Fulco AJ (1987) Identification and characterization of two functional domains in cytochrome P-450 BM-3, a catalytically self-sufficient monooxygenase induced by barbiturates in *Bacillus megaterium*. *J Biol Chem* 262:6683–6690
19. Warburg O, Christian W (1941) Isolierung und krystallisation des garungsferments enolase. *Biochem Z* 310:384–421
20. Mach H, Thomson JA, Middaugh CR (1989) Quantitative analysis of protein mixtures by second derivative absorption spectroscopy. *Anal Biochem* 181:79–85
21. Mach H, Middaugh R (1994) Simultaneous monitoring of the environment of tryptophan, tyrosine and phenylalanine residues in protein by near-ultraviolet second derivative spectroscopy. *Anal Biochem* 222:323–331
22. Bray MR, Carrierre AD, Clarke AJ (1994) Quantitation of tryptophan and tyrosine residues in proteins by fourth derivative spectroscopy. *Anal Biochem* 221:278–284
23. Kelly SM, Jess TJ, Price NC (2005) How to study proteins by circular dichroism. *Biochim Biophys Acta* 1751:119–139
24. Sreerama N, Woody RW (2004) Computation and analysis of protein circular dichroism spectra. *Methods Enzymol* 383:318–351
25. Sreerama N, Woody RW (2004) On the analysis of membrane protein circular dichroism spectra. *Protein Sci* 13:100–112
26. Sreerama N, Woody RW (1993) A self-consistent method for the analysis of protein secondary structure from circular dichroism. *Anal Biochem* 209:32–44
27. Manavalan P, Johnson WC Jr (1987) Variable selection method improves the prediction of protein secondary structure from circular dichroism spectra. *Anal Biochem* 167:76–85
28. Johnson WC (1999) Analyzing protein circular dichroism spectra for accurate secondary structures. *Proteins* 35:307–312
29. Andrade MA, Chacón P, Merelo JJ, Morán F (1993) Evaluation of secondary structure of proteins from UV circular dichroism using an unsupervised neural network. *Protein Eng* 6:383–390
30. Provencher SW, Glöckner J (1981) Estimation of globular protein secondary structure from circular dichroism. *Biochemistry* 20:33–37
31. Lobley L, Whitmore BAW (2002) DICHROWEB: an interactive website for the analysis of protein secondary structure from circular dichroism spectra. *Bioinformatics* 18:211–212
32. Whitmore L, Wallace BA (2004) DICHROWEB, an online server for protein secondary structure analyses from circular dichroism spectroscopic data. *Nucleic Acids Res* 32:W668–W673
33. Hardin Strickland E (1974) Aromatic contributions to circular dichroism spectra of proteins. *CRC Crit Rev Biochem* 2:113–175
34. Krell T, Horsburgh MJ, Cooper A, Kelly SM, Coggins JR (1996) Localization of the active site of type II dehydroquinases. Identification of a common arginine-containing motif in the two classes of dehydroquinases. *J Biol Chem* 271:24492–24497
35. Pain R (2005) Determining the CD spectrum of a protein. *Curr Protoc Protein Sci Chapter 7:Unit 7.6*
36. Venyaminov SY, Vassilenko KS (1994) Determination of protein tertiary structure class from circular dichroism spectra. *Anal Biochem* 222:176–184
37. Kyrp J, Kejnovska I, Renciuik D, Vorlickova M (2009) Circular dichroism and conformational polymorphism of DNA. *Nucleic Acids Res* 37(6):1713–1725
38. Marty R, N'soukpoé-Kossi CN, Charbonneau DM, Kreplak L, Tajmir-Riahi H (2009) Structural characterization of cationic lipid-tRNA complexes. *Nucleic Acids Res* 37(15):5197–5520
39. Greenfield NJ (1996) Methods to estimate conformation of proteins and polypeptides from CD data. *Anal Biochem* 235(1):1–10

40. Perczel A, Hollosi M, Tusnady G, Fasman GD (1991) Convex constraint analysis: a natural deconvolution of circular dichroism curves of proteins. *Protein Eng* 4:669–679
41. Perczel A, Fasman GD (1993) Effect of spectral window size on circular dichroism spectra deconvolution of proteins. *Biophys Chem* 48:19–29
42. Venyaminov SW, Baikalov I, Chuen-Shang C, Yang JT (1991) Some problems of CD analysis of protein conformation. *Anal Biochem* 198:250–255
43. Cover TM, Hart PE (1967) Nearest neighbor pattern classification. *IEEE Trans Inf Theory* 13(1):21–27
44. Thermo OMNIC software manual (TQ Analyst Algorithm) (1998) QC compare method for classifying materials
45. Li C, Nguyen X, Narhi LO, Chemmalil L, Towers E, Muzammil S, Gabrielson JP, Jiang Y (2011) Applications of circular dichroism for structural analysis of proteins: qualification of near- and far-UV CD for protein higher order structural analysis. *J Pharm Sci* 100(11):4642–4654
46. D'Antonio J, Murphy B, Manning M, Al-Azzam W (2012) Comparability of protein therapeutics: quantitative comparison of second-derivative amide I infrared spectra. *J Pharm Sci* 101(6):2025–2033
47. Teska B, Li C, Winn B, Arthur K, Jiang Y, Gabrielson J (2013) Comparison of quantitative spectral similarity analysis methods for protein higher order structure confirmation. *Anal Biochem* 434:153–165
48. Klewpatinond M, Viles JH (2007) Fragment length influences affinity for Cu<sup>2+</sup> and Ni<sup>2+</sup> binding to His96 or His111 of the prion protein and spectroscopic evidence for a multiple histidine binding only at low pH. *Biochem J* 404:393–402
49. Jemth P, Gianni S, Day R, Li B, Johnson CM, Daggett V, Fersht AR (2004) Demonstration of a low-energy on-pathway intermediate in a fast-folding protein by kinetics, protein engineering, and simulation. *Proc Natl Acad Sci U S A* 101:6450–6455
50. Zitzewitz JA, Bilsel O, Luo J, Jones BE, Matthews CR (1995) Probing the folding mechanism of a leucine zipper peptide by stopped-flow circular dichroism spectroscopy. *Biochemistry* 34:12812–12819
51. Andersson LA, Peterson JA (1995) Active-site analysis of ferric P450 enzymes: hydrogen bonding effects on the circular dichroism spectra. *Biochem Biophys Res Commun* 211:389–395
52. Wallace BA (2005) Shining new light on protein structure and function thru synchrotron radiation circular dichroism (SRCD) spectroscopy. *Aust Biochem* 36:47–50
53. Wallace BA, Janes RW (2010) Synchrotron radiation circular dichroism (SRCD) spectroscopy—an enhanced method for examining protein conformations and protein interactions. *Biochem Soc Trans* 38:861–873
54. Keiderling TA, Yasui SC, Narayanan U, Annamalai A, Malon P, Kobrinskaya R, Yang L (1988) Vibrational circular dichroism of biopolymers. In: Schmid ED, Schneider FW, Siebert F (eds) *Spectroscopy of biological molecules new advances*. Wiley, New York, NY, pp 73–76
55. Yasui SC, Keiderling TA (1988) Vibrational circular dichroism of polypeptides and proteins. *Mikrochim Acta* 95:325–327
56. Keiderling TA (1993) Vibrational circular dichroism of proteins polysaccharides and nucleic acids. In: Baijanu I, Pessen H, Kumosinski T (eds) *Physical chemistry of food processes*, vol 2 advanced techniques, structures and applications. Van Nostrand Reinhold, New York, NY, pp 307–337
57. Keiderling TA, Qi X (2002) Spectroscopic characterization of unfolded peptides and proteins studied with infrared absorption and vibrational circular dichroism spectra. *Adv Protein Chem* 62:111–161
58. Keiderling TA (2002) Protein and peptide secondary structure and conformational determination with vibrational circular dichroism. *Curr Opin Chem Biol* 6(5):682–688
59. Malon P, Kobrinskaya R, Keiderling TA (1988) Vibrational circular dichroism of polypeptides XII. Re-evaluation of the Fourier transform vibrational circular dichroism of polygamma-benzyl-L-glutamate. *Biopolymers* 27(5):733–746

60. Mao D, Wallace BA (1984) Differential light scattering and absorption flattening optical effects are minimal in the circular dichroism spectra of small unilamellar vesicles. *Biochemistry* 23:2667–2673
61. Lakowicz JR (1996) Principles of fluorescence spectroscopy, 2nd edn. Kluwer Academic/Plenum, New York, NY
62. Szabo AG, Stephanik TM, Wayner DM, Young NM (1983) Conformational heterogeneity of the copper binding site in azurin. *Biophys J* 41:233–244
63. Latypov RF, Liu D, Gunasekaran K, Harvey TS, Razinkov VI, Raibekas AA (2008) Structural and thermodynamic effects of ANS binding to human interleukin-1 receptor antagonist. *Protein Sci* 17(4):652–663
64. Eftink M (2000) Intrinsic fluorescence in proteins. In: Lakowicz JR (ed) Topics in fluorescence spectroscopy: protein fluorescence, vol 6. Springer, New York, NY, pp 1–16
65. Narhi LO, Kenney WC, Arakawa T (1991) Conformational changes of recombinant human granulocyte-colony stimulating factor induced by pH and guanidine hydrochloride. *J Protein Chem* 10(4):359–367
66. Kolvenbach CG, Elliott S, Sachdev R, Arakawa T, Narhi LO (1993) Characterization of two fluorescent tryptophans in recombinant human granulocyte-colony stimulating factor: comparison of native sequence protein and tryptophan-deficient mutants. *J Protein Chem* 12(2):229–236
67. Brems DN (2002) The kinetics of G-CSF folding. *Protein Sci* 11(10):2504–2511
68. Calhoun DB, Vanderkooi JM, Holtorn GR, Englander SW (1986) Protein fluorescence quenching by small molecules: protein penetration versus solvent exposure. *Proteins* 1:109–115
69. Thakkar SV, Kim JH, Samra HS, Sathish HA, Bishop SM, Joshi SB, Volkin DB, Middaugh CR (2012) Local dynamics and their alteration by excipients modulate the global conformational stability of an IgG1 monoclonal antibody. *J Pharm Sci* 101(12):4444–4457
70. Lukas TJ, Burgess WH, Prendergast FG, Lau W, Watterson DM (1986) Calmodulin binding domains: characterization of a phosphorylation and calmodulin binding site from myosin light chain kinase. *Biochemistry* 25:1458–1464
71. Cogen U, Shinitzky M, Weber G, Nishida T (1973) Micro-viscosity and order in the hydrocarbon region of phospholipid and phospholipid-cholesterol dispersions determined with fluorescent probes. *Biochemistry* 12:521–528
72. Daniel E, Weber G (1966) Cooperative effects in binding by bovine serum albumin I. The binding of 1-anilino-8-naphthalene-sulfonate. Fluorimetric titrations. *Biochemistry* 5:1893–1900
73. He F, Phan DH, Hogan S, Bailey R, Becker GW, Narhi LO, Razinkov VI (2010) Detection of IgG aggregation by a high throughput method based on extrinsic fluorescence. *J Pharm Sci* 99:2598–2608
74. Lakowicz JR, Keating-Nakamoto S (1984) Red-edge excitation of fluorescence and dynamic properties of proteins and membranes. *Biochemistry* 23(13):3013–3021
75. Chattopadhyay A, Mukherjee S (1993) Fluorophore environments in membrane-bound probes: a red edge excitation shift study. *Biochemistry* 32(14):3804–3811
76. Shih WM, Gryczynski Z, Lakowicz JR, Spudich JA (2000) A FRET-based sensor reveals large ATP hydrolysis-induced conformational changes and three distinct states of the molecular motor myosin. *Cell* 102(5):683–694
77. Rajan RS, Illing ME, Bence NF, Kopito RR (2001) Specificity in intracellular protein aggregation and inclusion body formation. *Proc Natl Acad Sci U S A* 98(23):13060–13065
78. Miyawaki A, Llopis J, Heim R, McCaffery JM, Adams JA, Ikura M, Tsien RY (1997) Fluorescent indicators for Ca<sup>2+</sup> based on green fluorescent proteins and calmodulin. *Nature* 388:882–887
79. Aoki V, Fukumori LMI, Freitas EL, Sousa JX Jr, Perigo AM, Oliveira ZNP (2010) Direct and indirect immunofluorescence. *An Bras Dermatol* 85(4):490–500
80. Johnston JA, Ward CL, Kopito RR (1998) Aggresomes: a cellular response to misfolded proteins. *J Cell Biol* 143(7):1883–1898

81. Tsou MF, Wang WJ, George KA, Uryu K, Stearns T, Jallepalli PV (2009) Polo kinase and separase regulate the mitotic licensing of centriole duplication in human cells. *Dev Cell* 17(3):344–354
82. Kim J, Lee J, Kwon D, Lee H, Grailhe R (2011) A comparative analysis of resonance energy transfer methods for Alzheimer related protein-protein interactions in living cells. *Mol Biosyst* 7:2991–2996
83. Prestrelski SJ, Arakawa T, Carpenter JF (1993) Separation of freezing- and drying-induced denaturation of lyophilized proteins using stress specific stabilization: II. Structural studies using infrared spectroscopy. *Arch Biochem Biophys* 303:465–473
84. Sharma VK, Kalonia DS (2003) Steady-state tryptophan fluorescence spectroscopy study to probe tertiary structure of proteins in solid powders. *J Pharm Sci* 92(4):890–899
85. Ramachander R, Jiang Y, Li C, Eris T, Young M, Dimitrova M, Narhi L (2008) Solid state fluorescence of lyophilized proteins. *Anal Biochem* 376(2):173–182
86. Araki A, Sako Y (1987) Determination of free and total homocysteine in human plasma by high-performance liquid chromatography with fluorescence detection. *J Chromatogr* 422:43–52
87. Koivisto P, Peltonen K (2010) Analytical methods in DNA and protein adduct analysis. *Anal Bioanal Chem* 398:2563–2572
88. Nishikida K, Nishio E, Hannah RW (1995) Selected applications of modern FTIR techniques. Gordon and Breach/Kodansha Ltd., Tokyo
89. Dong A, Huang P, Caughey WS (1990) Protein secondary structures in water from second-derivative amide I infrared spectra. *Biochemistry* 29(13):3303–3308
90. Surewicz WK, Mantsch HH, Chapman D (1993) Determination of protein secondary structure by Fourier transform infrared spectroscopy: a critical assessment. *Biochemistry* 32(2):389–394
91. Vedantham G, Sparks HG, Sane SU, Tzannis S, Przybycien TM (2000) A holistic approach for protein secondary structure estimation from infrared spectra in H<sub>2</sub>O solutions. *Anal Biochem* 285(1):33–49
92. Prestrelski SJ, Tedeschi N, Arakawa T, Carpenter JF (1993) Dehydration-induced conformational transitions in proteins and their inhibition by stabilizers. *Biophys J* 65:661–671
93. Prestrelski SJ, Pikal KA, Arakawa T (1995) Optimization of lyophilization conditions for recombinant human interleukin-2 by dried state conformational analysis using Fourier transform infrared spectroscopy. *Pharm Res* 12(9):1250–1259
94. Costantino HR, Carrasquillo KG, Cordero RA, Mumenthaler M, Hsu CC, Griebenow K (1998) Effect of excipients on the stability and structure of lyophilized recombinant human growth hormone. *J Pharm Sci* 87(11):1412–1420
95. Van Straaten J, Peppas NA (1991) ATR-FTIR analysis of protein adsorption on polymeric surfaces. *J Biomater Sci* 2(2):113–121
96. Tunc S, Maitz MF, Steiner G, Vazquez L, Pham MT, Salzer R (2005) In situ conformational analysis of fibrinogen absorbed on Si surfaces. *Colloids Surf B Biointerfaces* 42:219–225
97. Byler DM, Susi H (1986) Examination of the secondary structure of proteins by deconvolved FTIR spectra. *Biopolymers* 25:469–487
98. Dong A, Hyslop RM, Pringle DL (1996) Differences in conformational dynamics of RNase A and S as observed by infrared spectroscopy and hydrogen-deuterium exchange. *Arch Biochem Biophys* 333:275–281
99. Zhang Y, Lewis RAH, Hodges RS, McElhaney RN (1992) FTIR spectroscopic studies of the conformation and amide hydrogen exchange of a peptide model of the hydrophobic trans-membrane  $\alpha$ -helices of membrane. *Biochemistry* 31(46):11572–11578
100. Dong A, Matsuura J, Allison SD, Chrisman E, Manning MC, Carpenter JF (1996) Infrared and circular dichroism spectroscopic characterization of structural differences in beta-lactoglobulin A and B. *Biochemistry* 35:1450–1457
101. Kaiden K, Matsui T, Tanaka S (1987) A study of the amide III band by FT-IR spectrometry of the secondary structure of albumin, myoglobin, and  $\gamma$ -globulin. *Appl Spectrosc* 41(2):180–184

102. Lewandowska K, Balachander N, Sukenik CN, Culp LA (1989) Modulation of fibronectin adhesive functions for fibroblasts and neural cells by chemically derivatized substrata. *J Cell Physiol* 141(2):334–345
103. Sukenik CN, Balachander N, Culp LA, Lewandowska K, Merritt K (1990) Modulation of cell adhesion by modification of titanium surfaces with covalently attached self-assembled monolayers. *J Biomed Mater Res* 24(10):1307–1323
104. Eikje NS, Aizawa K, Ozaki Y (2005) Vibrational spectroscopy for molecular characterisation and diagnosis of benign, premalignant and malignant skin tumours. *Biotechnol Annu Rev* 11:191–225
105. Mackanos MA, Contag CH (2010) Fiber-optic probes enable cancer detection with FTIR spectroscopy. *Trends Biotechnol* 28(6):317–323
106. Baker MJ, Gazi E, Brown MD, Shanks JH, Clarke NW, Gardner P (2009) Investigating FTIR based histopathology for the diagnosis of prostate cancer. *J Biophotonics* 2(1–2):104–113
107. Ostrowska KM, Garcia A, Meade AD, Malkin A, Okewumi I, O’Leary JJ, Martin C, Byrne HJ, Lyng FM (2011) Correlation of p16INK4A expression and HPV copy number with cellular FTIR spectroscopic signatures of cervical cancer cells. *Analyst* 136:1365–1373
108. Fu K, Griebenow K, Hsieh L, Klibanov AM, Langer R (1999) FTIR characterization of the secondary structure of proteins encapsulated with PLGA microspheres. *J Control Release* 58:357–366
109. Dong A, Jones LS, Kerwin BA, Krishnan S, Carpenter JF (2006) Secondary structures of proteins adsorbed onto aluminum hydroxide adjuvant: infrared spectroscopic analysis of proteins from low solution concentrations. *Anal Biochem* 351:282–289
110. Hoehne M, Samuel F, Dong A, Wurth C, Mahler HC, Carpenter JF, Randolph T (2010) Adsorption of monoclonal antibodies to glass microparticles. *J Pharm Sci* 100:123–132
111. Goormaghtigh E, Ruyschaert JM, Raussens V (2006) Evaluation of the information content in infrared spectra for protein secondary structure determination. *Biophys J* 90(8):2946–2957
112. Griebenow K, Klibanov AM (1995) Lyophilization induced reversible changes in the secondary structure of proteins. *Proc Natl Acad Sci U S A* 92:10969–10976
113. Chittur KK (1998) FTIR/ATR for protein adsorption to biomaterial surfaces. *Biomaterials* 19(4–5):357–369
114. Goldberg ME, Chaffotte AF (2005) Undistorted structural analysis of soluble proteins by attenuated total reflectance infrared spectroscopy. *Protein Sci* 14(11):2781–2792
115. Service RJ, Hillier W, Debus RJ (2010) Evidence from FTIR difference spectroscopy of an extensive network of hydrogen bonds near the oxygen-evolving Mn[4]Ca cluster of photosystem II involving D1–Glu, 65, D2–Glu312, and D1–Glu329. *Biochemistry* 49(31):6655–6669
116. Hastings G, Bandaranayake KM, Carrion E (2008) Time-resolved FTIR difference spectroscopy in combination with specific isotope labeling for the study of A1, the secondary electron acceptor in photosystem I. *Biophys J* 94(11):4383–4392
117. Barth A (2000) Review, the infrared absorption of amino acid side chains. *Prog Biophys Mol Biol* 74:141–173
118. Mäntele W (1993) Reaction-induced infrared difference spectroscopy for the study of protein function and reaction mechanisms. *Trends Biochem Sci* 18(6):197–202
119. Zscherp C, Barth A (2001) Reaction-induced infrared difference spectroscopy for the study of protein reaction mechanisms. *Biochemistry* 40(7):1875–1883
120. Barth A (2007) Infrared spectroscopy of proteins. *Biochim Biophys Acta* 1767(9):1073–1101
121. Lacob RE, Engen JR (2012) Hydrogen exchange mass spectrometry, are we out of the quicksand? *J Am Soc Mass Spectrom* 23:1003–1010
122. Norris AL et al (2009) NMR detected hydrogen–deuterium exchange reveals differential dynamics of antibiotic- and nucleotide-bound aminoglycoside phosphotransferase 3’-IIIa. *J Am Chem Soc* 131(24):8587–8594
123. Houde D, Berkowitz SA, Engen JR (2011) The utility of hydrogen/deuterium exchange mass spectrometry in biopharmaceutical comparability studies. *J Pharm Sci* 100:2071–2086

124. Narhi LO, Wood SJ, Steavenson S, Jiang Y, Wu GM, Anafi D, Kaufman SA, Martin F, Sitney K, Denis P, Louis JC, Wypych J, Biere AL, Citron M (1999) Both familial Parkinson's disease mutations accelerate alpha-synuclein aggregation. *J Biol Chem* 274:9843–9846
125. Baenziger JE, Méthot N (1995) Fourier transform infrared and hydrogen/deuterium exchange reveal an exchange-resistant core of  $\alpha$ -helical peptide hydrogens in the nicotinic acetylcholine receptor. *J Biol Chem* 270:29129–29137
126. Rath P, DeGrip WJ, Rothschild KJ (1998) Photoactivation of rhodopsin causes an increased hydrogen-deuterium exchange of buried peptide groups. *Biophys J* 74(1):192–198
127. French DL, Arakawa T, Li T (2004) Fourier transform infrared spectroscopy investigation of protein conformation in spray-dried protein/trehalose powders. *Biopolymers* 73(4):524–531
128. Yu S, Fan F, Flores SC, Mei F, Cheng X (2006) Dissecting the mechanism of Epac activation via hydrogen-deuterium exchange FT-IR and structural modeling. *Biochemistry* 45(51):15318–15326
129. Kamerzell TJ, Middaugh CR (2007) Two-dimensional correlation spectroscopy reveals coupled immunoglobulin regions of differential flexibility that influence stability. *Biochemistry* 46:9762–9776
130. Fabian H, Naumann D (2006) Methods to study protein folding by stopped-flow FT-IR. *Methods* 34(1):28–40
131. Reinstädler D, Fabian H, Backmann J, Naumann D (1996) Refolding of thermally and urea-denatured ribonuclease A monitored by time-resolved FTIR spectroscopy. *Biochemistry* 35(49):15822–15830
132. Panick G, Winter R (2000) Pressure-induced unfolding/refolding of ribonuclease A, static and kinetic Fourier transform infrared spectroscopy study. *Biochemistry* 39(7):1862–1869
133. Sethuraman A, Belfort G (2005) Protein structural perturbation and aggregation on homogeneous surfaces. *Biophys J* 88(2):1322–1333
134. Sharma S, Berne BJ, Kumar SK (2010) Thermal and structural stability of adsorbed proteins. *Biophys J* 99(4):1157–1165
135. Noda I (1986) Two-dimensional infrared (2D-IR) spectroscopy of synthetic and biopolymers. *Bull Am Phys Soc* 31:520–524
136. Noda I (1989) Two-dimensional infrared spectroscopy. *J Am Chem Soc* 111:8116–8118
137. Noda I (1990) Two-dimensional infrared (2D IR) spectroscopy, theory and applications. *Appl Spectrosc* 44:550–561
138. Sosa LDV et al (2011) The structure, molecular dynamics, and energetics of centrin–melittin complex. *Proteins* 79:3132–3143
139. Jiang Y et al (2011) Qualification of FTIR spectroscopic method for protein secondary structural analysis. *J Pharm Sci* 100(11):4631–4641
140. Kendrick BS et al (1996) Quantitation of the area of overlap between second-derivative amide I infrared spectra to determine the structural similarity of a protein in different states. *J Pharm Sci* 85(2):155–158
141. Keiderling TA, Silva RAGD (2002) Review: conformational studies of peptides with infrared techniques. In: Goodman M, Herrman G (eds) Houben-Weyl synthesis of peptides and peptidomimetics, vol 22Eb. Georg Thiem, New York, NY, pp 715–738
142. Chou KC (1983) Identification of low-frequency modes in protein molecules. *Biochem J* 215:465–469
143. Chou KC (1984) Low-frequency vibration of DNA molecules. *Biochem J* 221:27–31
144. Ellis DI, Goodacre R (2006) Metabolic fingerprinting in disease diagnosis: biomedical applications of infrared and Raman spectroscopy. *Analyst* 131(8):875–885
145. Callender R, Deng H (1994) Nonresonance Raman difference spectroscopy: a general probe of protein structure, ligand binding, enzymatic catalysis, and the structures of other biomacromolecules. *Ann Rev Biophys Biomol Struct* 23:215–245
146. Spiro TG, Gaber BP (1977) Laser Raman scattering as a probe of protein structure. *Annu Rev Biochem* 46:553–570

147. Tuma R (2005) Raman spectroscopy of proteins: from peptides to large assemblies. *J Raman Spectrosc* 36:307–319
148. Benevides, JM, Overman, SA, Thomas GJ (2004) Raman spectroscopy of proteins. *Curr Protoc Protein Sci* Chapter 17:Unit 17.8
149. Lednev IK, Karnoup AS, Sparrow MC, Asher SA (1999) Alpha-helix peptide folding and unfolding activation barriers: a nanosecond UV resonance Raman study. *J Am Chem Soc* 121:8074–8086
150. Siamwiza MN, Lord RC, Chen MC, Takamatsu T, Harada I, Matsuura H, Shimanouchi T (1975) Interpretation of the doublet at 850 and 830  $\text{cm}^{-1}$  in the Raman spectra of tyrosyl residues in proteins and certain model compounds. *Biochemistry* 14:4870–4876
151. Arp Z, Autrey D, Laane J, Overman SA, Thomas GJ Jr (2001) Tyrosine Raman signatures of the filamentous virus Ff are diagnostic of non-hydrogen-bonded phenoxyls: demonstration by Raman and infrared spectroscopy of *p*-cresol vapor. *Biochemistry* 40:2522–2529
152. Takeuchi H, Harada I (1986) Normal coordinate analysis of the indole ring. *Spectrochim Acta* 42A:1069–1078
153. Takeuchi H, Matsuno M, Overman SA, Thomas GJ Jr (1996) Raman linear intensity difference of flow-oriented macromolecules: orientation of the indole ring of tryptophan-26 in filamentous virus fd. *J Am Chem Soc* 118:3498–3507
154. Miura T, Takeuchi H, Harada I (1989) Tryptophan Raman bands sensitive to hydrogen bonding and side-chain conformation. *J Raman Spectrosc* 20:667–671
155. Miura T, Takeuchi H, Harada I (1991) Raman spectroscopic characterization of tryptophan side chains in lysozyme bound to inhibitors: role of the hydrophobic box in the enzymatic function. *Biochemistry* 30:6074–6080
156. Kitagawa T, Azuma T, Hamaguchi K (1979) The Raman spectra of Bence-Jones proteins. Disulfide stretching frequencies and dependence of Raman intensity of tryptophan residues on their environments. *Biopolymers* 18:451–465
157. Li H, Thomas GJ Jr (1991) Cysteine conformation and sulfhydryl interactions in proteins and viruses. I. Correlation of the Raman S-H band with hydrogen bonding and intramolecular geometry in model compounds. *J Am Chem Soc* 113:456–462
158. Li H, Wurrey CJ, Thomas GJ Jr (1992) Cysteine conformation and sulfhydryl interactions in proteins and viruses. 2. Normal coordinate analysis of the cysteine side chain in model compounds. *J Am Chem Soc* 114:7463–7469
159. Li H, Hanson C, Fuchs JA, Woodward C, Thomas GJ Jr (1993) Determination of the pKa values of active-center cysteines, cysteines-32 and -35, in *Escherichia coli* thioredoxin by Raman spectroscopy. *Biochemistry* 32:5800–5808
160. Takeuchi H, Kimura Y, Koitabashi I, Harada I (1991) Raman bands of N-deuterated histidinium as markers of conformation and hydrogen bonding. *J Raman Spectrosc* 22:233–236
161. Tasumi M, Harada I, Takamatsu T, Takahashi S (1982) Raman studies of L-histidine and related compounds in aqueous solutions. *J Raman Spectrosc* 12:149–151
162. Harada I, Takeuchi H (1986) Raman and ultraviolet resonance Raman of proteins and related compounds. In: Clark RJH, Hester RE (eds) *Advances in spectroscopy*. John Wiley & Sons, New York, NY, pp 113–175
163. Russell MP, Vohník S, Thomas GJ Jr (1995) Design and performance of an ultraviolet resonance Raman spectrometer for proteins and nucleic acids. *Biophys J* 68:1607–1612
164. Arzhantsev S, Vilker V, Kauffman J (2012) Deep-ultraviolet (UV) resonance Raman spectroscopy as a tool for quality control of formulated therapeutic proteins. *Appl Spectrosc* 66(11):1262–1268
165. Bai Y, Sosnick TR, Mayne L, Englander SW (1995) Protein folding intermediates: native-state hydrogen exchange. *Science* 269:192–197
166. Barron LD, Hecht L, Blanch EW, Bell AF (2000) Solution structure and dynamics of biomolecules from Raman optical activity. *Prog Biophys Mol Biol* 73:1–49



167. Benevides JM, Li T, Lu XJ, Srinivasan AR, Olson WK, Weiss MA, Thomas GJ Jr (2000) Protein-directed DNA structure. II. Raman spectroscopy of a leucine zipper bZIP complex. *Biochemistry* 39:548–556
168. Thomas GJ Jr, Benevides JM, Overman SA, Ueda T, Ushizawa K, Saitoh M, Tsuboi M (1995) Polarized Raman spectra of oriented fibers of A DNA and B DNA: anisotropic and isotropic local Raman tensors of base and backbone vibrations. *Biophys J* 68:1073–1088
169. Thomas GJ Jr (1999) Raman spectroscopy of protein and nucleic acid assemblies. *Annu Rev Biophys Biomol Struct* 28:1–27
170. Benevides JM, Thomas GJ Jr (1983) Characterization of DNA structures by Raman spectroscopy: high-salt and low-salt forms of double helical poly(dG-dC) in H<sub>2</sub>O and D<sub>2</sub>O solutions and application to B, Z and A-DNA. *Nucleic Acids Res* 11:5747–5761
171. Thomas GJ Jr, Agard DA (1984) Quantitative analysis of nucleic acids, proteins and viruses by Raman band deconvolution. *Biophys J* 46:763–768
172. Wen Z, Cao X, Phillips J (2010) Application of Raman spectroscopy in biopharmaceutical manufacturing. *Am Pharm Rev* 13:46–53
173. Cao X, Wen Z, Vance A, Torraca G (2009) Raman microscopic applications in the biopharmaceutical industry: in situ identification of foreign particulates inside glass containers with aqueous formulated solutions. *Appl Spectrosc* 63(7):830–834
174. Zhu F, Isaacs NW, Hecht N, Barron LD (2005) Raman optical activity: a tool for protein structure analysis. *Structure* 13(10):1409–1419
175. Wyatt PJ (1993) Light scattering and the absolute characterization of macromolecules. *Anal Chim Acta* 272:1–40
176. Goldberg DS, Bishop SM, Shah AU, Sathish HA (2011) Formulation development of therapeutic monoclonal antibodies using high-throughput fluorescence and static light scattering techniques: role of conformational and colloidal stability. *J Pharm Sci* 100(4):1306–1315
177. Wen J, Arakawa T, Philo JS (1996) Size exclusion chromatography with on-line light scattering, absorbance, and refractive index detectors for studying protein and their interactions. *Anal Biochem* 240:155–166
178. Mandel M (1993) Applications of dynamic light scattering to polyelectrolytes in solution. In: Brown W (ed) *Dynamic light scattering: the method and some applications*. Oxford, New York, NY, pp 319–371
179. Philo JS (2009) A critical review of methods for size characterization of non-particulate protein aggregates. *Curr Pharm Biotechnol* 10:359–372
180. Narhi LO (ed) (2013) *Biophysics of protein therapeutic development*. Springer, NY

# Chapter 4

## Diffraction and Scattering by X-Rays and Neutrons

Ivan Rayment

**Abstract** X-ray and neutron scattering methods have played a historically pivotal role in the development of molecular biophysics and biochemistry. Today a large proportion of papers that address a question in macromolecular structure carry with them a pictorial representation based on structural features derived from scattering methods. These images are often compelling and yet it is often difficult to assess the presented information based on pictures alone. The purpose of this chapter is to allow the non-expert to develop a sense of how much can be accepted or what can be learned from the images derived from scattering methods.

**Keywords** X-ray diffraction • Neutron diffraction • Small-angle scattering • Molecular structure

### 4.1 Introduction to X-Ray Scattering and Diffraction Methods

#### 4.1.1 *Theory of X-Ray Scattering*

X-ray scattering can be used to investigate many aspects of biological molecules depending on the nature of the interactions of the X-rays with the material of interest. The focus of this section is on the group of techniques that utilize elastic scattering of X-rays by electrons. This includes X-ray crystallography, fiber diffraction, and small-angle scattering.

---

I. Rayment (✉)

Department of Biochemistry, University of Wisconsin-Madison,  
433 Babcock Drive, Madison, WI 53706, USA  
e-mail: [ivan\\_rayment@Biochem.wisc.edu](mailto:ivan_rayment@Biochem.wisc.edu)

In the simplest terms X-rays scattering arises from the interaction of the electromagnetic wave of the X-rays with an electron. This causes the electron to oscillate, which in terms of classical electromagnetic theory allows absorption and reemission of the X-rays. The emitted radiation will have the same wavelength as the incident wave, but is scattered in all directions. The manner in which the scattered radiation from one electron interacts with that scattered from other electrons in the biological material determines the type of experiment. The long range order in the samples used for X-ray crystallography and fiber diffraction creates interference which leads to wide-angle coherent diffraction (a specialized form of scattering), which in turn leads to detailed molecular models. Conversely, in small-angle X-ray scattering (SAXS) the random orientation of the molecules in the sample limits the information in the scattered radiation and yields structural knowledge at the level of molecular envelopes. Each of these experimental approaches has a unique place in structural biology.

### ***4.1.2 X-Ray Crystallography***

Macromolecular crystallography is a well established and extensively utilized technique with a long history. In its early days it took many years to determine a single protein structure; today this can be accomplished within days or less once crystals have been obtained. Indeed, in many cases X-ray crystallographic studies are now a routine component of biochemical research. From a practical point of view many years of training or apprenticeship are no longer necessary to participate in a structural determination. There are numerous introductory texts available that cover all aspects of this discipline [3, 18, 35]. Furthermore, there are outstanding software packages available that facilitate structural determinations [1, 44] and graphical representation of the results [7, 29]. A list of software or applications that are useful for structural analysis can be found at the Protein Data Bank [40]. Thus, the purpose of this brief introduction is to describe the general limitations of this technique and what can easily be determined or accepted from an X-crystallographic study.

The work flow for a crystallographic study shown in Fig. 4.1 illustrates an important point. A crystallographic study starts from crystals. That is obvious from the name of the technique, but what is not immediately obvious is that the inherent quality and quantity of information in the final structural model are dependent on the intrinsic order of the crystals. This arises because X-ray crystallography is an imaging technique, where the experimental data forms the basis for creating an image of the distribution of electrons in the crystal lattice. The structural model is obtained by first fitting atoms into that electron density followed by iterative refinement against the original X-ray data. Confidence in the position of the model atoms is increased by the incorporation of stereochemical restraints during the refinement process, but fundamentally, the accuracy of the model is directly related to the quality of the crystals (not necessarily the size). Thus, there is a lot of benefit in growing good crystals. For this reason, protein expression, purification, and crystal growth occupy most of the time required for a modern structural study.

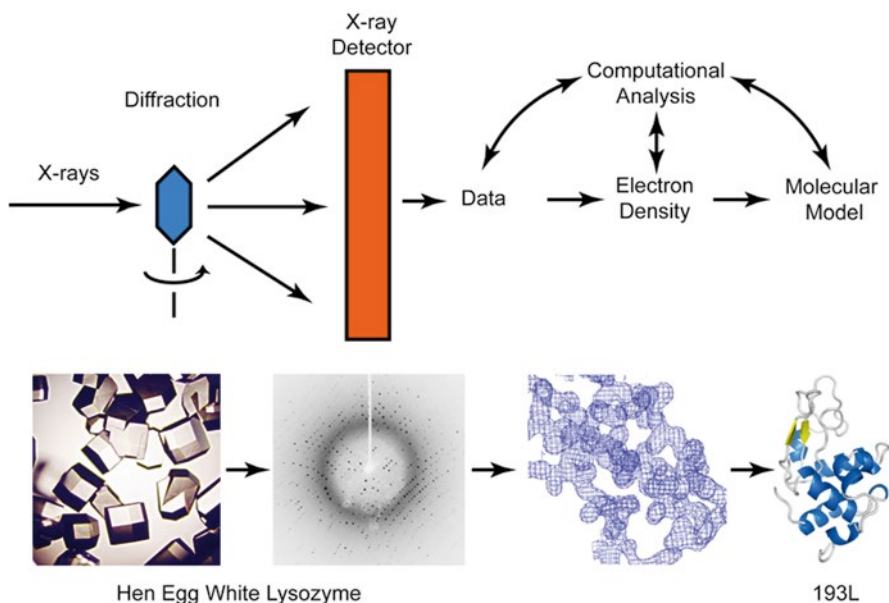


**Fig. 4.1** Work flow for an X-ray crystallographic study. The ribbon representation of lysozyme (PDB accession number 193L) was prepared with the program Pymol [7]

After the macromolecule has been purified and crystallized, the next step is data collection. In its simplest terms this involves rotating the crystal in a high intensity X-ray beam while recording the diffracted radiation with a detector. In 2011 80 % of structures deposited in the Protein Data Bank were determined with X-rays generated at synchrotron facilities as opposed to X-ray sources in home laboratories. There are primarily two reasons for the increased use of synchrotron radiation compared to 20 years ago when virtually all structures were determined with conventional X-ray sources. First, the intensity of the X-ray source is many orders of magnitude more intense than can be achieved with in-house X-ray generators. This increases the intensity of the scattered radiation which improves the signal to noise observed in the data collection statistics. Hence, synchrotron radiation dramatically reduces the time needed to record a data set (from days to minutes) and, in turn, allows very much smaller crystals to be studied. Second, synchrotron radiation provides a relatively straightforward way to solve the “phase problem” in crystallography discussed later.

A macromolecular crystal acts as a three-dimensional diffraction grating and yields a complementary three-dimensional array of X-ray diffraction maxima whose intensities can be transformed into an electron density distribution by a Fourier transform according to the formulae below

$$\rho(x,y,z) = \sum_{h=-\infty}^{\infty} \sum_{k=-\infty}^{\infty} \sum_{l=-\infty}^{\infty} |F(hkl)| e^{i\phi(hkl)} e^{-i2\pi(hx+ky+lz)} \quad (4.1)$$

**Table 4.1** Guide to the interpretation of “resolution”

Resolution (Å)	Structural implication	Data/parameter ratio <sup>a</sup>
>5	Positions of $\alpha$ -helices might be correct, but the location of individual atoms is subject to question	0.15
3–5	Protein fold might be correct, but positions of side chains are uncertain. A hydrogen bonding pattern based on the electron density map is meaningless	0.7–0.15
2.5–3.0	Fold likely correct, but surface loops might be ill-determined, which might lead to an incorrect model if the protein is not homologous to a known structure. Detailed hydrogen bonding pattern can be questionable, especially for side chains	1.2–0.7
2.0–2.5	Acceptable hydrogen bonding pattern. Water structure and ligands visible	2.4–1.2
1.5–2.0	Well-defined hydrogen bonding pattern with few errors in the side chain conformations	5.6–2.4
0.7–1.5	Atoms become resolved. Many multiple conformations become visible	5.5–5.6

<sup>a</sup>Theoretical value based on 50 % solvent in the crystalline lattice assuming four parameters per atom ( $x, y, z$  and a temperature factor)

where  $\rho(x, y, z)$  is the electron density at a position  $x, y, z$  in the crystals and  $|F(hkl)|$  is a structure factor amplitude derived from the X-ray diffraction intensities.  $\Phi(hkl)$  is the phase of the diffracted beam relative to the incoming radiation, which is lost when the data is recorded. This is unfortunate, because the phase term contributes strongly to resulting electron density maps. The loss of the phase information is known as the “phase problem” in X-ray crystallography. This simple relationship shows that all of the X-ray data contributes to the electron density at every point in the crystal lattice. The level of detail in the electron density depends on the extent of the X-ray diffraction, where this is defined in terms of the “resolution” of the data and is normally defined with units of Å. In simple terms, details finer than  $0.61 \times$  “resolution” cannot be resolved within an electron density map [14]. Strictly speaking the resolution of the data is related to the maximum angle of recorded diffraction according to the expression

$$\frac{1}{\text{resolution}} = \frac{2 \sin \theta}{\lambda}$$

where  $2\theta$  is the scattering angle and  $\lambda$  is the wavelength of the X-rays. The reported resolution provides a hint of what might be expected from an X-ray structural determination as summarized in Table 4.1. Thus, if the purpose of the structure is to understand ligand interactions, a resolution of at least 2.5 Å is required, whereas if the fold alone will suffice to answer the biological question, 3 Å resolution might be adequate. A resolution better than 2.0 Å is needed before any significant atomicity can be observed. The term “atomic resolution” is best reserved for structures with a resolution of better than 1 Å.

The resolution defines the amount of detail that can in principle be derived from the experimental data, but there are two other components that influence the reliability of the resultant structure. These are the quality of the X-ray data itself, and the thoroughness of the structural refinement. Both of these are typically judged in terms of  $R_{\text{factors}}$ . The quality of the X-ray data is typically defined by

$$R_{\text{merge or sym}} = \sum_{hkl} \frac{|I_{hkl} - \bar{I}_{hkl}|}{I_{hkl}}$$

where  $R_{\text{merge}}$  describes how well multiple measurements of the same or symmetry-related X-ray diffraction intensity ( $I_{hkl}$ ) data merge together. This typically has a value of less than 0.1 for high quality data, but is often higher for weakly diffracting crystals. The quality of the final refined structure is often judged by three other numbers,  $R_{\text{factor}}$ ,  $R_{\text{work}}$ , and  $R_{\text{free}}$ , which take the form

$$R_{\text{factor, work, or free}} = \sum_{hkl} \frac{|F_o - \bar{F}_c|}{F_o}$$

$R_{\text{factor}}$ ,  $R_{\text{work}}$ , and  $R_{\text{free}}$  are used to assess the quality of the final model as measured by the similarity between the observed data and that calculated from the model. Essentially all of the models in the Protein Data Bank have been refined against the observed data.

What can be expected from a model at a given resolution is described in Table 4.1. From the point of view of refinement this table presents an interesting problem because, except for very high resolution structures, there is insufficient data to refine a model against the X-ray data alone. Examination of the X-ray diffraction pattern shown in Fig. 4.1 suggests that X-ray crystallography can provide a very large number of independent data points since each spot or reflection on the image represents a unique experimental measurement. Ironically, the number of experimental observations is usually far less than the number of parameters required to independently describe the position of atoms in a protein. The minimal number is four parameters per atom, where these consist of three positional parameters ( $x$ ,  $y$ , and  $z$ ) and one thermal parameter to describe the movement of the atom in the crystalline lattice. The ratio between the data and number of parameters must be substantially greater than one to allow independent refinement of the model against that data.

The problem of insufficient data is overcome by including stereochemical restraints such as bond distances, conformational angles, and nonbonding contacts. The shortage of data means that it is possible to over-fit a model to the data. A measure of over-fitting is given by  $R_{\text{free}}$  [4]. This is the  $R_{\text{factor}}$  for 5–10 % of the data that has been excluded at random from the refinement calculations. For example, a test case in which a cellular retinoic acid-binding protein type II was deliberately built backwards into the electron density maps yielded an  $R_{\text{work}}$  of 0.21 with good geometry, but an  $R_{\text{free}}$  of 0.62, which exceeds the value anticipated for a random structure [15]. Although this is an extreme case, it illustrates that large disparities between the

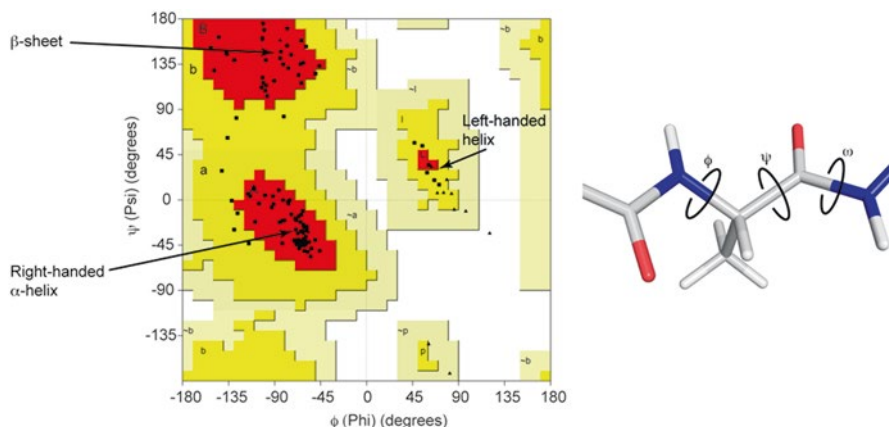


**Fig. 4.2** Ramachandran plot for hen egg white lysozyme (PDB accession number: 193L). The conformational angles for non-glycine residues (*black squares*) in well-defined X-ray structures should reside within or close to the fully allowed regions of the Ramachandran plot as indicated by the *arrows*

$R_{\text{work}}$  and  $R_{\text{free}}$  indicate that something is amiss with the model or experimental data. In practice  $R_{\text{free}}$  is 2–5 % higher than  $R_{\text{work}}$  for a satisfactory model. Greater differences indicate that something is amiss with the model or experimental data.

There is considerable difference of opinion in what a satisfactory  $R_{\text{work}}$  should be for a satisfactory model. In general, models derived from high quality data ( $R_{\text{merge}} < 0.08$ ) should have an  $R_{\text{work}}$  of considerably less than 0.20. Lesser quality data will generally yield a model with an  $R_{\text{work}}$  of 0.2–0.24. In general,  $R_{\text{work}}$  should be less than 0.25. In those cases where a high  $R_{\text{factor}}$  is reported for a structure accompanied by high quality data it can be assumed that either the refinement is incomplete or there is something wrong with the analysis. The Protein Data Bank may also list an overall refinement  $R_{\text{factor}}$  where this is the statistic for the final round of refinement in which both the working set and test data set combined. It is difficult, and perhaps incorrect, to assess the correctness of a model based on a single global parameter. Consideration of the stereochemistry and quality of the localized electron density will almost always lead to a better assessment of the true information content of the model.

Comparison of the stereochemistry of the model with standard parameters is an important measure of the quality of the coordinates. This is usually listed as deviations of bond distances and angles from the normal values, but is easiest to see for proteins on a Ramachandran plot. This displays the distribution of backbone conformational angles ( $\psi$  and  $\phi$ ) on a background that indicates the conformationally allowed regions. A good structure shows a tight distribution of angles falling within the conformationally allowed space adopted by  $\alpha$ -helices,  $\beta$ -strands, turns, and random-coil (Fig. 4.2). All of the information necessary to assess the geometry of an X-ray structure is available from the Protein Data Bank [40, 45]. This database contains a wealth of statistical information and a large array of tools and links that

help in evaluating the quality of a structural model. Numerous other servers exist of which the MolProbity and PDBsum servers are particularly useful sources for structural validation and provide scoring functions that help the user assess the quality of models [6, 21, 28].

Statistics are certainly useful for validating macromolecular structures, but visual tools are especially compelling since structural studies lead to visual representations. At the most basic level examination of the electron density superimposed on the model is one of the best methods for assessing the validity of a model. For this reason, many publishers still demand a figure that shows electron density for a section of the model or for a ligand. This should always be presented from an “omit map” in which the region of the molecule shown was omitted from the refinement and phase calculation. This is necessary in order to remove model bias and is particularly important for verification of the correct modeling for a ligand. As a general rule if the electron density does not cover or fit the atoms under consideration the location of those atoms is not supported by the experimental data. Real-space correlation functions are also a useful method of mathematically defining how well a model matches the electron density and can identify unreliable regions of a model.

To summarize, it is important to consider the limitations of a crystallographic model in the context of the statistical descriptors that assess quality, not only at a global level, but also at the level of individual atoms in the macromolecule. Visual representations provided by graphical applications such as Pymol [7] do not necessarily provide any indication of quality.

The manner in which the phase problem was solved can also influence an assessment of the correctness of a structure. As noted earlier, X-ray diffraction data is the result of constructive interference of radiation scattered from a three-dimensional array of atoms. The scattered radiation has both an amplitude and a phase. The amplitudes can be measured, but the phase information is lost; however, the latter is necessary in order to reconstruct an image of the electron density from the amplitudes (4.1). There are two fundamentally different ways that phases are obtained. Either experimental phases are obtained or phases are estimated from a preexisting structure. Experimental phases are obtained by perturbing the diffraction through the inclusion of heavier atoms in the crystal lattice. Determination of the location of the heavier atoms leads to a structural solution for the entire macromolecule. This is the basis for multiple isomorphous replacement and anomalous scattering techniques. Multiple isomorphous replacement with heavy metals was the first method used to determine X-ray structures. Today, most experimental phases are determined with anomalous scattering techniques that utilize synchrotron radiation to determine phases from the location of elements such as selenium in selenomethionine-substituted proteins which replaces the sulfur of methionine. Experimental phasing yields an unbiased structural determination and is the most powerful way for obtaining new structures, but it does require crystals that contain a heavy atom substitution or one that absorbs X-rays at an accessible wavelength.

The alternative way to solve the phase problem is to use the structure of a related macromolecule to derive phases. This is known as “molecular replacement” and has been used to determine more than half the structures in the Protein Data Bank.



With this approach care must be taken to remove the “model bias” introduced from the search structure [9], which is most easily achieved for high resolution and high quality data. The normal metrics for structural quality described above should provide guidance on whether a molecular replacement structure is meaningful, but examination of the electron density for the places that differ in the target and search model is often the best indication that model bias has been removed.

As of summer 2012 there were over 80,000 X-ray structures in the Protein Data Bank. Although the majority of the coordinates describe proteins, X-ray crystallography is also useful to determine the structure of DNA, RNA, and carbohydrates, as well as hetero-polymeric complexes comprising, for example, protein and RNA. Thus, it is appropriate to ask whether there are any inherent limitations to X-ray crystallography. The obvious limitation is that the material must form a well-ordered crystalline lattice. The question is whether the need for a crystal lattice limits the problem that can be investigated or the information that can be derived.

Over the years there has been an extensive discussion over whether the conformation of a macromolecule captured in a crystal lattice reflects the conformation in solution. In many cases enzymes are active in the crystal lattice so that it is generally accepted that the structure of domains seen in a crystal reflects the structure in solution. Clearly, the conformation of loops involved in crystal contacts may not represent those favored in solution, but a greater issue surrounds macromolecules that contain multiple domains whose relationships with each other influence biological function. In this case, it is quite likely that the arrangement of domains seen in a crystal lattice could be different from the “active” state. The solution to this problem is typically gained from determining the structures of the same macromolecule, but in different states and under different conditions, and perhaps complexed with ligands or interacting partners.

A fundamental limitation to almost all X-ray structures is that they represent a time-averaged view of the contents of the crystal. Consequently, many of the dynamic properties of individual macromolecules are lost. The exception to this general rule is time-resolved X-ray crystallography that uses exceedingly short exposures (nanoseconds or less) to follow coordinated reactions within a crystal lattice [32]. There is some information about movement embedded within the temperature factors associated with every atom, but in an absolute sense this information is inaccurate because temperature factors accommodate other crystallographic issues such as lattice disorder, radiation damage, absorption effects, and errors in modeling.

The sizes of molecules that have been crystallized have steadfastly increased since the first structures of myoglobin and hemoglobin. The structures of the 80S ribosome represent the largest macromolecular assemblies whose structures have been determined by X-ray crystallography with molecular weights of over four million [2], but doubtless the structures of larger molecules will be determined. Thus, size is not necessarily a limitation, though in general, as the contents of the crystal lattice grow larger the angular extent or resolution of the X-ray data is lower.

At the end of the day it can be argued that any structural information about a macromolecule is better than none. An X-ray crystallographic structure does not

answer all of the questions and it certainly does not establish biological relevance. It does however provide a molecular framework for understanding the relationship between sequence and function. Consideration of the resolution and quality of the data within the context of how well the structure fits into the biological problem will allow a realistic appreciation of the true information content of a structural model. An X-ray structure should complement existing biological data. A structure might lead to new interpretations, but these hypotheses must mirror fundamental principles of chemistry, biochemistry, and physics. The major errors that have occurred in X-ray crystallography biology have all deviated from these principles. An X-ray structure should be judged by these criteria rather than the aesthetic quality of the visual representations of the structures generated with programs such as Pymol or Chimera [7, 29].

### ***4.1.3 Diffraction from Noncrystalline Materials***

X-ray scattering and diffraction from noncrystalline materials is a powerful source of structural knowledge that complements that available from X-ray crystallography. It allows the study of fibrous materials that are not amenable to crystallization, and can provide information about assemblies in solution (small-angle and wide-angle scattering). These techniques have become much more accessible with the development of high intensity synchrotron facilities and improved detectors [42]. Synchrotron sources are generally preferred since the scattered X-ray radiation from noncrystalline materials is usually very weak. From the perspective of this brief introduction the question that must be asked is: what can be gained or expected from application of these techniques? The unique contributions of fiber diffraction and small-angle scattering to the study of biological materials are described below.

### ***4.1.4 Fiber Diffraction***

Many fibrous biological materials are composed of helical biopolymers. These are not amenable to crystallization, but can still adopt ordered arrays due to their tendency to line up in parallel arrays. These fibers can provide important structural information by X-ray diffraction, even though they are rotationally disordered around the fiber axis. Indeed, fiber diffraction has played a pivotal role in the development of structural biology. The early studies of keratin (wool) (Fig. 4.4a) by William Asbury provided the vital information necessary for the definition of the  $\alpha$ -helix by Pauling, Corey, and Branson [27]. Likewise, fiber diffraction patterns from DNA by Rosalind Franklin (Fig. 4.4b) as interpreted by Crick and Watson played a central role in the discovery of the genetic code.

In principle, the experimental arrangement for fiber diffraction is quite simple (Fig. 4.3), because a few orientations of the fiber should be sufficient to yield the

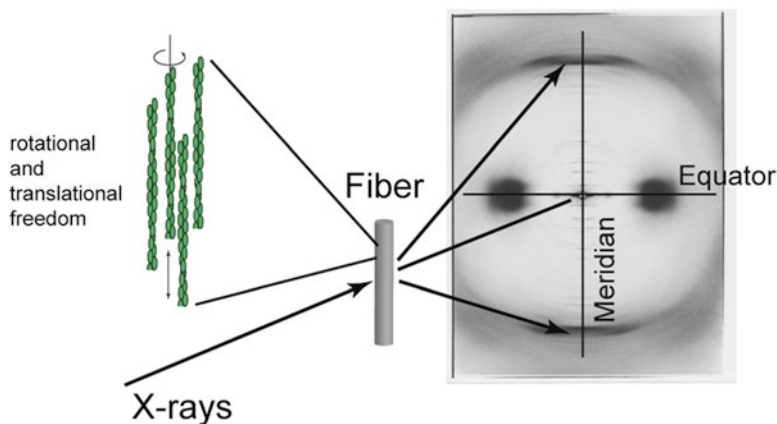


**Fig. 4.3** Experimental arrangement for fiber diffraction

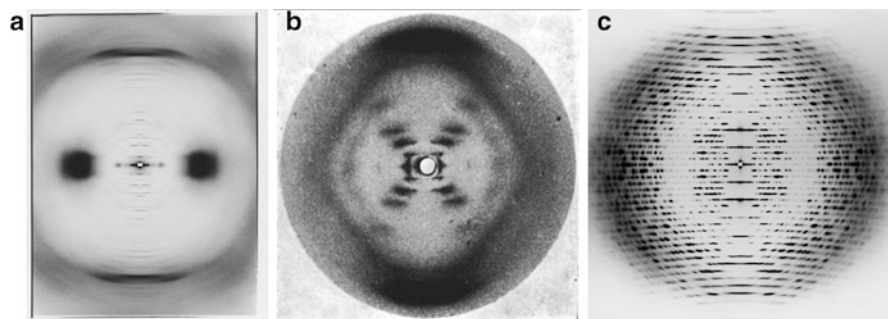


**Fig. 4.4** X-ray fiber diffraction patterns from (a)  $\alpha$ -keratin from a Crested African Porcupine (*Hystrix cristata*) (courtesy of Bruce Frasier and David Parry), (b) B-DNA [11], and (c) tobacco mosaic virus (Gerald Stubbs, Vanderbilt University, [25])

diffraction data. In practice, modern instrumentation is highly sophisticated because the diffraction is weak and the samples are often very small. The use of synchrotron radiation coupled with high resolution CCD-based detectors or, more recently, photon-counting devices has allowed the study of wide range of biopolymers, including simple polypeptides, polynucleotides, cytoskeletal filaments (actin and myosin), filamentous viruses, and larger biological assemblies such as muscle fibers. Synchrotron radiation now provides X-ray beams that are just a few microns in diameter, which permits direct examination of biological materials.

The information content of the diffraction pattern depends on the longitudinal order in the polymeric material and relative orientation of the fibers within the sample (Fig. 4.4). In the initial studies of wool which is built from intermediate filament proteins, the diffraction pattern revealed only diffuse diffraction maxima along the equator related to the packing of the intermediate filaments and a strong diffraction

maximum along the meridian at a spacing of 5.1 Å. The peak at 5.1 Å spacing led to some confusion in the development of the model for the  $\alpha$ -helix since the helical repeat of a standard  $\alpha$ -helix is 5.4 Å. (The history of the  $\alpha$ -helix has been elegantly summarized by David Eisenberg [10].) This discrepancy was resolved by Francis Crick who proposed that  $\alpha$ -keratin contains dimeric coiled-coils in which the  $\alpha$ -helices are inclined at an angle of 20° to the coiled-coil axis so that the apparent repeat along the fiber axis is reduced compared to that of a canonical  $\alpha$ -helix. This is a good example of the importance of starting from the correct structural model when interpreting limited amounts of experimental data.

In most fiber diffraction studies there is insufficient experimental data to determine the three-dimensional structure of the protein or macromolecular assembly from first principles. Thus, prior structural knowledge is usually needed in order to develop a model for a filamentous macromolecular assembly. Typically, an existing structure for a subunit is fitted to the diffraction data to provide the overall orientation of the molecule within the fiber. The difficulty arises when the molecule undergoes a conformational change when it polymerizes to become a filament. This problem can be overcome by molecular dynamics and energy minimization; however, it is not easy for the nonspecialist reader to appreciate the uniqueness of the structural solution or the coordinate error for the model. In the first instance, the resultant models should show tight distributions of conformational angles as assessed by a Ramachandran plot (Fig. 4.2) and the intermolecular interactions within the filament must accommodate the hydrogen bonding characteristics of the main-chain atoms and side chains. Furthermore, hydrophobic residues that are normally found in the buried intermolecular interfaces should be in close proximity to residues of the same character. Despite its limitations, fiber diffraction provides access to unique structural information, which is particularly evident in studies of amyloid proteins.

Amyloid fibrils have been implicated in numerous pathological conditions including, Alzheimer's disease and prion infections such as Creutzfeldt–Jakob disease. These fibrils occur when a protein that is normally soluble folds aberrantly to become an insoluble aggregate that exhibits cross- $\beta$  structure [26, 37, 41]. These protein aggregates have proven difficult to study because the proteins are completely insoluble. The term “cross- $\beta$ ” arises from the characteristic diffraction pattern. This includes a strong meridional intensity at around  $\sim 4.7$  Å coupled with a weaker equatorial intensity at  $\sim 10$  Å. The intense reflection at  $\sim 4.7$  Å (cross- $\beta$  diffraction) arises from the mean separation of hydrogen-bonded  $\beta$ -strands that lie perpendicular to the fiber axis and form sheets that lie parallel to the axis. The equatorial intensity reflects the packing of the  $\beta$ -sheets parallel to the fibril axis. Detailed examination of the diffraction pattern reveals that many fibrils exhibit a similar structure even though there is often negligible sequence similarity between sections that form amyloids [37]. Fiber diffraction places constraints on the organization of the amyloids in the fiber that is not available by other means. For example, a fiber diffraction study of infectious natural prions and recombinant amyloids showed that these assemblies are not alike at low resolution, even though they both show the characteristic cross- $\beta$  meridional diffraction at 4.75 Å (Fig. 4.5). This has important implications for understanding the structural properties of infectious prion proteins.

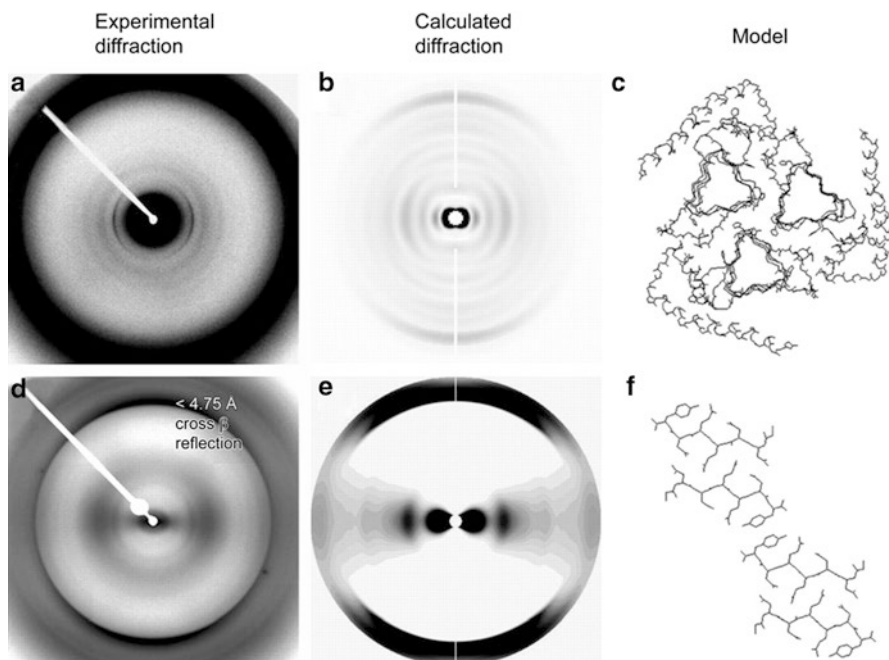


**Fig. 4.5** Comparison of observed and calculated diffraction patterns for natural Syrian hamster and recombinant prion proteins which can be modeled by  $\beta$ -helical and stacked-sheet amyloid models, respectively. (a, b) Experimental and calculated diffraction patterns from natural Syrian hamster prion protein (SHaPrP 27–30). (c) Disordered noncrystalline trimeric  $\beta$ -helical model used to calculate data in (b). (d, e) Experimental and calculated diffraction patterns from a recombinant Syrian hamster amyloid. (f) Stacked-sheet model used to calculate data in (e). In both models, the filament axis is *perpendicular* to the figure plane. Reproduced with permission from [43]

In some cases, such as ordered gels of filamentous viruses, the information content derived from fiber diffraction is very high (Fig. 4.4c) and permits an *ab initio* structural determination [36]. The first example of this was the structural determination of tobacco mosaic virus [25]. Independent phasing by the use of heavy atom derivatives coupled with molecular dynamics refinement yielded not only the interactions between subunits in the helical filament, but also the path and binding determinants for the enclosed RNA (Fig. 4.6). Although a partial structure of the individual protein subunit was known previously from the structure of a symmetric disk, this information was not required to determine the structure of the virus from the fiber diffraction data.

Highly ordered gels have also been obtained for actin and bacterial flagella. These share with filamentous viruses the property that they are built from many identical subunits that are organized in a helical manner within the filament. The key to all of these types of study is obtaining a well-ordered sample. The use of magnetic fields of the order of 10 T has proven to be increasingly important for obtaining ordered fibers [36, 46].

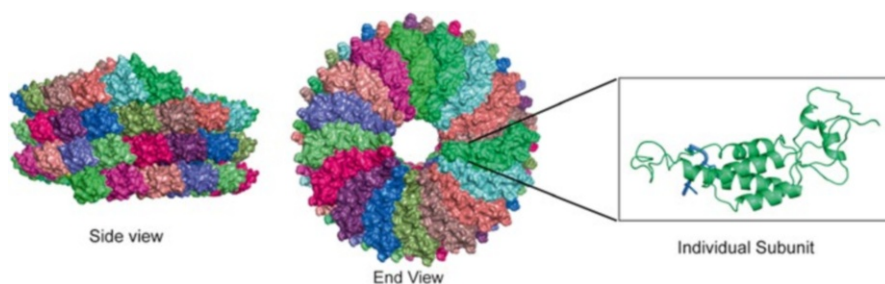


**Fig. 4.6** Structure of tobacco mosaic virus determined by fiber diffraction [25] (PDB accession number 2TMV). In this instance, the fiber diffraction pattern (Fig. 4.4c) yielded sufficient information to not only trace the polypeptide chain, but also define the path of the RNA for this viral assembly

X-ray fiber diffraction has played a central role in understanding the molecular transitions during muscle contraction. X-ray diffraction is the only technique that can provide molecular structural information from muscle in its physiological hydrated state. Indeed, this technique can follow the changes that occur during muscle contraction [30, 34]. As might be expected from the complexity of muscle, most of the diffraction is limited to low resolution and is very weak. This demands high intensity X-ray sources that are only available at synchrotron facilities and very small X-ray beams that can match the size of a single muscle fiber. X-ray microbeams have permitted studies of muscle contraction from living *Drosophila* during tethered flight [8].

## 4.2 Small-Angle Scattering

Constructive interference of scattered X-rays from ordered or partially ordered macromolecules is the basis of X-ray crystallography and fiber diffraction. This yields an enormous amplification of the signal compared to the scattering from an ensemble of molecules that lack any positional order. Even so, scattering from solutions of molecules in solution can provide unique structural information about the size, shape, and oligomerization state of a macromolecule. This is the rationale behind small-angle scattering measurements. Excellent reviews of the fundamentals of small-angle and wide-angle scattering and application to macromolecules are found in ref. [16] and in refs. [31, 42] respectively.

Both X-ray and neutron low-angle scattering provide information at 10–20 Å resolution. This level of detail encompasses the shape and oligomerization state of the macromolecule. It has the benefit that it encompasses the molecular size range that lies between that readily accessible by NMR and electron microscopy. Furthermore, the experimental requirements are quite simple. A dilute sample of the macromolecule (low micromolar concentrations) is exposed to a collimated or

focused beam of radiation. The key requirements are that the macromolecule must be monodisperse and stable in solution. The stability is less important for experiments performed with synchrotron radiation since these can be performed in seconds, but is much more of a concern for data collected with conventional X-ray sources.

Solution X-ray scattering from macromolecules in solution is exceedingly weak compared to the scattering from the solvent. At low resolution the signal is derived from the contrast between the solvent and protein. For pure water, the average electron density is  $\sim 0.33$  electrons/ $\text{\AA}^3$ , whereas proteins are typically around  $0.44$  electrons/ $\text{\AA}^3$ . Obviously, this is higher for RNA and DNA. The signal is obtained by subtracting the scattering of a buffer sample from that of the biological sample. This must be done very precisely. The resultant scattering curve,  $I(q)$ , is radially symmetric because the molecules are randomly oriented in solution.  $I(q)$  is the intensity of the scattering as a function of scattering angle, where  $q = (4\pi \sin \theta) / \lambda$ .  $q$  is known as the momentum transfer vector.

The equation that describes the scattering from the electron density of a homogeneous sample is given by:

$$I(q) = 4\pi \int_0^{D_{\max}} P(r) \frac{\sin(qr)}{qr} dr$$

where  $P(r)$  is the pair density distribution function (PDDF) and  $D_{\max}$  is the maximum distance present in the sample. One of the simplest items that can be derived from small-angle scattering is the radius of gyration ( $R_G$ ). At low angles the scattering can be described by the Guinier approximation:

$$I(q) = I(0) \exp(-q^2 R_G^2 / 3)$$

This is typically plotted as  $\ln[I(q)] = \ln[I(0) - q^2(R_G^2/3)]$  (Fig. 4.7b), where the slope will yield the radius of gyration, and the extrapolation to zero scattering angle can provide the molecular weight of the species in solution. For most globular biological macromolecules, this analysis should only be performed in the region closest to the beam stop or center of the scattering pattern where the product  $qR_G$  is less than 1.3, although the range is considerably smaller for asymmetric molecules. This type of analysis can be performed very rapidly and has been utilized for well over 55 years [12]. It provides valuable first sight into the oligomerization state of the molecule, but the complete scattering pattern contains considerably more information.

The small-angle scattering typically extends well beyond the range of the Guinier approximation, where this part of the profile is controlled by the shape of the molecular envelope (Fig. 4.7a). The molecular envelope controls the profile because the scattering signal is derived from the difference between the average electron density of the solute molecules and the bulk solvent. The variation in electron density within a macromolecule is lost at low resolution. Thus, SAXS is ideal for identifying or characterizing unfolded proteins. This is often evaluated from a Kratky plot (Fig. 4.8)



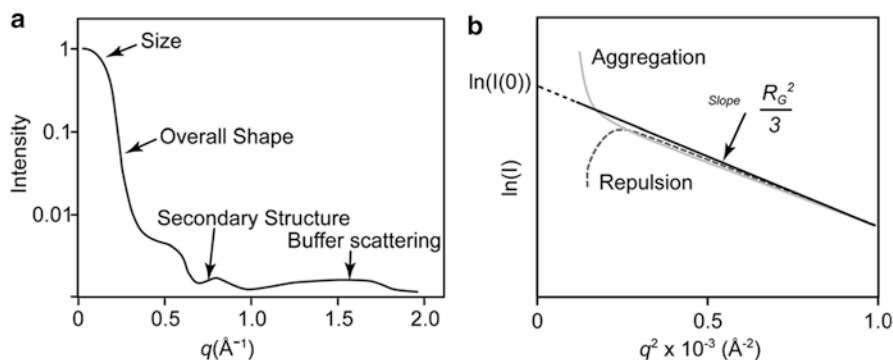
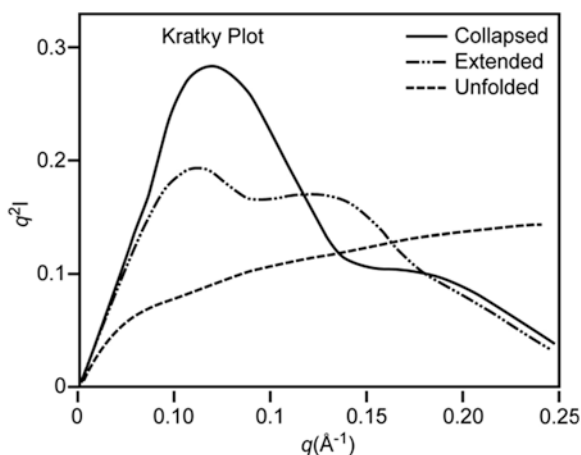


**Fig. 4.7** Small-angle X-ray scattering (SAXS) data. (a) X-ray scattering intensity  $\log(I)$  vs. scattering angle ( $q$ ). Arrows point to regions of the plot that correspond to structural information. (b) A Guinier plot,  $\ln(I)$  vs.  $q^2$ , provides information about the size of the molecule and the quality of the sample. For a globular particle, this plot should be linear at small values of  $q$  ( $q_{\max} \cdot R_G < 1.3$ ). A sharp drop-off in the plot is indicative of interparticle repulsion while an upward curve is indicative of aggregation. Dashed line indicates data extrapolation, based on the Guinier equation, to  $q=0$  (arrow). Reprinted with permission from [22]

**Fig. 4.8** The Kratky plot,  $q^2 I$  vs.  $q$ , indicates the extent of folding within a macromolecule. Molecules with an extensive tertiary fold (collapsed) result in a different profile than non-globular molecules (extended) or unfolded molecules



in which  $q^2 I$  is plotted against  $q$ . Globular proteins typically show a parabola-shaped plot, whereas unstructured proteins do not exhibit a peak and are approximately linear with respect to  $q$  at high values of  $q$ .

Careful analysis of the scattering profile can provide unique information about the shape of the molecular envelope. This is often analyzed in terms of the pair distribution function  $P(r)$  (also known as the PDDF), which describes the spherically averaged distribution of intermolecular vectors within the molecular envelope and is somewhat analogous to the crystallographic Patterson function, a Fourier calculated with interatomic vectors. The nature of the PDDF varies considerably



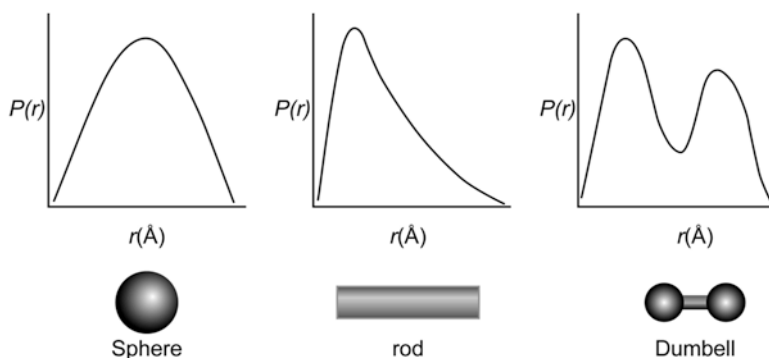


**Fig. 4.9** Theoretical examples of pair distance distribution functions

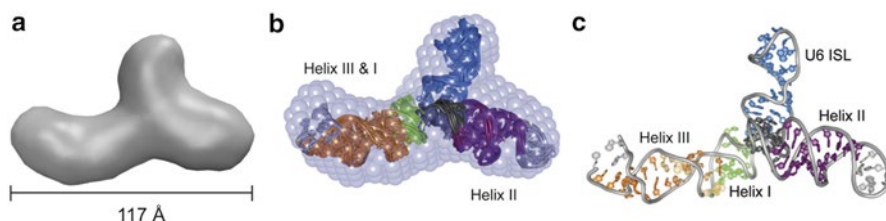


**Fig. 4.10** Combination of SAXS with NMR in the structural determination of RNA. **(a)** The ab initio structure of U2/U6 spliceosome RNA determined by SAXS. **(b)** The fit of the ten lowest energy models determined from the NMR to the SAXS envelope. **(c)** The lowest energy model of that ensemble. Modified with permission from [5]. The SAXS data was used both to select the best models from the ensemble of NMR coordinates and as a restraint in the final model refinement

depending on the overall shape of the molecule (Fig. 4.9), and can be calculated through a Fourier transform of the scattering curve. As important is the fact that a theoretical scattering curve can be calculated by a Fourier transform of a  $P(r)$  computed from a trial model and compared with the experimental function.

Construction and validation of low-resolution three-dimensional models from SAXS data is the focus of most current applications of SAXS as reviewed in [20]. Most ab initio approaches create a simplified model for the macromolecular envelope based on dummy atoms or amino acid residues (Fig. 4.10a). This provides insight into the molecular shape, but the number of statistically independent data points for most SAXS curves is quite limited. Consequently, the most successful applications of SAXS utilize this data in conjunction with other macromolecular information [33]. This often takes the form of building solution-state models starting from domains or components that have been determined independently at high resolution. SAXS data has also proved to be an enormously valuable restraint in NMR structural determinations [20, 33]. An example of the latter is seen in the structural determination of the U2/U6 snRNA complex (Fig. 4.10) [5].

Assessment of the quality of the structural models derived from SAXS is an important component of any study that utilizes this technique [31]. Once an envelope has been derived, the fit of an ensemble of high resolution models to that envelope is usually judged by its normalized spatial discrepancy (NSD) [17]. For satisfactory models NSD should be less than 0.8. Several criteria have been developed for measuring how well the experimental data itself fits the model [31]. One of these is the normalized discrepancy function  $\chi^2$ , which is defined as:

$$\chi^2 = \frac{1}{N_p - 1} \sum_i \left[ \frac{I(q_i) \exp - cI(q_i)_{calc}}{\sigma(q_i)} \right]$$

where  $c$  is a scaling factor,  $\sigma(q_i)$  is the experimental error, and  $N_p$  is the number of observations. This function is minimized during the construction of ab initio models, and ideally, should be around 1.5 for an optimal model. Values of  $\chi^2$  less than unity indicate over-fitting of the model to the data [20, 38].

### 4.3 Neutron Scattering and Diffraction Methods

Neutron scattering provides complementary information to that derived from X-ray scattering. The major difference is that neutrons are scattered by the nucleus while X-rays are scattered by electrons. Furthermore, the extent of scattering is related to the nuclear structure rather than just the number of nucleons, where this is defined in terms of a scattering length for each atom. For example, hydrogen, deuterium, carbon, nitrogen, and oxygen have scattering lengths of  $-3.7$ ,  $6.7$ ,  $6.7$ ,  $9.4$ , and  $5.8 \times 10^{-13}$  cm, respectively. This means that hydrogen and deuterium, in an absolute sense, scatter with similar efficiency to the other atoms in the polypeptide chain, and implies that hydrogen and deuterium atoms should be readily visible in Fourier synthesis maps (Fig. 4.11a, b). This is in contrast to electron density maps derived from X-ray crystallography where hydrogen atoms are usually not observed, except in ultrahigh resolution X-ray studies, due to the weak scattering power of a single electron. The negative sign for the scattering length for hydrogen compared to other atoms means that hydrogen nuclei appear as negative density in a Fourier map and are thus readily discernable from other atoms. Another benefit of neutron diffraction is that the intensity of scattering does not fall off at large scattering angles because the scattering nuclei are so small. There are two related factors that limit the application of neutron scattering to structural biology. The first is that there are only a small number of facilities that can provide a beam of thermal neutrons that have a wavelength of  $\sim 1$  Å, and the second is that the intensity of the neutron sources themselves is limited compared to X-ray sources. The latter factor generally demands large samples and lengthy data collection times in comparison to those required for X-ray scattering.

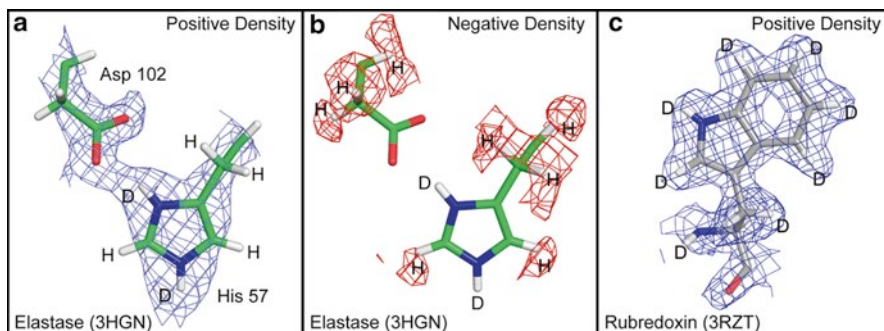


**Fig. 4.11** Neutron diffraction reveals the location of hydrogen atoms. **(a, b)** The neutron density for elastase contoured at positive and negative density levels [39]. **(c)** The neutron density for rubredoxin [23]. The crystals of elastase were grown from protein isolated from normal water and transferred to  $D_2O$ , and the neutron data were recorded to 1.65 Å resolution. Here, protons replaced by deuterons show as positive neutron density due to the positive scattering factor for deuterium. Conversely, non-exchangeable hydrogen atoms show as negative density due to their negative scattering length **(b)**. This study clearly shows that a deuterium atom is in close proximity to the ring nitrogen of the histidine and is not participating in a low barrier hydrogen bond. **(c)** The neutron density from a perdeuterated sample of rubredoxin that was recorded from a 14 h data collection run demonstrating that recent developments in detector technology and improvements in neutron sources make neutron crystallography an exciting option for locating hydrogen atoms in macromolecules (PDB accession numbers shown in parentheses)

## 4.4 Neutron Crystallography

In general, neutron crystallography is applied to problems for which the structure has already been determined by X-ray crystallography. There are three reasons for this. First, it is difficult to solve a structure by neutron scattering since the scattering length of metals or other elements that might be substituted is not very different from that of carbon, nitrogen, or oxygen. Consequently, it is difficult to solve the phase problem by neutron diffraction. Second, access to neutron facilities is limited and the sources are comparatively weak compared to synchrotron sources. Third, large crystals by X-ray standards are generally required in order to enhance the amplitude of the scattered radiation. Crystals with a volume of over 1 mm<sup>3</sup> were originally required, though the new radiation sources have reduced this volume considerably [23, 24]. In many instances it is challenging to grow very large crystals. Another problem that is not often appreciated is that neutron beams are not monochromatic (single wavelength), but exhibit a range of wavelengths. This is necessary in order to obtain a high flux, but causes overlap between adjacent reflections (measurements), which in turn reduces the completeness of the data. Even with these limitations, neutron crystallography has made significant contributions to macromolecular structure, particularly in those instances where the protonation state of an amino acid or ligand is important.

A good example of the value of neutron crystallography is seen in the study of serine proteases. This class of proteases utilizes a catalytic triad of residues in their

active site. This consists of an aspartic acid, histidine, and serine residue where the serine functions as the nucleophile that attacks the substrate carbonyl moiety. The histidine functions as a catalytic base and acid in the mechanism. A question has surrounded the role of the aspartate residue and whether a low barrier hydrogen bond exists between the histidine and aspartate side chains. There is no question that these two residues are connected by strong hydrogen bond, but the exact location of the hydrogen in that bond has been the subject of considerable discussion. A low barrier hydrogen bond requires that the hydrogen be close to the middle or shared by the carboxylate oxygen of the aspartate and the side chain nitrogen of the histidine. Despite several ultrahigh resolution X-ray crystallographic studies of serine proteins, the controversy has continued. A recent combined X-ray and neutron study clearly shows that in elastase, when complexed with a transition state analog, the hydrogen bond, is 2.6 Å long where the hydrogen is 0.80–0.96 Å from the histidine nitrogen (Fig. 4.11a) [39]. This position is consistent with a short but conventional hydrogen bond, and is not consistent with a low barrier hydrogen bond. The ability to observe the hydrogen (deuterium in this case) resolves the question of whether or not a low barrier hydrogen bond is present in this particular complex. It does not answer the question whether a low barrier hydrogen bond ever exists in serine proteases, so the discussion continues.

Generally, macromolecules are perdeuterated where possible or at least transferred to D<sub>2</sub>O for data collection. This is necessary because hydrogen has an anomalously large incoherent scattering cross section compared to other nuclei. In nuclear scattering the unit of measurement is the “barn” ( $10^{-28}$  m<sup>2</sup>), which was originally defined as the area cross section of a uranium nucleus. The nuclear cross section varies dramatically from one isotope to another for the same element and is not related simply to the number of nucleons. Thus, the scattering cross section for hydrogen is ~80 barns, whereas that for deuterium, nitrogen, and carbon is zero, 0.49, and zero, respectively. This incoherent scattering from hydrogen results in a large increase in the background. Full deuteration requires expression systems adapted to growth in D<sub>2</sub>O and deuterated carbon sources. Together these increase the signal-to-noise ratio in the diffraction pattern and allow for smaller sample sizes. Considerable improvements have also been made in detector technology and neutron sources [13, 23]. Consequently, increased application of neutron crystallography can be anticipated in future years. An example of these improvements is seen in the electron density for rubredoxin that was recorded in 14 h to 1.5 Å resolution (Fig. 4.11c).

## 4.5 Small-Angle Neutron Scattering

The concepts described for SAXS can be applied to neutron small-angle scattering. However, in this case the difference in sign for the scattering length for hydrogen and deuterium atoms means that it is possible to adjust the scattering density or contrast of the macromolecule relative to the solvent by varying the ratio of H<sub>2</sub>O to D<sub>2</sub>O.

This implies that a sample comprising two polymers can be prepared to distinguish the location and conformation of each individual chain. In such a case, one chain is hydrogenated and the other is perdeuterated. By adjusting the solvent contrast to match that of the hydrogenated sample, one can observe the scattering of a single polymer. This has profound implications for the examination of multicomponent macromolecules by [19]. Use of this powerful technique is limited by access to suitable facilities.

## 4.6 Summary

Elastic scattering techniques by X-rays and neutrons have had a profound influence on the development of the fundamentals of biology. These constitute a versatile set of tools that can provide information over a wide range of scales of both resolution and molecular size. Understanding the limitations of these methods allows the information they yield to be incorporated appropriately into molecular studies of biological systems.

## References

1. Adams PD, Afonine PV, Bunkoczi G, Chen VB, Davis IW, Echols N, Headd JJ, Hung LW, Kapral GJ, Grosse-Kunstleve RW, McCoy AJ, Moriarty NW, Oeffner R, Read RJ, Richardson DC, Richardson JS, Terwilliger TC, Zwart PH (2010) PHENIX: a comprehensive Python-based system for macromolecular structure solution. *Acta Crystallogr D Biol Crystallogr* 66(pt 2):213–221. doi:[10.1107/S0907444909052925](https://doi.org/10.1107/S0907444909052925)
2. Ben-Shem A, Garreau de Loubresse N, Melnikov S, Jenner L, Yusupova G, Yusupov M (2011) The structure of the eukaryotic ribosome at 3.0 Å resolution. *Science* 334(6062):1524–1529. doi:[10.1126/science.1212642](https://doi.org/10.1126/science.1212642)
3. Blow DM (2002) *Outline of crystallography for biologists*. Oxford University Press, Oxford, New York
4. Brunger AT (1992) Free R value: a novel statistical quantity for assessing the accuracy of crystal structures. *Nature* 355(6359):472–475
5. Burke JE, Sashital DG, Zuo X, Wang YX, Butcher SE (2012) Structure of the yeast U2/U6 snRNA complex. *RNA* 18(4):673–683. doi:[10.1261/ma.031138.111](https://doi.org/10.1261/ma.031138.111)
6. Chen VB, Arendall WB III, Headd JJ, Keedy DA, Immormino RM, Kapral GJ, Murray LW, Richardson JS, Richardson DC (2010) MolProbity: all-atom structure validation for macromolecular crystallography. *Acta Crystallogr D Biol Crystallogr* 66(pt 1):12–21. doi:[10.1107/S0907444909042073](https://doi.org/10.1107/S0907444909042073)
7. DeLano WL (2002) The PyMOL molecular graphics system. <http://www.pymol.org>
8. Dickinson M, Farman G, Frye M, Bekyarova T, Gore D, Maughan D, Irving T (2005) Molecular dynamics of cyclically contracting insect flight muscle in vivo. *Nature* 433(7023):330–334. doi:[10.1038/nature03230](https://doi.org/10.1038/nature03230)
9. Dodson E (2008) The before and after of molecular replacement. *Acta Crystallogr D Biol Crystallogr* 64(pt 1):17–24. doi:[10.1107/S0907444907049736](https://doi.org/10.1107/S0907444907049736)
10. Eisenberg D (2003) The discovery of the alpha-helix and beta-sheet, the principal structural features of proteins. *Proc Natl Acad Sci U S A* 100(20):11207–11210. doi:[10.1073/pnas.2034522100](https://doi.org/10.1073/pnas.2034522100)

11. Franklin RE, Gosling RG (1953) Molecular configuration in sodium thymonucleate. *Nature* 171(4356):740–741
12. Guinier A, Fournet G (1955) Small-angle scattering of X-rays. Structure of matter series. Wiley, New York
13. Hazemann I, Dauvergne MT, Blakeley MP, Meilleur F, Haertlein M, Van Dorsselaer A, Mitschler A, Myles DA, Podjarny A (2005) High-resolution neutron protein crystallography with radically small crystal volumes: application of perdeuteration to human aldose reductase. *Acta Crystallogr D Biol Crystallogr* 61(pt 10):1413–1417. doi:[10.1107/S0907444905024285](https://doi.org/10.1107/S0907444905024285)
14. James RW (1962) The optical principles of the diffraction of X-rays. OxBow Press, Woodbridge
15. Kleywegt GJ, Jones TA (1995) Where freedom is given, liberties are taken. *Structure* 3(6):535–540
16. Koch MHJ, Vachette P, Svergun DI (2003) Small-angle scattering: a view on the properties, structures and structural changes of biological macromolecules in solution. *Q Rev Biophys* 36(2):147–227. doi:[10.1017/S0033583503003871](https://doi.org/10.1017/S0033583503003871)
17. Kozin MB, Svergun DI (2001) Automated matching of high- and low-resolution structural models. *J Appl Crystallogr* 34:33–41
18. Lattman E, Loll P (2008) Protein crystallography: a concise guide. Johns Hopkins University Press, Baltimore
19. Lu Y, Jeffries CM, Trehwella J (2011) Invited review: probing the structures of muscle regulatory proteins using small-angle solution scattering. *Biopolymers* 95(8):505–516. doi:[10.1002/bip.21624](https://doi.org/10.1002/bip.21624)
20. Mertens HD, Svergun DI (2010) Structural characterization of proteins and complexes using small-angle X-ray solution scattering. *J Struct Biol* 172(1):128–141. doi:[10.1016/j.jsb.2010.06.012](https://doi.org/10.1016/j.jsb.2010.06.012)
21. Molprobiy server. <http://molprobiy.biochem.duke.edu/>
22. Mouzakis KE, Burke JE, Butcher SE (2012) Investigating RNAs involved in translational control by NMR and SAXS. In: Dinman JD (ed) The biophysics of translational control of gene expression. Springer, New York
23. Munshi P, Chung SL, Blakeley MP, Weiss KL, Myles DA, Meilleur F (2012) Rapid visualization of hydrogen positions in protein neutron crystallographic structures. *Acta Crystallogr D Biol Crystallogr* 68(pt 1):35–41. doi:[10.1107/S0907444911048402](https://doi.org/10.1107/S0907444911048402)
24. Myles DA (2006) Neutron protein crystallography: current status and a brighter future. *Curr Opin Struct Biol* 16(5):630–637. doi:[10.1016/j.sbi.2006.08.010](https://doi.org/10.1016/j.sbi.2006.08.010)
25. Namba K, Pattanayek R, Stubbs G (1989) Visualization of protein-nucleic acid interactions in a virus. Refined structure of intact tobacco mosaic virus at 2.9 Å resolution by X-ray fiber diffraction. *J Mol Biol* 208(2):307–325
26. Pauling L, Corey RB (1951) Configurations of polypeptide chains with favored orientations around single bonds: two new pleated sheets. *Proc Natl Acad Sci U S A* 37(11):729–740
27. Pauling L, Corey RB, Branson HR (1951) The structure of proteins; two hydrogen-bonded helical configurations of the polypeptide chain. *Proc Natl Acad Sci U S A* 37(4):205–211
28. PDBsum server. <http://www.ebi.ac.uk/pdbsum/>
29. Pettersen EF, Goddard TD, Huang CC, Couch GS, Greenblatt DM, Meng EC, Ferrin TE (2004) UCSF Chimera—a visualization system for exploratory research and analysis. *J Comput Chem* 25(13):1605–1612. doi:[10.1002/jcc.20084](https://doi.org/10.1002/jcc.20084)
30. Piazzesi G, Reconditi M, Linari M, Lucii L, Bianco P, Brunello E, Decostre V, Stewart A, Gore DB, Irving TC, Irving M, Lombardi V (2007) Skeletal muscle performance determined by modulation of number of myosin motors rather than motor force or stroke size. *Cell* 131(4):784–795. doi:[10.1016/j.cell.2007.09.045](https://doi.org/10.1016/j.cell.2007.09.045)
31. Putnam CD, Hammel M, Hura GL, Tainer JA (2007) X-ray solution scattering (SAXS) combined with crystallography and computation: defining accurate macromolecular structures, conformations and assemblies in solution. *Q Rev Biophys* 40(3):191–285. doi:[10.1017/S0033583507004635](https://doi.org/10.1017/S0033583507004635)
32. Rajagopal S, Kostov KS, Moffat K (2004) Analytical trapping: extraction of time-independent structures from time-dependent crystallographic data. *J Struct Biol* 147(3):211–222. doi:[10.1016/j.jsb.2004.04.007](https://doi.org/10.1016/j.jsb.2004.04.007)

33. Rambo RP, Tainer JA (2010) Bridging the solution divide: comprehensive structural analyses of dynamic RNA, DNA, and protein assemblies by small-angle X-ray scattering. *Curr Opin Struct Biol* 20(1):128–137. doi:[10.1016/j.sbi.2009.12.015](https://doi.org/10.1016/j.sbi.2009.12.015)
34. Reconditi M (2006) Recent improvements in small angle X-ray diffraction for the study of muscle physiology. *Rep Prog Phys* 69(10):2709–2759. doi:[10.1088/0034-4885/69/10/R01](https://doi.org/10.1088/0034-4885/69/10/R01)
35. Rupp B (2010) *Biomolecular crystallography: principles, practice, and application to structural biology*. Garland Science, New York
36. Stubbs G (1999) Developments in fiber diffraction. *Curr Opin Struct Biol* 9(5):615–619
37. Sunde M, Serpell LC, Bartlam M, Fraser PE, Pepys MB, Blake CC (1997) Common core structure of amyloid fibrils by synchrotron X-ray diffraction. *J Mol Biol* 273(3):729–739. doi:[10.1006/jmbi.1997.1348](https://doi.org/10.1006/jmbi.1997.1348)
38. Svergun DI (1999) Restoring low resolution structure of biological macromolecules from solution scattering using simulated annealing. *Biophys J* 76(6):2879–2886
39. Tamada T, Kinoshita T, Kurihara K, Adachi M, Ohhara T, Imai K, Kuroki R, Tada T (2009) Combined high-resolution neutron and X-ray analysis of inhibited elastase confirms the active-site oxyanion hole but rules against a low-barrier hydrogen bond. *J Am Chem Soc* 131(31):11033–11040. doi:[10.1021/ja9028846](https://doi.org/10.1021/ja9028846)
40. The Protein Data Bank. <http://www.pdb.org/>
41. Toyama BH, Weissman JS (2011) Amyloid structure: conformational diversity and consequences. *Annu Rev Biochem* 80:557–585. doi:[10.1146/annurev-biochem-090908-120656](https://doi.org/10.1146/annurev-biochem-090908-120656)
42. Tsuruta H, Irving TC (2008) Experimental approaches for solution X-ray scattering and fiber diffraction. *Curr Opin Struct Biol* 18(5):601–608. doi:[10.1016/j.sbi.2008.08.002](https://doi.org/10.1016/j.sbi.2008.08.002)
43. Wille H, Bian W, McDonald M, Kendall A, Colby DW, Bloch L, Ollesch J, Borovinskiy AL, Cohen FE, Prusiner SB, Stubbs G (2009) Natural and synthetic prion structure from X-ray fiber diffraction. *Proc Natl Acad Sci U S A* 106(40):16990–16995. doi:[10.1073/pnas.0909006106](https://doi.org/10.1073/pnas.0909006106)
44. Winn MD, Ballard CC, Cowtan KD, Dodson EJ, Emsley P, Evans PR, Keegan RM, Krissinel EB, Leslie AG, McCoy A, McNicholas SJ, Murshudov GN, Pannu NS, Potterton EA, Powell HR, Read RJ, Vagin A, Wilson KS (2011) Overview of the CCP4 suite and current developments. *Acta Crystallogr B Biol Crystallogr* 67(pt4):235–242. doi:[10.1107/S0907444910045749](https://doi.org/10.1107/S0907444910045749)
45. Worldwide PDB. <http://www.wwpdb.org/>
46. Yamashita I, Suzuki H, Namba K (1998) Multiple-step method for making exceptionally well-oriented liquid-crystalline sols of macromolecular assemblies. *J Mol Biol* 278(3):609–615. doi:[10.1006/jmbi.1998.1710](https://doi.org/10.1006/jmbi.1998.1710)

## Chapter 5

# Nuclear Magnetic Resonance Spectroscopy

Thomas C. Pochapsky and Susan Sondej Pochapsky

**Abstract** Nuclear magnetic resonance (NMR) has developed into an important tool for investigating the structure and dynamics of biomacromolecules in solution, associated with membranes and in solids. This chapter provides an introduction to the theory of NMR and a description of basic concepts (excitation of NMR transitions, spin populations and coherence, relaxation phenomena, signal detection and processing). Types of structural and dynamic information available from NMR experiments are noted. Standard experiments used for sequential assignment of resonances in biomolecules in solution and solid state are discussed, along with instrumentation and sample requirements. In particular, the need for selective and uniform isotope labeling is detailed. Software used to process NMR data and generate structural and dynamic information are noted, and data needed for structure determinations and dynamic analysis outlined.

**Keywords** Stable isotopes • TROSY • Nuclear Overhauser effect • Dipolar coupling • Solid-state NMR • Protein • Nucleic acid • Deuteration

---

All references to commercially available products and software are for the reader's convenience and information only. No guarantees of product safety, availability, comprehensiveness of listings or completeness of descriptions/pricing are made or implied.

T.C. Pochapsky (✉) • S.S. Pochapsky  
Department of Chemistry and Rosenstiel Basic Medical Sciences Research Institute,  
Brandeis University, 415 South Street, Waltham, MA 02454-9110, USA  
e-mail: pochapsk@brandeis.edu; ssp@brandeis.edu



## 5.1 What Is Nuclear Magnetic Resonance Spectroscopy?

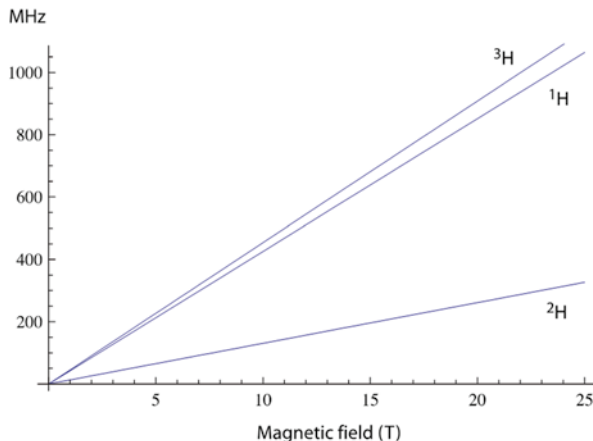
Perhaps no single technique since the advent of protein X-ray crystallography has made as great an impact on our understanding of biomolecular structure and dynamics as nuclear magnetic resonance (NMR) spectroscopy. While a thorough technical description of NMR is beyond the scope of what can be accomplished in a single chapter, we will attempt to provide readers with a sufficient overview of the potential of NMR in biophysical research that they can judge for themselves whether it might be usefully applied to their own work. For those desiring a more detailed description of the technical and theoretical aspects of NMR, we direct them to our textbook on the subject [1].

NMR makes use of radio frequencies (RF) between  $\sim 10$  and  $1,000$  MHz to probe the transitions of nuclear spins in the presence of a static magnetic field. Nuclear spin, designated by a quantum number  $I$ , is determined by the relative number and arrangement of protons and neutrons in the atomic nucleus and, as such, depends upon which isotope of an element is present. For example, hydrogen has three isotopes, protium ( $^1\text{H}$ ,  $I=1/2$ ), deuterium ( $^2\text{H}$ ,  $I=1$ ) and tritium ( $^3\text{H}$ ,  $I=1/2$ ). If  $I$  is not equal to zero, the magnetic quantum number  $m$ , with allowed values of  $-I, -I+1, \dots, I-1, I$ , determines in which spin state the nucleus resides. For example,  $^1\text{H}$  and  $^3\text{H}$  can each occupy either of two spin states,  $m=-1/2$  and  $m=1/2$ , while  $^2\text{H}$  has three allowed states,  $m=-1, m=0$  and  $m=1$ . In the absence of a magnetic field (or in the case of  $^2\text{H}$ , an electric field gradient), all of the allowed spin states are degenerate, or energetically equal. However, in the presence of a static magnetic field, the spin states become nondegenerate, and transitions between those states can be probed spectroscopically. The degree of (Zeeman) splitting between nondegenerate spin states is determined by (5.1):

$$2\pi\nu = \omega = \gamma B_0 \quad (5.1)$$

where  $\nu$  is the transition frequency in  $\text{s}^{-1}$  (Hertz or Hz),  $\omega$  is the transition frequency (also called the *Larmor frequency*) in radial units (radians/s),  $B_0$  the strength of the magnetic field (expressed in Tesla), and  $\gamma$  the gyromagnetic ratio, a constant that depends upon the identity of the nuclide. As such, the frequency of an NMR transition depends upon both the strength of the applied magnetic field and identity of the nucleus being observed. Figure 5.1 shows the Zeeman splitting for the three isotopes of hydrogen as a function of magnetic field strength. Because the signal to noise ratio ( $S/N$ ) in the NMR experiment is proportional to  $\sqrt{\gamma^3 B^3}$ , all other things being equal, the highest  $S/N$  is obtained by observing the nucleus present with the largest  $\gamma$  at the highest available magnetic field strength. As can be seen from Fig. 5.1,  $^3\text{H}$  (which is radioactive) has the largest  $\gamma$  of the three hydrogen isotopes, and at  $11.74$  T has a transition frequency of  $533.3$  MHz. However,  $^1\text{H}$  is not much lower in frequency than tritium, resonating at  $500$  MHz at the same field strength, and as  $^1\text{H}$  is abundant and not radioactive, it is the nuclide of choice for hydrogen NMR. Deuterium is not only less sensitive than either  $^1\text{H}$  or  $^3\text{H}$ , it is also

**Fig. 5.1** Resonance frequencies for the three isotopes of hydrogen as a function of magnetic field strength. Gyromagnetic ratios are 26.7510, 4.1064, and 28.5335  $\text{rad s}^{-1} \text{T}^{-1}$  for  $^1\text{H}$ ,  $^2\text{H}$ , and  $^3\text{H}$  respectively



a nuclear quadrupole ( $I > 1/2$ ), which introduces some complications for the NMR experiment that will not be discussed in detail here. In fact,  $^1\text{H}$  has the highest  $\gamma$  of any stable nuclide, and based on its abundance in biomolecules, is usually the nucleus of choice for detection in solution biomolecular NMR experiments. We will see that this is not the case for solid-state NMR, for reasons to be discussed later in this chapter.

## 5.2 Excitation of NMR Transitions

Nuclear Zeeman splitting in standard NMR magnets yields transition frequencies between  $\sim 10$  and 1,000 MHz, which lie in the radio frequency (RF) range of the electromagnetic spectrum, and excitation of NMR transitions on modern spectrometers is almost exclusively performed using *RF pulses*. An RF pulse consists of a short burst of RF energy defined by the frequency of the RF used to generate it ( $\nu_{\text{RF}}$ , called the *carrier frequency*, often but not exclusively the RF frequency near the center of the spectral region of interest), the amplitude of the RF (usually measured in decibels of attenuation of the full power available from the RF amplifier hardware), the shape of the pulse (i.e., amplitude as a function of time) and the pulse duration  $\tau_p$ . Despite the fact that the pulse is generated from a single RF frequency ( $\nu_{\text{RF}}$ ), the finite duration of the pulse results in “blurring,” so that a range of frequencies on either side of the carrier frequency are also excited by the pulse. The *excitation bandwidth* of a rectangular pulse with duration  $\tau_p$  (in seconds) is determined by the expression:

$$\Delta\nu = \nu_{\text{null}} - \nu_{\text{RF}} = \tau_p^{-1} \quad (5.2)$$

$\Delta\nu$  is the distance in Hz between the center frequency of the pulse and the first excitation null,  $\nu_{\text{null}}$ . Note that (5.2) is an inverse relationship. The shorter the pulse duration, the wider the range of frequencies it excites. Thus, for selective excitation (where only a narrow spectral region is excited) a long-duration pulse is applied, while for broadband excitation of all or most of spectral region of interest, a shorter pulse is used. Figure 5.2 shows graphically the relationship between pulse length and excitation bandwidth. Another important variable is pulse power, a measure of energy input into the sample (and probe) per unit time. Too much power over too long a time can damage the delicate components that make up the NMR probe or destroy the sample through dielectric heating. Thus, longer pulses at lower power are occasionally preferred over their shorter, higher power counterparts.

Another defining characteristic of the RF pulse is *pulse phase*. Any wave can be described in terms of its frequency and phase shift, which defines the amplitude of the wave at the origin ( $t=0$ ). If the amplitude of a sine wave at the beginning of the pulse is zero, the phase shift is 0. However, if the wave at  $t=0$  has maximum amplitude  $A_0$ , the phase of the wave has shifted by  $90^\circ$ , or  $\pi/2$  rad. A further  $90^\circ$  phase shift ( $180^\circ$  or  $\pi$  radians total shift) results in a return to zero amplitude. A  $270^\circ$  phase shift results in a negative amplitude ( $-A_0$ ) at  $t=0$ , while a  $360^\circ$  ( $2\pi$  rad) shift returns to the beginning of the cycle. We will find that pulse phase plays a critical role in selecting particular pathways of excitation in multiple-pulse NMR experiments.

What happens when an RF pulse is applied to a sample in the NMR spectrometer? Recall that the energy provided by the pulse is absorbed by nuclear spins in the sample undergoing a transition from a lower energy to a higher energy state as determined by (5.1). In order to absorb the energy provided by the RF, the nuclear spins must be in phase with the applied RF. To visualize this, consider the individual nuclear spin dipoles as being randomly oriented, but precessing around the applied magnetic field at their transition frequency (called the *Larmor frequency*). Boltzmann weighting of the spin dipole vectors implies that there is a net magnetization  $M$  along the  $+z$  axis (aligned with the applied field  $B_0$ ). When an RF pulse is applied, the magnetic component of the RF results in a “tipping” of the net magnetization  $M$  away from the  $z$  axis, generating a *coherent ensemble* (Fig. 5.3) [2], that induces a macroscopic RF signal at the Larmor frequency, which is detected in the NMR experiment.

The RF signal detected in an NMR experiment appears as a (weak) time-domain oscillating current at the Larmor frequency in the receiver coil of the NMR probe. This time-domain oscillation (called a *free-induction decay*, or FID) is passed to a device called a “mixer,” which subtracts the observed frequency from standard carrier frequency  $\nu_{\text{RF}}$ , shifting the very high-frequency NMR signal down into the audio range so that it can be easily handled by standard electronics. The FID is amplified, digitized (so that it can be handled by a computer) and then subjected to Fourier transformation, a mathematical operation that converts the time-domain FID to a frequency-domain spectrum.

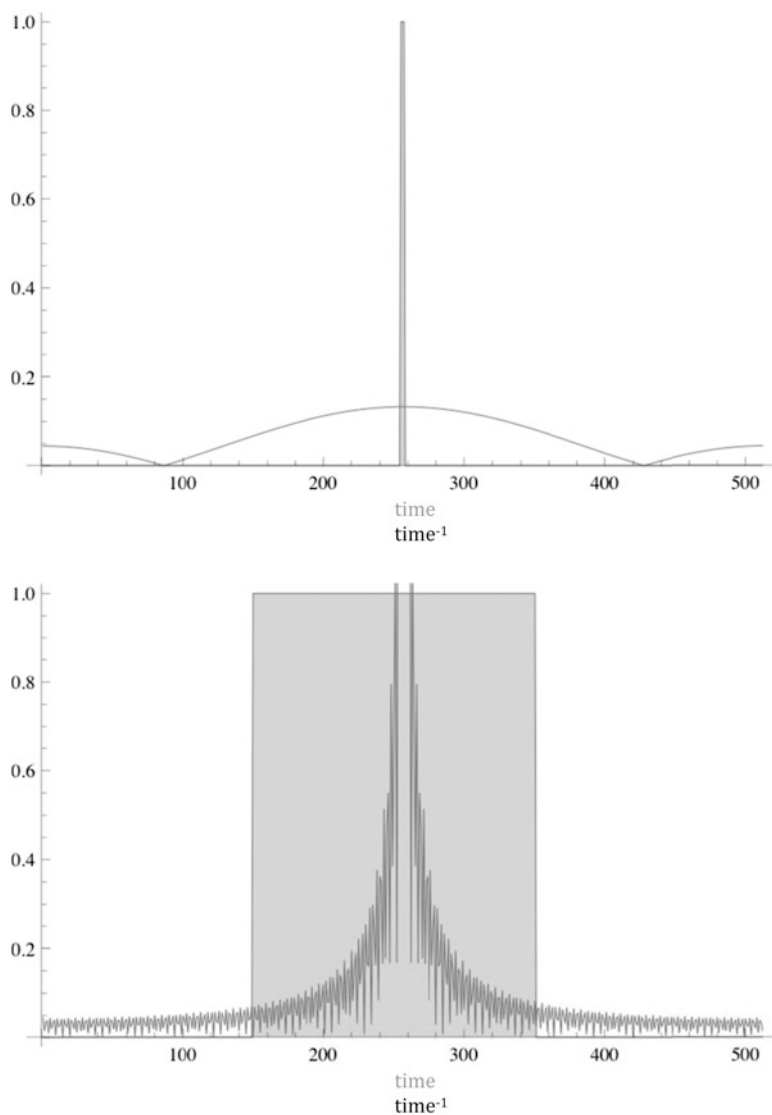


**Fig. 5.2** Inverse relationship between pulse length and excitation bandwidth. Amplitude (pulse or absolute value of excitation envelope) is in arbitrary units on the *vertical axis*. Note that the *horizontal axis* is in arbitrary units of time for pulse length (time), represented by shaded *rectangles*, or  $\text{time}^{-1}$  (frequency) for power spectra. *Top*: short duration pulse (three arbitrary time points, indicated by shaded *rectangle*), with power spectrum plotted in units of radians/time point. Nulls in the excitation envelope are located at  $\sim 85 \text{ rad/time}$  and  $425 \text{ rad/time}$ . *Bottom*: long-duration (200 time points, indicated by shaded *rectangle*) pulse, with nulls located close to the center of the frequency plot

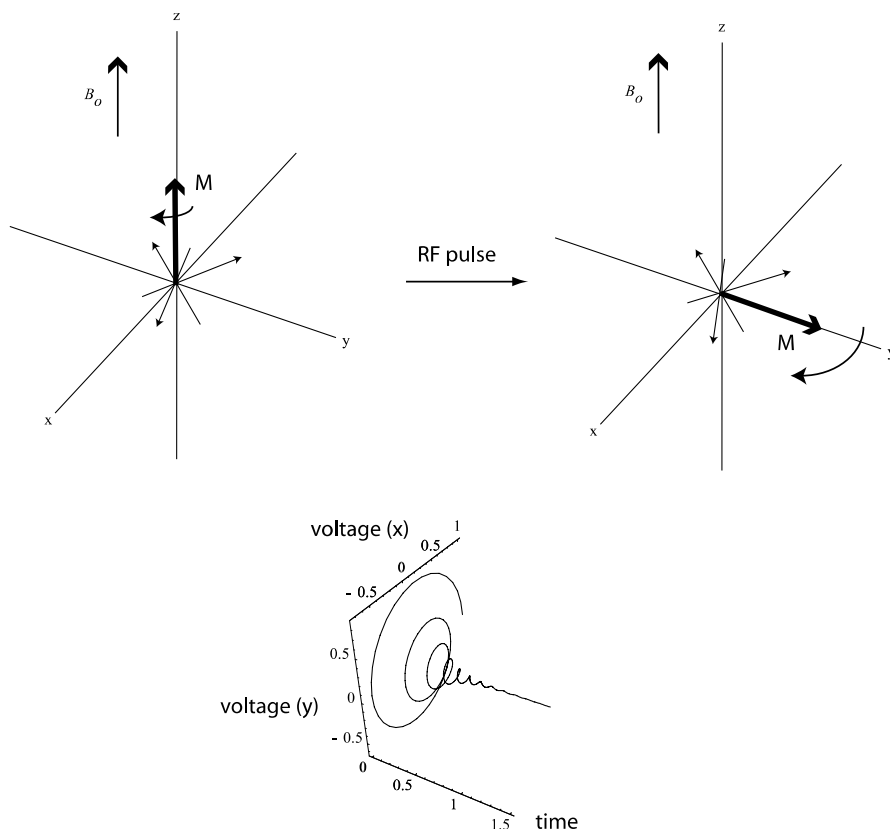


**Fig. 5.3** Generation of a coherent ensemble by an RF pulse in the NMR experiment. *Top left:* an incoherent ensemble of spin dipoles (*light lines*), oriented randomly and precessing at the Larmor frequency around the applied field  $B_0$ . Boltzmann weighting results in a net magnetization  $M$  along  $+z$ . Note that most of the spins are still randomly oriented. *Top right:* after an RF pulse is applied, the magnetic component of the RF field tilts the net magnetization away from  $+z$ , still precessing around the applied field  $B_0$  (precession indicated by *curved arrows*). The orthogonal detector circuits detect the precession as an oscillating voltage, generating a free-induction decay (*bottom*)

## 5.3 Relaxation of NMR Transitions

### 5.3.1 Return to Equilibrium Spin Populations: Spin–Lattice ( $T_1$ ) Relaxation

NMR spectroscopic transitions are typically much lower in energy than the thermal energy available from the environment as measured by  $kT$  (Boltzmann's constant,  $k = 1.380\,6505 \times 10^{-34} \text{ JK}^{-1}$ , with  $T$  the absolute temperature). As such, NMR is a relatively non-perturbing spectroscopic probe: While sample heating can occur if care is not taken, Boltzmann populations of biomolecule conformations are usually not

perturbed by the NMR experiment, and vibrational and electronic states are unaffected. The price of the non-perturbing nature of NMR is that it is very insensitive relative to other forms of molecular spectroscopy, and NMR experiments typically take much longer to run than other types of spectroscopic measurements. Because the transitions involved are low energy ( $\ll kT$ ), the Boltzmann population difference between spin states connected by an NMR transition is small, unlike most other forms of molecular spectroscopy, in which the ground state is almost exclusively populated at the beginning of the experiment. However, in order to obtain an NMR signal, there must be *some* population difference between the connected spin states. The net absorption of RF energy moves spins from a lower energy (more populated) spin state to a higher energy state until the populations of the two states are equal, at which point no further net RF absorption can occur. This phenomenon is called *saturation* of a transition, and at this point the experiment cannot be repeated until the states linked by the transition return to a near-Boltzmann population distribution. The process by which energy is lost to the surroundings, thus restoring an equilibrium distribution of spin populations, is called *spin-lattice relaxation*. In the simplest case, spin-lattice relaxation can be fit to a simple exponential decay, with a characteristic relaxation rate constant  $R_1$ . The inverse of this rate constant is  $T_1$ , the spin-lattice relaxation time, and can be thought of as the time required for the NMR signal amplitude to be restored to  $A_0/e$ , where  $e$  is the base of the natural logarithms and  $A_0$  is the amplitude of the signal generated by equilibrium population distributions (that is, after a very long delay between successive signal acquisitions). Because the energy differences between excited and ground states in NMR are very small (and coupling with local magnetic field fluctuations inefficient as a result),  $T_1$  relaxation times of nuclear spins commonly observed in NMR experiments can often be quite long, on the order of a second or more. This means that the rate at which an NMR experiment can be repeated is much lower than for other spectroscopic methods, so that signals take longer to build up to usable levels.

### 5.3.2 Loss of Coherence: Spin-Spin ( $T_2$ ) Relaxation

A second limiting factor in NMR experiments is the loss of coherence over time. Recall that the coherent ensemble of spins that produces the NMR signal is generated by the application of an RF pulse. After the pulse, the spins that form the coherent ensemble precess in phase at their Larmor frequency. However, local magnetic field fluctuations due to local spin-spin interactions result in the decay and eventual loss of the coherence. Such processes do not necessarily return spins to their equilibrium populations, as in spin-lattice relaxation, but only remove them from the coherent ensemble. Again, this loss of signal can often be modeled as a simple exponential decay of signal intensity with time, with a decay constant  $R_2$ . The inverse of  $R_2$  is  $T_2$ , the *spin-spin relaxation* time. As with  $T_1$ ,  $T_2$  can be considered as the time required for a coherence-induced signal in the NMR detector to decay in amplitude from the original  $A_0$  to  $A_0/e$ . Clearly, spin-lattice relaxation contributes to

$T_2$  ( $T_2$  is never longer than  $T_1$  for a given coherence) but time-dependent local fluctuations in the magnetic field that have nothing to do with spin–lattice relaxation nevertheless contribute to spin–spin interactions that do not result in loss of energy to the environment, but only to loss of coherence. We will see later that the frequencies of these local fluctuations provide valuable information regarding molecular dynamics, and can be extracted from experimentally measured relaxation times. However, at present, the important consideration is that  $T_2$  processes limit the lifetime of a coherence generated in an NMR experiment. In biological macromolecules,  $T_2$  is often the overriding consideration in designing multi-pulse experiments, since this relaxation time determines whether the coherence generated at the beginning of an experiment will survive long enough to be detected at the end.

Experimentally,  $T_2$  (or at least an approximate value  $T_2^*$ ) can be estimated for a given resonance from line width. Ideally, absorptive NMR resonances have Lorentzian lineshapes, with the width of a resonance at half height in Hz ( $\Delta\nu_{1/2}$ ) inversely proportional to the lifetime of the coherence from which it arises (5.3). In other words, spectral lines are narrower for longer-lived coherences. Thus, a line width of 35 Hz (typical for a  $^1\text{H}$  resonance in a protein) corresponds to a  $T_2^*$  of 9 ms. For small molecules, line widths on the order of 1 Hz are common ( $T_2^*$  of 320 ms). Note that the value of  $T_2^*$  includes not only the intrinsic  $T_2$  relaxation time of the coherence but experimental contributions as well (inhomogeneous magnetic fields, sample inhomogeneities, etc.).

$$\Delta\nu_{1/2} = (\pi T_2^*)^{-1} \quad (5.3)$$

## 5.4 Structural Information Available from NMR

Given the challenges it presents, why is NMR still so useful and important for biophysics? It turns out that relatively long relaxation times are both the bane and boon of NMR. As we show above, the line width of a spectroscopic transition is inversely proportional to the lifetime of the coherence as measured by  $T_2$ . For small molecules in nonviscous solution, lifetimes of  $\sim 1$  s are not uncommon. Even for biological macromolecules, coherence lifetimes  $>50$  ms can be observed under favorable circumstances. This leads to relatively narrow spectral lines and a high degree of distinguishability for transitions that are close in energy. In UV/visible and IR spectroscopy, excited state lifetimes are usually in the ps–ns range ( $10^{-12}$ – $10^{-9}$  s), with correspondingly broader lines, and poorer distinguishability. A second benefit of relatively long coherence lifetimes in NMR is that *coherences generated on one spin last long enough to be transferred via coupling to other spins, and the results analyzed in terms of coherence transfer pathways* [3]. This statement is italicized to indicate its importance: The benefits of multidimensional NMR arise from the fact that spins that are coupled to each other in some fashion can be connected by

**Table 5.1** Gyromagnetic ratios ( $\gamma$ ), sensitivity relative to  $^1\text{H}$  and resonance frequencies at 11.75 T for nuclei commonly used in biomolecular NMR

Nuclide	$\gamma$ (rad s <sup>-1</sup> T <sup>-1</sup> ) $\times 10^{-7}$	Sensitivity	Frequency (MHz) at 11.74 T
$^1\text{H}$	26.7510	1.00000	500.0
$^2\text{H}$ (quadrupole, $I=1$ )	4.1064	0.00362	76.7
$^{13}\text{C}$	6.7263	0.01590	125.7
$^{15}\text{N}$	-2.7116	0.00104	50.7
$^{19}\text{F}$	25.1665	0.83262	470.6
$^{31}\text{P}$	10.8289	0.06333	202.6

coherence transfer and the results analyzed in terms of that coupling. How coupling occurs and what types of coherence transfer pathways are commonly analyzed will be examined in more detail below.

Finally, NMR benefits from the sheer numbers of available spectroscopic targets. Besides  $^1\text{H}$ , a variety of other NMR-active isotopes present themselves in a typical biomolecule. Although the most common isotope of carbon,  $^{12}\text{C}$ , has no spin,  $^{13}\text{C}$  ( $I=1/2$ , 1.1 % natural abundance) is common enough that it is also a spectroscopic target and can be enriched by appropriate synthetic or biosynthetic means. The same is true for  $^{15}\text{N}$  ( $I=1/2$ , natural abundance <0.5 %), which is commonly enriched by expression of proteins on minimal media containing a  $^{15}\text{N}$ -labeled ammonium salt.  $^{31}\text{P}$  ( $I=1/2$ , 100 % natural abundance), while having some drawbacks, is a potential NMR target in nucleic acids.  $^{19}\text{F}$  ( $I=1/2$ , 100 % natural abundance) can often be substituted for hydrogen in amino acids and nucleotide bases, and is a useful NMR probe. By comparison, UV-visible spectroscopy rarely has more than a few distinguishable transitions in a biomolecule, and IR-based techniques, which have far more spectroscopic targets than even NMR (vibrational modes), suffer from the difficulty of detecting coherence transfer between coupled modes due to short excited state lifetimes.

### 5.4.1 Chemical Shift and Nuclear Shielding

Equation 5.1 allows us to calculate the resonance frequency of a given nuclide as a function of gyromagnetic ratio and applied magnetic field strength. Table 5.1 lists some commonly observed NMR nuclides, their gyromagnetic ratios and resonance frequencies in an applied magnetic field ( $B_0$ ) of 11.74 T. In general, only one nuclide is observed at a time, although schemes for simultaneous detection of more than one nuclide have been described [4–6]. From Table 5.1, it is expected that in an 11.74 T magnetic field,  $^1\text{H}$  will resonate at ~500 MHz. If all of the  $^1\text{H}$  spins in a molecule resonated at exactly the same frequency, they would not be distinguishable and NMR would not be particularly useful. However, local variations in the magnetic field arise from interactions between electrons in the chemical environment surrounding the observed nuclear spin and the applied field. Depending on the spatial



distribution of electron density surrounding the observed nuclear spin relative to the applied magnetic field  $B_o$ , these local variations can either increase or decrease the net magnetic field  $B_{\text{eff}}$  sensed by the nuclear spin. If the effect is additive ( $B_{\text{eff}} > B_o$ ), the Zeeman splitting increases slightly, the resonance moves to a higher frequency, and the nucleus is *deshielded*. If  $B_{\text{eff}} < B_o$ , the resonance moves to a lower frequency, and the nuclear spin is *shielded*. Such variation in resonant frequencies of spins as a function of chemical environment is referred to as *chemical shift*. Chemical shifts,  $\delta$ , are usually reported as a ratio of the difference in resonance frequency of the nucleus in question ( $\nu_{\text{obs}}$ ) relative to a standard  $\nu_{\text{ref}}$ :

$$\delta_{\text{obs}} = \frac{\nu_{\text{obs}} - \nu_{\text{ref}}}{\nu_{\text{ref}}} \quad (5.4)$$

Chemical shifts tend to be quite small relative to the reference frequency  $\nu_{\text{ref}}$ , often in the parts per million (ppm) range, and are so reported. This convention has the added convenience of being field-independent, so that chemical shifts can be compared between different spectrometers and different magnetic field strengths.

Because the net shielding/de-shielding of a nuclear spin depends on the spatial distribution of electron density around the nucleus as well as the orientation of that density relative to the applied magnetic field  $B_o$ , chemical shift is determined by the *shielding tensor*, the value of which depends upon the orientation of the molecular frame in the applied magnetic field. For samples in which motions are restricted (solids, liquid crystals), this leads to a spread of chemical shifts for a given nuclear spin over a range determined by the principal components of the shielding tensor. However, in isotropic liquids, the random tumbling of the molecule averages the chemical shielding over all orientations, reducing the chemical shift to a scalar value so that only a single resonance line is observed.

The most commonly observed nuclei in biomolecules are  $^1\text{H}$ ,  $^{13}\text{C}$ , and  $^{15}\text{N}$ . Of the three, the chemical shift of  $^1\text{H}$  is most obviously affected by environmental factors (temperature, pH, hydrogen bonding and shielding/de-shielding from nearby aromatic rings known as *ring current* effects). Indeed, the extent of folding of a protein can often be determined qualitatively by a quick examination of the  $^1\text{H}$  spectrum. A folded protein generally shows greater  $^1\text{H}$  chemical shift dispersion than the same protein unfolded, since close packing of aliphatic and aromatic amino acid side chains give rise to distinctive *upfield* (towards lower  $\delta$ ) shifts, while regular hydrogen bonding patterns in secondary structures such as turns and  $\beta$ -sheets yield *downfield* (towards higher  $\delta$ ) shifts for the involved amide protons. Note from Fig. 5.4 that aliphatic protons (attached to  $sp^3$  carbon) resonate between  $\sim 0$  and 5 ppm, aromatic ( $sp^2$ -C-attached) protons tend to cluster between 6 and 7 ppm, while amide protons cover a range between 6 and 10 ppm.

The chemical shift range of  $^1\text{H}$  is limited relative to other nuclei in that the allowed electron distribution around the hydrogen atom (in a  $1s$  orbital) is relatively spherical and not easily distorted.  $^{13}\text{C}$ , on the other hand, is much more sensitive to bonding and hybridization effects than  $^1\text{H}$ . The shielding patterns and electron distribution of  $sp^3$  vs.  $sp^2$  hybridization, the type and electronegativity of atoms bonded

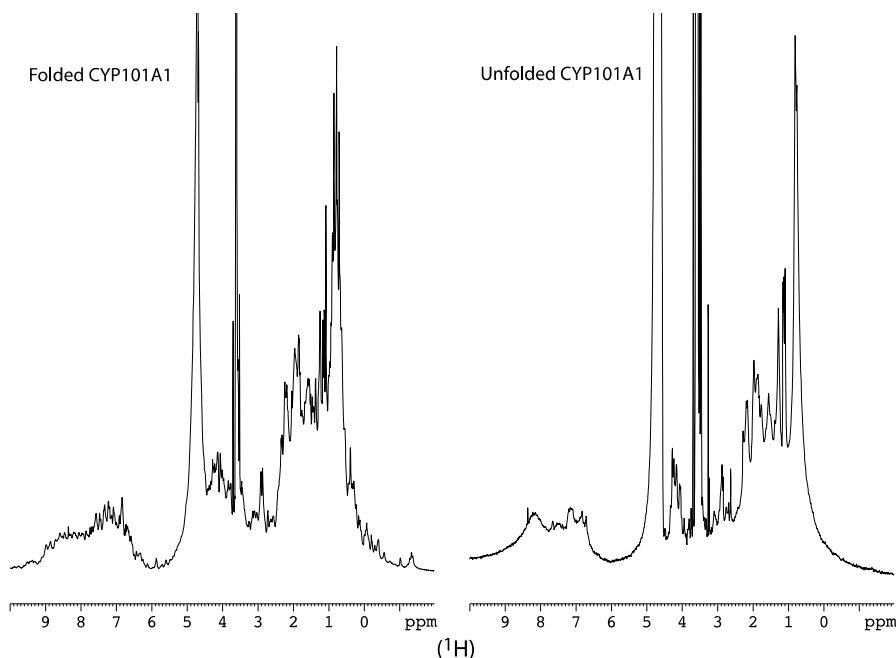


**Fig. 5.4**  $^1\text{H}$  NMR spectrum of folded (*left*) vs. unfolded (*right*) cytochrome P450cam (CYP101A1), showing increased spectral dispersion for the folded 46 kDa enzyme

to the observed  $^{13}\text{C}$ , and even branching patterns and dihedral angles formed by attached functionality have well-characterized and predictable effects on  $^{13}\text{C}$  shifts [7]. Analysis of  $^{13}\text{C}$  chemical shifts as a way of predicting or determining secondary structures in proteins is now common, and multiple programs and web-accessible resources are available for this purpose, as discussed below.

#### 5.4.2 Paramagnetic Effects on Chemical Shift

The above generalizations regarding  $^1\text{H}$ ,  $^{13}\text{C}$ , and  $^{15}\text{N}$  shifts hold true under most circumstances in diamagnetic molecules (i.e., molecules with no unpaired electronic spins present). However, in the presence of a metal center or metal-containing prosthetic group with unpaired electronic spins, such as a heme or iron-sulfur cluster, the effects of electronic spin on chemical shifts are often quite large. In solution NMR, these effects fall into two classes, *contact* and *pseudocontact shifts*. The contact shift results from overlap between orbitals containing unpaired electron spin density and those involving the shifted nuclear spin, and is therefore usually restricted to spins that are part of the same bonded unit as the paramagnetic center. Contact shifts are often observed to  $^1\text{H}$ ,  $^{15}\text{N}$ , and  $^{13}\text{C}$  resonances in Fe(III) and

high-spin Fe(II) hemes, as well as to  $^1\text{H}$  and  $^{15}\text{N}$  spins that are involved in hydrogen bonding or other direct interactions with iron-sulfur clusters or other paramagnetic metal centers in proteins.

Pseudocontact shifts result from through-space interactions between the electronic and nuclear spin dipoles, and can thus be observed for nuclear spins that are not directly part of the bonded system containing the unpaired spin. For example,  $^1\text{H}$  spins located above or below the plane of a heme prosthetic group in a protein often experience exaggerated shifts due to pseudocontact interactions.

A detailed examination of NMR of paramagnetic molecules is beyond the scope of this article. For the interested reader, there are a number of useful monographs and reviews [8, 9]. However, it is worth noting here that not only are chemical shifts affected by paramagnetism, but relaxation tends to be much more efficient for nuclear spins in the presence of unpaired electrons. This means that coherence transfer experiments are typically more difficult in paramagnetic systems, because coherences relax too quickly to be efficiently transferred between spins. However, enhanced relaxation due to paramagnetism has been used to advantage by the introduction of paramagnetic centers in the form of spin labels and paramagnetic metal ions to examine protein–protein interactions [10], oligomerization [11], surface exposure [12], and characterization of membrane proteins [13].

### 5.4.3 *J-Coupling and Coherence Transfer—the Basis of Multidimensional NMR*

As discussed above, one of the major advantages of NMR is the potential for creating relatively long-lived coherences on one spin that can then be transferred to a coupled spin for further evolution before detection. The appropriate excitation, evolution, and transfer of coherence allow the correlation between coupled spins to be established. In solution NMR, the primary mechanism for coherence transfer is *J*-coupling, also known as *scalar coupling*. *J*-coupling results from the interactions between nuclear spins mediated by the electrons in the overlapping orbitals that link the coupled nuclei. Because electrons have spin, they are affected by the spin state of the nuclei, changing their energies slightly depending upon whether they have the same or opposite spin relative to the nucleus with which they interact. This change in energy is detected by nuclear spins that are part of the same bonded system, resulting in slightly different energy levels (splitting) that depend upon the spin states of coupled nuclear spins in the same system. Thus, a  $^{15}\text{N}$ – $^1\text{H}$  bonded pair in a peptide bond will have two signals for each nuclear spin, with intensities reflecting the populations of  $+1/2$  and  $-1/2$  spins of the coupling partner. The separation of the signals is the same for both nuclei, and is termed the *coupling constant*. The *J*-coupling constant is represented by a superscript indicating the number of bonds by which the coupled spins are separated and a subscript indicating which atoms are involved. For example, the NH pair in an amide is coupled by  $^1J_{\text{NH}}$ , and the splitting observed is usually on the order of 94 Hz (Fig. 5.5). One-bond couplings are usually the largest in magnitude, since orbital overlap between bonded atoms is the most

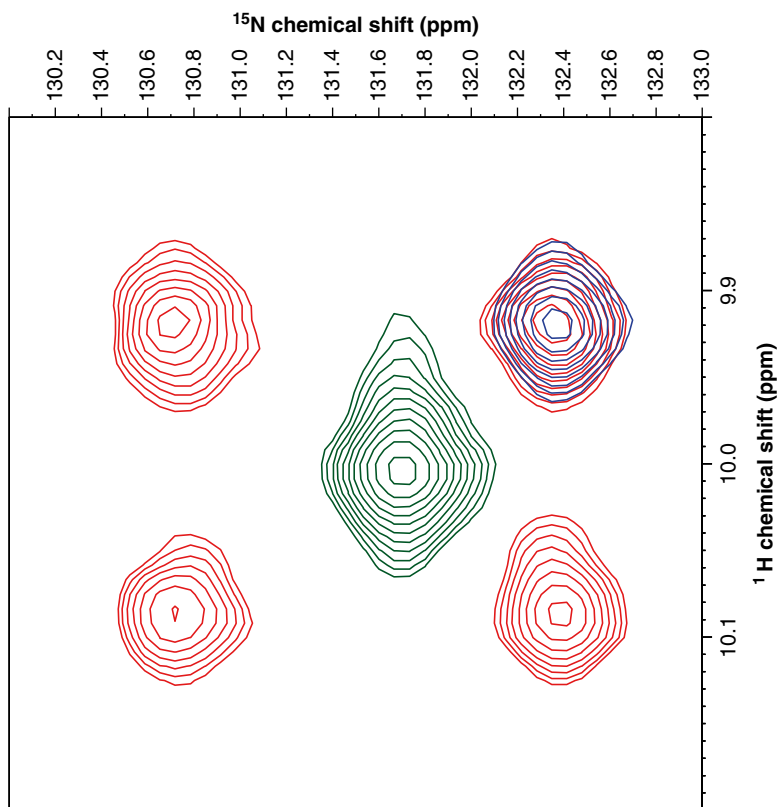


**Fig. 5.5** Superimposed coupled (red), decoupled (green), and TROSY-HSQC (blue) spectral correlations for a single N–H pair in an enzyme. The four red peaks comprise the correlation in the coupled spectrum, and are split from the adjacent peaks in both dimensions by the  $^1J_{\text{NH}}$  coupling ( $\sim 90$  Hz). Decoupling during evolution and acquisition results in a collapse of the four peaks into a single correlation (green central peak), simplifying the spectrum. Note that the lower right component is the narrowest and most intense, and can be selected exclusively using TROSY phase cycling. The TROSY spectrum (blue) is superimposed on the coupled spectrum

direct. Two protons attached to the same carbon (geminal coupling) are coupled to each other by  $^2J_{\text{HH}}$ , ranging from 5 to 15 Hz. Two protons on adjacent carbons show vicinal couplings  $^3J_{\text{HH}}$  between 0 and 15 Hz. Because of the requirement that orbitals overlap for  $J$ -coupling to occur, three-bond couplings are quite sensitive to dihedral angle, and the measured values for  $^3J$ -couplings can be used as restraints for calculations of polypeptide and polynucleic acid structures [14, 15]. Weak heteronuclear couplings can sometimes be observed even across a strong  $^{15}\text{N}$ – $^1\text{H}\cdots\text{O}=\text{C}$  hydrogen bond, as in nucleic acid base pairing [16].

This leads to an important observation for coherence transfer in NMR: Coherence transfer efficiency is directly proportional to the size of the mutual coupling of the spins between which coherence is transferred. This is a critical consideration for

multistep coherence transfers, such as those found in three-dimensional NMR experiments. As such, one-bond couplings are the most commonly used for coherence transfer in multidimensional NMR. A more complete description of such experiments is provided later in this article, and Scheme 5.1 lists some of the more common couplings used in biomolecular NMR for coherence transfer.

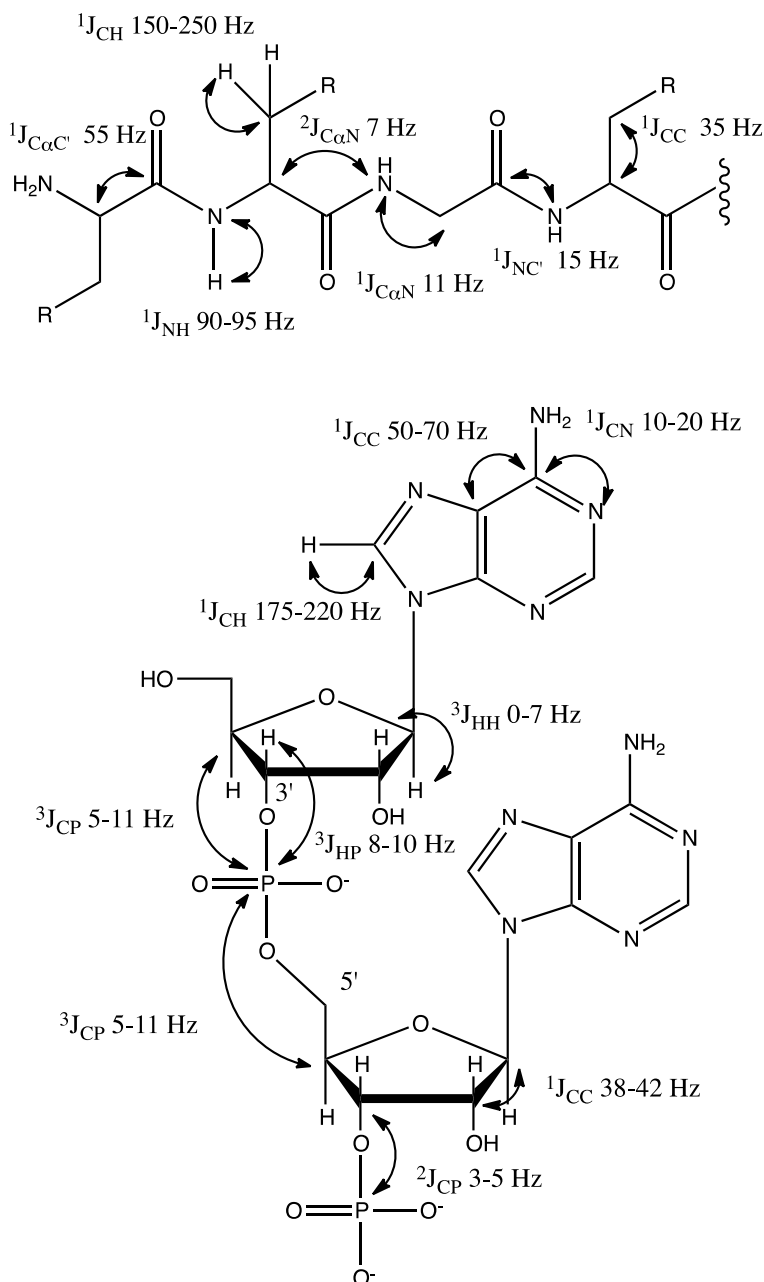
As  $^1\text{H}$  is never directly bonded to another  $^1\text{H}$  (except in  $\text{H}_2$ ),  $^1\text{H}$ – $^1\text{H}$   $J$ -correlation experiments must rely on 2- and 3-bond couplings. However, given the relative abundance and sensitivity of  $^1\text{H}$ , this is not as large a drawback as it is for other nuclei. Indeed, one of the first two-dimensional NMR experiments to enter common use, COSY (for *correlated spectroscopy*), showed that it was possible to map complete  $^1\text{H}$  spin systems (e.g., the side chain and backbone  $^1\text{H}$  resonances of a single amino acid residue) by through-bond correlations for small proteins and nucleic acids [17]. A later refinement of COSY, double-quantum filtered (DQF) COSY, is still frequently used for characterizing small organic molecules, peptides, and oligonucleotides [18] (Fig. 5.6).

An important breakthrough in identifying and correlating  $^1\text{H}$  spin systems was the development of the TOCSY experiment [19, 20] Fig. 5.6. TOCSY (for *totally correlated spectroscopy*) takes advantage of the ability of coupled oscillators with the same natural frequency to transfer energy from one to another. Under normal circumstances, free precession of coupled coherences at their respective Larmor frequencies prevents this type of transfer, known as the *Hartmann–Hahn effect*. However, if a relatively long low-power RF pulse is applied appropriately, a phenomenon known as “spin-locking” takes place: The free precession of individual coherences is halted, and components of the coherences are forced to remain in phase with each other, yielding Hartmann–Hahn matching. Under these circumstances, energy transfer occurs between coupled coherences, and once the spin-locking field is released and the coherences detected, the resulting signal amplitudes will be modulated by the frequencies of all of the spins that transferred energy to each other during the spin lock. The TOCSY experiment has the advantage over DQF-COSY in that all of the  $J$ -correlations involving a particular signal are observed simultaneously, reducing ambiguity in crowded spectra.

While  $^1\text{H}$  is the only naturally abundant spin that typically occurs in multi-spin coupled systems, introduction of uniform  $^{13}\text{C}$  labeling into a biomolecule allows similar experiments to identify complete  $^{13}\text{C}$  spin systems as well. The HCCH-TOCSY experiment [21], which will be described more completely in the next section, involves spin locking of the  $^{13}\text{C}$  nuclei within a coupled spin system, so that all of the coupled carbons can be identified in a single data set.

#### 5.4.4 Sequential Resonance Assignments, Polarization Transfer, and Triple-Resonance Experiments

Most of the value of biomolecular NMR can only be realized if resonances have been assigned to a specific atom in the macromolecule. This is true regardless of whether the macromolecule under consideration is a protein or a nucleic acid. Knowing, for



**Scheme 5.1** Approximate values of  $J$ -coupling constants commonly used for coherence transfer and dihedral angle measurements in biomolecular NMR. *Top*, protein, *bottom* RNA. Values for proteins adapted from [154], and for RNA adapted from [155]

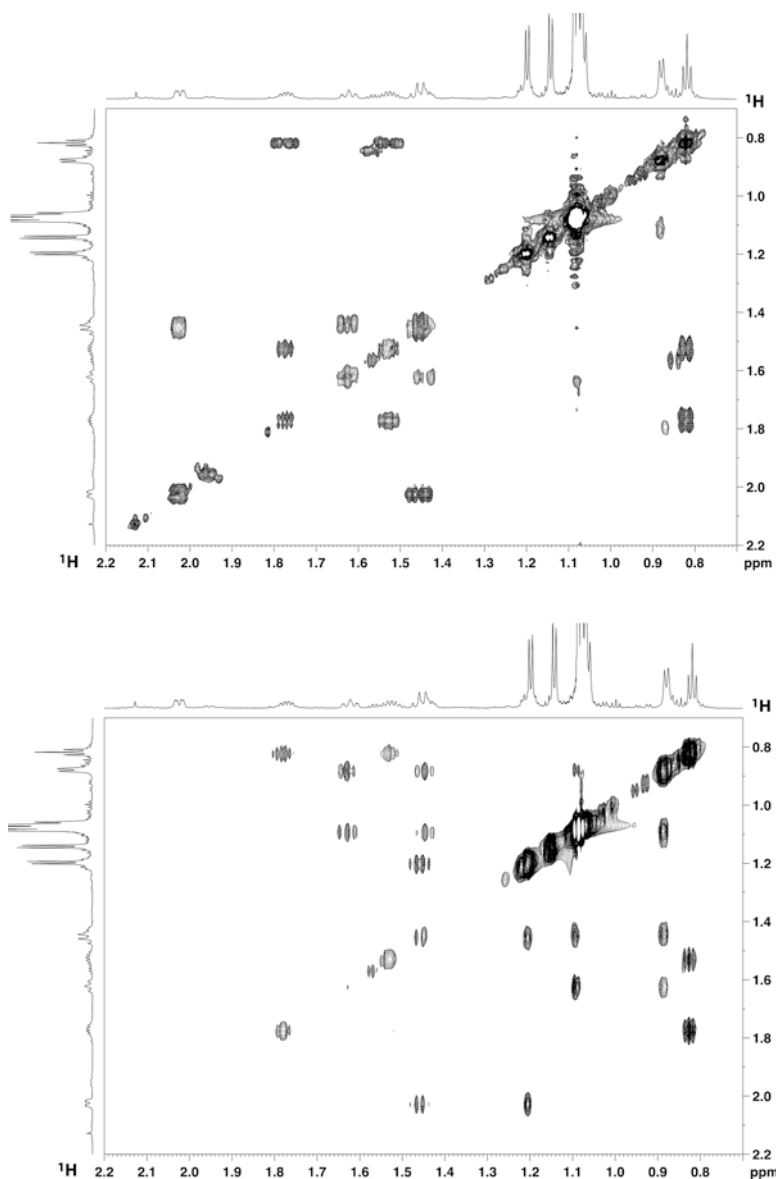


**Fig. 5.6** Corresponding regions of the two-dimensional 800 MHz  $^1\text{H}$  COSY (*top*) and TOCSY (*bottom*) spectra of mycinamicin, a macrolide antibiotic. Direct correlations that are obvious in the COSY spectrum are either less intense or completely absent in the TOCSY spectrum, where multistep coherence transfers predominate

example, that a valine spin system identified by HCCH-TOCSY in an enzyme is affected by adding substrate doesn't help much if one doesn't know to which of the 35 valine residues in the enzyme the spin system belongs. The process of sequential resonance assignment is therefore a critical (if sometimes challenging) part of the analysis of biomolecular NMR data. A useful guide as to whether a protein, nucleic acid, or complex can be assigned by NMR methods is provided by the Biological Magnetic Resonance Data Bank (BMRB, [www.bmrb.wisc.edu](http://www.bmrb.wisc.edu)). This well-curated database is organized so as to allow search by keyword or molecule type, as well as by the methodology used, and so is a convenient first stop for considering the viability of a project. Deposition of experimental NMR data (sequential assignments, NOEs, coupling constants, residual dipolar couplings (RDCs), etc.) in the BMRB is a prerequisite for the deposition of NMR-determined biomolecule structures in the RCSB Protein Data Bank ([www.rcsb.org/pdb](http://www.rcsb.org/pdb)).

While homonuclear ( $^1\text{H}$ ,  $^1\text{H}$ ) 2D NMR experiments are still widely used for the characterization of peptides, oligonucleotides, and small proteins [22], sequential resonance assignments in proteins >5 kDa are made almost exclusively using uniformly  $^{15}\text{N}$  and  $^{13}\text{C}$  labeled samples via a suite of triple-resonance three-dimensional NMR experiments [23]. These experiments take advantage of 1- and 2-bond  $J$ -couplings between  $^{15}\text{N}$ ,  $^{13}\text{C}$  and their attached protons to “connect the dots,” that is, determine the sequential connectivity of the individual amino acid spin systems via couplings involving backbone  $^{13}\text{C}$ ,  $^1\text{H}$ , and  $^{15}\text{N}$  resonances. As “triple-resonance” implies, each nucleus is resolved along one axis of a three-dimensional data set, with the observed correlations indicating connectivity between a particular set of resonances, one in each dimension.

The names of the various experiments describe the particular correlations that are observed in each. For example, the HNCA experiment [24, 25], a mainstay of the sequential assignment process, correlates an amide  $^1\text{H}$  with the  $^{15}\text{N}$  nitrogen to which it is bonded. In turn, the 1-bond coupling between that amide nitrogen and the  $\text{C}\alpha$  carbons of the residue to which the amide belongs as well as the 2-bond coupling to the  $\text{C}\alpha$  of the previous residue ( $i-1$ ) serve to connect two amino acid spin systems. The HN(CO)CA experiment, on the other hand, correlates the amide N with only the  $i-1$   $\text{C}\alpha$ , removing any ambiguity as to which  $\text{C}\alpha$  correlation is which in the HNCA experiment. The parentheses around (CO) in the experiment name mean that although coherence is passed through the carbonyl carbon from the amide to the preceding  $\text{C}\alpha$ , the carbonyl carbon is not resolved in the experiment, that is, the three axes are  $^1\text{H}$ ,  $^{15}\text{N}$ , and  $^{13}\text{C}\alpha$ . Another pair of experiments, HN(CO)CACB and HNCACB, use the same methodology, but extend correlations to the  $\text{C}\beta$  carbons, one carbon atom out from the polypeptide backbone into the side chains of adjacent amino acids. These experiments are particularly useful for sequential assignments, inasmuch as the combination of  $\text{C}\alpha$  and  $\text{C}\beta$  shifts are often diagnostic of amino acid type, while either shift alone is less so. Figure 5.7 provides representative views of these experiments to show how the correlations are made.

The observant reader might notice that all of these experiments involve the amide proton, and this is no accident. Because  $^1\text{H}$  has the largest gyromagnetic ratio of the three nuclei under observation, it is advantageous to detect  $^1\text{H}$  directly for the



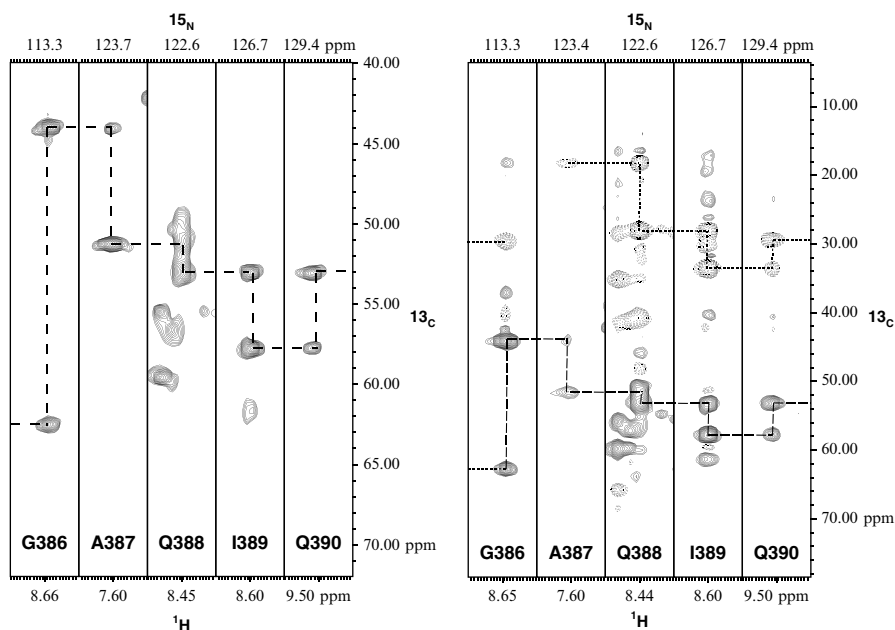


**Fig. 5.7** Strips from  $^{15}\text{N}$  planes of HNCA (left) and HNCACB (right) showing sequential connectivities for residues 386–390 of cytochrome P450<sub>cam</sub>, a 414-residue metalloenzyme. The  $^{15}\text{N}$  chemical shift of the correlating amide NH group is shown at the top of each strip, the NH  $^1\text{H}$  chemical shift is shown at the bottom, with  $^{13}\text{C}$  shifts shown along the right side of each set of strips. Darker correlations are for C $\alpha$  with either the adjacent NH or the NH of the following residue. Lighter dotted line correlations show similar information for C $\beta$

greatest sensitivity. However, the  $^1\text{H}$  advantage can be further exploited using a trick called *polarization transfer*. Because the proton has the largest  $\gamma$  of the nuclei involved, it exhibits the largest Boltzmann population difference between Zeeman states at a given magnetic field. By applying the appropriate series of simultaneous pulses to  $^1\text{H}$  and  $^{15}\text{N}$ , it is possible to “sort” the  $^{15}\text{N}$  spins by the spin state of the attached  $^1\text{H}$ , essentially transferring the  $^1\text{H}$  population difference (and the corresponding improvement in sensitivity) that naturally occurs for proton to the attached  $^{15}\text{N}$  [26]. This is the first step in all of the triple-resonance experiments noted above. Polarization is transferred from amide  $^1\text{H}$  to amide  $^{15}\text{N}$ . Subsequent simultaneous pulses on  $^{15}\text{N}$  and  $^{13}\text{C}$  pass this polarization on to the appropriate  $^{13}\text{C}$  atoms. At each nucleus along the way, the transferred polarization is allowed to evolve at the Larmor frequency of the nucleus on which it resides, thus labeling the resulting coherence with the chemical shift of each nucleus. After the coherence is appropriately labeled, it is passed back through reverse polarization transfers to the amide  $^1\text{H}$  from which it started, where it is detected.

The pulse sequence of an HNCA experiment is shown in Fig. 5.8, with the various polarization transfer steps marked. Coherence transfer pathways are selected by appropriate pulse and receiver phase cycling, and the application of *pulsed field*

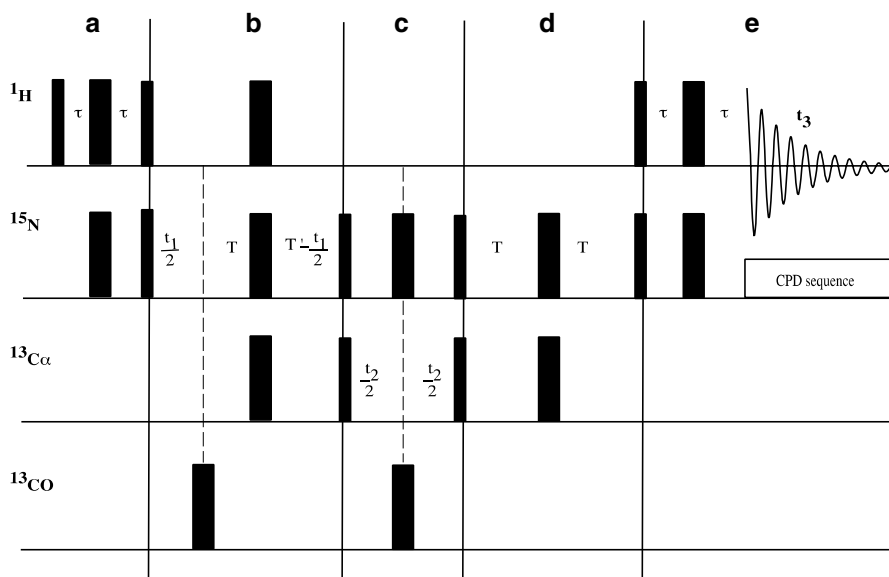


**Fig. 5.8** Simplified HNCA pulse sequence. No phase cycling or pulsed field gradients are shown. Pulses are indicated by vertical black bars on the RF channels on which they are applied. Thinner bars are 90° pulses, thicker bars are 180° pulses. (a) Polarization transfer from amide  $^1\text{H}$  to  $^{15}\text{N}$ . (b) Frequency labeling of coherence on  $^{15}\text{N}$  during independent time variable  $t_1$ , and refocusing of carbonyl (CO) coupling with  $^{15}\text{N}$ . (c) Coherence transfer from  $^{15}\text{N}$  to  $^{13}\text{C}_\alpha$  and frequency labeling of coherence on  $^{13}\text{C}_\alpha$  during independent time variable  $t_2$ . (d) Return coherence transfer from  $^{13}\text{C}_\alpha$  to  $^{15}\text{N}$ . (e) Return coherence transfer from  $^{15}\text{N}$  to  $^1\text{H}$  and detection during independent time variable  $t_3$ , with composite pulse decoupling (CPD) on  $^{15}\text{N}$  during  $^1\text{H}$  signal acquisition. Three independent time variables ( $t_1$ ,  $t_2$ , and  $t_3$ ) transform into three frequency domains in three dimensions for  $^{15}\text{N}$ ,  $^{13}\text{C}_\alpha$ , and  $^1\text{H}$ .

*gradients* (PFGs). The “frequency labeling periods” during which chemical shift evolution occurs are called  $t_1$ ,  $t_2$ , and  $t_3$ . In the experiments shown, the frequency-labeling periods  $t_1$  and  $t_2$  change in duration incrementally throughout the course of the 3D experiment, providing a time-domain modulation of the resulting signal that reflects the Larmor frequencies of the spins evolving during that frequency-labeling period. The third period,  $t_3$ , is the usual acquisition of the NMR signal. The resulting time-domain data set is then subjected to three separate Fourier transforms, one with respect to each of the three frequency-domain dimensions, yielding the final three-dimensional frequency-domain spectrum. The HCCH-TOCSY experiment mentioned previously also begins with polarization transfer, in this case between  $^1\text{H}$  and the directly bonded  $^{13}\text{C}$ . Thus, the coherence that is passed via Hartmann–Hahn transfer between carbon atoms during the spin-lock is the result of polarization transfer. The Hartmann–Hahn transfer therefore benefits from the improvement in sensitivity. A related experiment is CBCA(CO)NH, in which initial polarization transfer occurs from  $^1\text{H}$  to directly bonded  $^{13}\text{C}_\alpha$  and  $^{13}\text{C}_\beta$ , and eventually passed to the NH of the ( $i+1$ ) residue, yielding information similar to HN(CO)CACB.



must proceed through two-bond and three-bond  $^{13}\text{C}$ – $^{31}\text{P}$  couplings (HPC experiment). For this reason, nucleic acid sequential assignments are typically more dependent on internucleotide nuclear Overhauser effects, discussed below, than on coherence transfer experiments [28, 31].

#### 5.4.5 Dipolar Coupling and Nuclear Overhauser Effects

In addition to  $J$ -coupling, another mechanism for information and energy transfer between nuclear spins is *dipolar coupling*. Unlike  $J$ -coupling, dipolar coupling is a direct through-space interaction between two spins, and so does not require that the spins be part of the same bonded system, or even that they be part of the same molecule. Dipolar coupling ( $D$ -coupling) only requires spatial proximity of the coupled spins. In the case of  $^1\text{H}$  in solution, internuclear distances  $<5 \text{ \AA}$  are typical for observable dipolar interactions. Consider two bar magnets held close to each other. They clearly exhibit preferred orientations with respect to each other. Similarly,  $D$ -coupled nuclear spins also affect the energy levels of their coupling partners. The dipolar coupling constant  $D$  between two spins is proportional to the inverse cube of the distance between the coupled spins,  $r$ , and the angle  $\theta$  made by the internuclear vector  $\vec{r}$  with respect to the applied magnetic field:

$$D = \frac{3\cos^2\theta - 1}{r^3} \quad (5.5)$$

For a freely tumbling molecule in solution, the averaging of the angle  $\theta$  over all possible orientations means that there is no splitting of resonances due to the dipolar coupling, as  $D$  is averaged over all values, positive and negative. Despite the fact that  $D$  splitting is not observed in solution, dipolar interactions between spins are active, and provide important mechanisms for both  $T_1$  and  $T_2$  relaxation. Let us examine spin–spin ( $T_2$ ) relaxation. Consider a coherence generated by an RF pulse as in Fig. 5.3. Dipolar coupling provides a mechanism for random energy exchange between spins, so that a coherent spin may change its spin state by passing energy along to a  $D$ -coupling partner. This random spin state change (sometimes called a “spin flip”) results in a decrease in coherence, that contributes to  $T_2$  relaxation. Indeed, this type of  $D$ -modulated interaction is the origin of the term spin–spin relaxation. The  $D$ -modulated interaction between spins can also result in both coupled spins either gaining or losing energy simultaneously to the surroundings (or lattice). This results in a net population change for both spins (as opposed to just a loss of coherence) and in this case,  $D$ -coupling contributes to  $T_1$  relaxation (return towards an equilibrium distribution of spin states) as well as  $T_2$ .

Because  $D$ -coupling provides a mechanism for spin energy exchange both between coupled spins and with the surroundings, it renders the state populations (and therefore signal amplitudes) of spins dependent upon the corresponding state populations of their  $D$ -coupling partners. If, for example, one saturates the transition of one spin (by applying a long low-power pulse at the transition frequency of

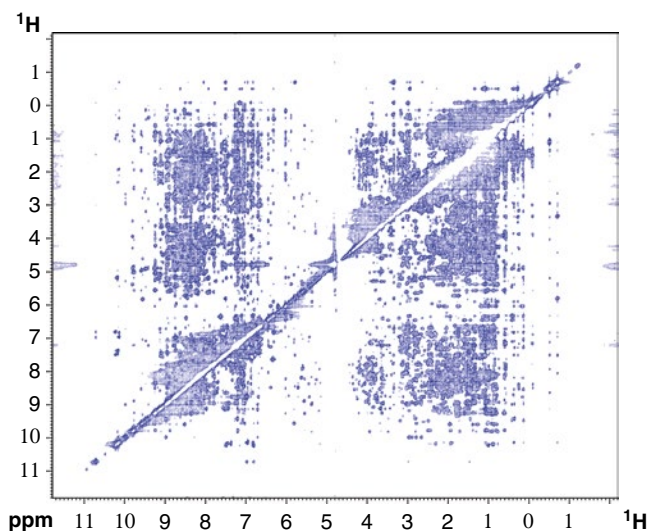


**Fig. 5.10**  $^1\text{H}$  NOESY of acireductone dioxygenase in 90 %  $\text{H}_2\text{O}$  obtained at 750 MHz  $^1\text{H}$ . Note the high degree of overlap in the two-dimensional spectrum

that spin), the signal intensities of that spin's  $D$ -coupling partners will be affected. This change in signal intensity for one spin upon perturbing the spin population of a  $D$ -coupling partner is termed a *nuclear Overhauser effect (NOE)*, and is an important source of structural information for solution NMR. Before the advent of multi-dimensional NMR methods, NOEs were typically measured by RF saturation of one signal in the NMR spectrum while the change in intensities of other signals were monitored, thereby identifying spins close in space to the saturated spin. However, the experiment is more conveniently accomplished as a two-dimensional experiment called NOESY [32]. As in other two-dimensional experiments, the first pulse generates coherence that evolves during the frequency-labeling period  $t_1$ . This is followed by a second pulse that initiates the *mixing time*, during which frequency-labeled coherences exchange spin energy with their  $D$ -coupled partners. The mixing time can vary in length depending upon the size of the molecule and  $T_1$  relaxation rates of the various spins, but mixing times of 50–100 ms are typical for proteins and nucleic acids. Finally, the mixing time is ended with another pulse that generates the labeled coherences that are detected during  $t_2$ . Fourier transformation with respect to both time dimensions yields a two-dimensional spectrum in which coupled spins give rise to cross-peaks indicating their dipolar connectivity (Fig. 5.10).

Typically, NOESY is a  $^1\text{H}$ ,  $^1\text{H}$  correlation experiment, since  $^1\text{H}$  is usually the only spin in sufficient abundance to form  $D$ -coupled networks without isotopic labeling. Until the advent of triple-resonance sequential assignment experiments, the NOESY experiment formed a critical piece of the sequential assignment puzzle, because it was the only way to get connectivity between spin systems of adjacent amino acid residues in a protein or adjacent bases in a polynucleotide. Furthermore, identification of NOEs between sequentially nonadjacent residues forms the basis of three-dimensional

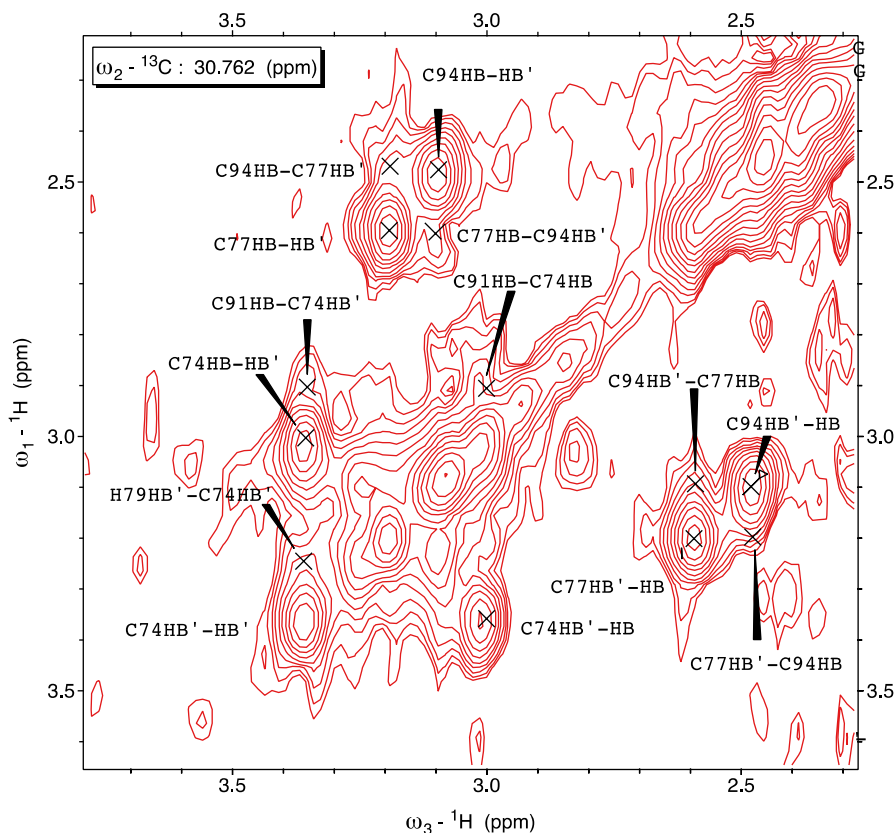


**Fig. 5.11** Plane from  $^{13}\text{C}$ -edited NOESY (800 MHz  $^1\text{H}$ ) of HypA, a nickel chaperone from *H. pylori*, at 30.76 ppm, corresponding to the  $^{13}\text{C}\beta$  shifts of the four cysteine ligands of bound  $\text{Zn}^{2+}$ . Labeled NOE cross-peaks indicate close approach of the  $\text{C}\beta\text{H}_2$  groups of pairs of ligands

structure determination of biological macromolecules by NMR. NOE-based distance restraints are incorporated into a variety of computational approaches for calculating structures, and while other sources of information are available and will be discussed, the NOESY experiment remains a mainstay of biomolecular structure determination. For larger, more complex systems, the NOESY spectrum can be resolved by marrying the NOESY experiment to HSQC, generating a three-dimensional experiment, NOESY-HSQC [33, 34]. Depending upon whether the HSQC correlates  $^1\text{H}$  to  $^{13}\text{C}$  or  $^{15}\text{N}$ , one can identify NOEs observed for a particular  $^1\text{H}$  spin resolved according to the chemical shift of the  $^{13}\text{C}$  or  $^{15}\text{N}$  to which the  $^1\text{H}$  spin is bonded (Fig. 5.11).

The sign of the observed NOE (that is, whether the NOE increases the signal intensity of coupling partners or decreases it) depends upon which mechanism discussed above predominates, the spin flip (exchange of spin states without a net change in overall spin populations), or simultaneous gain or loss of spin energy by both coupled spins, with concomitant change in overall spin populations. Typically, for small

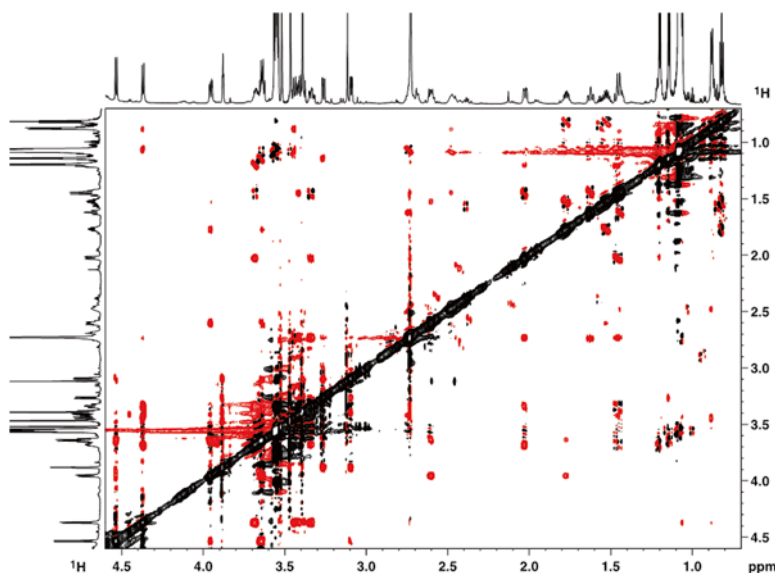


**Fig. 5.12** Portion of the 800 MHz  $^1\text{H}$  ROESY spectrum of mycinamicin, a macrolactone antibiotic ( $\sim 750$  Da). Anti-phase (red-black alternating) cross-peaks are due to  $J$ -coupling, while pure phase peaks are primarily through-space (ROE) correlations

molecules in nonviscous solvents, the simultaneous mechanism predominates, and direct NOEs are positive (i.e., signals are enhanced), while for large molecules or molecules in viscous solvents, the spin flip mechanism predominates and NOE decreases overall signal intensity. In small molecules, indirect NOEs (passed from one spin to another via a common  $D$ -coupled partner) tend to be small and negative, and can be distinguished from direct effects by the change in sign. The reasons for this observation are detailed in several monographs [35, 36]. On the other hand, for most proteins and nucleic acids, both direct and indirect NOE are negative in sign and are not readily distinguishable. This does not matter for the typical NOESY experiment with relatively short mixing times, although if the mixing time is too long, the information content decreases because NOEs can be observed between spins that are not directly  $D$ -coupled to each other. However, a major issue arises for molecules that fall in the molecular weight range of  $\sim 1,000$  Da, in that the two mechanisms balance each other and often no NOE is observed.

In such cases, an alternative experiment, called ROESY (for *rotating frame NOE spectroscopy*) can be used [37, 38]. During the mixing time of ROESY, a spin-lock field is applied to the precessing spins, much as in the TOCSY experiment. Now coherences are kept in phase that would otherwise evolve and  $D$ -coupled spins can cross-relax. The simultaneous mechanism predominates for all molecular weight ranges in the ROESY experiment, so all ROEs (rotating-frame NOEs) are positive, even for molecules in the 1,000 Da range (Fig. 5.12). Because the spin-lock RF field enables TOCSY transfers, care must be taken to distinguish true ROE ( $D$ -coupling



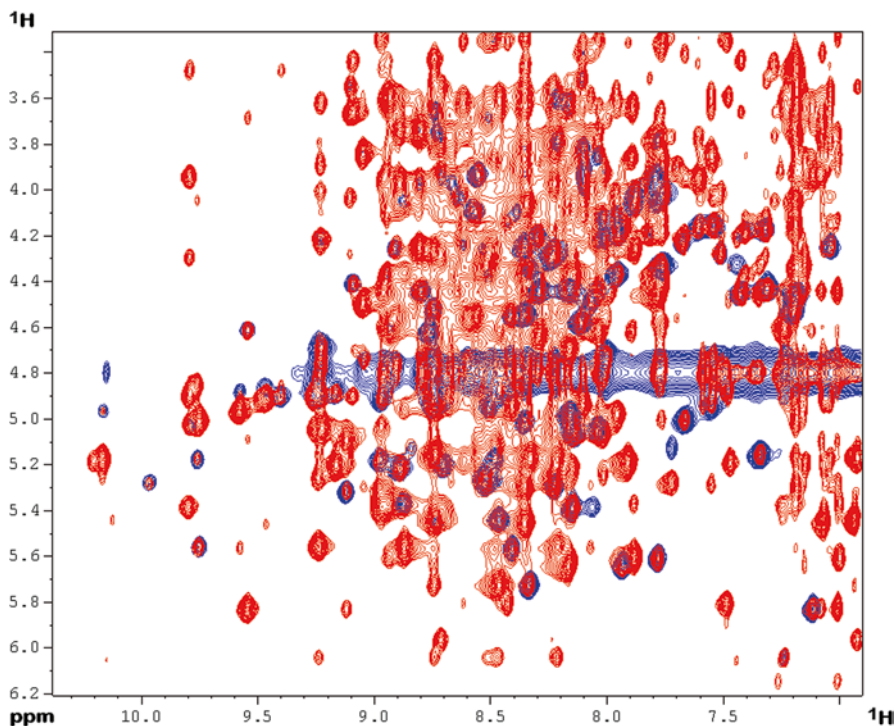


**Fig. 5.13** Overlay of a  $^1\text{H}$  TOCSY spectrum (blue) onto the  $^1\text{H}$  NOESY of acireductone dioxygenase (red). Both spectra were obtained at 750 MHz  $^1\text{H}$ . Region shown correlates NH (horizontal axis) with CoH resonances (vertical axis). TOCSY peaks correspond to intra-residue through-bond correlations, while NOESY cross-peaks indicate both intra- and inter-residue connectivities. Superimposed red-blue peaks indicate an intra-residue connectivity, while those only in red are inter-residue

effects) from TOCSY-type  $J$ -coupling transfers in ROESY datasets. Figure 5.13 shows an overlay of a TOCSY and NOESY experiment that illustrates this concept.

#### 5.4.6 Residual Dipolar Couplings (RDCs)

We will find that  $D$ -couplings are the primary mechanism of information and energy transfer between spins in solid-state NMR (SSNMR), because they are not averaged to zero by molecular tumbling as they are in solution. In fact,  $D$ -coupling constants can be very large (on the order of kHz for directly bonded atoms, as opposed to tens to hundreds of Hz for 1-bond  $J$ -couplings), and special techniques are required to simplify solid-state NMR spectra as a result of this. Furthermore, the orientation dependence of the  $D$ -coupling (due to the  $3\cos^2\theta - 1$  term in 5.4) is an important source of structural information. Each NOE exists in a unique frame of reference,



providing a distance between two  $D$ -coupled spins, but no orientation with respect to the molecular frame. Consider a globular protein structure, calculated only with NOE and secondary structure ( $J$ -coupling and chemical shift) restraints. One can think of the NOE as a rubber band connecting two atoms in the structure, holding them together with a flexible tether. If enough rubber bands are used to hold together disparate parts of the polypeptide, a reasonable structure can be obtained. However, if the molecule under consideration contains multiple domains, does not contain compact tertiary structure (as in DNA [39]) or contains regions that for some reason do not yield clean NOE connectivities, the relative orientations of those domains or regions remain in doubt. In this case, while local structural features (helices, sheets, turns) might be well defined structurally, the overall arrangement of these local features in the tertiary or quaternary structure is difficult to determine. Under these circumstances, *residual dipolar couplings* (RDCs) become an important source of structural information.

RDCs are measured by placing the molecule under investigation in a medium that introduces a slight orientational preference with respect to the applied magnetic field. Under these circumstances, the  $D$ -coupling is no longer averaged to zero, as it is in an isotropic medium. The (highly attenuated) dipolar coupling can then be measured as a variation of the  $J$ -coupling observed between the coupled spins in an isotropic medium. The RDC reflects the orientation of the vector connecting the coupled spins with respect to an alignment tensor, which is usually calculated in the course of structural refinement. Given that there are four independent solutions to RDC fittings, there is considerable ambiguity associated with RDC data in the case of an a priori structure determination [40]. This problem can be dealt with by measuring RDCs in more than one orienting medium, so that multiple independent alignment tensors are used in the fitting.

A variety of orienting media have been tested for measuring RDCs, and which is chosen often depends upon the physical and chemical properties of the molecule of interest. Indeed, any species with a high degree of *magnetic susceptibility anisotropy* (that is, the energy of the molecule varies depending on its orientation in the magnetic field) has the potential to provide an alignment medium. Some alignment media are oriented by the applied field (phage particles [41, 42], nematic liquid crystals [43–45] and bicelles/micelles [46, 47]), while in others, particularly stretched and compressed polyacrylamide gels, alignment is generated mechanically. Even chemical modification can be used for orienting macromolecules: If a polydentate ligand is introduced by covalent linkage, a paramagnetic metal ion with a high degree of magnetic anisotropy (e.g., Co(II)) can be used to obtain alignment [48]. Some of the earliest characterizations of RDCs were made using heme proteins, in which the metalloporphyrin exhibits sufficient magnetic anisotropy to induce a degree of alignment without addition of an external alignment medium [49]. Indeed, any species that has nonzero magnetic susceptibility anisotropy will likely exhibit some alignment; most globular proteins fall into this category [50]. However, the degree of alignment is almost always much smaller than what can be obtained using a defined aligning medium, and in order to distinguish the RDC from  $J$ -coupling and other effects, measurements must be made at multiple magnetic field strengths using specialized experiments for precise measurement of coupling constants.

### 5.4.7 Solid-State NMR (SSNMR)

The first NMR experiments were performed on a solid sample (paraffin wax) [51]. However, for many years, the relative simplicity of performing and analyzing solution NMR experiments meant that nonexperts were unwilling to venture into SSNMR, which is technically demanding and more difficult for the nonexpert to analyze. The reasons for this are understandable: The orientational dependence of the chemical shift in the absence of isotropic averaging means that in un-oriented (“powder”) samples, all orientations of a given species are present, so each spin gives rise to a complex resonance bounded by the maximum and minimum frequencies possible given the chemical shielding tensor of the spin in question (Fig. 5.14). The situation is further complicated by the presence of non-averaged dipolar couplings. As noted above, the dipolar coupling is typically much larger than  $J$ -couplings, and also has an orientational dependence, so that the  $J$ -coupling between two spins (which does not depend upon magnetic field strength or molecular orientation) is typically swamped by much larger (and variable) dipolar splittings (Fig. 5.15). Finally, while  $T_2$  relaxation is usually very efficient in solid-state samples, leading to broad lines, particularly for  $^1\text{H}$  spins,  $T_1$  is generally less efficient, so that unless special methods are employed, experiments for acquiring data of acceptable signal to noise are longer than for solution methods. Nevertheless, it is often the case that a macromolecule of interest is unsuited for solution NMR methods due to issues such as molecular weight, spectral complexity, membrane association, or limited solubility. In these instances, SSNMR provides some distinct advantages, and developments in commercially available SSNMR accessories and implementations of SSNMR experiments have made SSNMR more accessible to nonexperts. Probably the two most important such developments are the use of *magic-angle spinning* and *cross-polarization* methods.

### 5.4.8 Magic-Angle Spinning

Magic-angle spinning (MAS) involves spinning a randomly oriented (powder) SSNMR sample at high speeds, with the spinning axis placed at an angle  $\theta = 54.73^\circ$  (the “magic angle”) with respect to the applied magnetic field. MAS accomplishes two things. First, the spinning averages all orientations of the molecules in the sample except those that lie along the spinning axis. The observed chemical shift  $\sigma_{\text{obs}}$  of a spin is related to  $\theta$ , the angle between the applied field and the spinning axis by:

$$\sigma_{\text{obs}} = \sigma_{\text{iso}} + \frac{1}{2}(3\cos^2\theta - 1)(\sigma_{\text{iso}} + \sigma_{33}) \quad (5.6)$$

where  $\sigma_{\text{iso}}$  is the isotropic (solution) shift of the resonance under consideration and  $\sigma_{33}$  is the upfield limit of the chemical shift observed in the powder pattern SSNMR spectrum. Because the second term in (5.6) goes to zero when  $\theta = 54.73^\circ$ , the

**Fig. 5.14** Effect of magic-angle spinning on the  $^{13}\text{C}$  SSNMR spectrum of glycine. Note that as spinning speed increases (shown on the right of each spectrum), the spacing between the side bands increase, and greater intensity is observed for the center transition. The x-axis is the chemical shift of  $^{13}\text{C}$ . Courtesy of Prof. Janet Blümel, Texas A&M University

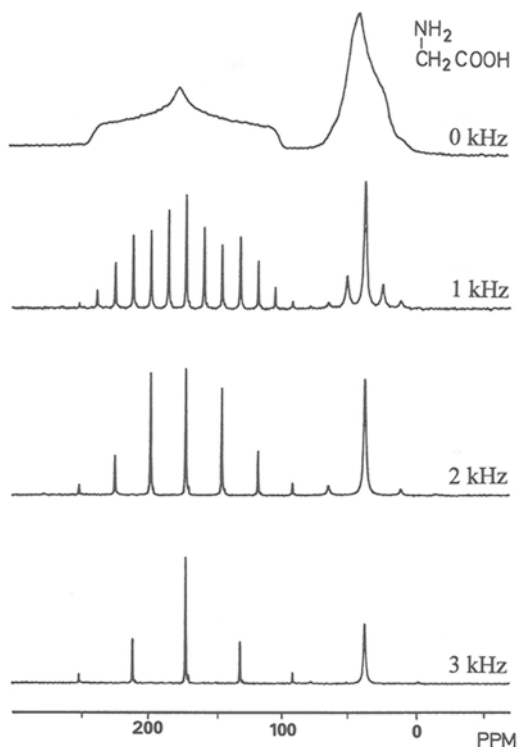
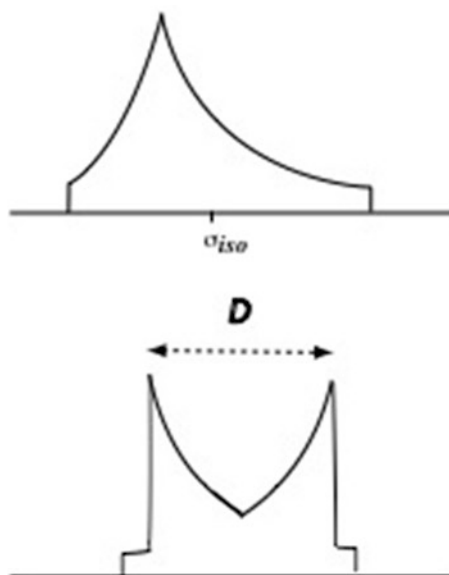


**Fig. 5.15** *Top*: representation of a powder pattern SSNMR spectrum, with  $\sigma_{\text{iso}}$  indicating the position of the isotropic (solution) shift of the observed resonance. *Bottom*: doubling due to dipolar coupling  $D$  between two nuclei. For directly bonded nuclei and protons bonded to the same atom, the coupling constant  $D$  can be on the order of kHz



resonance is observed at  $\sigma_{\text{iso}}$ , the same frequency as in solution. Secondly, the most significant terms contributing to the dipolar coupling also contain the form  $(3\cos^2\theta - 1)$ , and also go to zero with MAS. In principle, if the spinning speed is sufficiently high, a spectrum of singlets with CSA and  $D$ -coupling removed is observed. There are complications for MAS, however. First, if sample spinning is insufficiently fast, each resonance resolves into a series of lines separated from the central band  $\sigma_{\text{iso}}$  by the spinning frequency (Fig. 5.14). Secondly, even the highest obtainable spinning rates are usually insufficient to completely average the  $D$ -coupling between  $^1\text{H}$  and directly bonded heteronuclei (e.g.,  $^{15}\text{N}$ ,  $^{13}\text{C}$ ). This retained coupling results in considerable line broadening of the heteronuclear spins. As such, most SSNMR experiments also employ high-power  $^1\text{H}$  decoupling during acquisition of heteronuclear signals. Such decoupling rapidly interchanges the  $^1\text{H}$  spin states, so that the attached heteronuclear spin “sees” an average spin state for  $^1\text{H}$  and the dipolar coupling is removed.

#### 5.4.9 Cross-Polarization and Selective Reintroduction of $D$ -Couplings

The problems presented by large  $D$ -couplings and efficient  $T_2$  relaxation of  $^1\text{H}$  means that, except in unusual circumstances (e.g., very high spinning speeds and dilution of  $^1\text{H}$  spins),  $^1\text{H}$  is not the observed nucleus in SSNMR experiments on macromolecules. However, heteronuclei such as  $^{13}\text{C}$  and  $^{15}\text{N}$  have the same drawbacks that plague their direct observation in solution NMR, namely low sensitivity and, often, long  $T_1$  relaxation times. To circumvent these issues, most SSNMR experiments incorporate a *cross-polarization* step in which the Hartmann–Hahn condition is achieved by the application of high-power, relatively long-duration RF pulses to  $^1\text{H}$  and the heteronuclear spins simultaneously. This permits  $^1\text{H}$  to be used as a reservoir for both spin polarization and  $T_1$  relaxation.  $T_1$  relaxation is relatively efficient for  $^1\text{H}$ , even in solids, and cross-polarization allows the reservoir of  $^1\text{H}$  spins to “drain” non-Boltzmann populations from  $D$ -coupled heteronuclei, so that experiments can be repeated more rapidly for an improved signal to noise ratio. The other benefit of cross-polarization is the transfer of the inherently greater  $^1\text{H}$  sensitivity to the  $D$ -coupled heteronuclei. The mechanism of polarization transfer differs between solution and SSNMR: With the exception of the NOESY experiment, polarization transfer between spins in solution is mediated by  $J$ -coupling, whereas in SSNMR,  $D$ -couplings are used.

The  $D$ -coupling is also exquisitely sensitive to internuclear distances and orientations, and is used to transfer magnetization between spins in multidimensional SSNMR experiments. It is clear that in order to recover the information content inherent in  $D$ -coupling, it must be selectively reintroduced into the SSNMR experiment (as the point of MAS combined with high-power  $^1\text{H}$  decoupling is to get rid of unwanted  $D$ -coupling effects). A common way to reintroduce  $D$ -couplings is to use rotor-synchronized RF pulses. If an RF pulse is applied such that the pulse occurs at

the same point in the MAS rotation cycle each time, the motional averaging is removed for a fraction of the rotation period, and the  $D$ -coupling between spins affected by the RF pulse is reinstated momentarily. Because the RF pulse is always applied at the same point in the rotor cycle, the spins in the sample are affected in the same way each time, and an attenuated but non-averaged  $D$ -coupling develops between affected spins. An example of this type of experiment is called REDOR [52], in which the distance between two heteronuclei (e.g.,  $^{15}\text{N}$  and  $^{13}\text{C}$ ) can be measured relative to a known reference by the difference in signal intensity of one of the coupling partners as a function of whether or not rotor-synchronized pulses are applied to the other during the pulse sequence.

#### 5.4.10 Resonance Assignments by Solid-State NMR

REDOR is a 1D NMR sequence and is most useful when both heteronuclear signals have already been assigned to specific atoms in the structure. As with solution-state NMR, the usefulness of SSNMR as applied to biological macromolecules is exponentially improved by the availability of specific resonance assignments. For many years, such assignments were limited to targets of opportunity (labeled cofactors, unique residues, etc.). However, a variety of multidimensional SSNMR experiments developed over the past 10 years have made it possible to make sequential resonance assignments for small to midsize proteins [53–55]. The naming protocol for many of these experiments is similar to that used for solution NMR of proteins: The spin types that are correlated within the experiment give rise to the names: NCO and NCA correlate amide  $^{15}\text{N}$  resonances with those of adjacent carbonyl (CO) and C $\alpha$   $^{13}\text{C}$  spins, respectively, and NCOCX and NCACX extend the correlations to the next carbon in the coupling path, similar to the HNCACB experiment for solution-state NMR. For these types of two-dimensional heteronuclear SSNMR experiments, the detected nucleus is  $^{13}\text{C}$ , with cross-polarization between  $^1\text{H}$  and  $^{15}\text{N}$  in the first step. Polarization transfer between the spins of interest in many of these experiments is achieved by Hartmann–Hahn transfer. In order to insure that all spins of interest reach the Hartmann–Hahn condition at some point during the mixing period, amplitude- or frequency-modulated pulses are applied to one of the coupled spins so that a range of frequencies covering the spectral region of interest are present during the mixing period. Polarization transfer can also be achieved in SSNMR using REDOR sequences (for  $^{15}\text{N}$ ,  $^{13}\text{C}$  transfers) [56] or radio frequency-driven recoupling (RFDR) [57].

Recently, there has been renewed interest in direct  $^1\text{H}$  observation and assignment in SSNMR using a combination of very high MAS spinning speeds (28 kHz) and dilution of proton spins. The high spinning speeds reduce  $^1\text{H}$  line widths sufficiently to provide an acceptable degree of resolution in 2D  $^1\text{H}$ – $^{15}\text{N}$  correlation spectra, and  $^1\text{H}$  dilution can be obtained by expression of protein in perdeuterated media, and then allowing limited amide NH exchange for amides. This reduces  $^1\text{H}$ – $^1\text{H}$   $D$ -coupling sufficiently for the detection of resolved NH correlations [58, 59].

### 5.4.11 *Macromolecular Structure Determination by NMR*

The first use of two-dimensional NMR to determine the de novo structure of a protein (bull semen protease inhibitor, or BUSI) by the Wüthrich group in 1985 was rightly hailed as a milestone of structural biology [60]. While small by today's standards (57 residues), the BUSI structure demonstrated that NMR could stand alone as a method for determining biomolecular structures, once the exclusive domain of X-ray crystallography. In the intervening years, increasing magnetic field strength, improvements in instrumentation and data handling, introduction of multidimensional and multinuclear assignment methods, and selective and uniform isotope labeling, have rendered the determination of small soluble protein structures routine. Once a reasonably complete set of resonance assignments are in hand, the process of structure determination can begin. For compact soluble proteins, with molecular weights up to ~30 kDa, the process is relatively straightforward. NOEs must be identified and tabulated, especially those that are diagnostic of particular types of secondary structures. For example,  $\alpha$ -helices are characterized by strong sequential NH–NH NOEs and reasonably strong C $\alpha$ H–NH and C $\alpha$ H–C $\beta$ H NOEs between residues  $i$  and  $i+3$  within the helix, while antiparallel  $\beta$ -sheets are often identified by inter-strand C $\alpha$ H–C $\alpha$ H and NH–NH NOEs. Parallel sheets also exhibit characteristic NOE patterns, as do  $\beta$ -turns. An excellent summary of NOEs patterns typical of different secondary structural features can be found in Wüthrich's classic text on the subject [61]. Equally important are NOEs relating disparate secondary structural features to determine a global fold. NOEs between nonsequential secondary structures are typically observed between side chain resonances, and require reasonably complete side chain assignments. Dihedral angle restraints are another important source of structural information. Coupling constants can be measured and related to dihedral angles by means of Karplus-type relationships, which are empirically derived relations observed 3-bond  $J$ -couplings and the dihedral angle between the coupled spins. Furthermore,  $^1\text{H}$ ,  $^{15}\text{N}$ , and  $^{13}\text{C}$  chemical shifts of identified resonances can be related to backbone and side chain dihedral angles using a variety of statistical methods. Finally, RDCs can often relate the orientations of disparate secondary structural features that are too far apart to exhibit NOEs between each other. We have recently described the use of RDCs to characterize the solution conformations of cytochrome P450cam (46 kDa) via a restrained "gentle annealing" molecular dynamics (MD) protocol that found families of best-fit conformers that the enzyme occupies in solution [62, 63]. A number of other large proteins have been successfully characterized using RDC restraints [64, 65].

### 5.4.12 *Dealing with Larger Macromolecules and Membrane-Bound Proteins by NMR*

Above 30 kDa, structure determination becomes more difficult. While signal to noise and resolution issues have receded with improved technology, the problem of spectral complexity and overlap makes the process of resonance assignment for

larger soluble biomacromolecules by NMR less straightforward. Furthermore,  $T_2$  relaxation rates increase with longer correlation times (slower molecular tumbling), to the point where efficient coherence transfer required for multidimensional NMR experiments take longer than the lifetimes of the coherences involved. This problem can be ameliorated to a large extent by the preparation of extensively deuterated samples. By decreasing the  $^1\text{H}$  density of the sample via deuteration, cross-relaxation ( $T_2$ ) pathways are made less efficient, and many of the standard triple-resonance experiments for sequential backbone assignments are applicable to biomolecules with molecular weights  $>50$  kDa. However, deuteration comes at the cost of reducing the concentration of the most desirable nucleus for detection,  $^1\text{H}$ . In order to make use of standard triple-resonance experiments with uniformly deuterated samples, the NH protons critical for these experiments must be reintroduced either by unfolding-refolding (when possible) or by hydrogen-deuterium exchange using protonated buffers. For well-folded proteins and those not amenable to unfolding/refolding, buffer exchange is often incomplete, and non-exchangeable and isolated exchangeable NH groups will be difficult to assign. The deuteration of side chains also prevents the use of HCCH-TOCSY or other  $^1\text{H}$ - $^{13}\text{C}$  correlation experiments to assign or even detect side chain-side chain NOEs, which are critical for de novo characterization of tertiary structure in NOE-based structure determinations. Selective reprotonation schemes have been described that allow limited reprotonation of side chain methyl groups, which in turn can be used to detect nonsequential NOEs for structural work.

Even in the absence of sample deuteration, it is possible to extend many  $^1\text{H}$ -detected experiments for use with molecules over 30 kDa by modifying the detection portion(s) of the sequence with TROSY selection. TROSY (for *transverse relaxation optimized spectroscopy*) takes advantage of cross-correlation between the local fluctuations in magnetic fields that result in spin-spin relaxation of  $^1\text{H}$ - $^{15}\text{N}$  coupled spin pairs [66]. These local magnetic field fluctuations have both magnitude and sign, and can superimpose either constructively (both with the same sign) or destructively (opposite sign). If a  $^1\text{H}$ - $^{15}\text{N}$  HSQC experiment is acquired in un-decoupled mode, one observes a quartet of peaks, split by  $J_{\text{NH}}$  in both the  $^1\text{H}$  and  $^{15}\text{N}$  dimensions (see Fig. 5.5). Of the four peaks, one is considerably narrower and more intense than the other three, indicating a destructive interference between the fields that gives rise to spin-spin relaxation. TROSY-based experiments make use of phase cycling to select for just the narrowest peak of the quartet. This allows molecules that would otherwise give rise to broad overlapped spectra to be characterized in detail by NMR methods. CRINEPT (cross-correlated relaxation enhanced polarization transfer) is a passive version of this experiment, in which no selection is performed, but the broader components of the multiplets are not observed simply because of their large line widths [67]. CRINEPT works best for very large molecules ( $>60$  kDa), while TROSY often improves spectral appearance and interpretability even for relatively modest-sized molecules ( $>25$  kDa).

Many proteins of interest to the biophysicist are membrane-bound or membrane-associated. Even if the protein itself is of manageable size and appropriately

labeled for NMR purposes, the presence of a lipid bilayer of large and/or indeterminate size complicates the proceedings considerably. Membrane association always increases NMR line widths, rendering many coherence transfer experiments difficult because of short coherence lifetimes. Furthermore, unless appropriately deuterated lipids are used, unsuppressed signals from alkyl chains in the lipid create problems for observation of  $^1\text{H}$  signals upfield from water (in the alkyl region of the  $^1\text{H}$  spectrum). Often, structural determinations of membrane-bound species are best approached by using a combination of SSNMR and solution methods [68]. Given that MAS SSNMR yields the same chemical shifts as solution methods (assuming no change in environment), a useful approach is to prepare samples in micelles or bicelles of relatively defined size that are amenable to solution NMR assignment methods, and use these assignments in the analysis of SSNMR data, from which structural information can be obtained. A reasonable number of membrane protein structures have been determined by NMR to date, often using a combination of methods [13, 69, 70].

## 5.5 Dynamic Information Available from NMR

While NMR is an important structural tool, the advent of high-throughput structural genomics projects, with the automation of crystallization trials, wide access to beam lines and user-friendly diffraction analysis software means that, with the exception of small proteins, polypeptides, and polynucleotides that resist crystallization, initial structure determinations of biological macromolecules will most often be done using X-ray diffraction. Where NMR comes into its own is in characterizing the solution dynamics of macromolecules. Crystallization usually captures only one major conformation, although some regions of the molecule may exhibit polymorphism in different members of the asymmetric unit, or show multiple conformations locally. Often, a significant problem with a crystallographic structure is determining what relationship it has (if any) with the biological function of the macromolecule: It may be that the conformer that crystallizes is considerably different from the preferred ensemble of conformers in solution or the biologically functional form. A recent example of this is the case of IscU, a scaffold protein from *E. coli* that aids in the construction of iron-sulfur clusters in vivo. The crystallographic structure of IscU in complex with desulfurase IscS shows a well-folded IscU [71], while NMR data suggest that IscU is mostly unfolded in the solution complex with IscS [72]. Furthermore, it has become apparent that in vivo many proteins sample multiple conformations and oligomerization states, and NMR can provide insight at atomic resolution in such cases [11, 73]. The value of NMR in these cases comes from its ability to characterize macromolecular dynamics on a wide range of timescales (Fig. 5.16) [74]. We will describe some of the methods used to extract dynamic information in approximate order of the decreasing timescales that they represent.



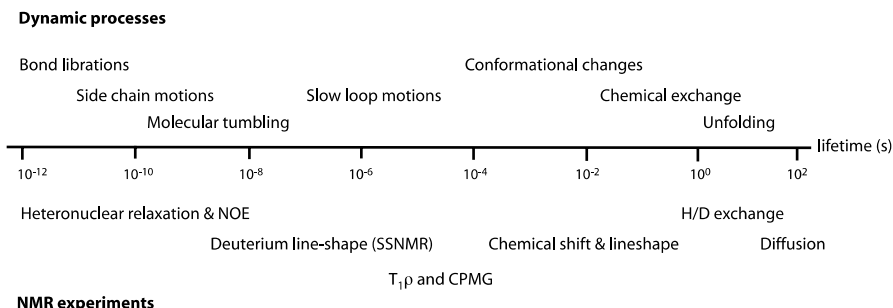


**Fig. 5.16** Approximate time scales of macromolecular motions and appropriate NMR methods that access those motions

### 5.5.1 Diffusion Measurements

In a typical NMR experiment, considerable effort is expended in making sure that the magnetic field is homogeneous throughout the sample volume, to ensure that individual resonance lines are as narrow and symmetric as possible. However, it is possible, through the application of linear magnetic field gradients, to extract position-specific data for a small volume of a sample. Indeed, this is the basis of magnetic resonance imaging; the appropriate application of PFGs allows 3D images of nonhomogenous samples to be constructed. In molecular spectroscopy, PFGs can be used to encode positions of a given molecule within the sample. This positional information can then be decoded at a later time by application of a second PFG. In the time between encoding and decoding, the molecule will diffuse out of the volume in which it was encoded. Depending upon how far the molecule diffuses, the decoding by the second PFG will be more or less complete. If a molecule does not move far from the position it occupied during the encoding PFG, it will decode more completely (and give rise to a more intense spectral peak) than those molecules that diffuse farther from their starting position. From these data, a diffusion coefficient for a given species can be extracted. Besides providing information about molecular size, shape, and degree of oligomerization, diffusion measurements can be used to screen small molecules that bind to macromolecules. Because macromolecules diffuse more slowly, they tend to lose less signal intensity during the diffusion delay between the encoding and decoding PFGs than their smaller counterparts. However, if a small molecule binds preferentially to a macromolecule, its diffusion will be slowed relative to other small molecules in the mixture, and its signals will be correspondingly less attenuated upon decoding. Because the target macromolecule does not have to be characterized (or indeed even be in high enough concentration to be observed in the experiment), diffusion-ordered spectroscopy (DOSY) provides a convenient rapid screen of small molecule mixtures for binding to a macromolecular target [75].

### 5.5.2 Hydrogen-Deuterium (H/D) Exchange

The slowest internal dynamic process that can be measured by solution NMR ( $10^{-7} \rightarrow 10^{-4} \text{ s}^{-1}$ ) is the chemical exchange of internal amide (or imino) protons for deuterium. Experimentally, these measurements are straightforward: The macromolecule is prepared fully protonated with  $^{15}\text{N}$  labeling, rapidly exchanged into a perdeuterated buffer, and the loss of signal intensity for individual exchangeable protons is followed by a convenient experiment such as  $^1\text{H}, ^{15}\text{N}$  HSQC. While many surface-exposed protons will exchange before the first HSQC experiment is started, internal protons, particularly those involved in hydrogen bonding within regular secondary structures, will exchange slowly enough that the time course of exchange can be followed and exchange constants calculated. H/D exchange rates have been modeled as a measure of local unfolding and de-protection of particular protons, and provides insight into the likelihood that a particular region of the macromolecule is solvent-accessible on a given time scale. Although few biologically important processes happen on the time scale of H/D exchange, this method can be used to identify more mobile parts of the protein that are likely to be dynamic on functionally relevant time scales. Because H/D exchange rates are sensitive to pH, it is important to monitor this variable in the course of exchange experiments.

### 5.5.3 Chemical Shift Perturbation and Line Width Changes

Because chemical shifts are sensitive to environmental factors (hydrogen bonding, solvation, steric interactions, etc.), local environmental perturbations can result in chemical shift changes of nearby spins. The extent of these shifts contains dynamic information resulting from the chemical shift time scale, which extends from  $\sim 10^1$  to  $10^4$  Hz. In the case of a spin exchanging between two environments, A and B, the extent of the perturbation (in Hz, or  $\text{s}^{-1}$ ) relative to the exchange rate ( $k_{\text{ex}}$ , also in  $\text{s}^{-1}$ ) determines how the phenomenon affects the appearance of the spectrum. If the rate of exchange between sites is less than the difference in chemical shifts  $|\nu_{\text{A}} - \nu_{\text{B}}|$  for the spin at the two sites, there will be two peaks in the spectrum, one at  $\nu_{\text{A}}$  and one at  $\nu_{\text{B}}$ , with integrations proportional to the relative populations of the sites. The exchange in this case is referred to as being **slow on the chemical shift time scale**. However, as the exchange rate increases, the line widths of the two peaks also increase, reflecting the shortened lifetimes of the spin at each of the two sites. When the rate of exchange equals the difference in chemical shifts of the two sites, the two peaks coalesce into a single very broad peak at the weighted average shift  $\nu_{\text{obs}} = \chi_{\text{A}}\nu_{\text{A}} - (1 - \chi_{\text{A}})\nu_{\text{B}}$ , here  $\chi_{\text{A}}$  is the fractional population of site A. Increasing the exchange rate even further results in a narrowing of the single peak, until at very fast exchange, the single line exhibits a line width similar to those of other, non-exchanging peaks assigned to the molecule. Such exchange is **fast on the chemical shift time scale** (Fig. 5.17). For two-site exchange, the broadening that occurs as the

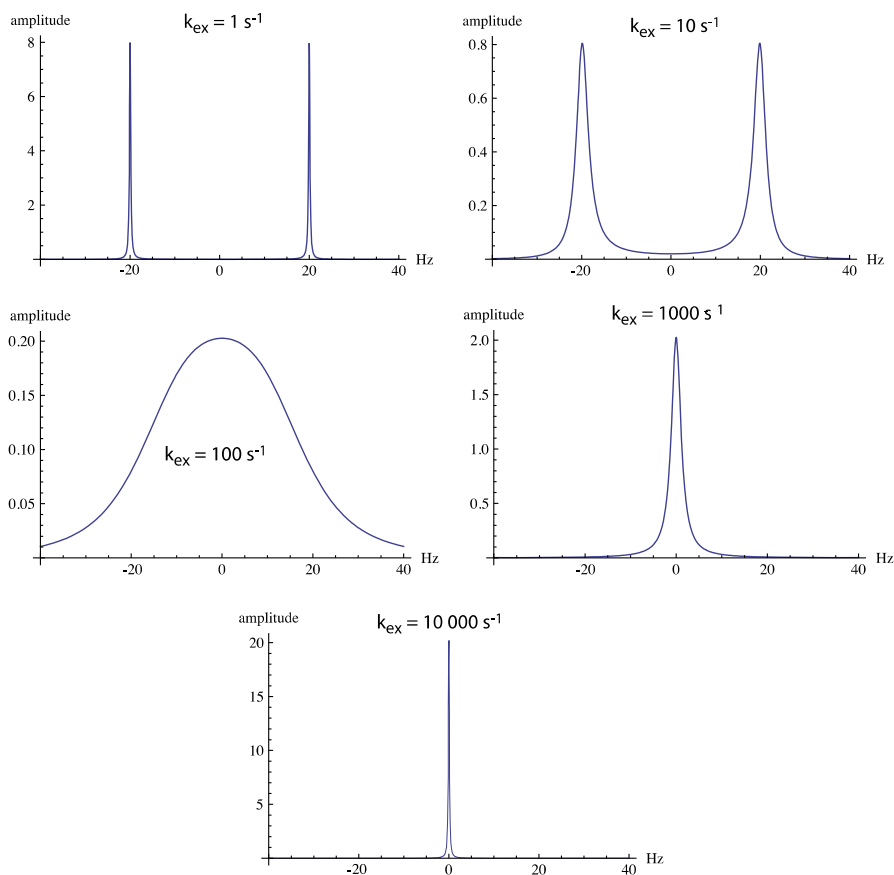


**Fig. 5.17** Spectral appearance as a function exchange rate ( $k_{ex}$ ) of chemical exchange between two equally populated sites. The two sites differ in chemical shift by 40 Hz. The separation in chemical shift affects the transition between slow and fast exchange: The greater the separation, the faster the exchange must be to cause the two peaks to coalesce. Note that the integration of the peak areas does not change (see amplitude scales)

exchange rate slows towards the slow exchange limit provides information about the rate of the dynamic process affecting the line width according to (5.7):

$$\Delta\nu_{1/2} = \left( \frac{1}{2\pi} \right) (\nu_A - \nu_B)^2 k_{ex}^{-1} \quad (5.7)$$

where  $\Delta\nu_{1/2}$  is the line width in Hz at half height. As such, comparison of line widths as a function of experimental variables, as in titration of an enzyme by a substrate or cofactor, provides direct information about the rate of exchange processes near the slow-fast exchange limit.

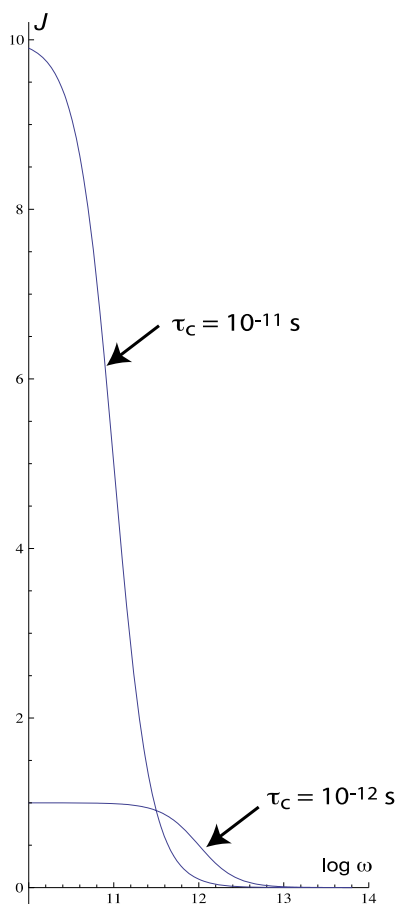
### 5.5.4 EXSY and *zz*-Exchange Spectroscopy

Most internal macromolecular dynamics are fast on the chemical shift timescale, with a few notable exceptions. X-proline *cis-trans* amide isomerizations are usually slow ( $<0.06\text{ s}^{-1}$ ), but have been found to accompany functionally important conformational changes. There is increasing evidence that X-Pro isomerizations provide a general mechanism for biological switches between active and inactive conformations of proteins and enzymes [76]. Aromatic ring flips (resulting in the exchange of nominally equivalent atoms on either side of a tyrosine or phenylalanine ring) are occasionally observed to be slow on the chemical shift time scale, and provide information on slow dynamics of protein interiors. An intriguing example of this is heme reorientation in cytochrome  $b_5$ . Despite ligation by two axial histidine ligands, the heme porphyrin exhibits exchange between two orientations related by rotation around a pseudosymmetry axis [77]. On the other hand, many important bimolecular events, such as substrate and cofactor binding, are often slow on the chemical shift time scale [78]. Rate constants for such phenomena can often be extracted by magnetization transfer between sites, using experiments such as EXSY (exchange spectroscopy) and *zz*-exchange HSQC, in which exchange-related peaks in these two-dimensional experiments are correlated by cross-peaks, the intensity of which varies with the mixing time  $\tau_m$  during which the exchange takes place [79]. By relating the cross-peak volumes with  $\tau_m$ , rate constants for the exchange processes can be calculated. It should be noted that  $T_1$  relaxation competes with exchange transfer, and if the exchange rate is much lower than the spin-lattice relaxation rate constant, the EXSY experiment will not report on the exchange.

### 5.5.5 Heteronuclear Relaxation

In the section above dealing with nuclear spin relaxation, we noted in passing that spin relaxation is induced by local random electromagnetic fluctuations at the frequency corresponding to that of the spectroscopic transition involved. It is now time to consider this in greater detail. In a  $^1\text{H}$ - $^{15}\text{N}$  bonded pair, there are four dipolar relaxation pathways that require local electromagnetic fluctuations at the appropriate frequencies. These include a single  $^{15}\text{N}$  spin state change (Larmor frequency  $\omega_N$ ), a single  $^1\text{H}$  spin state change ( $\omega_H$ ), a two-quantum ( $\omega_H + \omega_N$ ) and a zero-quantum ( $\omega_H - \omega_N$ ) transition ( $\omega = 2\pi\nu$ ). The relative probabilities of any of these transitions occurring are directly related to the motional behavior of the molecule to which the spin pair belongs. The random motion of molecules in a magnetic field produce an electromagnetic “white noise” that can cause the transitions leading to relaxation. However, that “noise” must contain frequency elements corresponding to the transition of interest in order for that transition to occur. The frequency range over which electromagnetic noise is nonzero is described by the *spectral density* (Fig. 5.18). For small molecules tumbling rapidly in a nonviscous solvents, the spectral density is

**Fig. 5.18** Spectral density,  $J(\omega)$ , plotted for two correlation times,  $\tau_c = 10^{-11}$  s and  $10^{-12}$  s. Because curves are plotted on a logarithmic scale, the areas under the curves are not equal. However, the available power is constant at a constant temperature. The efficiency of any relaxation process connecting spin states with a transition frequency  $\omega$  is proportional to the spectral density  $J(\omega)$  at that frequency



nonzero over a wide range of frequencies, so that all of the relaxation pathways of interest are available. However, large molecules tumble slowly, resulting in spectral densities that are poor in high-frequency elements, and relaxation reflects this by mostly taking place via lower frequency pathways (zero- and single-quantum transitions). Because spin–lattice ( $T_1$ ) relaxation requires that energy be removed from the spin system, not just moved from one spin to another, the lack of a two-quantum transition results in  $T_1$  processes being less significant relative to  $T_2$  (spin–spin) relaxation in large molecules without major internal motions.

Experiments have been designed to measure heteronuclear (X)  $T_1$ ,  $T_2$ , and X, { $^1\text{H}$ } NOE in macromolecules that enable numerical values for the correlation time,  $\tau_c$ , to be calculated, and a measure of the random motions of the molecules involved to be obtained [80]. The correlation time can be thought of as the mean time required for the molecule to reorient by 1 rad in any direction, and is the reciprocal of the high-frequency cut-off for the spectral density. Above  $\omega = \tau_c^{-1}$ , the spectral density

decreases rapidly to zero, militating against any relaxation pathways requiring frequencies greater than  $\tau_c^{-1}$ . Note that for many macromolecules, this cut-off frequency is  $\sim 10^8 \text{ s}^{-1}$ , well below the frequency required to stimulate double-quantum transitions at high magnetic field. However, if there are local motions within the macromolecule, these will be reflected in an increase in higher frequency fluctuations, and relaxation in the affected regions will reflect this increased local motion. Relaxation of  $^{15}\text{N}$  in proteins is often interpreted semi-quantitatively as the ratio between  $^{15}\text{N}$   $T_1$  and  $T_2$  graphed as a function of sequence, since this ratio reflects the relative contributions of possible relaxation pathways. The ratio tends to remain near a constant value for regions of the biomolecule that do not exhibit a high degree of conformational flexibility, but shows deviations for regions of greater mobility.

The simplest method for extracting numerical dynamic information from heteronuclear relaxation is the model-free approach [81], which is based on the assumption that motional behavior can be represented by two correlation times, an overall molecular correlation time  $\tau_m$  and a local effective correlation time  $\tau_e$ . For the model-free approach to be effective, the overall correlation time  $\tau_m$  must be much longer than  $\tau_e$ . Fitting of experimental  $T_1$ ,  $T_2$ , and heteronuclear NOE yields values of  $\tau_m$ ,  $\tau_e$ , and an order parameter ( $S^2$ ), which is a measure of the degree of freedom that a local structural feature exhibits with respect to the overall tumbling of the macromolecule. An order parameter  $S^2=1$  indicates that there is no motion of the local structure independent of the overall motion of the molecule, while  $S^2=0$  indicates that the local structure moves independently of the molecule as a whole.

The frequencies of motions accessible to standard relaxation experiments are quite high (Fig. 5.16), and although such motions often correlate with longer timescale dynamics, they are much faster than are typically expected for functionally important motions, such as those involved in signal transduction or enzyme activity. For this reason, experiments have been developed to measure field-dependent  $T_2$  relaxation, which allows the detection of lower frequency components of spectral densities. The standard pulse sequence for measurement of heteronuclear  $T_2$  is called the Carr–Purcell–Meiboom–Gill experiment (CPMG) [82]. The power of the RF pulses used to generate and invert transverse relaxation in the CPMG experiment is related to how fast the net magnetization is rotated around the applied RF, and power levels for these pulse trains are usually described in terms of the frequency with which the magnetization rotates around a transverse axis. For example, a 200 Hz CPMG field rotates bulk magnetization around a transverse (that is,  $x$  or  $y$ ) axis 200 times per second, corresponding to a  $90^\circ$  pulse length of  $(0.25 \times 1/200 \text{ s}^{-1}) = 1.25 \text{ ms}$ . If an exchange process moves a spin between magnetically nonequivalent sites on a time scale similar to that of the CPMG field rotational frequency, the exchange process has a measurable effect on  $T_2$ . The exchange rate for that process,  $k_{\text{ex}}$ , can be extracted from the measured value of  $T_2$  as a function of changing the CPMG field strength (dispersion curve). Resonances that are unaffected by the exchange process exhibit  $T_2$  values that are invariant relative to the CPMG field strength. Even in the absence of stringent quantitative interpretation, this series of experiments can be used to identify resonances that are undergoing exchange. In many cases, this method enables identification of the exchanging

conformers. Structural information about the conformers is obtained from the chemical shift differences that are extracted from the dispersion curves.

A related measurement is that of  $T_1\rho$ , the relaxation time of a resonance that is spin-locked around the effective field  $B_{\text{eff}}$ , the vector sum of the chemical shift offset and the RF field  $B_1$ , as in TOCSY and ROESY [83]. In the spin-locking frame of reference, spins precess (“nutate”) around  $B_{\text{eff}}$  at a frequency  $\nu$  determined by the expression  $2\pi\nu = \omega = \gamma B_{\text{eff}}$ . As  $B_{\text{eff}}$  is many orders of magnitude lower than the  $B_0$  field of the magnet in which the experiment is performed, nutation frequencies in the spin-lock frame are also much lower than the Larmor frequency. As such, the spectral density components needed for relaxation are provided by low frequency motions, and the frequencies of these motions can be extracted from measurement of  $T_1\rho$  as a function of  $B_{\text{eff}}$ .

### 5.5.6 Solid-State $^2\text{H}$ Lineshape Analysis

Macromolecular motions on time scales between the ns and ms range are difficult to probe by solution NMR. However, the nuclear quadrupole of  $^2\text{H}$  interacts with electric field gradients with couplings on the order of  $10^5$  Hz, and motions in this range ( $\mu\text{s}$  time scale) will affect the observed  $^2\text{H}$  line shapes in solid-state NMR spectra. Motional parameters can be varied to get the best fit the predicted and observed  $^2\text{H}$  line shapes in solid-state spectra, yielding information about local motions on the  $\mu\text{s}$  timescale.

## 5.6 Instrumentation

Macromolecular NMR spectroscopy is today almost exclusively performed using stable superconducting magnets to provide the primary magnetic field. As noted in Sect. 5.1, signal to noise ratio scales with field strength as  $B^{3/2}$ , and spectral dispersion scales linearly with field, so reaching higher fields has been a primary focus of the industry for many years. Often, instruments available in-house at nonspecialized sites do not exceed 14.1 T (600 MHz  $^1\text{H}$ ), and while much worthwhile biophysical research has been accomplished using 500 and 600 MHz instruments, for larger macromolecules ( $>20$  kDa), there is significant benefit to moving to higher fields. Currently, the highest field magnet in operation for spectroscopy is 23.5 T (1 GHz  $^1\text{H}$ ), and 18.8 T (800 MHz  $^1\text{H}$ ) and 21.1 T (900 MHz) magnets are not uncommon. Unfortunately, the cost of high-field spectrometers is a significant drawback. There was a rule of thumb for many years that NMR spectrometers cost “\$1K per MHz.” However, above 600 MHz, this rule broke down long ago, and prices increase nonlinearly for fields above 600 MHz. Thus it is often necessary to concentrate high-field NMR spectrometers in central locations, with a staff of experts and engineers to help maintain the instrumentation and train/assist outside users. This is true both for academic and industrial research institutions.

First-time users and nonexperts in NMR spectroscopy can usually find training and assistance in acquiring and analyzing their data at such facilities, which can also provide guidance about the feasibility and cost of a particular project. A quick on-line search yields many possibilities for collaborative NMR research.

### 5.6.1 *Solution-State NMR Probes*

At least as important as the magnet is the probe used for a particular experiment. The standard probe for biomolecular solution-state NMR as applied to proteins is called a “triple-resonance” or “inverse detection” probe, and consists of an inner coil (closest to the sample, and enclosing the sample volume as completely as possible) for excitation and detection of  $^1\text{H}$  and  $^2\text{H}$ , and an outer coil tuned for  $^{13}\text{C}$  and  $^{15}\text{N}$  excitation and decoupling.  $^2\text{H}$  capability is primarily used for locking the spectrometer frequencies relative to signals in the sample and for  $^2\text{H}$  decoupling. The related “quadruple-resonance” probe includes  $^{31}\text{P}$  excitation/decoupling capability for nucleic acid work. On many modern spectrometers, the transceiver coils and preamplifier (which boosts the very weak detected signal prior to transmission to the spectrometer console) are cooled to cryogenic temperatures ( $\sim 32\text{ K}$ ) by a flow of cold helium gas. This results in a significant reduction in thermal noise within the detection and preamplifier circuits and corresponding improvement in signal to noise (by a factor of 4 under ideal conditions). Cryogenically cooled probes are particularly useful for dilute ( $<1\text{ mM}$ ) samples of biological macromolecules, and provide the greatest sensitivity improvement when used with low-salt buffers.

While direct detection of  $^{13}\text{C}$ ,  $^{31}\text{P}$ , and  $^{15}\text{N}$  is possible using the outer coil on inverse-detection probes, the signal to noise ratio suffers significantly due to the lack of proximity and poorer filling of the coil-enclosed sensitive volume by the sample. For large perdeuterated proteins and some paramagnetic species, it is often desirable to directly observe  $^{13}\text{C}$ , because of its favorable relaxation characteristics and, in many cases, simplified pulse sequences. For such experiments, inner coils that are doubly tuned for  $^1\text{H}$  and  $^{13}\text{C}$  are available on specialized probes.

Almost all modern NMR probes are equipped with coils for applying PFGs in the course of an experiment. The coils are referred to by the axis in the laboratory frame along which the gradient is applied ( $x$ ,  $y$ , and  $z$ ). Single-axis gradients are usually applied along  $z$  (the long axis of the sample), and are sufficient for most applications.

### 5.6.2 *Solid-State NMR Probes*

The requirements for MAS and, in many cases, pulse-rotor synchronization for SSNMR experiments mean that these probes are very different in design from solution-state probes. Power requirements for cross-polarization, high-power  $^1\text{H}$



decoupling, sample alignment at the magic angle and high rotation speeds demand rugged construction and more mechanical parts than for solution work. Until relatively recently, the magnets used for SSNMR required wider bores than was typically used for solution work, so the same magnets would not normally be used for both. However, it is now possible to purchase SSNMR probes that fit into a standard-bore magnet, so the same magnet can be used for both solution and SSNMR.

### 5.6.3 *Electronics*

Typically, a separate amplifier/transmitter (termed a “channel”) is required for each nucleus involved in an NMR experiment. For the detected nucleus and lock nucleus channels, receivers, and mixer circuits as well as analog-to-digital converters (ADCs) are also required. Each channel must be coordinated with the others using timing circuits associated with a digital frequency synthesizer to insure phase coherence and appropriate timing of each pulse in the NMR experiment. Dedicated  $^1\text{H}$  amplifiers for solution NMR are typically lower power (50 W) than those used for other nuclei, as the spectral range covered by  $^1\text{H}$  is relatively small. Broadband amplifiers used for other nuclei with wider chemical shift ranges are usually at least 200 W, and a separate amplifier is usually used for each channel. Amplifiers used for  $^2\text{H}$  lock and decoupling are low power due to the narrow spectral range of  $^2\text{H}$ . Amplifiers used for SSNMR are typically more powerful than those required for solution NMR, because power requirements for  $^1\text{H}$  decoupling in CP-MAS are determined not by the chemical shift range of  $^1\text{H}$ , but the magnitude of dipolar couplings, which can be in the 10s of kHz.

## 5.7 Experimental Requirements

### 5.7.1 *Sample Requirements for Solution NMR*

The primary requirement for solution NMR characterization of a biomolecule is, obviously, solubility. However, the definition of “soluble” has changed dramatically since the inception of biomolecular NMR, and samples with concentrations as low as 100  $\mu\text{M}$  are often adequate for structural determinations and dynamics measurements with appropriate instrumentation. “Solubility with assistance,” e.g., by introduction of lipids, detergents/surfactants or stabilizing agents such as glycerol and high salt, is often required for membrane-bound and membrane-associated proteins, or proteins that aggregate or oligomerize [68, 70, 84]. One intriguing alternative for solubilization of membrane proteins is the “nanodisc,” a lipid bilayer discoid with dimensions defined by the number of turns of  $\alpha$ -lipoprotein used to generate it [85]. Nanodiscs can be prepared with a single membrane-bound protein associated with

each discoid, reducing the problems of self-association and heterogeneity often observed with standard membrane protein solubilization techniques. Still, whichever method is used, assisted solubilization often results in complications such as increased sample viscosity (which broadens lines), large residual signals due to additives and buffers, and “lossy” samples, that require longer RF pulses to achieve maximum excitation and can result in sample heating. While many commonly used surfactants, detergents, and buffer additives are available in deuterated form (reducing otherwise intense resonances), not all are, and these can give rise to very large signals in important regions of the spectrum. However, the use of deuterated additives can complicate sample locking. The  $^2\text{H}$  lock signal (usually the HDO line from ~5 % added  $\text{D}_2\text{O}$  in aqueous samples) is used to adjust the spectrometer frequency in response to small magnetic field fluctuations in the course of a long acquisition. The presence of other strong  $^2\text{H}$  signals from additives can render the lock less stable or allow the lock to “jump” from one signal to another during the experiment.

Another critical requirement is sample stability. As will be seen, a comprehensive set of data acquired for complete characterization of a biomacromolecule can take up to 2 weeks on the spectrometer. One of the most common causes of decomposition is the presence of trace amounts of protease (for proteins) and nucleases (for nucleic acids). The addition of small amounts of appropriate inhibitors can help in these cases. Sterile handling techniques, deoxygenation and the addition of a small amount of sodium azide to NMR buffers will inhibit the growth of microorganisms in NMR samples.

### 5.7.2 *Isotope Labeling*

The most common sample modification required for NMR is the introduction of isotope labels. It is no accident that biomolecular NMR came into its own as an independent structural methodology as methods for protein over-expression in bacterial hosts became available, allowing both selective and uniform isotope labeling to be performed. Although many types of samples (peptides, small proteins, and oligonucleotides) are still usefully characterized by homonuclear ( $^1\text{H}$ ) correlation experiments such as COSY, DQF-COSY, NOESY, and TOCSY, for larger proteins, biomolecular NMR is best performed using  $^{15}\text{N}$ ,  $^{13}\text{C}$  labeled samples. This labeling scheme allows sequential assignments to proceed via standard three-dimensional heteronuclear correlation experiments without resorting to sequential NOEs, which can be ambiguous, especially in crowded spectra. Virtually any recombinant protein or synthetic polynucleotide can be isotopically labeled, although protein yields from *in vivo* expression systems (usually bacterial) often decrease significantly when using defined minimal media commonly used for expression of isotopically labeled samples. Alternatively, good yields of isotope-labeled proteins have been obtained using labeled algal extracts as bacterial growth media, expression in yeast [86], insect cells [87] or by *in vitro* expression using wheat-germ extracts for translational machinery [88, 89]. Eukaryotic proteins are sometimes not expressed well

in bacterial expression systems, particularly if disulfide bond formation or glycosylation is required for correct folding, but success has been had expressing protein in eukaryotic (yeast, insect, and mammalian) expression systems [90]. Obtaining a usable amount of labeled sample is sometimes the rate-limiting step in the NMR characterization of a macromolecule, so it is usually worth testing a number of expression systems and methods in unlabeled media before committing to the expense of preparing a labeled sample.

The best labeling scheme depends upon the experiments to be performed and, generally, the size of the molecule under investigation. For sequential assignments and structural determination of proteins less than 25 kDa in molecular mass, uniform  $^{13}\text{C}$  and  $^{15}\text{N}$  labeling is generally sufficient for all of the needed experiments (see below). Above 25 kDa, the situation can become more complicated. Slower tumbling rates make  $^1\text{H}$ -mediated  $^{13}\text{C}$   $T_2$  relaxation more efficient, and  $^{13}\text{C}$  coherences become shorter-lived, to the point where the standard 3D triple-resonance experiments begin to fail. In such cases, fractional or complete deuteration of the macromolecule is an option. Replacing protons bonded to  $^{13}\text{C}$  with  $^2\text{H}$  greatly increases the lifetimes of  $^{13}\text{C}$ -based coherences, and make it possible for standard sequential assignment experiments to be performed with much larger macromolecules. We routinely make sequential assignments on molecules >46 kDa using samples perdeuterated to suppress  $^1\text{H}$ -mediated  $T_2$  relaxation [91], and assignments for malate synthase G (81.4 kDa monomer) have been reported [64]. Growth media for expression of perdeuterated and  $^{13}\text{C}$ ,  $^{15}\text{N}$ -labeled samples are prepared from commercially available  $^{13}\text{C}$ ,  $^2\text{H}$ -labeled carbon sources such as glycerol and glucose, with  $\text{H}_2\text{O}$  replaced in the medium by  $\text{D}_2\text{O}$ . Care must be taken to insure other nonobvious sources of  $^1\text{H}$  (e.g., hydrated salts added to the growth medium and additives such as vitamins, antibiotics, and inducers) are identified and suppressed. If care is taken in protecting spent  $\text{D}_2\text{O}$  growth media from moisture after cell harvest, it can be recycled by distillation from a strong aprotic base ( $\text{MgO}$  or  $\text{CaO}$ ) and filtration of the distillate through activated charcoal to remove volatile amines and thiols. Densitometry provides a rapid assay for determining the %  $\text{D}_2\text{O}$  present in the recycled material.

The absence of  $^1\text{H}$  spins in perdeuterated samples has drawbacks. Most current sequential assignment experimental schemes require  $^1\text{H}$ – $^{15}\text{N}$  pairs for detection, so the samples as isolated are not suitable for triple-resonance experiments. While purification of the protein in protonated buffers will exchange a large fraction of the amide  $^2\text{H}$  for protons, stable folded proteins usually contain a significant number of amide groups that are protected from exchange, and an unfolding/refolding step can be included (if feasible) to get complete backbone amide exchange. Also, any experiment that requires transfer of coherence between  $^1\text{H}$  and  $^{13}\text{C}$  (HCCH-TOCSY and  $^{13}\text{C}$ -edited NOESY, e.g.) cannot be performed with such samples, foregoing side chain  $^1\text{H}$  resonance assignments. To recover some of this information, selectively labeled samples can be prepared. In the simplest method, the growth medium is enriched in one particular amino acid with  $^1\text{H}$  and  $^{13}\text{C}$  labels, so that only these side chains show up in  $^{13}\text{C}$ -edited spectra. Scrambling of label can sometimes be problematic, particularly between amino acids that are part of the same biosynthetic

pathway. However, scrambling usually follows a predictable pattern, and so can be accounted for in data analysis. Schemes for the introduction of stereospecific  $^1\text{H}$ ,  $^{13}\text{C}$  methyl labels at valine, leucine, isoleucine, and alanine have also been described [92, 93]. These are particularly useful for structure determinations in that nonsequential NOEs can be observed and RDCs measured for specific methyl groups, providing structural restraints for large proteins.

### 5.7.3 *Type-Selective, Residue-Selective, and Segmental Labeling*

It is often useful to introduce labels selectively into a protein, both as an aid to sequential assignment for larger proteins and to characterize a particular structural or dynamic feature. Type-selective labeling, that is, labeling one type of amino acid residue, is usually straightforward. For amino acids that are not intermediates in the synthesis of multiple other amino acids, introduction of the labeled amino acids into a defined growth medium at the point of expression is usually sufficient for good selective labeling with a minimum of scrambling. Glycine, alanine, isoleucine, leucine, phenylalanine, proline, lysine, valine, and serine are usually good candidates for this type of labeling at either  $^{15}\text{N}$  or  $^{13}\text{C}$  [94]. Glutamate and glutamine are intermediates in the transaminase cycle, and so are not good candidates for  $^{15}\text{N}$  selective labeling. Cysteine is often back-scrambled to serine, and in general, an auxotrophic bacterial strain is best used for cysteine labeling.

Residue-selective labeling is generally much more laborious, and usually requires the use of pre-charged tRNAs that recognize the *amber* codon, introduced at the appropriate point in the DNA sequence [95]. Alternatively, double-labeling schemes can be used whereby residues can be assigned sequence-specifically via the occurrence of a unique or rare connection (e.g., V-A or G-S) which gives rise to an observable  $^{15}\text{N}$ – $^{13}\text{C}$  correlation. This scheme has been used for identifying residues in the vicinity of paramagnetic centers that are otherwise undetectable due to broadening of  $^1\text{H}$  signals [96–98]. Segmental labeling can be accomplished through the use of semi-synthetic protein synthesis (inteins) [99], in which two or more protein domains are expressed but only one is labeled. The domains are then spliced together to generate a complete protein in which only one domain is labeled.

### 5.7.4 *SSNMR Sample Requirements*

SSNMR sample preparation for MAS-based experiments is in some ways less restrictive than for solution NMR. Because cross-polarization between  $^1\text{H}$  and heteronuclear spins is an important element in most SSNMR experiments, such samples are generally protonated regardless of molecular mass. The extent of  $^{15}\text{N}$  and

$^{13}\text{C}$  labeling depends upon the type of experiment, but a variety of modern SSNMR multidimensional pulse sequences are available for sequential assignments with uniformly labeled samples, so this is a reasonable place to begin. Obviously, solubility is not an issue for SSNMR sample preparation. However, sample heterogeneity is a concern: If multiple static or slowly interconverting conformers of a macromolecule are present in a sample, lines will be broadened and spectra become more difficult to interpret. Typically, the best quality heteronuclear correlation SSNMR data sets are obtained with homogenous microcrystalline samples [100]. This insures a minimum of sample heterogeneity both at the molecular and mesoscopic levels.

Static SSNMR on oriented samples is often used to characterize orientation of helices bound to membranes (PISEMA, [101, 102]). For such experiments, samples are mechanically oriented in thin layers between microscope cover slips and placed within the transceiver coil. A specialized probe (without sample spinning) is required for these types of experiments.

### 5.7.5 Solvent Suppression

Efficient solvent signal suppression has always been a primary concern of biomolecular NMR. Almost all solution biomolecular NMR experiments are performed in aqueous media, which is approximately 55 M  $\text{H}_2\text{O}$  (and thus, 110 M aqueous  $^1\text{H}$ !). A small fraction (<10 %) of the buffer is typically  $\text{D}_2\text{O}$ , which is used for spectrometer lock. Nevertheless, this still results in a very large dynamic range problem, if the protons that need to be observed are present in  $\sim 0.001$  M concentration. Conversion of the analog RF signal detected in the NMR receiver coil to a digital number required for signal processing is accomplished by a device known as an ADC. ADCs are defined by their “bits,” that is, the number of binary places available to digitize the signal. An 18-bit ADC can generate a number as large as  $2^{17}$  (one bit being reserved for sign), with a designated voltage change ( $\Delta V$ ) required to flip a bit from 0 to 1. Thus the smallest signal that can be digitized results in a voltage change in the receiver circuit of  $\Delta V$ , and the maximum is  $\Delta V \times 2^{17}$ . Any signal inducing a voltage greater than this will be “clipped” and will not be correctly digitized. Typically, the unattenuated signal from  $\text{H}_2\text{O}$  is sufficient to completely fill the ADC, and the weak signals due to the macromolecule are lost or distorted.

Simply replacing  $\text{H}_2\text{O}$  with  $\text{D}_2\text{O}$  is usually undesirable except in special cases, since the NH correlations that are required for many multidimensional NMR experiments are lost due to exchange with the deuterated buffer. Instead, most early solvent suppression was accomplished by pre-saturation, that is, continuous low-power irradiation of the water signal that equalized populations of the water proton spin states and reducing the water signal to a minimum. However, there are many important resonances near the water line in  $^1\text{H}$  spectra that are also lost by pre-saturation, and “saturation transfer” via chemical exchange and spin diffusion leads to the weakening of other signals that are not near the water line [103].

An alternative, and now almost universally adopted scheme for water suppression is the use of selective excitation pulses that are constructed in order to avoid exciting the water signal in the first place, or else returning it to the  $+z$  axis before detection. The WATERGATE (*water* suppression by *gradient tailored excitation*) sequence [104] accomplishes this quite nicely, and is commonly found as part of the final pulse train on  $^1\text{H}$  before detection in many multidimensional NMR experiments. Another issue that often arises in the course of a multi-pulse NMR is that of *radiation damping*, which can occur when the  $\text{H}_2\text{O}$  spin Boltzmann population is inverted via a nonselective pulse. If allowed to remain inverted, a self-induced coherence analogous to that observed in lasers and masers can occur, generating a strong signal in the receiver coil, resulting in spectral distortion and receiver overload. To avoid radiation damping, multi-pulse experiments often include “flip-back” pulses, which are selective for the water signal and return it to the  $+z$  axis [105, 106]. Flip-back pulses have the added benefit of reducing attenuation of exchangeable  $^1\text{H}$  signals due to saturation transfer from water. Finally, PFG selection of heteronuclear correlation pathways, found in most modern multinuclear NMR experiments, effectively reduces the water signal of uniformly labeled samples, even without other forms of solvent suppression, since the water signal does not involve any correlation with  $^{15}\text{N}$  or  $^{13}\text{C}$ .

### 5.7.6 Standard Experiments for Solution State $^{13}\text{C}$ , $^{15}\text{N}$ -Labeled Samples (Including TROSY Modifications)

As a rule, the following set of 3D experiments are comprehensive, and provide all of the data needed for sequential assignments, chemical shift-based dihedral angle, and NOE-based distance restraints for proteins: HNCA, HN(CO)CA, HNCO, HNCACB, CBCA(CO)NH, HCCH-TOCSY,  $^{15}\text{N}$ -edited TOCSY/NOESY, and  $^{13}\text{C}$ -edited NOESY [21, 23, 33, 107]. Because of the large chemical shift range of  $^{13}\text{C}$ , the  $^{13}\text{C}$ -edited NOESY and HCCH-TOCSY experiments can be run twice, in one case with the  $^{13}\text{C}$  frequency centered on the aliphatic region ( $-10 \rightarrow 70$  ppm) and then centered on the aromatic region ( $\sim 70 \rightarrow 150$  ppm). The appropriate 2D experiments (usually  $^{15}\text{N}$  and  $^{13}\text{C}$  HSQC) experiments are generally interspersed with the 3D runs to monitor changes in sample and to provide convenient references for interpreting the 3D datasets. Most of these experiments are available and ready to run on standard commercial spectrometers.

There are a number of options that need to be considered when choosing which variants of a given experiment are best. For proteins with molecular weights  $<25$  kDa, the default setup is usually sufficient, at least for preliminary experiments. However, for larger proteins, the TROSY option is usually preferable [66]. As described earlier, TROSY detection takes advantage of the fact that the four lines of a  $^1\text{H}$ ,  $^{15}\text{N}$  multiplet (split by  $^1J_{\text{NH}}$  in both dimensions of a  $^1\text{H}$ ,  $^{15}\text{N}$  HSQC experiment obtained without decoupling of  $^{15}\text{N}$  during either  $t_1$  or  $t_2$ ) are differentially broadened. The least efficiently relaxed (and hence narrowest and sharpest) line of the

multiplet can be selected with the appropriate phase cycling. While the differential line broadening increases with field strength, we have found significant improvement in resolution for a 46 kDa enzyme even at 600 MHz using TROSY-based detection. For very large molecules, the CRINEPT experiment takes advantage of the almost complete loss of signal intensity for the non-TROSY peaks via passive detection of the narrowest line, without phase cycling. However, CRINEPT-based detection is not commonly used in 3D experiments, since the experiment works best for very large molecules (>100 kDa), and coherence transfer is difficult to maintain through multiple transfer steps [67].

### ***5.7.7 Solution State Experiments with Deuterated Proteins, Including Direct $^{13}\text{C}$ Observation***

If a protein is perdeuterated (as well as  $^{13}\text{C}$  and  $^{15}\text{N}$  labeled), the molecular mass range of standard sequential assignment experiments (HNCA, HN(CO)CA, HNCACB, CBCA(CO)NH,  $^{15}\text{N}$ -edited NOESY) is considerably extended. Backbone assignments for a number of proteins ~50 kDa in mass have been reported, and oligomeric proteins >100 kDa with internal symmetry have been assigned. In such cases, TROSY selection is appropriate, and the presence of  $^2\text{H}$  bound to  $^{13}\text{C}$  requires that  $^2\text{H}$  decoupling be applied during  $^{13}\text{C}$  evolution. Because there are no  $^{13}\text{C}$ -bound protons in such samples, experiments such as HCCH-TOCSY and  $^{13}\text{C}$ -edited NOESY are not options. However, the advent of cryogenically cooled probes capable of directly detecting  $^{13}\text{C}$  has made possible another class of experiments for sequential assignment of side chain resonances [108]. These include experiments such as CON, COCA, and CAN [109–111] for sequential backbone assignments of  $^{13}\text{C}$  and  $^{15}\text{N}$ , as well as CC-COSY and CC-TOCSY that can be used to extend assignments to side chains [112]. The lack of  $^1\text{H}$ s also make it possible to detect  $^{13}\text{C}$ ,  $^{13}\text{C}$  NOEs [113], which can replace  $^1\text{H}$ ,  $^1\text{H}$  NOEs as structural restraints.

### ***5.7.8 Sequential Assignment and Structural Determination Experiments for Nucleic Acids***

Because nucleic acids have a smaller set of monomers (ACTG or ACUG) and their tertiary structures are less varied than proteins, degeneracy is a more serious problem in the sequential assignment of nucleic acid polymers. Also, unlike proteins, in which 1- and 2-bond  $^{15}\text{N}$ – $^{13}\text{C}$  couplings can be used to move from one residue to the next in the assignment process, nucleic acid polymers are linked by phosphodiester, which require the use of relatively weak 2-bond ( $^{31}\text{P}$ – $^{13}\text{C}$ ) and 3-bond  $^1\text{H}$ – $^{31}\text{P}$  and  $^{13}\text{C}$ – $^{31}\text{P}$  couplings for coherence transfer between monomers [114]. This, combined with the relatively poor dispersion of  $^{31}\text{P}$  signals in polynucleotides, makes



the assignment process generally more dependent upon  $^{13}\text{C}$  and  $^{15}\text{N}$ -edited  $^1\text{H}$ ,  $^1\text{H}$  NOESY experiments [30, 115]. On the other hand, because nucleic acids are straightforward to synthesize in an automated fashion, it is easy to include sequence-specific labels. For structural determinations of multidomain RNA molecules, assignments and structures are determined for single domains, and then the domains are combined for characterization of the complete structure [28].

### 5.7.9 Residual Dipolar Coupling and Diffusion Measurements

RDC-based restraints are now a standard part of NMR-based structural determinations. In the simplest cases,  $^1\text{D}_{\text{NH}}$  RDCs, which are the most straightforward to obtain and analyze, can be measured by comparison of 2D spectra (often an HSQC) obtained in isotropic and aligned media without decoupling of  $^{15}\text{N}$  during acquisition of the  $^1\text{H}$  signal (or alternatively, without refocusing of NH coupling during  $^{15}\text{N}$  evolution). In the isotropic medium, each NH correlation is split in the appropriate dimension by  $^1J_{\text{NH}}$  (usually ~92–94 Hz). Upon alignment, the observed splitting is modulated by the RDC, which is then obtained by comparison with the splitting of the same correlation in the unaligned spectrum. Of course, as this approach results in doubling the number of peaks in the normal HSQC spectrum and line broadening usually increases in the presence of the aligning medium, this approach becomes unwieldy for larger proteins. In that case, the use of a combination of TROSY/semi-TROSY or IPAP (in-phase anti-phase) spectra yields a set of HSQC spectra that are offset from each other by the coupling constants of the correlated spins from each NH group. This reduces the complexity of the spectra to that of a typical decoupled HSQC or TROSY spectrum, reducing overlap and allowing for easier peak picking and analysis. RDC measurements are by no means limited to NH pairs. IPAP experiments have been described to measure a wide variety of RDCs, including  $\text{C}\alpha\text{--C}'$ ,  $\text{N--C}'$ , and  $\text{N--C}\alpha$  for proteins and imino NH and aromatic CH RDCs for nucleic acids [116, 117]. RDCs are particularly useful for nucleic acid structural work due to the lack of large numbers of long-range restraints.

Very early on, it was observed by Hahn that it should be possible to measure diffusion by NMR via the application of field gradients, in the same classic paper in which spin-echo and stimulated echo experiments are described [118]. However, it was some years before a practical realization of this experiment was described, using a time-dependent gradient [119], and the commercial availability of PFGs made the experiment practical on most spectrometers [75]. For macromolecules, a limitation of NMR-based diffusion measurement is that as the diffusing species increases in size and diffuses more slowly, the gradient strength required for accurate measurement also increases. For most commercial spectrometers, safe maximum gradient strengths are often too weak for accurate diffusion measurements on macromolecules. However, an interesting application of diffusion-based measurements is to characterize tight-binding fragments to the target macromolecule of choice by observing relative diffusion rates of the fragments [120]. Combined with other



methods, such as saturation transfer surface mapping [121], “pharmacophores” (small molecules that can be combined into pharmacologically active compounds) can be screened to aid in drug design.

## 5.8 Data Analysis

### 5.8.1 Data Processing and Assignment Software

NMR data analysis software can be classified roughly into three types, raw data processing (that is, applying digital after-processing such as linear prediction, window functions for optimizing data analysis, Fourier transformation of the data and phasing), resonance assignment (including automated and semi-automated assignment tools) and structural/dynamic modeling from the assigned NMR data. Some packages encompass more than one of the functions, but usually at the expense of compromising some functionality. Our discussion of such programs is necessarily incomplete, as much of the software is freeware (or close to freeware) and new programs are introduced while old ones are abandoned fairly often. Still, most NMR spectroscopists find a package that they are comfortable with, and stick with it, so there are often user groups and wikis associated with the various packages, even obsolete ones.

All spectrometer vendors (Bruker and Varian/Agilent being the most commonly used for biophysical applications at the time of this writing) provide software with the instrument that controls data acquisition and provides reasonable processing capability. However, for users with multiple NMR platforms, it is often useful to process raw NMR data using a single program that can interpret data formats from different instruments and provide a common output format. NMRPipe [122], originally provided by the NMR groups at the National Institutes of Health, is capable of advanced processing that produce spectra that in turn can be read by a variety of analysis software. NMRPipe has a relatively simple graphical user interface (GUI), NMRDraw, that allows interaction to establish optimum processing parameters. NMRPipe has the advantage of being free to academic users, and is easily mounted on UNIX and Linux operating systems. A more extensive GUI is provided by Felix [123], a distant descendant of one of the first stand-alone NMR processing programs, Dennis Hare’s FTNMR [124]. Felix incorporates peak-picking algorithms as well as interactive processing tools and multidimensional spectrum visualization.

The next step in analysis, sequential resonance assignment and tabulation of structural and dynamic restraints, can be accomplished using a variety of programs, again each with strengths and weaknesses. The choice of program is a matter of personal preference. An early data analysis program, XEASY, was developed in the Wüthrich laboratory at the ETH in Zurich, and provided considerable flexibility in viewing and analyzing multidimensional NMR data [125]. The XEASY suite has since been replaced by CARA, which has more flexible project management capability, runs on a wider range of platforms, and is still supported [126]. Another

commonly used freeware analysis program is SPARKY [127], developed at the University of California San Francisco. Originally developed for analyzing nucleic acid NMR data, SPARKY has been adapted reasonably well for the analysis of protein NMR data, but strip plot functionality (used for analysis of 3D NMR data) is somewhat limited. If one is willing to pay for analysis software, there are a number of useful packages available. The popular NMRview program, originally developed as freeware, is now offered in supported form for academic users [128]. Felix remains a powerful analysis program, and was recently spun off by Accelrys.

Over the years, a great deal of effort has been spent on development of automated or semi-automated assignment methods for multidimensional NMR spectra [129, 130]. While there has been some success in this area [131], particularly with smaller proteins, completely automated resonance assignments for larger proteins is still not possible. A major part of the problem is the accurate determination of what in a given spectrum constitutes a peak (as opposed to noise) and how the program distinguishes peak identities in regions of significant spectral overlap. In many cases, the human eye is still the best judge of whether a peak is (a) really a peak and (b) where the maximum of the peak lies. Even for fairly well resolved spectra of biomolecules, the results of automatic peak picking (available in all of the standard processing and analysis packages) should always be at least spot-checked by eye for accuracy.

Once peaks have been picked, the resulting peak lists can be incorporated into automated assignment routines. Again, a wide variety of automated assignment programs are available, each with a defined minimum set of experiments that are required. A thorough review of these programs is beyond the scope of this article; the field is changing fairly rapidly with ongoing improvements in the extent to which assignments can be made by automated methods and increased flexibility of required input data. Given that most of the programs are based on pattern recognition for particular residue types, the availability of accurate and relatively complete peak lists is critical in determining the degree to which the programs are successful.

To save time in structural genomics efforts, it might be desirable to avoid the sequential assignment process altogether, and go directly to the structure determination step [132]. (The author admits to serious philosophical arguments with this approach, since one learns a lot about one's pet protein/nucleic acid in the process of doing assignments!) Nevertheless, using sequence and chemical shift information, supplemented by NOEs and/or RDC data, it has been demonstrated with simple systems that it is possible to generate families of structures based on structural homology and statistically likely fits of the experimental data [133].

### 5.8.2 *Structural and Dynamic Analysis of NMR Data*

Once sequential assignments have been obtained, the extraction of useful structural and dynamic information from acquired data can begin in earnest. The first NMR structural determinations were carried out using distance geometry, using NOEs to

represent distances between pairs of  $^1\text{H}$ s, which were used to determine unknown distances by determining the geometric relationships between different pairs with known and unknown distances [134]. While distance geometry calculations are available as part of many computational packages, and often provide a useful front end for structural refinement, the vast majority of NMR-based structural refinements are now carried out using simulated annealing, a form of restrained molecular dynamics (MD). As in all MD simulations, kinetic energy is randomly distributed (as a function of the simulation temperature) to individual atoms in the simulation. This randomly assigned energy imparts a finite speed to the atom as the simulation begins. All of the forces acting on the individual atoms are calculated and a velocity assigned. After allowing motion for a very short time ( $\sim\text{ps}$ ), the forces are recalculated before the next step. Unlike standard MD simulations, SA is not intended to reproduce actual motions of the molecule in question. Instead, the molecule is raised (computationally) to a very high temperature, so that energetic barriers between the starting structure and the “correct” structure can be overcome. As the simulation proceeds, the temperature is gradually lowered and experimental restraints applied more strongly. Restraints are defined in terms of penalty functions, that is, a violation of the restraint raises the energy of the system. Although Cartesian dynamics (that is, motion is calculated in three-dimensional space) is still commonly used, torsional dynamics, in which rotation around appropriate bonds provide the degrees of freedom for motion, is computationally more efficient and is often used for calculating structures from NMR data.

Multiple computational platforms are available for SA calculations. Some of the oldest programs, including AMBER [135] and XPLOR (now XPLOR-NIH) [136] are still actively supported, with new releases matching developments in the field. Given that these programs were first written when GUIs were nonexistent, graphical interfaces are for the most part add-ons. However, XPLOR-NIH can be interfaced with the visualization software VMD [137], and AMBER supports a graphical molecule building interface, Xleap. Python scripting is preferred for input in the newer releases of XPLOR-NIH. A menu-driven descendant of XPLOR, CNS, is also in common use [138]. Most molecular graphics and visualization software can be used to examine the results of XPLOR and AMBER calculations, often by simply exporting the results as a PDB (protein data base) format file. DYANA is another widely used package, and combined with automated NOE assignment methods it forms the basis of the CYANA program, which iteratively assigns NOEs and generates test structures based on those assignments [139–141].

The most common restraint used in structure determination is the NOE-based distance. Each identified NOE is converted to a distance, and if the two restrained atoms deviate from that distance, the energetic penalty is applied. The NOE can be calibrated fairly precisely by measuring the NOE as a function of the buildup time (%NOE versus  $t_{\text{mix}}$ ), so these distances can be constrained quite tightly. However, it is generally more useful to divide the NOE into several classes (weak, medium and strong), and choose an approximate distance for each class (e.g., strong  $<3\text{ \AA}$ , medium  $<4\text{ \AA}$  and weak  $<5\text{ \AA}$ ). There are several reasons why this approximation is appropriate. First, multiple relaxation pathways and spin diffusion can attenuate the

NOE between protons in  $^1\text{H}$ -rich regions relative to those in  $^1\text{H}$ -poor regions of the macromolecule, making a single calibration difficult to use. Furthermore, if an NOE is incorrectly assigned, the more stringent restraints magnify the introduced error. Finally, if there is increased dynamics in one region of the macromolecule relative to another, a stringent distance restraint may mask local conformational flexibility. Generally, it is better to have many loosely constrained distances (many NOEs) as opposed to a few, strongly restrained distances.

Another important source of restraints are those on backbone and side chain dihedral angles. Traditionally, these were obtained by measuring coupling constants of spins across the angle of interest, and applying the appropriate Karplus relationship to obtain an allowable range of dihedral angles [142]. For nucleic acid structure determinations, the accurate measurement of  $^3J_{\text{CP}}$  couplings across phosphodiester linkages provide critical information regarding DNA and RNA backbone conformations [143]. However, in recent years, the availability of a large database of chemical shift assignments for known protein structures has made it possible to predict dihedral angles based solely on the chemical shifts of the atoms involved. One algorithm for extracting dihedral angle information for polypeptides from chemical shifts is TALOS+, which bases predictions on a sliding three-residue frame [144]. Generally, the more shifts that are assigned (e.g.,  $^1\text{H}$ ,  $^{15}\text{N}$ ,  $^{13}\text{C}$ ) the more reliable the predictions. Some MD packages (XPLOR-NIH, for example) can incorporate the shift data directly, without need for preparing an explicit set of angular restraints.  $^1\text{H}$  chemical shift data can also be used quantitatively for determining the relative orientation and distance between a shifted  $^1\text{H}$  spin and nearby aromatic rings. Aromatic rings often induce fairly dramatic  $^1\text{H}$  chemical shift changes due to “ring currents,” with de-shielding occurring in the plane of the ring and shielding above and below the plane. The SHIFTS program can incorporate this information as distance and angle restraints in AMBER [145].

RDCs have in recent years become a critical component of NMR structure determination. Unlike other NMR-based restraints, RDCs provide information regarding the relative orientations of internuclear vectors with respect to a single frame of reference provided by the alignment tensor. In a sense, RDCs provide a “whole-molecule” perspective that is absent from other types of NMR-based restraints. RDCs are of particular value for multi-domain and extended structures, where small errors in local restraints might lead to much larger displacements remotely. The use of RDCs in structural calculations not only requires the measured values of the RDCs as input, but the principal components of the alignment tensor as well. If a preliminary or model structure is known, a starting tensor can be calculated using singular value decomposition (SVD), in which the alignment tensor components are considered as unknown but overdetermined. Alternatively, for a completely unknown structure, the tensor elements can be calculated using histograms by grid-search or simplex fitting. In either case, once the tensor components are determined, they are iteratively refined in the course of the structure calculations, ideally resulting in a best-fit structure and tensor for the experimental RDCs. A number of programs are available for accomplishing these tasks, including REDCAT [146] and PALES [147]. If more than one alignment medium is used to measure RDCs, separate alignment tensors are required for each data set.

### 5.8.3 *Application of NMR Spectroscopy to Fundamental Questions of Biophysics*

As the reader is by now aware, NMR spectroscopy is a powerful tool for characterizing structural and dynamic features of macromolecules, with applicability to questions of protein folding [148, 149], ligand [150], cofactor [77], effector [94] and substrate binding [151–153], and characterization of modifications and mutations [76]. This chapter is not intended to be a comprehensive survey of the applications of NMR spectroscopy to biophysical research problems. Such a list would include thousands of references and would still be incomplete. We hope that we have provided the reader with the information needed to evaluate the usefulness of NMR spectroscopy in their own research, and that they will seek out local expertise for help in designing and performing the appropriate NMR experiments.

**Acknowledgment** Both authors acknowledge partial support from NIH grant R01-GM44191.

## References

1. Pochapsky TC, Pochapsky SS (2007) NMR for physical and biological scientists. Taylor and Francis, New York, London
2. Hanson LG (2008) Is quantum mechanics necessary for understanding magnetic resonance? *Concepts Magn Reson* 32A:329–340
3. Jeener J (1971) Lecture notes from Ampere Summer School in Basko Polje, Yugoslavia, September, 1971. In: Porneuf M, Goldman M (eds) Ampere International Summer School. Les editions de physique, Basko Polje, Yugoslavia
4. Kupce E, Freeman R (2008) Molecular structure from a single NMR experiment. *J Am Chem Soc* 130:10788–10792
5. Kupce E, Freeman R, John BK (2006) Parallel acquisition of two-dimensional NMR spectra of several nuclear species. *J Am Chem Soc* 128:9606–9607
6. Chakraborty S, Paul S, Hosur RV (2012) Simultaneous acquisition of  $^{13}\text{C}(\alpha)\text{-}^{15}\text{N}$  and  $^1\text{H}\text{-}^{15}\text{N}\text{-}^{15}\text{N}$  sequential correlations in proteins: application of dual receivers in 3D HNN. *J Biomol NMR* 52:5–10
7. Wehrli FW, Marchand AP, Wehrli S (1988) Interpretation of carbon-13 spectra. Wiley, New York
8. Bertini I, Luchinat C (1986) NMR of paramagnetic molecules in biological systems. Benjamin-Cummings, Menlo Park, CA
9. Telser J (2003) Paramagnetic resonance of metallobiomolecules. American Chemical Society, Washington, DC
10. Zhang W, Pochapsky SS, Pochapsky TC, Jain NU (2008) Solution NMR structure of putidaredoxin-cytochrome P450cam complex via a combined residual dipolar coupling-spin labeling approach suggests a role for Trp106 of putidaredoxin in complex formation. *J Mol Biol* 384:349–363
11. Wang W, Perovic I, Chittuluru J, Kaganovich A, Nguyen LTT, Liao JL, Auclair JR, Johnson D, Landeru A, Simorellis AK, Ju SL, Cookson MR, Asturias FJ, Agar JN, Webb BN, Kang CH, Ringe D, Petsko GA, Pochapsky TC, Hoang QQ (2011) A soluble alpha-synuclein construct forms a dynamic tetramer. *Proc Natl Acad Sci U S A* 108:17797–17802

12. Yuan T, Ouyang H, Vogel HJ (1999) Surface exposure of the methionine side chains of calmodulin in solution—a nitroxide spin label and two-dimensional NMR study. *J Biol Chem* 274:8411–8420
13. Liang BY, Bushweller JH, Tamm LK (2006) Site-directed parallel spin-labeling and paramagnetic relaxation enhancement in structure determination of membrane proteins by solution NMR spectroscopy. *J Am Chem Soc* 128:4389–4397
14. Zhu GA, Renwick A, Bax A (1994) Measurement of 2-Bond and 3-Bond  $^1\text{H}$ - $^{13}\text{C}$  J-couplings from quantitative heteronuclear J-correlation for molecules with overlapping  $^1\text{H}$  resonances, using  $t_1$  noise reduction. *J Magn Reson A* 110:257–261
15. Schmidt JM, Sorensen OW, Ernst RR (1994) Measurement of homonuclear long-range J-Couplings by relayed E- COSY. *J Magn Reson A* 109:80–89
16. Cordier F, Nisius L, Dingley AJ, Grzesiek S (2008) Direct detection of N-H[ $\cdots$ ]O=C hydrogen bonds in biomolecules by NMR spectroscopy. *Nat Protoc* 3:235–241
17. Kumar A, Wagner G, Ernst RR, Wüthrich K (1980) Studies of J-connectivities and selective  $^1\text{H}$ - $^1\text{H}$  Overhauser effects in  $\text{H}_2\text{O}$  solutions of biological macromolecules by two-dimensional NMR experiments. *Biochem Biophys Res Commun* 96:1156–1163
18. Rance M, Sorensen OW, Bodenhausen G, Wagner G, Ernst RR, Wüthrich K (1983) Improved spectral resolution in COSY  $^1\text{H}$ -NMR spectra of proteins via double quantum filtering. *Biochem Biophys Res Commun* 117:479–485
19. Braunschweiler L, Ernst RR (1983) Coherence transfer by isotropic mixing—application to proton correlation spectroscopy. *J Magn Reson* 53:521–528
20. Davis DG, Bax A (1985) Assignment of complex  $^1\text{H}$ -NMR spectra via two-dimensional homonuclear Hartmann–Hahn spectroscopy. *J Am Chem Soc* 107:2820–2821
21. Bax A, Clore GM, Gronenborn AM (1990)  $^1\text{H}$ - $^1\text{H}$  correlation via isotropic mixing of  $^{13}\text{C}$  magnetization, a new 3-dimensional approach for assigning  $^1\text{H}$  and  $^{13}\text{C}$  spectra of  $^{13}\text{C}$ -enriched proteins. *J Magn Reson* 88:425–431
22. Moehle K, Freund A, Kubli E, Robinson JA (2011) NMR studies of the solution conformation of the sex peptide from *Drosophila melanogaster*. *FEBS Lett* 585:1197–1202
23. Kay LE, Ikura M, Tschudin R, Bax A (1990) 3-Dimensional triple-resonance NMR spectroscopy of isotopically enriched proteins. *J Magn Reson* 89:496–514
24. Yamazaki T, Lee W, Revington M, Mattiello DL, Dahlquist FW, Arrowsmith CH, Kay LE (1994) An HNCA pulse scheme for the backbone assignment of  $^{15}\text{N}$ ,  $^{13}\text{C}$ ,  $^2\text{H}$ -labeled proteins—application to a 37-kDa Trp repressor DNA complex. *J Am Chem Soc* 116:6464–6465
25. Salzmann M, Pervushin K, Wider G, Senn H, Wüthrich K (1999)  $^{13}\text{C}$ -constant-time [ $^{15}\text{N}$ ,  $^1\text{H}$ ]-TROSY-HNCA for sequential assignments of large proteins. *J Biomol NMR* 14:85–88
26. Bodenhausen G, Ruben DJ (1980) Natural abundance  $^{15}\text{N}$  NMR by enhanced heteronuclear spectroscopy. *Chem Phys Lett* 69:185
27. Kay LE, Keifer P, Saarinen T (1992) Pure absorption gradient enhanced heteronuclear single quantum correlation spectroscopy with improved sensitivity. *J Am Chem Soc* 114:10663–10665
28. Lukavsky PJ (2007) Basic principles of RNA NMR spectroscopy. In: Puglisi JD (ed) *Structure and biophysics—new technologies for current challenges in biology and beyond*. Springer, New York, pp 65–80
29. Fiala R, Czernek J, Sklenar V (2000) Transverse relaxation optimized triple-resonance NMR experiments for nucleic acids. *J Biomol NMR* 16:291–302
30. Patel DJ (1997) Structural analysis of nucleic acid aptamers. *Curr Opin Chem Biol* 1:32–46
31. Pardi A (1995) Multidimensional heteronuclear NMR experiments for structure determination of isotopically labeled RNA. *Methods Enzymol* 261:350–380
32. Kumar A, Ernst RR, Wüthrich K (1980) A two-dimensional nuclear Overhauser enhancement (2D NOE) experiment for the elucidation of complete proton-proton cross-relaxation networks in biological macromolecules. *Biochem Biophys Res Commun* 95:1–6
33. Marion D, Kay LE, Sparks SW, Torchia DA, Bax A (1989) 3-Dimensional heteronuclear NMR of  $^{15}\text{N}$ -labeled proteins. *J Am Chem Soc* 111:1515–1517

34. Ikura M, Kay LE, Tschudin R, Bax A (1990) 3-Dimensional NOESY-HMQC spectroscopy of a  $^{13}\text{C}$ -labeled protein. *J Magn Reson* 86:204–209
35. Neuhaus D, Williamson MP (2000) The nuclear Overhauser effect in structural and conformational analysis, 2nd edn. Wiley, New York
36. Noggle JH, Schirmer RE (1971) The nuclear Overhauser effect: chemical applications. Academic, New York
37. Bothner-By AA, Stephens RL, Lee JM, Warren CD, Jeanloz RW (1984) Structure determination of a tetrasaccharide—transient nuclear Overhauser effects in the rotating frame. *J Am Chem Soc* 106:811–813
38. Bax A, Davis DG (1985) Practical aspects of two-dimensional transverse NOE spectroscopy. *J Magn Reson* 63:207–213
39. Tjandra N, Tate S, Ono A, Kainosho M, Bax A (2000) The NMR structure of a DNA dodecamer in an aqueous dilute liquid crystalline phase. *J Am Chem Soc* 122:6190–6200
40. Prestegard JH, Bougault CM, Kishore AI (2004) Residual dipolar couplings in structure determination of biomolecules. *Chem Rev* 104:3519–3540
41. Hansen MR, Mueller L, Pardi A (1998) Tunable alignment of macromolecules by filamentous phage yields dipolar coupling interactions. *Nat Struct Biol* 5:1065–1074
42. Clore GM, Starich MR, Gronenborn AM (1998) Measurement of residual dipolar couplings of macromolecules aligned in the nematic phase of a colloidal suspension of rod-shaped viruses. *J Am Chem Soc* 120:10571–10572
43. Tjandra N, Bax A (1997) Direct measurement of distances and angles in biomolecules by NMR in a dilute liquid crystalline medium. *Science* 278:1111–1114
44. Wang H, Eberstadt M, Olejniczak ET, Meadows RP, Fesik SW (1998) A liquid crystalline medium for measuring residual dipolar couplings over a wide range of temperatures. *J Biomol NMR* 12:443–446
45. Prosser RS, Losonczy JA, Shiyanovskaya IV (1998) Use of a novel aqueous liquid crystalline medium for high-resolution NMR of macromolecules in solution. *J Am Chem Soc* 120:11010–11011
46. Ottiger M, Bax A (1999) Bicelle-based liquid crystals for NMR measurement of dipolar couplings at acidic and basic pH values. *J Biomol NMR* 13:187–191
47. Ottiger M, Bax A (1998) Characterization of magnetically oriented phospholipid micelles for measurement of dipolar couplings in macromolecules. *J Biomol NMR* 12:361–372
48. Gaponenko V, Dvoretzky A, Walsby C, Hoffman BM, Rosevear PR (2000) Calculation of  $z$ -coordinates and orientational restraints using a metal binding tag. *Biochemistry* 39:15217–15224
49. Tolman JR, Flanagan JM, Kennedy MA, Prestegard JH (1995) Nuclear magnetic dipole interactions in field-oriented proteins—information for structure determination in solution. *Proc Natl Acad Sci U S A* 92:9279–9283
50. Tjandra N, Grzesiek S, Bax A (1996) Magnetic field dependence of nitrogen-proton  $J$  splittings in  $^{15}\text{N}$ -enriched human ubiquitin resulting from relaxation interference and residual dipolar coupling. *J Am Chem Soc* 118:6264–6272
51. Purcell EM, Torrey HC, Pound RV (1946) Resonance absorption by nuclear magnetic moments in a solid. *Phys Rev* 69:37–38
52. Gullion T, Schaefer J (1989) Rotational-echo double resonance NMR. *J Magn Reson* 81:196–200
53. Xu Y, Lorieau J, McDermott AE (2010) Triosephosphate isomerase:  $^{15}\text{N}$  and  $^{13}\text{C}$  chemical shift assignments and conformational change upon ligand binding by magic-angle spinning solid-state NMR spectroscopy. *J Mol Biol* 397:233–248
54. Habenstein B, Wasmer C, Bousset L, Sourigues Y, Schuetz A, Loquet A, Meier BH, Melki R, Boeckmann A (2011) Extensive *de novo* solid-state NMR assignments of the 33 kDa C-terminal domain of the Ure2 prion. *J Biomol NMR* 51:235–243
55. Takegoshi K, Nakamura S, Terao T (2001)  $^{13}\text{C}$ - $^1\text{H}$  dipolar-assisted rotational resonance in magic-angle spinning NMR. *Chem Phys Lett* 344:631–637
56. Gullion T (2009) Recent applications of REDOR to biological problems. In: Webb GA (ed) Annual report on NMR spectroscopy, vol 65., pp 111–137

57. Pauli J, van Rossum B, Forster H, de Groot HJM, Oschkinat H (2000) Sample optimization and identification of signal patterns of amino acid side chains in 2D RFDR spectra of the alpha-spectrin SH3 domain. *J Magn Reson* 143:411–416
58. Demers JP, Chevelkov V, Lange A (2011) Progress in correlation spectroscopy at ultra-fast magic-angle spinning: basic building blocks and complex experiments for the study of protein structure and dynamics. *Solid State Nucl Magn Reson* 40:101–113
59. Amoureux JP, Hu B, Trebosc J (2008) Enhanced resolution in proton solid-state NMR with very fast MAS experiments. *J Magn Reson* 193:305–307
60. Williamson MP, Havel TF, Wüthrich K (1985) Solution conformation of proteinase inhibitor-IIa from bull seminal plasma by  $^1\text{H}$  nuclear magnetic resonance and distance geometry. *J Mol Biol* 182:295–315
61. Wüthrich K (1986) *NMR of proteins and nucleic acids*, vol 3. Wiley, New York
62. Ascietto EK, Young MJ, Madura JD, Pochapsky SS, Pochapsky TC (2012) Solution structural ensembles of substrate-free cytochrome P450(cam). *Biochemistry* 51:3383–3393
63. Ascietto EK, Dang M, Pochapsky SS, Madura JD, Pochapsky TC (2011) Experimentally restrained molecular dynamics simulations for characterizing the open states of cytochrome P450(cam). *Biochemistry* 50:1664–1671
64. Grishaev A, Tugarinov V, Kay LE, Trewhella J, Bax A (2008) Refined solution structure of the 82-kDa enzyme malate synthase G from joint NMR and synchrotron SAXS restraints. *J Biomol NMR* 40:95–106
65. Evenas J, Mittermaier A, Yang DW, Kay LE (2001) Measurement of  $^{13}\text{C}(\alpha)$ - $^{13}\text{C}(\beta)$  dipolar couplings in  $^{15}\text{N}$ ,  $^{13}\text{C}$ ,  $^2\text{H}$ -labeled proteins: application to domain orientation in maltose binding protein. *J Am Chem Soc* 123:2858–2864
66. Pervushin K, Riek R, Wider G, Wüthrich K (1997) Attenuated  $T_2$  relaxation by mutual cancellation of dipole-dipole coupling and chemical shift anisotropy indicates an avenue to NMR structures of very large biological macromolecules in solution. *Proc Natl Acad Sci U S A* 94:12366–12371
67. Riek R, Wider G, Pervushin K, Wüthrich K (1999) Polarization transfer by cross-correlated relaxation in solution NMR with very large molecules. *Proc Natl Acad Sci U S A* 96:4918–4923
68. Pielak GJ, Tian F (2012) Membrane proteins, magic-angle spinning, and in-cell NMR. *Proc Natl Acad Sci U S A* 109:4715–4716
69. Zhou YP, Cierpicki T, Jimenez RHF, Lukasik SM, Ellena JF, Cafiso DS, Kadokura H, Beckwith J, Bushweller JH (2008) NMR solution structure of the integral membrane enzyme DsbB: functional insights into DsbB-catalyzed disulfide bond formation. *Mol Cell* 31:896–908
70. Gautier A, Mott HR, Bostock MJ, Kirkpatrick JP, Neitlispach D (2010) Structure determination of the seven-helix transmembrane receptor sensory rhodopsin II by solution NMR spectroscopy. *Nat Struct Mol Biol* 17:768–U147
71. Shi R, Proteau A, Villarroja M, Moukadi I, Zhang L, Trempe J-F, Matte A, Armengod ME, Cygler M (2010) Structural basis for Fe-S cluster assembly and tRNA thiolation mediated by IscS protein-protein interactions. *PLoS Biol* 8:e1000354
72. Kim JH, Tonelli M, Markley JL (2012) Disordered form of the scaffold protein IscU is the substrate for iron-sulfur cluster assembly on cysteine desulfurase. *Proc Natl Acad Sci U S A* 109:454–459
73. Rezaei-Ghaleh N, Blackledge M, Zweckstetter M (2012) Intrinsically disordered proteins: from sequence and conformational properties toward drug discovery. *Chembiochem* 13:930–950
74. Torchia DA (2011) Dynamics of biomolecules from picoseconds to seconds at atomic resolution. *J Magn Reson* 212:1–10
75. Morris KF, Johnson CS (1993) Resolution of discrete and continuous molecular-size distributions by means of diffusion-ordered 2D NMR spectroscopy. *J Am Chem Soc* 115:4291–4299
76. OuYang B, Pochapsky SS, Dang M, Pochapsky TC (2008) A functional proline switch in cytochrome P450(cam). *Structure* 16:916–923



77. Pochapsky TC, Sligar SG, McLachlan SJ, Lamar GN (1990) Relationship between heme binding-site structure and heme orientations of two ferrocycytochrome b5s—a study in prosthetic group recognition. *J Am Chem Soc* 112:5258–5263
78. Wei JY, Pochapsky TC, Pochapsky SS (2005) Detection of a high-barrier conformational change in the active site of cytochrome P450(cam) upon binding of putidaredoxin. *J Am Chem Soc* 127:6974–6976
79. Bosco DA, Eisenmesser EZ, Pochapsky S, Sundquist WI, Kern D (2002) Catalysis of cis/trans isomerization in native HIV-1 capsid by human cyclophilin A. *Proc Natl Acad Sci U S A* 99:5247–5252
80. Peng JW, Wagner G (1992) Mapping of spectral density functions using heteronuclear NMR relaxation measurements. *J Magn Reson* 98:308–332
81. Lipari G, Szabo A (1982) Model-free approach to the interpretation of nuclear magnetic resonance relaxation in macromolecules. 1. Theory and range of validity. *J Am Chem Soc* 104:4546–4559
82. Meiboom S, Gill D (1958) Modified spin-echo method for measuring nuclear relaxation times. *Rev Sci Instrum* 29:688–691
83. Deverell C, Morgan RE, Strange JH (1970) Studies of chemical exchange by nuclear magnetic relaxation in the rotating frame. *Mol Phys* 18:553
84. Van Horn WD, Kim HJ, Ellis CD, Hadziselimovic A, Sulistijo ES, Karra MD, Tian C, Sonnichsen FD, Sanders CR (2009) Solution nuclear magnetic resonance structure of membrane-integral diacylglycerol kinase. *Science* 324:1726–1729
85. Kijac AZ, Li Y, Sligar SG, Rienstra CM (2007) Magic-angle spinning solid-state NMR Spectroscopy of nanodisc-embedded human CYP3A4. *Biochemistry* 46:13696–13703
86. Laroche Y, Storme V, Demeutter J, Messens J, Lauwereys M (1994) High-level secretion and very efficient isotopic labeling of tick anticoagulant peptide (TAP) expressed in methylotrophic yeast *Pichia pastoris*. *Biotechnology* 12:1119–1124
87. Strauss A, Bitsch F, Fendrich G, Graff P, Knecht R, Meyhack B, Jahnke W (2005) Efficient uniform isotope labeling of Abl kinase expressed in *Baculovirus*-infected insect cells. *J Biomol NMR* 31:343–349
88. Lohr F, Reckel S, Karbyshev M, Connolly PJ, Abdul-Manan N, Bernhard F, Moore JM, Dotsch V (2012) Combinatorial triple-selective labeling as a tool to assist membrane protein backbone resonance assignment. *J Biomol NMR* 52:197–210
89. Sobhanifar S, Reckel S, Junge F, Schwarz D, Kai L, Karbyshev M, Lohr F, Bernhard F, Dotsch V (2010) Cell-free expression and stable isotope labelling strategies for membrane proteins. *J Biomol NMR* 46:33–43
90. Lustbader JW, Birken S, Pollak S, Pound A, Chait BT, Mirza UA, Ramnarain S, Canfield RE, Brown JM (1996) Expression of human chorionic gonadotropin uniformly labeled with NMR isotopes in Chinese hamster ovary cells: an advance toward rapid determination of glycoprotein structures. *J Biomol NMR* 7:295–304
91. Pochapsky SS, Dang M, OuYang B, Simorellis AK, Pochapsky TC (2009) Redox-dependent dynamics in cytochrome P450(cam). *Biochemistry* 48:4254–4261
92. Zwahlen C, Vincent SJF, Gardner KH, Kay LE (1998) Significantly improved resolution for NOE correlations from valine and isoleucine (C-Gamma 2) methyl groups in  $^{15}\text{N}$ ,  $^{13}\text{C}$ - and  $^{15}\text{N}$ ,  $^{13}\text{C}$ ,  $^2\text{H}$ -labeled proteins. *J Am Chem Soc* 120:4825–4831
93. Neri D, Szyperski T, Otting G, Senn H, Wüthrich K (1989) Stereospecific nuclear magnetic resonance assignments of the methyl groups of valine and leucine in the DNA-binding domain of the 434 repressor by biosynthetically directed fractional C-13 labeling. *Biochemistry* 28:7510–7516
94. Pochapsky SS, Pochapsky TC, Wei JW (2003) A model for effector activity in a highly specific biological electron transfer complex: the cytochrome P450(cam)-putidaredoxin couple. *Biochemistry* 42:5649–5656
95. Cellitti SE, Jones DH, Lagpacan L, Hao XS, Zhang Q, Hu HY, Brittain SM, Brinker A, Caldwell J, Bursulaya B, Spraggon G, Brock A, Ryu Y, Uno T, Schultz PG, Geierstanger BH

- (2008) In vivo incorporation of unnatural amino acids to probe structure, dynamics, and ligand binding in a large protein by nuclear magnetic resonance spectroscopy. *J Am Chem Soc* 130:9268–9281
96. Westler WM, Stockman BJ, Markley JL (1988) Correlation of  $^{13}\text{C}$  and  $^{15}\text{N}$  chemical shifts in selectively and uniformly labeled proteins by heteronuclear two-dimensional NMR spectroscopy. *J Am Chem Soc* 110:6256–6258
97. Chan TM, Markley JL (1983) Nuclear magnetic resonance studies of 2-iron-2-sulfur ferredoxins.3. Heteronuclear ( $^{13}\text{C}, ^1\text{H}$ ) two-dimensional NMR spectra,  $^{13}\text{C}$  peak assignments, and  $^{13}\text{C}$  relaxation measurements. *Biochemistry* 22:5996–6002
98. Jain NU, Pochapsky TC (1998) Redox dependence of hyperfine-shifted  $^{13}\text{C}$  and  $^{15}\text{N}$  resonances in putidaredoxin. *J Am Chem Soc* 120:12984–12985
99. Kobayashi H, Swapna GVT, Wu KP, Afinogenova Y, Conover K, Mao BC, Montelione GT, Inouye M (2012) Segmental isotope labeling of proteins for NMR structural study using a protein S tag for higher expression and solubility. *J Biomol NMR* 52:303–313
100. Bockmann A, Lange A, Galinier A, Luca S, Giraud N, Juy M, Heise H, Montserret R, Penin F, Baldus M (2003) Solid state NMR sequential resonance assignments and conformational analysis of the  $2 \times 10.4$  kDa dimeric form of the *Bacillus subtilis* protein Crh. *J Biomol NMR* 27:323–339
101. Kim Y, Valentine K, Opella SJ, Schendel SL, Cramer WA (1998) Solid-state NMR studies of the membrane-bound closed state of the colicin E1 channel domain in lipid bilayers. *Protein Sci* 7:342–348
102. Mote KR, Gopinath T, Traaseth NJ, Kitchen J, Gor'kov PL, Brey WW, Veglia G (2011) Multidimensional oriented solid-state NMR experiments enable the sequential assignment of uniformly  $^{15}\text{N}$  labeled integral membrane proteins in magnetically aligned lipid bilayers. *J Biomol NMR* 51:339–346
103. Kazanis S, Pochapsky TC (1997) Structural features of the metal binding site and dynamics of gallium putidaredoxin, a diamagnetic derivative of a  $\text{Cys}_4\text{Fe}_2\text{S}_2$  ferredoxin. *J Biomol NMR* 9:337–346
104. Piotto M, Saudek V, Sklenar V (1992) Gradient-tailored excitation for single-quantum NMR spectroscopy of aqueous solutions. *J Biomol NMR* 2:661–665
105. Kuboniwa H, Grzesiek S, Delaglio F, Bax A (1994) Measurement of H-N-H- $\alpha$  J couplings in calcium-free calmodulin using new 2D and 3D water flip-back methods. *J Biomol NMR* 4:871–878
106. Grzesiek S, Bax A (1993) The importance of not daturating  $\text{H}_2\text{O}$  in protein NMR—application to sensitivity enhancement and NOE measurements. *J Am Chem Soc* 115:12593–12594
107. Ikura M, Kay LE, Bax A (1990) A novel approach for sequential assignment of  $^1\text{H}$ ,  $^{13}\text{C}$ , and  $^{15}\text{N}$  spectra of larger proteins - Heteronuclear triple-resonance 3-dimensional NMR spectroscopy—application to calmodulin. *Biochemistry* 29:4659–4667
108. Bermel W, Bertini I, Felli IC, Matzapetakis M, Pierattelli R, Theli EC, Turano P (2007) A method for C- $\alpha$  direct detection in protonless NMR. *J Magn Reson* 188:301–310
109. Bermel W, Bertini I, Duma L, Felli IC, Emsley L, Pierattelli R, Vasos PR (2005) Complete assignment of heteronuclear protein resonances by protonless NMR spectroscopy. *Angew Chem Int Ed* 44:3089–3092
110. Kostic M, Pochapsky SS, Pochapsky TC (2002) Rapid recycle  $^{13}\text{C}'$ ,  $^{15}\text{N}$  and  $^{13}\text{C}$ ,  $^{13}\text{C}'$  heteronuclear and homonuclear multiple quantum coherence detection for resonance assignments in paramagnetic proteins: example of  $\text{Ni}^{2+}$ -containing acireductone dioxygenase. *J Am Chem Soc* 124:9054–9055
111. Pochapsky SS, Sunshine JC, Pochapsky TC (2008) Completing the circuit: direct-observe  $^{13}\text{C}$ ,  $^{15}\text{N}$  double-quantum spectroscopy permits sequential resonance assignments near a paramagnetic center in acireductone dioxygenase. *J Am Chem Soc* 130:2156
112. Machonkin TE, Westler WM, Markley JL (2002)  $^{13}\text{C}\{^{13}\text{C}-2\text{D}$  NMR: a novel strategy for the study of paramagnetic proteins with slow electronic relaxation rates. *J Am Chem Soc* 124:3204–3205

113. Matzapetakis M, Turano P, Theil EC, Bertini I (2007)  $^{13}\text{C}$ - $^{13}\text{C}$  NOESY spectra of a 480 kDa protein: solution NMR of ferritin. *J Biomol NMR* 38:237–242
114. Szyperski T, Fernandez C, Ono A, Wüthrich K, Kainosho M (1999) The 2D 31P spin-echo-difference constant-time [ $^{13}\text{C}$ ,  $^1\text{H}$ ]-HMQC experiment for simultaneous determination of 3J(H3'P) and 3J(C4'P) in  $^{13}\text{C}$ -labeled nucleic acids and their protein complexes. *J Magn Reson* 140:491–494
115. Riek R, Pervushin K, Fernandez C, Kainosho M, Wüthrich K (2001) [ $^{13}\text{C}$ ,  $^{13}\text{C}$ ]- and [ $^{13}\text{C}$ ,  $^1\text{H}$ ]-TROSY in a triple resonance experiment for ribose base and intrabase correlations in nucleic acids. *J Am Chem Soc* 123:658–664
116. Ding K, Gronenborn AM (2004) Sensitivity-enhanced IPAP experiments for measuring one-bond  $^{13}\text{C}'$ - $^{13}\text{C}(\alpha)$  and  $^{13}\text{C}(\alpha)$ - $^1\text{H}(\alpha)$  residual dipolar couplings in proteins. *J Magn Reson* 167:253–258
117. Ding KY, Gronenborn AM (2003) Sensitivity-enhanced 2D IPAP, TROSY-anti-TROSY, and E.COSY experiments: alternatives for measuring dipolar  $^{15}\text{N}$ - $^1\text{H}(\text{N})$  couplings. *J Magn Reson* 163:208–214
118. Hahn EL (1950) Spin echos. *Phys Rev* 80:580–594
119. Stejskal EO, Tanner JE (1965) Spin diffusion measurements: spin echoes in the presence of a time-dependent field gradient. *J Chem Phys* 42:288–292
120. Scaglioni L, Mazzini S, Mondelli R, Dallavalle S, Gattinoni S, Tinelli S, Beretta GL, Zunino F, Ragg E (2009) Interaction between double helix DNA fragments and a new topopyrone acting as human topoisomerase I poison. *Bioorg Med Chem* 17:484–491
121. Mizukoshi Y, Abe A, Takizawa T, Hanzawa H, Fukunishi Y, Shimada I, Takahashi H (2012) An accurate pharmacophore mapping method by NMR spectroscopy. *Angew Chem Int Ed* 51:1362–1365
122. Delaglio F, Grzesiek S, Vuister GW, Zhu G, Pfeifer J, Bax A (1995) NMRpipe—a multidimensional spectral processing system based on UNIX pipes. *J Biomol NMR* 6:277–293
123. NMR Felix (2007) Felix. Felix NMR Inc., San Diego, CA
124. Hare DR (1986) FTNMR. Hare Research, Woodinville, WA
125. Bartels C, Xia TH, Billeter M, Guntert P, Wüthrich K (1995) The program XEASY for computer-supported NMR spectral analysis of biological macromolecules. *J Biomol NMR* 6:1–10
126. Bettendorff P, Damberger F, Rochus L, Keller J, Guntert P CARA (computer assisted resonance assignment). ETH, Zurich
127. Goddard TD, Kneller DG Sparky 3. UCSF, San Francisco
128. NMRView. One Moon Scientific, Inc., Newark, NJ
129. Moseley HNB, Sperling LJ, Rienstra CM (2010) Automated protein resonance assignments of magic angle spinning solid-state NMR spectra of beta 1 immunoglobulin binding domain of protein G (GB1). *J Biomol NMR* 48:123–128
130. O'connell JF, Pryer KD, Grant SK, Leiting B (1999) A high quality nuclear magnetic resonance solution structure of peptide deformylase from *Escherichia coli*: application of an automated assignment strategy using GARANT. *J Biomol NMR* 13:311–324
131. Crippen GM, Rousaki A, Revington M, Zhang YB, Zuiderweg ERP (2010) SAGA: rapid automatic mainchain NMR assignment for large proteins. *J Biomol NMR* 46:281–298
132. Zweckstetter M (2003) Determination of molecular alignment tensors without backbone resonance assignment: aid to rapid analysis of protein-protein interactions. *J Biomol NMR* 27:41–56
133. Guerry P, Herrmann T (2011) Advances in automated NMR protein structure determination. *Q Rev Biophys* 44:257–309
134. Wagner G, Braun W, Havel TF, Schaumann T, Go N, Wüthrich K (1987) Protein structures in solution by nuclear magnetic resonance and distance geometry—the polypeptide fold of the basic pancreatic trypsin inhibitor determined using 2 different algorithms, DISGEO and DISMAN. *J Mol Biol* 196:611–639
135. Case DA, Cheatham TE, Darden T, Gohlke H, Luo R, Merz KM, Onufriev A, Simmerling C, Wang B, Woods RJ (2005) The AMBER biomolecular simulation programs. *J Comput Chem* 26:1668–1688

136. Schwieters CD, Kuszewski JJ, Tjandra N, Clore GM (2003) The Xplor-NIH NMR molecular structure determination package. *J Magn Reson* 160:65–73
137. Humphrey W, Dalke A, Schulten K (1996) VMD: visual molecular dynamics. *J Mol Graph* 14:33–38
138. Brunger AT, Adams PD, Clore GM, DeLano WL, Gros P, Grosse-Kunstleve RW, Jiang JS, Kuszewski J, Nilges M, Pannu NS, Read RJ, Rice LM, Simonson T, Warren GL (1998) Crystallography & NMR system: a new software suite for macromolecular structure determination. *Acta Crystallogr D Biol Crystallogr* 54:905–921
139. Guntert P (2004) Automated NMR protein structure calculation with CYANA. *Methods Mol Biol* 278:353–378
140. Banci L, Bertini I, Cremonini MA, Gori-Savellini G, Luchinat C, Wüthrich K, Guntert P (1998) Pseudodyana for NMR structure calculation of paramagnetic metalloproteins using torsion angle molecular dynamics. *J Biomol NMR* 12:553–557
141. Guntert P, Mumenthaler C, Wüthrich K (1997) Torsion angle dynamics for NMR structure calculation with the new program DYANA. *J Mol Biol* 273:283–298
142. Gorlach M, Wittekind M, Farmer BT, Kay LE, Mueller L (1993) Measurement of  $^3\text{J}(\text{HN}-\text{Alpha})$  vicinal coupling constants in proteins. *J Magn Reson B* 101:194–197
143. Mollova ET, Pardi A (2000) NMR solution structure determination of RNAs. *Curr Opin Struct Biol* 10:298–302
144. Shen Y, Delaglio F, Bax A (2009) TALOS+: a hybrid method for predicting protein backbone torsion angles from NMR chemical shifts. *J Biomol NMR* 44:213–223
145. Case DA (1998) The use of chemical shifts and their anisotropies in biomolecular structure determination. *Curr Opin Struct Biol* 8:624–630
146. Valafar H, Prestegard JH (2004) REDCAT: a residual dipolar coupling analysis tool. *J Magn Reson* 167:228–241
147. Zweckstetter M (2008) NMR: prediction of molecular alignment from structure using the PALES software. *Nat Protoc* 3:679–690
148. Fedukina DV, Cavagnero S (2011) Protein folding at the exit tunnel. In: Rees DC, Dill KA, Williamson JR (eds) *Annual review on biophysics*, vol 40., pp 337–359
149. Cioni P, Gabellieri E (2011) Protein dynamics and pressure: what can high pressure tell us about protein structural flexibility? *Biochim Biophys Acta* 1814:934–941
150. Cozzolino S, Sequi P, Valentini M (2011) Probing interactions between small molecules and polymers by means of NMR spectroscopy. In: Webb GA (ed) *Annual report on NMR spectroscopy*, vol 74., pp 181–213
151. Manley G, Loria JP (2012) NMR insights into protein allostery. *Arch Biochem Biophys* 519:223–231
152. Bhunia A, Bhattacharjya S, Chatterjee S (2012) Applications of saturation transfer difference NMR in biological systems. *Drug Discov Today* 17:505–513
153. Barelier S, Krimm I (2011) Ligand specificity, privileged substructures and protein drug-gability from fragment-based screening. *Curr Opin Chem Biol* 15:469–474
154. Sattler M, Schleucher J, Griesinger C (1999) Heteronuclear multidimensional NMR experiments for the structure determination of proteins in solution employing pulsed field gradients. *Prog Nucl Magn Reson Spectrosc* 34:93–158
155. Ippel JH, Wijmenga SS, de Jong R, Heus HA, de Vroom E, van der Marel GA, van Boom JH (1996) Heteronuclear scalar couplings in the bases and sugar rings of nucleic acids: their determination and application in assignment and conformational analysis. *Magn Reson Chem* 34:S176

# Chapter 6

## Electron Paramagnetic Resonance Spectroscopy

John H. Golbeck and Art van der Est

**Abstract** Electron paramagnetic resonance (EPR) spectroscopy is widely used to study proteins that contain naturally occurring paramagnetic centers and/or artificially introduced spin labels. In this chapter we present a mainly qualitative overview of the application of EPR spectroscopy to the study biological systems. The chapter begins with a short description of the physical principles underlying the method and the basic experimental techniques. An overview of characteristic line-shapes observed under various experimental conditions is then presented to show how quantities such as hyperfine couplings,  $g$ -anisotropy and zero-field splitting manifest themselves in EPR data. A number of specific examples are used to illustrate how these quantities can be used to obtain information about the geometry, bonding, electronic structure, etc. of biological systems.

**Keywords** CW EPR • Transient EPR • Pulse EPR • Zeeman splitting • Spin orbit coupling • Hyperfine coupling • Organic radicals • Metalloproteins • Molecular triplet states • Light-induced radical pairs

---

J.H. Golbeck (✉)

Department of Biochemistry and Molecular Biology, The Pennsylvania State University,  
University Park, PA 16802, USA

Department of Chemistry, The Pennsylvania State University,  
University Park, PA 16802, USA  
e-mail: jhg5@psu.edu

A. van der Est

Department of Chemistry, Brock University, St. Catharines, ON, Canada, L2S 3A1  
e-mail: avde@brocku.ca

## 6.1 Introduction

Electron paramagnetic resonance (EPR) detects the magnetic susceptibility associated with unpaired electrons in atoms or molecules. The presence of unpaired electrons is a rather unusual condition, as most stable molecules have filled electron shells and the Pauli Exclusion Principle specifies that their electrons be paired. Nevertheless, four important exceptions occur in biological systems. The transition metals typically have partially filled *d*-shells and many of them are paramagnetic in one or more of their oxidation states. The first row transition elements V, Mn, Fe, Co, Ni, Cu, the second row transition element Mo and the third row transition element W are found in metalloproteins. The metastable intermediates found in photoactive proteins and radical enzymes form a second class of paramagnetic species found in nature. These intermediates include excited triplet states, carbon-, oxygen-, and sulfur-centered radicals and biradicals such as formed in photosynthetic systems. Molecular oxygen, which makes up ~20 % of the atmosphere, also has a paramagnetic triplet ground state. Finally, stable nitroxide radical-based spin labels, such as *S*-(2,2,5,5-tetramethyl-2,5-dihydro-1H-pyrrol-3-yl)methyl methanesulfonothioate (MTSL), can be incorporated into proteins and used as probes of the molecular environment. Here, we give a brief, largely qualitative introduction to EPR spectroscopy in which we will use examples from three of these classes of systems to illustrate the physical principles of the method and its application in biophysics. For more in-depth treatments of EPR, readers are referred to the excellent introductory textbooks by Weil, Bolton, and Wertz (Electron paramagnetic resonance, elementary theory and practical applications, Wiley, New York) [1], Atherton (Principles of electron spin resonance, Ellis Horwood/Prentice Hall, New York) [2], and Hagen (Spectroscopy, CRC Press, Boca Raton, FL) [3] as well as overviews of practical aspects of the technique by Brustolon and Giamello (Electron paramagnetic resonance: a practitioner's toolkit, Wiley, Hoboken, NJ) [4] and advanced texts on pulsed EPR by Schweiger and Jeschke (Principles of pulsed electron paramagnetic resonance, Oxford University Press, Oxford) [5], high field EPR by Möbius and Savitsky (High field EPR spectroscopy on proteins and their model systems: characterization of transient paramagnetic states, RSC, Cambridge) [6], and on spin labeling by Berliner (Spin labeling, the next millenium, Plenum Press, New York) [7].

## 6.2 Physical Principles

### 6.2.1 Basic Principle of EPR

Magnetism is the result of the motion of charges. On a macroscopic level a current passing through a loop generates a magnetic field perpendicular to the plane of the loop. On a microscopic scale, a circulating negatively charged particle generates a magnetic moment,  $\vec{\mu}$ , that is, antiparallel to the angular momentum vector  $\vec{l}$  as

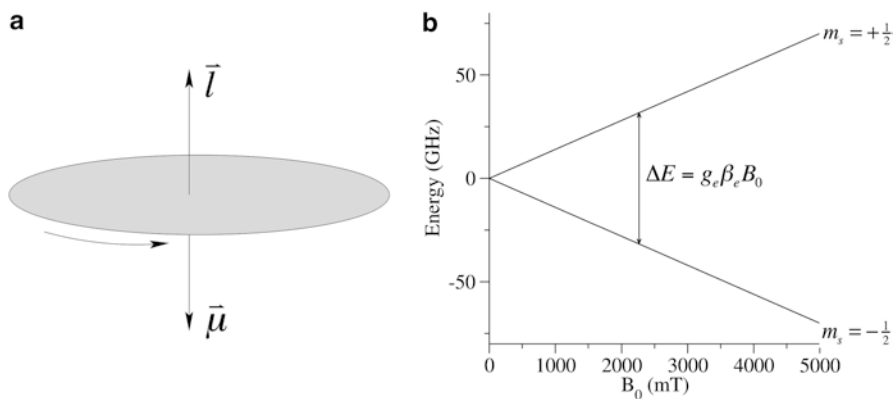


**Fig. 6.1** (a) Magnetic moment and angular momentum of a circulating negatively charged particle. (b) Zeeman energy levels for a free electron

shown in Fig. 6.1a. Free electrons do not circulate but have intrinsic angular momentum;  $\vec{S}$  referred to as spin and the magnetic moment of a free electron is antiparallel to its spin angular momentum. The two quantities are related by:

$$\vec{\mu} = -g_e \beta_e \vec{S}, \quad (6.1)$$

where  $g_e$  is the free electron  $g$ -factor (2.0023193) and  $\beta_e$  is the electron Bohr magneton ( $9.27401 \times 10^{-24}$  J T $^{-1}$ ). Bound electrons, on the other hand, have both orbital and spin angular momentum and both of these contribute to the magnetic moment. In light atoms and organic molecules, the orbital angular momentum is small and hence the magnetic moment is usually discussed in terms of the spin angular momentum. In the presence of a magnetic field,  $\vec{B}$ , a magnetic moment experiences an interaction energy that depends on the relative orientation of  $\vec{\mu}$  and  $\vec{B}$ . Classically, the interaction energy is given by:

$$E = -B_0 \mu_z, \quad (6.2)$$

where  $B_0$  is the magnitude of the magnetic field, which is defined to lie along the  $z$ -direction.

Quantum mechanically, the Hamiltonian operator for the energy is obtained by replacing  $\mu_z$  in (6.2) with the corresponding operator  $\hat{\mu}_z$ :

$$\hat{H} = -B_0 \hat{\mu}_z = g_e \beta_e B_0 \hat{S}_z, \quad (6.3)$$

where  $\hat{S}_z$  is the operator for the  $z$ -component of the spin angular momentum. Solving the Schrödinger equation for the energy gives:

$$E = g_e \beta_e B_0 m_s. \quad (6.4)$$

For a free electron, the quantum number  $m_s$  for the  $z$ -component of the spin angular momentum can take values of  $+1/2$  and  $-1/2$ . Thus, in a magnetic field a free electron has two energy states with  $E = +\frac{1}{2}g_e\beta_e B_0$  and  $E = -\frac{1}{2}g_e\beta_e B_0$  as shown in Fig. 6.1b. The interaction between the magnetic moment and the field is known as the Zeeman interaction and the basic principle of EPR spectroscopy is the measurement of the absorption of electromagnetic radiation as a result of transitions between the Zeeman energy levels. For atoms and molecules, there are additional interactions (hyperfine coupling, dipolar coupling, zero-field splitting, etc.) that lead to extra terms in the Hamiltonian operator and cause shifts and/or splittings of the energy levels. The effect of these terms on the EPR spectrum will be described below when the characteristic lineshapes are described. From a biophysics point of view, the interactions that lead to the additional terms are extremely important because they depend on the local environment of the unpaired electrons and hence, EPR spectra contain information about geometry, bonding, electronic structure, etc., of the paramagnetic species. Examples of the information contained in EPR data will be presented in the Sect. 6.5 of this chapter. First, however, we give a brief description of the EPR experiment and introduce the concept of magnetization that is important for understanding pulsed experiments and relaxation. This is followed by a short discussion of several important experimental aspects of EPR.

### 6.2.2 The EPR Experiment

Figure 6.2 shows a schematic diagram of the main components of a continuous wave EPR spectrometer using lock-in detection. The microwave components are contained in a microwave bridge indicated by the dashed line in Fig. 6.2. The microwave source is typically either a klystron or a Gunn diode and the microwaves exiting the source are split into a signal arm and a reference arm. The signal arm has an attenuator to adjust the microwave power reaching the sample and a circulator is used to direct microwaves to the resonator, which is mounted in the magnet. Reflected power from the resonator passes through the circulator to detector. The reference arm has a phase shifter that allows the relative phase of the microwaves in the two arms to be varied. The microwave signals from the two arms are then mixed and converted to a DC signal, or slowly oscillating signal, by the detector, which is typically either a diode or a mixer. The signal from the detector is then amplified by a preamplifier and fed to a lock-in amplifier. The lock-in amplifier modulates the EPR signal by modulating the magnetic field using a set of modulation coils mounted on the resonator and it amplifies only those signals from the bridge that oscillate at the modulation frequency. The output of the lock-in amplifier is recorded as the magnetic field is swept through a region of interest to generate the EPR spectrum.



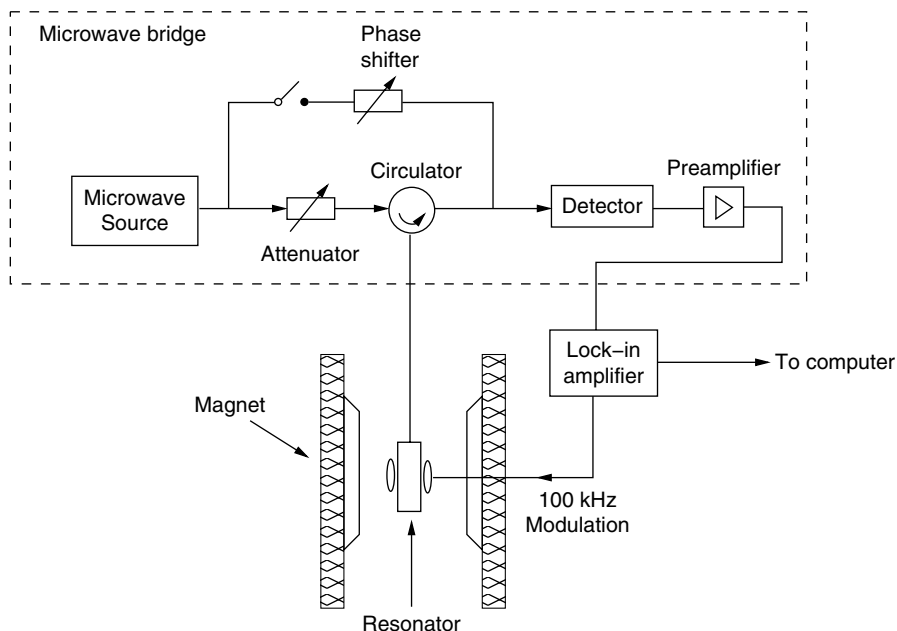


**Fig. 6.2** Schematic diagram of a basic continuous wave EPR spectrometer using field modulation detection

### 6.2.3 Magnetization

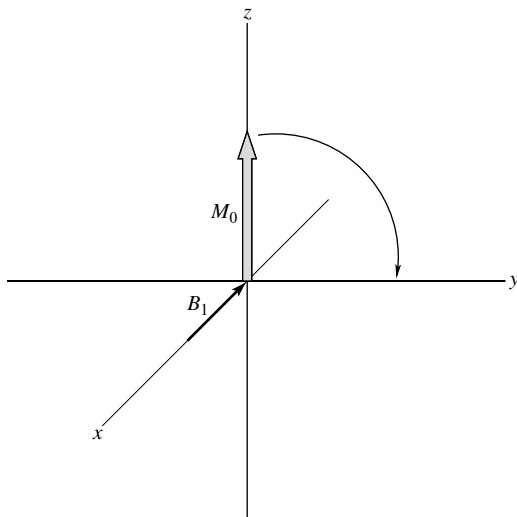
In a typical EPR experiment, the sample contains on the order of  $10^{16}$  spins and it is useful to describe the ensemble average behavior of the system. When a paramagnetic substance is placed in a magnetic field, it becomes magnetized and EPR experiments can be understood in terms of the response of the magnetization to the applied electromagnetic radiation. The magnetization of the sample is defined as the ensemble average magnetic moment. At thermal equilibrium, the  $x$  and  $y$  components of the magnetic moment average to zero and the magnetization is the average magnetic moment along the magnetic field,

$$\bar{M} = \rho \bar{\mu} = \rho \bar{\mu}_z, \quad (6.5)$$

where  $\rho$  is the number of spins per unit volume. Using the Boltzmann distribution to calculate  $\bar{\mu}_z$  gives:

$$\bar{M} = \frac{\rho g_e^2 \beta_e^2 S(S+1)}{3kT} \bar{B}_0 = \frac{\chi_m}{\mu_r \mu_0} \bar{B}_0, \quad (6.6)$$

**Fig. 6.3** Behavior of the magnetization in an EPR experiment in the laboratory frame and in the rotating frame



where  $S$  is the spin quantum number,  $\chi_m$  is the magnetic susceptibility,  $\mu_r$  and  $\mu_0$  are the relative and free space permeabilities, respectively. Equation (6.6) shows that the magnetic susceptibility depends on the inverse temperature, which is known as the Curie law. In an EPR experiment the response of the magnetization (or magnetic susceptibility) to the oscillating field of the electromagnetic radiation is measured. Experimentally, the microwaves are applied to the sample such that the magnetic field component oscillates in a plane perpendicular to the static field. The response of the system is measured by phase-sensitive detection of the microwaves in this plane. The in-phase response is defined as  $\chi'$  and the response  $90^\circ$  out of phase is  $\chi''$ . As shown in Fig. 6.2, the microwave signal from the sample is mixed with a reference microwave beam to produce a DC (or slowly oscillating) signal. Mathematically, this is equivalent to observing the  $x$  or  $y$  component of the magnetization in a frame of reference rotating at the frequency of the reference beam. Vector diagrams of the behavior of the magnetization in the rotating frame, such as shown in Fig. 6.3, are useful for understanding the observed signals especially in pulsed EPR experiments. Initially, without the microwave field present (Fig. 6.3a) the magnetization,  $M_0$ , is aligned along the static field,  $B_0$ , in the  $z$ -direction. When the microwave field,  $B_1$ , is applied perpendicular to the external field, the magnetization precesses about the sum of the two fields. This results in the spiral motion of the magnetization is shown in Fig. 6.3b. If we transform to a frame of reference rotating with the microwave frequency (Fig. 6.3c), the microwave field is now static and if the phase is chosen so that  $B_1$  is along the negative  $x'$ -direction, the magnetization precesses towards the  $y'$  direction. With the phase of the detection set to  $y'$  the precession of the magnetization results an increase of the observed signal. However, as the magnetization continues to precess the signal decreases, becomes negative, then positive again, and so on, in an oscillatory fashion. This oscillatory motion of the magnetization about the microwave field in the rotating frame is referred to as nutation.

## 6.3 Experimental Techniques

### 6.3.1 Choice of Magnetic Field and Microwave Frequency

The frequency of the radiation needed to cause a transition between the energy levels of a free electron is  $\nu = \Delta E/h = g_e \beta_e B_0/h$ . The choice of  $B_0$  and  $\nu$  is governed largely by available magnet and microwave or far infrared technology. Microwave sources and components are generally produced for specific, relatively narrow frequency bands each designated by a letter. X-band components operate at  $\sim 9.3$  GHz and inexpensive klystron or Gunn diode sources are available. The corresponding magnetic field,  $B_0 \approx 0.33$  T, can be easily produced by a moderately low power/current electromagnet. In general, the  $g$ -value depends on the orientation of the molecule with respect to the magnetic field. Hence, low temperature EPR spectra of randomly ordered samples are broad and have features corresponding to molecules at different orientations. The resolution of these features depends on the field/frequency combination that is used. Commercial spectrometers are now available at the following frequencies (along with their coded designations): 1.2 GHz (L-band), 2.4 GHz (S-band), 9.3 GHz (X-band), 34 GHz (Q-band), 94 GHz (W-band), and 263 GHz (mm-band). X-band spectrometers remain by far the most popular because of their comparatively low cost and ease of operation while providing sufficient resolution for metalloproteins. Q-band spectrometers are also widely used because they allow the spectra of some organic radicals to be partially resolved at a field strength that is achievable with an electromagnet. The higher frequency bands (W-band and higher) require superconducting magnets but provide an order of magnitude better spectral resolution compared to X-band. In practice, the most appropriate frequency band for a particular experiment depends on many factors and it is usually advantageous to have data at several frequency bands.

### 6.3.2 Sensitivity and Its Consequences for EPR Measurements

The population difference between the  $m_s = +1/2$  and  $m_s = -1/2$  states, which is required to observe the absorption of radiation, plays a crucial role in the design of EPR spectrometers. At thermal equilibrium the population difference is governed by the Boltzmann distribution:

$$N_\alpha / N_\beta = \exp(-E/kT), \quad (6.7)$$

where  $N_\alpha$  and  $N_\beta$  refer to the populations of the  $m_s = +1/2$  and  $-1/2$  states, respectively, and  $\Delta E = h\nu = g_e \beta_e B_0$ . At 298 K and  $B_0 = 0.33$  T ( $\nu = 9.25$  GHz, X-band),  $N_\alpha/N_\beta$  is 0.998, which is given as  $\Delta N/N = 10^{-3}$  where  $\Delta N = (N_\beta - N_\alpha)$  and  $N = (N_\alpha + N_\beta)$ . In comparison, transitions in the visible region have  $\Delta N/N \approx 1$ . Because the transition probability is directly proportional to  $\Delta N$ , EPR is a much less sensitive

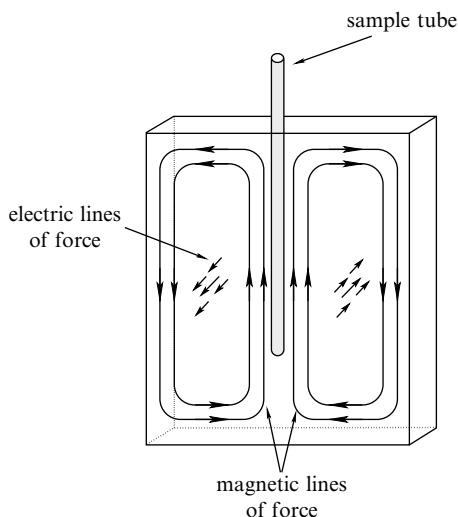
technique than is optical spectroscopy. On the other hand,  $\Delta N/N = 5 \times 10^{-5}$  for proton NMR spectroscopy, which is much less sensitive than EPR. As shown in (6.7), the population difference and hence, the transition probability can be increased by either lowering the temperature or increasing the magnetic field strength. With  $B_0 = 0.33$  T, about a 20-fold increase in signal strength is obtained by lowering the temperature from 298 to 10 K and a further tenfold increase is obtained by going to 1 K. Temperatures to 4.2 K are possible with the use of liquid He gas-flow cooling systems whereas temperatures to 1.6 K require a specialized cryostat and pumped He. Increasing the magnetic field strength from 0.33 T (X-band) to 1.2 T (Q-band) at 10 K results in a 3.5-fold increase in the signal strength. A tenfold increase in signal strength is obtained at 3.3 T (W-band) compared to X-band. However, the dimensions of the components scale with the wavelength of the microwave, and hence the sample size becomes smaller as the frequency increases. This can be an advantage when dealing with biological samples that are difficult to prepare but it also means that the total number of spins in the sample is lower. Another drawback is the increased cost of the microwave components and the magnets at higher fields. At very high frequencies, quasi-optical technologies must be used.

As a consequence of the small Boltzmann factors involved in EPR experiments, direct measurement of the microwave absorption is hampered by very poor signal to noise. To overcome this problem, the absorption is measured indirectly using a resonator and a microwave bridge. There are many different possible designs for the resonator but most commonly it is a closed cavity lined with highly conductive metal with dimensions similar to that of the wavelength of the microwave radiation. It is the microwave equivalent of a tuned, resonant circuit; hence, it stores energy at its resonance frequency. The microwave bridge is coupled to the resonator and tuned to its resonance frequency so that all of the incoming microwave energy is stored. When an EPR transition occurs in the sample, the resonator is perturbed and some of the incoming power from the microwave bridge is reflected. The amount of reflected power is considerably larger than the amount absorbed by the EPR transition and so a larger signal is obtained than in a direct absorption experiment.

### ***6.3.3 Resonator Design and the Problem of Damping***

In an ideal resonant cavity, the electrical properties of conductors dictate that the tangential electric field component of the microwaves must be zero at the walls if they are made of a highly conductive material [8]. This constrains the microwaves in space and causes the formation of standing waves. The result is a separation of the magnetic field lines of force from the electric field lines of force into different regions of the resonant cavity. This separation satisfies three important requirements for an EPR experiment. First, because only the magnetic component of the microwave radiation promotes EPR transitions, and because the amplitude of the detected signal is proportional to the amount of energy absorbed, the sample should be located in the region of the highest magnetic field lines of force. Second, absorption of microwaves via electric-dipole transitions in the sample should be minimized and

**Fig. 6.4** Magnetic and electric field lines in a rectangular resonator



therefore the sample should be located in the region of the lowest electric field lines of force. Third, to satisfy the selection rules for the spin transitions, the microwave magnetic field must be perpendicular to the direction of the laboratory magnetic field. Note that this requirement applies when the Zeeman interaction dominates, which is the usual situation. However, for integer ( $S=1, 2, 3$ , etc.) spin systems in which the zero-field splitting is larger than the Zeeman splitting (non-Kramer's systems) the magnetic component of the microwave radiation should be parallel to the direction of the laboratory magnetic field [9]. These conditions can be readily met in a rectangular resonator as depicted in Fig. 6.4. When the sample is placed in the center of the resonator, it is exposed maximally to the magnetic lines of force and minimally to the electric lines of force. A rather serious complication for biological materials is that if the sample is in a high dielectric solvent such as water, the electric component of the microwaves will be quenched, and along with it, the magnetic component. This can be avoided in one of two ways. First, the sample can be placed in a quartz tube and frozen; the phase change lowers the dielectric constant of water from 80.1 at 20 °C to 4 at 0 °C. Second, if the sample needs to remain a liquid, the so-called flat cell can be used which places the high dielectric sample in the nodal plane of the electric field. Alternatively, inexpensive, small diameter capillaries can be used at both X- and Q-bands, with a considerable savings in sample volume and ease of filling and cleaning.

### 6.3.4 Relaxation

Another important factor governing the sensitivity of EPR spectroscopy is spin relaxation. In a continuous wave experiment microwave power is applied continuously to the sample and both absorption and stimulated emission occur between the spin

states. Both the applied microwave field and oscillating fields in the local environment of the paramagnetic center induce these transitions. The relative rates of absorption and emission determine the net absorption of energy by the sample and hence the amplitude of the EPR signal. If the spin system is perturbed from thermal equilibrium, the transitions induced by the local fields return the system to equilibrium with a characteristic time known as the spin–lattice relaxation time,  $T_1$ . In the rotating frame picture,  $T_1$  is the time constant associated with the return of the magnetization to the  $z$ -direction. In the absence of relaxation, the populations of the spin states would eventually become equal under continuous irradiation and hence no net absorption would be observed. In the presence of relaxation, however, the population difference is maintained. The size of the population difference depends on the relative rates of relaxation, absorption, and stimulated emission. As the microwave power is increased, the rate of absorption and stimulated emission can become faster than the relaxation rate and equalization of the populations, and hence loss of signal, occurs. This phenomenon is known as power saturation and tends to occur when  $T_1$  is long. Since  $T_1$  usually increases as the temperature is lowered, power saturation occurs more easily at cryogenic temperatures. Thus, slow relaxing systems such as organic radicals are best observed at low microwave power and higher temperatures.

The relaxation rate also has an influence on the width of absorption lines. Here, both spin–lattice relaxation and spin–spin or phase relaxation governed by  $T_2$  play a role. In EPR the resonant absorption of microwaves is damped by  $T_1$  and  $T_2$  relaxation, and the larger the damping the broader the spectrum. Thus, if the relaxation is fast, the width of the spectrum is large, often to the point that it cannot be detected. Considered quantum mechanically, the phenomenon of lifetime broadening can be traced to the Heisenberg uncertainty principle, which can be restated as  $\tau\delta E \geq \hbar/2\pi$ , where  $\tau$  is the mean lifetime and  $\delta E$  is the uncertainty in the energy of the system. As the lifetime becomes shorter,  $\delta E$  becomes greater. Thus, as the relaxation becomes faster, the probability that a transition will be distributed over a larger magnetic field range increases. In general, the linewidth has two contributions: (1) the inhomogeneous linewidth, which is due to a distribution of local environments and (2) the homogeneous linewidth associated with the intrinsic properties of the paramagnetic species, which defines a minimum linewidth for a given spin system. Lifetime broadening usually determines the homogeneous linewidth and it is particularly problematic for certain metal ions. For example, [4Fe-4S] clusters typically cannot be observed at temperatures much above 20 K, although [2Fe-2S] clusters can be observed at temperatures as high as 77 K.

A plot of signal amplitude vs. inverse temperature (Fig. 6.5) shows two regions. The rise in signal amplitude as the temperature is lowered is termed the Curie law region and is due to the increased population difference between the spin energy levels as the temperature is lowered. The decline in signal amplitude beyond a certain optimum is due to power saturation as spin–lattice and spin–spin relaxation times become longer as the temperature is lowered. The shape of the saturation curve at low temperature depends on the relaxation mechanism.

A more quantitative approach [10] to determine the onset of saturation is to plot  $I/\sqrt{P}$  vs.  $\sqrt{P}$  for a given temperature, where  $I$  is the signal intensity and  $P$  is the

**Fig. 6.5** Temperature dependence of the intensity of an EPR signal. At high temperature the intensity follows Curie-law behavior. At low temperature the signal intensity decreases due to power saturation as  $T_1$  becomes long

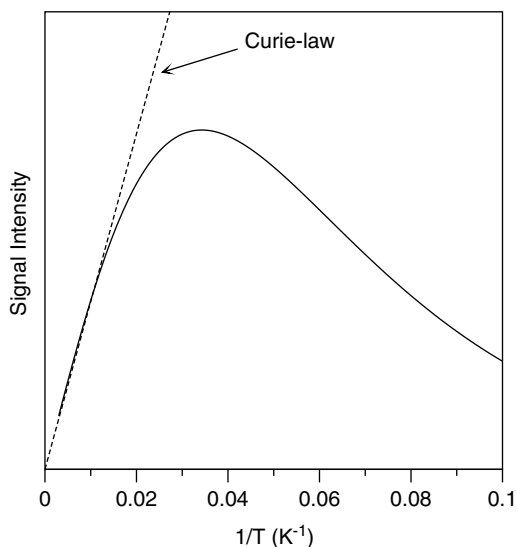
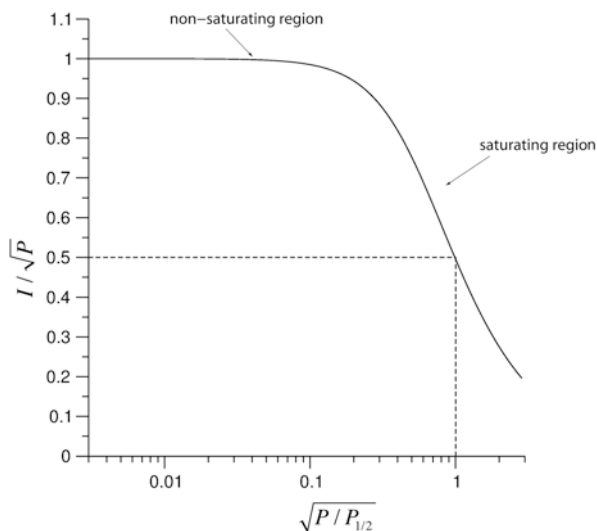


**Fig. 6.6** Saturation behavior of a homogeneously broadened line



microwave power (Fig. 6.6). In the non-saturating region, (low power) the signal intensity is proportional to the square root of the power and the plot is horizontal. At the onset of power saturation, the plot shows a break and a downward slope. The point at which  $I/\sqrt{P}$  drops by 50 % is labeled  $P_{1/2}$ , and is particularly useful in identifying interactions between two spin systems. If a rapidly relaxing spin system is in proximity of a slower relaxing spin system, the former will enhance the relaxation of the latter, and this can be measured by a change in the  $P_{1/2}$  of the slower spin system.

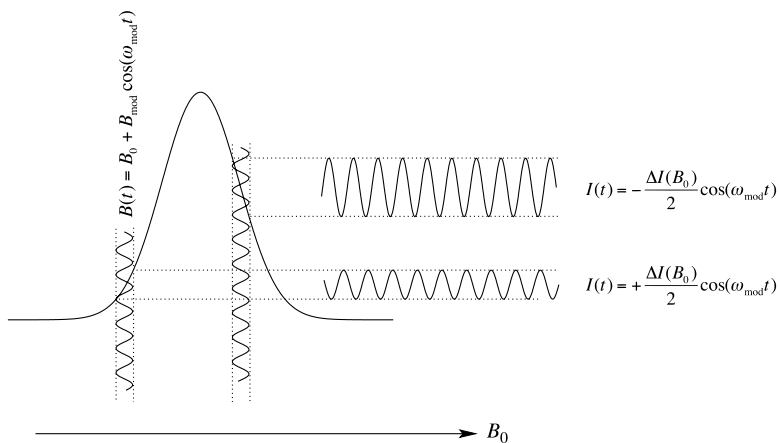
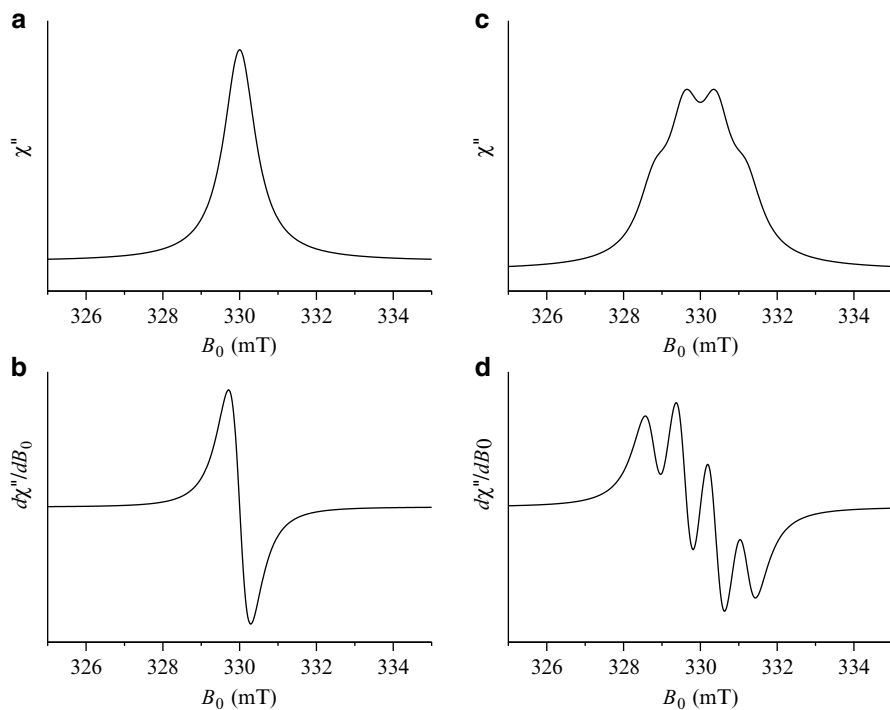
### 6.3.5 *Conventional Field-Swept CW EPR and Field Modulation Lock-In Detection*

To obtain an EPR spectrum, the microwave absorption must be measured as either the microwave frequency or the magnetic field is swept over a finite range. When a resonator is used for detection, the microwave frequency can only be varied over a range that is small compared to the bandwidth of the resonator. For many samples, the width of the EPR spectrum is much larger than the bandwidth of the resonator. Thus, the field must be swept. Despite the use of a resonator, EPR signals are still very weak and difficult to detect. The problem arises because of the characteristics of  $1/f$  noise; the issue is that direct detection of the signal falls in the noisy DC region of the electromagnetic spectrum. The  $S/N$  can be improved by converting the DC signal to an AC signal that is in a quieter region of the spectrum, applying a narrow bandpass filter to reject noise above and below that frequency, and demodulating the signal to bring it back to DC (actually, a time-varying, low frequency signal). This scheme is termed “phase-sensitive” detection and employs what is known as a “lock-in” amplifier. In practice, the AC frequency is applied with a small set of modulation coils attached to the resonator. The coils modulate the static magnetic field by as much as several mT, typically at a frequency of 100 kHz, while  $B_0$  is swept slowly over a fixed range (Fig. 6.7). The height of the modulated signal is proportional to the slope of the absorption line and it oscillates in phase and  $180^\circ$  out-of-phase with field modulation when the slope is positive and negative, respectively. Thus, the phase-sensitive detection produces a lineshape that is the first derivative of the absorption line. The absorption spectrum can be reconstructed by integrating the spectrum obtained using field modulation, but because EPR signals are usually broad, the derivative signal is normally retained, as it reveals subtle features that would be less pronounced in the integrated signal. Figure 6.8 shows the relationship between an absorptive signal (Fig. 6.8a) and its derivative (Fig. 6.8b), and in the case of a more complex signal (Fig. 6.8c, d) how the derivative brings out features that would be difficult to detect in the absorption spectrum.

### 6.3.6 *Pulsed EPR*

In magnetic resonance experiments, the use of pulses provides an attractive alternative to sweeping the field or frequency. When a short pulse is applied to the sample, the spin system is brought out of equilibrium. Then, as the spin system relaxes back to thermal equilibrium, it reemits some of the radiation as a free-induction decay (FID). The Fourier transform of the FID corresponds to the absorption spectrum. One of the many advantages of carrying out the experiment in this way is that by collecting all of the frequencies simultaneously, the measurement time is shorter and hence less noise is collected, which is the so-called multiplex advantage. In addition, multiple pulses can be used to manipulate the spin system to obtain information about specific interactions. These methods are standard



**Fig. 6.7** Field modulation of an EPR absorption line**Fig. 6.8** Comparison between absorption lineshapes and their first derivatives as detected using field modulation. (a) A single absorption line. (b) Its first derivative. (c) A broadened 1:2:2:1 quartet. (d) Its first derivative

practice in NMR spectroscopy but significant obstacles are encountered when they are applied to EPR.

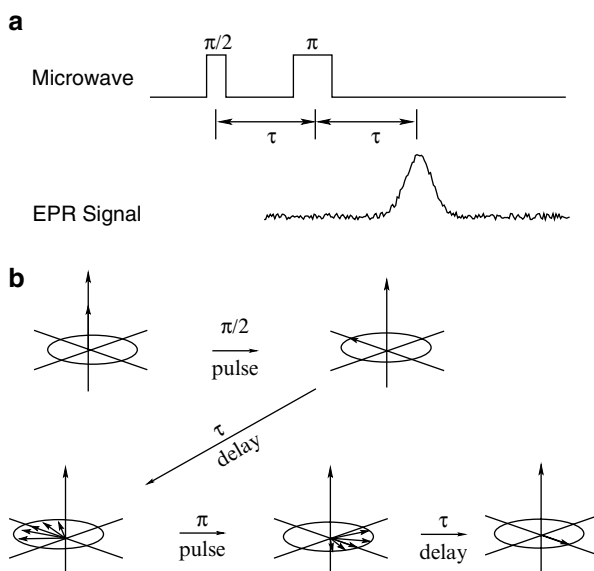
The first problem is that of the excitation bandwidth. The range of frequencies contained within a pulse is inversely proportional to the pulse length. Thus, the broader the required frequency range, the shorter the pulses must be. The shortest microwave pulses that can be easily produced are on the order of a few nanoseconds. This is sufficient to excite a spectral width of several hundred MHz or  $\sim 10$  mT. However, many EPR spectra are much broader than this. The second problem is that as the pulse length is shortened and the excitation bandwidth increases, the amount of power at any given frequency decreases. As a result, high power pulses must be used to achieve sufficient intensity across the excitation bandwidth. Finally, the spectrometer deadtime is also problematic. Following a short high intensity microwave pulse, the microwave cavity must “ring down” before the signal can be measured. The ring-down time can be longer than the decay time of the FID depending on the sample and type of resonator used. Because of these constraints, single pulse Fourier transform methods are only useful for systems with very sharp lines and a relatively narrow overall spectral width. The EPR spectra of most biological samples do not fall into this category. However, it is possible to study systems with broad spectra by pulsed EPR if spin-echo methods are used.

By applying two pulses separated by a time,  $\tau$ , the magnetization of the sample can be refocused to generate a spin-echo at a time  $\tau$  after the second pulse as shown in Fig. 6.9a. The lengths of the two pulses are chosen so that the magnetization is rotated through  $90^\circ$  and  $180^\circ$ , respectively. As can be seen in the vector diagrams in Fig. 6.9b, the first pulse rotates the magnetization into the  $x'y'$  plane. Different spin packets in the sample have different precession frequencies and so their contributions to the magnetization fan out. The second pulse inverts the magnetization so that the precession refocuses the magnetization at time  $2\tau$ . There are many other pulse sequences that also produce echoes but they will not be described here and readers are referred to [5] for details.

Several basic types of pulsed EPR experiments can be performed using spin-echo detection. The first is the so-called field swept echo spectrum. Usually, the width of the EPR spectrum is much larger than the excitation bandwidth so that the height of the echo varies depending on the value of the magnetic field at which it is measured. If the height of the echo is plotted as a function of the magnetic field, the EPR absorption spectrum is obtained. This method is particularly useful when two species with different linewidths are present in the sample. If field modulation is used in such cases, the relative amplitudes of the two components depend on the modulation amplitude. Hence, it is difficult to determine their relative intensities in a single experiment. This problem does not occur in the field swept echo spectrum provided that the same fraction of the magnetization can be refocused for both species pulse sequence for the four-pulse DEER experiment.

In the second class of experiments, the height of the echo is measured as a function of one or more of the delay times or pulse lengths in the pulse sequence. It is these types of experiments for which pulsed EPR is particularly useful because specific interactions in the spin system can be measured independently. A complete

**Fig. 6.9** Basic pulse sequence for detection of a spin-echo



list of the various pulse experiments goes beyond the scope of this chapter and we summarize only the few most common sequences here.

**Relaxation:** The spin–lattice relaxation time can be measured by the inversion recovery sequence  $(\pi) - t_d - (\pi/2) - \tau - (\pi) - \tau - \text{echo}$ . The first pulse inverts the magnetization then the second and third pulses generate an echo that probes the magnetization as it relaxes. The relaxation times are determined by measuring the height of the echo as a function of the delay time  $t_d$ . The relaxation time  $T_2$  can be obtained by applying the Hahn echo sequence followed by a train of  $180^\circ$  pulses  $(\pi/2)_x - \{\tau - (\pi)_y - \tau - \text{echo} - \}_n$ . This is the Carr–Purcell–Meiboom–Gill sequence [11, 12] and the height of the echo decays with  $T_2$  as a function of the time of the echo after the first pulse.

**Hyperfine coupling:** In a magnetic field the nuclei in a paramagnetic compound experience both the external magnetic field and a local field caused by the magnetic moment of the unpaired electron(s). In a pulsed EPR experiment the microwave pulses reorient the local field suddenly, which leads to coherent oscillation of the nuclear spin. As a result, the height of the echo in the Hahn sequence  $(\pi/2) - \tau - (\pi)$  is modulated as a function of the delay time,  $\tau$ . Taking the Fourier transform of the modulation gives an electron spin-echo envelope modulation (ESEEM) [13] spectrum from which hyperfine couplings and the types of coupled nuclei can be obtained. Hyperfine sublevel correlation spectroscopy (HYSCORE) [14] is a two-dimensional variation of this method. The pulse sequence  $(\pi/2) - \tau - (\pi/2) - t_1 - (\pi) - t_2 - (\pi/2) - \tau - \text{echo}$  is applied and the echo height is measured as a function of  $t_1$  and  $t_2$ . Double Fourier transformation of the data gives a two-dimensional dataset, which can be plotted as a contour plot. Such contour plots are widely used to determine the hyperfine couplings of cofactors in proteins and probe the protein–cofactor interactions.

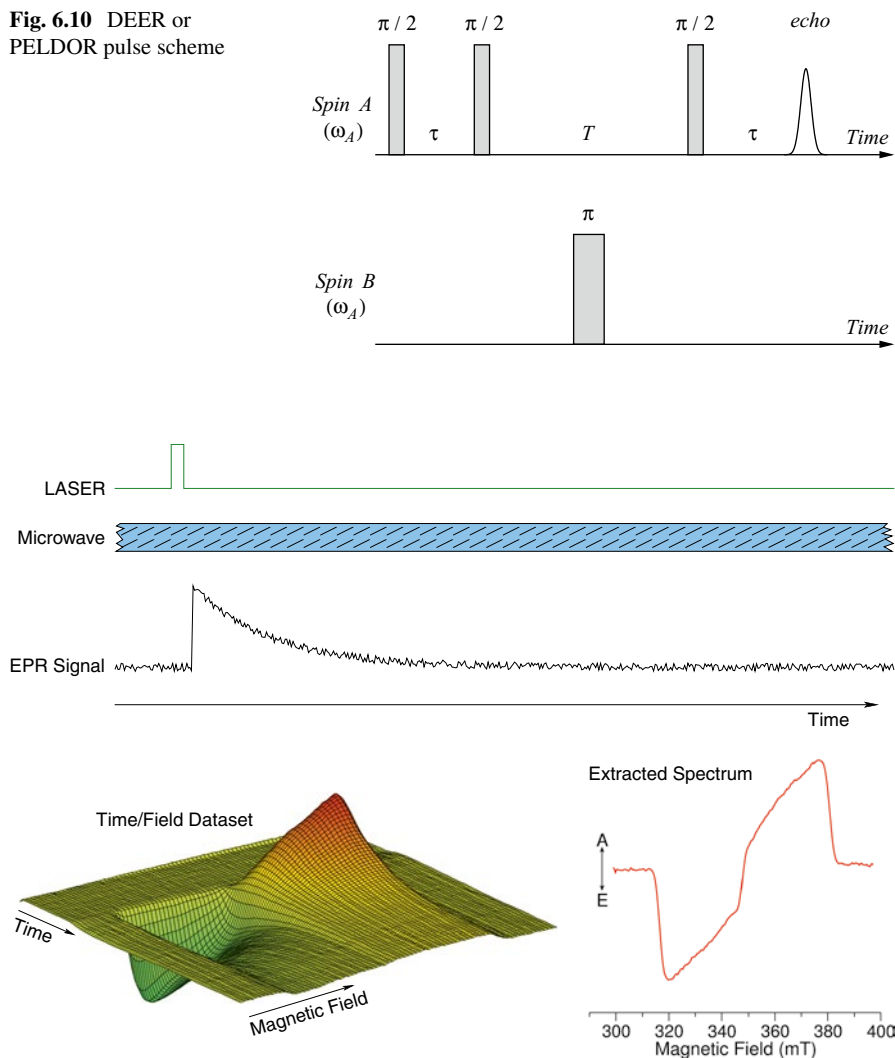
ESEEM and HYSCORE spectroscopy are relatively recent developments and electron-nuclear double resonance (ENDOR) is the more established method [6, 15, 16] for measuring hyperfine couplings. In an ENDOR experiment, radio frequency (RF) irradiation is used to manipulate the nuclear spins while microwaves are applied to observe the electron spins. Changes in the EPR signal of the electron spins are monitored as the frequency of the applied RF is varied. The original ENDOR experiments [17] were carried out using continuous wave methods; however, pulse methods [18–20] are more common today. There are several different pulse sequences that can be used but in all of them a preparation pulse is applied first to the electron spins. A frequency selective RF pulse is then applied to the nuclear spins and finally an echo sequence is applied to the electron spins. The height of the echo is measured as a function of the frequency of the RF pulse to generate the ENDOR spectrum.

*Electronic spin–spin coupling:* In systems containing more than one paramagnetic center, the electron magnetic moments couple to one another through the exchange interaction and the dipolar interaction. The exchange coupling shifts the energies of the possible spin configurations relative to one another as a result of the Pauli principle. The strength of the exchange coupling drops off exponentially as the distance between the centers increases. The dipolar coupling is the interaction of each of the spins with the magnetic field produced by the other spin. Importantly, the dipolar coupling depends on the inverse cube of the distance between the paramagnetic centers. For distances greater than  $\sim 1$  nm, the dipolar coupling dominates and measuring the spin–spin coupling in such systems can be very useful for structure determination. There are two common methods for determining the spin–spin coupling. In double electron electron resonance (DEER) [21] or pulsed electron double resonance (PELDOR) [22] two different microwave frequencies are used. There are several pulse schemes that can be used for the experiment but all of them have an echo sequence consisting of a preparation sequence, a mixing period and a detection pulse that is applied to one radical and an inversion pulse at a different frequency that is applied to the other radical during the mixing period. The four-pulse DEER sequence shown in Fig. 6.10 is used most widely for distance determination

In photosynthetic reactions centers and the cryptochrome/photolyase family of proteins, light excitation leads to sudden generation a radical pair from the excited singlet state of a chlorophyll or flavin. When the Hahn echo sequence is applied to radical pairs generated in this way, the echo is formed  $90^\circ$  out-of-phase, i.e., parallel to the direction of the microwave radiation rather than perpendicular to it [23]. This out-of-phase echo shows deep modulation as a function of the pulse separation in the echo sequence, from which the spin–spin coupling can be obtained [24].

### 6.3.7 Transient EPR

Most photoreactions generate short-lived paramagnetic species and time-resolved EPR methods can be extremely useful for studying such processes because they provide kinetic rates as well as detailed information about the geometry and local

**Fig. 6.10** DEER or PELDOR pulse scheme**Fig. 6.11** The transient EPR experiment

environment. These methods fall into two general classes: pulsed methods and transient EPR. In transient EPR continuous microwave irradiation is used and the EPR response to pulsed light excitation of the sample is monitored at a fixed magnetic field as illustrated in Fig. 6.11.

At a given magnetic field a transient response is obtained and the transients collected over a range of magnetic field strengths can be assembled to create a

time/field dataset. Transient EPR spectra can be extracted from the dataset by plotting the average signal in a given time window against magnetic field. An important parameter in such experiments is the response time. If the signal is measured using lock-in detection, the frequency of the field modulation and the bandwidth of the lock-in amplifier limit the rise time to  $\sim 100 \mu\text{s}$ . Some improvement, in the rise time can be obtained by using higher frequency for the field modulation but impedance problems make it difficult to use frequencies much above 1 MHz. Thus, transient EPR data are generally collected without using field modulation in what is referred to as “direct detection.” Without the field modulation the response time is determined by the bandwidth of the resonator and the preamplifier and is typically  $\sim 50 \text{ ns}$ . An important feature of transient EPR spectra is that they are spin-polarized. Because of selection rules involved in the photoreaction the spin states of the paramagnetic species generated by the laser flash are usually selectively populated. As a result, both absorptive and emissive signals are observed. The analysis of the polarization pattern can be useful for determining the pathway by which the paramagnetic species has been generated.

## 6.4 Characteristic Lineshapes

EPR spectra and indeed all types of magnetic resonance spectra show characteristic lineshapes depending on the conditions under which they have been measured. The nature of the spectrum depends on which terms contribute to the Hamiltonian, which is governed largely by motion of the molecules and how they interact with their surroundings.

### 6.4.1 *Rapid Tumbling Regime*

In dilute solution at room temperature, the solute molecules can be treated as being isolated from one another and in low viscosity solvents the correlation time for rotation of small organic molecules is on the order of  $10^{-10} \text{ s}$ , which is fast enough to cause the interactions in the Hamiltonian to be averaged. The zero-field splitting interaction averages to zero and in most cases the Hamiltonian contains terms for the average Zeeman energy of the electrons and nuclei and average hyperfine coupling between the electrons and nuclei. To a good approximation, the nuclear Zeeman energy does not change for EPR transitions, and hence need not be considered further. Thus, the Hamiltonian can be written as:

$$\hat{H} = g_{iso}\beta_e B_0 \hat{S}_z + \sum_i A_i \hat{S}_z \hat{I}_z, \quad (6.8)$$

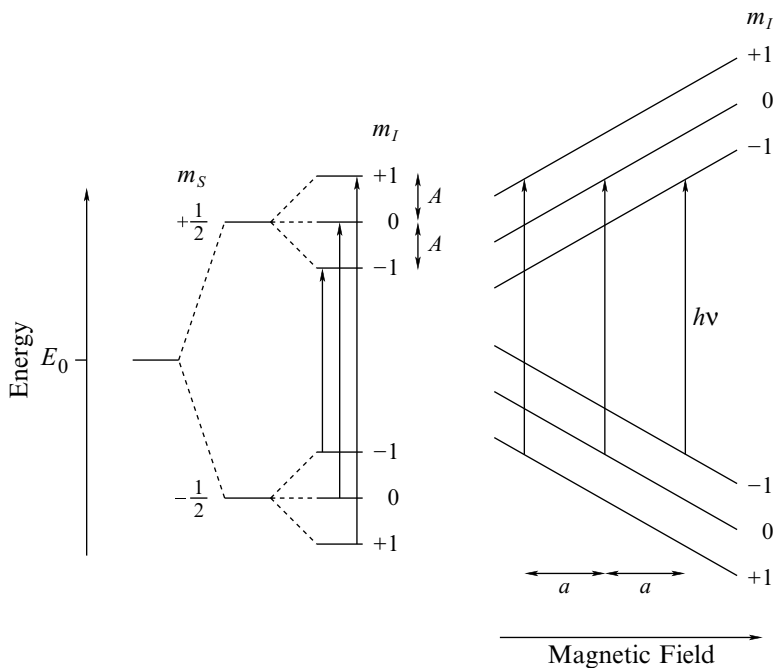


**Fig. 6.12** Energy level diagram for a system consisting of a single unpaired electron and an  $I=1$  nucleus. *Left*: Splitting due to the electron Zeeman interaction and the hyperfine interaction. *Right*: Field swept EPR experiment

where the sum is over all magnetic nuclei and it has been assumed that the magnetic field is high enough to make the Zeeman term much larger than the hyperfine term. The corresponding energies are:

$$E = g_{iso}\beta_e B_0 m_S + \sum_i A_i m_{Si} m_{Ii}, \quad (6.9)$$

where  $m_S$  and  $m_I$  are the quantum numbers for the  $z$ -components of electron and nuclear magnetic moments, respectively. Figure 6.12 shows the energy level diagram for a single unpaired electron coupled to a single  $I=1$  nucleus like nitrogen as found in nitroxide radicals. As can be seen, the hyperfine coupling splits each of the two energy levels of the unpaired electron into three equally spaced levels separated by the hyperfine coupling constant,  $A$ . The selection rules for the transitions are  $\Delta m_S = 1$ ,  $\Delta m_I = 0$ , since the microwaves flip the electron spin but not the nuclear spins. Thus the energies of the EPR lines are:

$$E = h\nu = g_{iso}\beta_e B_0 + \sum_i A_i m_{Ii}. \quad (6.10)$$

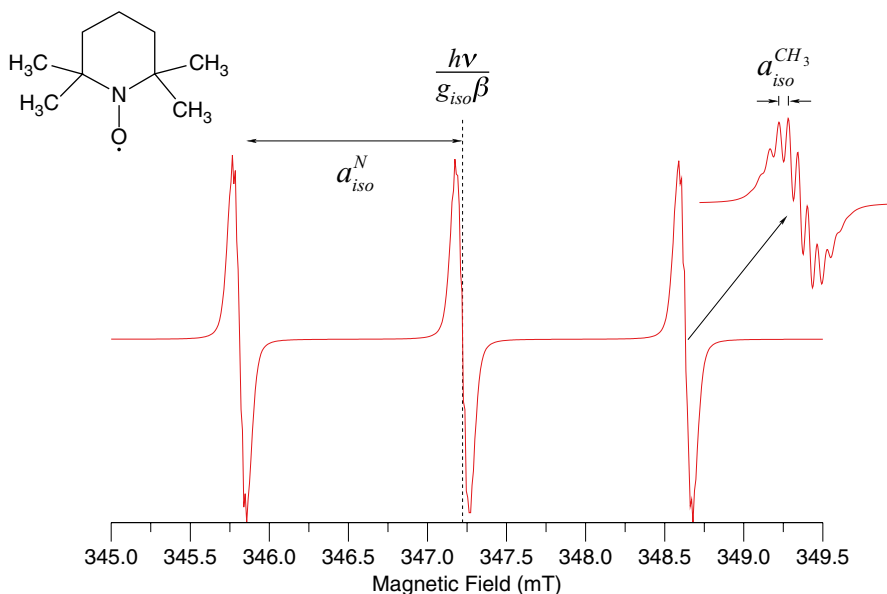


**Fig. 6.13** Calculated solution spectrum of a nitroxide radical showing the isotropic  $g$ -factor and hyperfine couplings. The couplings to the low abundance nuclei  $^{15}\text{N}$  and  $^{13}\text{C}$  have not been included

This results in spectra with sharp lines centered around  $B_0 = h\nu / g_{\text{iso}}\beta_e$ . Note that the hyperfine term does not include the laboratory magnetic field (which has no effect on the magnetic coupling of the fixed nuclear spin with the fixed electron spin). Because  $m_I = I, I-1, \dots, -I+1, -I$ , where  $I$  is the nuclear spin, each nucleus splits the signal into  $2I+1$  components. A group of  $n$  equivalent nuclei splits the signal into  $2nI+1$  components. The total number of lines is  $n_{\text{total}} = \prod_i (2n_i I_i + 1)$ . In a field swept experiment (Fig. 6.12, right), the separation between lines that differ by one in  $m_I$  is the hyperfine splitting constant and is equal to  $a = A / g_{\text{iso}}\beta_e$  with  $A$  in energy units. Usually, the hyperfine coupling constant (hfc),  $A$ , and the hyperfine splitting constant,  $a$  are specified in MHz and mT, respectively. In these units,  $a = hA / g_{\text{iso}}\beta_e$  with  $h/\beta_e = 0.07144773 \text{ mT MHz}^{-1}$ . An example of the solution spectrum of a nitroxide radical is shown in Fig. 6.13. As can be seen, the  $I=1$  nitrogen nucleus splits the EPR signal into three equal intensity lines. Each line is split further into a 13-line pattern by the 12 equivalent methyl protons ( $I=1/2$ ). For groups of equivalent nuclei, the intensities of the lines are the coefficients of a binomial expansion that can be determined using Pascal's triangle for  $I=1/2$ . The strength of the hyperfine coupling depends on the spin density at the nucleus. Hence, the nitrogen splitting is much larger than the splitting from the protons. The splitting from the remaining protons on the ring is too small to be observed.



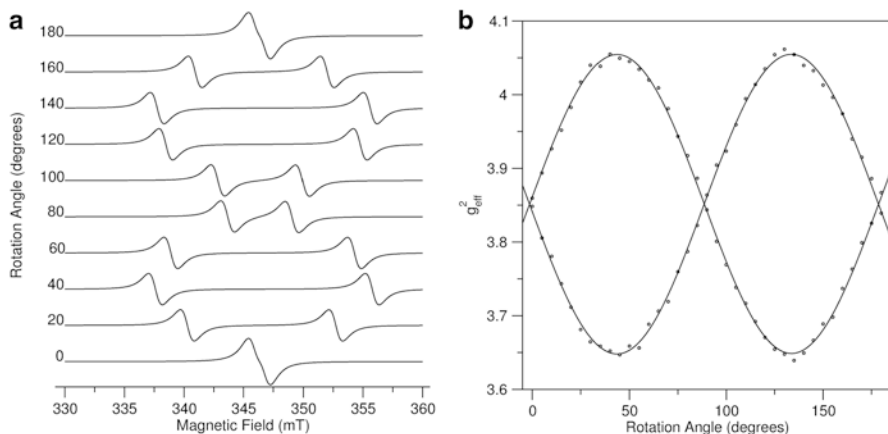


**Fig. 6.14** Demonstration of the EPR spectra and rotation patterns from a single crystal. **(a)** Calculated EPR spectra for the rotation of the crystal about one of the crystal axes. **(b)** Rotation pattern of the line positions. The crystal is assumed to have two paramagnetic centers per unit cell

### 6.4.2 Rigid Limit Regime

In frozen solution, the motion becomes too slow to cause averaging of the Hamiltonian and the system is said to be in the rigid limit. Indeed many biomolecules are sufficiently large that their motion is in the rigid limit even at room temperature in liquid solution. The slow rate of tumbling has a profound impact on the EPR spectrum. This is because essentially all of the interactions that contribute to EPR spectra depend on the orientation of the molecule with respect to the magnetic field. If, for example, a protein contains a paramagnetic center and a single crystal of the protein can be grown, the EPR spectrum changes as the orientation of the crystal is changed in the magnetic field. The series of spectra taken as the crystal is rotated about a particular axis is illustrated in Fig. 6.14a.

The positions of the lines in the spectra give effective  $g$ -values and the plot of  $g_{\text{eff}}^2(\theta)$  against  $\theta$  is known as a rotation pattern (Fig. 6.14b) and can be described by the function:

$$g_{\text{eff}}^2(\theta) = a_1 + a_2 \cos(2\theta) + a_3 \sin(2\theta). \quad (6.11)$$

A fit of the rotation patterns gives values for  $a_1$ ,  $a_2$ , and  $a_3$ . Typically, there are several molecules in symmetry-related positions in the unit cell and the values of  $a_1$ ,  $a_2$ , and  $a_3$  obtained from them are not independent. Rotation of the crystal about three mutually perpendicular axes gives six independent values, which can be written as the elements of a symmetric  $3 \times 3$  matrix. This matrix is known as the  $g$ -tensor and it depends on the choice of the three rotation axes. However, there exists a unique set of axes known as the principal axes in which the  $g$ -tensor is diagonal.

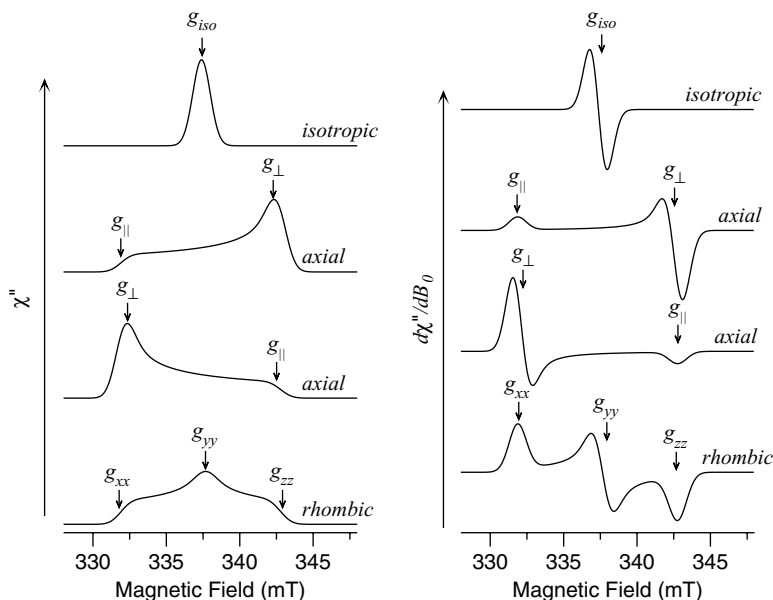


**Fig. 6.15** Examples of powder patterns arising from  $g$ -anisotropy. *Left*: Powder patterns as detected in absorption (e.g., by field-swept echo detection). *Right*: Corresponding first derivative spectra

In this frame of reference, the diagonal elements are known as the principal values. The  $g$ -tensor obtained from the rotation patterns can be diagonalized numerically to give the principal values,  $g_{xx}$ ,  $g_{yy}$ , and  $g_{zz}$  and the angles between the principal axes  $x$ ,  $y$ , and  $z$  and the chosen rotation axes. If the orientation of the molecules in the unit cell is known, then the rotation patterns allow the orientation of the principal axes of the  $g$ -tensor in the molecule to be determined.

For biological samples, it is relatively rare to have single crystals available and experiments are usually carried out on unordered samples, e.g., frozen solution. In this case, the EPR spectrum is the sum of the spectra arising from the randomly oriented molecules in the sample. This random distribution gives the characteristic *powder patterns* shown in Fig. 6.15. The absorption spectra that would be obtained in a field-swept echo experiment are shown on the left of Fig. 6.15, and those obtained using field modulation are shown on the right. From these spectra, the principal  $g$ -values are easily determined but no information about the orientation of the principal axes is obtained. Three possibilities for  $g$ -value anisotropy are illustrated in Fig. 6.15. When the paramagnetic center has cubic symmetry, the three principal  $g$ -values are equivalent, i.e.,  $g_{xx} = g_{yy} = g_{zz}$  and the spectrum is a single symmetrical line (Fig. 6.15, top) and is said to be “isotropic.” In systems with orthorhombic symmetry, all three principal  $g$ -values are inequivalent, i.e.,  $g_{xx} \neq g_{yy} \neq g_{zz}$  and the spectrum is referred to as “rhombic” (Fig. 6.15, bottom). When depicted as

an absorption signal, the spectrum has a low field turning point, a midfield peak, and a high field turning point. In derivative mode, the signal appears as a low field peak, a midfield derivative, and a high field trough. These three features arise from molecules with their  $x$ -,  $y$ -, and  $z$ -axes parallel to the field, respectively, and the intensity observed between the three features is from molecules at other orientations. Notice that because  $B_0$  is inversely proportional to the  $g$ -value, the high field end of the spectrum (largest value of  $B_0$ ) corresponds to the smallest of the three principal  $g$ -values and the low field end of the spectrum to the largest principal  $g$ -value. In practice, the principal  $g$ -values are obtained as the maximum and the inflection points of the rising and falling edges of the absorption spectrum. Using field modulation, these correspond to the midpoint of the derivative-shaped signal and the centers of mass of the positive and negative peaks, respectively.

Paramagnetic centers with threefold or higher rotational symmetry about a unique symmetry axis are said to have axial symmetry. In such cases, two of the principal  $g$ -values are equal such that  $g_{xx} = g_{yy} \neq g_{zz}$ . Here, there are two possible labeling conventions for the axes. The symmetry axes are labeled such that the axis with the highest rotational symmetry is the  $z$ -axis. In EPR, the axis associated with the smallest  $g$ -value is usually labeled  $z$ . To avoid confusion when there is a conflict between these two schemes, the  $g$ -factor associated with the principal axis that is parallel to symmetry  $z$ -axis is often labeled  $g_{\parallel}$  and the  $g$ -value associated with the other two axes is labeled  $g_{\perp}$ . Since the  $z$ -axis has a higher probability of being oriented perpendicular to the field than parallel to it, the signal corresponding to  $g_{\perp}$  is more intense than that corresponding to  $g_{\parallel}$ . Taking the case where  $g_{\parallel} > g_{\perp}$ , this means that the low field end of the spectrum is weak and the high field end is strong as shown in (Fig. 6.15, second spectrum from top). When  $g_{\parallel} < g_{\perp}$  the situation is reversed (Fig. 6.15, third spectrum from top).

The hyperfine interaction is also anisotropic and is characterized by three principal values  $A_{xx}$ ,  $A_{yy}$ , and  $A_{zz}$ . The powder patterns shown in Fig. 6.15 occur when the spectrum is dominated by the Zeeman interaction and the hyperfine interactions (or any other interactions) are sufficiently weak that they contribute only to the line-width at a given orientation. In practice, however, resolved hyperfine splitting is sometimes observed. In such cases, the principal  $g$ -values and hyperfine coupling constants are obtained by simulation of the spectrum.

For systems with  $S > 1/2$ , spin-orbit coupling and the dipolar coupling between the electrons lead to zero-field splitting. The term zero-field splitting refers to the fact that the splitting of the energy levels caused by these interactions does not depend on the magnetic field and can be observed by optical methods at zero field. In systems with weak spin-orbit coupling, the zero-field splitting is generally much larger than the anisotropy in the  $g$ -tensor but much smaller than the Zeeman energy and the EPR spectrum is dominated by this splitting. An example for a molecular triplet state ( $S = 1$ ) is shown in Fig. 6.16. In this case the triplet state gives a pair of lines for each orientation and the resulting powder pattern is referred to as a Pake doublet. From the positions of the features in the Pake doublet, the zero-field splitting parameters  $D$  and  $E$  can be obtained.

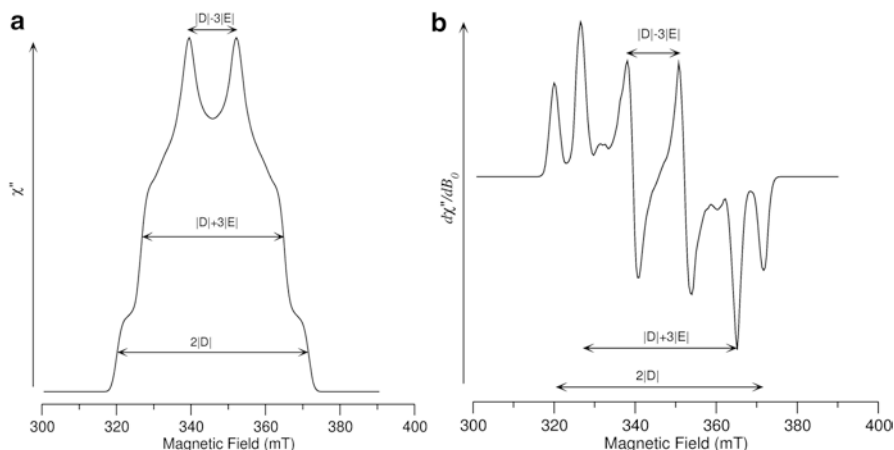


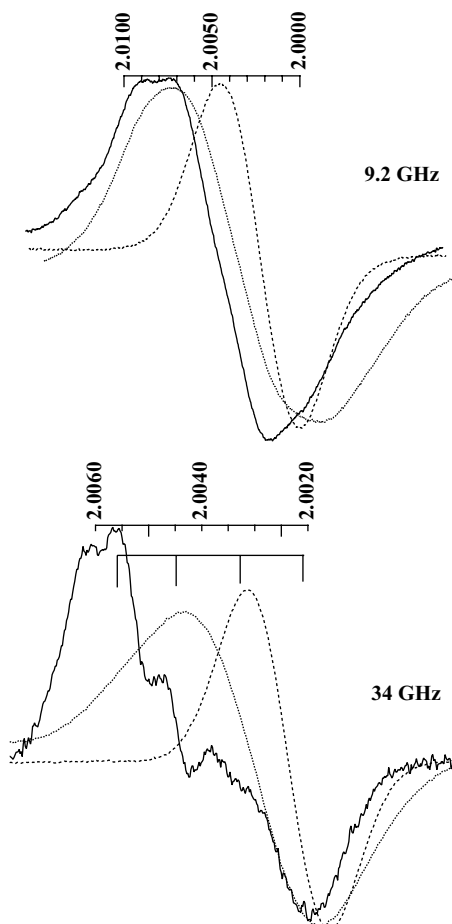
**Fig. 6.16** Pake doublet powder pattern arising from the zero-field splitting of a triplet state. (a) Absorption spectrum. (b) Corresponding first derivative spectrum

## 6.5 Applications in Biophysics

### 6.5.1 Spin-Orbit Coupling and $g$ -Value Anisotropy

In the paramagnetic centers found in biological systems, the electrons occupy atomic and molecular orbitals, and as a result, the total angular momentum consists of the inherent spin angular momentum plus the orbital angular momentum. The latter is normally zero for molecules in the ground state (it is said to be “quenched”), but mixing of the ground and excited states through spin-orbit coupling allows the ground state to acquire some orbital angular momentum. The amount of spin-orbit coupling depends on the size of the atom; it is small for oxygen, nitrogen, and carbon, and is large for metals. As a result of spin-orbit coupling,  $g = g_e + \Delta g$ , where  $g_e$  is the free-electron  $g$ -factor (2.0023193) and the latter is a correction that depends on the degree of spin-orbit coupling. Hence, the energy to induce a transition between the Zeeman components is altered. In organic-free radicals,  $\Delta g$  is small, and the spectra are similar to that of a free electron, whereas in metals,  $\Delta g$  can be large and  $g$  can deviate significantly from  $g_e$ . Because orbitals in molecules do not have spherical symmetry, the magnitude of the spin-orbit coupling is direction-dependent, i.e., the admixture is anisotropic. Hence, the contribution to the magnetic moment from orbital motion depends on the orientation in an external field. It is this orientation dependence of the magnetic moment that leads to the  $g$ -anisotropy and the rotation patterns and powder spectra shown in Fig. 6.14a, b.

**Fig. 6.17** EPR spectra of three organic cofactor radicals in Photosystem I. *Dashed line:*  $A_0^-$ , radical anion of the primary electron acceptor; *dotted line:*  $P_{700}^+$  radical cation of the chlorophyll special pair donor, *solid line:*  $A_1^-$  phylloquinone radical anion. The four prominent hyperfine couplings from the ring methyl group are indicated in the 34 GHz spectrum. The relevant  $g$ -value scale is depicted above each spectrum



### 6.5.1.1 Organic Cofactor Radicals

Spin-orbit coupling in organic radicals (centered on C, O, S, and N) is typically weak, hence the  $g$ -factor anisotropy is small and the resolution at X-band is often insufficient to obtain the components of the  $g$ -tensor. For some oxygen-containing species such as tyrosine radical anions or semiquinones, partial resolution of the  $g$ -tensor components can be achieved at Q-band. However, in general high field EPR (W-band or higher) is required to resolve the  $g$ -anisotropy in organic radicals. Figure 6.17 depicts three organic radicals:  $P_{700}^+$  (a chlorophyll cation radical),  $A_0^-$  (a chlorophyll anion radical), and  $A_1^-$  (a phylloquinone anion radical). At X-band, the spectrum of  $A_0^-$  appears as a single derivative lineshape with a  $g$ -value of 2.003 and a linewidth of 0.12 mT.  $P_{700}^+$  is a special pair of chlorophyll molecules, and because the spin is distributed over not one but two macrocycles, the linewidth is correspondingly narrower (ideally by a factor of  $\sqrt{2}$  for an equal distribution of the

spin). It is characterized by a derivative-shaped signal with a  $g$ -value of 2.002 at the crossover point and a linewidth of 0.09 mT. The  $g$ -tensor anisotropy in  $A_1^-$  is larger than that of  $A_0^-$  due to the presence of electron density at the electronegative oxygen atom. In quinone radicals the  $g$ -anisotropy is primarily a result of mixing of the lone-pair orbitals of the oxygen with  $\pi^*$  orbitals by spin-orbit coupling. The larger  $g$ -anisotropy leads to an X-band spectrum for phylloquinone that is characterized by a distorted derivative signal with a  $g$ -value of 2.0050 at the crossover point and a linewidth of 0.14 mT (Fig. 6.17, top). At Q-band, the resolution is enhanced by a factor of 3.8 and although this is insufficient to resolve the  $g$ -tensor components of the chlorophyll anion and  $P_{700}^+$  radicals, it does allow a more precise measurement of their average  $g$ -factors and reveals a slight difference of 2.0035 for  $A_0^-$  and 2.0028 for  $P_{700}^+$ . Both signals still appear isotropic due to the large number of overlapping, unresolved hyperfine couplings from the ring protons (see below). The  $A_1^-$  phylloquinone radical, however, shows a more complicated lineshape that incorporates a contribution from a partially resolved set of four hyperfine components from the three equivalent protons of the ring  $-CH_3$  group (Fig. 6.17, bottom). The hyperfine splitting can be eliminated by substituting the hydrogen atoms with deuterium, which has a spin 1 nucleus and a relatively small magnetic moment because of its higher mass. In deuterated samples, a near-rhombic spectrum with  $g_{xx}=2.0062$ ,  $g_{yy}=2.0050$ , and  $g_{zz}=2.0021$  is obtained for the  $A_1^-$  radical (Fig. 6.18). These examples additionally show that spin-orbit coupling leads to a downfield shift of  $g_{xx}$  and  $g_{yy}$ , but not  $g_{zz}$ , as the magnetic field strength increases.

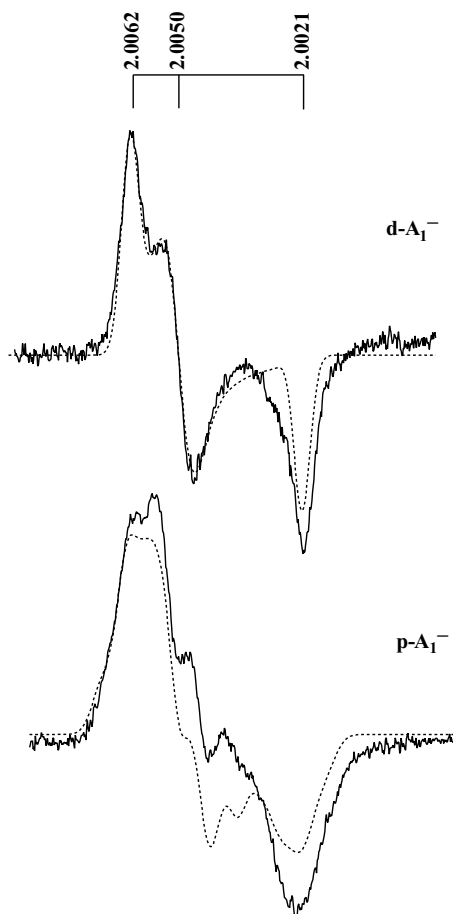
### 6.5.1.2 Metal Centers in Iron Proteins

Compared to organic radicals, the spin-orbit coupling in transition metal centers is large due to the presence of partially filled  $d$ -orbitals; hence, the  $g$ -factor anisotropy is typically spread over a large spectral range. A microwave frequency of 9 GHz (X-band) is usually sufficient to extract the principal values of the  $g$ -tensor. The EPR spectrum of the reduced [4Fe-4S]  $F_A$  cluster in Photosystem I (PS I), for example, shows a well-resolved  $g$ -tensor with principal  $g$ -values of 2.07, 1.93, and 1.89 (Fig. 6.19).

### 6.5.2 Hyperfine Coupling and Spin-Density Distributions

Hyperfine couplings are particularly useful for studying the interaction of organic cofactors with the surrounding protein. From such couplings it is possible to detect the presence of hydrogen bonds or deduce whether the unpaired electron is localized on the cofactor or delocalized onto the binding site or over several cofactors. Such conclusions can be very important for understanding the function of enzymes, particularly those that perform electron transfer reactions. The hyperfine coupling is composed of two parts, an isotropic Fermi contact term and an anisotropic

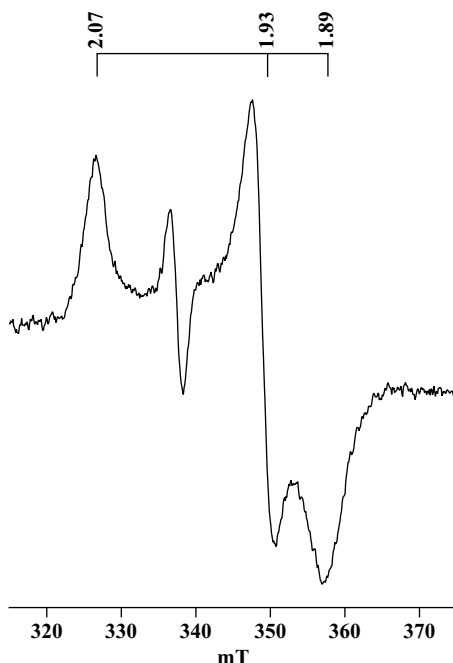
**Fig. 6.18** Q-band EPR spectrum of per-deuterated phyloquinone radical anion (*top*) compared with natural abundance phyloquinone radical anion (*bottom*). Simulated spectra are shown in the *dotted lines*. The principal *g*-values are depicted



dipole–dipole interaction term. In isotropic solution the latter term averages to zero and only the contribution from the orientation-independent Fermi contact term is observed. However, for most biological samples experiments are carried out in the rigid limit regime and both terms contribute. The magnitude of the Fermi contact term ultimately depends on the unpaired electron density from the  $1s$  orbital at the nucleus. The influence of valence electrons occurs through a mechanism known as core polarization.

The primary donors and quinone acceptors in photosynthetic reaction centers are two good examples of how hyperfine couplings can be used to deduce details of the local environment of organic cofactors. In reaction centers of purple bacteria, the chlorophylls are arranged in a cofacial dimer and the hyperfine couplings have been determined in single crystals. The couplings cannot be resolved in the EPR spectrum and ENDOR is needed to obtain them. ENDOR spectra from single crystal measurements give rotation patterns similar to those shown in Fig. 6.14b from

**Fig. 6.19** Low temperature X-band spectrum of the  $[4\text{Fe-4S}]^2\text{-F}_A$  cluster in Photosystem I. The resonance at 335 mT is due to  $P_{700}^+$ . The principal  $g$ -values are depicted

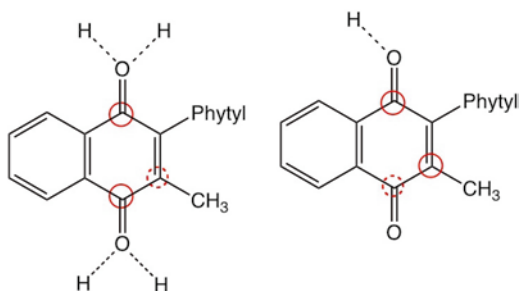


which the principal values and principal axis orientations of the hyperfine coupling tensors can be obtained. The rotation patterns of the primary donor cation in *Rhodobacter sphaeroides* R-26 have been measured [25] and the couplings and axis orientations allow the ENDOR signals to be assigned to individual nuclei in each of the two chlorophyll molecules. From the magnitudes of the couplings, a spin density map of the system is obtained that shows higher spin density on one half of the dimer. The asymmetry of the spin density indicates that although the dimer shows a high degree of symmetry in the positions of the atoms, electronically the two chlorophylls are inequivalent.

As shown in Fig. 6.17, partially resolved hyperfine splitting is observed in the Q-band spectrum of the reduced phylloquinone acceptor in PS I. The coupling is a direct result of the hydrogen bonding of the quinone to its binding site. Several studies have shown that the splitting is due to the protons of the 2-methyl group [26, 27] and that in the phylloquinone binding site in PS I, the splitting is about 20 % larger than in isopropanol solution [28]. This difference is a result of the fact that in protic solvents both oxygen atoms of phylloquinone are hydrogen-bonded. In contrast, in the phylloquinone binding site in PS I, only one of the two oxygens is H-bonded to the protein. In the presence of asymmetric H-bonding, the spin density on the quinone headgroup is distorted as shown in Fig. 6.20. If the oxygen at the 4-position of the ring is more strongly H-bonded than the oxygen in the 1-position, e.g., if there is only a single H-bond (Fig. 6.20, right) the distortion increases the spin density next to the methyl group in the 2-position. Thus, the strength of the methyl hyperfine coupling can be used to probe the nature of the hydrogen bonding.



**Fig. 6.20** Spin density distribution in phylloquinone with different H-bonding configurations. *Left:* Symmetric H-bonding, low spin density adjacent to the 2-methyl group. *Right:* Asymmetric H-bonding high spin density adjacent to the 2-methyl group



## 6.5.3 Electron–Electron Spin–Spin Interactions

### 6.5.3.1 Site-Directed Spin Labeling

The dipole–dipole coupling between magnetic moments is dependent on the distance between the magnetic moments and is widely used to obtain structural information. In NMR the Nuclear Overhauser Effect, which is the transfer of polarization between nuclei via the dipolar interaction, is routinely used to place constraints on the structure of the protein. With nuclear spins, distances up to about 0.5 nm can be estimated. If electrons are measured, the much larger magnetic moment means that it is possible to determine distances up to several nm. The main drawback, however, is the lack of naturally occurring unpaired electrons. A solution to this problem has been found by using the reactivity of the cysteine sulfhydryl group towards methane sulfonates to form sulfide bonds. If a stable nitroxide radical is substituted with a methane sulfonate side chain, it can be attached to cysteine-containing proteins so that they are spin labeled at specific sites. Using point mutagenesis techniques, it is possible to introduce cysteine residues at specific locations and thus the protein can be site-specifically spin-labeled. If a variant of the protein is constructed with only two cysteines, two spin labels can be introduced and the distance between them can then be determined by measuring the dipolar coupling between the unpaired electrons. The spin–spin coupling is not easily determined from the CW EPR spectra of spin-labeled proteins but can be obtained most accurately from the modulation curves in DEER or PELDOR measurements. If the distance between the two unpaired electrons is large compared to the dimensions of the distribution of the electrons, the point-dipole approximation can be used and the dipolar coupling is related to the distance by:

$$D = -\frac{2.786}{r^3} mT \text{ nm}^3. \quad (6.12)$$

Recent examples of the use of this technique include studies of the ATP hydrolysis cycle in ABC transporters [29] and of the self-association of the histidine kinase CheA [30].

### 6.5.3.2 Light-Induced Radical Pairs

Weakly coupled two-electron spin systems are also found in proteins that undergo light-induced electron transfer. The two main classes of such proteins are the photosynthetic reaction centers and the photolyase and cryptochrome flavin proteins. In both of these systems one or more chains of electron transfer cofactors extend away from a chromophore (a chlorophyll dimer or a flavin) that acts as either an electron donor or an electron acceptor in its excited state. When the chromophore absorbs light, electron transfer generates a series of radical-ion pairs. By passing electrons rapidly along the chain of cofactors, the charge separation is stabilized. The first of the radical pairs that can be detected by transient EPR is weakly coupled, that is, the spin–spin coupling is smaller than the difference in the resonance frequencies of the two radicals. In the excited state of the chromophore the two electrons are strongly correlated because they reside on the same molecule. The fact that the radical pairs are generated from this highly correlated state on a timescale that is short compared to the precession and relaxation of the spins means that they have an unusual population distribution and dynamic properties. Figure 6.21a shows the energy level diagram and the EPR transitions in a weakly coupled radical pair. Because the state of the chromophore from which the radical pair is generated is either a singlet state or a triplet state, it is useful to express the states of the radical pair in a singlet–triplet basis. As can be seen in Fig. 6.21a, only the two middle levels have singlet character. Thus, if the electron transfer is initiated from the excited singlet state of the chromophore, only the states 2 and 3 of the radical pair are populated because they are the only ones with any singlet character. This selective population of the radical pair spin states leads to both absorptive and emissive transitions in the direct detection mode spectra as shown in Fig. 6.21b. Such a spectrum is said to be *spin polarized* and the pattern of absorptive and emissive features is called a *polarization pattern*. The polarization patterns of weakly coupled radical pairs depend on the internal geometry of the pair. In particular they are sensitive to the orientation of the  $g$ -tensors of the two radicals relative to the distance vector between them [31]. This orientation dependence has been widely used to study the quinone acceptors in photosynthetic reaction centers of purple bacteria and PS I [32]. A comparison of the W-band spectra of the radical pair  $P^+Q^-$  in PS I and purple bacterial reaction centers is shown in Fig. 6.22. Here P stands for the respective primary donors  $P_{700}$  and  $P_{865}$  and Q for the quinone acceptors phyloquinone and ubiquinone, respectively. The differences on the low field end of the spectra are primarily due to the different orientations of the quinones.

The selective population of the spin states in light-induced radical pairs also has a strong influence on their spin echoes. As shown in the single orientation EPR spectrum (Fig. 6.21b, left), each radical contributes the so-called antiphase doublet split by the spin–spin coupling. Overall there is no net magnetization of the sample. Under these conditions when the Hahn echo sequence is applied, the spin-echo is phase shifted by  $90^\circ$  so that if the pulses are applied along the  $x$  direction the echo also appears in the  $x$ -direction rather than in the  $y$ -direction. As illustrated in Fig. 6.23, a dispersion signal is obtained in the in-phase channel ( $M_y$ ) while the echo

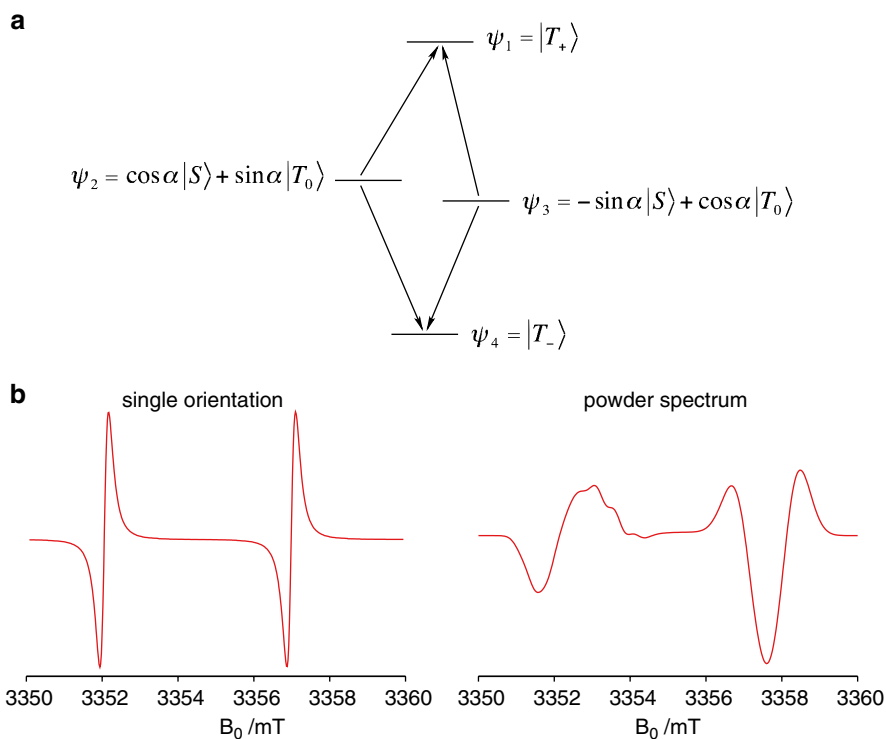
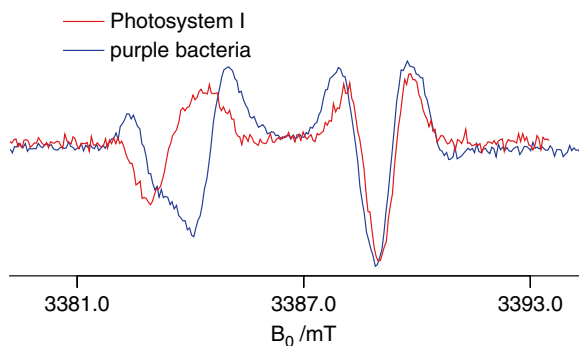


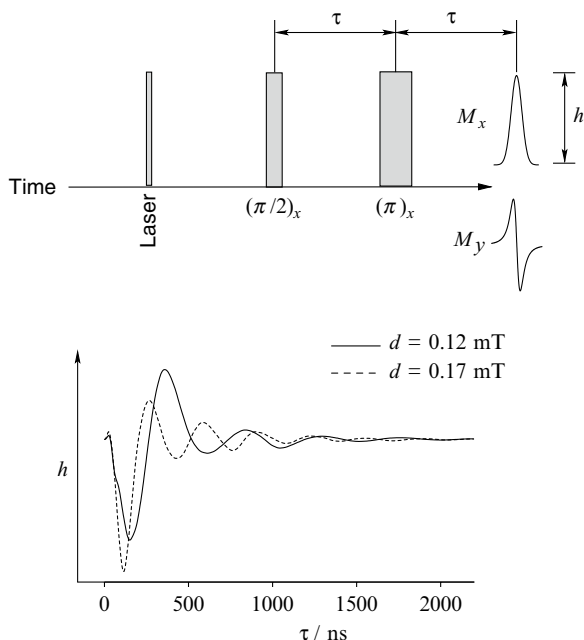
**Fig. 6.21** Energy level diagram and spectra of a weakly coupled radical pair formed from a singlet precursor. (a) Energy level diagram (b) W-band spectra

**Fig. 6.22** W-band spectra of the radical pair  $\text{P}^+\text{Q}^-$  in purple bacterial reaction centers and Photosystem I [33]



absorption signal is observed in the out-of-phase channel ( $M_x$ ). When the spacing between the two pulses in the echo sequence is varied, the echo amplitude shows deep modulations that depend strongly on the spin–spin coupling. This dependence is illustrated in the bottom part of Fig. 6.23, which shows the echo height plotted as

**Fig. 6.23** The out-of-phase echo modulation experiment for light-induced singlet-born radical pairs



a function of the pulse spacing for values of the dipolar coupling of 0.17 and 0.12 mT. As can be seen this small change in the coupling, which corresponds to a change of 0.3 nm in the distance, has a dramatic effect on the modulation curve. Thus, the out-of-phase echo modulation allows distances between the cofactors in light-induced radical pairs to be determined to an accuracy that is usually better than that which can be obtained by X-ray crystallography. A drawback, however, is that the distance obtained is between the centers of the spin density and the positions of these points relative to the positions of the atoms is not always unambiguous.

### 6.5.3.3 Molecular Triplet States

In many photoactive proteins triplet states of chromophores are formed that can also be detected by time-resolved EPR methods. In the excited states of molecules, the exchange coupling between the electrons is generally orders of magnitude larger than the Zeeman energy but the dipolar coupling is typically an order of magnitude or more smaller than the Zeeman energy depending on the magnetic field. This results in EPR spectra that are dominated by the zero-field splitting as discussed above with Fig. 6.16.

For the triplet state of a chromophore to be populated, a mechanism by which a spin-flip can occur must be present. There are two such mechanisms that commonly operate. The first of these is spin-orbit coupling, in which a change in the spin

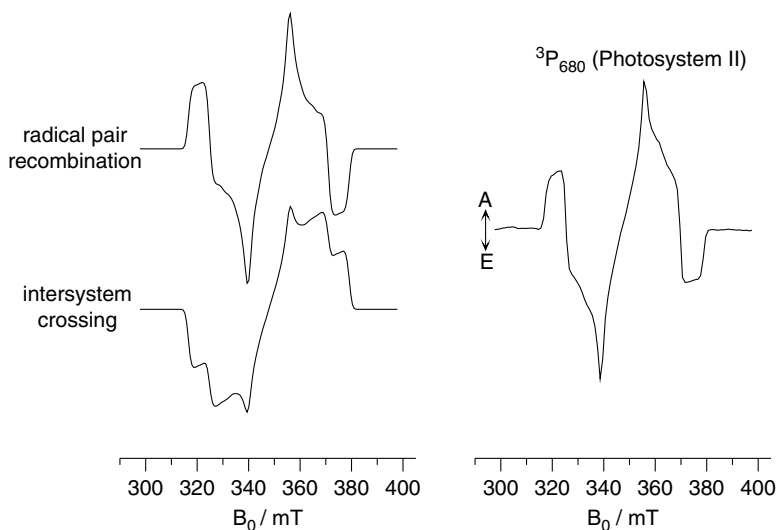
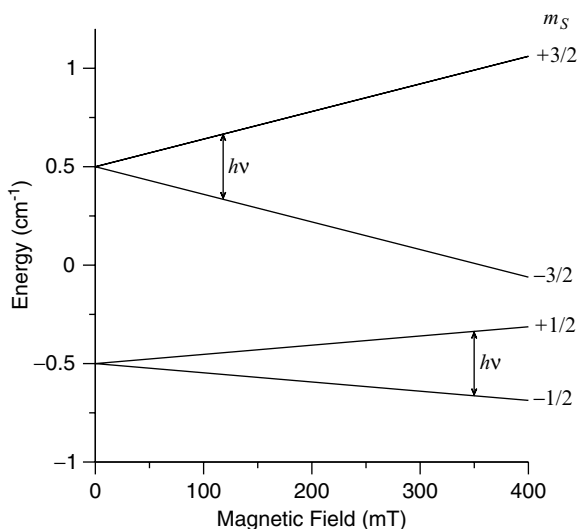


**Fig. 6.24** Spin-polarized chlorophyll triplet state spectra. *Left*: Calculated spectra for different possible pathways to the triplet state. *Right*: Experimental spectrum from Photosystem II D1/D2 particles at 40 K

angular momentum is accompanied by a change in the orbital angular momentum such that the total angular momentum remains unchanged. The second is singlet–triplet mixing that can occur in radical pairs due to the different precession frequencies of the spins of the two radicals. Because of this mixing, radical pairs formed initially in the singlet state often recombine to a molecular triplet state. In both cases, the process is spin-selective and hence the triplet state is spin-polarized. However, the spin selectivity is different in the two cases and the polarization patterns obtained are not the same. In the case of intersystem crossing, the strength of the spin-orbit coupling is orientation-dependent and is governed by the symmetry of the molecule. Singlet–triplet mixing in a radical pair, on the other hand, depends on the singlet character of the radical pair spin states. For a weakly coupled radical pair at high magnetic field, the singlet state mixes only with the  $T_0$  state. Thus, charge recombination occurs exclusively to the  $T_0$  level of the molecular triplet state and the polarization does not depend on orientation. Figure 6.24, left shows the polarization patterns expected for charge recombination and spin-orbit coupling mediated intersystem crossing. In the latter case it is assumed that spin-orbit coupling is strongest along the molecular  $z$ -direction and negligible in the  $x$ - and  $y$ -directions. As can be seen, the patterns differ significantly from one another so that it is possible to deduce the pathway by which the triplet state was generated. The right side of the Fig. 6.24 shows the experimental transient EPR spectrum obtained from Photosystem II particles that lack the terminal quinone acceptors. In these particles, charge separation generates the primary radical pairs which then recombines on a nanosecond timescale. From the transient EPR spectrum it is readily apparent that the triplet state of the primary donor  $P_{680}$  is populated via the recombination.

**Fig. 6.25** Energy level diagram for a spin  $3/2$  system with zero-field splitting parameters  $D=+0.5\text{ cm}^{-1}$  and  $E=0$ . The applied magnetic field is parallel to the  $z$ -axis of the zero-field splitting tensor. The *double-headed arrows* indicate the field positions at which X-band EPR transitions occur



#### 6.5.3.4 High Spin ( $S=3/2$ , $5/2$ ) Metal Center Systems

Metalloproteins with  $S=1/2$  are relatively straightforward to analyze by EPR because the spectra are only a function of the interaction of a single electron with the external magnetic field (Zeeman splitting) and with the field of nearby magnetic nuclei (hyperfine interactions). However, when  $S>1/2$ , the dipolar interaction between two or more unpaired electrons also contributes and spin-orbit coupling causes shifts of the spin states with different values of  $|m_S|$  relative to one another. High spin systems are found in heme proteins, which can exist with  $S=5/2$  as well as  $S=1/2$ , and in simple [4Fe-4S] clusters, which can exist with  $S=3/2$  as well as  $S=1/2$ . The relevant parameters in a high spin system are  $D$ , the axial zero-field splitting parameter, and  $E$ , the rhombic splitting parameter. The ratio of  $E$  to  $D$  is termed the “rhombicity” and it varies from  $E/D=0$  in an exclusively axial system to  $E/D=1/3$  in an exclusively rhombic system. In metalloproteins, the value of  $D$  is often much larger than the Zeeman energy at X-band (i.e., it is larger than  $\sim 0.3\text{ cm}^{-1}$ ), so that the separation of states with different values of  $|m_S|$  is large. The pairs of states with  $m_S=\pm 1/2$ ,  $\pm 3/2$ , etc., can be treated as pseudo  $S=1/2$  systems termed Kramer’s doublets (Fig. 6.25). In general, an  $S=n/2$  multiplet forms  $(n+1)/2$  Kramer’s doublets (i.e.,  $S=3/2$  forms two Kramer’s doublets and  $S=5/2$  forms three Kramer’s doublets). At zero field, the microwaves are not able to cause transitions between the doublets due to the large splitting, but as a magnetic field is applied, each doublet gives rise to its own set of resonances as if it were an  $S=1/2$  system. One important consideration is that if the zero-field splitting is larger than  $kT$  some of the Kramer’s doublets may have low population according to the Boltzmann distribution. However, in heme and iron-sulfur proteins,  $D$  is sufficiently small that even at 4 K, all of the doublets will be populated. In the case of an  $S=3/2$  system

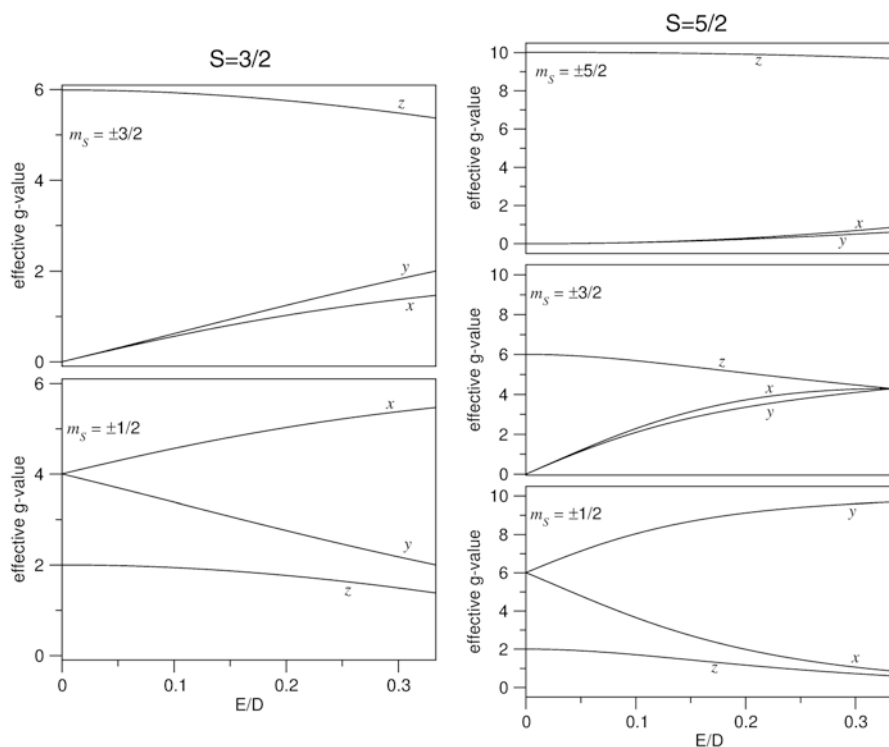


**Fig. 6.26** Rhombograms for  $S=3/2$  and  $S=5/2$  species showing the effective  $g$ -values of the powder spectrum features. The  $g$ -tensors of the species have been assumed to be isotropic and equal to the free electron value. The zero-field splitting is assumed to be large compared to the Zeeman energy

(Fig. 6.25), two sets of transitions can be observed, one from the  $\pm 1/2$  Kramer's doublet and the other from the  $\pm 3/2$  Kramer's doublet. If  $D$  is positive, the  $\pm 1/2$  Kramer's doublet is lower in energy and is termed the ground doublet and the  $\pm 3/2$  doublet is higher and is called the excited state. For  $D < 0$ , the situation is reversed. In both cases the lower Kramer's doublet will be preferentially populated.

These concepts can be generalized for systems with  $E/D > 0$  through a visual formalism termed a "rhombogram," which depicts the  $g$ -values of the features in the EPR powder spectra for the ground and excited state doublets as a function of the ratio of  $E/D$ . In an  $S=3/2$  system (Fig. 6.26, left), two Kramer's doublets will be present and for each of these, three features are observed corresponding to the three principal axes of the zero-field splitting tensor. For an axial system with  $E/D=0$ , the features from the  $x$  and  $y$  orientations overlap in the ground doublet, while in the excited doublet they occur at infinite field ( $g=0$ ) so only three features are observed at  $g=2, 4$ , and  $6$ . For rhombic systems with  $E/D > 0$ , six features will occur, three in the ground state doublet and three in the excited state doublet. The resonances associated with the ground state and excited state doublets can be distinguished by

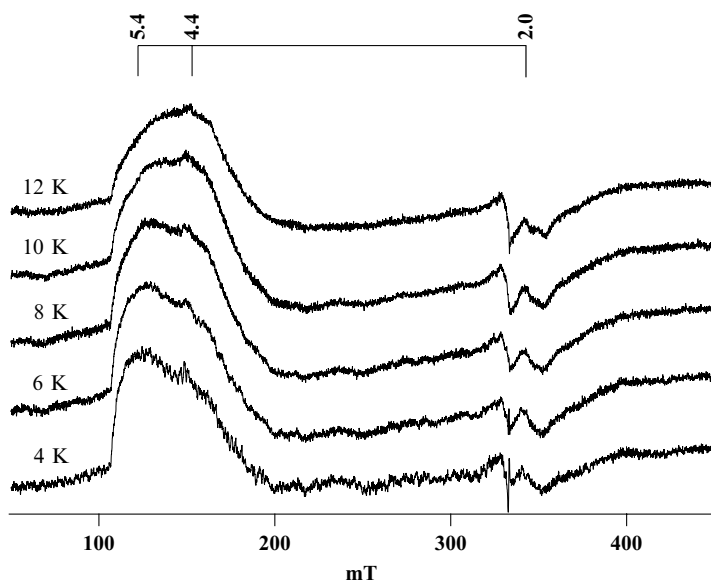


**Fig. 6.27** EPR spectrum of the  $S=3/2$  ground state [4Fe-4S] cluster  $F_X$  in the photosynthetic reaction center of *Heliobacterium modesticaldum* as a function of temperature. The principal  $g$ -values are depicted

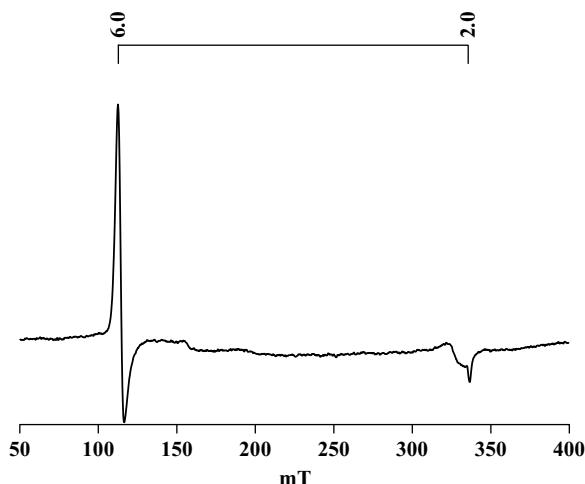
temperature studies. The ground state is preferentially populated relative to the excited state at lower temperatures but if  $D > 0$ , the excited state is preferentially populated relative to the ground state at higher temperatures because of its higher multiplicity.

In practice, if the ground state resonances can be identified, the  $E/D$  value can be determined and the excited state resonances will be specified by the rhombogram, and conversely, if the excited state resonances can be identified, the  $E/D$  value can be similarly determined, and the ground state resonances will be specified by the rhombogram. Such  $S=3/2$  systems are typically present in [4Fe-4S] clusters in which one cysteine ligand has been replaced either by an oxygen ligand or an external thiolate, and in [4Fe-4S] clusters that are shared between a protein homodimer. Figure 6.27 shows the EPR spectrum of the  $S=3/2$  system present in the interpoly-peptide  $F_X$  cluster of *Heliobacterium modesticaldum*. At 4.2 K, the spectrum shows two distinctive features: a peak at  $g=5.4$  and a shoulder at  $g=4.4$ . As the temperature is raised, the  $g=5.4$  peak decreases in intensity while the  $g=4.4$  shoulder increases in intensity. The temperature dependence suggests that the former signal is associated with the ground Kramer's doublet, whereas the latter feature is associated with the excited Kramer's doublet. The  $g$ -values of approximately 5.4 and 4.4 are roughly that expected for an  $S=3/2$  spin system exhibiting a rhombicity,  $E/D$ , of approximately 0.2 (Fig. 6.26).

In an  $S=5/2$  system three Kramer's doublets will be present. The rhombogram (Fig. 6.26, right) depicts the resonances expected as the  $E/D$  value is varied from an exclusively axial system to an exclusively rhombic system. Such  $S=5/2$  systems are



**Fig. 6.28** X-band EPR spectrum of horse myoglobin at pH 6.0. The principal  $g$ -values are depicted



present in heme proteins such as horse myoglobin at pH 6.0, which is a pure rhombic system with an  $E/D$  value close to 0 (Fig. 6.28). According to the rhombogram, the ground state  $S = 1/2$  Kramer's doublet, which will be preferentially populated at low temperatures, will show two  $g$ -values around 2 and 6. The middle Kramer's doublet will also show the  $g = 6$  resonance, but the  $g = 0$  resonances will not be observed. The highest Kramer's doublet, which will be lightly populated at low temperature, as well as the  $g = 1$  resonance will also not likely be observed. Hence, high spin heme proteins typically show a strong resonance around  $g = 6$  with only a minor feature around  $g = 2$ .

Another interesting example of an  $S = 5/2$  is octahedrally coordinated ferric iron (commonly known as "junk iron"), which is present in most biological samples. It is a rhombic system with an  $E/D$  value of  $1/3$ . According to the rhombogram, the ground state  $S = 1/2$  Kramer's doublet, which is preferentially populated at low temperatures, shows two  $g$ -values less than 1 and one  $g$ -value greater than 9, but the former are unlikely to be observed. The same consideration holds for the highest excited state Kramer's doublet, with the added provision that it will be less populated than the ground state doublet. In the middle Kramer's doublet, all three  $g$ -values converge to 4.29 at the rhombic limit, hence, this is the only prominent resonance observed from aqueous  $\text{Fe}^{3+}$  ions. These resonances are therefore relatively intense, making it easy to overestimate the amount of adventitiously bound iron present in a biological sample.

## 6.6 Concluding Remarks

Our goal in this overview of biological EPR is to give an introduction to the method without delving into the complicated mathematics that is needed for a complete description. In the interest of clarity and because of space constraints, we have not

been able to touch on many elegant and important aspects of EPR spectroscopy. However, we hope that we have been able to encourage readers and students new to the field of EPR to further explore the rich literature of the technique.

**Acknowledgements** This work was supported by the Molecular and Cellular Biosciences Division of the National Science Foundation (MCB-1021725) and by the U.S. Department of Energy, Basic Energy Sciences, Division of Materials Sciences and Engineering, under Contract DE-FG-05-05-ER46222 to JHG; and by a Discovery Grant from the Natural Science and Engineering Council Canada to AvdE.

## References

1. Weil JA, Bolton JR, Wertz JE (1994) *Electron paramagnetic resonance, elementary theory and practical applications*. Wiley, New York
2. Atherton NM (1993) *Principles of electron spin resonance*. Ellis Horwood/Prentice Hall, New York
3. Hagen WR, Biomolecular EPR (2009) *Spectroscopy*. CRC Press, Boca Raton, FL
4. Brustolon M, Giamello E (eds) (2009) *Electron paramagnetic resonance: a practitioner's toolkit*. Wiley, Hoboken, NJ
5. Schweiger A, Jeschke G (2001) *Principles of pulsed electron paramagnetic resonance*. Oxford University Press, Oxford
6. Möbius K, Savitsky A (2009) *High field EPR spectroscopy on proteins and their model systems: characterization of transient paramagnetic states*. RSC, Cambridge
7. Berliner L, Reuben J (eds) (1998) *Spin labeling, the next millenium*. Plenum Press, New York
8. Eom HJ (2004) *Electromagnetic wave theory for boundary-value problems: an advanced course on analytical methods*. Springer, Berlin
9. Abragam A, Bleaney B (1986) *Electron paramagnetic resonance of transition metal ions*. Dover, New York
10. Portis AM (1953) Electronic structure of F-centers—saturation of the electron spin resonance. *Phys Rev* 91(5):1071–1078
11. Carr HY, Purcell EM (1954) Effects of diffusion on free precession in nuclear magnetic resonance experiments. *Phys Rev* 94:630–638
12. Meiboom S, Gill D (1958) Modified spin-echo method for measuring nuclear relaxation times. *Rev Sci Instrum* 29:688–691
13. Rowan LG, Hahn EL, Mims WB (1965) Electron-spin-echo envelope modulation. *Phys Rev* 137(1A):A61–A71
14. Höfer P, Grupp A, Nebenführ H, Mehring M (1986) Hyperfine sublevel correlation (hyscore) spectroscopy—a 2D electron-spin-resonance investigation of the squaric acid radical. *Chem Phys Lett* 132:279–282
15. Kurreck H, Kirste B, Lubitz W (1988) In: Marchand AP (ed) *Electron nuclear double resonance spectroscopy of radicals in solution: application to organic and biological chemistry*. Wiley, Weinheim
16. Hoffman BM (2003) ENDOR of metalloenzymes. *Acc Chem Res* 36(7):522–529
17. Feher G (1956) Observation of nuclear magnetic resonances via the electron spin resonance line. *Phys Rev* 103(3):834–835
18. Mims WB (1965) Pulsed endor experiments. *Proc R Soc Lond Ser A* 283(1395):452–457
19. Davies ER (1974) New pulse endor technique. *Phys Lett A* 47(1):1–2
20. Gemperle C, Schweiger A (1991) Pulsed electron nuclear double-resonance methodology. *Chem Rev* 91(7):1481–1505

21. Larsen RG, Singel DJ (1993) Double electron–electron resonance spin-echo modulation—spectroscopic measurement of electron-spin pair separations in orientationally disordered solids. *J Chem Phys* 98:5134–5146
22. Milov AD, Maryasov AG, Tsvetkov YD (1998) Pulsed electron double resonance (PELDOR) and its applications in free-radicals research. *Appl Magn Reson* 15:107–143
23. Thurnauer MC, Norris JR (1980) An electron-spin echo phase-shift observed in photosynthetic algae—possible evidence for dynamic radical pair interactions. *Chem Phys Lett* 76(3):557–561
24. Bittl R, Zech SG (2001) Pulsed EPR spectroscopy on short-lived intermediates in Photosystem I. *Biochim Biophys Acta* 1507:194–211
25. Lendzian F, Huber M, Isaacson RA, Endeward B, Plato M, Bonigk B et al (1993) The electronic-structure of the primary donor cation-radical in rhodobacter-sphaeroides R-26—ENDOR and triple-resonance studies in single-crystals of reaction centers. *Biochim Biophys Acta* 1183:139–160
26. Niklas J, Gupta O, Epel B, Lubitz W, Antonkine ML (2010) Investigation of the stationary and transient  $A_1^-$  radical in Trp → Phe mutants of Photosystem I. *Appl Magn Reson* 38:187–203
27. Niklas J, Epel B, Antonkine ML, Sinnecker S, Pandelia ME, Lubitz W (2009) Electronic structure of the quinone radical anion  $A_1^-$  of Photosystem I investigated by advanced pulse EPR and ENDOR techniques. *J Phys Chem B* 113:10367–10379
28. Epel B, Niklas J, Sinnecker S, Zimmermann H, Lubitz W (2006) Phylloquinone and related radical anions studied by pulse electron nuclear double resonance spectroscopy at 34 GHz and density functional theory. *J Phys Chem B* 110:11549–11560
29. Hellmich UA, Lyubenova S, Kaltenborn E, Doshi R, van Veen HW, Prisner TF et al (2012) Probing the ATP hydrolysis cycle of the ABC multidrug transporter LmrA by pulsed EPR spectroscopy. *J Am Chem Soc* 134:5857–5862
30. Bhatnagar J, Sircar R, Borbat PP, Freed JH, Crane BR (2012) Self-association of the histidine kinase CheA as studied by pulsed dipolar ESR spectroscopy. *Biophys J* 102:2192–2201
31. Kandrashkin Y, van der Est A (2001) A new approach to determining the geometry of weakly coupled radical pairs from their electron spin polarization patterns. *Spectrochim Acta A Mol Biomol Spectrosc* 57:1697–1709
32. Kandrashkin YE, van der Est A (2007) Time-resolved EPR spectroscopy of photosynthetic reaction centers: from theory to experiment. *Appl Magn Reson* 31:105–122
33. van der Est A, Prisner T, Bittl R, Fromme P, Lubitz W, Mobius K et al (1997) Time-resolved X-, K-, and W-band EPR of the radical pair state  $P700^+ A_1^-$  of Photosystem I in comparison with  $P865^+ QA^-$  in bacterial reaction centers. *J Phys Chem B* 101(8):1437–1443

# Chapter 7

## Mass Spectrometry

Igor A. Kaltashov and Cedric E. Bobst

**Abstract** Mass spectrometry is now an indispensable tool in the armamentarium of molecular biophysics, where it is used for tasks ranging from covalent structure determination to studies of higher order structure, conformational dynamics, and interactions of proteins and other biopolymers. This chapter considers the basics of biological mass spectrometry and highlights recent advances in this field (with particular emphasis on hydrogen exchange, chemical cross-linking, and native electrospray ionization mass spectrometry), evaluates current challenges, and reviews possible future developments.

### 7.1 Physical Principles and Instrumentation

Mass spectrometry (MS) is one of the oldest methods of instrumental analysis in chemistry, this year being the centennial of the construction of the first mass spectrometric device [1]. In addition to rather mundane applications related to molecular mass measurements (as implied by its name), MS can be used for a variety of other tasks, many of which are uniquely suited to address challenging questions in molecular biophysics and structural biology. However, it was not until the advent of the two ionization techniques capable of producing ions of large and polar molecules, electrospray ionization (ESI), and matrix-assisted laser desorption/ionization (MALDI), that MS became a commonly accepted tool in the armamentarium of modern molecular biophysics.

---

I.A. Kaltashov (✉) • C.E. Bobst  
Department of Chemistry, University of Massachusetts-Amherst,  
710 North Pleasant Street, Amherst, MA 01003, USA  
e-mail: kaltashov@chem.umass.edu

### 7.1.1 Methods of Producing Biomolecular Ions

MS is unique among the analytical techniques commonly applied to study biomolecular structure and behavior in that the actual physical measurements are carried out in vacuum or in the gas phase, where either electric field alone or its combination with a magnetic field are used to determine ionic mass-to-charge ratios ( $m/z$ ). Placing a large biomolecular ion in vacuum is no trivial task, and the absence of robust methods to do so were limiting the utility of MS in the biophysical arena until the early 1990s.

#### 7.1.1.1 Electrospray Ionization

The advent of ESI MS in the mid-1980s [2] provided a means to observe spectra of intact proteins with no apparent mass limitation, an invention honored with a Nobel Prize in Chemistry to John Fenn in 2002 [3]. Although the ESI phenomenon was known and extensively studied for over a century, and the realization of its great analytical potential in the macromolecular realm had become apparent as early as 1960s [4], the practical applications of this ionization technique were limited to small biomolecules, such as nucleobases, amino acids [5], and short peptides [6, 7]. It was not until the demonstration of the ability of ESI to generate ionic signals for protein molecules in the form suitable for MS analysis [8] that this technique rapidly gained acceptance and recognition among MS practitioners and quickly became a tool of choice in a variety of studies of biomolecular structure.

ESI is a convoluted process, whose detailed discussion is beyond the scope of this chapter. Briefly, the protein (or, generally speaking, any biopolymer) solution is sprayed at atmospheric pressure in the presence of a strong electrostatic field, which generates metastable electrically charged droplets of the solvent encapsulating the protein molecules. Such droplets undergo a series of fission events, eventually producing either solvent-free or partially solvated protein ions. A very distinct feature of the ESI process is the accumulation of multiple charges on a single protein molecule, which leads to the appearance of multiple peaks in a mass spectrum even when a single protein is present in solution (Fig. 7.1a, b). In most cases multiple charging is the result of protonation of a number of different sites within the protein molecule, although other ubiquitous charge carriers (such as  $\text{Na}^+$ ,  $\text{K}^+$ ,  $\text{NH}_4^+$ ) may also contribute. A set of ion peaks, each representing the same protein molecule and differing from the rest by the extent of multiple charging, is usually referred to as a *charge state distribution*. Determination of the protein mass based on the experimentally measured charge state distribution is relatively straightforward, and can be easily accomplished using a variety of deconvolution routines even if the mass spectrum contains several overlapping charge state distributions representing different biomolecules.

Most ESI MS analyses are carried out in the positive ion mode (where biopolymer molecules are represented in mass spectra with polycationic species), but one

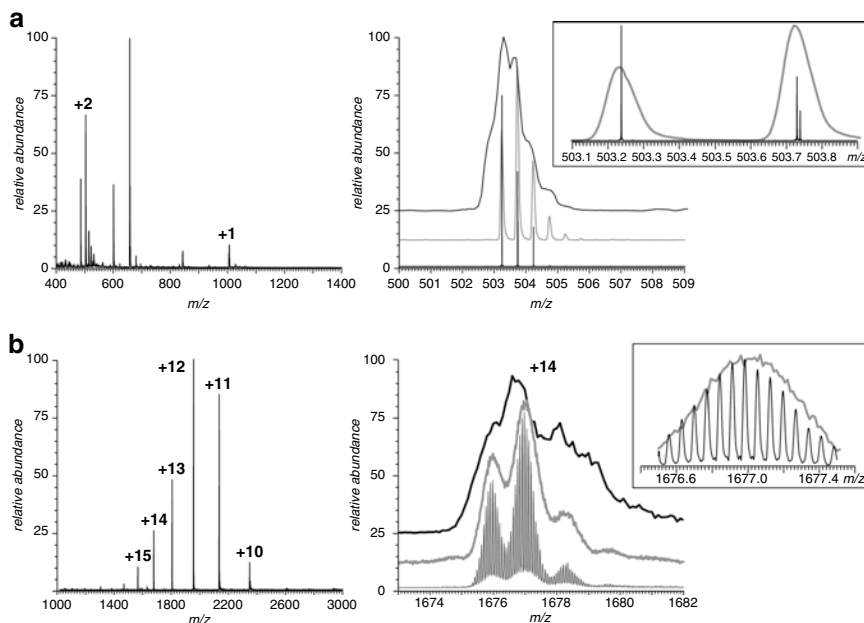


**Fig. 7.1** ESI mass spectra of a peptide SWANGDEAR (a) and trypsin (b). The panels on the *left* represent full-scan mass spectra, and the panels on the *right* show detailed views of a single charge state (the three traces in each case represent mass spectra acquired with a triple quadrupole MS, hybrid quadrupole/TOF MS, and FT ICR MS), with the *insets* showing zoomed views of mass spectra acquired with quadrupole/TOF and FT ICR MS. Note that although the resolving power of TOF is sufficient to resolve isotopic peaks of the peptide ion, it fails to detect the presence of a degraded (de-amidated) form of this peptide (between  $m/z$  503.7 and 503.8). Isotopic distribution of trypsin ions can only be resolved by FT ICR MS, although both quadrupole/TOF and FT ICR MS can resolve contributions of three different isoforms of this protein

can easily produce polyanionic species as well simply by switching the polarity of the ESI source. In this case multiple charging of macromolecules will be achieved by removing labile protons from the analyte molecule (de-protonation). While proteins are usually analyzed by ESI MS in the positive ion mode, switching to the negative ion mode could be advantageous for certain other biopolymers, such as nucleic acids. It must be stressed, however, that for any biopolymer both positive and negative ion spectra can be produced, and the charge state distributions in these spectra do not reflect the charge balance in solution [9].

### 7.1.1.2 MALDI

Another approach to producing macromolecular ions and transferring them to vacuum was introduced at about the same time ESI MS was developed; unlike ESI it produces ions not from the bulk of the solution, but from the interface of a

condensed phase (usually solid crystals) and the vacuum. This task is accomplished by mixing the analyte molecules with an excess of UV light-absorbing small organic molecules, which form the sample matrix, followed by irradiation with a UV laser beam. This results in rapid local heating of the matrix and subsequent ejection of a plume containing both matrix and analyte molecules from the solid surface to the gas phase and their ionization. This technique, presently known as MALDI was developed simultaneously by Koichi Tanaka [10] and Franz Hillenkamp and Michael Karas [11].

Biopolymer ions produced by MALDI can also carry multiple charges; however, the extent of protonation is significantly below that achieved with ESI. Generally, MALDI MS surpasses conventional ESI MS in terms of sensitivity and is more tolerant to salts. Superior sensitivity, relative simplicity of operation, and ease of automation have made it a top choice as an analytical technique for a variety of proteomics-related applications. On the other hand, MALDI mass spectra generally are not as reproducible as ESI mass spectra. Also, interfacing MALDI with separation techniques, such as liquid chromatography (LC), is more difficult than coupling LC to ESI MS.

### 7.1.2 Mass Measurements

Mass (or, more precisely, *mass-to-charge ratio*,  $m/z$ ) of an ion can be determined by MS, because this characteristic of a charge-carrying particle uniquely defines its trajectory in electric ( $E$ ) and magnetic ( $B$ ) fields, as well as their combinations:

$$m\ddot{\vec{r}} = ze(\vec{E} + [\dot{\vec{r}} \times \vec{B}]). \quad (7.1)$$

Here  $ze$  is the ionic charge expressed as a multiple of the elementary charge  $e$  ( $1.6022 \times 10^{-19}$  C in SI),  $m$  is its mass, while the first and second time derivatives of the trajectory vector represent its velocity and acceleration, respectively. Mass measurements are actually carried out by first separating the ions (either spatially or temporally) according to their  $m/z$  ratios, followed by detection of each type of ion, although other schemes exist where no physical separation of ions is required prior to their detection and mass measurement (*vide infra*).

The ionic  $m/z$  ratio measured by MS in most cases can be easily converted to the *ionic mass* (after taking into the account the multiple charging effect) and, ultimately, to the *molecular mass* of the analyte (after taking into the account the finite mass of the charge carriers, residual solvent, and other adducts). The notion of molecular mass (measured in unified atomic mass units, defined by IUPAC as 1/12 of the mass of a  $^{12}\text{C}$  atom in its ground state,  $u \approx 1.660\,5402(10) \times 10^{-27}$  kg) is closely related to the concept of *molecular weight*, a sum of the *atomic weights* of all atoms in a given molecule. However, the *atomic weight* of an element is a weighted average of the atomic masses of all of its stable isotopes, and the isotopic make-up is implicitly included in the definition. Contributions of isotopes are

not necessarily averaged out when ionic masses are measured by MS, and in many cases such measurements produce a distribution of masses, rather than a single value. This, of course, depends on the physical size of the analyte molecule and the mass resolution characteristics of the MS instrument (*vide infra*). Most modern MS instruments are capable of resolving isotopic distributions for relatively short peptides (Fig. 7.1a), while accomplishing the same task for proteins requires more technologically advanced (and alas, more expensive) instrumentation (Fig. 7.1b).

To avoid ambiguity in reporting molecular masses, one can use the notion of an *average mass*, which is calculated based on the entire isotopic distribution and is closely related to the *molecular weight* as used elsewhere in chemistry and related disciplines. In some applications, however, a *monoisotopic mass* would be a preferred way of reporting the molecular mass with high precision and accuracy (it is calculated based on contributions only from the lightest isotope for each element). Obviously, the use of the monoisotopic mass in reporting the MS measurement results is justified only if the resolution is high enough to afford separation of isotopic peaks in the mass spectra and the monoisotopic peak is one of the most abundant peaks in the distribution.

### 7.1.3 Tandem Mass Spectrometry

The most attractive features of both ESI and MALDI are their ability to generate intact macromolecular ions in the form suitable for mass measurement. However, this information is not sufficient in most instances for unequivocal identification of even small peptides, let alone large macromolecules. This task requires at least some knowledge of the covalent structure, which can be obtained by inducing dissociation of macromolecular ions and measuring the masses of the resulting fragment ions. Since most proteins and peptides are linear polymers, cleavage of a single covalent bond along the backbone generates a fragment ion (or two complementary fragment ions if the charge of the precursor ion  $z=2$  or higher) classified as an *a*-, *b*-, *c*- or *x*-, *y*-, *z*-type [12, 13], depending on (1) the type of the bond cleaved and (2) whether the fragment ion contains an N- or C-terminal portion of the peptide (Fig. 7.2). Ion dissociation is usually carried out following isolation of the ion of interest from other ionic species that may be present in the mass spectrum. This approach, known as *tandem mass spectrometry* or *MS/MS*, allows the fragment ion/precursor ion correlation to be established easily [14] and is indispensable for many biophysical applications of MS (*vide infra*).

The majority of tandem MS experiments employ various means of increasing internal energy of the precursor ion to induce its dissociation. Collisional activation remains the most widely used method of elevating ion internal energy [15], which typically yields *b*- and *y*-ions, although collision-induced dissociation (CID) at high energy may also lead to formation of other fragments, particularly *a*- and *x*-type (Fig. 7.3a, b). Excitation of ions leading to their dissociation can also be



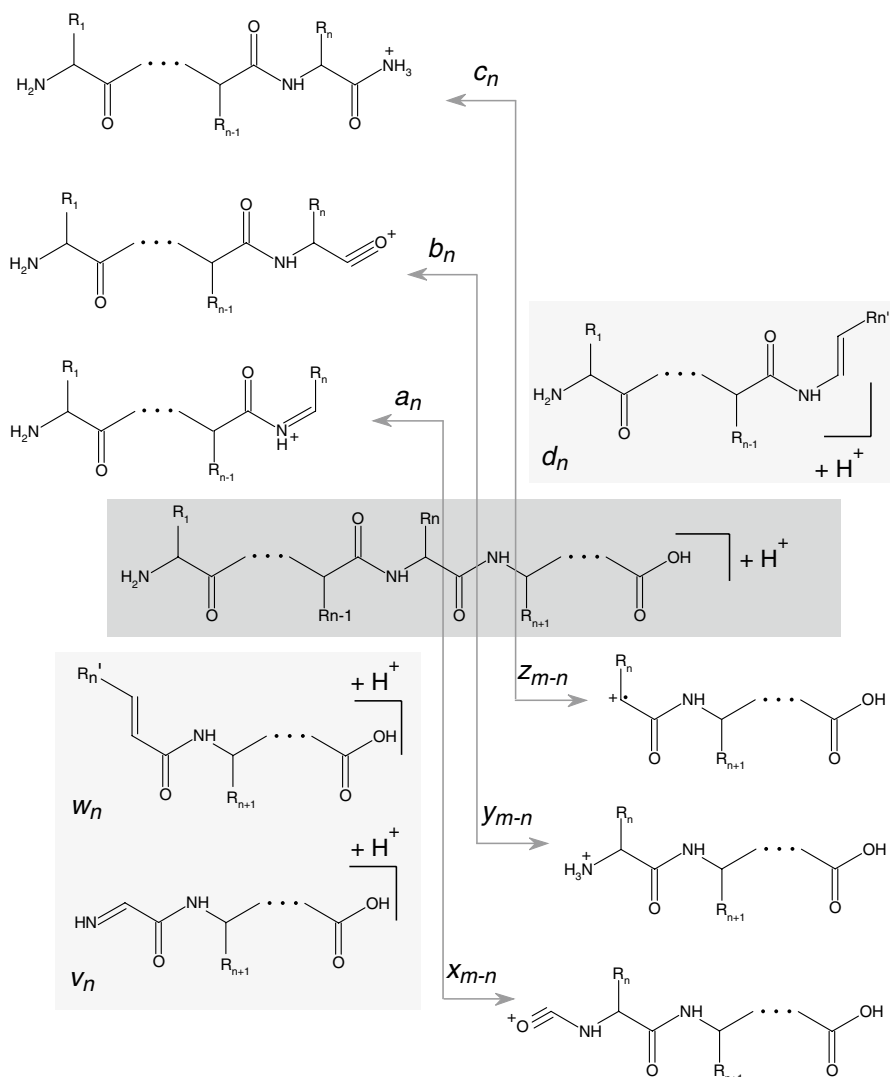


**Fig. 7.2** Biemann's nomenclature of peptide ion fragments [12]. Fragment ions shown in gray boxes correspond to either complete or partial loss of the side chains and are usually observed only in high-energy CID

achieved using other means, such as interaction with photons (a technique known as *infrared multi-photon dissociation*, IRMPD [16]) or with electrons (two closely related techniques, known as *electron capture dissociation*, ECD [17] and *electron transfer dissociation*, ETD [18]). While the outcome of IRMPD is usually very similar to low-energy CID, ECD, and ETD typically generate *c*- and *z*-fragments, and often provide more extensive sequence coverage in polypeptides compared to

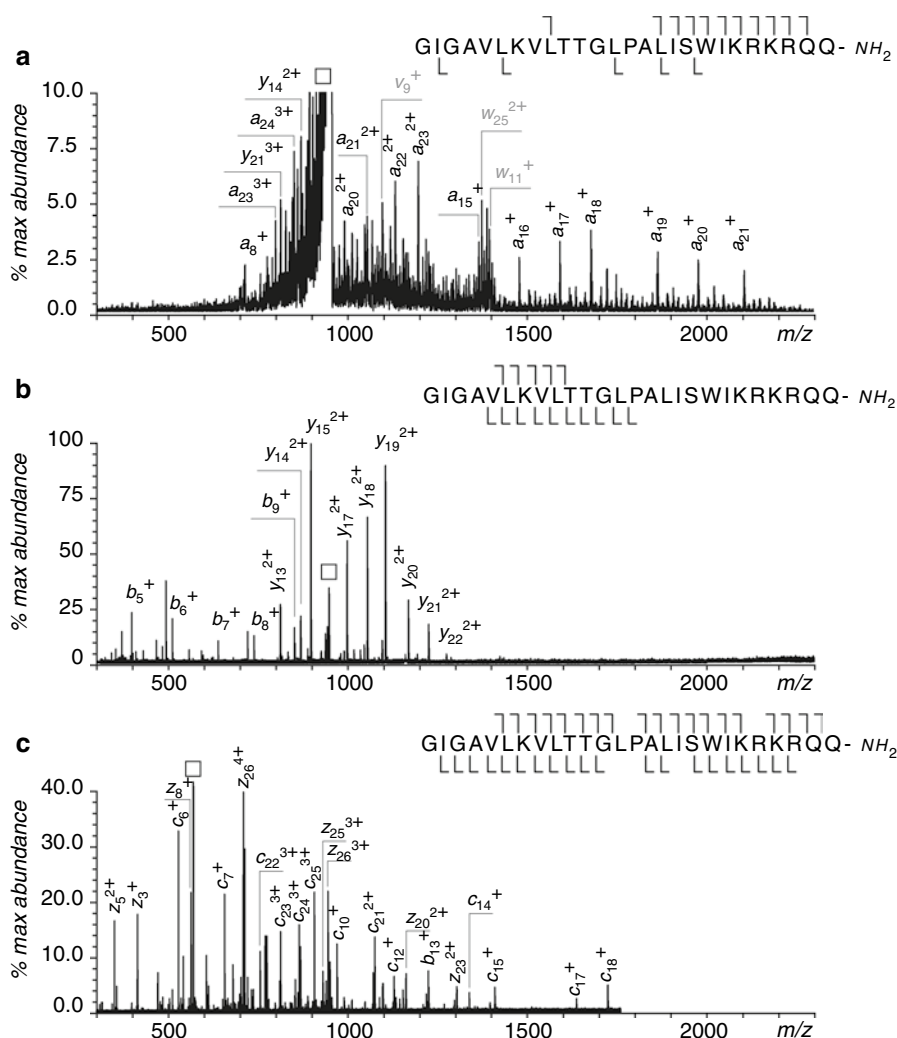


**Fig. 7.3** High-energy CID (a), low-energy CID (b), and ECD (c) fragmentation spectra of a 2.8 kDa melittin peptide. Only the most abundant fragment ions are labeled in the spectra

conventional CID (Fig. 7.3c). Another very attractive feature of electron-based fragmentation techniques is their ability to preserve labile groups introduced through posttranslational modification (PTM) of proteins and cleave disulfide bonds in peptide polycations [19], a challenging task when other methods of ion activation are employed. The fragmentation patterns produced by ECD and ETD are frequently complementary to the CID-generated fragments [20], hence the benefit of using multistage fragmentation (the so-called MS<sup>n</sup> experiments) consisting of both CID and ECD (or ETD).

### 7.1.4 Common Types of Mass Analyzers

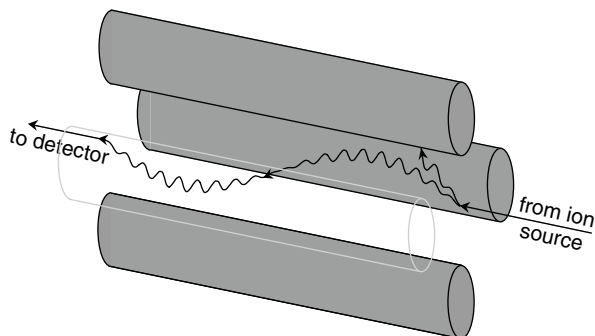
As has been already mentioned in this chapter,  $m/z$  measurements of macromolecular ions by MS rely on the unique dependence of the ionic trajectory in electric and magnetic fields on this parameter as shown in equation (7.1). The practical implementation of this principle takes a wide variety of approaches, hence a great number of mass analyzers which differ from each other not only by the amount and quality of information that can be extracted from mass measurements but also by price. Given the obvious space limitations of this volume, we cannot provide extensive coverage of all available types of mass analyzers, but instead focus our attention on three different types representing the ends and the middle of both performance and price scales. These are quadrupole, time-of-flight (TOF), and Fourier transform ion cyclotron resonance (FT ICR) mass spectrometers.

#### 7.1.4.1 Quadrupole, Triple Quadrupole, and Ion Trap MS

Strictly speaking, *quadrupole MS* should be called a mass filter, rather than a mass analyzer, since the dynamic quadrupolar electric field employed by this device allows ions within a narrow  $m/z$  range to be transmitted through this device and eventually reach a detector, while all other ions assume unstable trajectories and are lost prior to detection (Fig. 7.4). The  $m/z$  range of a typical quadrupole MS is limited to 4,000 (with many commercial instruments having even less generous  $m/z$  limits). The mass resolution of a quadrupole MS is not constant across the  $m/z$  scale, and rarely exceeds the level of several thousands. On the other hand, these devices provide good sensitivity and are capable of obtaining mass spectra fast enough to allow direct coupling to LC. MS/MS experiments can be carried out if three quadrupoles are arranged in tandem (a configuration referred to as QqQ, or so-called *triple quadrupole MS*). The first quadrupole is set to transmit ions of certain  $m/z$  value (precursor ions), while the second is used as a collision cell and transmits all ions (precursor and CID fragments) into the third quadrupole, which is scanned to obtain a fragment ion spectrum.

Other MS/MS experiments can be designed; for example, the third quadrupole can be set to allow the transmission of fragment ions at certain  $m/z$  values, while the first quadrupole is scanned. Mass spectra acquired in this mode contain peaks of all ions whose fragmentation gives rise to a selected fragment (the so-called *precursor ion scans*). Alternatively, scanning both first and third quadrupole filters at the same rate but with a fixed  $m/z$  offset while generating fragment ions in the second nondiscriminating quadrupole produces a spectrum of ions that undergo fragmentation via loss of a specific neutral fragment (the so-called *constant neutral loss scans*). Triple quadrupole mass spectrometers are indispensable in applications that require quantitation of both small organic and biological analytes to be carried out. However, modest resolution and  $m/z$  range of such mass spectrometers limit their use in biophysical and structural biology studies, although these devices are

**Fig. 7.4** A schematic representation of a quadrupole mass filter with examples of stable and unstable ion trajectories



often interfaced with other (higher-end) mass analyzers to produce hybrid mass spectrometers.

Quadrupolar devices can also be used to construct a different type of a mass analyzer, one where instead of being analyzed in a single pass through the dynamic quadrupolar field region, ions are stored (trapped) for prolonged periods of time [21]. The simplest design of such an ion trap is a segmented quadrupole (based on a triple quadrupole design), in which the central pressurized segment confines the ions radially in a dynamic (radio frequency) quadrupolar field, while the terminal segments provide repulsive DC potentials at either end that prevents the ions from escaping the central quadrupole in the axial direction. An alternative design (which is frequently referred to as a 3D ion trap to distinguish it from the linear trap described above) can be viewed as a single quadrupole filter that has been made into a toroidal device by connecting the opposite ends of each quadrupole rod and then “collapsing” this four-ring structure towards its axis of radial symmetry. In this case only one ring (the furthest from the axis) remains a ring, while the one closest to the axis completely disappears, and two other rings become endcaps flanking the remaining ring. This three-electrode system can be used to create a 3D quadrupolar electrical field, which confines ions within this device, a process that is greatly facilitated by the presence of He gas, which remove excess energy from ions via the so-called collisional damping [22, 23]. Gradual variation of electrode potentials destabilizes the trapped ions in an  $m/z$ -sensitive fashion and forces them to leave the confines of the trap, a feature that enables both MS measurements and precursor ion selection for MS/MS experiments; this field-induced external excitation can also be used to ramp-up the energy of the ions, which is then converted to internal energy upon collisions with He atoms, and eventually leads to ion dissociation [22–25].

A very significant advantage of both types of ion trapping devices described above over their progenitor quadrupole MS is that MS/MS measurements can be carried out within a single analyzer, without the need to have a dedicated collision cell and a second mass analyzer. Furthermore, any of the fragment ions produced in the course of an MS/MS experiment can also be isolated in the trap, collisionally

activated and fragmented, followed by the acquisition of a mass spectrum of the second generation of fragment ions. This process can be repeated any number of times, as long as the number of ions remaining in the trap is high enough to provide a usable signal-to-noise ratio. Such experiments are referred to as *multi-stage tandem MS*, or simply *MS<sup>n</sup>*. Due to significant improvements in the performance of ion traps in the past 2 decades, ease of operation and relatively low cost, they have become very popular, both as standalone mass spectrometers and as part of hybrid instruments. Limitations of ion traps are similar to those of quadrupole MS: modest mass resolution and relatively low upper limit of the *m/z* range where MS (and MS/MS) data can be collected.

#### 7.1.4.2 TOF MS and Hybrid Quadrupole/TOF MS

Ion separation in the *TOF MS* is based on the fact that the velocity *v* of an ion accelerated in an electrostatic field will be determined by the magnitude of the acceleration potential *U*<sub>0</sub> and the ionic *m/z* ratio. Measuring the time period needed to traverse a field-free drift region of length *D* would then allow the ionic *m/z* ratio to be determined:

$$t = \frac{D}{v} = \sqrt{\frac{m}{2zeU_0}} \cdot D \quad (7.2)$$

This approach, however, results in relatively poor mass resolution, mostly due to a significant spread of ionic kinetic energies prior to acceleration. To correct this, several approaches can be used, where energy focusing of the ions is done by delaying ion acceleration using pulsed (delayed) extraction [26] or by using the so-called ion mirror or *reflectron* [27]. The principle of the reflectron operation is illustrated in Fig. 7.5: if two identical ions have different velocities, the faster ion will penetrate deeper into the decelerating region of the reflectron, and its overall trajectory path will be longer. After its reemergence from the reflectron, this ion would still have a higher velocity, but it will be lagging behind the slower ion due to spending longer time in the decelerating region. Such relatively simple single-stage reflectrons can only perform first order velocity focusing, but more sophisticated devices (e.g., double stage ion mirrors) can provide velocity focusing to a higher order [28, 29].

Reflectrons also allow MS/MS measurements to be carried out with a single TOF mass analyzer [28], although a combination of two TOF analyzers or a hybrid instrument consisting of TOF and another, lower resolution, mass analyzer (such as a quadrupole MS) usually offer more flexibility in experiment design and deliver better data quality. A hybrid quadrupole-TOF instrument is a particularly popular configuration, which is offered by several manufacturers of MS instrumentation. Typically, a front-end quadrupole is used for mass-selection of precursor ions, followed by an RF-only quadrupole serving as a collision cell, the fragment ions are then analyzed with high resolution by a reflectron-equipped TOF section of the

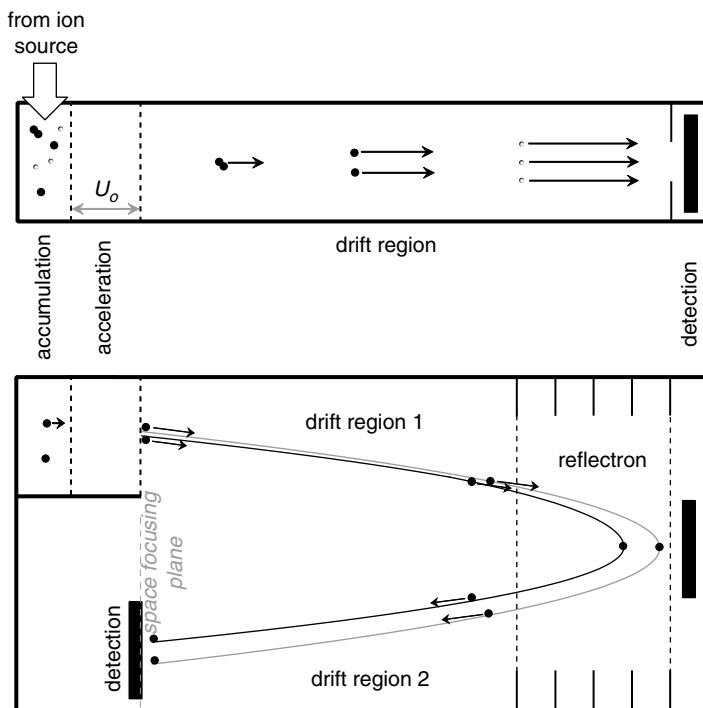


**Fig. 7.5** Schematic diagrams of linear (*top*) and single-stage reflectron (*bottom*) time-of-flight mass spectrometers

instrument. MS1 measurements are carried out by operating both quadrupole segments in the RF-only mode, so that they only serve as ion guides; all mass measurements are carried out by the TOF analyzer, which offers both better resolution ( $>10,000$ ) and  $m/z$  range vastly superior to that of the quadrupole MS.

### 7.1.4.3 FT ICR MS

*FT ICR MS* is an example of a high-performance mass spectrometer employing an ion trapping mass analyzer. However, unlike its relatively inexpensive cousins, the quadrupolar ion trap and linear ion trap considered in Sect. 1.4.1, it offers unparalleled mass resolution and unmatched mass accuracy (another high-performance mass analyzer based on the ion trapping principle is the orbitrap MS [30, 31]). Ion trapping is achieved in FT ICR MS by using a combination of electrostatic and magnetic fields, as shown in a schematic form in Fig. 7.6. A DC potential applied to the front and back plates of the cubic cell restricts the ionic motion along the  $z$ -axis, essentially locking the ions in the cell following their injection from the external source. A strong magnetic field (typically 4.7–12.0 T) applied in the direction of the

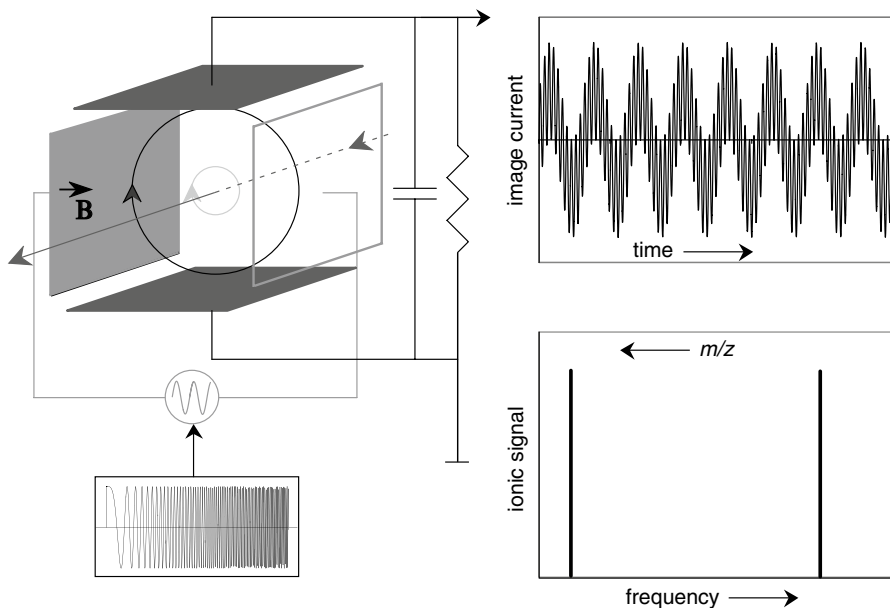


**Fig. 7.6** Principal of ion trapping, broadband excitation and detection in FT ICR MS. Reproduced with permission from [132]

$z$ -axis exerts a Lorentz force on the trapped ions, which acts as a centripetal force, inducing a circular (cyclotron) motion in the  $(x, y)$  plane. The frequency of the cyclotron motion  $\omega_c$  is independent of the ionic energy, but is uniquely determined by its  $m/z$  ratio and the strength of the magnetic field  $B$ :

$$\omega_c = \frac{zeB}{m}, \quad (7.3)$$

providing the physical basis of the mass measurement. Since frequency is a physical parameter that can be measured very accurately, mass spectrometers based on the principle of cyclotron motion can provide the highest accuracy in  $m/z$  measurements.

Ion detection in FT ICR MS is done by measuring the magnitude of the image current induced on the detection plates by the ion orbiting in the space between them (Fig. 7.6). Since unsynchronized motion of a large number of ions generates zero net current, ion detection must be preceded by ion excitation (e.g., by applying a uniform harmonic electric field in the direction orthogonal to the magnetic field). If the field frequency is the same as the cyclotron frequency of the orbiting ions, they will be synchronized (brought in phase with the field). Such resonant excitation also elevates ion kinetic energy, increasing the radii of their orbits, which leads to the increase of the image current induced by each ion. Synchronized ions of the same  $m/z$  ratio induce an image current, whose angular frequency  $\omega$  is equal to their

cyclotron frequency  $\omega_c$  and the current amplitude is proportional to the number of ions in the cell [32]. If several types of ions (with different  $m/z$  ratios) are present in the cell, their excitation/synchronization requires application of a broadband chirp as opposed to a harmonic signal, and the resulting image current is a superposition of several sinusoidal signals (the actual cyclotron frequency in a real ICR cell is lower than  $\omega_c$  due to the influence of a trapping electrostatic potential). Fourier transformation of such a spectrum allows the cyclotron frequencies of all ions to be determined and their  $m/z$  values calculated (Fig. 7.6).

Apart from ultra-high mass resolution and accuracy, a great advantage offered by FT ICR MS over most other mass analyzers is that it allows all ions across a wide  $m/z$  range to be detected (1) simultaneously within a very short period of time and (2) in a nondestructive fashion. The latter feature allows the data acquisition to be carried out with the same ion population over an extended period of time using multiple remeasurements, forming the basis of the  $MS^n$  (as opposed to  $MS/MS$  or  $MS^2$ ) experiments. Ion isolation in the ICR cell can be achieved using inverse FT (from the frequency to the time domain), and fragmentation of the isolated ions can be induced by either collisional activation or electron capture (other methods of ion activation, such as IRMPD, are also available). Combining FT ICR MS with another mass analyzer (e.g., quadrupole) as a front end leads to further expansion of the repertoire of the ion fragmentation techniques, e.g., by allowing ETD to be carried out under conditions of relatively high pressure prior to introduction of fragment ions to the ICR cell for either high-resolution mass analysis or interrogation with orthogonal ion fragmentation techniques that can be performed in the high-vacuum environment of the ICR cell. Combination of several ion fragmentation techniques in one experiment often provides significant improvement of the sequence coverage of macromolecular ions [33].

## 7.2 Analysis of Covalent Structure

### 7.2.1 Covalent Structure of Polypeptides and Proteins

Tandem mass spectrometry provides the means to obtain information on covalent structure of polypeptides and proteins by employing a combination of various MS-based techniques. Typically, these are grouped in two broad categories, the so-called *bottom-up* and *top-down* approaches, which are considered in the following sections.

#### 7.2.1.1 Polypeptide Sequencing: The Bottom-Up Approach

The classical approach to polypeptide sequencing by MS relies on enzymatic cleavage of a protein to relatively short peptides, followed by their separation by LC and



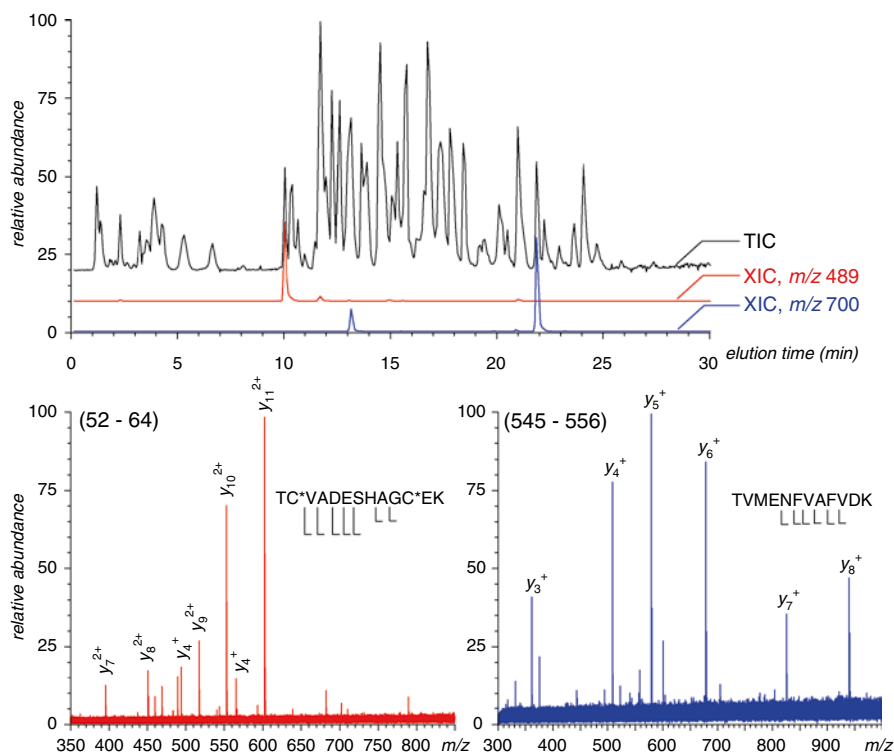


**Fig. 7.7** An example of using LC/MS/MS to obtain protein sequence information. A purified 66 kDa protein bovine serum albumin has been digested with trypsin, followed by separation of proteolytic fragments on a reversed-phase ( $C_{18}$ ) column with online ESI MS detection. The black trace in the top panel shows the total ionic signal recorded by ESI MS as a function of the elution time, while the red and blue traces represent ionic signals at two specific  $m/z$  values, which correspond to two proteolytic peptide ions, TCVADESHAGCEK<sup>64</sup> (charge state +3; both cysteine side chains are fully reduced and methylated) and TVMENFVAFVDK<sup>556</sup> (charge state +2). The MS/MS spectra of these two peptide ions acquired in a data-dependent fashion (by selecting the most abundant ion in MS1 spectrum as a precursor for CAD) are shown in the bottom panels. All structurally diagnostic ions are labeled in the mass spectra, and the corresponding backbone cleavage positions are shown within each peptide's sequence

analysis of their structure using MS/MS methods [34]. The chromatographic step is usually combined with MS and/or MS/MS analysis, which frequently allows a great wealth of sequence information to be obtained in a single LC/MS/MS experiment (Fig. 7.7). The entire procedure can be automated on most commercial instruments, which allows MS/MS operation to be performed in a data-dependent fashion, while the data interpretation step is frequently assisted by database searches. The latter allows peptides and proteins to be identified even if the fragmentation patterns contain significant sequence gaps.

### 7.2.1.2 Polypeptide Sequencing: The Top-Down Approach

The top-down approach to polypeptide and protein sequencing completely bypasses the enzymatic degradation step, with all structural information derived from dissociation of the intact protein or polypeptide ion in the gas phase [35]. While this approach has been used successfully by many groups to obtain sequence information on relatively small proteins (<30 kDa), its application to larger proteins is not straightforward even when high-end instrumentation is used. Nevertheless, successful utilization of this methodology was demonstrated for identification of proteins beyond 500 kDa [36], although such examples remain very rare.

### 7.2.1.3 Posttranslational Modifications

Analysis of PTM of proteins is another area where MS-based methods of analysis are now playing a major role. Due to the labile nature of many PTMs, application of traditional MS/MS approaches to identify specific modifications and localize them within the protein sequence meets only with limited success. For example, collisional activation of glyco- and phospho-peptides frequently leads to facile removal of PTM moieties prior to cleavage of the peptide backbone, leaving no mass tags on amino acid residues that were modified and making their identification a challenging task. However, the electron-based ion dissociation techniques (such as ECD and ETD) allow this conundrum to be solved, since the fragmentation events are highly localized and do not require accumulation of vibrational energy within the peptide ion over an extended period of time (as does CAD).

### 7.2.1.4 Covalent Structure of Other Biopolymers

While the analysis of protein covalent structure by MS-based methods gained the most recognition and is in fact the default approach to obtaining both amino acid sequence information and mapping PTMs, structural analysis of other biopolymers also benefitted enormously from recent improvements in MS hardware and methodology. For example, both MALDI and ESI MS had been used successfully to measure masses of intact RNA molecules and other nucleic acids; however, these analyses frequently present a number of challenges, mostly due to the ability of the phosphodiester backbone of nucleic acids to form adducts with alkali and alkaline earth metal cations. This typically leads to very broad peaks in mass spectra (Fig. 7.8), although extensive buffer exchange into volatile ammonium salts to displace metal cations, desalting by metal chelation or HPLC can improve the spectral quality. Sequence information can be obtained by means of MS/MS, or simply by inducing fragmentation in the ionization source, e.g., by increasing the laser power in MALDI measurements. Dissociation of nucleic acids along the phosphodiester backbone produces structurally diagnostic ions, and these fragment ion ladders (Fig. 7.9) can be used to determine the oligonucleotide sequence. This approach to

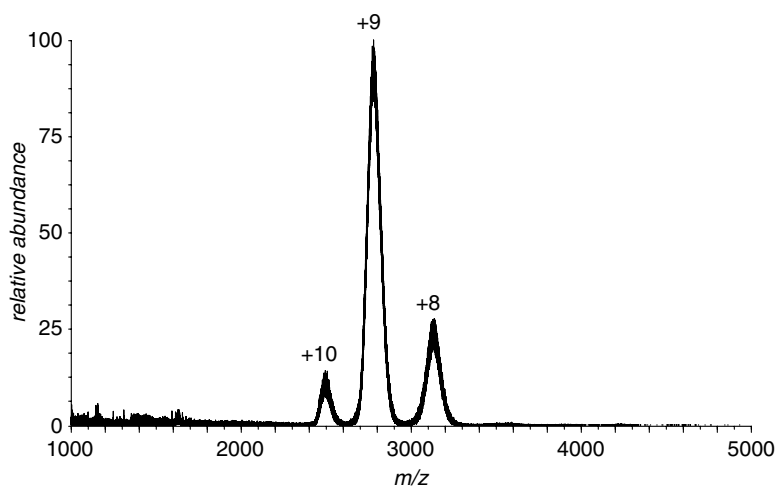


**Fig. 7.8** ESI mass spectrum of  $rRNA^{\text{Thr}}$  acquired with a hybrid quadrupole/TOF MS (10  $\mu\text{M}$  in 20 mM ammonium acetate)

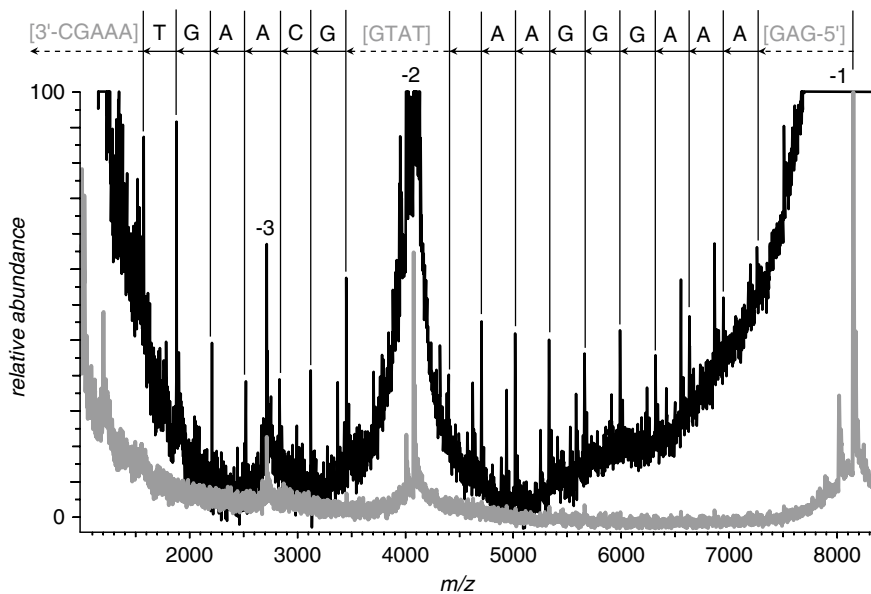


**Fig. 7.9** Prompt fragmentation in MALDI MS: UV-MALDI spectra of an oligonucleotide strand acquired at increased (*top* trace) and moderate laser power. Adapted with permission from [132]

oligonucleotide sequencing is analogous to how peptide fragmentation patterns reveal the amino acid sequence (*vide supra*), although it currently remains practical only for relatively short oligonucleotides.

MS/MS methods can also be applied to obtain information on covalent structure of another type of biopolymer, polysaccharides, although these analyses tend to be less straightforward. Dissociation of polypeptide and short oligonucleotide ions tends to follow well-defined pathways, primarily occurring along the backbone. This conveniently generates structurally diagnostic fragments from which the sequence of the intact biopolymer can be derived. By contrast, dissociation of carbohydrate ions frequently leads to much more complex fragmentation patterns. Chemical bond fission commonly occurs not only between saccharide units but also across the glycosidic ring [37], and multiple rearrangement pathways are available to activated species that render analysis of tandem MS data extremely complex. Further complication arises due to the fact that unlike polypeptides and oligonucleotides, polysaccharides in general are not linear polymers, and the presence of multiple branching points makes the interpretation of MS/MS data a challenging task. Data analysis can be simplified by inducing fragmentation of polysaccharide ions with low-energy collisional activation, which typically leads to dissociation of glycosidic bonds, while leaving the rings intact. Fragmentation processes are also strongly influenced by the nature of the parent ion (alkali metal cationized species produce different fragmentation patterns compared to protonated species). Additional information can be also gained by using various chemical derivatization techniques.

Glycopeptides are another area of great interest and their structural analysis entails localization of glycosylation sites within the polypeptide chain in addition to structural studies of the carbohydrate moieties. Glycosylation site analysis is typically carried out by identifying glycopeptides among proteolytic fragments (e.g., by comparing peptide maps for intact and de-glycosylated protein). If peptide mapping of de-glycosylated protein is not feasible (e.g., due to poor solubility of the carbohydrate-free form of the protein), glycopeptides can be identified in the digest of intact glycoprotein by observing characteristic losses (e.g., 162 Da for hexose residues) in survey MS/MS spectra obtained with low-energy CID of peptide ions, since the labile nature of glycosidic bonds in the gas phase leads to their facile dissociation (*vide supra*). Precise localization of glycosylation sites can be accomplished with electron-based ion fragmentation techniques, as they preferentially cleave peptide backbone, leaving the carbohydrate chains mostly intact [38]. Complete determination of structure (especially with novel glycans) frequently requires the use of orthogonal methods, such as NMR and X-ray crystallography in addition to MS [39].

### 7.3 Analysis of Higher Order Structure with MS Tools

The ability of various MS-based techniques to examine covalent structure of proteins, other biopolymers and their derivatives also makes them indispensable in the studies of the higher order structure and conformational dynamics of such macromolecular

systems, which rely on various chemical probes (such as chemical labeling and cross-linking studies, to be considered later in this section). Furthermore, the unique ability of ESI to generate biomolecular ions directly from solutions kept under physiologically relevant conditions provides other opportunities to examine higher order architecture, dynamics and interactions of biopolymers, as detailed below.

### ***7.3.1 Direct ESI MS Measurements: Characterization of Non-covalent Interactions by ESI MS***

Both ESI and MALDI are rightfully credited as being soft ionization techniques, since they allow intact biopolymers to be transferred from a condensed phase to the vacuum without damaging their covalent structure. Furthermore, it was recognized soon after the introduction of these techniques into the mainstream of bioanalysis that ESI is also capable of generating ions representing intact non-covalent macromolecular complexes if the transition from solution to the gas phase is carried out under mild desolvation conditions in the ESI MS interface. The two parameters that are most critical for the survival of non-covalent complexes upon this transition are the ESI interface temperature and the electrical field in the ion desolvation region, which determines the average kinetic energy of ions undergoing frequent collisions with neutral molecules in this region. Keeping these parameters at relatively low levels allows the composition and stoichiometry of macromolecular assemblies to be determined reliably and with minimal sample consumption (Fig. 7.10). Not only can such experiments provide information on the stoichiometry of multi-protein complexes [40–44], but they may also reveal the presence of smaller ligands (e.g., metal ions and small organic molecules) within these non-covalent assemblies (see the right-hand panel in Fig. 7.10).

Reducing the efficiency of ion desolvation to ensure the survival of non-covalent complexes in ESI MS is needed in order not only to avoid collisional excitation of these species in the gas phase but also to preserve a layer of residual solvent molecules and small counterions, which are often critical for the survival of large macromolecular complexes in the gas phase [45, 46]. A frequent (and unfortunate) consequence of less-than-optimal ion desolvation in ESI MS interface is a decrease of the accuracy of mass measurements, a problem that can be dealt with very effectively by supplementing mild ESI MS measurements with those carried out under harsher conditions [47]. Although the latter step leads to partial dissociation of non-covalent complexes in the gas phase (Fig. 7.11), the surviving assemblies have lower residual solvation, and a stepwise increase of the electrostatic field in the interface region eventually results in dissociation of cofactors from the subunits, thereby allowing low molecular weight species present in each subunit to be identified and the stoichiometry established.

The ability of ESI MS to preserve non-covalent interactions has been used in the past two decades in numerous studies aimed at establishing quaternary structure of protein complexes [48]. These range from relatively modest structures to large

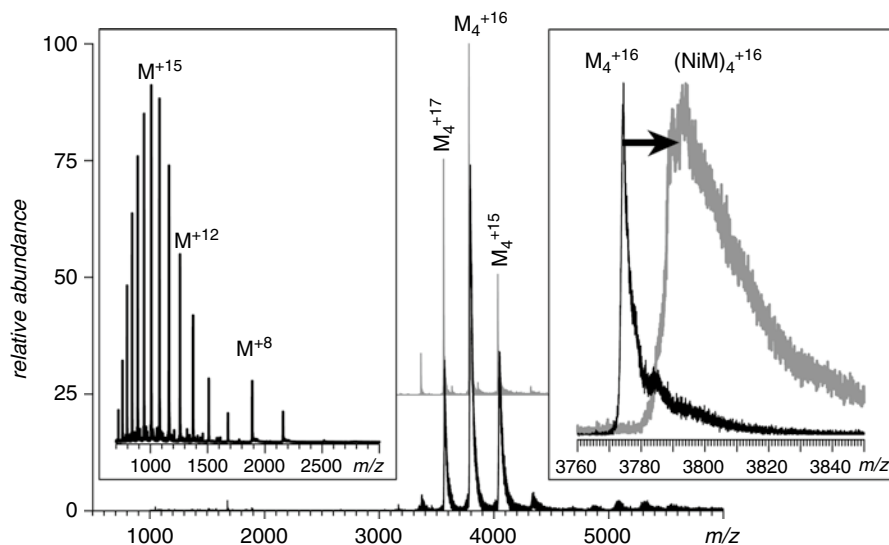


**Fig. 7.10** ESI mass spectra of the apo- (gray trace) and holo- (black trace) forms of a regulatory metalloprotein NikR from *E. coli*. The main panel shows the spectra acquired under near-native conditions, when both forms assume a tetrameric structure, while the denaturing conditions (inset on the left-hand side) result in complete loss of the physiologically relevant quaternary structure and reveal only the presence of monomeric polypeptide chains. The detailed view of ionic peaks of NikR at charge state +16 (inset on the right-hand side) shows the mass difference between the ions representing the apo- and holo-forms, revealing the presence of a single metal ion in each protein subunit of holo-NikR

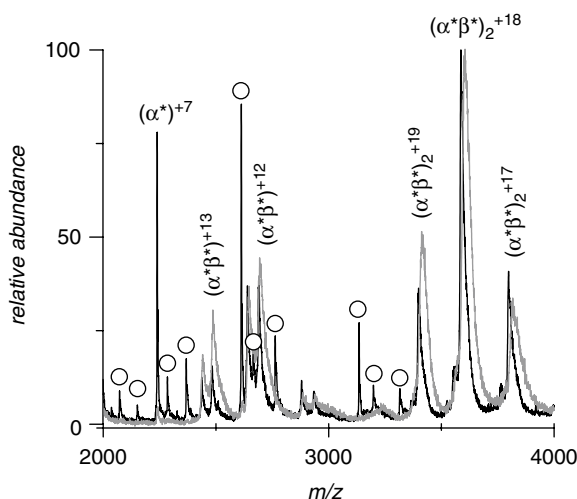
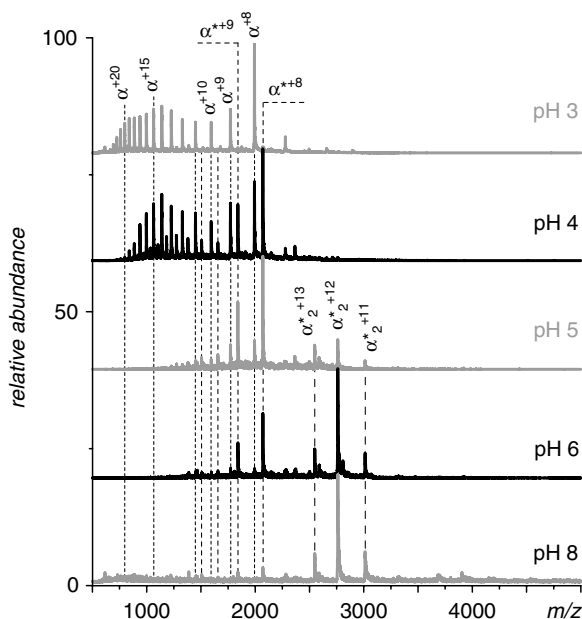


**Fig. 7.11** ESI mass spectra of bovine hemoglobin acquired under very mild desolvation conditions (gray trace) to preserve all non-covalent complexes and with elevated collisional activation in the ESI interface (black trace) to enhance ionic desolvation. Note the mass shifts of ionic peaks corresponding to tetramers  $(\alpha^*\beta^*)_2$  and dimers  $\alpha^*\beta^*$  due to removal of a substantial fraction of residual solvent molecules. Products of gas phase fragmentation are indicated with white circles (not observed under the mild desolvation conditions)

**Fig. 7.12** ESI MS monitoring of acid-induced dissociation and unfolding of homo-dimeric hemoglobin from *Scapharca* (data courtesy of Prof. Wendell P. Griffith, University of Toledo)



macromolecular assemblies whose molecular weight exceeds 1 MDa, such as intact ribosomes [49] and viral capsids [43]. This approach has also been extremely successful in probing other types of physiologically relevant non-covalent interactions, such as protein–receptor binding [50]. ESI MS can also be used to monitor changes in the composition of non-covalent associations in response to environmental factors (such as solvent composition, protein concentration, etc.). This is illustrated in Fig. 7.12 with acid-induced dissociation of dimeric hemoglobin from a mollusk *Scapharca*, where the onset of subunit dissociation clearly manifests itself via the appearance of the ionic signal representing globin monomers. Consequent dissociation of the heme group from the polypeptide chain is manifested by a mass shift of globin monomer ions corresponding to a loss of ca. 617 Da. Early stages of protein aggregation can also be monitored by ESI MS, e.g., by observing appearance of oligomeric protein ions in ESI MS in response to heat stress [51].

### 7.3.2 Ionic Charge State Distribution as an Indicator of Protein Compactness in Solution

So far, our discussion has been focused solely on changes of the ionic mass in ESI MS as an indicator of the changes in the protein architecture in solution. However,

careful examination of ESI MS data presented in Fig. 7.12 reveals another interesting phenomenon in addition to the dimer-to-monomer transition triggered by the acidification of the protein solution. Unlike the charge state distribution of dimer ions ( $\alpha^*$ )<sub>2</sub>, which remains narrow and contains only three charge states (+11, +12, and +13) as long as the dimer ions can be detected in the mass spectra, the charge state distributions of the monomer ions (both with and without the heme group,  $\alpha^*$  and  $\alpha$ ) evolve as the solvent conditions change and become very convoluted below pH 5. The distributions of ionic charges of both of these species at pH 4 are bimodal, a feature that is usually attributed to the coexistence of two or more protein conformations in solution [9]. Native or near-native protein structures are usually very compact, and they can accommodate only a limited number of charges upon their transfer from solution to the gas phase. At the same time, even partial unfolding of a polypeptide chain results in an increase of the solvent-accessible surface area, which allows a significantly higher number of charges to be accommodated by the protein upon its transfer to the gas phase. Native and nonnative protein states often coexist at equilibrium under mildly denaturing conditions; in such situations protein ion charge state distributions in ESI MS become bimodal (as can be seen in the two top panels in Fig. 7.12), reflecting the presence of both native and denatured states. Therefore, dramatic changes of protein charge state distributions often serve as gauges of large-scale conformational changes.

The less compact the protein becomes, the higher the extent of multiple charging of the ions representing these conformers in ESI MS: as can be seen in Fig. 7.12, continuing acidification of the protein solution results in expansion of the charge state envelope of globin monomers (e.g., the mass spectrum acquired at pH 3 contains charge states +25 and higher, which are not present in the spectrum acquired at pH 4). This behavior may be indicative of the presence of several nonnative conformers in solution; however, making a distinction between the contributions made by such (partially) unfolded species to the total ionic signal is not very straightforward. Therefore, changes in the protein ion charge state distributions are frequently regarded as qualitative indicators of re- or denaturation that do not provide much information beyond loss or gain of the native fold.

This problem can be addressed at least in some cases using a procedure that utilizes chemometric tools to extract semiquantitative data on multiple protein conformational isomers coexisting in solution under equilibrium [52, 53]. Experiments are carried out by acquiring an array of spectra over a range of both near-native and denaturing conditions to ensure adequate sampling of various protein states and significant variation of their respective populations within the range of experimental conditions. The total number of protein conformers sampled in the course of the experiment can be determined by subjecting the set of collected spectra to singular value decomposition, SVD [54]. The ionic contributions of each conformer to the total signal can then be determined by using a supervised minimization routine. Application of this method to several small model proteins has yielded a picture of protein behavior consistent with that based



on the results of earlier studies that utilized a variety of orthogonal biophysical approaches [53, 55–59].

### 7.3.3 *Hydrogen/Deuterium Exchange MS*

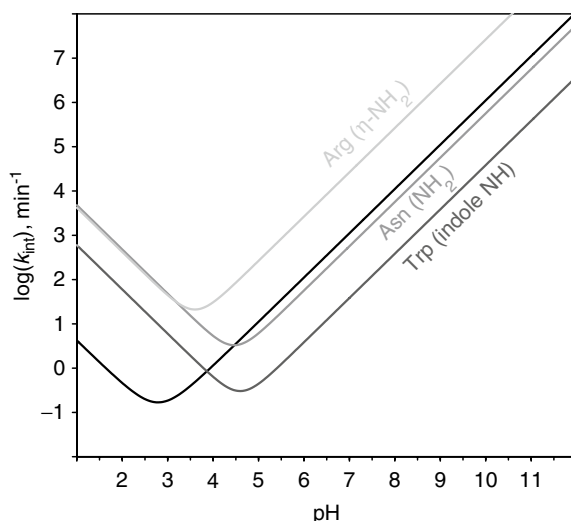
Perhaps one of the most popular and powerful MS-based experimental tools that is now widely used to study protein architecture and conformational dynamics is *hydrogen-deuterium exchange (HDX)*. The analytical value of HDX as a tool for probing macromolecular structure was recognized almost immediately after the discovery of deuterium [60] and subsequent development of the methods of production of heavy water. Initial studies of the exchange reactions between organic molecules and  $^2\text{H}_2\text{O}$  carried out by Bonhoeffer and colleagues indicated that the exchange rate is very high for hetero-atoms (e.g.,  $-\text{OH}$  groups), while the hydrogen atoms attached to carbon atoms (e.g.,  $-\text{CH}_3$  groups) do not undergo exchange [61]. As early as mid-1950s, Hvidt and Linderstrøm-Lang used HDX exchange to measure solvent accessibility of labile hydrogen atoms as a probe of polypeptide structure [62, 63], and Burley et al. suggested that the extent of deuterium incorporation into a protein molecule can be measured by monitoring its mass increase [64]. However, it was not until much later that the advent of ESI and MALDI MS dramatically expanded the range of biopolymers for which the extent of deuterium incorporation could be measured by monitoring the protein mass evolution directly under a variety of conditions [65].

While MS is not the only means of detection that can be used for HDX measurements (high-resolution NMR is another popular choice), MS does offer several important advantages, namely faster time scale, tolerance to high-spin ligands and cofactors, ability to monitor the exchange in a conformer-specific fashion, as well as much more forgiving molecular weight limitations. The ability of MS to handle larger proteins and their complexes is particularly important when compared to high-field NMR, which still has limited application for proteins larger than ca. 30 kDa. Another significant advantage offered by ESI MS is its superior sensitivity, which allows many experiments to be carried out using only minute quantities of proteins.

#### 7.3.3.1 *Basic Principles of Protein HDX*

HDX targets all labile hydrogen atoms (i.e., those attached to nitrogen atoms at the backbone amides and heteroatoms at polar/charged side chains), although many labile hydrogen atoms would not readily undergo HDX due to their involvement in hydrogen bonding network or sequestration from the solvent in the protein interior. Therefore, protein HDX involves two different types of reactions: (1) reversible protein unfolding that disrupts the H-bonding network and/or exposes buried segments to solvent and (2) isotope exchange at individual unprotected sites. Since protein

**Fig. 7.13** Intrinsic exchange rates of several types of labile hydrogen atoms as functions of solution pH. Reproduced with permission from [132]

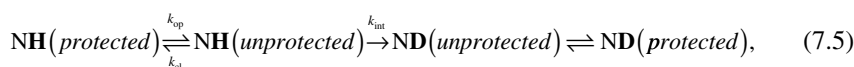


unfolding (either local or global) is a prerequisite for exchange at the sites that are protected in the native conformation, HDX reactions serve as a reliable and sensitive indicator of the unfolding events (*protection* means either involvement in the hydrogen bonding network or sequestration from solvent in the protein core). However, conformation and dynamics are not the only determinants of the HDX kinetics. Even in the absence of any protection, the exchange kinetics of a labile hydrogen atom is strongly dependent on the nature of the functional group. Furthermore, the exchange rate is strongly influenced by a variety of extrinsic factors, most notably solution pH and temperature, and the intrinsic rate constant can be expressed as [66]

$$k_{\text{int}} = k_{\text{acid}}[H^+] + k_{\text{base}}[OH^-] + k_w \quad (7.4)$$

The pH dependence of the cumulative intrinsic exchange rate for several types of labile hydrogen atoms, calculated based on the data compiled by Dempsey [66] is presented in Fig. 7.13.

Backbone amide hydrogen atoms constitute a particularly interesting class of labile hydrogen atoms due to their uniform distribution throughout the protein sequence, which makes them very convenient reporters of protein dynamics at the amino acid residue level (proline is the only naturally occurring amino acid lacking an amide hydrogen atom). Therefore, it is not surprising that the majority of HDX MS experiments are concerned with the exchange of the backbone amide hydrogen atoms. The mathematical formalism that is often used to describe HDX kinetics of backbone amides was introduced several decades ago and is based upon a simple two-state kinetic model [67]:



where  $k_{op}$  and  $k_{cl}$  are the rate constants for the opening (unfolding) and closing (refolding) events that expose/protect a particular amide hydrogen to/from exchange with the solvent.

In most HDX studies the exchange-incompetent state of the protein is considered to be its native state. The exchange-competent state is thought of as a nonnative structure, which can be either fully unfolded (random coil) or partially unfolded (intermediate states). Alternatively, it can represent a structural fluctuation within the native conformation, which exposes an otherwise protected amide hydrogen to solvent transiently through *local unfolding* or “structural breathing” without large-scale structure loss [68, 69]. Transitions between different nonnative states under equilibrium conditions are usually ignored in mathematical treatments of HDX, since the majority of HDX measurements are carried out under native or near-native conditions.

### 7.3.3.2 Global HDX MS Measurements

HDX MS measurements can provide information on *global protection* by measuring the deuterium content of the entire protein, rather than the exchange kinetics of individual amide hydrogen atoms (as done by high-resolution HDX NMR). Still, interpretation of HDX MS data often utilizes the kinetic model (7.5) by making an implicit assumption that NH(protected) and NH(unprotected) represent groups of amides, rather than individual amides that become unprotected upon transition from one state to another. Two extreme cases are usually considered: a situation when  $k_{cl} \gg k_{int}$  and  $k_{cl} \ll k_{int}$ . The former case (referred to as the *EX2 exchange regime*) is commonly observed under native or near-native conditions, when each unfolding event is very brief, and its lifetime ( $1/k_{cl}$ ) is much shorter than the characteristic time of exchange of an unprotected labile hydrogen atom ( $1/k_{int}$ ). In this case the probability of exchange for even a single amide during an unfolding event will be very low, and the overall rate of exchange will be defined by both the frequency of unfolding events ( $k_{op}$ ) and the probability of exchange during a single opening event:

$$k^{HDX} = k_{op} \cdot (k_{int} / k_{cl}) = k_{int} \cdot K, \quad (7.6)$$

where  $K$  is an effective equilibrium constant for the unfolding reaction, which is determined by the free energy difference between the two states of the protein. The overall exchange rate constant  $k^{HDX}$  in this case is a cumulative rate of exchange, i.e., an ensemble-averaged rate of deuterium incorporation into a molecule, and is measured as a mass shift of the isotopic cluster of a protein ion as a function of HDX time.

The opposite extreme ( $k_{cl} \ll k_{int}$ ) is observed either when the protein is placed under denaturing conditions (which dramatically decreases the refolding rate  $k_{cl}$ ), or by increasing the intrinsic exchange rate (e.g., by elevating the protein solution pH—see Fig. 7.13). As a result, the lifetime of the unprotected states become long enough to allow all exposed labile hydrogen atoms to be exchanged during a single unfolding event. In this case (commonly referred to as the *EX1 exchange regime*) the exchange rate will be determined simply by the rate of protein unfolding:

$$k^{\text{HDX}} = k_{\text{op}} \quad (7.7)$$

HDX MS measurements carried out under the EX1 conditions typically give rise to bi- or multimodal isotopic distributions, where the deuterium content of each part reflects the backbone protection levels of distinct protein conformers. This gives HDX MS the unique ability to visualize and track multiple protein states that may coexist in solution under equilibrium [70].

### 7.3.3.3 Local HDX MS Measurements

Replacement of each hydrogen with a deuterium (or vice versa) results in a protein mass change of about 1 Da, which makes MS a very sensitive and reliable detector of the progress of protein HDX reactions. Mass measurements of proteins undergoing HDX are usually carried out following rapid acidification of the protein solution to pH 2.5–3 and lowering the temperature to 0–4 °C, which results in significant deceleration of the chemical (intrinsic) exchange rates of backbone amide hydrogen atoms (see Fig. 7.13). These conditions, known as *HDX quenching* or *slow exchange conditions*, also result in unfolding of most proteins. Since the intrinsic exchange rates of labile side chain hydrogen atoms are not decelerated as significantly as those for backbone amides, all information on the side chain protection is generally lost during this step, leaving a single HDX reporter for each amino acid residue (again, with the exception of proline residues). Another fortunate consequence of quench-induced protein denaturation is dissociation of all non-covalently bound ligands (ranging from metal cations and small organic molecules to other biopolymers) from the protein. Therefore, measuring the protein mass under these conditions provides information only on the protein conformation and stability, rather than composition of non-covalent complexes formed by the protein and its ligands. In addition to characterizing protein conformation and stability globally, the protein can be digested with an acidic protease (e.g., pepsin) under the slow exchange conditions, and MS (usually following quick desalting and fast LC separation) can be used to measure the deuterium content of each proteolytic fragment. This produces information on protein conformation and dynamics at the local level. A typical workflow diagram of an HDX MS experiment is shown in Fig. 7.14.

Spatial resolution offered by HDX MS is usually limited only by the extent of proteolysis, which (along with other sample-handling steps) must be performed relatively quickly under the slow exchange conditions to avoid occurrence of significant *back-exchange* prior to MS measurements of the deuterium content of individual peptide fragments. In general, a large number of proteolytic fragments, particularly overlapping ones, would lead to greater spatial resolution, and hence more precise localization of the structural regions which have undergone exchange. In some cases, this may allow the backbone amide protection patterns to be determined at single-residue resolution [71], although such instances remain very rare. Supplementation of enzymatic digestion with peptide ion fragmentation in the gas phase may also enhance the spatial resolution of HDX MS measurements [72], but

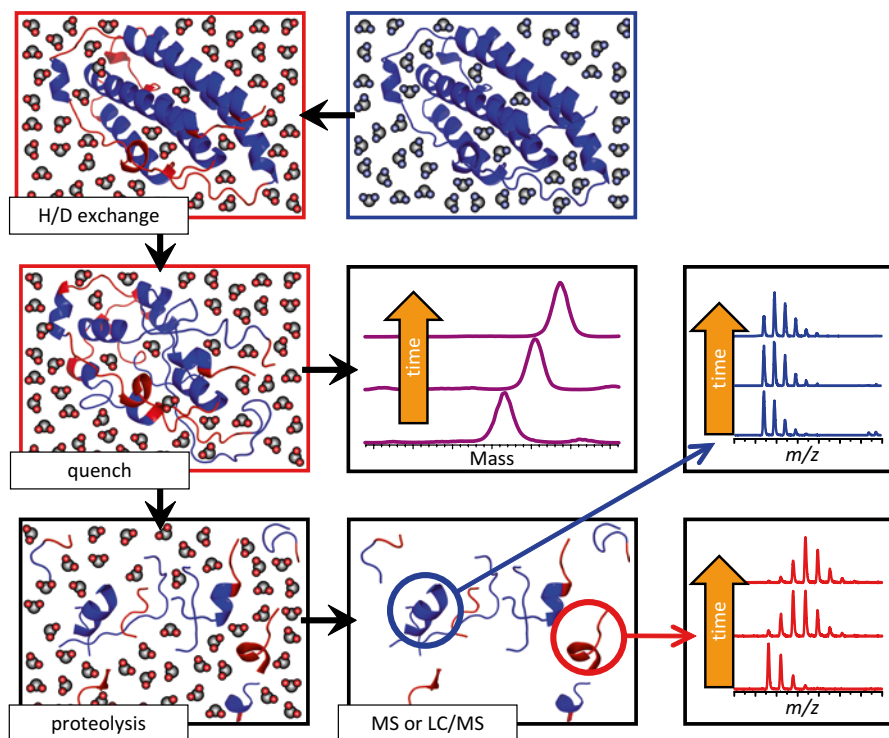


**Fig. 7.14** Schematic representation of HDX MS work flow to examine protein higher order structure and conformational dynamics. The exchange is initiated by placing the unlabeled protein into a D<sub>2</sub>O-based solvent system (e.g., by a rapid dilution). Unstructured and highly dynamic protein segments undergo fast exchange (blue and red colors represent protons and deuterons, respectively). Following the quench step (rapid solution acidification and temperature drop), the protein loses its native conformation, but the spatial distribution of backbone amide protons and deuterons across the backbone is preserved (all labile hydrogen atoms at side chains undergo fast back-exchange at this step). Rapid clean-up followed by MS measurement of the protein mass reports the total number of backbone amide hydrogen atoms exchanged under native conditions (a global measure of the protein stability under native conditions), as long as the quench conditions are maintained during the sample work-up and measurement. Alternatively, the protein can be digested under the quench conditions using acid-stable protease(s), and LC/MS analysis of masses of individual proteolytic fragments will provide information on the backbone protection of corresponding protein segments under the native conditions. Reproduced with permission from [133]

this technique has yet to be commonly accepted due to concerns over the possibility of introducing gas phase artifacts [73]. In addition to limited spatial resolution, HDX MS measurements frequently suffer from incomplete sequence coverage, especially when applied to larger and extensively glycosylated proteins. Proteins with multiple disulfide bonds constitute another class of targets for which adequate sequence coverage is difficult to achieve, although certain changes in experimental protocol can alleviate this problem, at least for smaller proteins [74]. Typically, an

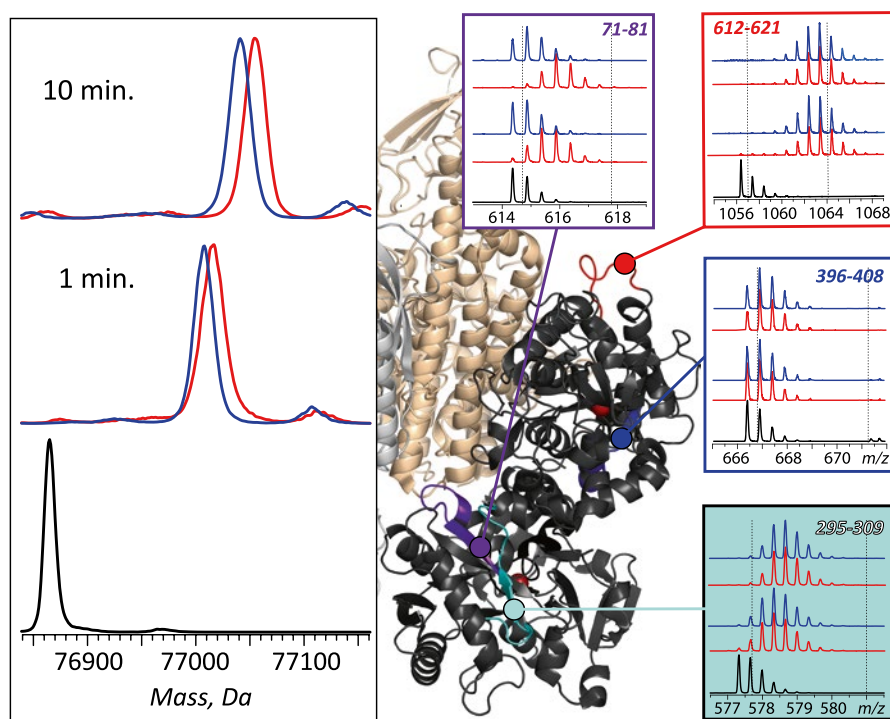


**Fig. 7.15** Localization of the receptor binding interface on the surface of human serum transferrin (Tf) with HDX MS. *Left* panel: HDX MS of Tf (global exchange) in the presence (*blue*) and the absence (*red*) of the receptor. The exchange was carried out by diluting the protein stock solution 1:10 in exchange solution (100 mM  $\text{NH}_4\text{HCO}_3$  in  $\text{D}_2\text{O}$ , pH adjusted to 7.4) and incubating for a certain period of time as indicated on each diagram followed by rapid quenching (lowering pH to 2.5 and temperature to near 0 °C). The *black* trace shows unlabeled protein. *Right* panel: isotopic distributions of representative peptic fragments derived from Tf subjected to HDX in the presence (*blue*) and the absence (*red*) of the receptor and followed by rapid quenching, proteolysis, and LC/MS analysis. *Dotted lines* indicate deuterium content of unlabeled and fully exchanged peptides. Colored segments within the Tf/receptor complex show localization of these peptic fragments (based on the low-resolution structure of the complex). Adapted with permission from [73]

80 % level of sequence coverage is considered good, although significantly lower levels may also be adequate, depending on the context of the study.

An example of using HDX MS to probe protein conformation and dynamics, as well as to identify binding interface regions in a protein/receptor complex is shown in Fig. 7.15, where hydrogen exchange kinetics are measured for a diferric form of human serum transferrin ( $\text{Fe}_2\text{Tf}$ ) alone and in complex with its cognate receptor. Both Tf-metal and Tf-receptor complexes dissociate under the slow exchange conditions prior to MS analysis; therefore, the protein mass evolution in each case reflects solely deuterium uptake in the course of exchange in solution (left panel in

Fig. 7.15). The extra protection afforded by the receptor binding to Tf persists over an extended period of time, and it may be tempting to assign it to shielding of labile hydrogen atoms at the protein–receptor interface. However, this view is overly simplistic, as the conformational effects of protein binding are frequently felt well beyond the interface region. The difference in the backbone protection levels of receptor-free and receptor-bound forms of Fe<sub>2</sub>Tf appears to grow during the initial hour of exchange, reflecting significant stabilization of Fe<sub>2</sub>Tf higher order structure by the bound receptor. Indeed, while the fast phase of HDX is often ascribed to frequent local fluctuations (transient perturbations of higher order structure) affecting relatively small protein segments, the slower phases of HDX usually reflect relatively rare, large-scale conformational transitions, such as transient partial or complete protein unfolding [75].

Evolution of the deuterium content of various peptic fragments of Fe<sub>2</sub>Tf (right panel in Fig. 7.15) reveals a wide spectrum of protection, which is distributed very unevenly across the protein sequence. While some peptides exhibit nearly complete protection of backbone amides (e.g., segment [396–408] sequestered in the core of the protein C-lobe), exchange in many others is fast (e.g., peptide [612–621] in the solvent-exposed loop of the C-lobe). The influence of receptor binding on backbone protection is also highly localized. While most segments appear to be unaffected by the receptor binding, there are several regions where exchange kinetics are noticeably decelerated (e.g., segment [71–81] of the N-lobe, which contains several amino acid residues that form the Tf/receptor interface according to the available model of the complex based on low-resolution cryo-EM data [76]).

#### 7.3.3.4 Local HDX MS Measurements Using a Top-Down Approach

An alternative method to probe HDX kinetics locally that does not require proteolytic fragmentation prior to MS analysis takes advantage of the ability of modern mass spectrometers to produce a wealth of structural information in tandem (MS/MS) experiments at the protein level (the top-down approach to protein sequencing discussed in Sect. 7.2.1.2). One unique advantage of the top-down HDX MS measurements that cannot be matched by the classic bottom-up type experiments is the ability to obtain protection patterns in a conformer-specific fashion. This can be accomplished by fragmenting subpopulations of protein ions, which are mass selected to include species with deuterium content representative of a certain protein conformer (this, of course, can be accomplished only under conditions favoring EX1 exchange regime in solution, so that different protein conformers can be visualized based on different levels in deuterium incorporation).

Despite the great promise of top-down HDX MS [73], applications of this technique have been limited so far due to concerns over the possibility of hydrogen scrambling accompanying dissociation of protein ions in the gas phase. Several recent studies demonstrated that the extent of scrambling is indeed negligible when ECD [77] or ETD [78] is used as a means of generating fragment ions in top-down HDX MS experiments. In addition to allowing hydrogen scrambling to be



eliminated in the top-down HDX MS experiments, both ECD and ETD appear to be superior to collisional activation in terms of generating a larger number of structurally diagnostic ions [79], allowing both better sequence coverage and enhanced spatial resolution to be achieved. In fact, in some cases it becomes possible to generate patterns of deuterium distribution across the protein backbone down to the single-residue level [77, 80].

### 7.3.4 Chemical Cross-Linking of Proteins

*Chemical cross-linking* is a classical biochemical technique used to characterize protein conformation, and it benefits tremendously from the ability of modern MS to detect and identify the products of the cross-linking reactions. Cross-linking reagents are generally classified based on their chemical specificity and the length of the *spacer arm* (cross-bridge formed between the two cross-linked sites when the reaction is complete). The chemical specificity of a cross-linker determines the overall pool of reactive groups within the polypeptide that may participate in the cross-linking reaction. Eight out of the 20 amino acid side chains are chemically reactive with good selectivity: Arg (guanidiny), Lys ( $\epsilon$ -amine), Asp and Glu ( $\beta$ - and  $\gamma$ -carboxylates), Cys (sulfhydryl), His (imidazole), Met (thioether), Trp (indoyl), and Tyr (phenolic hydroxylate) [81], although virtually no reagent is absolutely group-specific.

*Monofunctional* (or *zero-length*) *cross-linkers* induce direct coupling of two functional groups of the protein without incorporating any extraneous material into the protein. Obviously, this becomes possible only if the two functional groups are in a very close proximity to each other, in which case the cross-linker operates as a condensing agent, resulting in the cross-linked residues becoming directly inter-joined. *Bifunctional cross-linkers*, on the other hand, contain two reagents linked through a spacer arm, thus allowing the coupling of functional groups whose separation does not exceed the spacer's length. Bifunctional reagents are further subdivided into *homobifunctional* (i.e., both cross-linking groups within the reagent targeting the same reactive groups on the protein) and *heterobifunctional* cross-linkers (coupling different functional groups on the protein).

Heterobifunctional cross-linkers may incorporate a *photosensitive* (nonspecific) *reagent* in addition to a conventional (group-specific) functionality. Such photosensitive groups react indiscriminately upon activation by irradiation. Once the specific end of such a cross-linker is anchored to an amino acid residue, the photo-reactive end can be used to probe the surroundings of this amino acid. More information on chemical cross-linkers can be found in several excellent reviews on the subject [82–85] and an outstanding book by Wong [81].

MS-assisted cross-linking studies usually aim to identify the pairs of cross-linked residues within the protein or protein complex. Such information may provide through-space distance constraints that are extremely valuable for defining both tertiary (intra-subunit cross-links) and quaternary (inter-subunit cross-links) organization of the protein when no other structural information is available. Confident



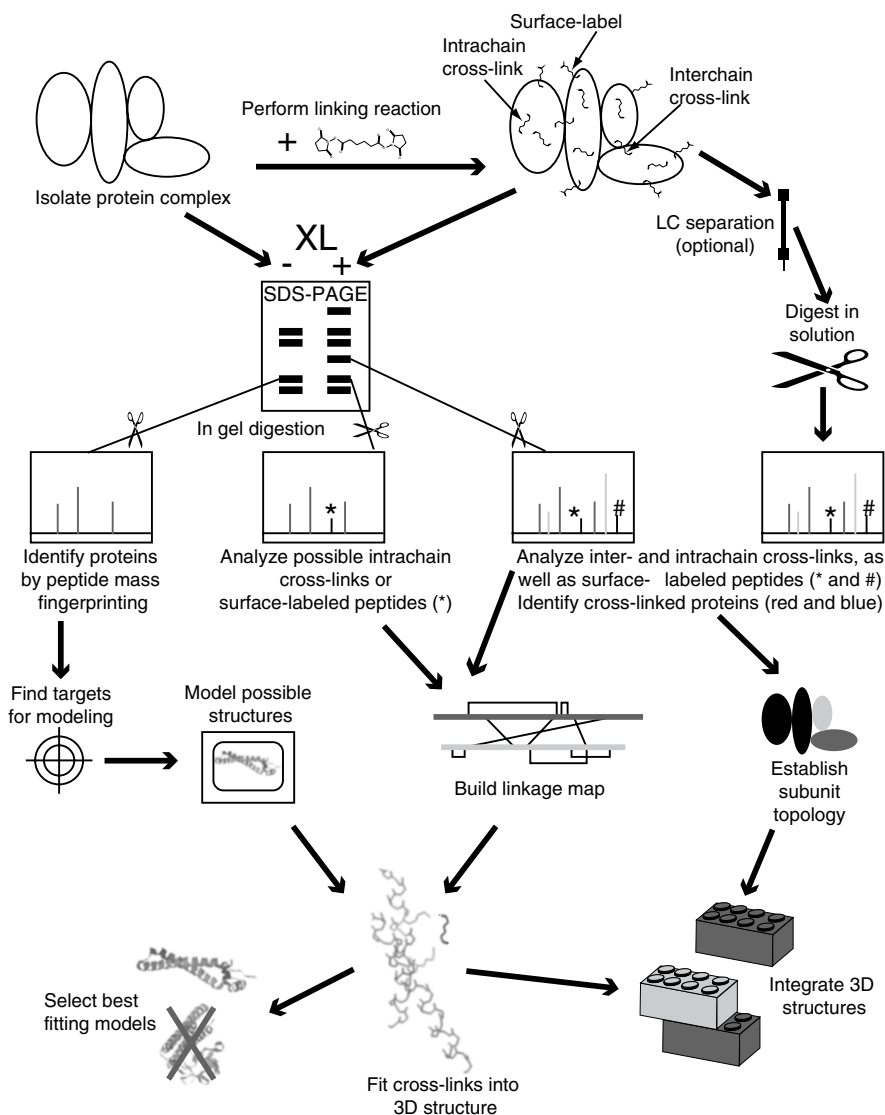


**Fig. 7.16** A schematic diagram of workflow of cross-linking a multi-protein complex and integrating the levels of information into a three-dimensional model of the structure. Reprinted with permission from [86]

assignment of the pairs of coupled residues within the cross-linked protein(s) is a rather challenging experimental task. A combination of proteolysis, separation methods (e.g., LC), and mass spectrometry (and, particularly, MS/MS) provides perhaps the most elegant and efficient way of solving this problem [84, 86, 87]. Figure 7.16 shows a workflow of a typical cross-linking experiment. Separation of

proteolytic fragments prior to MS analysis usually results in significant improvements in sensitivity by eliminating possible signal suppression effects that may otherwise result in discrimination against larger (cross-linked) fragments [86]. Although peptide mapping alone can sometimes lead to confident identification of the cross-linked residues [88–90], unambiguous assignment of cross-linked peptides requires that MS/MS sequencing of the proteolytic fragments be carried out [91, 92].

As the amount of information deduced from cross-linking experiments increases, so does the complexity of data interpretation, and the tools of bioinformatics become absolutely essential to interpret the results of cross-linking experiments [93]. The task of assigning the cross-linked peptides and localizing the modification sites can be greatly assisted by a variety of automated algorithms that use MS or MS/MS data as input [86, 93]. The database mining approach to identification of cross-linked peptides mentioned earlier in this section [94] can be used even in a situation when the protein complex composition is not known a priori [95]. More sophisticated approaches, such as Xlink-Identifier [96], allow the cross-linking sites to be localized with high precision by identifying inter- and intra-peptide cross-links in addition to dead-end products and underivatized peptides. Another comprehensive cross-linking data analysis platform is MS-Bridge [97], which is part of the Protein Prospector MS data analysis suite. While these platforms were developed to support label-free analyses, several other algorithms have been developed to take advantage of isotopically tagged cross-linkers [98–101]. A comprehensive list of data analysis programs developed for interpretation of the results of cross-linking experiments can be found in a recent review article [87].

### 7.3.5 Chemical Labeling

*Selective chemical modification* [102] is another classical biophysical technique that benefitted tremendously from the recent progress in MS hardware and methodology. The unique ability of MS to localize both shielded and modified residues within a protein molecule transformed the chemical labeling technique to a highly efficient probe of higher order macromolecular structure. Most chemical modifications of an amino acid side chain alter the protein mass, hence the appeal of mass spectrometry as a readout tool for the outcome of such experiments. Interpretation of the MS and MS/MS data on chemically modified proteins is usually relatively straightforward (as compared to the analysis of cross-linked proteins) and greatly benefits from a vast arsenal of experimental tools developed to analyze PTM of proteins.

In a typical experiment, protein exposure to a certain chemical probe is followed by digestion of the modified protein with a suitable proteolytic enzyme, and mass mapping of the fragment peptides. The position(s) of the modified residue(s) within each proteolytic fragment can be reliably established using tandem mass spectrometry, as the presence of a chemical modification manifests itself as a break or a shift in the ladder of the expected fragment ions. Inter-subunit binding topology is usually determined by comparing modification patterns of the protein obtained in the

presence and in the absence of its binding partner [103], although the two experiments can be combined if the labeling agent contains a stable isotope tag [104]. An added benefit of using isotope tags is the easy recognition and quantitation of label-containing peptides and their fragments in MS and MS/MS spectra.

In addition to selective chemical labeling, protein conformation can also be characterized with *non-selective labeling*, which also offers an additional advantage of being able to determine the solvent exposure of several types of amino acids simultaneously in a single experiment. So far, the hydroxyl radical  $\text{OH}^\bullet$  is the most popular nonspecific modifier, due to its ability to induce side chain oxidation for a variety of amino acids and the relative ease of its generation in solution. Although the hydroxyl radical is relatively nondiscriminatory, and can modify virtually all types of amino acid side chains [105], the most susceptible to  $\text{OH}^\bullet$  attack are side chains containing sulfur atoms (Cys and Met), including disulfide-bonded Cys residues. The least susceptible to the  $\text{OH}^\bullet$  attack are Gly, Asn, Asp, and Ala, whose reactivity is three orders of magnitude lower than that of Cys. The great variety of OH-induced oxidation products and the large number of potential targets place a premium on the ability to detect and identify the modification sites. Usually proteolytic degradation of the modified protein followed by LC/MS and MS/MS analyses is needed in order to achieve reliable identification of oxidatively labeled amino acid side chains [105–107]. As is the case with the analysis of the results of chemical cross-linking experiments, extracting useful information from covalent labeling experimental data greatly benefits from automation [108].

One important consideration that must be kept in mind when designing or interpreting the results of both selective chemical and nonselective (oxidative) labeling experiments relates to the fact that structural information derived from such measurements is reliable only if the protein maintains its conformation during the experiment [109]. Most chemical modifications result in changing the charge of the labeled amino acid residue, and a significant alteration of the protein surface charge distribution may obviously result in conformational change. Furthermore, even the sheer size of many groups used as covalent labels may interfere with the protein's ability to maintain its conformation by creating steric constraints, but despite the extreme seriousness of this concern, less than half of all studies utilizing selective chemical labeling that were conducted in the past decade employed any means of ensuring the integrity of protein higher order structure during the experiments [109]. Artifacts associated with the influence of chemical modifications on the protein conformation can be avoided by limiting the number of modifications to one per protein molecule (in this way, reactivity of any amino acid side chain is determined only by the unperturbed protein structure [109]). While the extent of protein modification can be kept low to minimize conformational perturbations [106], this inevitably has a negative impact on the sensitivity of the measurements. A very elegant solution to this problem is based upon the realization that the extent of artifacts introduced by chemical labeling depends not only on the extent of protein oxidation but also on the time frame of the oxidation process [110]. Should this reaction time window be significantly narrow compared to the time scale of conformational changes (sub-millisecond range), the labeling pattern would reflect only the native

structure of the protein, even if the number of modified sites on each protein is significant. These considerations form the basis of a highly successful technique called fast photochemical oxidation of proteins (FPOP), where solvent-exposed amino acid residues are oxidized by  $\text{OH}^\bullet$  radicals produced by the photolysis of  $\text{H}_2\text{O}_2$ . FPOP is designed to limit protein exposure to radicals to  $<1\ \mu\text{s}$  by employing a pulsed laser for initiation to produce the radicals and a radical-scavenger to limit their lifetimes [111].

### 7.3.6 Higher Order Structure of Other Biopolymers

#### 7.3.6.1 DNA Higher Order Structure

Until very recently, there was substantially less interest in developing MS-based methods to probe higher order structure of DNA molecules, since they were thought to adopt only relatively few favored conformations (unlike proteins). Nevertheless, apart from the Watson–Crick double helical DNA structure (which is also known as the B-form DNA), a large number of other structures have been shown to exist, which either differ from the B conformation by arrangement of the two strands in the double helix (the so-called A and Z conformations), or by incorporating more than just two strands (e.g., triplexes and quadruplexes) [112]. Several of these non-classical DNA conformations came to prominence recently either due to their importance in designing novel therapeutic strategies [113] or for their potential use in nano-technological applications, e.g., as scaffolds of building blocks in molecular devices [114].

Similar to the studies of protein non-covalent complexes discussed in Sect. 7.3.1, ESI MS can also be used to obtain mass spectra of intact double-stranded DNA [115], as well as tetramers of short oligonucleotides that assemble to form G-quadruplex-like structures [116, 117]. Direct ESI MS measurements have also been successful as a means of monitoring DNA interaction with small ligands, most notably DNA-targeting drugs. Numerous studies have been published where this technique was employed to evaluate not only the stoichiometry of such non-covalent complexes but also their binding affinity (reviewed in [118, 119]). Information on DNA higher order structure can also be provided by using selective chemical labeling and chemical cross-linking combined with MS analysis of the products, a technique similar to those discussed in Sects. 7.3.4 and 7.3.5. While a range of chemical probes for DNA structure are available [120], mass spectrometry has not been a prominent player in this field until recently. This is beginning to change, with the realization of the enormous potential of this technique as a tool to provide rapid and sensitive characterization of the reaction products of both cross-linking [121] and chemical labeling [122].

### 7.3.6.2 Higher Order Structure and Dynamics of RNA

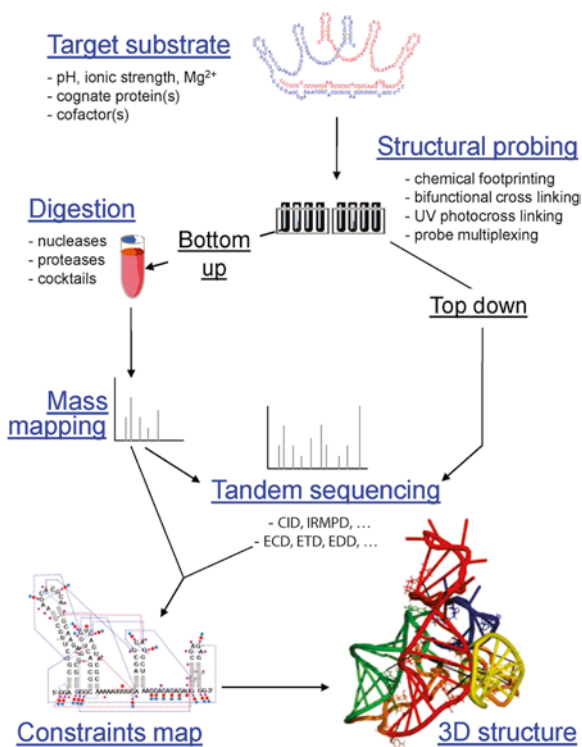
Unlike DNA, RNA molecules are known to form a rich variety of secondary and tertiary structures that make them extremely versatile, but the biophysical tools for the study of RNA structure are still somewhat less mature than those for studies of proteins. Among other things, HDX measurements have been employed to investigate structure in RNA using NMR [123, 124] and Raman spectroscopy [125]. Although the glycosidic hydrogen atoms exchange rapidly, it is possible to measure protection of the base amino and imino protons that are involved in structure, which provides information about base-pairing as opposed to bases that are involved in single stranded regions and/or bulges. While these exchange reactions are still too fast to be followed in solution by MS, hydrogen/deuterium exchange can be carried out in the gas phase, a method that shows promise for determining structural elements in oligonucleotides [126, 127].

Hydroxyl radical modification has been very successful as a means of probing oligonucleotide structure in solution, although other chemical modifications can be employed to investigate RNA structure as well. A variety of reagents are available that act as solvent accessibility probes, since they are unable to modify nucleotides involved in base-pairing, stacking, or other tertiary interactions. A similar approach can be used to probe RNA structure and RNA–protein interactions [128, 129], where the extent of chemical labeling is monitored by MS, and subsequent digestion with ribonuclease and analysis of the resulting fragments by high resolution MS allows the modification sites to be localized. In addition to solvent accessibility information, chemical labeling can also provide a measure of structural flexibility of RNA molecules [130]. Recently, a technique dubbed MS3D [92] was introduced to probe higher order structure of RNA, the workflow for which is shown in Fig. 7.17 [131]. Essentially, the structure of the polynucleotide under native conditions is probed by a series of chemical footprinting reagents. These solvent accessibility probes have varying specificity for different bases, and their reactivity is limited by the presence of base-pairing, stacking, or other tertiary interactions. Following labeling, the sites of modification are determined by a combination of bottom-up (digestion with ribonucleases) or top-down (gas phase fragmentation) methods. Additional MS/MS techniques can be used to pinpoint the labeled site to the individual nucleotide.

## 7.4 Current Challenges and Future Directions

Mass spectrometry has truly become a routine analytical tool in diverse fields of molecular biophysics and structural biology, although many areas remain where it still faces significant challenges. For examples, several classes of proteins are notoriously difficult to analyze using MS-based approaches, and chief among them are membrane proteins. The strongly hydrophobic or amphipathic character of membrane proteins results in their general insolubility, which makes any experimental

**Fig. 7.17** General workflow for 3D-structure determination of nucleic acids based on structural probing and MS analysis (MS3D). The substrate is probed under ideal conditions preserving its native fold. Characterization of the ensuing covalent adducts can be performed under denaturing conditions, following either bottom-up or top-down approaches. The positions of probed nucleotides provide spatial constraints that are summarized on 2D maps, from which a complete, all-atom 3D structure can be readily generated through established molecular modeling protocols. Reproduced with permission from [134]



study of these proteins an extremely difficult undertaking. Mass spectrometry is not an exception, since even sequencing of membrane proteins is often problematic due to their extreme instability in solutions that are commonly used in MS work. Another obstacle to MS analysis is presented by protein aggregation, a process that is now at the cross-hair of biophysical research due to its obvious importance in the etiology of the so-called conformational diseases (such as Alzheimer's and Parkinson's), as well as its importance in the burgeoning biotechnology and biopharmaceutical sectors. Finally, mass spectrometry increasingly finds itself in the midst of the on-going paradigm shift affecting the entire field of biophysics and structural biology, namely breaking away from the reductionist description of various biophysical and biochemical phenomena, and embracing the enormous complexity of living systems. While MS in general played a very visible role in catalyzing this shift (particularly in the fields of proteomics and interactomics), many more traditional MS-based approaches to study architecture and dynamics of biological molecules were slow to respond. Clearly, biological MS is and will continue to be a very dynamic area of research, which will certainly continue to evolve and make important contributions to the Life Sciences in general, and advance the fields of biophysics and structural biology in particular.

**Acknowledgements** Preparation of this manuscript was supported in part by a grant from the National Institutes of Health R01 GM061666. The authors are grateful to Prof. Wendell P. Griffith (University of Toledo), Dr. Rinat R. Abzalimov (University of Massachusetts-Amherst), Dr. Guanbo Wang (Universiteit Utrecht), and Dr. Shunhai Wang (Regeneron, Inc.) for sharing unpublished data sets for this manuscript.

## References

1. Thompson JJ (1912) Further experiments on positive rays. *Philos Mag* 24(140):209–253
2. Fenn JB, Mann M, Meng CK, Wong SF, Whitehouse CM (1989) Electrospray ionization for mass spectrometry of large biomolecules. *Science* 246:64–71
3. Fenn JB (2003) Electrospray wings for molecular elephants (Nobel lecture). *Angew Chem Int Ed Engl* 42(33):3871–3894
4. Dole M, Cox HL, Gieniec J (1973) Electrospray mass spectroscopy. *Adv Chem Ser* 125:73–84
5. Thomson BA, Iribarne JV, Dziedzic PJ (1982) Liquid ion evaporation/mass spectrometry/mass spectrometry for the detection of polar and labile molecules. *Anal Chem* 54:2219–2224
6. Alexandrov ML, Baram GI, Gall LN, Krasnov NV, Kusner YS, Mirgorodskaya OA, Nikolaev VI, Shkurov VA (1985) Formation of beams of quasi-molecular ions of peptides from solutions. *Bioorg Khim* 11(5):700–704
7. Alexandrov ML, Baram GI, Gall LN, Grachev MA, Knorre VD, Krasnov NV, Kusner YS, Mirgorodskaya OA, Nikolaev VI, Shkurov VA (1985) Application of a novel mass spectrometric method to sequencing of peptides. *Bioorg Khim* 11(5):705–708
8. Meng CK, Mann M, Fenn JB (1988) Of protons or proteins. *Z Phys D* 10:361–368
9. Kaltashov IA, Abzalimov RR (2008) Do ionic charges in ESI MS provide useful information on macromolecular structure? *J Am Soc Mass Spectrom* 19(9):1239–1246
10. Tanaka K, Ido Y, Akita S, Yoshida Y, Yoshida T (1987) Detection of high mass molecules by laser desorption time-of-flight mass spectrometry. In *Proceedings of the second Japan-China joint symposium on mass spectrometry*, Bando Press, Osaka, pp 185–188
11. Karas M, Hillenkamp F (1988) Laser desorption ionization of proteins with molecular masses exceeding 10,000 daltons. *Anal Chem* 60(20):2299–2301
12. Biemann K (1988) Contributions of mass spectrometry to peptide and protein structure. *Biomed Environ Mass Spectrom* 16(1–12):99–111
13. Biemann K (1990) Appendix 5. Nomenclature for peptide fragment ions (positive ions). *Methods Enzymol* 193:886–887
14. McLuckey SA, Wells JM (2001) Mass analysis at the advent of the 21st century. *Chem Rev* 101(2):571–606
15. Jennings KR (2000) The changing impact of the collision-induced decomposition of ions on mass spectrometry. *Int J Mass Spectrom* 200(1–3):479–493
16. Little DP, Speir JP, Senko MW, O'Connor PB, McLafferty FW (1994) Infrared multiphoton dissociation of large multiply charged ions for biomolecule sequencing. *Anal Chem* 66(18):2809–2815
17. Zubarev RA, Kelleher NL, McLafferty FW (1998) Electron capture dissociation of multiply charged protein cations. *J Am Chem Soc* 120:3265–3266
18. Syka JE, Coon JJ, Schroeder MJ, Shabanowitz J, Hunt DF (2004) Peptide and protein sequence analysis by electron transfer dissociation mass spectrometry. *Proc Natl Acad Sci U S A* 101(26):9528–9533
19. Zubarev RA (2003) Reactions of polypeptide ions with electrons in the gas phase. *Mass Spectrom Rev* 22(1):57–77

20. Savitski MM, Kjeldsen F, Nielsen ML, Zubarev RA (2006) Complementary sequence preferences of electron-capture dissociation and vibrational excitation in fragmentation of polypeptide polycations. *Angew Chem Int Ed* 45(32):5301–5303
21. Drees T, Paul W (1964) Beschleunigung von elektronen in einem plasmabetatron. *Z Chem* 180(4):340–361
22. March RE (1997) An introduction to quadrupole ion trap mass spectrometry. *J Mass Spectrom* 32(4):351–369
23. Jonscher KR, Yates JR 3rd (1997) The quadrupole ion trap mass spectrometer—a small solution to a big challenge. *Anal Biochem* 244(1):1–15
24. March RE (1998) Quadrupole ion trap mass spectrometry: theory, simulation, recent developments and applications. *Rapid Commun Mass Spectrom* 12(20):1543–1554
25. March RE (2000) Quadrupole ion trap mass spectrometry: a view at the turn of the century. *Int J Mass Spectrom* 200(1–3):285–312
26. Cotter RJ (1999) The new time-of-flight mass spectrometry. *Anal Chem* 71(13):445A–451A
27. Mamyrin BA (2001) Time-of-flight mass spectrometry (concepts, achievements, and prospects). *Int J Mass Spectrom* 206(3):251–266
28. Cotter RJ (1997) Time-of-flight mass spectrometry: instrumentation and applications in biological research. American Chemical Society, Washington, DC
29. Uphoff A, Grottemeyer J (2003) The secrets of time-of-flight mass spectrometry revealed. *Eur J Mass Spectrom* 9(3):151–164
30. Makarov A (2000) Electrostatic axially harmonic orbital trapping: a high-performance technique of mass analysis. *Anal Chem* 72(6):1156–1162
31. Hardman M, Makarov AA (2003) Interfacing the orbitrap mass analyzer to an electrospray ion source. *Anal Chem* 75(7):1699–1705
32. Marshall AG, Hendrickson CL (2002) Fourier transform ion cyclotron resonance detection: principles and experimental configurations. *Int J Mass Spectrom* 215(1–3):59–75
33. Horn DM, Ge Y, McLafferty FW (2000) Activated ion electron capture dissociation for mass spectral sequencing of larger (42 kDa) proteins. *Anal Chem* 72(20):4778–4784
34. Fenselau C (1991) Beyond gene sequencing: analysis of protein structure with mass spectrometry. *Annu Rev Biophys Biophys Chem* 20(1):205–220
35. McLafferty FW, Breuker K, Jin M, Han X, Infusini G, Jiang H, Kong X, Begley TP (2007) Top-down MS, a powerful complement to the high capabilities of proteolysis proteomics. *FEBS J* 274(24):6256–6268
36. Karabacak NM, Li L, Tiwari A, Hayward LJ, Hong PY, Easterling ML, Agar JN (2009) Sensitive and specific identification of wild type and variant proteins from 8 to 669 kDa using top-down mass spectrometry. *Mol Cell Proteomics* 8(4):846–856
37. Domon B, Costello CE (1988) A systematic nomenclature for carbohydrate fragmentations in FAB-MS/MS spectra of glycoconjugates. *Glycoconj J* 5:397–409
38. Mirgorodskaya E, Roepstorff P, Zubarev RA (1999) Localization of O-glycosylation sites in peptides by electron capture dissociation in a Fourier transform mass spectrometer. *Anal Chem* 71(20):4431–4436
39. Marino K, Bones J, Kattla JJ, Rudd PM (2010) A systematic approach to protein glycosylation analysis: a path through the maze. *Nat Chem Biol* 6(10):713–723
40. Loo JA (1997) Studying noncovalent protein complexes by electrospray ionization mass spectrometry. *Mass Spectrom Rev* 16(1):1–23
41. Hernandez H, Robinson CV (2007) Determining the stoichiometry and interactions of macromolecular assemblies from mass spectrometry. *Nat Protoc* 2(3):715–726
42. Yin S, Loo JA (2009) Mass spectrometry detection and characterization of noncovalent protein complexes. *Methods Mol Biol* 492:273–282
43. Heck AJR (2008) Native mass spectrometry: a bridge between interactomics and structural biology. *Nat Methods* 5(11):927–933
44. Uetrecht C, Versluis C, Watts NR, Roos WH, Wuite GJL, Wingfield PT, Steven AC, Heck AJR (2008) High-resolution mass spectrometry of viral assemblies: molecular composition and stability of dimorphic hepatitis B virus capsids. *Proc Natl Acad Sci USA* 105(27):9216–9220



45. Abzalimov RR, Frimpong AK, Kaltashov IA (2006) Gas-phase processes and measurements of macromolecular properties in solution: on the possibility of false positive and false negative signals of protein unfolding. *Int J Mass Spectrom* 253(3):207–216
46. Freeke J, Robinson CV, Ruotolo BT (2009) Residual counter ions can stabilise a large protein complex in the gas phase. *Int J Mass Spectrom* 298(1–3):91–98
47. Lei QP, Cui X, Kurtz DM Jr, Amster IJ, Chernushevich IV, Standing KG (1998) Electrospray mass spectrometry studies of non-heme iron-containing proteins. *Anal Chem* 70(9):1838–1846
48. Heck AJ, Van Den Heuvel RH (2004) Investigation of intact protein complexes by mass spectrometry. *Mass Spectrom Rev* 23(5):368–389
49. Gordiyenko Y, Robinson CV (2008) The emerging role of MS in structure elucidation of protein-nucleic acid complexes. *Biochem Soc Trans* 36(4):723–731
50. Leverence R, Mason AB, Kaltashov IA (2010) Noncanonical interactions between serum transferrin and transferrin receptor evaluated with electrospray ionization mass spectrometry. *Proc Natl Acad Sci U S A* 107(18):8123–8128
51. Wang G, Abzalimov RR, Kaltashov IA (2011) Direct monitoring of heat-stressed biopolymers with temperature-controlled electrospray ionization mass spectrometry. *Anal Chem* 83(8):2870–2876
52. Dobo A, Kaltashov IA (2001) Detection of multiple protein conformational ensembles in solution via deconvolution of charge state distributions in ESI MS. *Anal Chem* 73:4763–4773
53. Mohimen A, Dobo A, Hoerner JK, Kaltashov IA (2003) A chemometric approach to detection and characterization of multiple protein conformers in solution using electrospray ionization mass spectrometry. *Anal Chem* 75(16):4139–4147
54. Hendler RW, Shrager RI (1994) Deconvolutions based on singular value decomposition and the pseudoinverse: a guide for beginners. *J Biochem Biophys Methods* 28(1):1–33
55. Borysik AJH, Radford SE, Ashcroft AE (2004) Co-populated conformational ensembles of  $b_2$ -microglobulin uncovered quantitatively by electrospray ionization mass spectrometry. *J Biol Chem* 279(26):27069–27077
56. Frimpong AK, Abzalimov RR, Uversky VN, Kaltashov IA (2010) Characterization of intrinsically disordered proteins with electrospray ionization mass spectrometry: conformational heterogeneity of alpha-synuclein. *Proteins* 78(3):714–722
57. Testa L, Brocca S, Šamalikova M, Santambrogio C, Alberghina L, Grandori R (2011) Electrospray ionization-mass spectrometry conformational analysis of isolated domains of an intrinsically disordered protein. *Biotechnol J* 6(1):96–100
58. Natalello A, Benetti F, Doglia SM, Legname G, Grandori R (2011) Compact conformations of  $\alpha$ -synuclein induced by alcohols and copper. *Proteins* 79(2):611–621
59. Brocca S, Testa L, Sobott F, Samalikova M, Natalello A, Papaleo E, Lotti M, De Gioia L, Doglia SM, Alberghina L, Grandori R (2011) Compaction properties of an intrinsically disordered protein: Sic1 and its kinase-inhibitor domain. *Biophys J* 100(9):2243–2252
60. Urey HC, Brickwedde FG, Murphy GM (1932) A hydrogen isotope of mass 2. *Phys Rev* 39:164–165
61. Bonhoeffer KF, Klar R (1934) Über den austausch von schweren wasserstoffatomen zwischen wasser und organischen verbindungen. *Naturwissenschaften* 22:45
62. Hvidt A, Linderstrom-Lang K (1954) Exchange of hydrogen atoms in insulin with deuterium atoms in aqueous solutions. *Biochim Biophys Acta* 14(4):574–575
63. Hvidt A, Linderstrom-Lang K (1955) The kinetics of deuterium exchange of insulin with  $D_2O$ . An amendment. *Biochim Biophys Acta* 16:168–169
64. Burley RW, Nicholls CH, Speakman JB (1955) The crystalline/amorphous ratio of keratin fibres. Part II. The hydrogen-deuterium exchange reaction. *J Text Inst* 46:T427–T432
65. Katta V, Chait BT (1991) Conformational changes in proteins probed by hydrogen-exchange electrospray-ionization mass spectrometry. *Rapid Commun Mass Spectrom* 5(4):214–217
66. Dempsey CE (2001) Hydrogen exchange in peptides and proteins using NMR-spectroscopy. *Prog Nucl Magn Reson Spectrosc* 39(2):135–170

67. Hvidt A, Nielsen SO (1966) Hydrogen exchange in proteins. *Adv Protein Chem* 21:287–386
68. Maity H, Lim WK, Rumbley JN, Englander SW (2003) Protein hydrogen exchange mechanism: local fluctuations. *Protein Sci* 12(1):153–160
69. Qian H, Chan SI (1999) Hydrogen exchange kinetics of proteins in denaturants: a generalized two-process model. *J Mol Biol* 286(2):607–616
70. Eyles SJ, Kaltashov IA (2004) Methods to study protein dynamics and folding by mass spectrometry. *Methods* 34(1):88–99
71. Del Mar C, Greenbaum EA, Mayne L, Englander SW, Woods VL Jr (2005) Structure and properties of  $\alpha$ -synuclein and other amyloids determined at the amino acid level. *Proc Natl Acad Sci U S A* 102(43):15477–15482
72. Rand KD, Zehl M, Jensen ON, Jorgensen TJD (2009) Protein hydrogen exchange measured at single-residue resolution by electron transfer dissociation mass spectrometry. *Anal Chem* 81(14):5577–5584
73. Kaltashov IA, Bobst CE, Abzalimov RR (2009) H/D exchange and mass spectrometry in the studies of protein conformation and dynamics: is there a need for a top-down approach? *Anal Chem* 81(19):7892–7899
74. Burke JE, Karbarz MJ, Deems RA, Li S, Woods VL, Dennis EA (2008) Interaction of group IA phospholipase A2 with metal ions and phospholipid vesicles probed with deuterium exchange mass spectrometry. *Biochemistry* 47(24):6451–6459
75. Xiao H, Hoerner JK, Eyles SJ, Dobo A, Voigtman E, Mel'cuk AI, Kaltashov IA (2005) Mapping protein energy landscapes with amide hydrogen exchange and mass spectrometry: I. A generalized model for a two-state protein and comparison with experiment. *Protein Sci* 14(2):543–557
76. Cheng Y, Zak O, Aisen P, Harrison SC, Walz T (2004) Structure of the human transferrin receptor-transferrin complex. *Cell* 116(4):565–576
77. Pan J, Han J, Borchers CH, Konermann L (2008) Electron capture dissociation of electrosprayed protein ions for spatially resolved hydrogen exchange measurements. *J Am Chem Soc* 130(35):11574–11575
78. Abzalimov RR, Kaplan DA, Easterling ML, Kaltashov IA (2009) Protein conformations can be probed in top-down HDX MS experiments utilizing electron transfer dissociation of protein ions without hydrogen scrambling. *J Am Soc Mass Spectrom* 20(8):1514–1517
79. Zubarev RA, Zubarev AR, Savitski MM (2008) Electron capture/transfer versus collisionally activated/induced dissociations: solo or duet? *J Am Soc Mass Spectrom* 19(6):753–761
80. Pan J, Han J, Borchers CH, Konermann L (2009) Hydrogen/deuterium exchange mass spectrometry with top-down electron capture dissociation for characterizing structural transitions of a 17 kDa protein. *J Am Chem Soc* 131:12801–12808
81. Wong SS (1991) *Chemistry of protein conjugation and cross-linking*. CRC, Boca Raton, FL
82. Han K-K, Richard C, Delacourte A (1984) Chemical cross-links of proteins by using bifunctional reagents. *Int J Biochem* 16(2):129–145
83. Mattson G, Conklin E, Desai S, Nielander G, Savage MD, Morgensen S (1993) A practical approach to crosslinking. *Mol Biol Rep* 17(3):167–183
84. Andrea S (2006) Chemical cross-linking and mass spectrometry to map three-dimensional protein structures and protein-protein interactions. *Mass Spectrom Rev* 25(4):663–682
85. Petrotchenko EV, Borchers CH (2010) Crosslinking combined with mass spectrometry for structural proteomics. *Mass Spectrom Rev* 29(6):862–876
86. Back JW, de Jong L, Muijsers AO, de Koster CG (2003) Chemical cross-linking and mass spectrometry for protein structural modeling. *J Mol Biol* 331(2):303–313
87. Jin Lee Y (2008) Mass spectrometric analysis of cross-linking sites for the structure of proteins and protein complexes. *Mol Biosyst* 4(8):816–823
88. Yang T, Horejsh DR, Mahan KJ, Zaluzec EJ, Watson TJ, Gage DA (1996) Mapping cross-linking sites in modified proteins with mass spectrometry: an application to cross-linked hemoglobins. *Anal Biochem* 242(1):55–63

89. Bennett KL, Kussmann M, Bjork P, Godzwon M, Mikkelsen M, Sorensen P, Roepstorff P (2000) Chemical cross-linking with thiol-cleavable reagents combined with differential mass spectrometric peptide mapping—a novel approach to assess intermolecular protein contacts. *Protein Sci* 9(8):1503–1518
90. Sinz A, Wang K (2001) Mapping protein interfaces with a fluorogenic cross-linker and mass spectrometry: application to nebulin-calmodulin complexes. *Biochemistry* 40(26):7903–7913
91. Yu Z, Friso G, Miranda JJ, Patel MJ, Lo-Tseng T, Moore EG, Burlingame AL (1997) Structural characterization of human hemoglobin crosslinked by bis(3,5-dibromosalicyl) fumarate using mass spectrometric techniques. *Protein Sci* 6(12):2568–2577
92. Young MM, Tang N, Hempel JC, Oshiro CM, Taylor EW, Kuntz ID, Gibson BW, Dollinger G (2000) High throughput protein fold identification by using experimental constraints derived from intramolecular cross-links and mass spectrometry. *Proc Natl Acad Sci U S A* 97(11):5802–5806
93. Leitner A, Walzthoeni T, Kahraman A, Herzog F, Rinner O, Beck M, Aebersold R (2010) Probing native protein structures by chemical cross-linking, mass spectrometry, and bioinformatics. *Mol Cell Proteomics* 9(8):1634–1649
94. Rappsilber J, Siniosoglou S, Hurt EC, Mann M (2000) A generic strategy to analyze the spatial organization of multi-protein complexes by cross-linking and mass spectrometry. *Anal Chem* 72(2):267–275
95. Winters MS, Day RA (2003) Detecting protein-protein interactions in the intact cell of *Bacillus subtilis* (ATCC 6633). *J Bacteriol* 185(14):4268–4275
96. Du X, Chowdhury SM, Manes NP, Wu S, Mayer MU, Adkins JN, Anderson GA, Smith RD (2011) Xlink-Identifier: an automated data analysis platform for confident identifications of chemically cross-linked peptides using tandem mass spectrometry. *J Proteome Res* 10(3):923–931
97. Chu F, Baker PR, Burlingame AL, Chalkley RJ (2010) Finding chimeras: a bioinformatics strategy for identification of cross-linked peptides. *Mol Cell Proteomics* 9(1):25–31
98. Rinner O, Seebacher J, Walzthoeni T, Mueller L, Beck M, Schmidt A, Mueller M, Aebersold R (2008) Identification of cross-linked peptides from large sequence databases. *Nat Methods* 5(4):315–318
99. Gao QX, Xue S, Doneanu CE, Shaffer SA, Goodlett DR, Nelson SD (2006) Pro-CrossLink. Software tool for protein cross-linking and mass spectrometry. *Anal Chem* 78(7):2145–2149
100. Maiolica A, Cittaro D, Borsotti D, Sennels L, Ciferri C, Tarricone C, Musacchio A, Rappsilber J (2007) Structural analysis of multiprotein complexes by cross-linking, mass spectrometry, and database searching. *Mol Cell Proteomics* 6(12):2200–2211
101. Petrotchenko EV, Borchers CH (2010) ICC-CLASS: isotopically-coded cleavable crosslinking analysis software suite. *BMC Bioinformatics* 11:64–73
102. Glazer AN (1970) Specific chemical modification of proteins. *Annu Rev Biochem* 39(1):101–130
103. Hager-Braun C, Tomer KB (2002) Characterization of the tertiary structure of soluble CD4 bound to glycosylated full-length HIVgp120 by chemical modification of arginine residues and mass spectrometric analysis. *Biochemistry* 41(6):1759–1766
104. Hochleitner EO, Borchers C, Parker C, Bienstock RJ, Tomer KB (2000) Characterization of a discontinuous epitope of the human immunodeficiency virus (HIV) core protein p24 by epitope excision and differential chemical modification followed by mass spectrometric peptide mapping analysis. *Protein Sci* 9(3):487–496
105. Xu GH, Chance MR (2007) Hydroxyl radical-mediated modification of proteins as probes for structural proteomics. *Chem Rev* 107(8):3514–3543
106. Konermann L, Stocks BB, Pan Y, Tong X (2010) Mass spectrometry combined with oxidative labeling for exploring protein structure and folding. *Mass Spectrom Rev* 29(4):651–667
107. Roeser J, Bischoff R, Bruins AP, Permentier HP (2010) Oxidative protein labeling in mass-spectrometry-based proteomics. *Anal Bioanal Chem* 397(8):3441–3455

108. Kaur P, Kiselar JG, Chance MR (2009) Integrated algorithms for high-throughput examination of covalently labeled biomolecules by structural mass spectrometry. *Anal Chem* 81(19):8141–8149
109. Mendoza VL, Vachet RW (2009) Probing protein structure by amino acid-specific covalent labeling and mass spectrometry. *Mass Spectrom Rev* 28(5):785–815
110. Hambly D, Gross M (2005) Laser flash photolysis of hydrogen peroxide to oxidize protein solvent-accessible residues on the microsecond timescale. *J Am Soc Mass Spectrom* 16(12):2057–2063
111. Gau BC, Sharp JS, Rempel DL, Gross ML (2009) Fast photochemical oxidation of protein footprints faster than protein unfolding. *Anal Chem* 81(16):6563–6571
112. Suhnel J (2001) Beyond nucleic acid base pairs: from triads to heptads. *Biopolymers* 61(1):32–51
113. Balasubramanian S, Hurley LH, Neidle S (2011) Targeting G-quadruplexes in gene promoters: a novel anticancer strategy? *Nat Rev Drug Discov* 10(4):261–275
114. Krishnan Y, Simmel FC (2011) Nucleic acid based molecular devices. *Angew Chem Int Ed* 50(14):3124–3156
115. Lightwahl KJ, Springer DL, Winger BE, Edmonds CG, Camp DG, Thrall BD, Smith RD (1993) Observation of a small oligonucleotide duplex by electrospray ionization mass spectrometry. *J Am Chem Soc* 115(2):803–804
116. Goodlett DR, Camp DG, Hardin CC, Corregan M, Smith RD (1993) Direct observation of a DNA quadruplex by electrospray ionization mass spectrometry. *Biol Mass Spectrom* 22(3):181–183
117. Rosu F, Gabelica V, Poncelet H, De Pauw E (2010) Tetramolecular G-quadruplex formation pathways studied by electrospray mass spectrometry. *Nucleic Acids Res* 38(15):5217–5225
118. Rosu F, De Pauw E, Gabelica V (2008) Electrospray mass spectrometry to study drug-nucleic acids interactions. *Biochimie* 90(7):1074–1087
119. Brodbelt JS (2010) Evaluation of DNA/ligand interactions by electrospray ionization mass spectrometry. *Annu Rev Anal Chem* 3(1):67–87
120. Millard JT (1999) Molecular probes of DNA structure. *Compr Nat Prod Chem* 7:81–103
121. Smith SI, Brodbelt JS (2010) Rapid characterization of cross-links, mono-adducts, and non-covalent binding of psoralens to deoxyoligonucleotides by LC-UV/ESI-MS and IRMPD mass spectrometry. *Analyst* 135(5):943–952
122. Parr C, Pierce SE, Smith SI, Brodbelt JS (2011) Investigation of the reactivity of oligodeoxynucleotides with glyoxal and KMnO<sub>4</sub> chemical probes by electrospray ionization mass spectrometry. *Int J Mass Spectrom* 304(2–3):115–123
123. Gmeiner WH, Sahasrabudhe P, Pon RT (1995) Use of shaped pulses for semi-selective excitation of imino H-1 resonances in duplex DNA and RNA. *Magn Reson Chem* 33(6):449–452
124. Nonin S, Jiang F, Patel DJ (1997) Imino proton exchange and base-pair kinetics in the AMP-RNA aptamer complex. *J Mol Biol* 268(2):359–374
125. Li TS, Johnson JE, Thomas GJ (1993) Raman dynamic probe of hydrogen-exchange in bean pod mottle virus—base-specific retardation of exchange in packaged ssRNA. *Biophys J* 65(5):1963–1972
126. Hofstadler SA, Sannes-Lowery KA, Griffey RH (2000) Enhanced gas-phase hydrogen–deuterium exchange of oligonucleotide and protein ions stored in an external multipole ion reservoir. *J Mass Spectrom* 35(1):62–70
127. Hofstadler SA, Sannes-Lowery KA, Hannis JC (2005) Analysis of nucleic acids by FTICR MS. *Mass Spectrom Rev* 24(2):265–285
128. Yu E, Fabris D (2003) Direct probing of RNA structures and RNA-protein interactions in the HIV-1 packaging signal by chemical modification and electrospray ionization Fourier transform mass spectrometry. *J Mol Biol* 330(2):211–223
129. Kellersberger KA, Yu E, Kruppa GH, Young MM, Fabris D (2004) Top-down characterization of nucleic acids modified by structural probes using high-resolution tandem mass spectrometry and automated data interpretation. *Anal Chem* 76(9):2438–2445

130. Turner KB, Yi-Brunozzi HY, Brinson RG, Marino JP, Fabris D, Le Grice SFJ (2009) SHAMS: combining chemical modification of RNA with mass spectrometry to examine polypurine tract-containing RNA/DNA hybrids. *RNA* 15(8):1605–1613
131. Fabris D, Yu ET (2010) Elucidating the higher-order structure of biopolymers by structural probing and mass spectrometry: MS3D. *J Mass Spectrom* 45(8):841–860
132. Kaltashov IA, Eyles SJ (2012) *Mass spectrometry in structural biology and biophysics: architecture, dynamics, and interaction of biomolecules*, 2nd edn. Wiley, Hoboken, NJ
133. Bobst CE, Kaltashov IA (2011) Advanced mass spectrometry-based methods for the analysis of conformational integrity of biopharmaceutical products. *Curr Pharm Biotechnol* 12(10):1517–1529
134. Fabris D (2010) A role for the MS analysis of nucleic acids in the post-genomics age. *J Am Soc Mass Spectrom* 21(1):1–13

## Chapter 8

# Single-Molecule Methods

Paul J. Bujalowski, Michael Sherman,  
and Andres F. Oberhauser

**Abstract** Single-molecule methods have emerged as powerful tools in life science research. These techniques allow the detection and manipulation of individual biological molecules and investigate, with unprecedented resolution, their conformations and dynamics at the nanoscale level. These techniques overcome the restrictions of traditional bulk biochemical studies by focusing on individuals of molecules. Here we describe some of the most common single-molecule methods including atomic force microscopy, optical tweezers, and fluorescence microscopy. We also describe the use of cryo-electron microscopy methods to study large molecules and macromolecular assemblies. We outline the principles of operation for each technique and discuss prominent applications.

**Keywords** Single-molecule • Biophysics • Atomic force microscopy • Optical tweezers • Fluorescence microscopy • Electron microscopy

---

P.J. Bujalowski • M. Sherman

Department of Biochemistry and Molecular Biology, University  
of Texas Medical Branch at Galveston, Galveston, TX 77555, USA  
e-mail: pjbjalo@utmb.edu; mbsherma@utmb.edu

A.F. Oberhauser (✉)

Department of Biochemistry and Molecular Biology, University  
of Texas Medical Branch at Galveston, Galveston, TX 77555, USA

Department of Neuroscience and Cell Biology, University  
of Texas Medical Branch at Galveston, Galveston, TX 77555, USA

Sealy Center for Structural Biology and Molecular Biophysics,  
University of Texas Medical Branch at Galveston, Galveston, TX 77555, USA  
e-mail: afoberha@utmb.edu

## 8.1 Introduction

Single-molecule measurement techniques provide fundamental information on the structure and function of biomolecules and are becoming an indispensable tool to understand how biomolecules work. During the last 2 decades this field has grown at an almost exponential rate in terms of biological and biophysical applications. Single-molecule techniques have opened a new field of science that is at the crossroads of several disciplines, namely biology, physics, chemistry, material science, and computer science. Since the development of single-ion channel recording techniques in the 1970s [109], the family of single-molecule methods have expanded significantly to include, among others, optical and magnetic tweezers, atomic force microscopy (AFM), and single-molecule fluorescence. There are two main types of single-molecule methods: (1) those that do not use an external force such as single-molecule fluorescence microscopy or electron microscopy and (2) those imposing an external force to the system through an electric field (e.g., patch-clamp) or a mechanical manipulation (e.g., through tension or torsion). The latter subtype, the so-called single-molecule manipulation techniques, offers a unique opportunity to study the behavior of molecules under an external mechanical force, applied either directly using flexible beams (e.g., AFM, microneedles) or through external-field manipulators (e.g., optical and magnetic tweezers). Single-molecule methods span 5-orders of magnitude in terms of forces, distances, and dynamical ranges. A summary of the features of various methods is provided in Table 8.1 and discussed in greater detail in the different sections of this chapter. Single-molecule methods overcome the restrictions of traditional bulk biochemical studies by focusing not on a population of molecules but on the molecule itself. These methods are often the approach of choice to clarify and better understand the functions of molecular motors, transcription, replication, translation, protein folding, or the structure of membrane proteins. In this chapter we focus on the most commonly used single-molecule methods, namely AFM, optical tweezers, fluorescence microscopy, and single-particle imaging using electron microscopy. We describe their operating principles, practical implementation, and for each method we discuss a few noteworthy examples.

## 8.2 Range of Forces at the Single-Molecule Level

Biomolecules are subject to thermal forces, which are random in nature. When these forces act on small objects like protein nanomachines in solution, they result in what is called Brownian motion. It is through thermal energy that proteins reach the high-energy transition states that are essential in biochemical reactions. The energies involved in protein conformational changes are slightly above thermal energy levels (or thermal noise), typically ranging from  $1 k_B T$  (thermal energy;  $k_B T = 4.1 \text{ pN nm} = 0.6 \text{ kcal/mol}$ , at room temperature, where  $k_B$  is the Boltzmann constant and  $T$  is the absolute temperature) to  $25 k_B T$  (the energy released by ATP hydrolysis) such that the structures are stable enough to prevail at physiological

**Table 8.1** A comparison of several single-molecule methods

Method	Force range (pN)	Length scale range (nm)	Dynamical range (s)	Limitations	Typical applications
AFM	10–10,000	1–10,000	$10^{-3}$ – $10^2$	Random attachment of the force probe	DNA, oligomeric membrane proteins, protein elasticity and folding, mechano-chemistry, receptor–ligand interactions
Optical tweezers	0.1–100	0.1–1,000	$10^{-4}$ – $10^3$	Photodamage long handles	DNA, actin, molecular motors, DNA and RNA polymerases
Single-molecule fluorescence (FRET)	0	1–10	$10^{-4}$ – $10^2$	Dye photobleaching sensitive to orientation	Protein conformational transitions, protein–protein interactions



temperatures. Given that changes in protein conformation are measured in the Ångstrom to nanometer range ( $\text{\AA}$  to nm,  $1 \text{ \AA} = 10^{-10} \text{ m}$ ,  $1 \text{ nm} = 10^{-9} \text{ m}$ ) the relevant biological forces are expected to be in the piconewton range ( $1 \text{ pN} = 10^{-12} \text{ N}$ ). Because proteins are subject to thermal forces, the number of possible conformations is at its maximum when a protein forms a random coil or is denatured. Conformational entropy becomes progressively reduced with the formation of secondary and tertiary structures. Stretching random-coiled proteins in the low-force regime to overcome “entropic forces” requires the application of forces in the order of a few pN, which has been achieved experimentally using single-molecule-manipulation techniques. Several molecular motors such as myosin, kinesin, and RNA or DNA polymerases also generate forces in this range (see examples presented below). The next group consists of “enthalpic forces,” which includes the forces needed to unfold the folded domains of proteins (i.e., intramolecular interactions) as well as those required to overcome specific intermolecular interactions such as ligand/receptor or antigen/antibody. These forces are typically in the 50–300 pN range (at pulling speeds of  $1 \text{ }\mu\text{m/s}$ ). It must be noted that protein mechanical unfolding is typically a nonequilibrium dynamic process and therefore these forces depend on the pulling speed. The typical pulling speeds *in vivo* may in some cases be much lower and therefore the corresponding forces may also be lower. The forces needed to break covalent bonds apart are almost two orders of magnitude larger, in the range of a few nanonewtons ( $1 \text{ nN} = 10^{-9} \text{ N}$ ).

### 8.3 Atomic Force Microscopy Methods

The AFM was first described in 1986 and originally developed as a high resolution imaging tool [17] before it began to be used to probe and manipulate molecules. During the last two and half decades AFM has evolved as a very powerful and versatile tool in biology that can be used, for example, to manipulate and detect single proteins, DNA, or polysaccharides [72, 83, 92, 93, 112, 122, 124, 125], to image single molecules in physiological conditions with nanometer resolution [40, 75, 106], to measure the interaction forces between proteins [24, 45, 103], exocytotic fusion [20, 102], mapping of cell surface receptors [35, 62, 63, 105], and high-speed imaging of molecular motors in action [75]. One of the key advantages of the AFM as a single-molecule technique is the straightforward sample preparation, the ability to conduct imaging and manipulation experiments of biomolecules under physiological relevant conditions and the direct analysis of the dynamics of single molecules or complexes.

#### 8.3.1 Basic Principles

The AFM is a remarkably simple instrument that can measure forces down to few pico-newtons and distances of only few Ångstroms. The AFM consists of two main parts: the scanner (XYZ stage) and an optical head (Fig. 8.1a). The core of

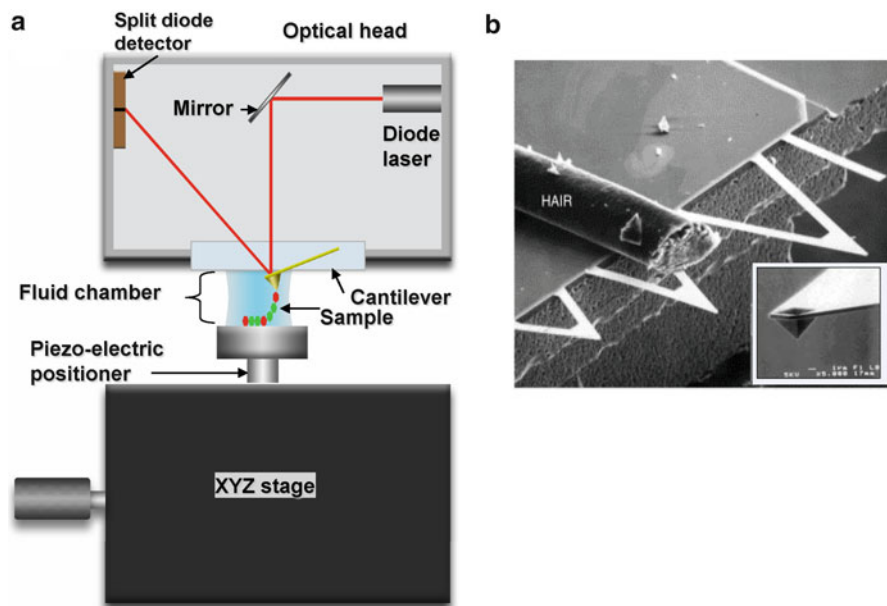


**Fig. 8.1** Schematic diagram of an AFM. (a) The AFM is a remarkably simple instrument that can measure forces down to few pico-newtons and distances of only few angstroms. The AFM consists of two main parts: the scanner (XYZ stage) and an optical head. The heart of the system is a small cantilever that functions as a microscopic spring. When the cantilever is brought into contact with a sample it bends. This bending can be easily detected by shining a laser on the back of the cantilever; the light that bounces off is captured by a photodetector. The optical amplification is such that a tiny deformation of a few nanometers causes a large in the photovoltage of the detector which is then converted into a force signal. (b) A scanning electron microscope image of commercially available AFM cantilevers showing both triangular and beam-shaped cantilevers. A human hair with a diameter of  $\sim 100\ \mu\text{m}$  diameter is included as a size reference. The *inset* shows a higher magnification image of the end of a cantilever showing the tip that has a radius of curvature of  $\sim 10\ \text{nm}$  (obtained with permission from Allison et al. [3])

the system is a small cantilever, a thin and flexible piece of silicon (about  $200\ \mu\text{m}$  in length and  $10\ \mu\text{m}$  in thickness) that works as a microscopic force sensor (Fig. 8.1b). At the very tip of the cantilever there is small stylus, which looks like a pyramid that is very sharp (in fact it may be atomically sharp, Fig. 8.1b). When a cantilever is brought into contact with a sample, by means of a three-dimensional nano-positioner, it bends. In order to track this bending a laser beam is shined on the back of the cantilever; the laser light that bounces off is captured by a position-sensitive photodetector that tracks the position of the laser spot (Fig. 8.1a). The optical amplification is such that a tiny deformation of the cantilever, of only a few nanometers, causes a large change in the photovoltage of the detector. In order to measure force one simply uses the relationship that relates the force that a spring develops when is stretched. The proportionality factor is the stiffness of the cantilever (or spring constant,  $k_c$ ) which is calculated from Hooke's law,  $F = k_c \Delta x$ , where  $\Delta x$  represents the cantilever deflection. A typical spring

constant is about 100 pN/nm, so a bending of only 10 Å (the size of three water molecules) causes a change in force of 100 pN (the noise level of the system is about 1 Å). For normal topographic imaging, the probe tip is brought into continuous or intermittent contact with the sample and raster-scanned over the surface. Several AFM imaging modes can be used which vary mainly in the way the tip of the cantilever is moved over the sample. The most popular is the contact mode in which topographical information is obtained by two methods: (1) by measuring the cantilever deflection while the sample is scanned at constant height or (2) by measuring cantilever displacement while maintaining the cantilever deflection constant using a feedback loop. In the intermittent mode the cantilever is oscillated at its resonant frequency and the amplitude and phase are recorded while scanning the sample.

### 8.3.2 *Imaging Single Biomolecules Using AFM*

One of the most stunning applications of the AFM is the imaging of single membrane proteins at subnanometer resolution under physiologically relevant conditions [39, 46]. The three-dimensional structure of gap junction channels obtained using cryo-electron microscopy at a resolution of 7.5 Å and X-ray crystallography at 3.5 Å resolution provided direct evidence for alpha-helical folding of four trans-membrane domains within each connexin subunit [90, 145]. AFM provided complementary information on the structural features of the extracellular surface of single gap junctions obtained physiological buffer conditions [65]. Later work demonstrated that it is possible to track conformational changes at subnanometer resolutions using AFM [104]. Figure 8.2a shows an example of a topographic image of the extracellular surface of split native connexin 26 gap junction plaque. The six individual subunits of the connexin are distinctly visible. The subunits protrude by about 1.5 nm above the lipid bilayer and are arranged into a donut-shaped structure surrounding a central pore. Connexin 26 gap junctions participate in cell–cell communication and respond to changes in the calcium concentration. Remarkably it was found that upon injection of calcium into the buffer solution, the extracellular channel entrance reduced its diameter from 1.5 to 0.6 nm, a conformational change that was fully reversible.

AFM allows direct nano-imaging of DNA–protein complexes at the single-molecule level [59, 88, 89]. In these experiments the protein is readily identified as a “blob” on the DNA. The change in length of the DNA upon binding the protein gives an indication of the extent to which the DNA is looped within or wrapped around the protein [56, 59]. For example, AFM was recently applied to the important problem of DNA mismatch repair [70]. Several proteins participate in detecting mismatch and directing repair. In bacteria MutS initiates the mismatch repair process. Figure 8.2b shows AFM images of DNA:MutS complexes containing a mismatch in the middle of the DNA molecule. The volume measurements suggested that each “blob” in these images correspond to MutS tetramers. This demonstrates the power of AFM methods in resolving individual nucleoprotein complexes in liquid.

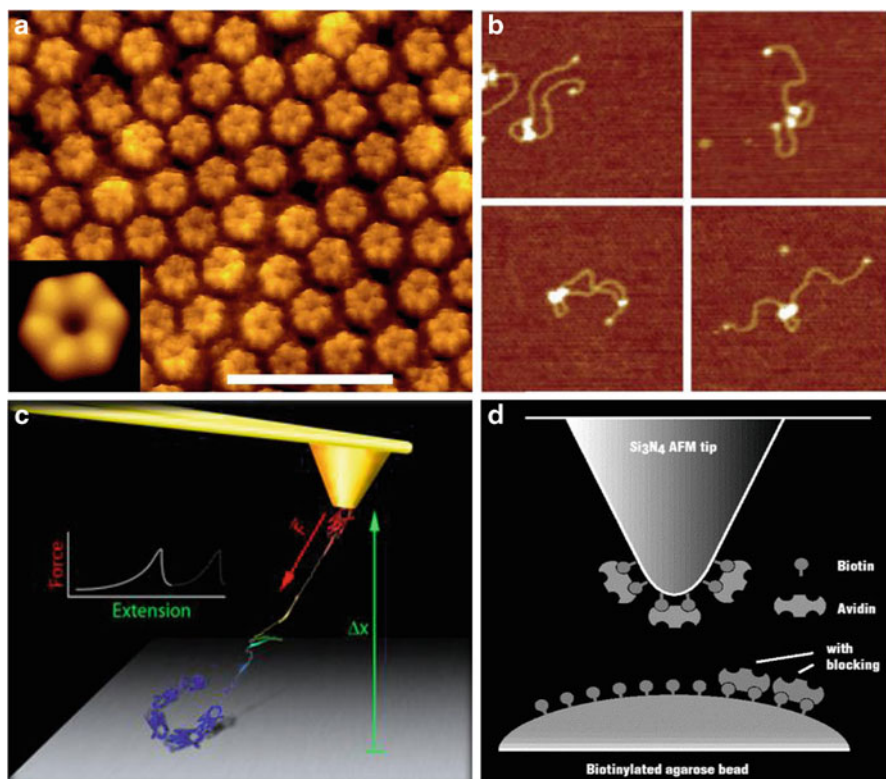


**Fig. 8.2** AFM: a nano-toolbox for single molecule detection and manipulation. **(a)** Tracking conformational changes in surface structures of isolated Connexin26 gap junctions. AFM topograph of individual connexons. *Inset*: Average of the raw data exhibiting a lateral resolution of  $\sim 1.2$  nm. The six individual subunits of the connexin are distinctly visible. The subunits protrude by about 1.5 nm above the lipid bilayer and are arranged into a donut-shaped structure surrounding a central pore. Reproduced with permission from Muller et al. [104]. **(b)** Imaging DNA–protein complexes at the single molecule level. AFM images of DNA:MutS complexes containing a mismatch in the middle of the DNA molecule. In these experiments the MutS protein is readily identified as a “blob” on the DNA. Each image is  $250 \times 250$  nm. Reproduced with permission from Jiang and Marszalek [70]. **(c)** The AFM can be also used to analyze the unfolding and refolding pathways of single proteins. This cartoon diagram depicts a multidomain protein (e.g., titin) being stretched by the AFM tip. As the protein is stretched ( $\Delta x$ ) the force raises until one of the domains unfolds resulting in a sudden decrease in the force. **(d)** Measuring ligand (biotin) and receptor (avidin) interactions using AFM. Schematic representation of the interaction between an AFM tip, functionalized with avidin molecules, and a biotin-derivatized agarose bead (not drawn to scale). The biotin molecules are covalently coupled to the bead. During the withdrawal of the AFM tip the tension across the avidin–biotin complex to increase gradually. Reproduced with permission from Florin et al. [44]

### 8.3.3 Single-Molecule Force Spectroscopy of Biomolecules

The so-called single-molecule force spectroscopy (SMFS) was designed to record force-extension curves obtained by pulling in a single direction ( $z$  axis; Fig. 8.2c) [28, 31, 122, 124]. Two basic SMFS modes are currently used depending on the variable

being controlled: the more common length-clamp, which yields a force-extension curve, and the force-clamp, which yields an extension-time curve (Fig. 8.3b, top panel). SMFS is a very sensitive technique that can measure forces of tens of piconewtons and changes in length with nanometer resolution. However, a common problem is that force peaks can originate from a variety of sources other than the interaction of interest (detachment of other molecules from any of the two anchoring points, protein-protein interactions, disentanglement of molecules, etc.) or from multiple molecules in parallel. This drawback was overcome by using long multidomain proteins (such as titin, tenascin, or spectrin) [82, 114, 124] or homo-oligomers recombinant proteins [27], in which their periodicity was used to infer single molecules unequivocally. The protein molecules are first immobilized between the substrate (a glass coverslip) and the tip of the cantilever. Typically, in these experiments proteins get attached by physisorption (i.e., nonspecific adsorption) although sometimes specific functionalization methods are also used (e.g., terminal cysteine residues in the protein that get covalently linked to the gold-coated surface of the substrate or/and the cantilever tip). Protein molecules are then stretched, by moving apart the AFM piezoelectric positioner, which applies a stretching force that unfolds the protein. The resulting force versus extension curve can be simply analyzed using the worm-like chain model for polymer elasticity which describes how a polypeptide chain behaves under a stretching force [23]. In the case of modular proteins such as titin the resulting force-extension curve displays the characteristic sawtooth pattern that results from the unfolding of individual immunoglobulin domains [124] (Fig. 8.3b). The typical range of the forces required to unfold single proteins is between 50 and 500 pN (at pulling speeds of about 1  $\mu\text{m/s}$ ) [112]. By retracting the AFM positioner, the protein can also be refolded in the presence or in absence of mechanical force. In the force-clamp mode (Fig. 8.3b, bottom panel), a feedback mechanism quickly corrects the distance between the coverslip and the AFM tip in order to control the applied force. After the application of a stretching force to a multidomain protein, such as titin, it unfolds in a staircase pattern where each step corresponds to the all-or-none unfolding of individual domains. The main advantage of this mode is the precise control of the end-to-end distance of the protein with subnanometer resolution in the millisecond time scale. Force-clamp SMFS techniques are currently being used to tackle fundamental problems in biology such as protein folding [2, 42, 115, 160] and chemical mechanisms in enzyme catalysis [15, 120, 141]. SMFS methods are constantly providing with exciting and promising new ways to study the molecular mechanisms of protein folding. For example SMFS allow the direct measurement of the main energy barriers in the unfolding and folding pathways and the location of these barriers with single amino acid resolution [26, 151].

The AFM has been also successfully used to analyze the magnitude of the interaction forces between single ligand-receptor pairs (Fig. 8.2d). In this method the tip of the cantilever, functionalized with one molecule, is brought into contact with a surface that is covered with the other molecule allow them to interact for a short time (milliseconds to seconds). Upon retraction of the cantilever tip from the surface molecular bonds are broken and the adhesion forces between the two molecules are quantified. For example, the interaction forces between avidin and its ligand,

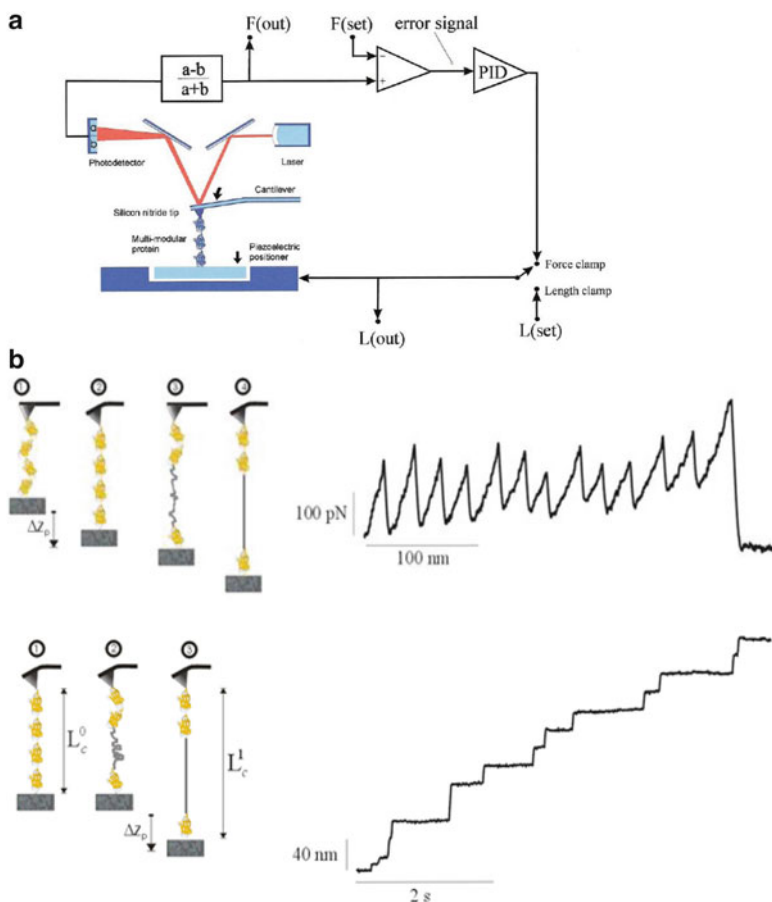


**Fig. 8.3** (a) Schematic diagram of the AFM apparatus and associated control electronics. When pressed against a layer of protein attached to a substrate, the silicon nitride tip of the AFM cantilever may adsorb a single protein molecule. Extension of the molecule by retraction of the piezoelectric positioner results in deflection of the cantilever. A single molecule is stretched by using either a length-clamp mode or a force-clamp mode. In the standard length-clamp mode the desired position ( $L$ ) is set and then measure the resulting force ( $F$ ) calculated from the laser deflection,  $(a-b)/(a+b)$ , where  $a$  and  $b$  correspond to the photovoltage in the position-sensitive detector. In the force-clamp mode, the measured force is compared with a set value generating an error signal that is fed to a proportional, integral, and differential amplifier (PID) whose output is connected directly to the piezoelectric positioner. Reproduced with permission from Oberhauser et al. [113]. (b) Example of stretching a multidomain protein using the length-clamp (*top panel*) and force-clamp (*bottom panel*) modes of the AFM. The AFM tip picks up a single protein (1) and starts pulling on it (2). When sufficient force is applied (around 200 pN) the domains begin to unfold (3). In the length-clamp mode this is seen as a “sawtooth” pattern where each peak corresponds to the unfolding of individual domains. In the force-clamp mode the unfolding is seen as a “staircase” pattern where each step corresponds to individual unfolding events



biotin, has been comprehensively studied using SMFS [44, 69, 103]. Avidin is a tetrameric protein that binds four molecules of biotin with particularly strong affinity ( $K_D \sim 10^{-15}$  M). In these experiments both the cantilever tip and a glass surface are functionalized with biotin; then avidin is added in order to block most of the biotin molecules. Under these conditions it is possible to pull a single biotin out its avidin binding site revealing the force needed to rupture ligand-receptor bonds. This was found to be around 150 pN which is equivalent to an unbinding free energy of about 23 kcal/mol making it one of the strongest known non-covalent bonds [68].

## 8.4 Optical Tweezers Methods

Optical tweezers, also known as optical traps, were first described in the late 1980s by Ashkin and colleagues. They based on the fact that small dielectric particles [6], including viruses and bacteria [5, 7], can be trapped by using a focused laser. Since then the field of single-molecule manipulations with optical tweezers has grown at an impressive pace and proven to be an important single-molecule method in a wide range of research fields [16, 41, 52, 76, 97, 101, 137]. For example, optical tweezers have been used to investigate molecular motors such as myosin [4, 43, 126, 137] and kinesin [129, 139, 140], processive enzymes such as DNA [152] and RNA polymerases [33, 81, 149] and DNA translocases [121], endonucleases [50] and helicases [30, 36], the bacteriophage packaging motor [135, 155], the unfolding and refolding of single proteins [29, 90, 138, 143] and RNA hairpins [85], the mechanism of action of molecular chaperones [13], and protein translocation by ATP-dependent proteases [8, 91].

### 8.4.1 Basic Principles

Optical tweezers take advantage of gradient force produced by a focused laser beam. The force exerted by an optical field on a small dielectric object (such as a plastic bead) falls within the range of 0.1–100 pN and is used to “trap” and manipulate it with sub-nanometer precision, allowing the simultaneous determination of force and displacement [41, 101, 110]. Optical tweezers use a microscope objective to create a focused Gaussian beam that exerts a force in the direction of the field gradient which draws it towards the center of the laser beam (Fig. 8.4a). When trapped, the bead behaves as a small Hookean spring, with the force given by  $F = k\Delta x$ , where  $k$  is the spring constant of the trap and  $\Delta x$  is the displacement of the bead from the focus of the trap (Fig. 8.4b, right inset). A restoring or trapping force arises whenever the bead is displaced from its equilibrium position. Photons carry momentum that is proportional to the energy of the laser beam and the direction of propagation. The photons interacting with the bead will undergo refraction and as a result they will change their momentum (Fig. 8.4b, left inset). Because of the conservation of momentum, the bead must experience also a rate of change of momentum of equal but opposite in magnitude that tends to restore the

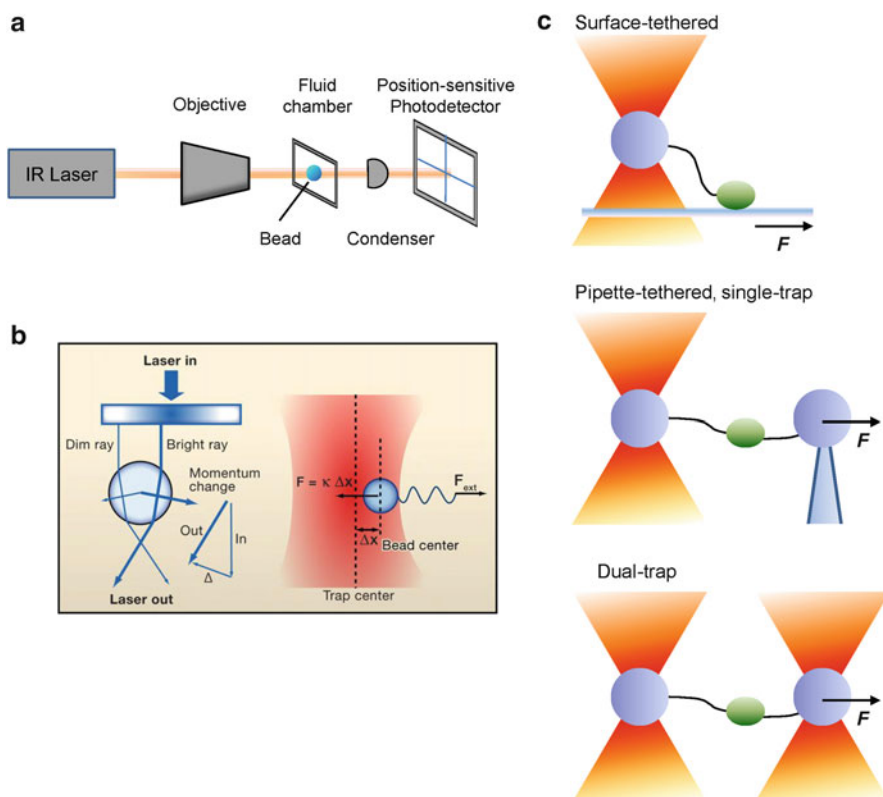


**Fig. 8.4** Basic principles of operation of optical tweezers. (a) Basic elements in an optical tweezers instrument. A laser beam (typically infrared, IR) is focused on a small dielectric bead (inside a fluid chamber) by means of a microscope objective, and the exiting light is collected by a position-sensitive photodetector to measure both the intensity (in the range of 0.1–100 pN) and its deflection. (b) Optical tweezers can be built by focusing a laser beam through a lens to form a “trap.” When trapped, the bead behaves as a small Hookean spring. A trapping force arises whenever the bead is displaced from its equilibrium position. Photons carry momentum that is proportional to the energy of the laser beam and the direction of propagation. The photons interacting with the bead will undergo refraction and as a result they will change their momentum; hence the bead will experience a rate of change of momentum of equal but opposite in magnitude that tends to restore the bead back to the center of the beam. Reproduced with permission from Bustamante et al. [22]. (c) Typical geometries used in optical tweezers experiments: the tethered particle assay (top), the pipette-tethered single-trap assay (center) and the dual-trap assay (bottom)

bead back to the center of the beam. This gives rise to a net force acting on the bead which can be measured by means of a position-sensitive photodetector. The spring constants of the optical trap are typically 1,000 times smaller than those for AFM cantilevers, in the range of 0.01–1 pN/nm, meaning that a lower range of forces are accessible (0.1–100 pN; Table 8.1). In order to minimize optically induced damage to the sample from the intense laser beam, wavelengths in the near-infrared (800–1,100 nm) are used because biological samples are relatively transparent to infrared light.



In single-molecule optical tweezers experiments, the molecule of interest is tethered to the optically trapped bead with different conjugation chemistries generally based on avidin–biotin or antibodies–epitope interactions. Different optical tweezers geometries have been designed according to the type of molecule and the requirements for resolution and stability (Fig. 8.4c) [52, 101]. In the tethered particle assay (Fig. 8.4c, top) the protein (e.g., cytoskeletal motors, such as kinesin or myosin) is attached onto the optically trapped bead and the filament (microtubule or actin) is attached by physisorption to the surface of a coverslip. Motions of the motor are monitored by the changes in the relative position of the trapped bead. This is the simplest geometry in optical tweezer instruments but it is prone to mechanical noise originating from thermal drift of the coverslip and laser fluctuations. In the pipette-tethered single-trap assay (Fig. 8.4c, center) [52, 134], one end of the molecule (e.g., a long segment of DNA or RNA) is attached to the trapped bead and the other end is bound to second a bead suctioned by a glass micropipette. The pipette can be moved away from the trapped bead to apply tension to the molecule and changes in length are monitored by tracking the motion of the optically trapped bead. In the double-trap assay (Fig. 8.4c, bottom) a second bead is held using a second optical trap. In this case the molecule under study is attached to one bead (e.g., RNA polymerase) and a DNA handle is tethered to a second bead via avidin–biotin linkages. The relative motions of both beads are independently monitored. The beads are held in separate optical traps free of the coverslip surface, greatly improving the stability and reducing the noise of the system. The dual-trap geometry offers the simplest way to implement a force-feedback or force-clamp mode of operation in which the position of one trap relative to the second trap is adjusted via a feedback loop to maintain a constant force on the beads at all times [147]. Recent technical advances in dual-trap optical tweezers have pushed the spatial resolution down to the angstrom scale [1, 21, 100]. With this resolution single base pair motions of the RNA polymerase were detected [1].

#### **8.4.2 *Examples of Biological Applications of Optical Tweezers: Motion of Single Molecular Motors and Folding/Unfolding Reactions of Single Proteins***

Some of the most important applications of optical tweezers were done in the 1990s, when these were used to measure the motions of motor proteins such as kinesin [140] and myosin [43] with nanometer resolution. Motor proteins are enzymes powered by ATP and drive a wide variety of subcellular movements such as organelle transport, cell and chromosomal division, and muscle contraction. These pioneering experiments demonstrated that these motors walk in nanometer-steps. In an assay for kinesin-driven motility, a bead carrying a single motor protein is first trapped and then brought into contact with a microtubule bound to a glass coverslip, as shown in Fig. 8.5a. The kinesin motor attaches to the microtubule filament and “walks” in steps along it ( $\Delta x$ ), pulling the bead from the trap and building up a force that resists further motion of the motor.

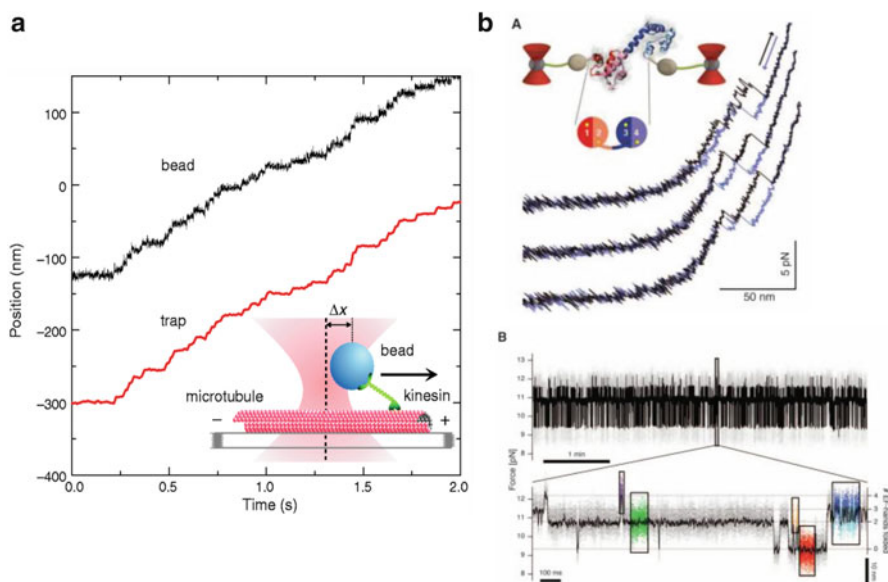


**Fig. 8.5** Examples of biological applications of optical tweezers. (a) Single kinesin molecules studied using optical tweezers techniques [148]. Record of the displacement of a single kinesin motor showing discrete 8 nm steps (*black trace*) as it walks along a microtubule (*inset*, not to scale). The position of the optical trap is under computer control to maintain a fixed distance behind the bead, thereby imposing a load of a few piconewtons in a direction that hinders movement (*red trace*). Reproduced with permission from Visscher et al. [148]. (b) Folding and unfolding reactions studied by optical tweezers techniques [138]. Traces representing stretching and relaxation cycles of calmodulin (*top panel*). The insert presents the experimental setup where calmodulin at its ends is linked with ubiquitins that are attached to DNA handles that are connected to functionalized silica beads. (*Bottom panel*) Traces of fluctuation of a single calmodulin molecule at constant trap separation at 5 min time intervals. The vertical scale represents force acting on single molecule. The identified intermediate states of protein are colored. The data at full resolution are shown in *grey* and low pass filtered data are shown in *black*. Reproduced with permission from Stigler et al. [138]

Optical traps can also exert forces while single proteins undergo structural changes such as unfolding and folding reactions. Optical tweezers have been used to pull the ends of a single folded protein molecules until it straightened out and then to reduce the tension to allow it to fold again [29, 90, 131, 138, 143]. Recent experiments on calmodulin showed that optical tweezers allow the dissection of protein folding pathways [138] (Fig. 8.5b). The calmodulin protein is stretched to a preset force value where complex fluctuations of full-length protein that occurs between folded and unfolded states of protein can be observed and analyzed. The equilibrium fluctuation data reveals number of intermediate states and allows reconstruction of possible transition pathways between the intermediates, thus these experiments can address the role of intermediates and the mechanism of protein folding.

## 8.5 Single-Molecule Fluorescence Methods

Fluorescence methods have been used for the detection of single molecules for several decades. One of the first papers describing the visualization of a single protein by fluorescence methods was in the 1970s by Hirschfeld [64], who showed the optical microscopic observation of single antibody molecules labeled with ~100 fluorophores. Since then the single-molecule fluorescence field has advances at a remarkable pace. For example nowadays it is possible to track the rotational motion of single proteins on living cells with millisecond resolution [144]. One of the main advantages of single-molecule fluorescence techniques over AFM or optical traps is that they are largely noninvasive and typically require less complex instrumentation and hence are fairly accessible to cell biologists, biochemists, and biophysicists.

### 8.5.1 Basic Principles

The basis of fluorescence is the relaxation of a fluorophore from an excited electron state (high energy) to the ground state (low energy) accompanied by the emission of radiation [78]. The emission rates are in the order of  $10^8 \text{ s}^{-1}$  meaning that typical fluorescence lifetimes are in the nanosecond range. Fluorescence typically occurs from aromatic molecules; in single-molecule experiments the favorite fluorophores are those based on cyanine (e.g., Cy3 and Cy5) and rhodamine (e.g., Texas red and Alexa dyes) [71, 78]. These dyes can be incorporated into the molecule of interest via chemical coupling to free sulfhydryl or amino groups. The quantum yield, fluorescence lifetime, and photostability are the most important properties of fluorophores used in single-molecule experiments [78]. Quantum yield refers to the number of emitted photons relative to the absorbed photons; lifetime determines the time available for the fluorophore to interact in its environment. The emission wavelength, quantum efficiency, and lifetime are highly dependent on the local physical and chemical microenvironment and hence the fluorophore relaxation process can be used to obtain structural and dynamical information at the single-molecule level.

Almost all fluorophores are photobleached upon continuous illumination. Photobleaching is an irreversible process that results in the loss of fluorescence. In typical single-molecule fluorescence experiments a single fluorophore emits about  $10^6$  photons before undergoing photobleaching [98]. The Alexa and Cy3, Cy5 dyes are commonly used in single-molecule experiments since several show high quantum yield and reasonable photostability and appear to have been developed for this reason [71].

The most common experimental optical geometries used in single-molecule fluorescence are confocal (Fig. 8.6a) [111] and total internal reflection fluorescence microscopy (TIRF, Fig. 8.6c) [9–11, 71, 73, 118]. In confocal microscopy a laser beam is focused by a high-numerical aperture objective lens on the sample [150], resulting in the excitation of a very small volume (on the order of femtoliters ( $10^{-15} \text{ L}$ )). The emitted fluorescence is collected by the objective and projected, via

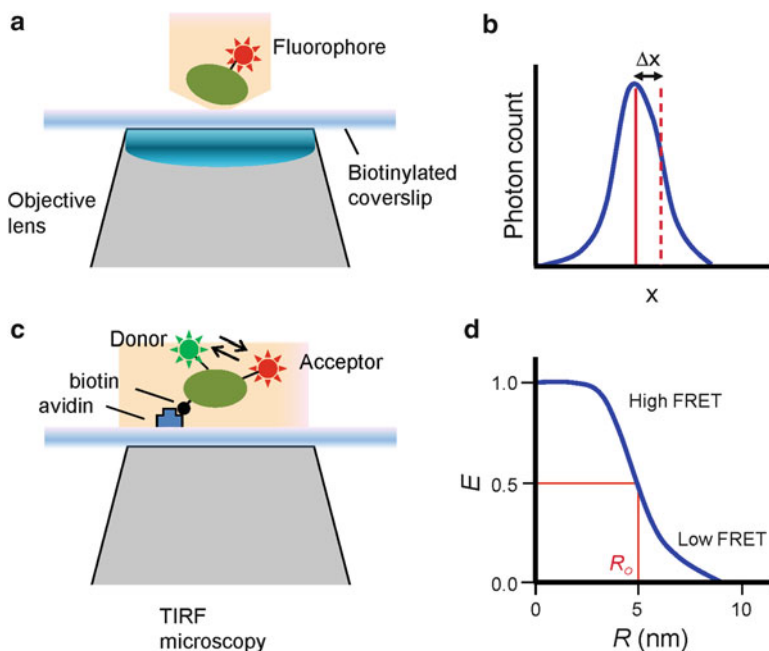


**Fig. 8.6** Typical experimental setups used in single-molecule fluorescence. Single-molecule fluorescence methods rely on the detection of photons from a small diffraction limited spot (confocal, **a**) or from a large area (wide-field, **c**). (**a**) In confocal microscopy the fluorescence emitted from a small volume (femtoliters) is detected using a detector, such as avalanche photodiodes, making it possible to achieve a time resolution in the order of picoseconds. (**b**) Diagram depicting the Gaussian distribution of a single fluorophore. By tracking the median of the distribution ( $\Delta x$ ) it is possible to follow the trajectories of single molecules. (**c**) In total internal reflection fluorescence (TIRF) microscopy the evanescent wave created ( $\sim 100$  nm in depth) is used to excite fluorescent molecules near the coverslip. The use of two fluorophores allows the tracking of conformational changes of a single biomolecule (e.g., labeled with green and red fluorophores) using FRET. In order to stably and specifically immobilize biomolecules to a glass coverslip, a biotin-streptavidin linkage is frequently used. (**d**) Diagram showing the dependence of the energy transfer efficiency ( $E$ ) on the distance  $R$ .  $R_0$  is the Förster distance

a pinhole positioned in the conjugate focal plane in order to avoid the collection of photons generated at locations different from the focal plane. The light is collected by a very fast detector, such as avalanche photodiodes, making it possible to achieve a time resolution on the order of picoseconds. In TIRF microscopy an evanescent wave is formed by the refraction of a laser beam through a high-numerical aperture objective lens or a prism [9–11, 118]. This laser beam is focused at the boundary between two optical media having different refraction indices at such an angle that all the light is reflected off the glass surface. However, an evanescent wave forms which is capable of exciting fluorophores near the surface. The intensity of the evanescent field decays exponentially with the distance from the surface allowing the selective excitation of fluorophores within only 100 nm resulting in a very low

background signal. The emitted light is collected by 2-dimensional detectors such as charge-coupled device (CCD) cameras allowing the simultaneous imaging of hundreds of single molecules with millisecond resolution.

One of the simplest methods to directly visualize fluorescently labeled molecules is to track motion using TIRF microscopy. The spatial resolution of conventional microscopy is limited by the Rayleigh criterion [132]; since the diffraction limit is approximately,

$\sigma = \lambda/2NA$ , where  $\lambda$  is the emitted wavelength and NA the numerical aperture of the objective lens. For a high-numerical aperture objective of 1.65, two molecules cannot be resolved if they are closer than  $\sim 150$  nm. Several methods have been developed to push the limit for single-molecule fluorescence localization to the nanometer range. For example, centroid-tracking methods have been recently used to directly analyze the stepping mechanism of myosin and kinesin molecular motors [126, 153, 154]. In this technique the intensity profile of the light emitted by the fluorophore is fitted to a Gaussian distribution function (Fig. 8.6b). The center of the fluorescence distribution (centroid) can be determined with an uncertainty,  $\Delta x$ , of

$$\Delta x = \frac{\sigma}{\sqrt{N}}, \text{ where } N \text{ is the number of photons counted and } \sigma \text{ is the width of the}$$

diffraction limited spot [52]. Hence, in this method the resolution is not limited by the Rayleigh criterion but instead by the number of photons counted over short periods of time. Tracking the motion of single molecules has reached the remarkable precision of 1 nm and with millisecond temporal resolution [77, 119, 153, 154]. This centroid-tracking method was fittingly named “fluorescence imaging with one nanometer accuracy” (FIONA) [136, 153, 154].

One of the most commonly used single-molecule fluorescence methods is FRET (fluorescent resonance energy transfer) or Fröster transfer [78]. FRET between two fluorophores occurs when the excitation energy of the donor is transferred to the acceptor via an induced dipole–dipole interaction. The energy transfer efficiency is given by

$E = 1/(1 + (R/R_0)^6)$ , where  $R$  is the distance between the donor and acceptor fluorophores and  $R_0$  is the so-called Förster radius, which is the distance at which  $E = 0.5$  (Fig. 8.6d). The efficiency of the transfer is a very sensitive function of the distance between the two fluorophores in the 2–10 nm range [34, 57, 58]. Experimentally  $E$  is obtained by using:

$E = [1 + \gamma I_d/I_a]^{-1}$ , where  $I_d$  and  $I_a$  are the donor and acceptor intensities and  $\gamma$  a correction factor that depends on the donor and acceptor quantum yield and detection efficiency [57, 73, 127]. This means that the FRET efficiency depends not only on the interdye distance but it also depends on the angles between the respective dipoles [78] making it difficult to convert  $E$  into quantitative distances.

Single-molecule FRET is perhaps the most flexible and successful single-molecule techniques in biology. This is because of its inherent sensitivity and the steep dependence of the energy transfer to the distance between the dyes (proportional to  $R^{-6}$ ). FRET can effectively measure distances between 2 and 10 nm making it ideal to track conformational changes [127]. Single-molecule FRET time

trajectories are most commonly acquired by imaging surface-immobilized molecules with the aid of TIRF microscopy (Fig. 8.6c) that allows high-throughput data acquisition [161]. Single-molecule FRET has been successfully used to track the conformational changes of a wide array of molecules, such as calcium-binding proteins [142], four-way DNA (Holliday) junctions [96], the reverse transcription initiation complex [18], the folding of single ribozyme [161], the folding of single proteins [74, 107], and the conformations of individual SNARE proteins in live cells [146].

A number of “super-resolution” fluorescence microscopy techniques have been recently developed that achieve lateral resolutions in the nanometer scale allowing the localization of single molecules on fixed or living cells [49, 55, 66, 74, 86, 133]. In these techniques the imaging setup and fluorophores are designed in such a way to circumvent the Rayleigh criterion for resolution. For instance photoactivated localization microscopy (PALM) [14], fluorescence photoactivation localization microscopy (FPALM) [61], and stochastic optical reconstruction microscopy (STORM) [128] can achieve extremely high resolution by localizing individual photoactivable fluorophores on cells or tissues. These techniques are opening exciting new opportunities for biologists to interrogate single cells at the molecular scale through direct observation of protein movement.

### 8.5.2 *Examples of Biological Applications of Single-Molecule Fluorescence Methods*

FIONA methods have been widely applied by several groups to track the motion of cytoskeleton motor proteins [77, 119, 153, 154]. For example, FIONA has been successfully used to measure step sizes of fluorescently labeled myosin VI molecules (Fig. 8.7a, left panel). In these experiments a single Cy5 dye was attached to one head of the myosin molecule and an *in vitro* motility assay combined with FIONA was used to track myosin VI walking on actin filaments [116]. Single fluorophores were localized with nanometer resolution by fitting the fluorescent peak to a two-dimensional Gaussian function (Fig. 8.7a, center panel). The authors observed the movement of the Cy5 fluorophore occurring in discrete steps (Fig. 8.7a, right panel). The average step size of myosin VI was 36 nm, a result is consistent with a hand-over-hand stepping mechanism.

Single-molecule FRET techniques have been applied to visualize DNA binding and translocation of ATP-powered enzymes. *Escherichia coli* Rep is a helicase that can translocate on ssDNA in the 3′–5′ direction using ATP hydrolysis. Rep helicase was labeled with both donor and acceptor dyes (Fig. 8.7b, left panel), where high FRET and low FRET would represent closed and open conformations of helicase, respectively [108]. Single-molecule FRET experiments revealed that Rep gradually closes as it approaches the duplex junction and abruptly opens up when it snaps back and starts another translocation process (Fig. 8.7b, right panel). Experiments with donor-labeled Rep helicase and acceptor-labeled DNA duplex showed repeatable

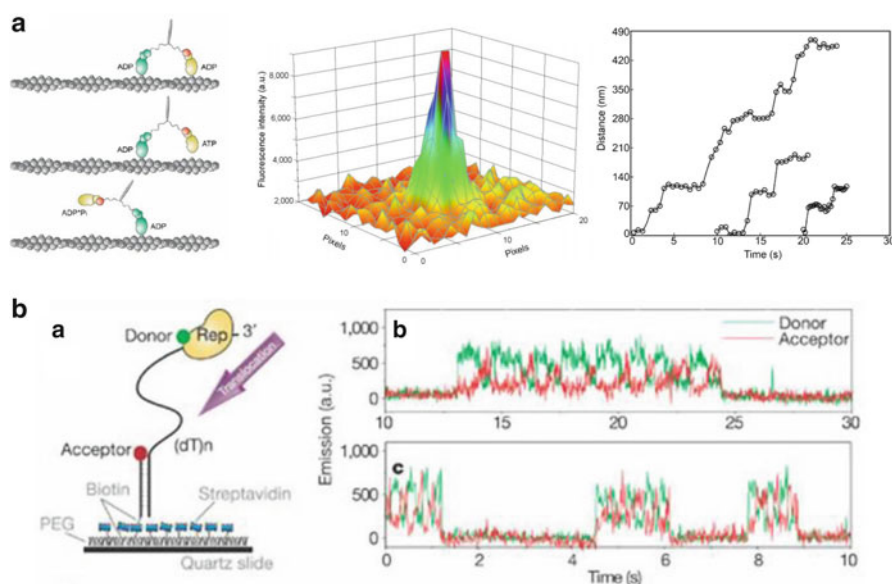


**Fig. 8.7** Examples of biological applications of single-molecule fluorescence methods. **(a)** Tracking the motion of myosin VI walking along actin filaments. *Left*: Sequence of events during hand-over-hand walking of myosin VI. As a result of ATP hydrolysis myosin head moves 36 nm. The trailing head (yellow) switch its place with previously leading head (green). Myosin molecules are labeled with Cy5 attached to one calmodulin. *Center*: Single photon localization. The centers of individual Cy5 dyes were calculated by a curve fitting to a two-dimensional (2D) Gaussian function which allowed measurement of displacement of the labeled motor domain. *Right*: Staircases of three different fluorescently labeled myosin VI molecules. The experiments were done in 40  $\mu\text{M}$  concentration of ATP. Reproduced with permission from Okten et al., Nature [116]. **(b)** *Left*: Diagram of the translocation of Rep helicase along ssDNA. Cy3-labeled Rep (donor) binds to a ssDNA and moves along it from 3' end towards acceptor-labeled duplex DNA. *Right*: b, c, Fluorescence FRET intensity traces for Rep translocation along the ssDNA. When donor-labeled Rep binds to 3' end of ssDNA fluorescence donor signal rises sharply. Then it steadily decreases which corresponds to Rep translocation along ssDNA towards acceptor-labeled duplex DNA. Decrease in acceptor fluorescence signal is accompanied by increase of acceptor fluorescence signal. Fluorescence traces shows cycles of FRET increases and decreases suggesting repeatable cycles of Rep translocation along the ssDNA. Experiments were done at 22  $^{\circ}\text{C}$  (b) and 37  $^{\circ}\text{C}$  (c). Reproduced with permission from [108]

cycles of helicase translocation along the ssDNA and its snapback. When both ends of ssDNA were labeled, FRET traces revealed formation of short lived ssDNA loops.

RNA is involved in storage of information and catalysis which makes it very versatile molecule. Analysis of folding and catalytic activity of terahymena ribozyme was performed by observing the FRET changes occurring between fluorescent dyes located at 3' and 5' ends of surface-immobilized ribozyme [161]. The experiments allow the observation of rarely docked states previously not observed by ensemble methods and discovery of new folding pathway. The applied method enabled the determination of rate constants and added new insight in our understanding of transition states.



## 8.6 Single-Particle Cryo-Electron Microscopy

Cryo-electron microscopy (cryo-EM) recently emerged as a powerful tool to study ultrastructure of biological macromolecules including large proteins, protein complexes, and nucleic acids. This single-particle method entails the purification of the biomolecules, spotting them onto an EM grid, flash freezing the sample (cryogenically), and then imaging the frozen sample using an electron microscope. The collected raw data consists of many (hundreds or thousands) images of the same macromolecule in different orientations, which are then processed to produce a three-dimensional model. The big advantage of electron microscopy is high resolving power of electron optics allowing the examination of fine structure details. Modern electron microscopes allow filling the gap between light optics resolving object details on a micron scale ( $10^{-6}$  m) and X-ray crystallography capable of solving structure of crystallized samples with 0.1–0.3 nm precision ( $10^{-9}$  m). Actually cryo-EM nowadays is closing in on the X-ray crystallography “monopoly” in that range and is yielding structures with comparable resolution of 0.35–0.4 nm [12, 54, 130, 156, 157, 159]. The current limit of resolution of cryo-EM in terms of molecular mass is about 200 kDa [117]; however, it is possible to resolve single proteins within macromolecular assemblies (e.g., ion channels, viruses) to near-atomic (0.33–0.46 nm) resolution [12].

### 8.6.1 Basic Principles

Electron microscope is analogous to traditional light optical microscope in concept but uses electrons to “shine” onto the samples and to form images (Fig. 8.8). That becomes possible owing to low mass of electrons and their electric charge allowing electromagnetic fields to bend their trajectories and to form images like in the light optics case. In addition to being discrete particles electrons have wave properties as well. Their wavelength depends on their energy and can be calculated using the de Broglie equation,  $\lambda = h/p$ , where  $h$  is Planck’s constant and  $p$  the relativistic momentum of the moving electron.  $\lambda$  is called the de Broglie wavelength and is usually extremely small. To calculate numerical values of  $\lambda$  for electrons used in electron microscopy let us find dependency of  $\lambda$  on high tension in an electron microscope. For electrons accelerated in electric field with  $U$  potential difference, their velocity is defined by the formula:  $v = \sqrt{\frac{2eU}{m}}$ . Here  $m$  is the mass of the electron and  $e$  is its charge. Therefore,

$$\lambda = \frac{h}{p} = \frac{h}{mv} = \frac{h}{\sqrt{2meU}}$$



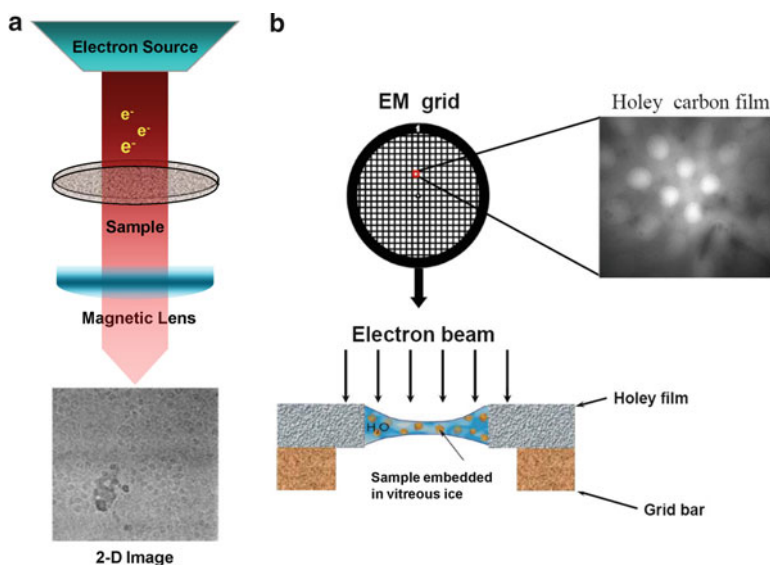


**Fig. 8.8** Schematic diagram of an EM instrument. (a) An electron beam is generated by an electron gun (electron source) which is then scattered by a sample and focused by an objective lens of the microscope creating an image. (b) The cryo-EM method entails the purification of the biomolecules and an application of suspension of biomolecules in a solvent to an EM grid with a holey carbon film (thin carbon film with small holes) to form very thin layers of the suspension. Then the sample is flash frozen in a cryogen, followed by its imaging using an electron microscope

Electrons are typically accelerated in electron microscopes to 60–300 keV energy and their wavelengths are ranging from  $\sim 4.8$  pm ( $10^{-12}$  m) to  $\sim 2$  pm. Electron microscopes have electron source, condenser system, objective lens, and a number of projector lenses to magnify an image formed by the objective lens. Instead of glass used to make lenses in light optics, electron microscopes use electromagnetic lenses that are just copper windings with magnetic field concentrators made of soft iron that is ferromagnetic in nature. The field inside a lens is quite strong reaching strength of several T (Tesla) (typical refrigerator magnet produces fields of only  $\sim 5$  mT). These strong fields are used to focus electrons both to illuminate very small regions in the specimens and to form their images.

The resolving power of electron microscopes is much higher compared to light microscopes owing to much shorter wavelength of electrons used to illuminate the samples. While the wavelengths of visible light used in light optics range from  $\sim 400$  to  $700$  nm, the wavelength of electrons used in electron microscopes is typically shorter than  $0.003$  nm. According to Rayleigh criterion of resolution for a diffraction limited optical system (system with ideal optics):

$\sigma = 1.22\lambda f/D$  where  $\sigma$  is the resolution,  $\lambda$  is the wavelength of the illuminating beam,  $D$  is the diameter of the aperture, and  $f$  is focal length of the objective lens. Since  $f/D$  is proportional to  $1/NA$  it's easy to see that the resolution in EM should be many orders of magnitudes better than in light optics. In practice though EM

resolution is worse than the value predicted by Rayleigh criterion owing to numerous aberrations present in the electron optics, radiation damage of specimens under study, and various instabilities present in the microscope and in environment. The latter include mechanical vibrations, acoustical noise, stray electromagnetic fields, temperature variations of the microscope and in the microscope room, air pressure changes, etc. Diffraction limited electron optics would have  $\sim 0.01$  nm or better resolution while the practical resolution limit in electron microscopy in biology currently at the very best is at 0.2–0.3 nm level.

Because of the strong electron interaction with surrounding molecules, one of the major requirements for electron microscope design is to provide an ultrahigh vacuum inside of the lenses along the beam path. Therefore the microscopes have their own vacuum systems with several pumps constantly pumping out residual gas molecules to prevent undesirable electron scattering before and after the beam hits the specimen. The vacuum should be good enough to allow electrons to travel at least the length of the microscope column (usually more than a meter in length) without seeing residual gas molecules. And that means high or ultrahigh vacuum with the pressure readings less than  $10^{-5}$ – $10^{-7}$  Torr ( $10^{-3}$ – $10^{-5}$  Pa).

More than 25 years ago EM moved to a new era when investigators realized that ultrafast specimens cooling could preserve them in a vitrified buffer. The cooling rate though should be so fast that ice crystals would not have time to form; and that is very difficult to achieve. First of all the specimens must be very thin to begin with, less than 1,000 nm in thickness. That excludes most of the cells and definitely tissues leaving the field with single particles that are single protein or nucleic acid molecules, or their aggregates or complexes, cellular organelles, viruses, etc. Secondly, specimens should be cooled to at least  $-150$  °C to prevent water crystallization since vitreous water is stable only at the temperatures below  $-140$  °C. This requires using liquid cryogenics (such as ethane or propane) with a very high specific heat constant and allows cooling down the samples very effectively and fast (with up to  $10^6$  °/s). The vitrification preserves the biomolecules in nearly native state and creates a temporal snapshot of all the biomolecules in the sample since they were immobilized on a microsecond time scale.

### 8.6.2 *Imaging Single Particles and Biomolecules*

Since electrons are invisible to human eye, the images formed by electron optics should be transformed to visible light images either by direct conversion, or by registering them by a sensor followed by conversion to visible to eye images, in both cases the images are made useable for human perception. One way to convert an electron image into visible to eye is to use phosphors that emit photons (fluoresce) when electrons hit them. Fluorescent screens are commonly used in electron microscope to directly observe images and photographic film was used as an image detector. Nowadays photographic films are commonly replaced by digital electron detectors (typically CCD or CMOS cameras) allowing to display electrons immediately after

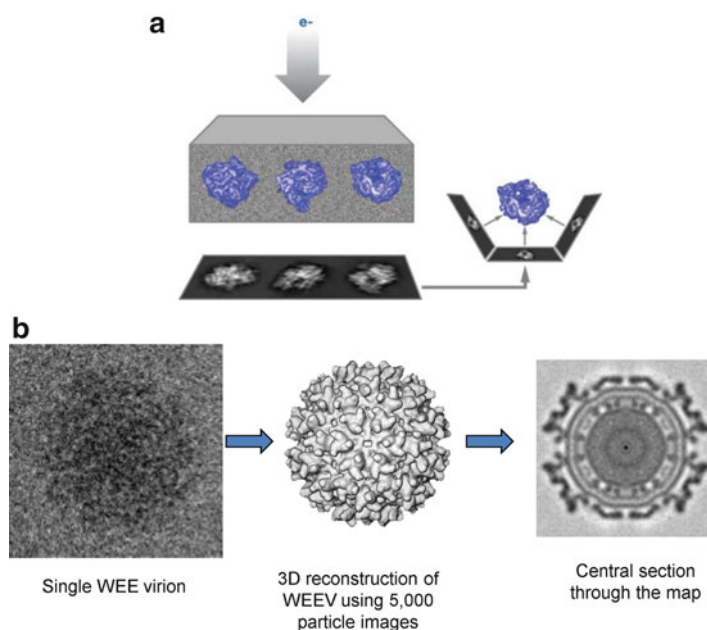


**Fig. 8.9** Principle of single-particle reconstruction from 2D images. (a) In the cryo-EM a coherent electron beam is shined onto a sample consisting of particles embedded in random orientations in the vitreous ice. The collected images are 2D projections of the 3D molecules. The collected raw data consists of many (hundreds or thousands) images of the same macromolecule in different orientations, which are then processed to produce a 3D model. Reproduced with permission from [99]. (b) Power of averaging. *Left panel*: raw image of a single virus particle (western equine encephalitis virus, WEEV, left); *central panel*: 3D reconstruction obtained by combining 5,000 individual raw images; *right panel*: view of the central cross-section through the reconstructed 3D image. The combination of these raw noisy individual WEEV images results in about 70-fold increase in the signal of the 3D map

acquisition on a computer screen. Typically a very thin phosphor layer is used in these cameras to convert electrons to visible light, which is then registered by the digital sensor. Recently a new class of electron detectors was developed, the direct electron detection devices, allowing registering electron images without their intermediate conversion to light.

EM images are “flat”; they represent two-dimensional (2D) projections of three-dimensional (3D) samples (Fig. 8.9). These projections are not just shadows originating from a shape of an object but rather true projections formed by summing all the densities within a sample along the projection direction. That means that information about the third dimension in the specimen is not readily accessible in an image, which is disappointing since one would like to know 3D structure of the samples under study. Fortunately the information is not lost completely; it is still possible to reconstruct the 3D structure of a sample using a number of its 2D projections—images (Fig. 8.9a). That was first formulated and proven by an Austrian mathematician Johann Radon back in 1917 [123]. For an accurate reconstruction

many projections are needed, the more, the better. At the same time combining large number of images allows one to greatly reduce noise in the reconstruction since that effectively increases the electron dose and consequently suppresses the shot noise in the reconstruction enhancing the signal, improving the quality of the reconstruction (Fig. 8.9b). Mathematically speaking the noise reduces proportionally to the square root of the number of individual images combined in a reconstruction, so if 10,000 images were used to reconstruct a volume, the noise is suppressed by 100 times.

### 8.6.3 Image Processing

Once an image set is acquired in an imaging session, the images have to be processed to obtain a 3D reconstruction. First, an image is assessed for defects that impair the image quality (e.g., specimen drift during exposure) and bad images are discarded from further analysis. The effect of the microscope optics on image formation is usually described by a “contrast transfer function” (CTF), which is an oscillating function affecting image Fourier transforms. The transforms have zero amplitudes in places where CTF is zero and since CTF depends on the defocus used to acquire an image, it is a good idea to collect images within a range of defocus values. Then information that is lost in a particular image (zero amplitude) could be extracted from other images where CTF has large values in that region of Fourier space. Good images are corrected for the CTF and then individual particles images are boxed out from them.

A critical assumption in image processing of single particles is that all the particle images represent the same 3D object. It then becomes possible to implement an extremely powerful idea of averaging or combining information from many different images to create a single, much less noisy, reconstruction of the object. If that assumption fails, none of the processing would work since one in such a case would try to compare apples and oranges and the result would correspond to neither. Combining information from many images is necessary for many reasons: individual images are so noisy that signal is buried frequently in the noise; CTF correction fails in some regions of Fourier space and information is lost in those; individual images represent single projections of a 3D object, consequently to restore the object in three dimensions one needs a large number of these projections at all possible orientations. It is usually assumed that particles are embedded in ice in random orientations so selecting many different images would provide many different orientations of an object they represent.

There are several groups of reconstruction algorithms that are used in cryo-EM. There are Fourier space-based methods where 3D Fourier transform of an object is reconstructed from the information from Fourier transforms of individual images followed by Fourier inversion back to the object space [32]. In back-projection algorithms one uses the idea that a superposition of projections stretched along their corresponding projection directions would produce a reconstruction of the original object. There are algebraic reconstruction algorithms where reconstructions are calculated iteratively with reconstruction errors diminishing at each iteration until the process converges [47, 53, 60, 79].

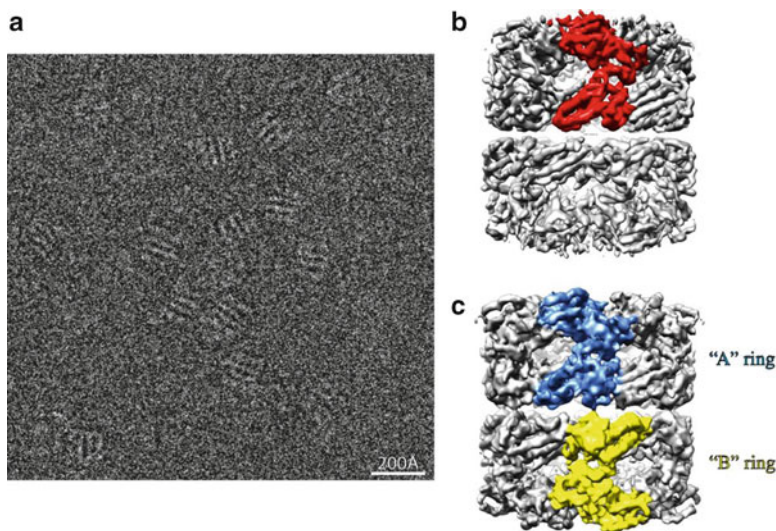


**Fig. 8.10** 3-Dimensional reconstructions of GroEL. (a) Cryo-EM image of GroEL molecules embedded in vitreous water shows a very low signal-to-noise ratio. (b) 3D reconstruction from a set of 135 micrographs resulting in a 0.42 nm resolution map (with a monomer highlighted in red). True D7 symmetry was used for reconstruction. (c) 0.47 nm reconstruction of the same sample using lower C7 symmetry. Independent “A” and “B” rings with monomers shown in blue and yellow, respectively. Reproduced with permission from Ludtke et al. [87]

#### 8.6.4 Examples of 3D Reconstructions Using Cryo-EM Techniques: Chaperonins, Ribosomes, and Viruses

GroE is a chaperonin that is required for the proper folding of a wide range of proteins [38, 94]. It has been proposed that GroE acts as an Anfinsen cage providing the proper chemical environment to promote protein folding [37]. GroE is composed of two proteins: GroEL and GroES. GroEL forms two back-to-back seven-membered rings that are responsible for accepting and folding of a polypeptide chain [19, 25]. Figure 8.10 shows an example how cryo-EM techniques are used to reconstruct GroEL to  $\sim 0.4$  nm resolution [87]. The raw 2D micrograph shows individual GroEL molecules which are hard to resolve because of the very low signal-to-noise ratio (Fig. 8.10a). Figure 8.10b, c show 3D reconstructions using a large set of micrographs resulting in a 0.42 nm resolution image (a single subunit is highlighted in red). This represents a significant milestone in resolution for low-symmetry, single-particle cryo-EM maps [87].

The ribosome structure has been studied by EM for a long time, since the 1960s. Cryo-EM and image processing allow now to reveal mechanism of protein synthesis followed by protein folding with the help of SecY–SecE1

complex that translocates nascent secretory proteins across cellular membranes and integrates membrane proteins into lipid bilayers. Typical resolutions achieved using single-particle cryo-EM are better than 1 nm, in some cases approaching 0.6 nm, and allowing to segment different ribosome components, mRNA and tRNAs along with elongation factors used in protein synthesis. It is an amazing achievement for cryo-EM since ribosome does not have any symmetry to improve the quality of the reconstruction [48].

Icosahedral viruses have the highest intramolecular symmetry in biology, having a 60-fold symmetry, so that a single cryo-EM image is equivalent to 60 images of asymmetric particles. In addition, these viruses are often well preserved and several viral structures have been reconstructed to better than 0.4 nm resolution. A cryo-EM structure of an infectious subviral particle of aquareovirus was recently reported at 0.33 nm resolution and revealed side-chain densities leading to de novo construction of a full-atom model of the viral particle [158].

## 8.7 Perspectives

Single-molecule methods are providing us more and more fundamental information on the structure and function of proteins. The progress in the visualization and manipulation of single proteins during the last 20 years has been impressive. The implementation of single-molecule methods by biochemists and biophysicists has grown almost exponentially; from a handful of papers published in the early 1990s to nearly 1,400 papers published just in 2011 (Web of Knowledge). Clearly, single-molecule methods are becoming an indispensable tool to understand how proteins work in real time. However, most single-molecule methods have an inherent problem: they are mainly concerned with *in vitro* studies of purified proteins that are removed from the cellular environment. The key future challenge is to bring single-molecule methods into living cells. This is not an easy task since it will require the combination of several single-molecule methods and bring together nanoscience, biophysics, and cell biology. For example, the combination of single-molecule manipulation techniques (e.g., tweezers or AFM) and single-molecule detection techniques (e.g., fluorescence) is an important development [51, 67, 80, 84, 95] and should enable us to tackle more complex problems. Through the information unveiled by the different single-molecule methods we are entering a new and exciting time in biology which, in combination with the knowledge generated in this proteomic era, is likely to move us closer to understanding how proteins work in living cells.

**Acknowledgements** This work was funded in part by NIH grant R01DK073394, by the UTMB Claude D. Pepper Older Americans Independence Center NIH/NIA Grant P30 AG024832, and the John Sealy Memorial Endowment Fund for Biomedical Research. We would like to acknowledge Barbara Rolls and Justin Drake for critically reviewing the super-resolution fluorescence microscopy section in this chapter.



## References

1. Abbondanzieri EA, Greenleaf WJ et al (2005) Direct observation of base-pair stepping by RNA polymerase. *Nature* 438(7067):460–465
2. Ainavarapu SR, Wiita AP et al (2008) A single-molecule assay to directly identify solvent-accessible disulfide bonds and probe their effect on protein folding. *J Am Chem Soc* 130(2):436–437
3. Allison DP, Hinterdorfer P et al (2002) Biomolecular force measurements and the atomic force microscope. *Curr Opin Biotechnol* 13(1):47–51
4. Altman D, Sweeney HL et al (2004) The mechanism of myosin VI translocation and its load-induced anchoring. *Cell* 116(5):737–749
5. Ashkin A, Dziedzic JM (1987) Optical trapping and manipulation of viruses and bacteria. *Science* 235(4795):1517–1520
6. Ashkin A, Dziedzic JM et al (1986) Observation of a single-beam gradient force optical trap for dielectric particles. *Opt Lett* 11(5):288
7. Ashkin A, Dziedzic JM et al (1987) Optical trapping and manipulation of single cells using infrared laser beams. *Nature* 330(6150):769–771
8. Aubin-Tam ME, Olivares AO et al (2011) Single-molecule protein unfolding and translocation by an ATP-fueled proteolytic machine. *Cell* 145(2):257–267
9. Axelrod D (1989) Total internal reflection fluorescence microscopy. *Methods Cell Biol* 30:245–270
10. Axelrod D (2003) Total internal reflection fluorescence microscopy in cell biology. *Methods Enzymol* 361:1–33
11. Axelrod D, Burghardt TP et al (1984) Total internal reflection fluorescence. *Annu Rev Biophys Bioeng* 13:247–268
12. Baker ML, Zhang J et al (2010) Cryo-EM of macromolecular assemblies at near-atomic resolution. *Nat Protoc* 5(10):1697–1708
13. Bechtluft P, van Leeuwen RG et al (2007) Direct observation of chaperone-induced changes in a protein folding pathway. *Science* 318(5855):1458–1461
14. Betzig E, Patterson GH et al (2006) Imaging intracellular fluorescent proteins at nanometer resolution. *Science* 313(5793):1642–1645
15. Bhasin N, Carl P et al (2004) Chemistry on a single protein, vascular cell adhesion molecule-1, during forced unfolding. *J Biol Chem* 279(44):45865–45874
16. Biais N, Higashi DL et al (2010) Force-dependent polymorphism in type IV pili reveals hidden epitopes. *Proc Natl Acad Sci U S A* 107(25):11358–11363
17. Binnig G, Quate CF et al (1986) Atomic force microscope. *Phys Rev Lett* 56(9):930–933
18. Block SM (2007) Kinesin motor mechanics: binding, stepping, tracking, gating, and limping. *Biophys J* 92(9):2986–2995
19. Braig K, Otwinowski Z et al (1994) The crystal structure of the bacterial chaperonin GroEL at 2.8 Å. *Nature* 371(6498):578–586
20. Brunger AT, Weninger K et al (2009) Single-molecule studies of the neuronal SNARE fusion machinery. *Annu Rev Biochem* 78:903–928
21. Bustamante C, Chemla YR et al (2009) High-resolution dual-trap optical tweezers with differential detection: managing environmental noise. *Cold Spring Harb Protoc* 2009(10):pdb ip72
22. Bustamante C, Cheng W et al (2011) Revisiting the central dogma one molecule at a time. *Cell* 144(4):480–497
23. Bustamante C, Marko JF et al (1994) Entropic elasticity of lambda-phage DNA. *Science* 265(5178):1599–1600
24. Cao Y, Balamurali MM et al (2007) A functional single-molecule binding assay via force spectroscopy. *Proc Natl Acad Sci U S A* 104(40):15677–15681
25. Carazo JM, Marco S et al (1991) Electron microscopy study of GroEL chaperonin: different views of the aggregate appear as a function of cell growth temperature. *J Struct Biol* 106(3):211–220

26. Carrion-Vazquez M, Marszalek PE et al (1999) Atomic force microscopy captures length phenotypes in single proteins. *Proc Natl Acad Sci U S A* 96(20):11288–11292
27. Carrion-Vazquez M, Oberhauser AF et al (1999) Mechanical and chemical unfolding of a single protein: a comparison. *Proc Natl Acad Sci U S A* 96(7):3694–3699
28. Carrion-Vazquez M, Oberhauser AF et al (2000) Mechanical design of proteins studied by single-molecule force spectroscopy and protein engineering. *Prog Biophys Mol Biol* 74(1–2):63–91
29. Cecconi C, Shank EA et al (2005) Direct observation of the three-state folding of a single protein molecule. *Science* 309(5743):2057–2060
30. Cheng W, Arunajadai SG et al (2011) Single-base pair unwinding and asynchronous RNA release by the hepatitis C virus NS3 helicase. *Science* 333(6050):1746–1749
31. Clausen-Schaumann H, Seitz M et al (2000) Force spectroscopy with single bio-molecules. *Curr Opin Chem Biol* 4(5):524–530
32. Crowther RA, Amos LA et al (1970) Three dimensional reconstructions of spherical viruses by fourier synthesis from electron micrographs. *Nature* 226(244):421–425
33. Davenport RJ, Wuite GJ et al (2000) Single-molecule study of transcriptional pausing and arrest by *E. coli* RNA polymerase. *Science* 287(5462):2497–2500
34. Deniz AA, Dahan M et al (1999) Single-pair fluorescence resonance energy transfer on freely diffusing molecules: observation of Forster distance dependence and subpopulations. *Proc Natl Acad Sci U S A* 96(7):3670–3675
35. Dufrene YF, Hinterdorfer P (2008) Recent progress in AFM molecular recognition studies. *Pflügers Arch* 456(1):237–245
36. Dumont S, Cheng W et al (2006) RNA translocation and unwinding mechanism of HCV NS3 helicase and its coordination by ATP. *Nature* 439(7072):105–108
37. Ellis RJ (1994) Molecular chaperones. Opening and closing the Anfinsen cage. *Curr Biol* 4(7):633–635
38. Ellis RJ, van der Vies SM (1991) Molecular chaperones. *Annu Rev Biochem* 60:321–347
39. Engel A, Gaub HE (2008) Structure and mechanics of membrane proteins. *Annu Rev Biochem* 77:127–148
40. Engel A, Muller DJ (2000) Observing single biomolecules at work with the atomic force microscope. *Nat Struct Biol* 7(9):715–718
41. Fazal FM, Block SM (2011) Optical tweezers study life under tension. *Nat Photonics* 5:318–321
42. Fernandez JM, Li H (2004) Force-clamp spectroscopy monitors the folding trajectory of a single protein. *Science* 303(5664):1674–1678
43. Finer JT, Simmons RM et al (1994) Single myosin molecule mechanics: piconewton forces and nanometre steps. *Nature* 368(6467):113–119
44. Florin EL, Moy VT et al (1994) Adhesion forces between individual ligand-receptor pairs. *Science* 264(5157):415–417
45. Florin E-L, Rief M, Lehmann H, Ludwig M, Dornmair C, Moy VT, Gaub HE (1995) Sensing specific molecular interactions with the atomic force microscope. *Biosens Bioelectron* 10(9–10):895–901
46. Fotiadis D (2011) Atomic force microscopy for the study of membrane proteins. *Curr Opin Biotechnol* 23(4):510–515
47. Frank J (1996) Three-dimensional electron microscopy of macromolecular assemblies. Academic, San Diego
48. Frauenfeld J, Gumbart J et al (2011) Cryo-EM structure of the ribosome-SecYE complex in the membrane environment. *Nat Struct Mol Biol* 18(5):614–621
49. Galbraith JA, Galbraith CG (2011) Super-resolution microscopy for nanosensing. *Wiley Interdiscip Rev Nanomed Nanobiotechnol* 3(3):247–255
50. Gemmell GJ, Millin R et al (2006) Tension-dependent DNA cleavage by restriction endonucleases: two-site enzymes are “switched off” at low force. *Proc Natl Acad Sci U S A* 103(31):11555–11560



51. Gorelik J, Shevchuk A et al (2002) Scanning surface confocal microscopy for simultaneous topographical and fluorescence imaging: application to single virus-like particle entry into a cell. *Proc Natl Acad Sci U S A* 99(25):16018–16023
52. Greenleaf WJ, Woodside MT et al (2007) High-resolution, single-molecule measurements of biomolecular motion. *Annu Rev Biophys Biomol Struct* 36:171–190
53. Gregor J, Benson T (2008) Computational analysis and improvement of SIRT. *IEEE Trans Med Imaging* 27(7):918–924
54. Grigorieff N, Harrison SC (2011) Near-atomic resolution reconstructions of icosahedral viruses from electron cryo-microscopy. *Curr Opin Struct Biol* 21(2):265–273
55. Gustafsson MG (2008) Super-resolution light microscopy goes live. *Nat Methods* 5(5):385–387
56. Guthold M, Zhu X et al (1999) Direct observation of one-dimensional diffusion and transcription by *Escherichia coli* RNA polymerase. *Biophys J* 77(4):2284–2294
57. Ha T, Enderle T et al (1996) Probing the interaction between two single molecules: fluorescence resonance energy transfer between a single donor and a single acceptor. *Proc Natl Acad Sci U S A* 93(13):6264–6268
58. Ha T, Ting AY et al (1999) Single-molecule fluorescence spectroscopy of enzyme conformational dynamics and cleavage mechanism. *Proc Natl Acad Sci U S A* 96(3):893–898
59. Hansma HG, Kasuya K et al (2004) Atomic force microscopy imaging and pulling of nucleic acids. *Curr Opin Struct Biol* 14(3):380–385
60. Herman GT, Lent A et al (1973) ART: mathematics and applications. A report on the mathematical foundations and on the applicability to real data of the algebraic reconstruction techniques. *J Theor Biol* 42(1):1–32
61. Hess ST, Girirajan TP et al (2006) Ultra-high resolution imaging by fluorescence photoactivation localization microscopy. *Biophys J* 91(11):4258–4272
62. Hinterdorfer P (2002) Molecular recognition studies using the atomic force microscope. *Methods Cell Biol* 68:115–139
63. Hinterdorfer P, Pohl P et al (2009) Microscopic and spectroscopic observations in the bioworld. *Chemphyschem* 10(9–10):1680–1682
64. Hirschfeld T (1976) Optical microscopic observation of single small molecules. *Appl Opt* 15(12):2965–2966
65. Hoh JH, Lal R et al (1991) Atomic force microscopy and dissection of gap junctions. *Science* 253(5026):1405–1408
66. Huang B, Bates M et al (2009) Super-resolution fluorescence microscopy. *Annu Rev Biochem* 78:993–1016
67. Ishijima A, Kojima H et al (1998) Simultaneous observation of individual ATPase and mechanical events by a single myosin molecule during interaction with actin. *Cell* 92(2):161–171
68. Isralewitz B, Baudry J et al (2001) Steered molecular dynamics investigations of protein function. *J Mol Graph Model* 19(1):13–25
69. Isralewitz B, Gao M et al (2001) Steered molecular dynamics and mechanical functions of proteins. *Curr Opin Struct Biol* 11(2):224–230
70. Jiang Y, Marszalek PE (2011) Atomic force microscopy captures MutS tetramers initiating DNA mismatch repair. *EMBO J* 30(14):2881–2893
71. Joo C, Balci H et al (2008) Advances in single-molecule fluorescence methods for molecular biology. *Annu Rev Biochem* 77:51–76
72. Ke C, Humeniuk M et al (2007) Direct measurements of base stacking interactions in DNA by single-molecule atomic-force spectroscopy. *Phys Rev Lett* 99(1):018302
73. Kellermayer MS (2005) Visualizing and manipulating individual protein molecules. *Physiol Meas* 26(4):R119–R153
74. Kner P, Chhun BB et al (2009) Super-resolution video microscopy of live cells by structured illumination. *Nat Methods* 6(5):339–342

75. Kodera N, Yamamoto D et al (2010) Video imaging of walking myosin V by high-speed atomic force microscopy. *Nature* 468(7320):72–76
76. Kuo SC, Sheetz MP (1993) Force of single kinesin molecules measured with optical tweezers. *Science* 260(5105):232–234
77. Kural C, Kim H et al (2005) Kinesin and dynein move a peroxisome in vivo: a tug-of-war or coordinated movement? *Science* 308(5727):1469–1472
78. Lakowicz JR (2006) Principles of fluorescence spectroscopy. Springer, New York
79. Lakshminarayanan AV, Lent A (1979) Methods of least squares and SIRT in reconstruction. *J Theor Biol* 76(3):267–295
80. Lang MJ, Fordyce PM et al (2004) Simultaneous, coincident optical trapping and single-molecule fluorescence. *Nat Methods* 1(2):133–139
81. Larson MH, Landick R et al (2011) Single-molecule studies of RNA polymerase: one singular sensation, every little step it takes. *Mol Cell* 41(3):249–262
82. Law R, Carl P et al (2003) Cooperativity in forced unfolding of tandem spectrin repeats. *Biophys J* 84(1):533–544
83. Li H, Linke WA et al (2002) Reverse engineering of the giant muscle protein titin. *Nature* 418(6901):998–1002
84. Li PT, Bustamante C et al (2007) Real-time control of the energy landscape by force directs the folding of RNA molecules. *Proc Natl Acad Sci U S A* 104(17):7039–7044
85. Liphardt J, Onoa B et al (2001) Reversible unfolding of single RNA molecules by mechanical force. *Science* 292(5517):733–737
86. Lippincott-Schwartz J, Manley S (2009) Putting super-resolution fluorescence microscopy to work. *Nat Methods* 6(1):21–23
87. Ludtke SJ, Baker ML et al (2008) De novo backbone trace of GroEL from single particle electron cryomicroscopy. *Structure* 16(3):441–448
88. Lyubchenko YL, Jacobs BL et al (1995) Atomic force microscopy of nucleoprotein complexes. *Scanning Microsc* 9(3):705–724, discussion 724–707
89. Lyubchenko YL, Shlyakhtenko LS et al (2011) Imaging of nucleic acids with atomic force microscopy. *Methods* 54(2):274–283
90. Maeda S, Nakagawa S et al (2009) Structure of the connexin 26 gap junction channel at 3.5 Å resolution. *Nature* 458(7238):597–602
91. Maillard RA, Chistol G et al (2011) ClpX(P) generates mechanical force to unfold and translocate its protein substrates. *Cell* 145(3):459–469
92. Marszalek PE, Oberhauser AF et al (1998) Polysaccharide elasticity governed by chair-boat transitions of the glucopyranose ring. *Nature* 396(6712):661–664
93. Marszalek PE, Lu H et al (1999) Mechanical unfolding intermediates in titin modules. *Nature* 402(6757):100–103
94. Martin J, Langer T et al (1991) Chaperonin-mediated protein folding at the surface of groEL through a “molten globule”-like intermediate. *Nature* 352(6330):36–42
95. Mathur AB, Truskey GA et al (2000) Atomic force and total internal reflection fluorescence microscopy for the study of force transmission in endothelial cells. *Biophys J* 78(4):1725–1735
96. McKinney SA, Declais AC et al (2003) Structural dynamics of individual Holliday junctions. *Nat Struct Biol* 10(2):93–97
97. Mehta AD, Pullen KA et al (1998) Single molecule biochemistry using optical tweezers. *FEBS Lett* 430(1–2):23–27
98. Michalet X, Weiss S (2002) Single-molecule spectroscopy and microscopy. *C R Phys* 3:619–644
99. Mitra K, Frank J (2006) Ribosome dynamics: insights from atomic structure modeling into cryo-electron microscopy maps. *Annu Rev Biophys Biomol Struct* 35:299–317
100. Moffitt JR, Chemla YR et al (2006) Differential detection of dual traps improves the spatial resolution of optical tweezers. *Proc Natl Acad Sci U S A* 103(24):9006–9011

101. Moffitt JR, Chemla YR et al (2008) Recent advances in optical tweezers. *Annu Rev Biochem* 77:205–228
102. Montana V, Liu W et al (2009) Single molecule measurements of mechanical interactions within ternary SNARE complexes and dynamics of their disassembly: SNAP25 vs. SNAP23. *J Physiol* 587(pt 9):1943–1960
103. Moy VT, Florin EL et al (1994) Intermolecular forces and energies between ligands and receptors. *Science* 266(5183):257–259
104. Muller DJ, Hand GM et al (2002) Conformational changes in surface structures of isolated connexin 26 gap junctions. *EMBO J* 21(14):3598–3607
105. Muller DJ, Krieg M et al (2009) New frontiers in atomic force microscopy: analyzing interactions from single-molecules to cells. *Curr Opin Biotechnol* 20(1):4–13
106. Muller DJ, Schabert FA et al (1995) Imaging purple membranes in aqueous solutions at sub-nanometer resolution by atomic force microscopy. *Biophys J* 68(5):1681–1686
107. Myong NH (2005) Tissue microarray analysis of Fas and FasL expressions in human non-small cell lung carcinomas; with reference to the p53 and bcl-2 overexpressions. *J Korean Med Sci* 20(5):770–776
108. Myong S, Rasnik I et al (2005) Repetitive shuttling of a motor protein on DNA. *Nature* 437(7063):1321–1325
109. Neher E, Sakmann B (1976) Single-channel currents recorded from membrane of denervated frog muscle fibres. *Nature* 260(5554):799–802
110. Neuman KC, Nagy A (2008) Single-molecule force spectroscopy: optical tweezers, magnetic tweezers and atomic force microscopy. *Nat Methods* 5(6):491–505
111. Nie S, Chiu DT et al (1994) Probing individual molecules with confocal fluorescence microscopy. *Science* 266(5187):1018–1021
112. Oberhauser AF, Carrion-Vazquez M (2008) Mechanical biochemistry of proteins one molecule at a time. *J Biol Chem* 283(11):6617–6621
113. Oberhauser AF, Hansma PK et al (2001) Stepwise unfolding of titin under force-clamp atomic force microscopy. *Proc Natl Acad Sci U S A* 98(2):468–472
114. Oberhauser AF, Marszalek PE et al (1998) The molecular elasticity of the extracellular matrix protein tenascin. *Nature* 393(6681):181–185
115. Oberhauser AF, Marszalek PE et al (1999) Single protein misfolding events captured by atomic force microscopy. *Nat Struct Biol* 6(11):1025–1028
116. Okten Z, Churchman LS et al (2004) Myosin VI walks hand-over-hand along actin. *Nat Struct Mol Biol* 11(9):884–887
117. Osenkowski P, Li H et al (2009) Cryoelectron microscopy structure of purified gamma-secretase at 12 Å resolution. *J Mol Biol* 385(2):642–652
118. Paige MF, Bjerneld EJ et al (2001) A comparison of through-the-objective total internal reflection microscopy and epifluorescence microscopy for single-molecule fluorescence imaging. *Single Mol* 2:191–201
119. Park H, Ramamurthy B et al (2006) Full-length myosin VI dimerizes and moves processively along actin filaments upon monomer clustering. *Mol Cell* 21(3):331–336
120. Perez-Jimenez R, Li J et al (2009) Diversity of chemical mechanisms in thioredoxin catalysis revealed by single-molecule force spectroscopy. *Nat Struct Mol Biol* 16(8):890–896
121. Ptacin JL, Nollmann M et al (2006) Identification of the FtsK sequence-recognition domain. *Nat Struct Mol Biol* 13(11):1023–1025
122. Puchner EM, Gaub HE (2009) Force and function: probing proteins with AFM-based force spectroscopy. *Curr Opin Struct Biol* 19(5):605–614
123. Radon J (1917) Über die bestimmung von funktionen durch ihre integralwerte längs gewisser mannigfaltigkeiten. *Ber Verh Sächs Akad Wiss Leipzig Math Nat Kl* 69:262–277
124. Rief M, Gautel M et al (1997) Reversible unfolding of individual titin immunoglobulin domains by AFM. *Science* 276(5315):1109–1112
125. Rief M, Oesterhelt F et al (1997) Single molecule force spectroscopy on polysaccharides by atomic force microscopy. *Science* 275(5304):1295–1297

126. Rock RS, Rice SE et al (2001) Myosin VI is a processive motor with a large step size. *Proc Natl Acad Sci U S A* 98(24):13655–13659
127. Roy R, Hohng S et al (2008) A practical guide to single-molecule FRET. *Nat Methods* 5(6):507–516
128. Rust MJ, Bates M et al (2006) Sub-diffraction-limit imaging by stochastic optical reconstruction microscopy (STORM). *Nat Methods* 3(10):793–795
129. Schnitzer MJ, Block SM (1997) Kinesin hydrolyses one ATP per 8-nm step. *Nature* 388(6640):386–390
130. Settembre EC, Chen JZ et al (2011) Atomic model of an infectious rotavirus particle. *EMBO J* 30(2):408–416
131. Shank EA, Cecconi C et al (2010) The folding cooperativity of a protein is controlled by its chain topology. *Nature* 465(7298):637–640
132. Slayter EM, Slayter HS (1992) *Light and electron microscopy*. Cambridge University Press, Cambridge
133. Small A (2012) Faster and more versatile tools for super-resolution fluorescence microscopy. *Nat Methods* 9(7):655–656
134. Smith SB, Cui Y et al (1996) Overstretching B-DNA: the elastic response of individual double-stranded and single-stranded DNA molecules. *Science* 271(5250):795–799
135. Smith DE, Tans SJ et al (2001) The bacteriophage straight phi29 portal motor can package DNA against a large internal force. *Nature* 413(6857):748–752
136. Snyder GE, Sakamoto T et al (2004) Nanometer localization of single green fluorescent proteins: evidence that myosin V walks hand-over-hand via telemark configuration. *Biophys J* 87:1776–1783
137. Spudich JA, Rice SE et al (2011) Optical traps to study properties of molecular motors. *Cold Spring Harb Protoc* 2011(11):1305–1318
138. Stigler J, Ziegler F et al (2011) The complex folding network of single calmodulin molecules. *Science* 334(6055):512–516
139. Svoboda K, Block SM (1994) Force and velocity measured for single kinesin molecules. *Cell* 77(5):773–784
140. Svoboda K, Schmidt CF et al (1993) Direct observation of kinesin stepping by optical trapping interferometry. *Nature* 365(6448):721–727
141. Szoszkiewicz R, Ainarapu SR et al (2008) Dwell time analysis of a single-molecule mechanochemical reaction. *Langmuir* 24(4):1356–1364
142. Truong K, Sawano A et al (2001) FRET-based in vivo Ca<sup>2+</sup> imaging by a new calmodulin-GFP fusion molecule. *Nat Struct Biol* 8(12):1069–1073
143. Tskhovrebova L, Trinick J et al (1997) Elasticity and unfolding of single molecules of the giant muscle protein titin. *Nature* 387(6630):308–312
144. Umemura YM, Vrljic M et al (2008) Both MHC class II and its GPI-anchored form undergo hop diffusion as observed by single-molecule tracking. *Biophys J* 95(1):435–450
145. Unger VM, Kumar NM et al (1999) Three-dimensional structure of a recombinant gap junction membrane channel. *Science* 283(5405):1176–1180
146. Valentine MT, Fordyce PM et al (2006) Individual dimers of the mitotic kinesin motor Eg5 step processively and support substantial loads in vitro. *Nat Cell Biol* 8(5):470–476
147. Visscher K, Block SM (1998) Versatile optical traps with feedback control. *Methods Enzymol* 298:460–489
148. Visscher K, Schnitzer MJ et al (1999) Single kinesin molecules studied with a molecular force clamp. *Nature* 400(6740):184–189
149. Wang MD, Schnitzer MJ et al (1998) Force and velocity measured for single molecules of RNA polymerase. *Science* 282(5390):902–907
150. Webb RH (1999) Theoretical basis of confocal microscopy. *Methods Enzymol* 307:3–20
151. Williams PM, Fowler SB et al (2003) Hidden complexity in the mechanical properties of titin. *Nature* 422(6930):446–449

152. Wuite GJ, Smith SB et al (2000) Single-molecule studies of the effect of template tension on T7 DNA polymerase activity. *Nature* 404(6773):103–106
153. Yildiz A, Forkey JN et al (2003) Myosin V walks hand-over-hand: single fluorophore imaging with 1.5-nm localization. *Science* 300(5628):2061–2065
154. Yildiz A, Tomishige M et al (2004) Kinesin walks hand-over-hand. *Science* 303(5658):676–678
155. Yu J, Moffitt J et al (2010) Mechanochemistry of a viral DNA packaging motor. *J Mol Biol* 400(2):186–203
156. Zhang X, Settembre E et al (2008) Near-atomic resolution using electron cryomicroscopy and single-particle reconstruction. *Proc Natl Acad Sci U S A* 105(6):1867–1872
157. Zhang R, Hryc CF et al (2011) 4.4 Å cryo-EM structure of an enveloped alphavirus venezuelan equine encephalitis virus. *EMBO J* 30(18):3854–3863
158. Zhang X, Jin L et al (2010) 3.3 Å cryo-EM structure of a nonenveloped virus reveals a priming mechanism for cell entry. *Cell* 141(3):472–482
159. Zhou ZH (2011) Atomic resolution cryo electron microscopy of macromolecular complexes. *Adv Protein Chem Struct Biol* 82:1–35
160. Zhuang X, Rief M (2003) Single-molecule folding. *Curr Opin Struct Biol* 13(1):88–97
161. Zhuang X, Bartley LE et al (2000) A single-molecule study of RNA catalysis and folding. *Science* 288(5473):2048–2051

**Part II**  
**Biological Macromolecules as Molecular**  
**Machines: Three Examples**

# Chapter 9

## Helicase Unwinding at the Replication Fork

Divya Nandakumar and Smita S. Patel

**Abstract** Ring-shaped hexameric helicases play an essential role of double-stranded DNA unwinding during genome replication. The NTPase-powered unwinding activity of the hexameric helicases is required both for replication initiation and fork progression. We describe ensemble biophysical methods to measure the unwinding activity of ring-shaped helicases during fork progression using the T7 bacteriophage replicative helicase gp4A' as a model enzyme. These assays provide insights into the stepping mechanism of translocation, active or passive mechanism of unwinding, and regulation by associated proteins such as single strand DNA binding protein, DNA polymerase, and primase enzymes.

**Keywords** Hexameric helicase • Replication • DNA unwinding • T7 bacteriophage • DNA polymerase • SSB • Primase • Unwinding assays • gfit • Global regression analysis • Unwinding mechanism

### 9.1 Introduction

Helicases are molecular motor proteins that unwind double-stranded (ds) DNA into single strands using the energy of NTP hydrolysis. This activity is required not only for DNA replication but also for DNA repair, recombination, and transcription [1–3]. Helicases are found from viruses to humans where they play essential roles in practically all DNA and RNA metabolic processes. Therefore, helicases are attractive targets for developing new antiviral, antibacterial, and therapeutic agents. In humans, defects in helicase activity due to mutations cause genome instability that can ultimately result in diseases such as cancer and premature aging.

---

D. Nandakumar • S.S. Patel (✉)

Department of Biochemistry and Molecular Biology, Robert Wood Johnson Medical School,  
Rutgers University, 675 Hoes lane, Piscataway, NJ 08854, USA  
e-mail: patelss@rwjms.rutgers.edu

DNA unwinding is a multistep process involving both chemical and mechanical steps. To initiate unwinding, the helicase must bind DNA and assemble into its functional monomeric/multimeric structure on the DNA. To unwind DNA, the helicase binds to NTP and hydrolyzes it forming intermediates that stabilize various conformational changes that support helicase translocation along single-stranded DNA (ssDNA) and separation of the dsDNA. The NTPase and translocation/unwinding cycling continue while the helicase remains attached to the DNA, leading to processive separation of the dsDNA strands. To understand helicase mechanisms, each step is kinetically and thermodynamically characterized and the relationships and dependencies between the various steps are determined. Additionally, this information is related to high-resolution structures of helicase complexes with DNA and NTP. Biochemical and biophysical methods such as pre-steady state kinetics, X-ray crystallography, electron microscopy, single molecule kinetics, and advancements in computational biophysics have been critical in enhancing our understanding of the functioning of helicases [4–6].

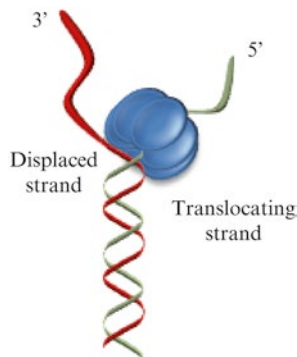
A class of helicases distinguished by their ring-shaped structure is found widely to be involved in genome replication. These ring-shaped helicases assemble from six identical subunits in most organisms, except in eukaryotes where the replicative hexameric helicase mini chromosome maintenance protein (MCM 2–7) assembles from six different subunits [7, 8]. The ring-shaped assembly creates a central channel that binds DNA and the topological linkage of the DNA and the ring confers high processivity to this class of helicases allowing them to unwind long segments of DNA for efficient replication. The central channel is flexible and it can accommodate ssDNA or dsDNA and many hexameric helicases can translocate on both types of DNA [9, 10].

The ssDNA translocation activity of hexameric helicases is important for DNA unwinding and is powered by the NTPase reaction that occurs at the active sites located at the hexamer subunit interfaces [11–14]. The direction of translocation can be either  $5' \rightarrow 3'$  or  $3' \rightarrow 5'$  depending on the helicase. Recent biochemical [15, 16] and structural studies support an ordered sequential mechanism of NTP hydrolysis around the ring. The crystal structure of bovine papilloma virus E1 and *Escherichia coli* Rho helicase indicates that at any given time, five consecutive subunits interact with five consecutive nucleotides of ssDNA (or ssRNA) in a spiral staircase conformation [13, 14]. Each subunit is in a distinct NTP ligation state as it goes through the steps of NTP binding, hydrolysis, Pi release, and NDP release steps in a sequential manner. During translocation, NTP binding promotes a subunit at the top of the staircase to bind to a free nucleotide of ssDNA while at the same time NDP release promotes its neighboring subunit to release its nucleotide of ssDNA. Thus, directional movement of helicase on ssDNA is akin to a wheel (helicase) rolling down the road (ssDNA) without slipping through interactions within the central channel of the helicase.

To separate the strands of dsDNA, the helicase must couple its ssDNA translocation activity to base pair melting at the replication fork junction. Almost all hexameric helicases unwind the fork DNA by a strand exclusion model [10, 17–22]. In this model, the helicase ring translocates along one of the ssDNA strands that it binds in its central channel while excluding the complementary strand (Fig. 9.1). Strand exclusion is important because if the helicase ring surrounds the dsDNA



**Fig. 9.1** Strand exclusion model of helicase unwinding. A representation of the strand exclusion model in which the ring-shaped helicase binds the translocating strand in the central channel and excludes the complementary strand to separate the two strands



instead of ssDNA, then strand separation does not occur because the helicase translocates along dsDNA without unwinding. The coupling of ssDNA translocation and base pair melting that leads to strand separation can occur by a passive or active mechanism [23]. In a passive mechanism, the helicase does not destabilize the junction base pair but simply translocates along ssDNA by capturing an opened base generated by thermal fraying, whereas in the active mechanism, the helicase actively disrupts the base pairs at the junction. We will discuss methods to distinguish between the two mechanisms.

Replicative helicases work in association with enzymes such as the DNA polymerase and DNA primase and accessory proteins such as the single strand DNA binding protein (SSB) [24–26] to ensure efficient and timely replication of genomic DNA. To understand the role of the helicase during DNA replication, it is necessary to study the unwinding activity of the isolated helicase as well as the helicase in complex with associated proteins. Bacteriophage T7 provides an ideal system to carry out such enzymological studies of DNA replication [25]. The replication machinery of phage T7 is one of the simplest consisting of the helicase-primase protein (T7 gp4), DNA polymerase (heterodimer of T7 gp5 and *E. coli* thioredoxin), and single strand binding protein (T7 gp2.5). There are no accessory loaders or connector proteins required and efficient DNA replication can be reconstituted in vitro from recombinant proteins.

Unwinding long stretches of DNA by the helicase occurs in a stepwise manner. In each step the helicase unwinds a certain number of base pairs (step size) at a certain rate (stepping rate). These biophysical parameters along with others such as the rate of unwinding a single base pair and how far the helicase travels before dissociating from the DNA (processivity) are critical for understanding the mechanism of action of this enzyme. In this chapter, we will discuss ensemble biophysical methods to characterize these most basic parameters of DNA unwinding by helicases. Although the methods described are using T7 helicase as an example, they are generally applicable to most helicases. We will show that the single base pair unwinding rate from ensemble methods can be used as a basic handle to determine if the helicase unwinds DNA by an active or passive mechanism and to probe how helicase activity is regulated by single strand binding protein (SSB), DNA polymerase, and primase.

## 9.2 Ensemble Unwinding Assay Conditions

The ensemble assays that we describe to measure DNA strand separation by the helicase are all-or-none assays that detect only the end product in the reaction. These assays do not detect partial unwinding of dsDNA for which other methods can be used [27, 28]. We use two kinds of assays; a radiometric discontinuous gel-based assay and a fluorescence-based real time assay to detect DNA strand separation. In this section, we describe the DNA substrate and the conditions for the assays in detail.

### 9.2.1 DNA Substrate

A typical DNA substrate to measure the unwinding activity of replicative ring-shaped helicases is a fork DNA that contains a linear dsDNA region and two noncomplementary ssDNA overhangs (Fig. 9.2a, b). This substrate mimics half of a replication fork advancing in one direction. The fork DNA substrates are chemically synthesized; therefore, both the length and sequence of the DNA can be easily controlled. The phage T7 helicase is a 5′–3′ translocase and strand separation occurs when the helicase assembles around the 5′-overhang and translocates in the 5′–3′ direction excluding the 3′-strand from its central channel. Optimum unwinding of dsDNA by T7 helicase requires the 5′-overhang to be 35-nt long and 3′-overhang to be 15-nt, which needs to be determined experimentally by comparing the unwinding rates and processivity values for DNA substrates with different lengths of 5′ and 3′ overhangs [18].

### 9.2.2 Steady State Versus Pre-steady State Kinetics

Steady state kinetic approaches are generally not suitable for determining the unwinding rates of helicases. Under steady state experimental conditions, the fork DNA substrate is used in excess amount over the helicase and one measures multiple rounds of helicase loading, unwinding, and helicase dissociation from the end. The observed rate under steady state conditions is dictated primarily by the slow rate of helicase dissociation and reassociation. DNA unwinding therefore needs to be monitored under pre-steady state conditions where the steps of helicase association and dissociation are decoupled from the steps of DNA unwinding. Synchronization of the enzyme molecules is important in determining the unwinding rate for which the helicase needs to be preassembled on the fork DNA without having unwinding of the dsDNA in the assembly mixture.

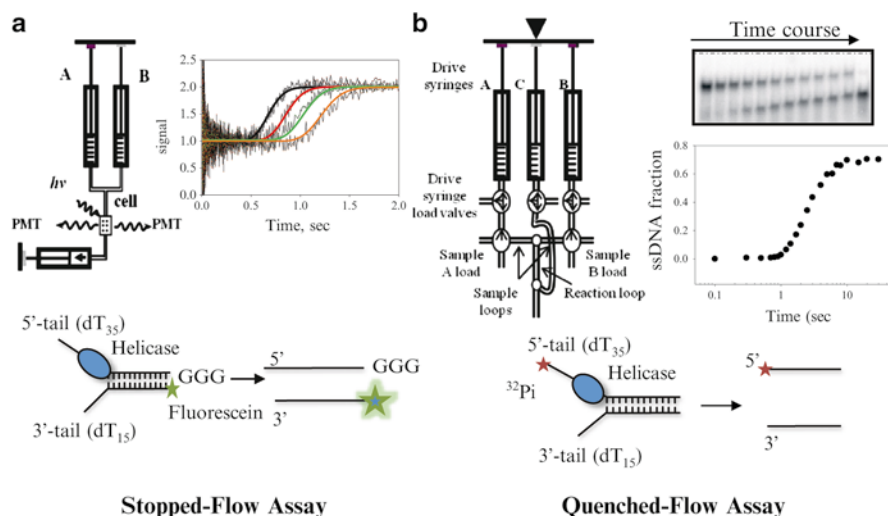


**Fig. 9.2** Ensemble DNA unwinding assays. **(a)** Instrumental design, DNA substrate, and representative kinetic traces for the fluorescence-based stopped-flow assay **(a)** and gel-based quenched-flow assay **(b)** to measure DNA unwinding. **(a)** The KinTek stopped-flow instrument rapidly fires reactants from the two drive syringes into a mixing cell for observation by fluorescence or absorbance with time resolution of 1 ms. The DNA substrate is labeled with fluorescein at the 5' end of the lower strand and has a GGG at the 3' end of the translocating strand to quench the fluorescence when present as dsDNA. Unwinding results in strand separation and a time-dependent increase in fluorescence as seen in the sample kinetic trace. **(b)** The quenched-flow instrument allows rapid mixing of two reactants followed by a delay line after which the mixed reactants are quenched. The duration of the reaction is determined by the volume of the delay line and the flow rate through the delay line. Radiolabeling of the translocating strand at the 5' end allows visualization of the forked DNA substrate and released ssDNA product at various time points when resolved on a native polyacrylamide gel. The kinetic trace shows a time-dependent increase in ssDNA fraction

### 9.2.3 Assembly of the Helicase on the DNA

Ring-shaped helicases assemble very slowly on DNA and many require special conditions or protein loaders to efficiently bind DNA. Although T7 helicase does not require a loader protein to bind DNA, it needs dTTP to form hexameric rings and to bind DNA but can do so without  $Mg^{2+}$  [29]. Since  $Mg^{2+}$  is required for dTTP hydrolysis, we prevent DNA unwinding in the preassembly mixture by leaving out  $Mg^{2+}$  and adding it to initiate the reaction. Single round conditions are established by including a trap such as SSB protein that would bind free ssDNA or excess ssDNA that would bind free helicase. The optimal concentration of the trap is determined experimentally by adding increasing amount of the trap in the preassembly mixture.

It is important to note that SSB can potentially have other effects on the unwinding mechanism apart from acting as a DNA trap (Sect. 9.6). When using ssDNA to trap excess helicase, the commonly used traps are the 5'-strand or 3'-strand itself or a polynucleotide DNA such as dT(30–90). With some helicases, the specific ssDNA used as the trap can influence the unwinding mechanism by the helicase [30]. Thus, it is important to ensure that the traps do not affect the mechanism of unwinding by verifying that different traps have a uniform effect on unwinding.

### 9.3 Unwinding Assays

T7 helicase unwinds short fork DNA substrates ranging in length from 20 to 90 bp within milliseconds time intervals. Hence, the pre-steady state single round kinetic measurements are carried out in rapid mixing apparatus such as the stopped-flow or quenched-flow instruments (Fig. 9.2a, b).

#### 9.3.1 *Real Time Unwinding Assay*

To measure DNA unwinding in real time, the fork DNA substrate is modified with a fluorophore (such as fluorescein), incorporated at the 5'-end of the displaced strand. When the DNA is double-stranded, the fluorescein fluorescence is quenched by a string of three guanines introduced in the 3' end of the complementary strand [31, 32]. When the helicase unwinds the dsDNA and the displaced strand becomes single-stranded, the fluorescein moves away from the string of Gs and the fluorescence increases when the strands are fully separated. This results in a time-dependent increase in fluorescence, which is measured continuously in a stopped-flow apparatus (Fig. 9.2a).

#### 9.3.2 *Gel-Based Unwinding Assay*

The gel-based assay is discontinuous where one of the DNA strands is 5'-end labeled with  $^{32}\text{P}$ i allowing detection of the fork DNA substrate and the ssDNA product (Fig. 9.2b). The reactions are mixed in a quenched-flow instrument and the unwinding reaction is stopped after defined periods with EDTA and sodium dodecyl sulfate (SDS) that dissociates the helicase from the DNA. The quenched reactions are analyzed by native polyacrylamide gel electrophoresis that resolves dsDNA from the fully unwound ssDNA, which are quantified using the phosphorimager software ImageQuant (GE Healthcare). The partially unwound intermediates reanneal after the unwinding reaction is stopped. The only intermediates that may not reanneal and fall apart into ssDNAs after quenching are the ones where only a very short portion of dsDNA remains to be

unwound. This short portion of dsDNA is defined as the minimal duplex length ( $L_m$ ) and it can be determined experimentally as described below (Sect. 9.4.2).

We describe only two ensemble experiments, but variations of these have been successfully used for studying other helicases [33–35]. Of the assays, the fluorescence-based assay has the advantage of being real time, high throughput, providing a large number of data points to accurately determine the unwinding rate, and has a smaller  $L_m$  compared to the gel-based assay (explained below). The radio-metric assay is discontinuous, but it provides a reliable way to determine the amplitude or the fraction of DNA unwound at any given time. The amplitude is used to determine the helicase processivity, which estimates how far the helicase moves along the DNA before it falls off.

## 9.4 The Unwinding Kinetic Trace

The pre-steady state single round kinetics of unwinding shows an initial lag followed by a steep increase in ssDNA product formation that plateaus after a certain time. The initial lag represents the time the helicase takes to unwind the dsDNA region before the strands become fully separated. The lag time depends on the dsDNA length and it increases as the length of the dsDNA increases (Fig. 9.3a). The steady increase in lag time with increasing dsDNA length is a good indication that the assay is measuring the steps of unwinding rather than rate-limiting initiation. The plateau in the trace represents the population of DNA strands that are fully separated at the end of the reaction. As the trace represents an all-or-none unwinding reaction, the slope should typically be steep corresponding to the synchronized generation of ssDNA. A shallow increase observed under certain conditions or with certain DNA substrates is an indication of a distribution of enzyme molecules over the intermediate steps in the reaction, generated by helicase pausing or nonuniform stepping rates.

### 9.4.1 *Quantifying the Assembled Helicase–DNA Complex*

To prevent the newly unwound DNA strands from reannealing during the course of the reaction, the fork DNA concentration is kept to a minimum (low nanomolar range). This is especially important when the unwinding rate is slow and reactions are monitored for minutes. The concentration of helicase is then adjusted to saturate the fork DNA substrate. To determine the concentration of helicase to add in the preassembly mixture, one needs to know the dissociation constant ( $K_d$ ) of the helicase–fork DNA complex under conditions of the experiment. The dissociation constant is a measure of strength of binding or affinity of an enzyme for its substrate. We describe here a method to determine the apparent  $K_d$  or  $K_{1/2}$  of T7 helicase–fork DNA complex in the presence of dTTP using the unwinding assay itself (Fig. 9.3b). The measured value is the apparent  $K_d$  as the readout for the experiment

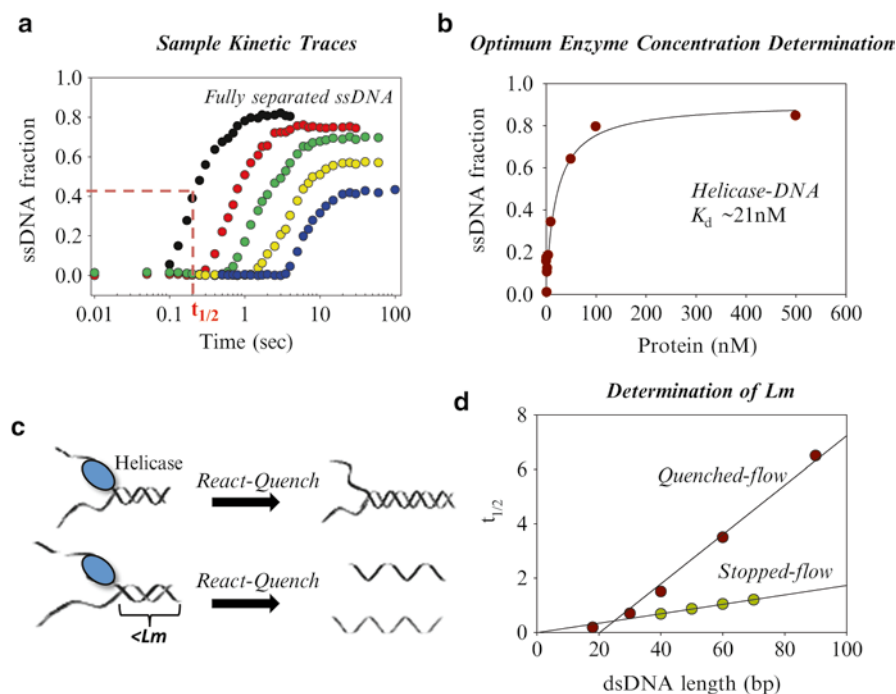


**Fig. 9.3** DNA unwinding assay parameters. **(a)** Pre-steady state sample kinetic traces showing unwinding of 18–90 bp length of fork DNA by 100 nM T7 helicase (T7 gp4A') at 18 °C in the presence of 2 mM dTTP and excess ssDNA trap using the gel-based assay. The time taken for half the molecules to be unwound is an approximate value of the  $t_{1/2}$  for the reaction. **(b)** Estimation of apparent  $K_d$ : Plot of fraction of substrate unwound at increasing concentrations of T7 helicase is fit to a hyperbola to obtain the apparent  $K_d$  in the absence of  $Mg^{2+}$ . In this experiment, 5 nM fork DNA was incubated with various concentrations of T7 helicase in the presence of 2 mM dTTP and 5 mM EDTA for 15 min. This was mixed with 2 mM dTTP, 3 mM ssDNA trap, and 9.4 mM  $MgCl_2$  to initiate the unwinding reaction which was quenched after 30 s. The fraction of DNA unwound was estimated from native polyacrylamide gel. **(c)** Quick estimation of  $L_m$ :  $L_m$  or the minimal duplex length refers to the shortest duplex length that does not fall apart in the absence of the helicase. The  $x$  intercept from a plot of  $t_{1/2}$  of unwinding versus DNA length for the gel-based and real time fluorescence assays provided  $L_m$  of 18 and 0.64 bp, respectively

(unwinding) is a step associated with binding but not binding itself. The  $K_m$  of dTTP ranges from 20 to 200  $\mu$ M depending on the stability of the dsDNA [36]. Near-saturation dTTP concentrations of 0.5 mM in the stopped-flow and 2 mM in the quenched-flow assays are used in the examples discussed here. Helicases can also use alternate NTPs as fuel in addition to the most commonly used NTP. For example, in addition to dTTP, T7 gp4A' can use dATP and ATP as substrates with unwinding being faster with ATP. However, use of ATP also promotes slippage during unwinding [37]. Similarly, the T4 bacteriophage helicase gp41 can also use ATP or GTP for unwinding with the rates being faster with GTP than ATP [38].

A mixture of 40 bp radiolabeled fork DNA (2 nM) and 1 mM dTTP incubated with various concentrations of T7 helicase (5–500 nM) is mixed with  $\text{Mg}^{2+}$  and ssDNA trap and quenched after 30 s in a quenched-flow instrument. A plot of the fraction of DNA unwound in 30 s versus helicase concentration fits to a hyperbola with  $K_{1/2}$  of 21 nM (Fig. 9.3b), which is the apparent  $K_d$  of the helicase–fork DNA complex in the presence of dTTP without  $\text{Mg}^{2+}$ . This assay provides a measure of the active enzyme–substrate complex in the preassembly mixture. This is more reliable than simply using the  $K_d$  obtained from other equilibrium binding methods, because it is possible that a fraction of the enzyme forms a nonproductive complex with the DNA and is not available for unwinding.

The same information can be obtained from the real time stopped-flow assay where a mixture of fluorescent-labeled fork DNA (2 nM) and T7 helicase (5–500 nM) is incubated with 1 mM dTTP in one syringe of the stopped-flow instrument and mixed with  $\text{Mg}^{2+}$  and ssDNA trap from the other syringe. The difference in the initial and final plateau values of fluorescence (amplitude,  $A$ ) increases as T7 helicase concentration is increased in the preassembly mixture. The plot of amplitude versus T7 helicase concentration fits to a hyperbola with  $K_{1/2}$  of 18 nM, which is very close to the value from the quenched-flow assay.

### 9.4.2 Estimation of $L_m$

To determine the unwinding parameters, the actual length of dsDNA that is unwound by the helicase needs to be determined. A portion of the dsDNA, defined as the  $L_m$  or the minimal stable dsDNA length, falls apart spontaneously before the helicase reaches the end of the fork DNA (Fig. 9.3c) of length  $L$ . The effective length of DNA that the helicase unwinds is therefore  $L - L_m$ . The value of  $L_m$  depends on the type of unwinding assay (real time versus discontinuous gel-based assay), the GC content of the dsDNA, and the temperature of the experiment. A quick way to estimate  $L_m$  is from the  $x$  intercept of  $t_{1/2}$  of unwinding versus  $L$ . An alternate method to determine  $L_m$  using methyl phosphonate-modified DNA has been used in the kinetic analysis of Dda helicase [39].

Typically the gel-based assay of unwinding provides a larger value of  $L_m$  than the real time assay. This is because the partially unwound duplexes, especially those intermediates that have a very short stretch of dsDNA remaining to be unwound, fall apart in the time period between reaction quenching and product analysis by gel electrophoresis. Using the semiquantitative method of  $t_{1/2}$  versus  $L$ , we obtained an  $L_m$  of 18 bp for the unwinding of 18–90 bp fork DNA (average GC content 32 %) by the gel-based assay ( $x$  intercept in Fig. 9.3c). The real time assay, on the other hand, provided  $L_m$  of 0.64 bp from the  $t_{1/2}$  of unwinding a set of 40–70 bp (average GC content 5 %) (Fig. 9.3c).  $L_m$  can be more accurately obtained from global fitting of unwinding a set of fork DNAs of different lengths, as described in section “Computational Model for Unwinding (Sect. 9.5.1).”

## 9.5 Stepping Model of DNA Unwinding

T7 helicase can unwind long stretches of DNA that exceed the DNA binding site of a single hexamer. Such processive unwinding of dsDNA can be represented by a stepping model, where the helicase moves unidirectionally along ssDNA in a series of discrete steps each one coupled to its biochemical cycle of NTP hydrolysis (Fig. 9.4). The number of base pairs unwound in each step is defined as the step size ( $s$ ) and the rate as the stepping rate ( $k$ ). The step size and stepping rate are the most basic parameters of the helicase motor, but are difficult to measure. The ensemble all-or-none unwinding assays described here can be computationally fit to a uniform stepping model that assumes equal step size and stepping rate (Fig. 9.4a). The average step size obtained from these measurements is referred to as the *kinetic* step size as it provides the number of base pairs unwound between two rate-limiting steps of unwinding a stretch of dsDNA and may not correspond to the elementary step size that is coupled to the NTPase cycle. The helicase stepping process could be affected by the composition of the DNA sequence and may not be uniform as assumed (Fig. 9.4b). Despite this limitation, the model provides reliable values of the average single base pair unwinding rates and processivity of the helicase, which allows us to make inferences on the helicase mechanism of action and effect of proteins that regulate helicase activity.

### 9.5.1 Computational Model for Unwinding

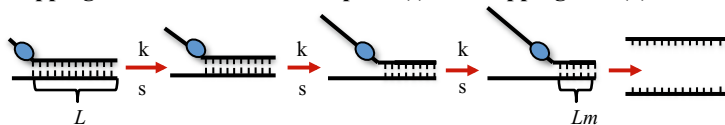
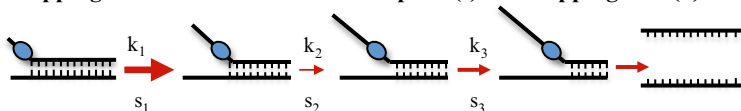
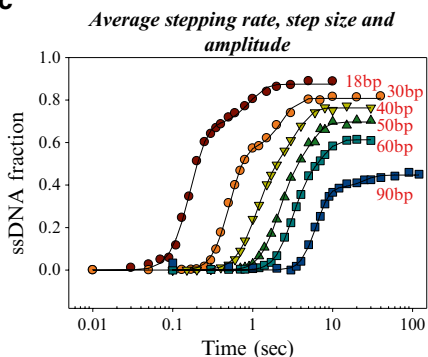
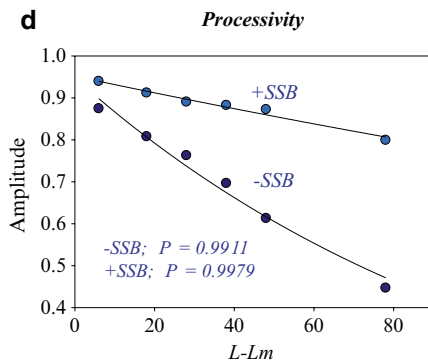
The uniform stepping model considers the total unwinding to consist of discrete steps of equal size ( $s$ ) and uniform stepping rate ( $k$ ). In the all-or-none unwinding experiments under single round conditions, we monitor only the product of the last step in the series of unwinding steps, which is described by the incomplete gamma function (9.1). The mathematical basis for use of the gamma function has been comprehensively described by Lucius et al. [40] and is beyond the scope of this chapter. The incomplete gamma function allows the number of unwinding steps ( $n$ ) to be continuous (not only integers) and hence allows us to float the parameter  $n$  in the computation. The fitting provides the stepping rate ( $k$ ) and step size ( $s$ ) to unwind the dsDNA of effective length ( $L - L_m$ ).

$$F(t) = \sum_i^N A_i \gamma(n_i, k_i t) + F_0 \quad (9.1)$$

where

$$\gamma(n, s) = \frac{\int_0^s e^{-x} x^{n-1} dx}{\int_0^\infty e^{-x} x^{n-1} dx}$$



**a** Stepping model with uniform step size( $s$ ) and stepping rate ( $k$ )**b** Stepping model with non-uniform step size( $s$ ) and stepping rate ( $k$ )**c****d**

**Fig. 9.4** Stepping model of unwinding. **(a)** Uniform stepping model: In the uniform stepping model, the unwinding reaction is considered to consist of a series of discrete steps of uniform step size ( $s$ ) and stepping rate ( $k$ ). The step size represents the number of bp unwound by the helicase between two rate-limiting steps. **(b)** Nonuniform stepping model: Effect of DNA composition or heterogeneity in helicase population can result in varying step size and stepping rate. This is accounted for in the nonuniform stepping model which assumes nonuniform stepping rate ( $k_1, k_2, k_3, \dots, k_n$ ) and step size ( $s_1, s_2, s_3, \dots, s_n$ ) of helicase movement where  $n$  is the total number of steps. The varying step size and stepping rate are indicated by different sized arrows. **(c)** Estimation of rate,  $L_m$ , amplitude, and step size by global data fitting: Time course of unwinding obtained by the gel-based assay for fork DNA substrates of different lengths (18–90 bp) by 100 nM T7 helicase at 18 °C in the presence of 2 mM dTTP and excess ssDNA trap, globally fit to a two-population uniform stepping model using the *gfit* application provided an average base pair unwinding rate of 15.5 bp/s. **(d)** Processivity: Plot of amplitude obtained through global fitting versus effective duplex length unwound ( $L - L_m$ ) is fit to  $A = A_0 \times P^{(L-L_m)}$  to obtain a processivity of 0.9911 for the isolated helicase and 0.9979 for T7 helicase in the presence of SSB

is the normalized incomplete gamma function,  $n = (L - L_m)/s$  is the number of unwinding steps required to observe the product,  $F(t)$  is the fraction of single-stranded DNA at time  $t$ , and  $F_0$  is the background signal.

An inherent problem in analyzing ensemble processes is the possibility of multiple species of starting enzyme–DNA complex or populations that unwind at different average rates. Our model accounts for this by calculating the sum of  $N$  unwinding processes,

providing amplitudes ( $A_i$ ) and stepping rates ( $k_i$ ) for each population. A similar model developed by Lucius et al. addresses the same problem by incorporating a term for a nonproductive enzyme–DNA complex and can fit the data to two populations [40]. The software *gfit* (MATLAB), developed by Mikhail Levin, allows us to fit the unwinding kinetic data to the model [unwinding.m] to obtain relevant parameters [41].

To estimate the minimal stable duplex length,  $L_m$ , the unwinding traces for a set of fork DNAs of different lengths ( $L$ ) are fit to the stepping model while globally constraining the apparent stepping rate, step size, and  $L_m$ . We show here gel-based time traces of unwinding fork DNAs from 18 to 90 bp with 32 % average GC content using ssDNA as a trap for which the global fit provided  $L_m$  of 14.8 bp,  $k_s$  of 18.6 steps/s, and  $s$  of 0.8 bp (Fig. 9.4c). The average single base pair unwinding rate  $k_u$  was calculated as  $k_s \times s = 18.6 \times 0.8 = 15.5$  bp/s.

### 9.5.2 Processivity of DNA Unwinding

Processivity of single base pair unwinding ( $P$ ) is defined as the probability that the helicase unwinds a base pair as opposed to dissociating from that position on the DNA and it estimates how far the helicase moves on the DNA before dissociating from the DNA. Processivity is determined from the amplitudes of DNA unwinding traces of fork DNAs of different lengths. The amplitude can be determined from computational fitting or simple examination of the unwinding time traces in single round experiments. For example, unwinding of fork DNAs from 18 to 90 bp fork DNA under single round conditions shows a decrease in amplitude with increasing dsDNA length. Fitting the plot of amplitude ( $A$ ) versus  $(L - L_m)$  to the relationship,  $A = A_0 \times P^{(L - L_m)}$  [40], provides processivity of 0.9911 for T7 helicase (Fig. 9.4d). This is a more accurate value obtained by fitting the unwinding data to the two-population stepping model compared to the previously published value of 0.9835 obtained by fitting the data to a one-population stepping model [42]. The  $P$  of 0.9911 indicates that T7 helicase unwinds on an average about 112 bp of DNA before dissociating based on the relation, average distance travelled =  $1/(1 - P)$  [40]. The single base pair processivity  $P$  is equal to  $k_u/k_u + k_d$ , where  $k_u$  is the average single base pair unwinding rate and  $k_d$  is the average helicase dissociation rate after each base pair unwinding. From the processivity data and average single bp unwinding rate, we determine that T7 helicase dissociates with an average rate of  $0.14 \text{ s}^{-1}$  during unwinding. The dissociation rate of T7 helicase during unwinding also increases with increase in GC content of the DNA. This could possibly be the effect of enhanced stalling observed for the helicase on GC patches in single molecule experiments. Contrary to expectations for a ring-shaped helicase that binds DNA in the central channel, the unwinding studies reveal a surprisingly low processivity for the T7 helicase compared to its processivity during ssDNA translocation (112 versus 7,500 bp). The low processivity is probably a consequence of interactions of the helicase with the fork junction. We show below that addition of *E. coli* SSB or DNA polymerase increases the processivity of the complex during unwinding.

### 9.5.3 *Active Versus Passive Mechanism of DNA Unwinding*

Helicases can unwind dsDNA by an active or passive mechanism. A passive helicase located at the fork junction does not destabilize the junction base pairs and can advance only when the junction base pairs are separated by thermal fluctuation. On the other hand, if the presence of the helicase or the forward motion of the helicase powered by the NTP hydrolysis reaction destabilizes the junction base pairs and shifts the equilibrium of base pair opening and closing toward opening, then the helicase is unwinding by an active mechanism (Fig. 9.5a).

One way to assess whether a helicase unwinds by an active or passive mechanism is to determine the sensitivity of helicase-catalyzed unwinding to base pair stability. A mathematical treatment by Betterton and Julicher [23] has shown that a helicase may show different sensitivities to base pair stability depending on whether the helicase uses an active or a passive mechanism of unwinding. If the helicase works by a passive mechanism mostly by trapping the thermally frayed DNA ends, then its unwinding rate will be influenced maximally by base pair stability. If the helicase interacts with the ss/ds junction or its conformational transitions entail motions aiming at base pair melting, then the unwinding rate will not be dramatically influenced by base pair stability. The degree of helicase's active involvement in the unwinding mechanism depends on the extent to which the helicase shifts the equilibrium to base pair opening, which in turn depends on the nature of the helicase's interaction with the fork junction and the coupling of NTP binding and hydrolysis to ssDNA translocation.

Substrates with different stabilities can be easily prepared by introducing different percentages of GC base pairs in the dsDNA. In the example shown here, we introduced 0–100 % GC content by uniformly distributing the GC base pairs in a 40-bp duplex DNA region. The average bp stability of the DNA substrates was calculated using the nearest neighbor analysis [43] and it ranges from 0.96 to 2.13 kcal/mol/bp. The gel-based unwinding traces show an increase in lag time with increasing GC content, indicating that the DNAs with the greater number of GC base pairs are unwound more slowly. The unwinding kinetics were fit to the uniform stepping model to determine the average single base pair unwinding rate ( $k_u$ ), which decreases from 30 to 3 bp/s (Fig. 9.5b).

To quantitatively fit the above data and determine if T7 helicase unwinds by a passive or active mechanism, we used the basic ideas developed by Betterton and Julicher [23] for a motor moving against a mobile obstacle. The opening and closing of the junction base pair is treated as a rapid equilibrium process and described by the free energy or  $\Delta G$  of base pair opening–closing. We assume that the helicase is located on the fork DNA next to the junction base pair and the interaction energy of the helicase with the junction base pair is  $U_o$ . We also assume that the helicase translocates with a step size of one nucleotide, and in this case the unwinding rate ( $k_u$ ) of the helicase with respect to its ssDNA translocation rate ( $k_{ss}$ ) is described by the following equation:

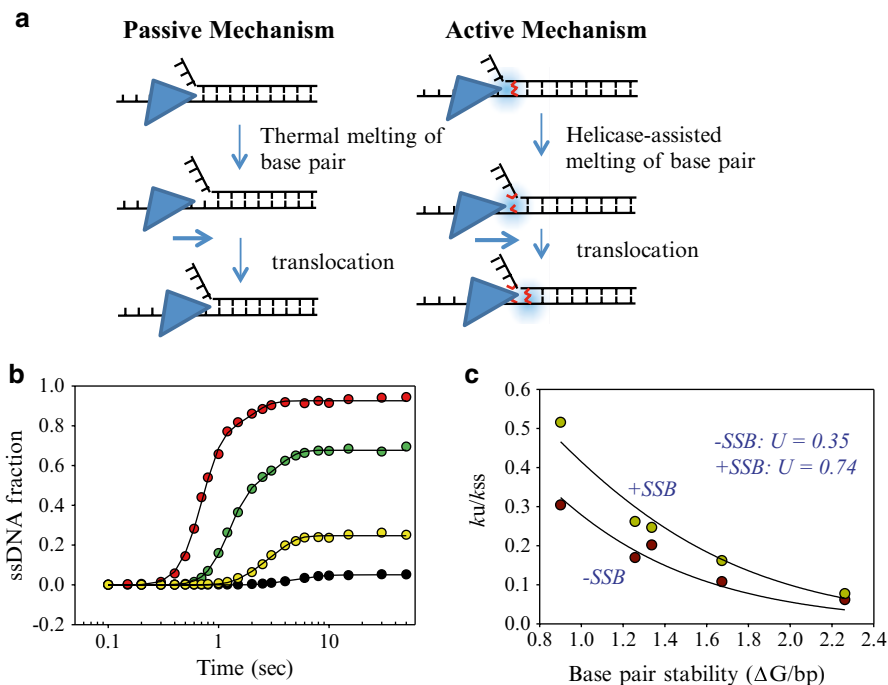


**Fig. 9.5** Mechanism of unwinding: **(a)** Illustration of active versus passive mechanism of unwinding: In the passive mechanism of unwinding, base pair separation occurs by thermal fluctuation of junction base pairs and when the ssDNA available is greater than or equal to the helicase step size, the helicase may move forward. In the active mechanism, the presence of the helicase at the junction or its NTP hydrolysis-coupled forward motion destabilizes the junction base pairs (represented by the *blue cloud*) and facilitates DNA melting. **(b)** DNA stability-dependent unwinding: Time course of unwinding obtained by the gel-based assay for DNA substrates of different stabilities generated by varying the GC content of the DNA. The reactions were carried out at 18 °C by 100 nM T7 helicase on 2.5 nM DNA in the presence of 2 mM dTTP, 2 mM free  $\text{Mg}^{2+}$ , and excess ssDNA trap. The kinetic traces show a decrease in amplitude and rate of unwinding with increasing GC content. **(c)** Interaction energy of the helicase with junction base pairs: A plot of single bp unwinding rates obtained for DNA substrates with different GC content by the gel-based assay as a function of the average single bp stability fit to (9.2) to determine the interaction energy exerted by the helicase on the junction base pair ( $U_o$ ), keeping  $f=0.05$ . The equation assumes that the helicase is at the junction and translocates with a step size of 1 bp. The presence of SSB increases the interaction energy  $U_o$ , which could be due to the effect exerted by the SSB directly on the DNA or indirectly through the helicase

$$\frac{k_u}{k_{ss}} = \frac{C \times \left( C + (1-C) \times e^{-f \times (U_o/RT)} \right)}{\left( C + (1-C) \times e^{-(U_o/RT)} \right)} \quad (9.2)$$

$$c = e^{-\Delta G/RT}$$

where  $R$  is the gas constant,  $T$  is temperature in degree Kelvin, and  $f$  is a dimensionless coefficient whose value lies between 0 and 1. It describes the relative effect of the interaction energy on the helicase's forward versus the backward rate or junctions opening versus closing rates. The exact value of  $f$  is unknown and it was fixed to a small value of 0.05 as treated by Betterton and Julicher [23]. The ssDNA translocation rate ( $k_{ss}$ ) of 130 nt/s was determined from independent experiments under the same solution conditions and dTTP concentrations as the unwinding reactions.

The plot of  $k_u/k_{ss}$  for T7 helicase unwinding fork DNAs of different GC content decreases with increasing average  $\Delta G$  of base pairing (Fig. 9.5c). The fit to 9.2 provides interaction energy  $U_o$  of 0.36 kcal/mol indicating that T7 helicase unwinds by an active mechanism. However, the small value of  $U_o$  indicates that it is not an optimally active helicase as was also observed by single molecule methods [44]. We expect that an optimally active helicase would unwind dsDNA as fast as it translocates on ssDNA and such a helicase would have interaction energy close to 2.2 kcal/mol. Similar conclusions have been made for other ring-shaped helicases such as *E. coli* DnaB and bacteriophage T4 helicase [45, 46]. It has been observed that the efficiency of a helicase greatly increases in the presence of other proteins such as the single strand binding (SSB) protein, DNA polymerase, and primase enzymes. We describe examples to show the effect of these proteins on the helicase activity and interpretations of how they modulate the mechanism of helicase action.

## 9.6 Effect of the SSB on DNA Unwinding

SSB proteins have been shown to stimulate DNA unwinding by many helicases [47]. The SSB protein binds to ssDNA intermediates and mediates steps in DNA replication and repair, although the exact mechanism is not well understood. *E. coli* SSB is a heterologous ssDNA binding protein for T7 helicase, but it is present in the cell during infection by phage T7 and it is a well characterized ssDNA binding protein [48]. To understand the effect of *E. coli* SSB, the unwinding parameters from the gel-based and real time unwinding assays by T7 helicase in the presence of SSB are compared to those obtained in its absence.

In the presence of *E. coli* SSB, the average unwinding rate per base pair is  $\sim$  twice the average unwinding rate in its absence using the same DNA substrates. The unwinding traces for the 18–90 bp DNA (32 % GC content) obtained from the gel-based assays fit to the uniform stepping model as described above, provided globally constrained  $k_s$  of 24 steps/s,  $s$  of 1.53 bp, and  $L_m$  of 10.4 bp in the presence of SSB as compared to 18.6 steps/s, 0.8 bp, and 14.8 bp in the absence of SSB. Thus, the rate of unwinding by T7 helicase increases in the presence of SSB from 15.5 to 36.6 bp/s. A sample unwinding curve to show the effect of SSB on a 60 % GC DNA is shown in Fig. 9.6a and Table 9.1.

The processivity of the helicase also increases in the presence of SSB (0.9979) indicating that T7 helicase unwinds on an average about 476 bp of dsDNA (Fig. 9.4d) (compared to 112 bp dsDNA) before dissociating and the average rate of helicase

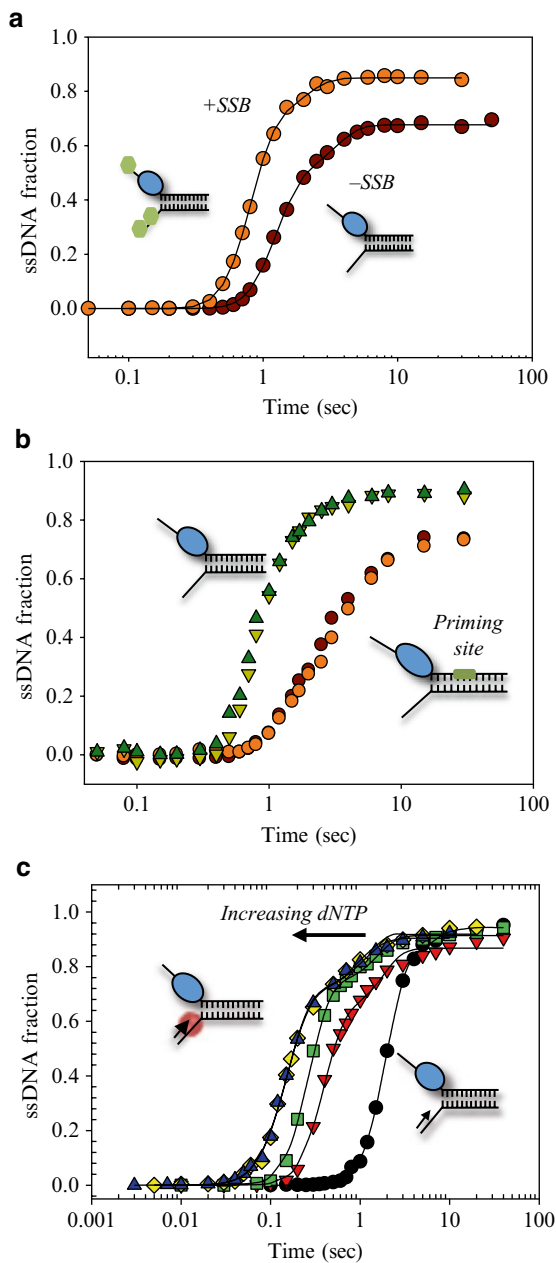


**Fig. 9.6** Effect of various replisome proteins on DNA unwinding by T7 helicase: **(a)** Effect of *E. coli* SSB on DNA unwinding: Time course of unwinding a 60 % GC DNA shows increase in rate and amplitude in the presence of SSB (1  $\mu$ M). DNA unwinding was measured by the gel-based assay at 18 °C by 100 nM gp4A' on 2.5 nM DNA in the presence of 2 mM dTTP and 2 mM free  $Mg^{2+}$ . **(b)** Effect of the priming site on DNA unwinding: Comparison of the time course of gel-based unwinding reactions shows that the presence of the T7 priming site slows down T7 helicase both in the presence

dissociation decreases to  $0.077 \text{ s}^{-1}$ . The interaction energy of the helicase on the junction base pair to destabilize it, obtained by plotting  $k_u/k_{ss}$  versus  $\Delta G/\text{bp}$  of the DNA in the presence of SSB, increased about 2 times in the presence of SSB (Fig. 9.5c). This increase in  $U_o$  could be due to a direct effect of the SSB on the ss/ds junction or an indirect effect through the helicase.

## 9.7 Effect of the Primase on DNA Unwinding

The primase provides the RNA primers required to initiate DNA replication on the lagging strand. The primase protein is closely associated with the replicative helicase and, in case of bacteriophage T7, the primase is part of the same polypeptide. The N-terminal half of T7 helicase contains the primase domain that recognizes 3'CTGG/TG/T sequence on ssDNA [49] and uses this priming sequence as a template to make short RNA primers when ATP+CTP are present. In the hexameric structure, the primase domains are positioned behind the helicase domains and the distance between the helicase and primase active sites is about 10 nt [50]. The primase synthesizes RNA primers in the opposite direction (3'–5') relative to the motion of the helicase domain (5'–3'). This raises the question as to how the primase affects the unwinding activity of the helicase.

To investigate if the DNA unwinding activity of T7 helicase is influenced by the priming activity, we made two fork substrates: one contained a single priming sequence (3'CTGGG) 22 bp downstream from the fork junction, and a control DNA without the priming sequence. DNA unwinding by T7 helicase was measured using the all-or-none gel-based assay under single round conditions. The lag kinetics were computationally fit to the uniform stepping model, which show that the priming substrate is unwound with an average single base pair unwinding rate of 15 bp/s whereas the control substrate is unwound with a rate of 47 bp/s (Fig. 9.6b). The experiments show that the priming activity slows the helicase [51]. We observed helicase slowing even in the absence of ATP+CTP, which indicates that primer synthesis is not required and simply binding of the primase domains to the priming site is sufficient to slow the helicase. Comparable results were obtained with the real time fluorescence assay when performed at varying dTTP (energy source of the helicase) concentrations as well. Thus, the effect of primase on helicase slowing is an allosteric effect in which the primase engaged with the priming site opposes the helicase's



**Fig. 9.6** (continued) and absence of priming NTPs. (c) Effect of T7 DNA polymerase on DNA unwinding: Time course of unwinding in the presence and absence of T7 DNA polymerase at increasing dNTP concentrations obtained by the gel-based assay shows that the presence of an active DNA polymerase stimulates DNA unwinding and at saturating dNTP concentrations the unwinding rates approach the helicase translocation rate on ssDNA. The reactions were carried out at 18 °C with 400 nM T7 helicase, 400 nM T7 DNA polymerase (T7 gp5:thioredoxin complex), 200 nM fork DNA with primer, 2 mM dTTP, and varying concentrations of dNTP (5, 10, 40, and 100  $\mu\text{M}$ )

**Table 9.1** Effect of replisomal proteins on the average single base pair unwinding rate and processivity of T7 gp4A<sup>a</sup>

	Effect of SSB		Effect of primase		Effect of polymerase	
	–SSB	+SSB	–Primase	+Primase	–Polymerase	+Polymerase
GC content (%)	32	32	20	20	33	33
Average single bp unwinding rate <sup>b</sup> (bp/s)	~15	~37	~47	~15	~9	~114
Processivity <sup>c</sup> (bp)	112	476	–	–	–	–
Interaction energy ( $U_o$ ) <sup>d</sup>	0.35	0.74	–	–	–	–

<sup>a</sup>The differences observed across experiments with only helicase is an effect of GC% and other experimental conditions

<sup>b</sup>Average single bp unwinding rate = stepping rate × step size

<sup>c</sup>Processivity: number of bp unwound per binding event

<sup>d</sup>Interaction energy: Measure of influence of helicase on junction base pair

forward movements. Interestingly, helicase slowing in the presence of the priming site was not observed when T7 helicase is coupled with T7 DNA polymerase [51].

Contrary to slowing down of the T7 helicase in the presence of priming sites, single molecule experiments using magnetic tweezers in the T4 system in which the primase enzyme (gp61) is a separate polypeptide has shown that the presence of the gp61 in the absence of NTPs does not modify the helicase unwinding activity on a DNA containing priming sites [38]. The mechanism of continued replication fork progression during primer synthesis appears to occur through the formation of a priming loop (T7 and T4) [38, 51], dissociation of one of the primase subunits from the primosome complex (*E. coli*) [52], or pausing of the leading strand synthesis (T7) [53].

## 9.8 Effect of the DNA Polymerase on DNA Unwinding

Leading strand DNA synthesis is catalyzed by the synergistic activity of T7 helicase and T7 DNA polymerase. To investigate how T7 DNA polymerase affects the unwinding rate of T7 helicase, we prepared a fork DNA that contained a primer-template in place of the 3'-overhang where the DNA polymerase could bind. The unwinding kinetics were measured using the all-or-none gel-based assay. The helicase and polymerase were preassembled on the replication fork DNA in the presence of dTTP and reactions were initiated with  $Mg^{2+}$  and the remaining dNTPs. The lag kinetics were computationally fit to the stepping model which shows that the isolated helicase unwinds the replication fork DNA with an average single base pair unwinding rate of 9 bp/s (30 % GC content), but in the presence of T7 DNA polymerase with saturating dNTPs this rate increased to ~120 bp/s close to the ssDNA translocation rate (Fig. 9.6c). The rate stimulation depended on the concentration of dNTPs that control the rate of DNA synthesis. As the concentration of the 3 dNTPs was increased from 5, 10, 40, and 100  $\mu M$ , the average single base pair unwinding rate increased from 45, 65, 116, and 117 bp/s, respectively. This shows that when



the DNA polymerase catalyzes DNA synthesis at its fastest rate at saturating dNTPs, it is able to stimulate the helicase activity to maximum resembling the helicase's speed of ssDNA translocation (130 nt/s). A heterologous polymerase such as T4 DNA polymerase does not cause similarly high stimulation [54]. Thus, both physical and functional couplings are necessary for effective leading strand DNA synthesis by the helicase-polymerase.

The stimulation on the leading strand unwinding synthesis could be a result of DNA polymerase providing a “push” for the helicase forward motion or acting as a “brake” to prevent slippage as suggested for the T7 system [54]. Recent single molecule studies on the T4 system indicate that the stimulation could be because the helicase allows the polymerase to adopt a polymerizing conformation versus an exonucleolytic conformation and the polymerase aids the helicase by unwinding the first few base pairs and thereby increasing the unwinding rate [55].

## 9.9 Conclusions

Obtaining accurate kinetic parameters that define the unwinding activity of helicases is critical to understanding both the mechanism and role of helicases in biological processes. The ensemble approaches, especially the pre-steady state kinetic methods, provide a facile way to obtain basic helicase parameters that can be used as handles to understand regulation of helicase by associated proteins such as DNA polymerase and single strand binding protein in DNA replication.

The ensemble methods measure averaged behavior of helicase molecules, which is an inherent limitation that precludes precise measurements of unsynchronized or heterogeneous populations. This limitation can be overcome by single molecule methods that track individual helicase molecules and can resolve behaviors of helicase populations. The single molecule methods are particularly powerful in observing the stepwise translocation of processive helicases. Such studies have helped in observing previously unobservable stalling/pausing behavior of individual helicase molecules during DNA unwinding [56].

All three types of single molecule methods, optical trap, magnetic tweezers, and fluorescence resonance energy transfer (FRET), have been used to measure the unwinding reaction by ring-shaped replicative helicases including T7 gp4A', T4 bacteriophage gp41, and *E. coli* DnaB. The optical trap and magnetic tweezers methods apply piconewton forces and measure nanometer distance changes during DNA unwinding. All of these helicases show faster unwinding rates with application of increasing destabilizing force on the fork DNA, and the force-velocity measurements are in agreement with the ensemble studies and indicate that these ring-shaped helicases do not function by an entirely active mechanism [44, 45, 55]. While the single molecule methods provide intricate details of helicase translocation, the stretching force on the DNA itself may affect the helicase mechanism. Experiments with DnaB helicase have shown that the geometry of the fork DNA and whether the force is applied to the strand occluded by the DnaB ring or to the

strand encircled by DnaB dictate the degree of activeness [46]. Similarly, separation of the two strands behind the translocating helicase under force could also modify the helicase mechanism if the excluded strand is involved in some aspect of unwinding as has been proposed for the eukaryotic MCM 2–7 protein [57].

Single molecule FRET provides an alternative way to measure nanometer distance changes during DNA unwinding without application of force. These experiments have been used to understand aspects of helicase unwinding such as enzyme conformational changes and interaction with other proteins in the replisome [5]. Such experiments showed slowing of T7 helicase by priming site on fork DNA and the formation of a priming loop when T7 helicase is coupled to the DNA polymerase during leading strand DNA replication [51]. The application of methods that combines FRET and force-based manipulation [58, 59] will be helpful in tracking the relative positioning of proteins on the replication fork and simultaneously monitoring the unwinding and replication process with application of force and distance measurements.

**Acknowledgements** We thank former and current Patel Lab members for developing and testing the methods and models described in this review. This work was supported by National Institute of Health (NIH) grant GM55310.

## References

1. Patel SS, Donmez I (2006) Mechanisms of helicases. *J Biol Chem* 281:18265–18268
2. Singleton MR, Dillingham MS, Wigley DB (2007) Structure and mechanism of helicases and nucleic acid translocases. *Annu Rev Biochem* 76:23–50
3. Lohman TM, Tomko EJ, Wu CG (2008) Non-hexameric DNA helicases and translocases: mechanisms and regulation. *Nat Rev Mol Cell Biol* 9:391–401
4. Egelman EH (1998) Bacterial helicases. *J Struct Biol* 124:123–128
5. Yodh JG, Schlierf M, Ha T (2010) Insight into helicase mechanism and function revealed through single-molecule approaches. *Q Rev Biophys* 43:185–217
6. Fischer CJ, Tomko EJ, Wu CG, Lohman TM (2012) Fluorescence methods to study DNA translocation and unwinding kinetics by nucleic acid motors. *Methods Mol Biol* 875:85–104
7. Costa A, Onesti S (2009) Structural biology of MCM helicases. *Crit Rev Biochem Mol Biol* 44:326–342
8. Patel SS, Picha KM (2000) Structure and function of hexameric helicases. *Annu Rev Biochem* 69:651–697
9. Rasnik I, Jeong YJ, McKinney SA, Rajagopal V, Patel SS, Ha T (2008) Branch migration enzyme as a Brownian ratchet. *EMBO J* 27:1727–1735
10. Kaplan DL, Davey MJ, O'Donnell M (2003) Mcm4,6,7 uses a “pump in ring” mechanism to unwind DNA by steric exclusion and actively translocate along a duplex. *J Biol Chem* 278:49171–49182
11. Sawaya MR, Guo S, Tabor S, Richardson CC, Ellenberger T (1999) Crystal structure of the helicase domain from the replicative helicase-primase of bacteriophage T7. *Cell* 99:167–177
12. Singleton MR, Sawaya MR, Ellenberger T, Wigley DB (2000) Crystal structure of T7 gene 4 ring helicase indicates a mechanism for sequential hydrolysis of nucleotides. *Cell* 101:589–600
13. Thomsen ND, Berger JM (2009) Running in reverse: the structural basis for translocation polarity in hexameric helicases. *Cell* 139:523–534

14. Enemark EJ, Joshua-Tor L (2006) Mechanism of DNA translocation in a replicative hexameric helicase. *Nature* 442:270–275
15. Liao JC, Jeong YJ, Kim DE, Patel SS, Oster G (2005) Mechanochemistry of  $\tau$ 7 DNA helicase. *J Mol Biol* 350:452–475
16. Crampton DJ, Mukherjee S, Richardson CC (2006) DNA-induced switch from independent to sequential dTTP hydrolysis in the bacteriophage T7 DNA helicase. *Mol Cell* 21:165–174
17. Hacker KJ, Johnson KA (1997) A hexameric helicase encircles one DNA strand and excludes the other during DNA unwinding. *Biochemistry* 36:14080–14087
18. Ahnert P, Patel SS (1997) Asymmetric interactions of hexameric bacteriophage T7 DNA helicase with the 5'- and 3'-tails of the forked DNA substrate. *J Biol Chem* 272:32267–32273
19. Jezewska MJ, Rajendran S, Bujalowska D, Bujalowski W (1998) Does single-stranded DNA pass through the inner channel of the protein hexamer in the complex with the *Escherichia coli* DnaB helicase? Fluorescence energy transfer studies. *J Biol Chem* 273:10515–10529
20. Kaplan DL (2000) The 3'-tail of a forked-duplex sterically determines whether one or two DNA strands pass through the central channel of a replication-fork helicase. *J Mol Biol* 301:285–299
21. Galletto R, Maillard R, Jezewska MJ, Bujalowski W (2004) Global conformation of the *Escherichia coli* replication factor DnaC protein in absence and presence of nucleotide cofactors. *Biochemistry* 43:10988–11001
22. Rothenberg E, Trakselis MA, Bell SD, Ha T (2007) MCM forked substrate specificity involves dynamic interaction with the 5'-tail. *J Biol Chem* 282:34229–34234
23. Betterton MD, Julicher F (2005) Opening of nucleic-acid double strands by helicases: active versus passive opening. *Phys Rev E Stat Nonlin Soft Matter Phys* 71:011904
24. Benkovic SJ, Valentine AM, Salinas F (2001) Replisome-mediated DNA replication. *Annu Rev Biochem* 70:181–208
25. Hamdan SM, Richardson CC (2009) Motors, switches, and contacts in the replisome. *Annu Rev Biochem* 78:205–243
26. Langston LD, Indiani C, O'Donnell M (2009) Whither the replisome: emerging perspectives on the dynamic nature of the DNA replication machinery. *Cell Cycle* 8:2686–2691
27. Eggleston AK, Rahim NA, Kowalczykowski SC (1996) A helicase assay based on the displacement of fluorescent, nucleic acid-binding ligands. *Nucleic Acids Res* 24:1179–1186
28. Cheng W, Hsieh J, Brenda KM, Lohman TM (2001) *E. coli* Rep oligomers are required to initiate DNA unwinding in vitro. *J Mol Biol* 310:327–350
29. Picha KM, Patel SS (1998) Bacteriophage T7 DNA helicase binds dTTP, forms hexamers, and binds DNA in the absence of  $Mg^{2+}$ . The presence of dTTP is sufficient for hexamer formation and DNA binding. *J Biol Chem* 273:27315–27319
30. Sen D, Nandakumar D, Tang GQ, Patel SS (2012) The human mitochondrial DNA helicase TWINKLE is both an unwinding and an annealing helicase. *J Biol Chem* 287(18):14545–14556
31. Torimura M, Kurata S, Yamada K, Yokomaku T, Kamagata Y, Kanagawa T, Kurane R (2001) Fluorescence-quenching phenomenon by photoinduced electron transfer between a fluorescent dye and a nucleotide base. *Anal Sci* 17:155–160
32. Noble JE, Wang L, Cole KD, Gaigalas AK (2005) The effect of overhanging nucleotides on fluorescence properties of hybridising oligonucleotides labelled with Alexa-488 and FAM fluorophores. *Biophys Chem* 113:255–263
33. Toseland CP, Webb MR (2010) Fluorescence tools to measure helicase activity in real time. *Methods* 51:259–268
34. Xi XG, Deprez E (2010) Monitoring helicase-catalyzed DNA unwinding by fluorescence anisotropy and fluorescence cross-correlation spectroscopy. *Methods* 51:289–294
35. Dou SX, Xi XG (2010) Fluorometric assays for characterizing DNA helicases. *Methods* 51:295–302
36. Donmez I, Patel SS (2008) Coupling of DNA unwinding to nucleotide hydrolysis in a ring-shaped helicase. *EMBO J* 27:1718–1726

37. Sun B, Johnson DS, Patel G, Smith BY, Pandey M, Patel SS, Wang MD (2011) ATP-induced helicase slippage reveals highly coordinated subunits. *Nature* 478:132–135
38. Manosas M, Spiering MM, Zhuang Z, Benkovic SJ, Croquette V (2009) Coupling DNA unwinding activity with primer synthesis in the bacteriophage T4 primosome. *Nat Chem Biol* 5:904–912
39. Eoff RL, Raney KD (2006) Intermediates revealed in the kinetic mechanism for DNA unwinding by a monomeric helicase. *Nat Struct Mol Biol* 13:242–249
40. Lucius AL, Maluf NK, Fischer CJ, Lohman TM (2003) General methods for analysis of sequential “n-step” kinetic mechanisms: application to single turnover kinetics of helicase-catalyzed DNA unwinding. *Biophys J* 85:2224–2239
41. Levin MK, Hingorani MM, Holmes RM, Patel SS, Carson JH (2009) Model-based global analysis of heterogeneous experimental data using gfit. *Methods Mol Biol* 500:335–359
42. Jeong YJ, Levin MK, Patel SS (2004) The DNA-unwinding mechanism of the ring helicase of bacteriophage T7. *Proc Natl Acad Sci U S A* 101:7264–7269
43. Breslauer KJ, Frank R, Blocker H, Marky LA (1986) Predicting DNA duplex stability from the base sequence. *Proc Natl Acad Sci U S A* 83:3746–3750
44. Johnson DS, Bai L, Smith BY, Patel SS, Wang MD (2007) Single-molecule studies reveal dynamics of DNA unwinding by the ring-shaped T7 helicase. *Cell* 129:1299–1309
45. Lionnet T, Spiering MM, Benkovic SJ, Bensimon D, Croquette V (2007) Real-time observation of bacteriophage T4 gp41 helicase reveals an unwinding mechanism. *Proc Natl Acad Sci U S A* 104:19790–19795
46. Ribbeck N, Kaplan DL, Bruck I, Saleh OA (2010) DnaB helicase activity is modulated by DNA geometry and force. *Biophys J* 99:2170–2179
47. Rajagopal V, Patel SS (2008) Single strand binding proteins increase the processivity of DNA unwinding by the hepatitis C virus helicase. *J Mol Biol* 376:69–79
48. Shereda RD, Kozlov AG, Lohman TM, Cox MM, Keck JL (2008) SSB as an organizer/mobilizer of genome maintenance complexes. *Crit Rev Biochem Mol Biol* 43:289–318
49. Frick DN, Richardson CC (2001) DNA primases. *Annu Rev Biochem* 70:39–80
50. Kusakabe T, Baradaran K, Lee J, Richardson CC (1998) Roles of the helicase and primase domain of the gene 4 protein of bacteriophage T7 in accessing the primase recognition site. *EMBO J* 17:1542–1552
51. Pandey M, Syed S, Donmez I, Patel G, Ha T, Patel SS (2009) Coordinating DNA replication by means of priming loop and differential synthesis rate. *Nature* 462:940–943
52. Yuzhakov A, Kelman Z, O'Donnell M (1999) Trading places on DNA—a three-point switch underlies primer handoff from primase to the replicative DNA polymerase. *Cell* 96:153–163
53. Lee JB, Hite RK, Hamdan SM, Xie XS, Richardson CC, van Oijen AM (2006) DNA primase acts as a molecular brake in DNA replication. *Nature* 439:621–624
54. Stano NM, Jeong YJ, Donmez I, Tummalapalli P, Levin MK, Patel SS (2005) DNA synthesis provides the driving force to accelerate DNA unwinding by a helicase. *Nature* 435:370–373
55. Manosas M, Spiering MM, Ding F, Croquette V, Benkovic SJ (2012) Collaborative coupling between polymerase and helicase for leading-strand synthesis. *Nucleic Acids Res* 40(13):6187–6198
56. Dumont S, Cheng W, Serebrov V, Beran RK, Tinoco I Jr, Pyle AM, Bustamante C (2006) RNA translocation and unwinding mechanism of HCV NS3 helicase and its coordination by ATP. *Nature* 439:105–108
57. Graham BW, Schauer GD, Leuba SH, Trakselis MA (2011) Steric exclusion and wrapping of the excluded DNA strand occurs along discrete external binding paths during MCM helicase unwinding. *Nucleic Acids Res* 39:6585–6595
58. Hohng S, Zhou R, Nahas MK, Yu J, Schulten K, Lilley DM, Ha T (2007) Fluorescence-force spectroscopy maps two-dimensional reaction landscape of the holliday junction. *Science* 318:279–283
59. Zhou R, Kozlov AG, Roy R, Zhang J, Korolev S, Lohman TM, Ha T (2011) SSB functions as a sliding platform that migrates on DNA via reptation. *Cell* 146:222–232

# Chapter 10

## Rotary Motor ATPases

Stephan Wilkens

**Abstract** The preceding chapters offered an introduction to a selection of biophysical tools most commonly used in the elucidation of the structure and mechanism of biological macromolecules. The following chapter describes how some of these tools were applied—and new ones developed—to gain an understanding of the catalytic mechanism of a particular class of membrane-bound transport proteins, the rotary motor ATPases. Rotary motor ATPases are highly efficient molecular machines that function to interconvert chemical energy (in form of ATP) into the potential energy of transmembrane ion motive force, and vice versa. Energy conversion in the rotary ATPases involves rotation of a central subdomain (the rotor) relative to a static portion called the stator. Most rotary motor ATPases can function in both directions, which means that the enzyme can either pump ions across lipid membranes at the expense of ATP hydrolysis or synthesize ATP driven by ion flow along a concentration gradient through the membrane-bound part of the complex. Catalysis involving subunit rotation was proposed before detailed structural information was available; however, proving the existence of a rotary mechanism turned out to be a biophysical challenge, and, along the way, novel single molecule observation techniques had to be developed to be able to confirm the rotary motor hypothesis. Rotary motor ATPases can be found in all domains of life including bacteria, archaea, and eukarya. The enzyme found in the inner membrane of mitochondria, the plasma membrane of bacteria, and the thylakoid membrane of chloroplasts is called  $F_1F_0$ -ATP synthase or F-ATPase. The enzyme found in archaea is called A-ATP synthase (or  $A_1A_0$ -ATP synthase or A-ATPase) and the enzyme found in the endomembrane system (and sometimes plasma membrane) of eukaryotic organisms is called vacuolar ATPase (or  $V_1V_0$ -ATPase or V-ATPase). The family of the rotary ATPases is characterized by a similar overall topology, a cytoplasmic ATPase

---

S. Wilkens (✉)

Department of Biochemistry and Molecular Biology, SUNY Upstate Medical University,  
750 East Adams Street, Syracuse, NY 13210, USA  
e-mail: wilkensp@upstate.edu

connected to a membrane-bound ion channel, with differences in subunit composition and structure that have evolved to accommodate different functional needs and mechanisms of enzyme regulation.

**Keywords** ATPase • Rotary molecular motor • F-ATP synthase • A-ATP synthase • Vacuolar ATPase • Biophysics • X-ray crystallography • Electron microscopy • NMR spectroscopy • Small angle X-ray scattering • Single molecule observation • Single molecule fluorescence resonance energy transfer (FRET) spectroscopy

## 10.1 The Family of Rotary Motor ATPases

The family of rotary motor ATPases is divided into three main subtypes that are believed to have originated from a common ancestor parallel to the divergence of the three kingdoms of life [1–4]. The enzymes found in the plasma membrane of archaea and bacteria are called A-ATPase and F-ATPase, respectively. Eukaryotic organisms harbor both an F-type ATPase (in the inner mitochondrial membrane and the thylakoid membrane of chloroplasts) and a complex structurally more similar to the A-ATPase that is called vacuolar ATPase (V-ATPase). The vacuolar ATPase is found in the endomembrane system of all eukaryotic cells but also in the plasma membrane of some specialized cell types in higher animals [5–8]. The presence of both F- and V-type ATPases in eukaryotic cells is consistent with the idea that modern eukaryotes have evolved from proto-eukaryotes (an early branch of the archaea) that formed a symbiotic relationship with  $\alpha$  proteobacteria, the precursors for the modern mitochondria [9].

A rotary motor ATPase structurally similar to the A-ATPase has also been found in some, mostly extremophilic, bacteria and it is believed that the genes for the archaeal-like enzyme in these organisms have been acquired by horizontal gene transfer from archaea sharing the same habitat [10]. This A- or A/V-like ATPase likely functions as ATP synthase, either replacing or duplicating the function of the F-ATPase in these bacteria [11, 12]. From here on in the chapter, vacuolar ATPase (V-ATPase) will be used in the context of the eukaryotic enzyme whereas the bacterial complex will be referred to as A/V-like ATPase as suggested in [13]. One of the structurally and functionally best characterized members of the bacterial A/V-like ATPases is the enzyme from the thermophilic bacterium, *Thermus thermophilus* [14]. Thanks to its thermostability, intact *T. thermophilus* A/V-ATPase and the enzyme's functional domains and individual subunits have been purified and their structure and stoichiometry analyzed by electron microscopy, X-ray crystallography, NMR spectroscopy, and native mass spectrometry (MS) (see below). A schematic of the bacterial F-, the archaeal A-, and the eukaryotic V-ATPase is shown in Fig. 10.1. The first rotary ATPase described was F-ATPase, also referred to as  $F_1F_o$ -ATP synthase with  $F_1$  representing “Factor 1,” the water-soluble ATP hydrolyzing factor that can be released from the, e.g., inner mitochondrial membrane, and  $F_o$  for the insoluble, membrane-bound Factor “o” (with the subscript “o” referring to the

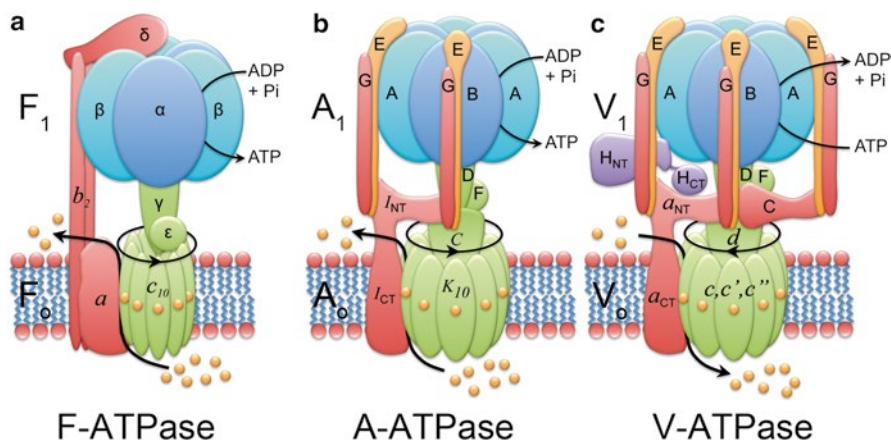


**Fig. 10.1** Structural models of bacterial F-, archaeal A-, and eukaryotic V-ATPase. Models of the subunit arrangement in the bacterial F-ATPase (a), archaeal A-ATPase (b), and eukaryotic V-ATPase (c). While F- and A-ATPase can function as both ATP synthase and ATP hydrolysis-driven ion pumps, eukaryotic V-ATPase is a dedicated proton pump. As can be seen, F-ATPase has one, while A-ATPase and V-ATPase have two and three stator stalks, respectively. Catalytic subunits are in blue, the rotor in green, and the stator stalk(s) or stator(s) in red/orange

macrolide oligomycin, a potent inhibitor of mitochondrial F-ATP synthase) [15, 16]. For consistency, archaeal A- and eukaryotic V-ATPase are therefore also referred to as  $A_1A_0$ -ATP synthase and  $V_1V_0$ -ATPase, respectively, even though oligomycin is not an inhibitor of these two enzymes.

The A-, V-, and F-ATPases function as the smallest rotary molecular motors described so far, and, depending on enzyme source, speed of subunit rotation can be  $>100$  rps, thereby catalyzing synthesis or hydrolysis of ATP at rates of up to  $500\text{ s}^{-1}$  (for the chloroplast ATP synthase [17]). Unequivocal proof that multi-site catalysis is accompanied by subunit rotation, first postulated for the F-ATPase from animal mitochondria [18], required development of sophisticated single molecule observation techniques that have since then provided a wealth of information on the molecular mechanism of subunit rotation and the movement of domains of catalytic and regulatory subunits during steady state catalysis. The functional data together with progress of atomic and near-atomic resolution structure determination by X-ray crystallography, NMR spectroscopy, and cryo electron microscopy makes the rotary ATPases one of the best characterized families of molecular machines.

## 10.2 Function of the Rotary Motor ATPases

Rotary molecular motor ATPases are energy converters that couple the free energy change associated with the synthesis or hydrolysis of MgATP to the release or storage of potential energy in form of a transmembrane electrochemical potential. According to Mitchell's chemiosmotic hypothesis ([19]; for an in-depth treatment,

see [20]), the potential energy (difference in free energy,  $\Delta G$ ) of the electrochemical ion gradient can be described as “ion motive force” (imf), which is given to:

$$\text{imf} (mV) = -\left(\Delta_{H^+}\right) \cdot F^{-1} = \Delta\phi - (2.3 \cdot RT) \cdot F^{-1} \cdot \Delta pH = \Delta\phi - 59 \cdot \Delta pH$$

with  $\Delta\mu H^+$  being the difference in electrochemical potential,  $F$  the Faraday constant ( $F$ ),  $\Delta\psi$  the transmembrane electrical potential difference, and  $\Delta pH$  (or  $\Delta pNa$  in case of sodium ion-coupled ATPases) the difference in ion concentration.

One of the structurally and functionally best characterized rotary ATPases is the F-ATPase ( $F_1F_0$ -ATP synthase) found in the plasma membrane of bacteria, the mitochondrial inner membrane, and the thylakoid membrane of chloroplasts [18, 21–24]. F-ATPase can function as a proton (or sodium) gradient-driven ATP synthase, harnessing the potential energy of the ion motive force across, e.g., the bacterial plasma or inner mitochondrial membrane to synthesize ATP from ADP and inorganic phosphate, or the enzyme can hydrolyze ATP to pump protons or sodium ions across a lipid bilayer. When growing under anaerobic conditions, certain bacteria (such as *Escherichia coli*) use F-ATPase in the reverse direction, that is, as an ATP hydrolysis-driven proton pump, to establish a proton motive force across the plasma membrane that serves to drive subsequent secondary transport processes for the import or export of nutrients and metabolites, respectively.

ATP synthesis by mitochondrial F-ATPase, which provides the bulk of chemical energy in all animals, is driven by the proton gradient established by the respiratory complexes I, III, and IV during electron transport from catabolically generated reducing equivalents to molecular oxygen [25]. ATP synthesis by the chloroplast enzyme in green plants is driven by a proton gradient established by the photosystems as a result of sunlight-driven oxidation of water into reduction equivalents (NADPH) and molecular oxygen.

Depending on the type of membrane, the individual contributions of membrane potential and pH difference can vary: most of the driving force in animal mitochondria is contributed by an electrical potential difference with only a minor difference in pH between inter-membrane space and matrix ( $\sim 1$  pH unit), allowing proteins to function on both sides of the inner membrane. In the thylakoid membrane of chloroplasts, however, the free energy difference is dominated by a proton gradient that can reach several pH units during light-driven electron transport ( $\sim 4$  pH units). Here, only few functional proteins are found in the thylakoid lumen that have adapted to function even under relatively acidic conditions ( $\sim pH 4$ ).

Most of what we know about the A- and A/V-like ATPases has been derived from studies with the bacterial enzymes from, e.g., *T. thermophilus* [14] and *Enterococcus hirae* [26]. Due to their similarity in subunit composition and overall architecture, it is generally assumed that both rotary ATPase subtypes share a similar enzymatic mechanism, and recent progress with purification and structural characterization of the archaeal enzyme, despite the difficulties with growing the often extremophilic organisms in the laboratory, appears to confirm the earlier assumption [11, 12]. The catalytic mechanism of the *T. thermophilus* A/V-ATPase (both for the intact complex and the soluble ATPase sector) has been studied extensively by using the single



molecule observation methods developed for characterizing rotational catalysis of the F-ATPase [27] (see below).

While F- and A-ATPase can function with high efficiency in both ATP synthesis and ATP hydrolysis directions, the eukaryotic vacuolar ATPase (V-ATPase) is a dedicated proton pump, hydrolyzing MgATP to acidify the lumen of subcellular organelles or the extracellular space in some specialized or polarized cells such as renal intercalated cells or bone osteoclasts [5–8]. This difference in physiological function between F- and A-ATPase on the one and V-ATPase on the other hand is not a fundamental difference in enzymatic mechanism as eukaryotic V-ATPase can be made to reverse direction and synthesize ATP, albeit at low efficiency [28]. Over the course of evolution, V-ATPase has acquired additional subunits that have no counterparts in the A- or F-ATPase. In addition, the proton pumping activity of the eukaryotic V-ATPase has been shown to be regulated by a unique mechanism referred to as reversible dissociation. In yeast, for example, under conditions of glucose deprivation,  $V_1$ -ATPase disengages from the membrane integral  $V_o$  proton turbine with concomitant silencing of ATPase and proton translocation activities and, at the same time, one of the V-ATPase subunits, C, is released from both domains of the complex [29]. V-ATPase dissociation is reversible; however, reassembly of intact V-ATPase from cytoplasmic  $V_1$ , membrane-bound  $V_o$ , and subunit C requires catalytic action of a chaperone complex called RAVE (regulator of  $H^+$ -ATPases of vacuolar and endosomal membranes) [30]. RAVE has been shown to bind subunits of the  $V_1$  and the chaperone likely acts as a scaffold to bring back together all components of the enzyme in a spatially ordered fashion. Nutrient availability-dependent reversible dissociation or developmentally regulated assembly of V-ATPase is also found in insects and higher animals [31–33], suggesting that this unique mode of activity regulation has been conserved throughout evolution. Most importantly, eukaryotic V-ATPase has been shown to be involved in or even responsible for a number of widespread human diseases such as osteoporosis [34], renal tubular acidosis [35, 36], diabetes [37], sensorineural deafness [38], and cancer [39]. Due to its established role in human health, the structure and mechanism of activity regulation by reversible disassembly of the V-ATPase are actively studied by many groups and efforts are underway to identify small molecule compounds that may be used to modulate the proton pumping activity of the enzyme [40, 41].

### 10.3 Structure of the Rotary Motor ATPases

Rotary motor ATPases are large, multisubunit enzyme complexes composed of two major functional units, a membrane peripheral, water-soluble ATPase that is characterized by an alternating hexameric arrangement of three catalytic and three non-catalytic nucleotide binding subunits, and a membrane-embedded ion channel made of a ring of hydrophobic “proteolipid” subunits with a transmembrane subunit located at the outer periphery of the ring (see Fig. 10.1 and Table 10.1). The cytoplasmic ATPase (referred to as  $F_1$ ,  $A_1$ , or  $V_1$ ) is connected to the membrane sector

**Table 10.1** Subunit composition of F-, A-, and V-ATPases

Sector	F-ATPase		A-ATPase	V-ATPase <sup>d</sup>	
	F <sub>1</sub>				
ATPase	Bacterial <sup>a</sup>	Mitochondrial <sup>b</sup>	A <sub>1</sub>	V <sub>1</sub>	Function
	α (3)	α (3)	B (3)	B (3)	Non-catalytic
	β (3)	β (3)	A (3)	A (3)	Catalytic
	γ (1)	γ (1)	D (1)	D (1)	Rotor
	δ (1)	OSCP (1)			Stator stalk
	ε (1)	δ (1)	F (1)	F (1)	Rotor, regulatory
		ε (1)			Rotor, regulatory
		d (1)	E (2)	E (3)	Stator stalk
		h (1)	G (2)	G (3)	Stator stalk
				C (1)	Stator
				H (1)	Regulation
Ion channel	F <sub>o</sub>		A <sub>o</sub>	V <sub>o</sub>	
	a (1)	a (1)	a (1) <sup>c</sup>	a (1)	Stator, ion channel
	b (2)	b (1)			Stator stalk
	c (8–15)	c (8–10)	c (10) <sup>c</sup>	c, c', c'' (10?)	Rotor, ion binding
			d (1) <sup>c</sup>	d (1)	Coupling spacer
		f, e, g, 8, i, k			Dimerization
				e	Unknown

<sup>a</sup>Subunit nomenclature of the bacterial enzyme  
<sup>b</sup>For yeast mitochondrial F-ATPase  
<sup>c</sup>Subunits *a*, *c*, and *d* in the A and A/V-type enzymes are also called I, K, and C, respectively  
<sup>d</sup>For yeast vacuolar ATPase

(F<sub>o</sub>, A<sub>o</sub>, or V<sub>o</sub>) via a rotating “central stalk” that couples conformational changes in the catalytic subunits to c ring rotation, and a static “stator stalk” that functions to resist the torque of rotational catalysis and keep the ATPase and ion channel in the correct spatial arrangement relative to one another for efficient energy coupling to take place. While X-ray crystallography has provided atomic resolution detail for the ATPase sectors, proteolipid rings, and stator stalks from a wide variety of rotary ATPases, only electron microscopic reconstructions are available for the overall structure of intact enzyme complexes.

**10.3.1 Structural Information from X-Ray Crystallography:  
ATPase Sectors, Rotor Rings, and Stator Stalks**

Mitochondria-rich animal tissues allowed purification of large amounts of F<sub>1</sub>-ATPase and most of the early biochemical and structural studies were conducted with the enzymes from, e.g., beef heart or rat liver [42, 43]. The first atomic resolution structure was reported for the beef heart enzyme and, at the time, the structure represented the largest asymmetric bio macromolecule solved to date (~380 kDa; see Fig. 10.2a) [44]. A novel solvent flattening protocol developed specifically for

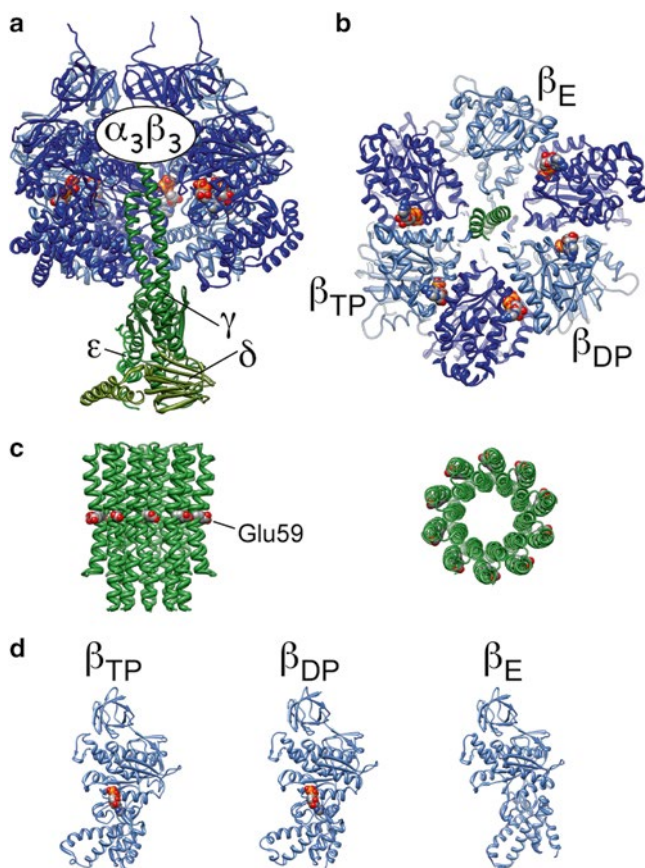


**Fig. 10.2** Crystal structure of mitochondrial F<sub>1</sub>-ATPase catalytic and proteolipid domains. **(a)** Side view parallel to the membrane of the X-ray crystal structure of bovine heart F<sub>1</sub>-ATPase (1e79). **(b)** A view of the structure from the membrane surface towards the matrix. The catalytic sites are in three different conformations with an empty ( $\beta_E$ ), a MgAMPPNP-bound site ( $\beta_{TP}$ ), and an MgADP-bound site ( $\beta_{DP}$ ). **(c)** Crystal structure of the rotor ring of yeast F-ATPase (3u2f). The Glu59 sidechain is shown in *spacefill*. **(d)** The three  $\beta$  subunits in the AMPPNP, ADP, and empty conformations

improving the electron density maps was crucial for tracing most of the catalytic and non-catalytic  $\alpha$  and  $\beta$  and part of the  $\gamma$  subunits [45]. The most striking aspect of the beef heart F<sub>1</sub> structure was that the three catalytic nucleotide binding sites were seen in three different conformations. One catalytic site had the non-hydrolyzable ATP analog AMPPNP bound, another one had ADP bound, and the third one was empty (see Fig. 10.2b, d). This configuration of the three catalytic sites was exactly what had been proposed more than 10 years earlier based on biochemical experiments in what was generally known under the name binding change mechanism of F<sub>1</sub>-ATPase [18]. The model predicted that at any given time, one catalytic site has ATP tightly bound, one site has ADP loosely bound, and that one site

is empty (see below for details of the binding change mechanism). Subsequent structures of the beef heart [46–48], rat liver [49], chloroplast [50], yeast [51, 52], and *E. coli* enzymes [53] crystallized in the presence of various nucleotide and/or inhibitor combinations revealed a variety of conformations of the catalytic nucleotide binding subunits including one where all three sites were (at least partially) filled with nucleotide [47]. In the first beef heart structure, only part of the central rotor subunit,  $\gamma$ , was resolved while the middle portion of  $\gamma$  as well as the other two rotor subunits,  $\delta$  and  $\epsilon$  (subunit nomenclature of the mitochondrial enzyme), was not visible due to disorder. The subunits and subunit domains not seen in the first structure, however, could be resolved using data collected from crystals that were slightly more compact likely due to dehydration [46]. Crystal structures are also available for the ATPase sectors of the bacterial A/V-type ATPase from *T. thermophilus*, albeit at moderate resolutions of between 2.8 and 4 Å [54, 55].

After solving the beef heart  $F_1$  structure, efforts intensified to obtain a structure of the intact  $F_1F_0$ -ATP synthase and while crystals of the detergent-solubilized yeast and bovine enzymes could be obtained [52, 56, 57], they only revealed electron density for the ATPase sector ( $\alpha\beta_3\gamma\delta\epsilon$ ) and the ring of proteolipids ( $c_{10}$  for yeast,  $c_8$  for bovine). While the quality of the electron density in the first yeast  $F_1$ - $c_{10}$  structure was not sufficient for unambiguous tracing for the proteolipid chains, the data clearly showed that there were 10  $c$  subunits in the ring [56], a number that had been speculated about extensively based on biochemical and crosslinking data conducted with the enzyme from *E. coli* [58, 59].

The first high resolution X-ray crystal structure for an isolated  $c$  subunit ring was obtained from crystals of purified, SDS-resistant proteolipid rings of the bacterial sodium pumping F-ATPase from *Ilyobacter tartaricus* [60]. The structure of the *I. tartaricus*  $c_{11}$  ring revealed the interaction of the individual  $c$  subunits and the residues involved in sodium binding. Following the *I. tartaricus* ring structure, a series of other rings with varying  $c$  subunit stoichiometries were reported, including a  $c_{10}$  ring of yeast F-ATPase [61], a  $c_{14}$  ring from the spinach chloroplast enzyme [62], and a 15- $c$  subunit ring from the proton transporting F-ATPase from *Spirulina platensis* [63]. The only ring seen so far with 12  $c$  subunits is the one from *T. thermophilus* A/V-type ATPase [64, 65], though no high resolution structure is currently available. A structure has been obtained for the 10- $c$  subunit ring of the sodium transporting A/V-like ATPase from *E. hirae* [66]. However, the *E. hirae*  $c$  subunits are more similar to the eukaryotic V-ATPase in that they contain four transmembrane segments, with the proton or sodium binding carboxyl residue in the C-terminal membrane spanning  $\alpha$  helix. With a total of 40 transmembrane  $\alpha$  helices, the *E. hirae* ring is the largest observed so far.

Dividing the number of  $c$  subunits by three gives the number of ions that need to cross the membrane sector for the synthesis or hydrolysis of one molecule of ATP, provided that each ion translocated is coupled to rotation of the central stalk. From the above  $c$  subunit stoichiometries, it follows that the ion to ATP ratio varies from  $\sim 2.7$  (for bovine mitochondrial  $F_1F_0$ ) to 5 (for the enzyme from *S. platensis*). Interestingly, experimental determination of the  $H^+$ /ATP ratio revealed that four protons have to be translocated per ATP in both the chloroplast and *E. coli* ATP synthases [67], suggesting a possible uncoupling of proton translocation and rotor movement (slippage)

under some conditions. Figure 10.2c shows the recent high resolution crystal structure of the  $c_{10}$  proteolipid ring from the F-ATPase from *S. cerevisiae* [61], highlighting the carboxylate residues (Glu59) located in the middle of the C-terminal helix of the  $c$  subunit where they are exposed to the middle of the lipid bilayer.

As discussed in more detail below, F-ATPase has a single stator stalk that functions to link the soluble ATPase with the membrane sector [68]. The bacterial stator stalk is composed of a homodimer of  $b$  subunits, with a more complex composition in the mitochondrial enzyme [69] (Fig. 10.1a). The stator stalks in A- and V-ATPase are formed from heterodimers of subunits E and G and while there are two copies of the stator stalk in A-ATPase [70], eukaryotic V-ATPase contains three [71] (Fig. 10.1b, c). Crystal structures for the mitochondrial F-ATPase stator stalk as well as bacterial and eukaryotic EG heterodimers have been obtained [69, 72–74], showing the A- and V-ATPase stator stalks folded in  $\alpha$  helical coiled coils with an unusual right-handed twist.

Together, the atomic resolution X-ray structures of ATPases, rotor rings, and stator stalks provide essential information on the catalytic mechanism of the ATPase and allowed generation of plausible models of how the free energy of ATP synthesis or hydrolysis released or consumed on the  $F_1$  is coupled to movements of ions across the membrane-bound  $F_o$ . However, X-ray crystallography as of today has not been able to provide a picture of an intact member of the rotary motor ATPase family, most likely due to the labile nature of the interaction of the proteolipid ring with the membrane-bound  $a$  subunit. Structural models of intact rotary ATPases are available from single particle 3D EM reconstructions and while the earlier models from negatively stained specimens were obtained at low to moderate resolutions of between 20 and 30 Å, advances in cryo electron microscopy have recently allowed generation of models in the 10–20 Å resolution range with one model providing subnanometer (9.7 Å) detail [65] (see below).

### 10.3.2 Structural Information from Protein NMR Spectroscopy: Individual Subunits and Subunit Domains

The first F-ATPase subunit to be analyzed by protein NMR spectroscopy was the  $c$  subunit of the proteolipid rotor ring of the  $F_o$  sector of *E. coli*  $F_1F_o$ -ATP synthase. The highly hydrophobic  $\alpha$  helical hairpin can be readily obtained from *E. coli* inner membranes by extraction with organic solvent. Multidimensional, heteronuclear NMR spectroscopy of the subunit in a mixture of chloroform/methanol/water allowed determination of the proteolipid structure, initially at neutral pH [75]. A later structure calculated from data collected at acidic pH (5.5) revealed a different conformation, in which the C-terminal helix that contains the proton binding Asp61 residue was rotated close to 180° [76]. However, recent crystal structures of intact rotor rings (see above) suggest that protonation/deprotonation of the carboxylate involves only local changes in sidechain conformation and it needs to be seen whether the pH-induced structural changes observed for the  $c$  subunit monomer play a role in the proton translocation mechanism.

While the first crystallographic structure of bovine  $F_1$ -ATPase allowed detailed insight into the structure and conformations of the catalytic and non-catalytic subunits, part of the  $\gamma$  as well as the  $\delta$  subunit was not resolved due to disorder in the crystal lattice [44]. However, biochemical experiments conducted with the F-ATPase from *E. coli* suggested that especially the  $\epsilon$  subunit (the homolog to mitochondrial  $\delta$  subunit, see Table 10.1) played a critical role in energy coupling by connecting the central rotor ( $\gamma$  subunit) to the proteolipid ring of the proton channel [77]. The structure of isolated *E. coli*  $\epsilon$  subunit was subsequently solved by NMR spectroscopy [78, 79] and X-ray crystallography [80]. NMR and crystal structure agreed well, showing the subunit to be folded in an N-terminal  $\beta$  sandwich and a C-terminal  $\alpha$  helix–turn–helix that could be seen packed against one side of the  $\beta$  sandwich. Interestingly, while isolated *E. coli*  $\epsilon$  adopts a compact conformation in solution, a recent X-ray crystal structure of *E. coli*  $F_1$ -ATPase showed  $\epsilon$  in an extended structure with the subunit's C-terminal  $\alpha$  helix inserted deeply into the catalytic  $\alpha_3\beta_3$  hexamer where it interacts with and thereby links catalytic  $\beta$  and central rotor  $\gamma$  subunits [53]. Certain bacteria utilize F-ATPase in both ATP synthesis and proton pumping directions and it is believed that inhibition by  $\epsilon$  subunit serves to prevent wasteful ATP hydrolysis under some growth conditions [53]. In the mitochondrial enzyme, the extended conformation of the homologous mitochondrial subunit ( $\delta$ ) is prevented by another small subunit (called mitochondrial  $\epsilon$  subunit; not to be confused with bacterial  $\epsilon$  subunit, see Table 10.1) with no counterpart in bacterial  $F_1F_0$  that binds right next to mitochondrial  $\delta$  [46]. However, wasteful ATP hydrolysis in mitochondrial F-ATPase is prevented by pH-dependent binding of an inhibitor protein (“inhibitory factor one,” IF1), that functions in a similar fashion as *E. coli*  $\epsilon$  subunit C-terminal domain in that it inserts into the catalytic interface from the bottom of the  $\alpha_3\beta_3$  hexamer [81, 82]. The structure of IF1 has been determined by NMR spectroscopy and contains a C-terminal dimerization and an N-terminal inhibitory domain [83].

Protein NMR spectroscopy was also successful in determining the structure of the N-terminal domain of the bacterial  $\delta$  [84] and its mitochondrial homologue, the OSCP subunit [85], which were seen to form a compact  $\alpha$  helical bundle binding to the very top of the  $\alpha_3\beta_3$  hexamer via the N-terminal 19 residues of one of the  $\alpha$  subunits [85, 86].

### ***10.3.3 Structural Information from Electron Microscopy: From Projection Images to 3D Reconstructions***

The first structural information for the rotary ATPases was obtained using transmission electron microscopy (TEM) of negatively stained mitochondrial membrane preparations [42]. The images showed globular proteins with a diameter of approximately 10 nm that were attached to the membrane by 2- to 3-nm-long slender stalks. Treatment of the membranes with low ionic strength buffer resulted in a water-soluble ATPase and a membrane fraction that had no ATP hydrolyzing activity [87]. TEM images of the globular particles detached from the membrane

revealed the hexameric architecture of the ATPase sector but the limited resolution of the negative stain images did not allow localization of the single copy subunits of the complexes. This was accomplished by a combination of cryo electron microscopy and enzyme decoration with monoclonal antibodies and antibody Fab fragments [88]. TEM analysis of detergent-solubilized membranes revealed the characteristic dumbbell appearance of the intact  $F_1F_o$ -ATP synthase particles [89] and the application of cryo electron microscopy for visualizing lipid vesicle-reconstituted enzyme confirmed the existence of the central stalk connecting  $F_1$  and  $F_o$  sectors [90, 91]. Subsequent application of statistical image analysis techniques revealed the presence of a second or stator stalk that could be seen to connect the top of the ATPase to the membrane at the periphery of the complex [92–94]. This structure was later shown to contain the  $\delta$  and  $b$  subunits of the enzyme (bacterial subunit nomenclature) [95]. Such stator stalks were also observed for the bacterial A/V-type ATPase [96] and later for the eukaryotic vacuolar ATPase [97] and, as mentioned above, it is now established that F-ATPase has a single stator stalk composed of the  $\delta$  and  $b$  subunits (bacterial enzyme nomenclature [68]; the single mitochondrial F-ATPase stator stalk contains additional subunits [69]) while archaeal A- and bacterial A/V-ATPase and eukaryotic V-ATPase have 2 [70] and 3 [71], respectively. The stator stalks in rotary ATPases are formed by homo- (for the bacterial enzyme) or heterodimeric coiled coil proteins with an unusual right-handed twist [72–74, 98]. Unlike in F-ATPase, the A- and V-ATPase stator stalks are not membrane-anchored but connect to subunits and subunit domains in the ATPase-ion channel interface for which there are no homologs in the F-ATPase (see Fig. 10.1).

Early 3D EM reconstructions of F- [99], A- [100, 101], and V-ATPases [102–105] calculated at resolutions of between 15 and 30 Å allowed determination of the overall subunit architecture of the complexes. Placing of crystal structures of catalytic sectors, proteolipid rings, and individual subunits into the EM-derived atomic density maps produced first “pseudo atomic resolution” models of the rotary ATPases. The limited resolution of these maps, however, sometimes produced contradictory interpretations as to the placement of some of the subunits. A more recent application of cryo electron microscopy allowed determination of a 3D map of the A/V-type ATPase from *T. thermophilus* that provided unprecedented structural detail [65]. At 9.7 Å resolution, the EM density was able to resolve individual  $c$  subunits in the proteolipid ring and provided a first glimpse into the interaction of the  $c$  subunit ring with the membrane-bound domain of the  $a$  subunit. The model clearly resolved eight transmembrane  $\alpha$  helices for the C-terminal domain of the  $a$  subunit, consistent with earlier biochemical studies conducted with the homologous subunit of the yeast vacuolar ATPase [106]. The eight TM segments appeared to be packed as 2 four- $\alpha$  helix bundles, leading the authors of the EM study to speculate that each four-helix bundle formed one of the water-accessible half channels that had been postulated earlier to form an integral part of the proton pathway across the subunit  $a$ – $c$  ring interface in F-ATPase [107, 108]. A selection of the most recent cryo EM reconstructions, fitted with the available crystal structures, is shown in Fig. 10.3.



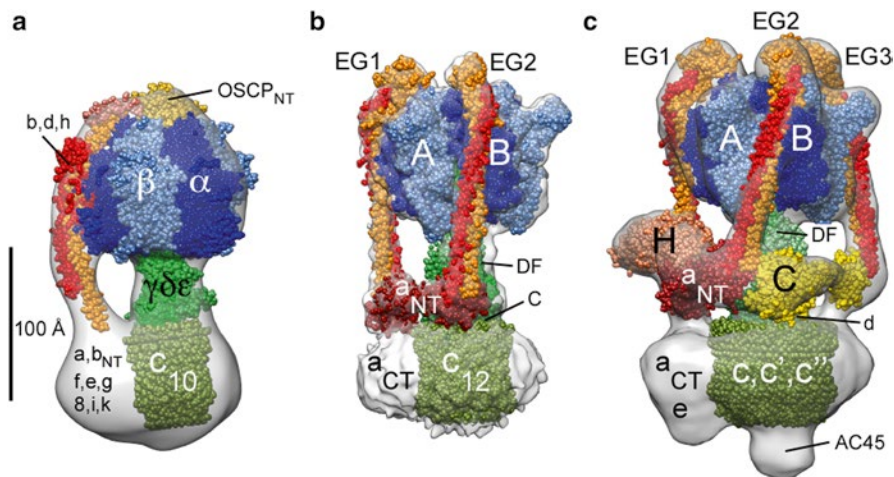


**Fig. 10.3** 3D EM reconstructions of F-, A/V-, and V-ATPase. **(a–c)** Cryo EM reconstructions of yeast F-ATPase (emd-2011), A/V-type ATPase of *T. thermophilus* (emd-5335), and insect V-ATPase (emd-1590). The crystal structures used for fitting were in **(a)** bovine F<sub>1</sub> (1e79), OSCP (2bo5), stator stalk assembly (2cly), and rotor ring (3u2f); in **(b)** A<sub>3</sub>B<sub>3</sub> (3a5c), DF (3aon), EG heterodimer (3k5b), *a* subunit N-terminal domain (3rrk), rotor ring with 12 *c* subunits (modeled; 1c17), and subunit *d* (1r5z); and in **(c)**, as in **(b)** plus subunit C (1u7l), subunit H (1ho8) and the K<sub>10</sub> ring of *E. hirae* (2bl2)

### 10.3.4 Structural Information from Native Mass Spectrometry

Mass spectrometry (MS) has become a powerful tool for analyzing structural features of large protein complexes. In native mass spectrometry, protein complexes are introduced into the gas phase by electrospray ionization (ESI) or laser-induced liquid bead ion desorption (LILBID) without denaturant, and, under suitable conditions, the proteins travel as intact multi-subunit complexes through the vacuum of the spectrometer. Mass spectrometry of native protein complexes can provide essential information which is often difficult to obtain by classical biochemical methods such as subunit stoichiometry and, in case of membrane proteins, lipid binding. Information about conformation can be obtained from an analysis of the proteins' cross section using ion mobility mass spectrometry. Several rotary motor ATPases and their sub-complexes have been analyzed by native MS. Native ESI-MS analysis conducted with A/V-type ATPase from *T. thermophilus* and V<sub>1</sub>-ATPase from yeast allowed unambiguous determination of the subunit stoichiometry, including the presence of 2 and 3 EG heterodimer stator stalks, respectively [70, 71]. LILBID analysis of the A-ATPase from the hyperthermophilic archaeon *Pyrococcus furiosus* allowed determination of the subunit stoichiometry of the intact enzyme,



including the number of *c* subunits in the membrane-bound proteolipid ring, information that has been difficult to obtain by traditional biochemical methods [100]. More recently, ESI native mass spectra of unprecedented resolution and clarity could be obtained for the intact A/V-type ATPases from *T. thermophilus* and (to a somewhat lesser degree) *E. hirae*, allowing detection of nucleotide-dependent conformational changes in the ATPase sector and binding of specific lipids to the detergent-solubilized membrane sector [109].

### **10.3.5 Structural Information from Small Angle X-Ray Scattering**

Much like TEM, small angle X-ray scattering of biological macromolecules (BioSAXS) was one of the early biophysical tools that was applied to obtain structural information for rotary motor ATPases and their functional domains. Initial pioneering studies were limited to the analysis of hydrodynamic parameters including radius of gyration ( $R_g$ ) and pairwise distance distribution functions ( $P(r)$ ), providing overall information on molecular mass and size of the complexes in solution [110]. Subsequent development of algorithms that allowed shape determination from SAXS intensities were used to obtain low resolution solution structures of  $F_1$ - and  $V_1$ -ATPase sectors as well as individual subunits and subunit complexes from the eukaryotic V-ATPase [111–114]. In one study, SAXS was used to determine the shape of yeast V-ATPase stator stalk complex bound to the regulatory C subunit, revealing an L-shaped structure [104]. Interestingly, the resulting envelope did not match the atomic density for the stator stalk as seen in a negative stain 3D EM reconstruction, a mismatch that leads the authors of the study to speculate that the stator stalks have to change conformation from a solution state to the structure when bound in the assembled enzyme [104].

## **10.4 Towards the Mechanism of Rotary Catalysis**

Conducted parallel to the structure determination of the rotary ATPases, which started with the early electron microscopy studies and is still ongoing to date, were efforts addressed at determining the molecular mechanism of enzyme catalysis, that is, reversible conversion of the potential energy stored in a transmembrane ion gradient to the chemical energy stored in the off equilibrium mass action ratio of ATP and ADP in the cell. The process of ion gradient-driven ATP synthesis or ATP hydrolysis-driven buildup of an ion gradient is generally referred to as “energy coupling” or “energy conversion.”

### 10.4.1 *The Beginnings: $^{18}\text{O}$ Exchange and a Hypothesis*

Early experiments had shown that F-ATPase contains three catalytic sites (on the  $F_1$ ) but only a single proton channel (in the transmembrane  $F_0$ ). How do the three catalytic sites communicate with each other and how are events in three catalytic sites coupled to a single proton pore? Early experiments conducted by the groups of Paul Boyer (using  $^{18}\text{O}$  oxygen exchange kinetics) and Harvey Penefsky (employing quench flow kinetics) showed that, under limiting ATP concentrations, the equilibrium constant of the ATP hydrolysis reaction on the catalytic sites is close to unity, suggesting that much of the energy of the ion gradient during ATP synthesis is used to open the catalytic site to allow release of synthesized ATP and not for the synthesis reaction itself [18, 115, 116]. These and other experiments then allowed Paul Boyer to formulate the “binding change mechanism” of F-ATPase, that, as mentioned above, predicted that three catalytic sites at any given time were in different conformations, with one tight (ATP-bound) site, one loose (ADP-bound) site, and one empty site. During ATP synthesis, each catalytic site undergoes cyclic changes from open (empty) to loose (ADP-bound) to tight (ATP) and opens again with the reversed order during ATP hydrolysis. The cyclic conversions of each site are coupled to the two other sites,  $120^\circ$  and  $-120^\circ$  out of phase. While ATP binding was found to occur with strongly negative cooperativity, the turnover rate increases from the so-called unisite catalysis, where only one site operates (due to limiting ATP concentration) to multi-site catalysis by a factor of  $\sim 10^6$  [18, 117]. However, the notion that maximal turnover rate can be achieved with only two catalytic sites filled has been challenged based on tryptophan fluorescence quenching experiments that showed that maximum turnover in *E. coli*  $F_1$ -ATPase requires nucleotide occupancy of all three sites [22, 118] as seen in the three-nucleotide X-ray crystal structure of bovine  $F_1$  [47].

A further prediction by Boyer was that coupling of the three catalytic sites to the single ion channel would involve rotation of some (or all) of the single copy subunits of the enzyme. In 1997, Paul Boyer (for the catalytic mechanism) and Sir John Walker (for the crystal structure determination of bovine  $F_1$ -ATPase) were awarded the Nobel Prize in chemistry ([http://nobelprize.org/nobel\\_prizes/chemistry/laureates/1997](http://nobelprize.org/nobel_prizes/chemistry/laureates/1997)).

### 10.4.2 *Proving Rotational Catalysis: Or Putting Biophysics to the Test*

While the hypothesis of subunit rotation seemed plausible early on considering the symmetry mismatch between three catalytic sites and one ion channel, validating or invalidating this hypothesis proved much more difficult than anticipated. For example, biochemical experiments using photo or disulfide crosslinking were mostly in support of rotational catalysis in that they showed that linking putative stator and rotor subunits leads to enzyme inhibition while

linking rotor and rotor or stator and stator components had little effect [24, 77]. However, in the end, the static crosslinking experiments fell short of a definitive proof as there may be alternative explanations to enzyme inhibition upon crosslinking. More direct evidence was obtained using reversible crosslinks that showed that the rotor subunit is indeed moving between different catalytic subunits [119] but by that time, researchers realized that only real-time experiments could provide sufficient evidence for rotational catalysis. The first observation of rotor dynamics on a timescale of catalysis was provided by fluorescence anisotropy relaxation measurements of immobilized  $F_1$ -ATPase molecules—but for technical reasons, even these experiments were limited to showing a rotation angle short of a full rotation ( $\pm 200^\circ$ ) [120].

### 10.4.3 Looking at Single Molecules: The Breakthrough

While the sum of biochemical and biophysical experiments available at the time left little doubt that subunit rotation was integral to the mechanism of energy coupling in F-ATPase, a direct and convincing proof was only obtained from single molecule observation that unequivocally showed unidirectional and continuous rotation of the gamma subunit in response to ATP hydrolysis. The experimental setup consisted of immobilized  $\alpha_3\beta_3\gamma$  sub-complexes that were tagged with a long fluorescently labeled actin filament attached to the mobile  $\gamma$  subunit for direct CCD camera-based observation under the fluorescence microscope (Fig. 10.4a; [121]). The resulting video recordings showed counterclockwise rotation of the  $\gamma$  subunit during ATP hydrolysis when viewing the complex from the bottom (corresponding to a direction from the membrane surface towards cytoplasm). From the rotation rate and length of the actin filament, it could be determined that ATP hydrolysis generated a torque of up to 80 pN·nm, suggesting that the  $F_1$ -ATPase motor was converting the free energy change generated during ATP hydrolysis to mechanical work with near 100 % efficiency (this is possible as  $F_1$ -ATPase is not a heat engine) [122].

Subsequent refinement of the experimental setup produced a wealth of detailed information on the catalytic mechanism of  $F_1$ -ATPase as well as intact, immobilized  $F_1F_0$ -ATP synthase. A crucial improvement of the time resolution could be accomplished by replacing the fluorescent actin filaments with small nylon beads [123] or gold nanorods [124] in combination with high speed CCD cameras. For example, improving the time resolution of the imaging showed that each  $120^\circ$  rotation step is divided into an  $80^\circ$  sub-step induced by ATP binding, and a  $40^\circ$  sub-step driven by phosphate and/or ADP release [123, 125]. Higher time resolution also allowed a thermodynamic analysis of  $F_1$  rotation, suggesting that the energy pathway of catalysis is relatively flat, allowing turnover without  $F_1$  having to overcome excessive energy barriers [126]. Sophisticated single molecule manipulation using magnetic beads allowed mechanical winding of the  $\gamma$  subunit and it could be shown that this forced  $\gamma$  rotation was able to synthesize ATP from ADP and inorganic phosphate [127].

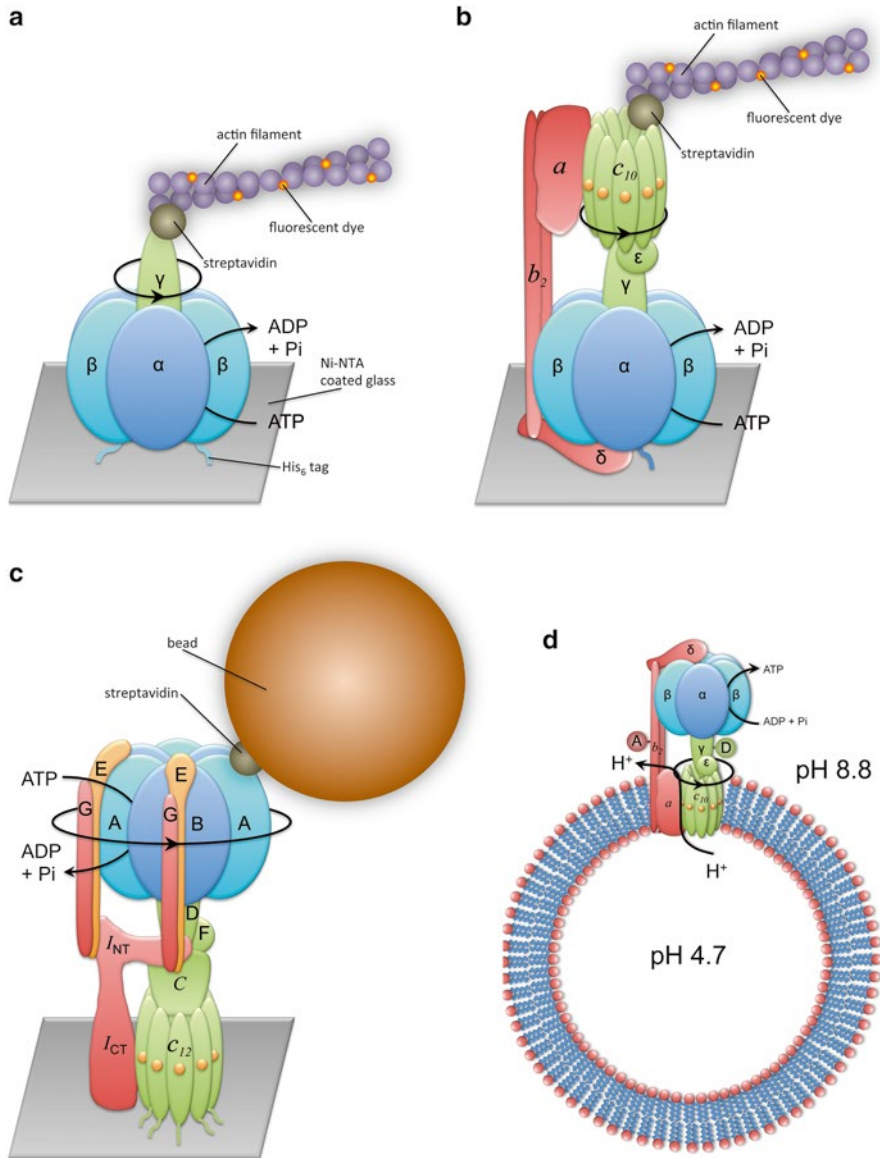


**Fig. 10.4** Experimental setup for single molecule observation by fluorescence microscopy and FRET spectroscopy. Observation of subunit rotation via actin filament attached to (a)  $\gamma$  subunit in  $F_1$ -ATPase and (b)  $c$  subunit in intact  $F_1F_0$ -ATP synthase (adapted from [121] and [128], respectively). (c) Observation of rotation in intact A/V-ATP synthase from *T. thermophilus* via nylon bead attached to the A subunit (adapted from [27]). (d) FRET-based observation of rotation in lipid vesicle-reconstituted *E. coli* ATP synthase. Donor and acceptor dyes were attached to the  $\gamma$  and  $b$  subunits, respectively (shown as green and red spheres). Liposomes containing in average one ATP synthase molecule were equilibrated in low pH buffer and then diluted into basic buffer containing ADP and inorganic phosphate ( $P_i$ ) to initiate ATP synthesis. Liposomes were allowed to diffuse through a laser focus in a confocal microscope, allowing recording of fluorescence bursts for a duration of between 50 and 250 ms. Fluorescence bursts showed three levels of donor and acceptor intensity, corresponding to the three positions of the donor dye attached to the rotor. The order of the levels changed when going from ATP synthesis to ATP hydrolysis (adapted from ref. [133])

The experimental setup used for single molecule observation of intact, detergent-solubilized ATP synthase using actin filaments [128] and spherical beads as probe is illustrated in Fig. 10.4b, c. Similar experimental setups were then used to show rotation of the proteolipid ring in lipid bilayer-reconstituted, intact ATP synthase [129]. Recent real-time observation by the atomic force microscope (AFM) revealed that cyclic up and down movements of the  $\beta$  subunit C-terminal domains can even be observed in rotorless “F<sub>1</sub>,” suggesting that communication of the subunits within the ring of the catalytic core is sufficient for providing directionality [130].

The single molecule rotation experiments were quickly adapted to bacterial A/V-ATPase sector and intact yeast vacuolar ATPase and the studies showed that, surprisingly, A/V-ATPase appeared to use a slightly different catalytic mechanism in that 80° and 40° sub-steps were not observed [27, 131]. It is possible that the turnover kinetics of A/V-ATPase is different with shorter dwell times for one of the sub-steps, too short to be resolved, but it is also possible that A/V-ATPase uses only one power stroke, e.g., as a result of ATP binding. The only single molecule observation of a eukaryotic rotary motor, conducted with the intact vacuolar ATPase from yeast confirmed subunit rotation, albeit with a slightly lower torque compared to F-ATPase [132].

All single molecule experiments using direct observation of actin filaments, polystyrene beads, or gold nanorods were with rotary motor complexes functioning in the direction of ATP hydrolysis (Fig. 10.4a–c). For observation of single molecules actively synthesizing ATP driven by a proton gradient and membrane potential, a different experimental setup had to be developed.

#### 10.4.4 Single Molecule Fluorescence Energy Transfer Spectroscopy

Until now, it was shown that rotary motor ATPases rotate unidirectionally (counter-clockwise when seen from the membrane surface towards the bottom of the  $\alpha_3\beta_3\gamma$  complex) and while there was little doubt that directionality is reversed when the enzyme switches from hydrolysis to synthesis of ATP, the change in the direction of rotation needed to be shown experimentally. This was ultimately accomplished using single molecule Förster resonance energy transfer (smFRET) spectroscopy of liposome-reconstituted *E. coli* ATP synthase labeled with donor and acceptor fluorophores at stator and rotor subunits, respectively [133] (see Fig. 10.4d). ATP synthesis was driven by a transient transmembrane pH gradient established by diluting liposomes equilibrated at low pH into a buffer of basic pH. For observation of single liposome-bound ATP synthase molecules, a confocal microscope setup was used where acceptor fluorescence is recorded while liposomes are allowed to diffuse through a femtoliter size laser focus. During the resulting “bursts” of fluorescence, three levels of fluorescence intensity were observed and it could be shown that during membrane potential-driven ATP synthesis, the order of the fluorescence levels in the bursts was reversed from the direction of rotation observed for ATP hydrolysis.

A similar smFRET setup was used in subsequent experiments to show that rotation of the proteolipid ring occurred in steps of  $\sim 36^\circ$  (the *E. coli* enzyme has 10 *c* subunits in the proteolipid ring) [134]. ATP hydrolysis-induced stepping of the proteolipid rings was subsequently also shown using high speed CCD-based direct observation of enzyme-coupled gold nanorods and nylon beads for *E. coli* F- [135] and *T. thermophilus* A/V-type [27] ATP synthases, respectively. Recording fluctuations in polarization of gold nanorods induced by subunit rotation using an ultra high speed CCD camera revealed a transient interaction of one of the loops of the *a* subunit with the cytoplasmic loops of the proteolipid ring as part of each stepped motion of the ring of *c* subunits. Such transient interaction between proteolipid rotor and *a* subunit stator may serve to bias the “Brownian ratchet” (see below) in the desired direction of rotation [135].

#### 10.4.5 Rotational Catalysis and Elastic Energy Coupling

As summarized above, both ATPase and membrane sectors function as stepper motors, with  $120^\circ$  steps for the central rotor of the ATPase and  $360^\circ/n$  steps for the ion channel with *n* being the number of *c* subunits in the proteolipid ring. With few exceptions, the number of *c* subunits in the ring is not divisible by three, resulting in a non-integer ratio of the number of ions translocated for each molecule of ATP synthesized or hydrolyzed. The much smaller rotational steps of the proteolipid ring ( $36^\circ$  for the *E. coli* F-ATPase *c*<sub>10</sub> ring) compared to the  $120^\circ$  steps of the central rotating stalk require transient storage of elastic energy by one or several components of the motor. Single molecule experiments conducted with the *E. coli* F-ATPase revealed that it is the  $\gamma$  subunit, with some contribution from the C-terminal domains of the catalytic  $\beta$  subunits, that functions in elastic energy storage [136]. In this model, the energy provided by the translocation of the first two (or three) protons serves to “wind up” the  $\gamma$  subunit before a third (or fourth) proton results in a  $120^\circ$  rotational step of the rotor with concomitant opening and closing of catalytic sites. The same study also suggested that the *b* subunit dimer is relatively stiff, indicating that the stator stalk does not play a significant role in transient energy storage [136]. However, modeling studies conducted with the bacterial A/V-ATPase suggest that the stator stalks have to be flexible to adapt to the different conformations of the catalytic subunits [73] and it remains to be seen whether stiffness of the stator stalk is a conserved feature of all rotary ATPases or limited to bacterial F-ATP synthase.

#### 10.4.6 Theoretical Considerations

As mentioned above, we still have no high resolution structure of the proteolipid ring–subunit *a* interface. Critical residues involved in proton transport (in *E. coli* F-ATPase) are Asp61 in subunit *c* and Arg210 in subunit *a*. The difficulty in obtaining crystals for

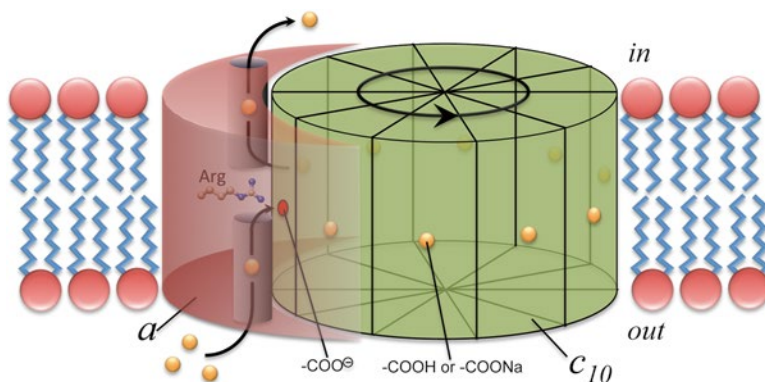


**Fig. 10.5** Mechanistic model of the rotary ATPase proton turbine. In the direction of ion gradient-driven ATP synthesis, protons (or sodium ions) enter the first half channel in subunit *a* and bind the ionized form of a carboxylate located in the middle of one of the transmembrane  $\alpha$  helices of subunit *c* (Asp61 in *E. coli* F-ATP synthase). Binding of the proton or sodium ion neutralizes the negatively charged carboxylate, allowing it to move away from the subunit *a*–*c* interface into the hydrophobic proteolipid–lipid interface. This movement will align another proton or sodium-bound carboxyl group with the second half channel, allowing its ion to dissociate and diffuse to the other side of the membrane. The sidechain of a critical arginine residue in subunit *a* acts as a gate to prevent that ions move directly from the exit of the first to the entry of the second half channel. According to the “Brownian ratchet” model of rotary ATPase-ion channel function [120], thermal fluctuations allow the ring to overcome local minima of the electrostatic potential, possibly biased by a transient “tether” interaction between subunits *a* and *c* [139]. Illustration adapted from ref. [107]

this part of the complex may be explained by the fact that the tether interactions at the subunit *a*–*c* interface mentioned above cannot be too tight. The surface of the *c* ring is likely covered with lipid molecules, a greasy surface that may provide lubrication for the *a*–*c* interface so that the two subunits can slide past each other several hundred times per second during steady state turnover. The *a*–*c* interface has been studied by disulfide crosslinking and, based on these data, models of the interface have been proposed [137]. Early on it was postulated that subunit *a* contains two water accessible hemi channels that are interrupted at the level of Asp61 and Arg210 in the membrane [107] (see Fig. 10.5). The model predicted that protons (hydronium ions) would enter from, e.g., the periplasmic half channel, bind the carboxylate of Asp61, and, after being carried around by one revolution of the ring, the proton would be released on the cytoplasmic side through the second half channel. While evidence from accessibility experiments has been obtained that supports a two half channel model [108], details of the proton pathway through subunit *a* remain to be determined. As mentioned above, the 2 four- $\alpha$  helix bundles seen in the cryo EM reconstruction of *T. thermophilus* ATPase have been proposed to act as the two half channels in A-, A/V-type, and V-ATPases [65]. F-ATPase *a* subunit, however, has likely only five TM segments, but since the presence of the *b* subunits is required for proton translocation [138], it cannot be ruled out that the two N-terminal TM helices of the *b* subunits contribute to the two half channels in F-ATPase.



It has been suggested that torque generation in the rotary ATPase proton channel functions according to a “Brownian ratchet” mechanism, where thermal fluctuations allow the ring to overcome local minima in the electrostatic potential influenced by the positively charged Arg210 sidechain and the carboxylate of Asp61 [139]. Once a proton (or sodium) is picked up by an Asp61 carboxylate, the now neutral sidechain can move away from the *a*–*c* interface into the lipid bilayer, moving another carboxylic acid into the interface where it will release its proton to the cytoplasm. This mechanism can be easily envisioned in the direction of proton transport along a pH gradient while in the direction of proton pumping, a change in *pK* of Asp61’s carboxyl may be required to allow release of the proton to a more acidic periplasm.

## 10.5 Current Developments and Remaining Challenges

Past biophysical and biochemical investigations of the rotary motor ATPase have produced a wealth of structural and mechanistic information, especially for the catalytic sectors. Much less detail is available for the membrane portions of the enzymes, in particular how the proteolipid ring interacts with the (membrane-bound part of) *a* subunit during rotational catalysis. Structural studies of an intact rotary motor ATPase have so far been limited to crystal structures of mitochondrial F<sub>1</sub>–proteolipid ring complexes or medium resolution cryo electron microscopy maps of bacterial A/V-ATPase. While the crystal structures provide some insight into the interaction of membrane subunits with subunits of the soluble ATPase sectors, as of now only the cryo EM models provide a glimpse of the interface of the proteolipid ring and the *a* subunit. Resolving this interface with atomic detail will be absolutely required for elucidating the mechanism by which protons (or sodium ions) are transported from one side of the membrane to the other, and how this ion transport generates the driving force for subunit rotation-driven synthesis of ATP.

## References

1. Muench SP, Trinick J, Harrison MA (2011) Structural divergence of the rotary ATPases. *Q Rev Biophys* 44:311–356
2. Wilkens S (2005) Rotary molecular motors. *Adv Protein Chem* 71:345–382
3. Pallen MJ, Bailey MC, Beatson SA (2006) Evolutionary links between FliH/YscL-like proteins from bacterial type III secretion systems and second-stalk components of the FoF1 and vacuolar ATPases. *Protein Sci* 15:935–940
4. Mulkidjanian AY, Makarova KS, Galperin MY, Koonin EV (2007) Inventing the dynamo machine: the evolution of the F-type and V-type ATPases. *Nat Rev Microbiol* 5:892–899
5. Forgac M (2007) Vacuolar ATPases: rotary pumps in physiology and pathophysiology. *Nat Rev Mol Cell Biol* 8:917–929
6. Marshansky V, Futai M (2008) The V-type H<sup>+</sup>–ATPase in vesicular trafficking: targeting, regulation, and function. *Curr Opin Cell Biol* 20:415–426



7. Saroussi S, Nelson N (2009) The little we know on the structure and machinery of V-ATPase. *J Exp Biol* 212:1604–1610
8. Li SC, Kane PM (2009) The yeast lysosome-like vacuole: endpoint and crossroads. *Biochim Biophys Acta* 1793:650–663
9. Margulis L (1996) Archaeal-eubacterial mergers in the origin of eukarya: phylogenetic classification of life. *Proc Natl Acad Sci U S A* 93:1071–1076
10. Hilario E, Gogarten JP (1993) Horizontal transfer of ATPase genes—the tree of life becomes a net of life. *Biosystems* 31:111–119
11. Müller V, Ruppert C, Lemker T (1999) Structure and function of the  $A_1A_o$ -ATPases from methanogenic Archaea. *J Bioenerg Biomembr* 31:15–27
12. Müller V, Grüber G (2003) ATP synthases: structure, function and evolution of unique energy converters. *Cell Mol Life Sci* 60:474–494
13. Hilario E, Gogarten JP (1998) The prokaryote-to-eukaryote transition reflected in the evolution of the V/F<sub>1</sub>A-ATPase catalytic and proteolipid subunits. *J Mol Evol* 46:703–715
14. Yokoyama K, Ohkuma S, Taguchi H, Yasunaga T, Wakabayashi T, Yoshida M (2000) V-type H<sup>+</sup>-ATPase/synthase from a thermophilic eubacterium, *Thermus thermophilus*. Subunit structure and operon. *J Biol Chem* 275:13955–13961
15. Pullman ME, Penefsky HS, Datta A, Racker E (1960) Partial resolution of the enzymes catalyzing oxidative phosphorylation. I. Purification and properties of soluble, dinitrophenol-stimulated adenosine triphosphatase. *J Biol Chem* 235:3322–3329
16. Kagawa Y, Racker E (1966) Partial resolution of the enzymes catalyzing oxidative phosphorylation. IX. Reconstruction of oligomycin-sensitive adenosine triphosphatase. *J Biol Chem* 241:2467–2474
17. Junge W, Engelbrecht S, Griwatz C, Groth G (1992) The chloroplast H<sup>+</sup>-ATPase: partial reactions of the proton. *J Exp Biol* 172:461–474
18. Boyer PD (1997) The ATP synthase—a splendid molecular machine. *Annu Rev Biochem* 66:717–749
19. Mitchell P (1961) Coupling of phosphorylation to electron and hydrogen transfer by a chemiosmotic type of mechanism. *Nature* 191:144–148
20. Nicholls DG, Ferguson SJ (2002) Bioenergetics, 3rd edn. Academic, London
21. Nakanishi-Matsui M, Sekiya M, Nakamoto RK, Futai M (2010) The mechanism of rotating proton pumping ATPases. *Biochem Biophys Acta* 1797:1343–1352
22. Senior AE, Nadanaciva S, Weber J (2003) The molecular mechanism of ATP synthesis by F<sub>1</sub>F<sub>o</sub>-ATP synthase. *Biochem Biophys Acta* 1553:188–211
23. Yoshida M, Muneyuki E, Hisabori T (2001) ATP synthase—a marvelous rotary engine of the cell. *Nat Rev Mol Cell Biol* 2:669–677
24. Capaldi RA, Aggeler R (2002) Mechanism of F<sub>1</sub>F<sub>o</sub>-type ATP synthase, a biological rotary motor. *Trends Biochem Sci* 27:154–160
25. Wilkens S (2009) Chemistry of ATP synthesis. Wiley's Encyclopedia of chemical biology. Wiley, New York
26. Murata T, Yamato I, Kakinuma Y (2005) Structure and mechanism of vacuolar Na<sup>+</sup>-transporting ATPase from *Enterococcus hirae*. *J Bioenerg Biomembr* 37:411–413
27. Furuike S, Nakano M, Adachi K, Noji H, Kinoshita K Jr, Yokoyama K (2011) Resolving stepping rotation in *Thermus thermophilus* H<sup>(+)</sup>-ATPase/synthase with an essentially drag-free probe. *Nat Commun* 2:233
28. Hirata T, Nakamura N, Omote H, Wada Y, Futai M (2000) Regulation and reversibility of vacuolar H<sup>+</sup>-ATPase. *J Biol Chem* 275:386–389
29. Kane PM, Parra KJ (2000) Assembly and regulation of the yeast vacuolar H<sup>+</sup>-ATPase. *J Exp Biol* 203:81–87
30. Smardon AM, Tarsio M, Kane PM (2002) The RAVE complex is essential for stable assembly of the yeast V-ATPase. *J Biol Chem* 277:13831–13839
31. Sumner JP, Dow JA, Earley FG, Klein U, Jäger D, Wieczorek H (1995) Regulation of plasma membrane V-ATPase activity by dissociation of peripheral subunits. *J Biol Chem* 270:5649–5653

32. Trombetta ES, Ebersold M, Garrett W, Pypaert M, Mellman I (2003) Activation of lysosomal function during dendritic cell maturation. *Science* 299:1400–1403
33. Voss M, Vitavska O, Walz B, Wiczorek H, Baumann O (2007) Stimulus-induced phosphorylation of vacuolar H<sup>+</sup>-ATPase by protein kinase A. *J Biol Chem* 282:33735–33742
34. Blair HC, Teitelbaum SL, Ghiselli R, Gluck S (1989) Osteoclastic bone resorption by a polarized vacuolar proton pump. *Science* 245:855–857
35. Finberg KE, Wagner CA, Bailey MA, Paunescu TG, Breton S, Brown D, Giebisch G, Geibel JP, Lifton RP (2005) The B1-subunit of the H(+) ATPase is required for maximal urinary acidification. *Proc Natl Acad Sci U S A* 102:13616–13621
36. Alper SL (2010) Familial renal tubular acidosis. *J Nephrol* 23(suppl 16):S57–S76
37. Sun-Wada GH, Wada Y, Futai M (2003) Lysosome and lysosome-related organelles responsible for specialized functions in higher organisms, with special emphasis on vacuolar-type proton ATPase. *Cell Struct Funct* 28:455–463
38. Karet FE, Finberg KE, Nelson RD, Nayir A, Mocan H et al (1999) Mutations in the gene encoding B1 subunit of H<sup>+</sup>-ATPase cause renal tubular acidosis with sensorineural deafness. *Nat Genet* 21:84–90
39. Martinez-Zaguilan R, Lynch RM, Martinez GM, Gillies RJ (1993) Vacuolar-type H(+)-ATPases are functionally expressed in plasma membranes of human tumor cells. *Am J Physiol* 265:C1015–C1029
40. Kartner N, Yao Y, Li K, Crasto GJ, Datti A et al (2010) Inhibition of osteoclast V-ATPase-mediated acid secretion by targeting the  $\alpha$ 3-B2 subunit interaction. *J Biol Chem* 285:37476–37490
41. Johnson RM, Allen C, Melman SD, Waller A, Young SM et al (2010) Identification of inhibitors of vacuolar proton-translocating ATPase pumps in yeast by high-throughput screening flow cytometry. *Anal Biochem* 398:203–211
42. Fernandez-Moran H, Oda T, Blair PV, Green DE (1964) A macromolecular repeating unit of mitochondrial structure and function. Correlated electron microscopic and biochemical studies of isolated mitochondria and submitochondrial particles of beef heart muscle. *J Cell Biol* 22:63–100
43. Amzel LM, Pedersen PL (1978) Adenosine triphosphatase from rat liver mitochondria. Crystallization and X-ray diffraction studies of the F<sub>1</sub>-component of the enzyme. *J Biol Chem* 253:2067–2069
44. Abrahams JP, Leslie AG, Lutter R, Walker JE (1994) Structure at 2.8 Å resolution of F<sub>1</sub>-ATPase from bovine heart mitochondria. *Nature* 370:621–628
45. Abrahams JP, Leslie AG (1996) Methods used in the structure determination of bovine mitochondrial F<sub>1</sub> ATPase. *Acta Crystallogr D Biol Crystallogr* 52:30–42
46. Gibbons C, Montgomery MG, Leslie AG, Walker JE (2000) The structure of the central stalk in bovine F<sub>1</sub>-ATPase at 2.4 Å resolution. *Nat Struct Biol* 7:1055–1061
47. Menz RI, Walker JE, Leslie AG (2001) Structure of bovine mitochondrial F<sub>1</sub>-ATPase with nucleotide bound to all three catalytic sites: implications for the mechanism of rotary catalysis. *Cell* 106:331–341
48. Bowler MW, Montgomery MG, Leslie AG, Walker JE (2007) Ground state structure of F<sub>1</sub>-ATPase from bovine heart mitochondria at 1.9 Å resolution. *J Biol Chem* 282:14238–14242
49. Bianchet M, Hüllihen J, Pedersen PL, Amzel M (1998) The 2.8-Å structure of rat liver F<sub>1</sub>-ATPase: configuration of a critical intermediate in ATP synthesis/hydrolysis. *Proc Natl Acad Sci U S A* 95:11065–11070
50. Groth G, Pohl E (2001) The structure of the chloroplast F<sub>1</sub>-ATPase at 3.2 Å resolution. *J Biol Chem* 276:1345–1352
51. Kabaleeswaran V, Puri N, Walker JE, Leslie AG, Mueller DM (2006) Novel features of the rotary catalytic mechanism revealed in the structure of yeast F<sub>1</sub> ATPase. *EMBO J* 25:5433–5443
52. Dautant A, Velours J, Giraud MF (2010) Crystal structure of the Mg-ADP-inhibited state of the yeast F<sub>1</sub>C<sub>10</sub>-ATP synthase. *J Biol Chem* 285:29502–29510

53. Cingolani G, Duncan TM (2011) Structure of the ATP synthase catalytic complex (F<sub>1</sub>) from *Escherichia coli* in an autoinhibited conformation. *Nat Struct Mol Biol* 18:701–707
54. Maher MJ, Akimoto S, Iwata M, Nagata K, Hori Y, Yoshida M, Yokoyama S, Iwata S, Yokoyama K (2009) Crystal structure of A<sub>3</sub>B<sub>3</sub> complex of V-ATPase from *Thermus thermophilus*. *EMBO J* 28:3771–3779
55. Numoto N, Hasegawa Y, Takeda K, Miki K (2009) Inter-subunit interaction and quaternary rearrangement defined by the central stalk of prokaryotic V<sub>1</sub>-ATPase. *EMBO Rep* 10:1228–1234
56. Stock D, Leslie AGW, Walker JE (1999) Molecular architecture of the rotary motor in ATP synthase. *Science* 286:1700–1705
57. Watt IN, Montgomery MG, Runswick MJ, Leslie AGW, Walker JE (2010) Bioenergetic cost of making an adenosine triphosphate molecule in animal mitochondria. *Proc Natl Acad Sci U S A* 107:16823–16827
58. Jones PC, Fillingame RH (1998) Genetic fusions of subunit c in the F<sub>0</sub> sector of H<sup>+</sup>-transporting ATP synthase. Functional dimers and trimers and determination of stoichiometry by cross-linking analysis. *J Biol Chem* 273:29701–29705
59. Jiang W, Hermolin J, Fillingame RH (2001) The preferred stoichiometry of c subunits in the rotary motor sector of *Escherichia coli* ATP synthase is 10. *Proc Natl Acad Sci U S A* 98:4966–4971
60. Meier T, Polzer D, Diedrichs K, Welte W, Dimroth P (2005) Structure of the rotor ring of F-type Na<sup>+</sup>-ATPase from *Ilyobacter tartaricus*. *Science* 308:659–662
61. Symersky J, Pagadala V, Osowski D, Krah A, Meier T, Faraldo-Gómez JD, Mueller DM (2012) Structure of the c(10) ring of the yeast mitochondrial ATP synthase in the open conformation. *Nat Struct Mol Biol* 19:485–491
62. Vollmar M, Schlieper D, Winn M, Büchner C, Groth G (2009) Structure of the c14 rotor ring of the proton translocating chloroplast ATP synthase. *J Biol Chem* 284:18228–18235
63. Pogoryelov D, Yildiz O, Faraldo-Gómez JD, Meier T (2009) High-resolution structure of the rotor ring of a proton-dependent ATP synthase. *Nat Struct Mol Biol* 16:1068–1073
64. Toei M, Gerle C, Nakano M, Tani K, Gyobu N, Tamakoshi M, Sone N, Yoshida M, Fujiyoshi Y, Mitsuoka K, Yokoyama K (2007) Dodecamer rotor ring defines H<sup>+</sup>/ATP ratio for ATP synthesis of prokaryotic V-ATPase from *Thermus thermophilus*. *Proc Natl Acad Sci U S A* 104:20256–20261
65. Lau WC, Rubinstein JL (2012) Subnanometre-resolution structure of the intact *Thermus thermophilus* H<sup>+</sup>-driven ATP synthase. *Nature* 481:214–218
66. Murata T, Yamato I, Kakinuma Y, Leslie AG, Walker JE (2005) Structure of the rotor of the V-type Na<sup>+</sup>-ATPase from *Enterococcus hirae*. *Science* 308:654–659
67. Steigmiller S, Turina P, Gräber P (2008) The thermodynamic H<sup>+</sup>/ATP ratios of the H<sup>+</sup>-ATP synthases from chloroplasts and *Escherichia coli*. *Proc Natl Acad Sci U S A* 105:3745–3750
68. Dunn SD, McLachlin DT, Revington M (2000) The second stalk of *Escherichia coli* ATP synthase. *Biochim Biophys Acta* 1458:356–363
69. Dickson VK, Silvester JA, Fearnley IM, Leslie AG, Walker JE (2006) On the structure of the stator of the mitochondrial ATP synthase. *EMBO J* 25:2911–2918
70. Esteban O, Bernal RA, Donohoe M, Videler H, Sharon M, Robinson CV, Stock D (2008) Stoichiometry and localization of the stator subunits E and G in *Thermus thermophilus* H<sup>+</sup>-ATPase/synthase. *J Biol Chem* 283:2595–2603
71. Kitagawa N, Mazon H, Heck AJ, Wilkens S (2008) Stoichiometry of the peripheral stalk subunits E and G of yeast V<sub>1</sub>-ATPase determined by mass spectrometry. *J Biol Chem* 283:3329–3337
72. Lee LK, Stewart AG, Donohoe M, Bernal RA, Stock D (2010) The structure of the peripheral stalk of *Thermus thermophilus* H<sup>+</sup>-ATPase/synthase. *Nat Struct Mol Biol* 17:373–378
73. Stewart AG, Lee LK, Donohoe M, Chaston JJ, Stock D (2012) The dynamic stator stalk of rotary ATPases. *Nat Commun* 3:687

74. Oot RA, Huang L-S, Berry EA, Wilkens S (2012) Crystal structure of the yeast vacuolar ATPase heterotrimeric EGChead peripheral stalk complex. *Structure* 20:1881–1892
75. Girvin ME, Rastogi VK, Abildgaard F, Markley JL, Fillingame RH (1998) Solution structure of the transmembrane H<sup>+</sup>-transporting subunit c of the F<sub>1</sub>F<sub>0</sub> ATP synthase. *Biochemistry* 37:8817–8824
76. Rastogi VK, Girvin ME (1999) Structural changes linked to proton translocation by subunit c of the ATP synthase. *Nature* 402:263–268
77. Capaldi RA, Aggeler R, Wilkens S (1995) Conformational changes in the  $\gamma$  and  $\epsilon$  subunits are integral to the functioning of the *Escherichia coli* H<sup>+</sup>-pumping ATPase (ECF<sub>1</sub>F<sub>0</sub>). *Trans Biochem Soc* 23:767–770
78. Wilkens S, Dahlquist F, McIntosh L, Donaldson L, Capaldi RA (1995) Structural features of the  $\epsilon$  subunit of the *Escherichia coli* ATP synthase (ECF<sub>1</sub>F<sub>0</sub>) from NMR spectroscopy. *Nat Struct Biol* 2:961–967
79. Wilkens S, Capaldi RA (1998) Solution structure of the  $\epsilon$  subunit of the F<sub>1</sub>-ATPase form *Escherichia coli* and interactions of this subunit with  $\beta$  subunits in the complex. *J Biol Chem* 273:26645–26651
80. Uhlin U, Cox G, Guss JM (1997) Crystal structure of the epsilon subunit of the proton-translocating ATP synthase from *Escherichia coli*. *Structure* 15:1219–1230
81. Pullman ME, Monroy GC (1963) A naturally occurring inhibitor of mitochondrial adenosine triphosphatase. *J Biol Chem* 238:3762–3769
82. Cabezón E, Montgomery MG, Leslie AG, Walker JE (2003) The structure of bovine F<sub>1</sub>-ATPase in complex with its regulatory protein IF<sub>1</sub>. *Nat Struct Biol* 10:744–750
83. Cabezón E, Runswick MJ, Leslie AG, Walker JE (2001) The structure of bovine IF<sub>1</sub>(1), the regulatory subunit of mitochondrial F-ATPase. *EMBO J* 20:6990–6996
84. Wilkens S, Dunn SD, Chandler J, Dahlquist FW, Capaldi RA (1997) Solution structure of the N-terminal domain (residues 1–134) of the  $\delta$  subunit of the *Escherichia coli* F<sub>1</sub>F<sub>0</sub> ATPsynthase. *Nat Struct Biol* 4:198–201
85. Carbajo RJ, Kellas FA, Runswick MJ, Montgomery MG, Walker JE, Neuhaus D (2005) Structure of the F<sub>1</sub>-binding domain of the stator of bovine F<sub>1</sub>F<sub>0</sub>-ATPase and how it binds an alpha-subunit. *J Mol Biol* 351:824–838
86. Wilkens S, Borchardt D, Weber J, Senior AE (2005) Structural characterization of the interaction of the  $\delta$  and  $\alpha$  subunits of the *Escherichia coli* F<sub>1</sub>F<sub>0</sub>-ATPsynthase by NMR spectroscopy. *Biochemistry* 44:11786–11794
87. Kresge N, Simoni RD, Hill RL (2006) Unraveling the enzymology of oxidative phosphorylation: the work of Efraim Racker. *J Biol Chem* 281:e4
88. Gogol EP, Aggeler R, Sagermann M, Capaldi RA (1989) Cryoelectron microscopy of *Escherichia coli* F<sub>1</sub> adenosinetriphosphatase decorated with monoclonal antibodies to individual subunits of the complex. *Biochemistry* 28:4709–4716
89. Tsuprun VL, Orlova EV, Mesyanzhinova IV (1989) Structure of the ATP-synthase studied by electron microscopy and image processing. *FEBS Lett* 244:279–282
90. Gogol EP, Lücken U, Capaldi RA (1987) The stalk connecting the F<sub>1</sub> and F<sub>0</sub> domains of ATP synthase visualized by electron microscopy of unstained specimens. *FEBS Lett* 219:274–278
91. Lücken U, Gogol EP, Capaldi RA (1990) Structure of the ATP synthase complex (ECF<sub>1</sub>F<sub>0</sub>) of *Escherichia coli* from cryoelectron microscopy. *Biochemistry* 29:5339–5343
92. Wilkens S, Capaldi RA (1998) ATP synthase's second stalk comes into focus. *Nature* 393:29
93. Karrasch S, Walker JE (1999) Novel features in the structure of bovine ATP synthase. *J Mol Biol* 290:379–384
94. Böttcher B, Schwarz L, Gräber P (1998) Direct indication for the existence of a double stalk in CF<sub>1</sub>F<sub>0</sub>. *J Mol Biol* 281:757–762
95. Wilkens S, Zhou J, Nakayama R, Dunn SD, Capaldi RA (2000) Localization of the  $\delta$  subunit in the *Escherichia coli* F<sub>1</sub>F<sub>0</sub>-ATPsynthase by immuno electron microscopy: the  $\delta$  subunit binds on top of the F<sub>1</sub>. *J Mol Biol* 295:387–391

96. Boekema EJ, Ubbink-Kok T, Lolkema JS, Brisson A, Konings WN (1997) Visualization of a peripheral stalk in V-type ATPase: evidence for the stator structure essential to rotational catalysis. *Proc Natl Acad Sci U S A* 94:14291–14293
97. Wilkens S, Vasilyeva E, Forgac M (1999) Structure of the vacuolar ATPase by electron microscopy. *J Biol Chem* 274:31804–31810
98. Del Rizzo PA, Bi Y, Dunn SD (2006) ATP synthase b subunit dimerization domain: a right-handed coiled coil with offset helices. *J Mol Biol* 364:735–746
99. Rubinstein JL, Walker JE, Henderson R (2005) Structure of the mitochondrial ATP synthase by cryo electron microscopy. *EMBO J* 22:6182–6192
100. Vonck J, Pisa KY, Morgner N, Brutschy B, Muller V (2009) Three-dimensional structure of  $A_1A_0$  ATP synthase from the hyperthermophilic archaeon *Pyrococcus furiosus* by electron microscopy. *J Biol Chem* 284:10110–10119
101. Bernal RA, Stock D (2004) Three-dimensional structure of the intact *Thermus thermophilus*  $H^+$ -ATPase/synthase by electron microscopy. *Structure* 12:1789–1798
102. Wilkens S, Inoue T, Forgac M (2004) Three-dimensional structure of the vacuolar ATPase—localization of subunit H by difference imaging and chemical cross-linking. *J Biol Chem* 279:41942–41949
103. Zhang Z, Zheng Y, Mazon H, Milgrom E, Kitagawa N, Kish-Trier E, Heck AJ, Kane PM, Wilkens S (2008) Structure of the yeast vacuolar ATPase. *J Biol Chem* 283:35983–35995
104. Diepholz M et al (2008) A different conformation for EGC stator subcomplex in solution and in the assembled yeast V-ATPase: possible implications for regulatory disassembly. *Structure* 16:1789–1798
105. Muench SP et al (2009) Cryo-electron microscopy of the vacuolar ATPase motor reveals its mechanical and regulatory complexity. *J Mol Biol* 386:989–999
106. Toei M, Toei S, Forgac M (2011) Definition of membrane topology and identification of residues important for transport in subunit a of the vacuolar ATPase. *J Biol Chem* 286:35176–35186
107. Vik SB, Antonio BJ (1994) A mechanism of proton translocation by  $F_1F_0$  ATP synthases suggested by double mutants of the a subunit. *J Biol Chem* 269:30364–30369
108. Angevine CM, Herold KA, Fillingame RH (2003) Aqueous access pathways in subunit a of rotary ATP synthase extend to both sides of the membrane. *Proc Natl Acad Sci U S A* 100:13179–13183
109. Zhou M, Morgner N, Barrera NP, Politis A, Isaacson SC, Matak-Vinković D, Murata T, Bernal RA, Stock D, Robinson CV (2011) Mass spectrometry of intact V-type ATPases reveals bound lipids and the effects of nucleotide binding. *Science* 334:380–385
110. Paradies HH, Schmidt UD (1979) Size and molecular parameters of adenosine triphosphatase from *Escherichia coli*. *J Biol Chem* 254:5257–5263
111. Svergun DI, Konrad S, Huss M, Koch MH, Wiczorek H, Altendorf K, Volkov VV, Grüber G (1998) Quaternary structure of V1 and F1 ATPase: significance of structural homologies and diversities. *Biochemistry* 37:17659–17663
112. Armbrüster A, Svergun DI, Coskun U, Juliano S, Bailer SM, Grüber G (2004) Structural analysis of the stalk subunit Vma5p of the yeast V-ATPase in solution. *FEBS Lett* 570:119–125
113. Basak S, Gayen S, Thaker YR, Manimekalai MS, Roessle M, Hunke C, Grüber G (2011) Solution structure of subunit F (Vma7p) of the eukaryotic V(1)V(O) ATPase from *Saccharomyces cerevisiae* derived from SAXS and NMR spectroscopy. *Biochim Biophys Acta* 1808:360–368
114. Oot RA, Wilkens S (2012) Subunit interactions at the  $V_1$ - $V_o$  interface in the yeast vacuolar ATPase. *J Biol Chem* 287:13396–13406
115. Boyer PD, Cross RL, Momsen W (1973) A new concept for energy coupling in oxidative phosphorylation based on a molecular explanation of the oxygen exchange reactions. *Proc Natl Acad Sci U S A* 70:2837–2839
116. Cross RL, Grubmeyer C, Penefsky HS (1982) Mechanism of ATP hydrolysis by beef heart mitochondrial ATPase. Rate constants for elementary steps in catalysis at a single site. *J Biol Chem* 257:12092–12100

117. Cross RL, Grubmeyer C, Penefsky HS (1982) Mechanism of ATP hydrolysis by beef heart mitochondrial ATPase. Rate enhancements resulting from cooperative interactions between multiple catalytic sites. *J Biol Chem* 257:12101–12105
118. Weber J, Senior AE (2001) Bi-site catalysis in  $F_1$ -ATPase: does it exist? *J Biol Chem* 276:35422–35428
119. Duncan TM, Bulygin VV, Zhou Y, Hutcheon ML, Cross RL (1995) Rotation of subunits during catalysis by *Escherichia coli*  $F_1$ -ATPase. *Proc Natl Acad Sci U S A* 92:10964–10968
120. Sabbert D, Engelbrecht S, Junge W (1996) Intersubunit rotation in active F-ATPase. *Nature* 381:623–626
121. Noji H, Yasuda R, Yoshida M, Kinosita K Jr (1997) Direct observation of the rotation of  $F_1$ -ATPase. *Nature* 386:299–302
122. Kinosita K, Yasuda R, Noji H, Adachi K (2000) A rotary molecular motor that can work at near 100% efficiency. *Philos Trans R Soc Lond B Biol Sci* 255:473–489
123. Yasuda R, Noji H, Yoshida M, Kinosita K Jr, Itoh H (2001) Resolution of distinct rotational substeps by submillisecond kinetic analysis of  $F_1$ -ATPase. *Nature* 410:898–904
124. Spetzler D, York J, Daniel D, Fromme R, Lowry D, Frasch W (2006) Microsecond time scale rotation measurements of single  $F_1$ -ATPase molecules. *Biochemistry* 45:3117–3124
125. Adachi K, Oiwa K, Nishizaka T, Furuike S, Noji H, Itoh H, Yoshida M, Kinosita K (2007) Coupling of rotation and catalysis in  $F_1$ -ATPase revealed by single-molecule imaging and manipulation. *Cell* 130:309–321
126. Sekiya M, Nakamoto RK, Al-Shawi MK, Nakanishi-Matsui M, Futai M (2009) Temperature dependence of single molecule rotation of the *Escherichia coli* ATP synthase  $F_1$  sector reveals the importance of  $\gamma$ - $\beta$  subunit interactions in the catalytic dwell. *J Biol Chem* 284:22401–22410
127. Itoh H, Takahashi A, Adachi K, Noji H, Yasuda R, Yoshida M, Kinosita K (2004) Mechanically driven ATP synthesis by  $F_1$ -ATPase. *Nature* 427:465–468
128. Sambongi Y, Iko Y, Tanabe M, Omote H, Iwamoto-Kihara A, Ueda I, Yanagida T, Wada Y, Futai M (1999) Mechanical rotation of the c subunit oligomer in ATP synthase (F<sub>0</sub>F<sub>1</sub>): direct observation. *Science* 286:1722–1724
129. Nishio K, Iwamoto-Kihara A, Yamamoto A, Wada Y, Futai M (2002) Subunit rotation of ATP synthase embedded in membranes:  $\alpha$  or  $\beta$  subunit rotation relative to the c subunit ring. *Proc Natl Acad Sci U S A* 99:13448–13452
130. Uchihashi T, Iino R, Ando T, Noji H (2011) High-speed atomic force microscopy reveals rotary catalysis of rotorless  $F_1$ -ATPase. *Science* 333:755–758
131. Imamura H, Takeda M, Funamoto S, Shimabukuro K, Yoshida M, Yokoyama K (2005) Rotation scheme of  $V_1$ -motor is different from that of  $F_1$ -motor. *Proc Natl Acad Sci U S A* 99:17929–17933
132. Hirata T, Iwamoto-Kihara A, Sun-Wada G-H, Okajima T, Wada Y, Futai M (2003) Subunit rotation of vacuolar-type proton pumping ATPase: relative rotation of the G as to the c subunit. *J Biol Chem* 278:23714–23719
133. Diez M, Zimmermann B, Börsch M, König M, Schweinberger E, Steigmüller S, Reuter R, Felekyan S, Kudryavtsev V, Seidel CA, Gräber P (2004) Proton-powered subunit rotation in single membrane-bound  $F_0F_1$ -ATP synthase. *Nat Struct Mol Biol* 11:135–141
134. Düser MG, Zarrabi N, Cipriano DJ, Ernst S, Glick GD, Dunn SD, Börsch M (2009) 36 Degrees step size of proton-driven c-ring rotation in FoF<sub>1</sub>-ATP synthase. *EMBO J* 28:2689–2696
135. Ishmukhametov R, Hornung T, Spetzler D, Frasch WD (2010) Direct observation of stepped proteolipid ring rotation in *E. coli*  $F_0F_1$ -ATP synthase. *EMBO J* 29:3911–3923
136. Wächter A, Bi Y, Dunn SD, Cain BD, Sielaff H, Wintermann F, Engelbrecht S, Junge W (2011) Two rotary motors in F-ATP synthase are elastically coupled by a flexible rotor and a stiff stator stalk. *Proc Natl Acad Sci U S A* 108:3924–3929

137. Fillingame RH, Dmitriev OY (2002) Structural model of the transmembrane Fo rotary sector of H<sup>+</sup>-transporting ATP synthase derived by solution NMR and intersubunit cross-linking in situ. *Biochim Biophys Acta* 1565:232–245
138. Schneider E, Altendorf K (1985) All three subunits are required for the reconstitution of an active proton channel (F<sub>o</sub>) of Escherichia coli ATP synthase (F<sub>1</sub>F<sub>o</sub>). *EMBO J* 4:515–518
139. Oster G, Wang H (2003) Rotary protein motors. *Trends Cell Biol* 13:114–121

# Chapter 11

## Biophysical Approaches to Understanding the Action of Myosin as a Molecular Machine

Mihály Kovács and András Málnási-Csizmadia

**Abstract** Many of the concepts of biological structure–function relationships were pioneered in muscle research, resulting in mechanistic knowledge spanning from molecular actions to macroscopic phenomena. Due to its abundance and spatial organization, the actomyosin system powering muscle contraction could readily be investigated by a wide variety of biophysical methods, and also provided fertile ground for the development of these techniques. For decades, muscle actomyosin was the only known biological motor system. It was later discovered that muscle contraction represents a highly specialized form of actomyosin-based contractility. All eukaryotic cells express a variety of myosin isoforms, which drive cellular processes including cell division, differentiation, movement, intracellular transport, and exo- and endocytosis. In this chapter we discuss how various biophysical methods have been used to elucidate the structural and functional properties of the actomyosin system and the physiological processes driven by its motor activity. We provide an overview of techniques applied to study molecular and supramolecular features of diverse myosin motors including their structure, kinetics, conformational transitions, force generation, assembly, cooperation, regulation, and the linkage of these properties to cellular and physiological functions.

**Keywords** Myosin • Actin • Structure • Kinetics • Mechanism • Muscle • Energy transduction • ATP • ATPase • Cytoskeleton • Method • Enzyme • Activation • Allostery • Motility • Molecular motors

---

M. Kovács (✉)

Department of Biochemistry, Eötvös Loránd University-Hungarian Academy of Sciences “Momentum” Motor Enzymology Research Group,  
Eötvös Loránd University, Budapest, Hungary  
e-mail: kovacsm@elte.hu

A. Málnási-Csizmadia

Department of Biochemistry, Eötvös Loránd University-Hungarian Academy of Sciences  
Molecular Biophysics Research Group, Eötvös Loránd University, Budapest, Hungary



## 11.1 Seminal Discoveries in Muscle Research Contributed to General Concepts of Biology

All life forms exhibit some form of motility, the capability to perform active movement and associated work. Motility is driven by proteins called molecular motors. These enzymes can convert chemical energy, stored most commonly in the anhydride bonds of ATP or a proton concentration gradient, to mechanical energy. This direct conversion mechanism is fundamentally different from that of man-made combustion engines in which the free enthalpy liberated in a chemical reaction is first converted to heat, and heat is then used to produce work.

The most obvious macroscopic manifestation of motility is muscle action. It is driven principally by two kinds of protein, actin and myosin. For a long time, muscle was the only system for studying biological motility. Studies on muscle initiated the field of mechanobiochemistry, which paved the way for protein mechanical studies also in various non-muscle systems. With advances in cell biological and molecular genetic techniques, a wide spectrum of non-muscle myosins as well as tubulin- and nucleic acid-based molecular motors were discovered and mechanistically characterized.

Classical advantages of muscle research include (1) the abundance of proteins allowing large-scale homogeneous preparations for biochemical studies, (2) the high level of spatial organization allowing diffractive and microscopic investigations, and (3) a macroscopic contractile phenomenon readily measurable by mechanical manipulation in physiological experiments [1].

Szent-Györgyi introduced the idea of structure–function relationships in biological systems, and chose muscle as the most regularly organized specimen to study. His group was the first to purify actin and myosin in isolation [2]. They made actomyosin threads from the isolated proteins, and investigated their contractile properties in correlation with the biochemical features of protein solutions and suspensions. In addition, they described the cyclic interaction between the two protein components and discovered that this interaction is coupled to the ATP hydrolytic cycle [2]. Together with the subsequent discovery of the actin-induced activation of myosin's ATPase activity by Bíró and Szent-Györgyi [3], these works lay the foundations for the concept of allosteric activation, which was later explored in detail in structural and kinetic studies (discussed in the next two sections). Decades later, the combination of structural and kinetic investigations with advanced force manipulation techniques revealed a special mode of large-scale allosteric communication in which the activities of individual catalytic sites are regulated and coordinated by external forces acting on proteins [4–7].

The principles of the allosteric regulation of specific events of the myosin ATPase cycle by myosin's interaction with actin proved to be generally applicable to a wide variety of motor-track and GTP-dependent signaling systems [8–10]. In this framework, actin can be viewed as a nucleotide exchange factor for myosin, accelerating the release of hydrolysis products. Other biological phenomena discovered in muscle research include the principles governing supramolecular assembly leading to formation of actin and myosin filaments; and the discovery of  $\text{Ca}^{2+}$  as second messenger, initiated by Weber and colleagues [1, 11–13].

## 11.2 Elucidation of Molecular and Supramolecular Structures

H.E. Huxley and Hanson, in parallel with A.F. Huxley and Niedergerke, proposed the sliding filament model of muscle contraction based on their interference, phase contrast, and electron microscopic (EM), and low-angle X-ray diffraction investigations [14–16]. Among several competing theories, this model has emerged and remained the prevalent conceptual framework for muscle action. The model explained contraction as resulting from the sliding of intercalated thick (myosin) and thin (actin) filaments past each other. Sliding was proposed to be powered by the action of crossbridge structures emanating from thick filaments. Crossbridges were proposed to swing during the force-generating step (powerstroke), thus exerting a rowing-like action to perform mechanical work.

Thin and thick filaments are assemblies mainly consisting of actin and myosin molecules, respectively. Actin monomers (G-actin) have a molecular weight of 42 kDa and, at physiological conditions, polymerize into long, helically structured filaments (F-actin). The first X-ray structures of G-actin were of those crystallized in complex with DNase I and other actin binding proteins [17–19]. These structures revealed that the actin monomer is organized into two domains with a bound nucleotide located between these two domains. The atomic structure of the actin filament was modeled by docking the G-actin structures into the cryo-EM envelope of F-actin [20]. Recently, more refined structures were published, which revealed the fine details of conformational rearrangements associated with actin polymerization [21, 22].

Myosin can be extracted from myofibrils at high ionic strength. The molecular weight of the myosin holoenzyme is around 500 kDa, as determined by analytical ultracentrifugation [1]. Electrophoretic analysis performed under denaturing conditions showed that the holoenzyme consists of two heavy chain subunits with a molecular weight around 220 kDa, and two pairs of light chains with molecular weights around 17–20 kDa. Historically, the light chains, which belong to the calmodulin family, have been termed as essential light chain (ELC) and regulatory light chain (RLC) (Fig. 11.1a).

Electron micrographs of rotary shadowed myosin molecules showed that the molecule consists of two head-like structures (forming the crossbridges in muscle) and an elongated rod [23]. Limited proteolytic experiments were fundamental in resolving the “gross anatomy” of the myosin holoenzyme. Myosin can be proteolytically digested to produce heavy and light meromyosin fragments (HMM and LMM, respectively) (Fig. 11.1a) [1, 24, 25]. HMM contains the heads and the proximal part of the rod, whereas LMM forms the distal part of the rod. The actin binding property and ATPase activity reside in HMM, whereas LMM confers the capability of filament formation. Further proteolysis of HMM liberates myosin heads (subfragment 1, S1) from the proximal rod fragment (subfragment 2, S2) (Fig. 11.1a). S1 confers catalytic activity and can bind to actin, whereas the S2 portion holds the heads together and provides a spacer from rest of the tail, which forms the filament backbone [26]. The flexibility of myosin

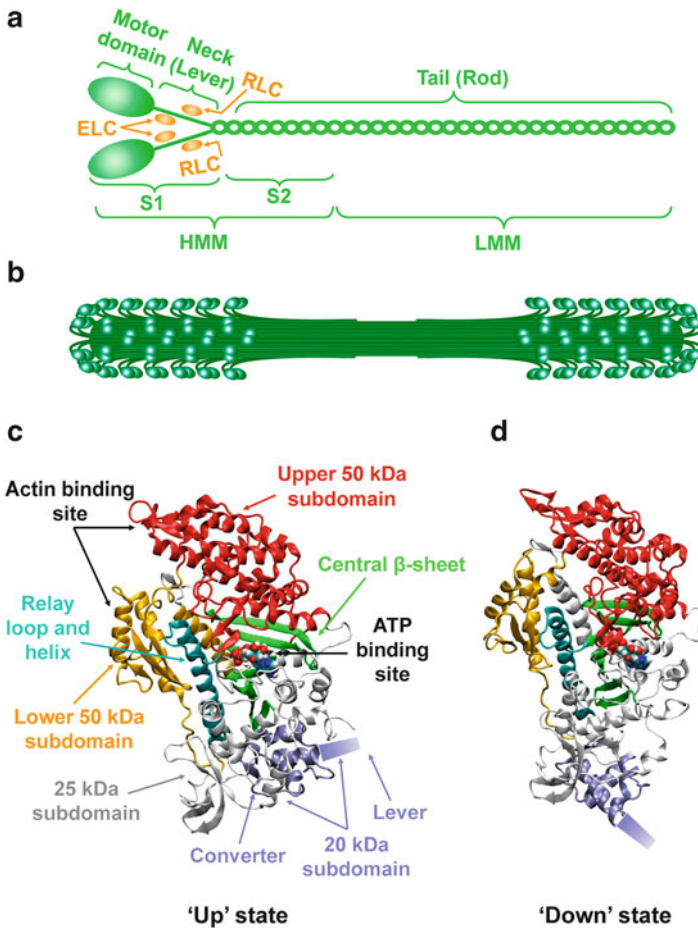


**Fig. 11.1** Overview of myosin structure. (a) Structure of the myosin 2 holoenzyme. (b) Schematic representation of a bipolar myosin 2 filament. (c, d) Ribbon diagrams of the crystal structure of *Dictyostelium discoideum* myosin 2 motor domain in the up-lever (c) and down-lever (d) conformations (based on PDB structures 1VOM and 1MMD, respectively)

at the S1–S2 and HMM–LMM junctions was detected by proteolysis, EM, and time-resolved fluorescence anisotropy decay experiments [23, 27].

X-ray diffraction, optical rotation, sequence analysis, and structural modeling studies revealed that the myosin rod is an elongated coiled-coil made up of two long  $\alpha$ -helical segments, mediating the dimerization of myosin heavy chains [1]. The structure is held together by a medial hydrophobic stripe, strengthened by charged residues at its sides. The pattern of the latter elements defines a staggered arrangement of coiled-coil dimers in the bipolar myosin filament (Fig. 11.1b) [28]. The double-headed arrangement and filament formation capability are shared by a large number of myosin isoforms classified as class 2 myosins, which are present in

various forms of muscle and in the cytoplasm of non-muscle cells [29]. The size and dynamics of myosin filaments varies considerably between sarcomeric (skeletal and cardiac muscle) and non-sarcomeric (smooth muscle and non-muscle) myosin 2 isoforms. Sarcomeric myosins form stable filaments comprising several hundred myosin holoenzymes, whereas non-sarcomeric ones are characterized by dynamic regulation of filament assembly and disassembly (Fig. 11.1b). Vertebrate non-muscle myosin 2 minifilaments consist of as few as 14 myosin molecules at each pole, as shown by EM both in vitro [30] and in vivo [31].

Unlike the myosin holoenzyme and the isolated myosin rod, the catalytic HMM and S1 fragments are soluble at physiological ionic strength, which has greatly facilitated their kinetic investigation. S1 was also further digested to produce three heavy chain fragments of 25, 50, and 20 kDa. These fragments were first considered as individual domains, but proved to be inactive [32, 33]. Two reactive sulfhydryl groups (SH1 and SH2) located in the 20 kDa segment proved to be useful in biophysical experiments as the attachment of spectroscopic probes to these groups enabled a wide range of kinetic and structural investigations [34].

According to the swinging crossbridge theory, the bulk of the crossbridge would have to rotate during force generation. In early electron paramagnetic (EPR) spectroscopic studies on muscle fibers, however, probes attached to SH1 failed to show such a reorientation [34]. This and several other unresolved questions regarding force generation were clarified upon the publication of the atomic structures of the myosin head. The first structure, solved by Rayment and coworkers, was that of chicken skeletal muscle S1 with methylated lysine side chains [35]. The structure was tadpole-like in which a large globular motor domain (MD) was sequentially followed by a long  $\alpha$ -helical segment of the heavy chain, to which the ELC and RLC were bound. The latter structural part (involving all three polypeptide chains) was termed as the neck, and its appearance immediately suggested a lever function. The previously identified proteolytic fragments turned out to be integral subdomains of S1, which were linked by flexible, protease-susceptible surface loops: loop 1 connecting the 25 and 50 kDa, and loop 2 connecting the 50 and 20 kDa fragments.

As depicted in the atomic structures of the MD shown in Fig. 11.1c, d, the ATP binding site is located at the interface of the 25 and 50 kDa subdomains. The 50 kDa subdomain is divided by a large cleft; thus the “upper” 50 kDa (U50) and “lower” 50 kDa (L50) subdomains were defined. Parts of these subdomains were postulated to form the actin binding site. The 20 kDa fragment contains a region (termed the converter) connecting the nucleotide binding site with the lever. This fragment also contains the long  $\alpha$ -helix of the heavy chain portion of the neck. SH1 turned out to be located at the pivot of the lever, which provided an explanation for the insensitivity of SH1-attached spectroscopic probes to lever orientation. Lever movement could be followed in later experiments using EPR and fluorescence spectroscopic probes attached to the light chains [36–38].

Subsequently, a series of crystal structures of a recombinantly expressed, catalytically active myosin 2 MD fragment from the amoeba *Dictyostelium discoideum*, and those of molluscan muscle S1 fragments were crystallized with a variety of nucleotide analogs mimicking different intermediates of the enzymatic

cycle (Fig. 11.1c, d) [39–44]. Some nucleotide analogs (including ADP, AMPPNP (adenylyl-imidodiphosphate), and ADP.BeF<sub>x</sub>) induced a conformation that closely resembled the previously described chicken S1 structure [40, 41, 43]. In contrast, other analogs (including ADP.AlF<sub>4</sub> and ADP.VO<sub>4</sub>) induced a conformation in which the C-terminal part of the MD, which forms the base of the lever, pointed in a direction 70° different from that seen in the other structures [40, 42, 43]. These findings were suggestive of the lever swing expected based on previous results. Some nucleotide analogs (chiefly ADP.BeF<sub>x</sub>) were able to induce both states, which implied the reversibility of the lever swing in the absence of actin (see also in next section). However, the assignment of the detected structural states to the functional states of the mechanochemical cycle remained to be addressed by kinetic and spectroscopic studies.

### 11.3 Kinetic Resolution of Structural States

The model proposed by Lymn and Taylor in 1971 lay the groundwork for the coupling of the ATP hydrolytic and mechanical cycles of actomyosin and placed the major (then postulated) structural states of actomyosin in the first kinetic framework (Fig. 11.2) [45]. The cycle was established by transient kinetic studies monitoring the interaction of F-actin, soluble myosin fragments (HMM and S1), and nucleotide. The cycle is usually described starting from the strongly actin-bound, nucleotide-free myosin (rigor) state. The rapid and high-affinity binding of ATP to the myosin head causes a drastic weakening of the acto-S1 interaction and the dissociation of the two proteins, as evidenced by a concomitant decrease in light scattering. The hydrolysis of ATP was found to occur mainly in the actin-detached state. A burst in phosphate (P<sub>i</sub>) liberation from ATP, detected in quenched-flow transient kinetic experiments, indicated that ATP hydrolysis precedes the rate-limiting step of the chemical cycle. Although not directly evidenced by experiments at the time, ATP hydrolysis was proposed to be linked to the priming of the myosin head. The myosin.ADP.P<sub>i</sub> products complex was shown to rebind to actin. The release of the hydrolysis products was thus proposed to be coupled to the strengthening of the actomyosin interaction and the force-generating powerstroke step, during which the crossbridge swings back to its rigor conformation.

A more detailed kinetic framework of the S1 ATPase cycle and the conformational changes occurring in the absence of actin was proposed some years later by Bagshaw and Trentham [46, 47]. In their detailed transient kinetic analysis they utilized the increase in the intrinsic tryptophan (Trp) fluorescence of rabbit skeletal muscle S1 occurring upon nucleotide binding and ATP hydrolysis. Their work revealed that the binding process occurs in two steps: a rapid formation of a weakly bound myosin–nucleotide collision complex is followed by a conformational transition leading to the strengthening of the complex, associated with an increase in Trp fluorescence. ATP hydrolysis was associated with a further fluorescence enhancement, indicating the formation of the primed (up-lever) crossbridge state. Quenched-flow experiments as well as isotope exchange studies (i.e., the incorporation of

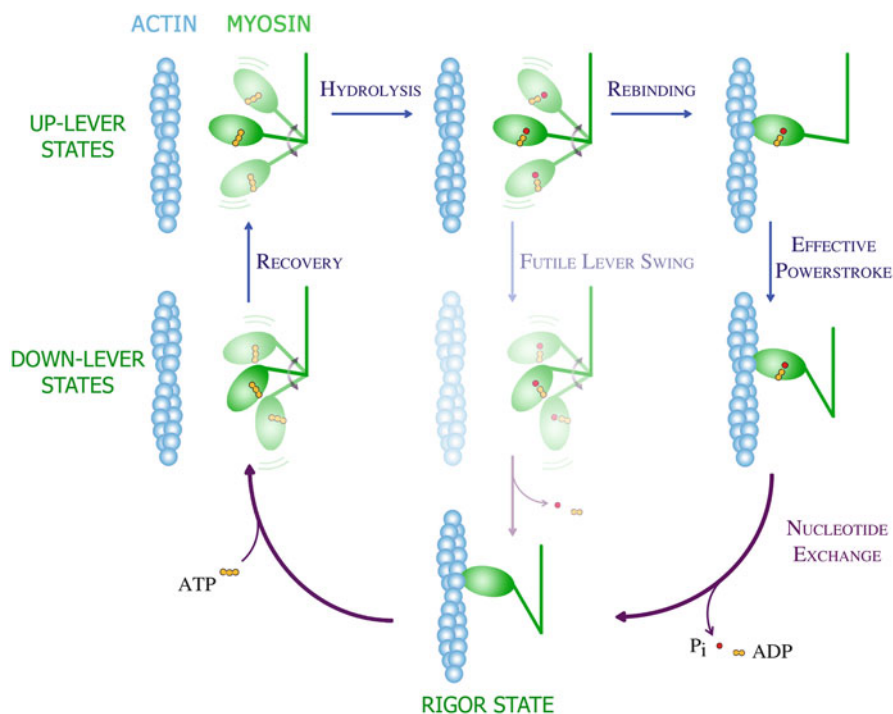


**Fig. 11.2** Mechanochemical cycle of the actomyosin motor. The mechanism shown incorporates the Lymn–Taylor model in conjunction with major conceptual advances gained from recent structural and kinetic investigations. Myosin and actin are shown in *green* and *blue*, respectively. During the working cycle, ATP binding to the myosin head dissociates the strongly bound actomyosin rigor complex (*lowest panel*). During the recovery step (*left two panels*), which occurs in ATP-bound myosin, the myosin lever moves from a “down” to an “up” (primed) position. Note the change in lever orientation relative to the motor domain. In the actin-detached states (*upper left four panels*), the myosin head (motor domain plus lever) is shown in several different orientations (connected by *double-sided arrows*) to indicate its free rotation about a flexible joint that connects it to the distal part of the molecule (and the thick filament in muscle). The hydrolysis of ATP to ADP and  $P_i$  (inorganic phosphate) occurs only in the up-lever state (*upper left panel*). The post-hydrolytic up-lever complex (*upper middle panel*) can continue the cycle in two pathways. If the lever swings back to a down position when the head is detached from actin (futile lever swing, *middle panels*), the ATP hydrolysis cycle is completed without work production. In order to undergo an effective powerstroke leading to force generation, the head must rebind to actin (*upper right panel*) before the lever swing (up-to-down movement, *right two panels*). Following the lever swing and the release of hydrolysis products ( $P_i$  and ADP), the myosin head binds a new ATP molecule. Note that this scheme does not indicate changes in actin affinity or motor domain structure, and thus it does not discriminate between alternative pathways of the powerstroke discussed in the text. Reproduced with permission from ref. [58]

multiple  $^{18}\text{O}$  atoms from water into the liberated  $P_i$ ) revealed the reversibility of the hydrolysis step [48]. The quasi-irreversible release of  $P_i$  was proposed to be the rate-limiting step in the absence of actin. ADP release was shown to be essentially the reversal of the two-step ATP binding process.



Almost three decades later, a series of kinetic and spectroscopic studies from various laboratories provided an extension of the Bagshaw–Trentham and Lymn–Taylor models by the determination of the precise correspondence between structural and kinetic states. Advances in molecular genetic techniques, recombinant protein expression, and mutagenesis allowed the precise placement of spectroscopic probes into specific locations of the myosin head [49–55]. The major source of Trp fluorescence changes upon nucleotide binding and ATP hydrolysis was assigned to conserved Trp residues located at the nucleotide binding site and the so-called relay loop, respectively. The relay loop is located at the interface of the L50 and converter subdomains (Fig. 11.1c, d). Trp fluorescence experiments showed that lever priming and ATP hydrolysis are distinct but coupled steps as hydrolysis can take place only in the primed (up-lever) myosin state [54, 56]. These findings were in line with structural results showing that the catalytic residues of the active site are in place for catalysis only in the up-lever conformation [40, 42].

Trp signals originating from the relay loop allowed the experimental verification of the earlier concept that the up-to-down lever movement occurring after hydrolysis in the myosin.ADP.P<sub>i</sub> complex is a distinct step preceding P<sub>i</sub> release [47, 57]. In addition, it was shown that, in the absence of actin, the rate-limiting step of the enzymatic cycle is the up-to-down lever movement and not the actual release of P<sub>i</sub>. The up-to-down lever movement is markedly accelerated by actin, which was pointed out as the key phenomenon to ensure that lever priming (down-to-up movement) and the force-generating powerstroke (up-to-down movement) occur in actin-detached and attached states, respectively. This feature leads to a kinetic pathway selection mechanism enabling efficient force generation, and explains why the powerstroke can start from the myosin.ADP.P<sub>i</sub> state, which has the lowest actin affinity among all intermediates of the enzymatic cycle (Fig. 11.2) [58–60].

Parallel advances in structural and kinetic–spectroscopic investigations also revealed many of the fine details of the allosteric linkage between the three most important functional parts of the myosin head: the actin and nucleotide binding sites and the lever. The ATPase active site contains three conserved loops termed the P-loop, switch-1, and switch-2. In the absence of actin, switch-2 and the lever show coupled movement. An open (non-catalytic) switch-2 conformation is associated with a down lever. Closure of switch-2, and thus the acquisition of catalytic competence, was found to coincide with lever priming (down-to-up movement). Kinetic studies revealed that lever priming is a rapid and reversible step, which is a prerequisite for the oncoming, relatively slower chemical step of ATP hydrolysis [54, 56].

The concept of weak and strong actin binding states of myosin emerged from kinetic and spectroscopic studies. Besides light scattering, the most useful signal used in these studies was site-specific labeling of actin by cysteine-reactive pyrene dyes at residue C<sup>374</sup> close to the actin C-terminus [61]. Quenching of pyrene fluorescence occurs upon the formation of the strongly bound actomyosin complex [62, 63].

The actin binding region of the myosin head involves several structural elements contributed from both sides of the large cleft separating the U50 and L50 subdomains [64]. The incomplete fitting of the available atomic structures of the myosin head and actin into cryo-EM envelopes of the actomyosin rigor complex implied

that the cleft must undergo closure in order to adopt a strongly actin-bound state [65]. Structural studies also revealed that a class 5 myosin is able to adopt a closed-cleft structure even in the absence of actin, which can be well fitted into cryo-EM maps of the rigor complex [66, 67]. Correspondingly, it was found that this myosin isoform binds actin in a rapid, quasi-diffusion-controlled manner [68]. The kinetics of the pyrene fluorescence quench occurring upon actin binding by myosin 5 did not show a saturating tendency with increasing actin concentration. Later it was found that muscle myosin 2 isoforms from various molluscan species are also able to adopt a rigor-like conformation in the absence of actin, and bind to actin rapidly in a manner similar to that observed in myosin 5 [69].

Coupling between the conformational changes in myosin's actin and nucleotide binding regions leads to an antagonistic relationship (negative thermodynamic coupling) between actin and nucleotide binding affinities. This coupling was characterized in detail and kinetically resolved by using a variety of intrinsic and extrinsic fluorescent and EPR probes [51, 70–72]. In addition, it was discovered that the conformation of the switch-1 loop of the active site is linked to changes in actin affinity, probably via cleft movement [73, 74]. An open switch-1 state is associated with low nucleotide affinity and a closed-cleft conferring high actin affinity. Switch-1 closure upon nucleotide binding leads to cleft opening and weakening of myosin's actin affinity. The results also revealed the role of the  $\gamma$ -phosphate of ATP in switch closure, as the binding of ADP to actomyosin induces limited switch-1 closure.

As discussed above, the processes of nucleotide-induced actomyosin dissociation and the subsequent conformational changes of actin-detached myosin constitute fairly well-described segments of the mechanochemical cycle. However, the functionally most intriguing part of the mechanism, i.e., force generation via the powerstroke, has remained elusive, mainly due to the low abundance and kinetically inaccessible nature of its key intermediates. A comprehensive model describing myosin's structural transitions leading to the powerstroke was set forth by Geeves and Holmes [64]. As a cardinal feature, the model proposes that the actin-attached powerstroke (up-to-down lever movement) occurs via a structural pathway that is markedly different from that of the well-characterized actin-detached lever priming process (down-to-up movement). In the actin-attached pathway, the lever swing starts from a closed-cleft, high actin-affinity “top-of-powerstroke” state that has a closed active site (switches 1 and 2) and the lever arm in the “up” orientation. The lever swing then occurs without switch-2 opening (in contrast to the situation in the absence of actin), but switch-1 opens to release the hydrolysis products. This proposition challenges the long-standing “back door” hypothesis, which stated that, following ATP hydrolysis,  $P_i$  releases via a route different from that of ATP entry [75]. The model of Geeves and Holmes also embraced the idea that the strengthening of the actomyosin interaction is associated with the movement of the P-loop and the twisting of the central  $\beta$ -sheet of the MD. This  $\beta$ -sheet, termed as the “transducer” together with associated elements, has been proposed to act as an energy-storing torsional spring within the MD (Fig. 11.1c, d) [68, 76].

Force production is generally conceived to occur in strongly bound actomyosin complexes. In line with this, the above model implies that the strengthening of the



actomyosin interaction precedes the actual swing of the lever. However, the limited available evidence does not exclude that the force generation process could occur via parallel pathways—even in ones in which the lever swing occurs in weakly actin-attached myosin. The subsequent strengthening of the actomyosin interaction could thermodynamically stabilize the post-powerstroke state [58]. The force dependence of the transition between weakly and strongly actin-bound myosin complexes can thus markedly influence the fluxes conveyed by the alternative pathways. This constitutes one of the key unresolved questions regarding force generation (see also in the next section).

The physical time scale of the kinetic transitions occurring during the working cycle (milliseconds to seconds) is several orders of magnitude slower than those accessible by computational simulation methods that could describe structural pathways, energy landscapes, and transition states. However, significant advances in these approaches including conjugate peak refinement (CPR), normal mode analysis (NMA), umbrella methods, and molecular dynamic simulations have enabled the description of structural trajectories of nucleotide-induced cleft opening, lever priming, and ATP hydrolysis [77–80].

## 11.4 Force Generation and Motility

Mechanoenzymes confer the specific feature that the enzymatic reaction is linked to mechanical action, which can be followed and analyzed by force manipulation and particle tracking techniques. Muscle produces a macroscopic mechanical response, which was investigated for many decades on intact muscles and muscle fibers. These techniques generally measure the mechanical response of the specimen to the addition of chemical agents (by applying changes in solution conditions) or on mechanical stimulus (by applying rapid stretch or release). Demembranated (skinned) fibers with an exposed contractile apparatus, produced first by Szent-Györgyi, allow the application of rapid changes in chemical conditions. Mechanical manipulation (length-jump) experiments have provided important insights into the kinetics and energetics of muscle contraction [81]. A crucial aim of these studies is to establish the linkage between macroscopic parameters of force production and the underlying molecular mechanisms. For instance, the linkage of the force-generating step to enzymatic product release steps has been a matter of great controversy. Based on the dependence of the mechanical response of muscle fibers on solute (mainly  $P_i$ ) concentrations, the majority of groups argue that force generation occurs before  $P_i$  release [82–85]. However, other workers propose that the force-generating step is a conformational transition between two ADP-bound states, and thus it occurs after  $P_i$  has released from the myosin head [86, 87].

It was discovered as early as 1923 by Fenn that the heat output of muscle increases when it is allowed to shorten against a load, as compared to the situation when it only holds tension (isometric contraction) [88]. Accordingly, force–velocity relationships of contracting muscles and fibers define an

optimum for power output, generally around 1/3 of the maximal (unloaded) shortening velocity [1]. Based on current knowledge of the molecular mechanisms, the Fenn effect is thought to arise from the load dependence of the kinetics of multiple key steps of the actomyosin ATPase cycle. As a result, lower loads will be associated with more rapid ATPase activity and shorter periods of actin attachment, whereas an increase in resistive load will prolong the actin attachment lifetime and slow down the enzymatic cycle of myosin heads [5, 7, 89–91]. Fiber techniques have provided estimates of 1–10 pN for the unitary isometric force produced by a single myosin head and values around 7 nm for the unitary displacement occurring during a single powerstroke [92, 93]. These values were refined by single molecule techniques more directly measuring unitary displacement and force generation (see below).

The swinging lever hypothesis implies that force generation requires the movement of a lever whose length will directly determine the unitary displacement. In vitro motility assays were the first to allow quantitative measurement of motile properties of experimental systems assembled from isolated protein components [94–97]. The most common form of these assays images and measures the velocity of the gliding of fluorescently labeled actin filaments over a myosin-coated surface, monitored by fluorescence microscopy. In vitro motility assays also allowed the mechanical properties on non-muscle myosins to be studied, for which macroscopic forces would be difficult to assess in vivo.

The combination of in vitro motility assays with the genetic manipulation of lever length provided the first solid support for the lever arm hypothesis [98, 99]. Myosin constructs of varying lever length could be produced either by modification of the number of light chain binding regions in the neck region or by appending artificial levers to the MD. The in vitro actin gliding velocity was found to increase in proportion with lever length. Further support for the lever theory came from experiments in which the orientation of the lever was redesigned by genetic manipulation. Myosin constructs with a reverse-oriented lever exhibited a reversal in the direction of the movement of actin filaments in the in vitro motility assay [100].

A further great technical breakthrough in the investigation of molecular motility was the application of the optical trap, which allowed direct measurement of forces produced by single molecules [101–104]. In this technique, a focused laser beam is used to hold a micrometer-size bead in position, which allows the measurement of molecular forces pulling the bead out of position. A widely used arrangement for the measurement of actin–myosin interactions is a three-bead dumbbell assay in which an actin filament is spanned between two beads, and a single myosin molecule is attached to a third bead serving as a pedestal. This arrangement also allows the application of rapid external force feedback to determine the effect of external load on the mechanical response of single myosin molecules. Besides the measurement of the main force-producing powerstroke step [105], these assays were also useful in determining the load-dependent kinetics of ADP release of various myosin isoforms [7, 89–91, 106]. This feature turned out to be an important mechanism regulating the actin attachment lifetime of myosin heads, which determines their sliding velocity and tension bearing properties.

Advances in the visualization of single molecules by fluorescence microscopic techniques have also been valuable in revealing motile mechanisms. To observe single molecules, one of the most widely applied techniques is total internal reflection fluorescence (TIRF) microscopy. This technique allows selective excitation of fluorophores in the vicinity of the microscope slide via an evanescent field, thereby eliminating background fluorescence originating from the bulk of the sample. Single enzymatic cycles were observed by following the interaction of fluorescently labeled nucleotides with surface-attached single myosin molecules [107, 108].

For the investigation of non-muscle myosin motility, the most widely applied TIRF arrangement involves the attachment of actin filaments to the slide surface via biotin–avidin bridges [109]. This arrangement allows monitoring of the movement of fluorescently labeled single myosin molecules on the actin tracks if they are processive, i.e., able to perform a series of steps along the actin filament before detachment. Movement observed in this assay is generally considered as direct evidence of the processive nature of a given type of motor protein.

A further sophistication of the TIRF assay is FIONA (fluorescence imaging with 1 nm accuracy), which allows precise determination of the position of a single fluorophore by applying two-dimensional Gaussian fits to the spatial distribution of fluorescence emission intensity [110]. Sizes and durations of individual steps during processive runs of various myosin isoforms have been resolved by FIONA [111–114].

Synthesis of the knowledge gained in biochemical and molecular mechanical investigations may provide clues regarding an important theoretical aspect of motor protein action, i.e., whether force generation is based on lever strain or a Brownian ratchet-like mechanism [115]. In the lever strain model, one ATPase cycle leads to strictly one lever swing event and coupled translocation. In contrast, a Brownian ratchet-like motor can freely fluctuate between pre- and post-powerstroke states. This fluctuation is rectified by the nucleotide hydrolytic cycle, which imposes a bias as different lever conformations may be preferred for track binding and dissociation. Ratchet mechanisms can thus act at lower coupling between the chemical cycles and translocation. The current thinking on actomyosin action embraces both lever- and the ratchet-type concepts. This conceptual framework has been applied also to other systems including DNA-based motor proteins.

## **11.5 Correspondence Between Molecular Properties and Physiological Functions**

The first so-called unconventional myosin (myosin 1) was discovered in 1973 [116]. This myosin does not contain sequences for dimerization and thus adopts a single-headed, nonfilamentous structure. The large amount of sequence information gained in the subsequent decades revealed the existence of a multitude of myosin isoforms whose subunit composition and domain structure showed wide variations in line with their supramolecular assemblies, regulatory mechanisms, and physiological functions [29, 117]. The activity of myosins is required for a

variety of life processes including muscle contraction, cell migration, division, sensory functions, membrane trafficking, and formation of cellular protrusions such as brush borders and filopodia [117]. The myosin superfamily is currently classified into 35 classes [118]. The MD has proved to be the most conserved part of myosin in terms of its sequence and structure, and therefore this domain was used as a basis for classification. Besides the MD, most myosins contain neck and tail domains. The neck is usually centered along an elongated  $\alpha$ -helix of the heavy chain containing varying numbers of conserved sequence elements called IQ motifs, each of which can bind calmodulin or a calmodulin-family light chain. It was also proposed that myosin necks may be extended by stable charged single  $\alpha$ -helices with no associated light chains [119–121]. The tails of myosins from different classes contain various effector and partner binding domains and, in some classes, induce heavy chain dimerization.

The size and stability of filamentous assemblies varies widely between different myosin 2 isoforms [1, 29]. Sarcomeric (skeletal and cardiac) muscle myosin 2 iso-enzymes form large and stable thick filaments. Regulation of the action of these myosins by  $\text{Ca}^{2+}$  is generally mediated by actin-associated protein complexes (mainly troponin and tropomyosin) by occluding or exposing the myosin binding sites on the actin filament [13, 122]. In smooth muscle and non-muscle myosin 2, filament assembly and myosin activity are dynamically regulated via myosin phosphorylation [123]. In the off-state with unphosphorylated RLC, the two heads of these myosins adopt an asymmetrical arrangement in which the actin binding site of one head interacts with the nucleotide binding site of the other [124]. Other myosin 2 isoforms, including those from molluscan muscle, are regulated by direct binding of  $\text{Ca}^{2+}$  ions to the ELC [125].  $\text{Ca}^{2+}$  binding also regulates the activity of many unconventional myosins [117].

Heavy chain dimerization is a prerequisite for the processive walking of cytoskeletal transporters acting as single holoenzymes. Dimerization of myosin 5 was obvious, but that of other transporters such as myosins 6 and 10 has been a contentious issue [119, 126, 127]. In myosin 6, the importance of a cargo-induced dimerization mechanism has been pointed out [126]. Myosin 6 displays other peculiar adaptations including reverse directionality (i.e., movement towards the minus end of actin tracks) dictated by a class-specific insert at the base of its lever, which also has a reversibly extendable domain [128, 129]. Membrane attachment can also regulate the targeting and supramolecular organization of various unconventional myosins [117]. Another intriguing adaptation is that other motor proteins or actin bundles can induce processive motility of some myosin isoforms that were previously shown to be non-processive on bare actin filaments [130, 131].

Assemblies of multiple motor units into dimers or filaments raise the possibility of large-scale allosteric communication between motor units via exerting forces on each other. It has long been known from muscle physiological studies that rapid pulling or release of activated muscle fibers can produce partial synchronization of myosin heads, implying a load-dependent mechanism. Biochemical and single molecule experiments have revealed the importance of such mechanisms in most filamentous myosins [117]. In the case of double-headed transporters, this form of

communication may keep the mechanochemical cycles of the two heads out of phase. This mechanism enables efficient processive movement by preventing simultaneous actin detachment of both heads [89]. In myosin 5 performing single molecule motility, the length of the neck also determines the optimal arrangement of myosin heads to reach the next subunit on the actin track [109]. Recent advances in time-resolved atomic force microscopy (AFM) have enabled the direct observation of the processive walking of myosin 5 molecules along actin filaments [132].

The general mechanokinetic framework set forth by Lynn and Taylor has proven to be applicable to most myosins, but there is a large variation between isoforms in the magnitude and ratio of the individual rate and equilibrium constants of transitions [133]. Simplistically, the mechanochemical cycle time can be divided into the lifetimes of actin-attached ( $t_{\text{on}}$ ) and actin-detached ( $t_{\text{off}}$ ) states, governed by the steps of the ATPase cycle, which are linked to changes in actin interaction. The important concept of duty ratio (or duty cycle,  $r$ ) can be defined by the fraction of cycle time spent in actin-bound states:  $r$  will thus equal  $t_{\text{on}}/(t_{\text{on}} + t_{\text{off}})$ . In the ergodic approximation, this will also equal the fraction of motor units (heads) bound to actin in a population at a given time point during steady-state cycling.

It is characteristic of most myosins that ATP binding causes rapid dissociation from actin, and hydrolysis occurs in the actin-detached state. Following this,  $P_i$  release and ADP release are accelerated to various extents by actin. As the myosin.ADP. $P_i$  and myosin.ADP states bind to actin weakly and strongly, respectively, the rate of  $P_i$  and ADP release will define various duty ratios ranging from 1 to 2 % in rapidly contracting fast skeletal muscle to more than 70 % in myosin 5. The physiological importance of the adaptable duty ratio is that (1) it must be sufficiently high to maintain continuous actin attachment of a supramolecular motor ensemble in order to produce prolonged translocation and (2) it must be sufficiently low that the individual motor units do not pose a drag force opposing the contraction driven by other motors.

A key kinetic and thermodynamic determinant of the duty ratio is ADP–actin coupling, i.e., the allosteric effect of binding of actin and ADP to the same myosin head. If the coupling is highly negative, as in rapidly contracting muscle myosins, ADP release from (and subsequent ATP binding to) actin-bound myosin heads will occur rapidly and the heads will only spend a short time attached to actin. In contrast, in load-bearing myosins, the actin–ADP coupling is low because ADP release is not or only weakly accelerated by actin, which results in longer lifetimes of actin attachment. For instance, this occurs in the case of smooth muscle and non-muscle myosin 2 isoforms [5, 91, 134]. The structural basis of load-dependent ADP release is that an additional lever swing occurs upon this step, first discovered by Milligan, Sweeney, and colleagues in smooth muscle myosin [135]. This structural feature varies greatly between isoforms, and is in correspondence with their mechanochemical properties [136].

In summary, the mechanokinetic properties of myosin motors are shaped by physiological demands. In general these features appear evolutionarily far less conserved than protein structure and sequence. These principles have proven generally applicable to various other motor-track systems and enzyme–nucleotide–effector ternary complexes [8–10].

**Acknowledgements** Work in MK's lab is supported by the Human Frontier Science Program (RGY0072/2010) and the "Momentum" Program of the Hungarian Academy of Sciences (LP2011-006/2011). MK is a Bolyai Fellow of the Hungarian Academy of Sciences. Work in AMC's lab is supported by the European Research Council (European Community's Seventh Framework Programme (FP7/2007-2013)/European Research Council grant agreement no. 208319), the Hungarian Academy of Sciences (HAS-ELTE research group ID: 01055), the European Union in collaboration with the European Social Fund (grant agreement no. TAMOP-4.2.1/B-09/1/KMR), the National Office for Research and Technology, and the European Union (European Regional Development Fund), under the sponsorship of the National Technology Programme (NTP TECH\_08\_A1/2-2008-0106). We thank Kata Sarlós, Zoltán Simon, and Zhenhui Yang for figure preparation.

## References

1. Bagshaw CR (1993) Muscle contraction, 2nd edn. Chapman & Hall, London
2. Banga I, Erdos T, Gerendas M, Mommaerts WFHM, Straub FB, Szent-Gyorgyi A (1942) Studies from the Institute of Medical Chemistry, University Szeged. S. Karger, Basel
3. Biro NA, Szent-Gyorgyi AG (1949) The effect of actin and physico-chemical changes on the myosin ATP-ase system, and on washed muscle. *Hung Acta Physiol* 2:120–133
4. Nyitrai M, Geeves MA (2004) Adenosine diphosphate and strain sensitivity in myosin motors. *Philos Trans R Soc Lond B Biol Sci* 359:1867–1877
5. Kovacs M, Thirumurugan K, Knight PJ, Sellers JR (2007) Load-dependent mechanism of nonmuscle myosin 2. *Proc Natl Acad Sci U S A* 104:9994–9999
6. Sellers JR, Veigel C (2006) Walking with myosin V. *Curr Opin Cell Biol* 18:68–73
7. Laakso JM, Lewis JH, Shuman H, Ostap EM (2008) Myosin I can act as a molecular force sensor. *Science* 321:133–136
8. Goody RS, Hofmann-Goody W (2002) Exchange factors, effectors, GAPs and motor proteins: common thermodynamic and kinetic principles for different functions. *Eur Biophys J* 31:268–274
9. Vale RD (1996) Switches, latches, and amplifiers: common themes of G proteins and molecular motors. *J Cell Biol* 135:291–302
10. Kull FJ, Vale RD, Fletterick RJ (1998) The case for a common ancestor: kinesin and myosin motor proteins and G proteins. *J Muscle Res Cell Motil* 19:877–886
11. Weber A (1959) On the role of calcium in the activity of adenosine 5'-triphosphate hydrolysis by actomyosin. *J Biol Chem* 234:2764–2769
12. Weber A, Herz R, Reiss I (1964) The regulation of myosin fibrillar activity by calcium. *Proc R Soc Lond B Biol Sci* 160:489–501
13. Ebashi S (1980) The Croonian lecture, 1979: regulation of muscle contraction. *Proc R Soc Lond B Biol Sci* 207:259–286
14. Huxley H, Hanson J (1954) Changes in the cross-striations of muscle during contraction and stretch and their structural interpretation. *Nature* 173:973–976
15. Huxley AF, Niedergerke R (1954) Structural changes in muscle during contraction; interference microscopy of living muscle fibres. *Nature* 173:971–973
16. Huxley HE (1953) X-ray analysis and the problem of muscle. *Proc R Soc Lond B Biol Sci* 141:59–62
17. Kabsch W, Mannherz HG, Suck D, Pai EF, Holmes KC (1990) Atomic structure of the actin:DNase I complex. *Nature* 347:37–44
18. McLaughlin PJ, Gooch JT, Mannherz HG, Weeds AG (1993) Structure of gelsolin segment 1-actin complex and the mechanism of filament severing. *Nature* 364:685–692
19. Schutt CE, Myslik JC, Rozycki MD, Goonesekere NC, Lindberg U (1993) The structure of crystalline profilin-beta-actin. *Nature* 365:810–816



20. Holmes KC, Popp D, Gebhard W, Kabsch W (1990) Atomic model of the actin filament. *Nature* 347:44–49
21. Murakami K, Yasunaga T, Noguchi TQ, Gomibuchi Y, Ngo KX, Uyeda TQ, Wakabayashi T (2010) Structural basis for actin assembly, activation of ATP hydrolysis, and delayed phosphate release. *Cell* 143:275–287
22. Oda T, Iwasa M, Aihara T, Maeda Y, Narita A (2009) The nature of the globular- to fibrous-actin transition. *Nature* 457:441–445
23. Elliott A, Offer G (1978) Shape and flexibility of the myosin molecule. *J Mol Biol* 123:505–519
24. Margossian SS, Lowey S (1973) Substructure of the myosin molecule. 3. Preparation of single-headed derivatives of myosin. *J Mol Biol* 74:301–311
25. Margossian SS, Lowey S (1973) Substructure of the myosin molecule. IV. Interactions of myosin and its subfragments with adenosine triphosphate and F-actin. *J Mol Biol* 74:313–330
26. Malnasi-Csizmadia A, Shimony E, Hegyi G, Szent-Gyorgyi AG, Nyitrai L (1998) Dimerization of the head-rod junction of scallop myosin. *Biochem Biophys Res Commun* 252:595–601
27. Mendelson RA, Morales MF, Botts J (1973) Segmental flexibility of the S-1 moiety of myosin. *Biochemistry* 12:2250–2255
28. Decker B, Kellermayer MS (2008) Periodically arranged interactions within the myosin filament backbone revealed by mechanical unzipping. *J Mol Biol* 377:307–310
29. Sellers JR (1999) *Myosins*. Oxford University Press, New York
30. Niederman R, Pollard TD (1975) Human platelet myosin. II. In vitro assembly and structure of myosin filaments. *J Cell Biol* 67:72–92
31. Verkhovsky AB, Svitkina TM, Borisy GG (1995) Myosin II filament assemblies in the active lamella of fibroblasts: their morphogenesis and role in the formation of actin filament bundles. *J Cell Biol* 131:989–1002
32. Mornet D, Pantel P, Audemard E, Kassab R (1979) The limited tryptic cleavage of chymotryptic S-1: an approach to the characterization of the actin site in myosin heads. *Biochem Biophys Res Commun* 89:925–932
33. Mocz G, Szilagyi L, Chen LR, Fabian F, Balint M, Gergely J (1984) Effect of nucleotides, divalent cations and temperature on the tryptic susceptibility of myosin subfragment 1. *Eur J Biochem* 145:221–229
34. Thomas DD (1987) Spectroscopic probes of muscle cross-bridge rotation. *Annu Rev Physiol* 49:691–709
35. Rayment I, Rypniewski WR, Schmidt-Base K, Smith R, Tomchick DR, Benning MM, Winkelmann DA, Wesenberg G, Holden HM (1993) Three-dimensional structure of myosin subfragment-1: a molecular motor. *Science* 261:50–58
36. Adhikari B, Hideg K, Fajer PG (1997) Independent mobility of catalytic and regulatory domains of myosin heads. *Proc Natl Acad Sci U S A* 94:9643–9647
37. Irving M, St Claire AT, Sabido-David C, Craik JS, Brandmeier B, Kendrick-Jones J, Corrie JE, Trentham DR, Goldman YE (1995) Tilting of the light-chain region of myosin during step length changes and active force generation in skeletal muscle. *Nature* 375:688–691
38. LaConte LE, Baker JE, Thomas DD (2003) Transient kinetics and mechanics of myosin's force-generating rotation in muscle: resolution of millisecond rotational transitions in the spin-labeled myosin light-chain domain. *Biochemistry* 42:9797–9803
39. Bauer CB, Holden HM, Thoden JB, Smith R, Rayment I (2000) X-ray structures of the apo and MgATP-bound states of Dictyostelium discoideum myosin motor domain. *J Biol Chem* 275:38494–38499
40. Fisher AJ, Smith CA, Thoden JB, Smith R, Sutoh K, Holden HM, Rayment I (1995) X-ray structures of the myosin motor domain of Dictyostelium discoideum complexed with MgADP.BeFx and MgADP.AlF<sub>4</sub><sup>-</sup>. *Biochemistry* 34:8960–8972

41. Gulick AM, Bauer CB, Thoden JB, Rayment I (1997) X-ray structures of the MgADP, MgATP $\gamma$ S, and MgAMPPNP complexes of the Dictyostelium discoideum myosin motor domain. *Biochemistry* 36:11619–11628
42. Smith CA, Rayment I (1996) X-ray structure of the magnesium(II).ADP.vanadate complex of the dictyostelium discoideum myosin motor domain to 1.9 Å resolution. *Biochemistry* 35:5404–5417
43. Houdusse A, Szent-Gyorgyi AG, Cohen C (2000) Three conformational states of scallop myosin S1. *Proc Natl Acad Sci U S A* 97:11238–11243
44. Houdusse A, Kalabokis VN, Himmel D, Szent-Gyorgyi AG, Cohen C (1999) Atomic structure of scallop myosin subfragment S1 complexed with MgADP: a novel conformation of the myosin head. *Cell* 97:459–470
45. Lynn RW, Taylor EW (1971) Mechanism of adenosine triphosphate hydrolysis by actomyosin. *Biochemistry* 10:4617–4624
46. Bagshaw CR, Eccleston JF, Eckstein F, Goody RS, Gutfreund H, Trentham DR (1974) The magnesium ion-dependent adenosine triphosphatase of myosin. Two-step processes of adenosine triphosphate association and adenosine diphosphate dissociation. *Biochem J* 141:351–364
47. Bagshaw CR, Trentham DR (1974) The characterization of myosin-product complexes and of product-release steps during the magnesium ion-dependent adenosine triphosphatase reaction. *Biochem J* 141:331–349
48. Bagshaw CR, Trentham DR, Wolcott RG, Boyer PD (1975) Oxygen exchange in the gamma-phosphoryl group of protein-bound ATP during Mg<sup>2+</sup>-dependent adenosine triphosphatase activity of myosin. *Proc Natl Acad Sci U S A* 72:2592–2596
49. Korman VL, Anderson SE, Prochniewicz E, Titus MA, Thomas DD (2006) Structural dynamics of the actin-myosin interface by site-directed spectroscopy. *J Mol Biol* 356:1107–1117
50. Thomas DD, Kast D, Korman VL (2009) Site-directed spectroscopic probes of actomyosin structural dynamics. *Annu Rev Biophys* 38:347–369
51. Yengo CM, Chrin L, Rovner AS, Berger CL (1999) Intrinsic tryptophan fluorescence identifies specific conformational changes at the actomyosin interface upon actin binding and ADP release. *Biochemistry* 38:14515–14523
52. Yengo CM, Chrin LR, Rovner AS, Berger CL (2000) Tryptophan 512 is sensitive to conformational changes in the rigid relay loop of smooth muscle myosin during the MgATPase cycle. *J Biol Chem* 275:25481–25487
53. Malnasi-Csizmadia A, Woolley RJ, Bagshaw CR (2000) Resolution of conformational states of Dictyostelium myosin II motor domain using tryptophan (W501) mutants: implications for the open-closed transition identified by crystallography. *Biochemistry* 39:16135–16146
54. Malnasi-Csizmadia A, Pearson DS, Kovacs M, Woolley RJ, Geeves MA, Bagshaw CR (2001) Kinetic resolution of a conformational transition and the ATP hydrolysis step using relaxation methods with a Dictyostelium myosin II mutant containing a single tryptophan residue. *Biochemistry* 40:12727–12737
55. Malnasi-Csizmadia A, Kovacs M, Woolley RJ, Botchway SW, Bagshaw CR (2001) The dynamics of the relay loop tryptophan residue in the Dictyostelium myosin motor domain and the origin of spectroscopic signals. *J Biol Chem* 276:19483–19490
56. Urbanke C, Wray J (2001) A fluorescence temperature-jump study of conformational transitions in myosin subfragment 1. *Biochem J* 358:165–173
57. Gyimesi M, Kintsés B, Bodor A, Perczel A, Fischer S, Bagshaw CR, Malnasi-Csizmadia A (2008) The mechanism of the reverse recovery step, phosphate release, and actin activation of Dictyostelium myosin II. *J Biol Chem* 283:8153–8163
58. Malnasi-Csizmadia A, Kovacs M (2010) Emerging complex pathways of the actomyosin powerstroke. *Trends Biochem Sci* 35:684–690



59. White HD, Belknap B, Webb MR (1997) Kinetics of nucleoside triphosphate cleavage and phosphate release steps by associated rabbit skeletal actomyosin, measured using a novel fluorescent probe for phosphate. *Biochemistry* 36:11828–11836
60. Varkuti BH, Yang Z, Kintsés B, Erdelyi P, Bardos-Nagy I, Kovacs AL, Hari P, Kellermayer M, Vellai T, Malnasi-Csizmadia A (2012) A novel actin binding site of myosin required for effective muscle contraction. *Nat Struct Mol Biol* 19:299–306
61. Cooper JA, Walker SB, Pollard TD (1983) Pyrene actin: documentation of the validity of a sensitive assay for actin polymerization. *J Muscle Res Cell Motil* 4:253–262
62. Geeves MA, Jeffries TE (1988) The effect of nucleotide upon a specific isomerization of actomyosin subfragment 1. *Biochem J* 256:41–46
63. Taylor EW (1991) Kinetic studies on the association and dissociation of myosin subfragment 1 and actin. *J Biol Chem* 266:294–302
64. Geeves MA, Holmes KC (2005) The molecular mechanism of muscle contraction. *Adv Protein Chem* 71:161–193
65. Holmes KC, Angert I, Kull FJ, Jahn W, Schroder RR (2003) Electron cryo-microscopy shows how strong binding of myosin to actin releases nucleotide. *Nature* 425:423–427
66. Coureux PD, Wells AL, Menetrey J, Yengo CM, Morris CA, Sweeney HL, Houdusse A (2003) A structural state of the myosin V motor without bound nucleotide. *Nature* 425:419–423
67. Holmes KC, Schroder RR, Sweeney HL, Houdusse A (2004) The structure of the rigor complex and its implications for the power stroke. *Philos Trans R Soc Lond B Biol Sci* 359:1819–1828
68. Sweeney HL, Houdusse A (2004) The motor mechanism of myosin V: insights for muscle contraction. *Philos Trans R Soc Lond B Biol Sci* 359:1829–1841
69. Yang Y, Gourinath S, Kovacs M, Nyitray L, Reutzel R, Himmel DM, O’Neill-Hennessey E, Reshetnikova L, Szent-Gyorgyi AG, Brown JH, Cohen C (2007) Rigor-like structures from muscle myosins reveal key mechanical elements in the transduction pathways of this allosteric motor. *Structure* 15:553–564
70. Yengo CM, De La Cruz EM, Chrin LR, Gaffney DP, Berger CL (2002) Actin-induced closure of the actin-binding cleft of smooth muscle myosin. *J Biol Chem* 277:24114–24119
71. Conibear PB, Bagshaw CR, Fajer PG, Kovacs M, Malnasi-Csizmadia A (2003) Myosin cleft movement and its coupling to actomyosin dissociation. *Nat Struct Biol* 10:831–835
72. Klein JC, Burr AR, Svensson B, Kennedy DJ, Allingham J, Titus MA, Rayment I, Thomas DD (2008) Actin-binding cleft closure in myosin II probed by site-directed spin labeling and pulsed EPR. *Proc Natl Acad Sci U S A* 105:12867–12872
73. Kintsés B, Gyimesi M, Pearson DS, Geeves MA, Zeng W, Bagshaw CR, Malnasi-Csizmadia A (2007) Reversible movement of switch 1 loop of myosin determines actin interaction. *EMBO J* 26:265–274
74. Holmes KC, Schroder RR (2003) Switch 1 opens on strong binding to actin. Molecular and cellular aspects of muscle contraction. *Adv Exp Med Biol* 538:159–166
75. Yount RG, Lawson D, Rayment I (1995) Is myosin a “back door” enzyme? *Biophys J* 68:44S–47S
76. Coureux PD, Sweeney HL, Houdusse A (2004) Three myosin V structures delineate essential features of chemo-mechanical transduction. *EMBO J* 23:4527–4537
77. Fischer S, Windshugel B, Horak D, Holmes KC, Smith JC (2005) Structural mechanism of the recovery stroke in the myosin molecular motor. *Proc Natl Acad Sci U S A* 102:6873–6878
78. Kuhner S, Fischer S (2011) Structural mechanism of the ATP-induced dissociation of rigor myosin from actin. *Proc Natl Acad Sci U S A* 108:7793–7798
79. Cecchini M, Houdusse A, Karplus M (2008) Allosteric communication in myosin V: from small conformational changes to large directed movements. *PLoS Comput Biol* 4:e1000129
80. Yu H, Ma L, Yang Y, Cui Q (2007) Mechanochemical coupling in the myosin motor domain. I. Insights from equilibrium active-site simulations. *PLoS Comput Biol* 3:e21

81. Huxley AF, Simmons RM (1971) Proposed mechanism of force generation in striated muscle. *Nature* 233:533–538
82. Dantzig JA, Goldman YE, Millar NC, Lacktis J, Homsher E (1992) Reversal of the cross-bridge force-generating transition by photogeneration of phosphate in rabbit psoas muscle fibres. *J Physiol* 451:247–278
83. Kawai M, Halvorson HR (1991) Two step mechanism of phosphate release and the mechanism of force generation in chemically skinned fibers of rabbit psoas muscle. *Biophys J* 59:329–342
84. Sleep J, Irving M, Burton K (2005) The ATP hydrolysis and phosphate release steps control the time course of force development in rabbit skeletal muscle. *J Physiol* 563:671–687
85. Caremani M, Dantzig J, Goldman YE, Lombardi V, Linari M (2008) Effect of inorganic phosphate on the force and number of myosin cross-bridges during the isometric contraction of permeabilized muscle fibers from rabbit psoas. *Biophys J* 95:5798–5808
86. Davis JS, Epstein ND (2009) Mechanistic role of movement and strain sensitivity in muscle contraction. *Proc Natl Acad Sci U S A* 106:6140–6145
87. Davis JS, Rodgers ME (1995) Indirect coupling of phosphate release to de novo tension generation during muscle contraction. *Proc Natl Acad Sci U S A* 92:10482–10486
88. Fenn WO (1923) A quantitative comparison between the energy liberated and the work performed by the isolated sartorius muscle of the frog. *J Physiol* 58:175–203
89. Veigel C, Schmitz S, Wang F, Sellers JR (2005) Load-dependent kinetics of myosin-V can explain its high processivity. *Nat Cell Biol* 7:861–869
90. Veigel C, Molloy JE, Schmitz S, Kendrick-Jones J (2003) Load-dependent kinetics of force production by smooth muscle myosin measured with optical tweezers. *Nat Cell Biol* 5:980–986
91. Norstrom MF, Smithback PA, Rock RS (2010) Unconventional processive mechanics of non-muscle myosin IIB. *J Biol Chem* 285:26326–26334
92. Linari M, Caremani M, Piperio C, Brandt P, Lombardi V (2007) Stiffness and fraction of myosin motors responsible for active force in permeabilized muscle fibers from rabbit psoas. *Biophys J* 92:2476–2490
93. Decostre V, Bianco P, Lombardi V, Piazzesi G (2005) Effect of temperature on the working stroke of muscle myosin. *Proc Natl Acad Sci U S A* 102:13927–13932
94. Sheetz MP, Block SM, Spudich JA (1986) Myosin movement in vitro: a quantitative assay using oriented actin cables from Nitella. *Methods Enzymol* 134:531–544
95. Toyoshima YY, Kron SJ, McNally EM, Niebling KR, Toyoshima C, Spudich JA (1987) Myosin subfragment-1 is sufficient to move actin filaments in vitro. *Nature* 328:536–539
96. Kron SJ, Toyoshima YY, Uyeda TQ, Spudich JA (1991) Assays for actin sliding movement over myosin-coated surfaces. *Methods Enzymol* 196:399–416
97. Sellers JR, Cuda G, Wang F, Homsher E (1993) Myosin-specific adaptations of the motility assay. *Methods Cell Biol* 39:23–49
98. Uyeda TQ, Abramson PD, Spudich JA (1996) The neck region of the myosin motor domain acts as a lever arm to generate movement. *Proc Natl Acad Sci U S A* 93:4459–4464
99. Anson M, Geeves MA, Kurzawa SE, Manstein DJ (1996) Myosin motors with artificial lever arms. *EMBO J* 15:6069–6074
100. Tsiavaliaris G, Fujita-Becker S, Manstein DJ (2004) Molecular engineering of a backwards-moving myosin motor. *Nature* 427:558–561
101. Spudich JA (1990) Optical trapping: motor molecules in motion. *Nature* 348:284–285
102. Finer JT, Simmons RM, Spudich JA (1994) Single myosin molecule mechanics: piconewton forces and nanometre steps. *Nature* 368:113–119
103. Molloy JE, Burns JE, Kendrick-Jones J, Tregear RT, White DC (1995) Movement and force produced by a single myosin head. *Nature* 378:209–212
104. Saito K, Aoki T, Aoki T, Yanagida T (1994) Movement of single myosin filaments and myosin step size on an actin filament suspended in solution by a laser trap. *Biophys J* 66:769–777

105. Steffen W, Smith D, Sleep J (2003) The working stroke upon myosin-nucleotide complexes binding to actin. *Proc Natl Acad Sci U S A* 100:6434–6439
106. Smith D, Sleep J (2006) Strain-dependent kinetics of the myosin working stroke, and how they could be probed with optical-trap experiments. *Biophys J* 91:3359–3369
107. Funatsu T, Harada Y, Tokunaga M, Saito K, Yanagida T (1995) Imaging of single fluorescent molecules and individual ATP turnovers by single myosin molecules in aqueous solution. *Nature* 374:555–559
108. Conibear PB, Kuhlman PA, Bagshaw CR (1998) Measurement of ATPase activities of myosin at the level of tracks and single molecules. *Adv Exp Med Biol* 453:15–26
109. Sakamoto T, Wang F, Schmitz S, Xu Y, Xu Q, Molloy JE, Veigel C, Sellers JR (2003) Neck length and processivity of myosin V. *J Biol Chem* 278:29201–29207
110. Yildiz A, Selvin PR (2005) Fluorescence imaging with one nanometer accuracy: application to molecular motors. *Acc Chem Res* 38:574–582
111. Sakamoto T, Yildiz A, Selvin PR, Sellers JR (2005) Step-size is determined by neck length in myosin V. *Biochemistry* 44:16203–16210
112. Yang Y, Kovacs M, Sakamoto T, Zhang F, Kiehart DP, Sellers JR (2006) Dimerized *Drosophila* myosin VIIa: a processive motor. *Proc Natl Acad Sci U S A* 103:5746–5751
113. Sun Y, Sato O, Ruhnaw F, Arsenault ME, Ikebe M, Goldman YE (2010) Single-molecule stepping and structural dynamics of myosin X. *Nat Struct Mol Biol* 17:485–491
114. Reifenberger JG, Toprak E, Kim H, Safer D, Sweeney HL, Selvin PR (2009) Myosin VI undergoes a 180 degrees power stroke implying an uncoupling of the front lever arm. *Proc Natl Acad Sci U S A* 106:18255–18260
115. Houdusse A, Sweeney HL (2001) Myosin motors: missing structures and hidden springs. *Curr Opin Struct Biol* 11:182–194
116. Pollard TD, Korn ED (1973) *Acanthamoeba* myosin. I. Isolation from *Acanthamoeba castellanii* of an enzyme similar to muscle myosin. *J Biol Chem* 248:4682–4690
117. Coluccio LM (2008) Myosins: a superfamily of molecular motors. Springer, Dordrecht
118. Odrionitz F, Kollmar M (2007) Drawing the tree of eukaryotic life based on the analysis of 2,269 manually annotated myosins from 328 species. *Genome Biol* 8:R196
119. Knight PJ, Thirumurugan K, Xu Y, Wang F, Kalverda AP, Stafford WF III, Sellers JR, Peckham M (2005) The predicted coiled-coil domain of myosin 10 forms a novel elongated domain that lengthens the head. *J Biol Chem* 280:34702–34708
120. Peckham M (2011) Coiled coils and SAH domains in cytoskeletal molecular motors. *Biochem Soc Trans* 39:1142–1148
121. Suveges D, Gaspari Z, Toth G, Nyitray L (2009) Charged single alpha-helix: a versatile protein structural motif. *Proteins* 74:905–916
122. Brown JH, Cohen C (2005) Regulation of muscle contraction by tropomyosin and troponin: how structure illuminates function. *Adv Protein Chem* 71:121–159
123. Smith RC, Cande WZ, Craig R, Tooth PJ, Scholey JM, Kendrick-Jones J (1983) Regulation of myosin filament assembly by light-chain phosphorylation. *Philos Trans R Soc Lond B Biol Sci* 302:73–82
124. Wendt T, Taylor D, Messier T, Trybus KM, Taylor KA (1999) Visualization of head-head interactions in the inhibited state of smooth muscle myosin. *J Cell Biol* 147:1385–1390
125. Szent-Gyorgyi AG (2007) Regulation by myosin: how calcium regulates some myosins, past and present. *Adv Exp Med Biol* 592:253–264
126. Pichith D, Travaglia M, Yang Z, Liu X, Zong AB, Safer D, Sweeney HL (2009) Cargo binding induces dimerization of myosin VI. *Proc Natl Acad Sci U S A* 106:17320–17324
127. Chibalina MV, Puri C, Kendrick-Jones J, Buss F (2009) Potential roles of myosin VI in cell motility. *Biochem Soc Trans* 37:966–970
128. Wells AL, Lin AW, Chen LQ, Safer D, Cain SM, Hasson T, Carragher BO, Milligan RA, Sweeney HL (1999) Myosin VI is an actin-based motor that moves backwards. *Nature* 401:505–508

129. Sweeney HL, Houdusse A (2010) Myosin VI rewrites the rules for myosin motors. *Cell* 141:573–582
130. Nagy S, Ricca BL, Norstrom MF, Courson DS, Brawley CM, Smithback PA, Rock RS (2008) A myosin motor that selects bundled actin for motility. *Proc Natl Acad Sci U S A* 105:9616–9620
131. Hodges AR, Bookwalter CS, Krementsova EB, Trybus KM (2009) A nonprocessive class V myosin drives cargo processively when a kinesin-related protein is a passenger. *Curr Biol* 19:2121–2125
132. Koder N, Yamamoto D, Ishikawa R, Ando T (2010) Video imaging of walking myosin V by high-speed atomic force microscopy. *Nature* 468:72–76
133. De La Cruz EM, Ostap EM (2004) Relating biochemistry and function in the myosin superfamily. *Curr Opin Cell Biol* 16:61–67
134. Cremo CR, Geeves MA (1998) Interaction of actin and ADP with the head domain of smooth muscle myosin: implications for strain-dependent ADP release in smooth muscle. *Biochemistry* 37:1969–1978
135. Whittaker M, Wilson-Kubalek EM, Smith JE, Faust L, Milligan RA, Sweeney HL (1995) A 35-a movement of smooth muscle myosin on ADP release. *Nature* 378:748–751
136. Iwamoto H, Oiwa K, Kovacs M, Sellers JR, Suzuki T, Wakayama J, Tamura T, Yagi N, Fujisawa T (2007) Diversity of structural behavior in vertebrate conventional myosins complexed with actin. *J Mol Biol* 369:249–264

## **Part III**

# **Future Prospects**

## Chapter 12

# Future Prospects

Norma M. Allewell, Igor A. Kaltashov, Linda O. Narhi, and Ivan Rayment

**Abstract** This chapter illustrates the dynamic, evolving nature of molecular biophysics by providing perspectives on future prospects in three major areas: X-ray and neutron scattering, mass spectrometry, and therapeutic drug development. In all three areas, major advances in the biological sciences, development of powerful new experimental and computational tools, and urgent real-world challenges are driving rapid progress. These developments have enabled and encouraged biophysicists to focus increasingly on studying systems of various sizes and the interactions between their components, rather than simply on their isolated constituents. As the examples demonstrate, these interactions are often transient, and may occur in massive macromolecular complexes, between macromolecules, or between macromolecules and ligands. A diverse set of emerging and advancing technologies are likely to spur future developments. These include advances in methods that enable individual molecules to be studied at atomic resolution; high throughput methods, increasing automation, development of massive databases that allow comparison and analysis of data of many types gathered worldwide; and increasingly powerful computational methods that enable ever larger systems to be modeled at high

---

N.M. Allewell (✉)

Department of Cell Biology and Molecular Genetics, University of Maryland,  
College Park, MD 20852, USA  
e-mail: allewell@umd.edu

I.A. Kaltashov

Department of Chemistry, University of Massachusetts-Amherst,  
710 North Pleasant Street, Amherst, MA 01003, USA

L.O. Narhi

Research and Development, Amgen, Inc., One Amgen Center Drive,  
Thousand Oaks, CA 91320, USA  
e-mail: lnarhi@amgen.com

I. Rayment

Department of Biochemistry, University of Wisconsin-Madison,  
433 Babcock Drive, Madison, WI 53706-1544, USA

resolution. Finally, the emerging field of synthetic biology will create exciting opportunities to create, explore, and manipulate the biophysics of novel systems.

**Keywords** Advances in computation • Database development • High throughput automation • Macromolecular interactions • Mass spectrometry • Membrane proteins • Single molecule methods • Structural biology • Therapeutic drug development • X-ray and neutron scattering

Molecular biophysics is a dynamic, evolving area of science that continues to undergo rapid change in terms of the kinds of questions that can be asked, and the experimental and computational tools that are available to address them. This chapter presents perspectives on current challenges and future prospects in three major areas that, in combination, provide a snapshot of where the field is now and where it is moving. The first section, on X-ray and neutron scattering, emphasizes the importance of biological questions in driving advances in these technologies. Many of these biological questions focus on interactions, often transient, in massive macromolecular complexes, between macromolecules, or between macromolecules and their ligands. These themes are amplified in the second section, which describes the explosive development of mass spectrometry as a powerful tool for characterizing the conformation and dynamics of membrane proteins, large macromolecular assemblies, highly heterogeneous proteins, and molecular interactions *in vivo*. Although the biological themes in the two sections are similar, their juxtaposition reveals the complementarity of these two major experimental approaches and the insights that they provide. The last section, on the use of biophysical methods in therapeutic protein development, illustrates another important trend, the rapidly increasing importance of molecular biophysics in solving real-world problems. These applications have also driven development of the technology, in this case towards small volume, high throughput methods. In all of these examples, the questions being asked have resulted in advances in the technology, which have led to increased understanding, and consequently the ability to address even more complicated questions. In this way, molecular biophysics and the fields to which it is applied constantly interact to advance together.

## 12.1 X-Ray and Neutron Scattering

X-ray diffraction and neutron scattering are relatively mature methods and thus their future prospects will be driven primarily by the biological questions that must be envisaged or answered. Scattering methods are also well advanced; however, considerable technical development can be anticipated in the foreseeable future, particularly in improved methods and facilities for data collection and advances in sample preparation. Together, it can be anticipated that problems that appear almost insurmountable at present will become routine. The most compelling change will be increasing

use of scattering methods by newcomers who have not previously used these methods, as a result of more widespread understanding of the fundamentals and consequent development of automated structural determination. These prospects are outlined for crystallography, fiber diffraction, and small angle scattering, with challenges that lie at the forefront of scattering and diffraction methods described first.

### ***12.1.1 Challenges at the Frontier of Structural Biology***

For the most part, these challenges are conceptually well established, many are under active investigation and great progress is expected in the near future. Areas where there are major opportunities to enhance understanding of cellular function include the architecture of microtubule organizing centers, kinetochores, nuclear pore complexes, multiprotein membrane complexes found at the interfaces between cells, and spliceosomes. Inherent in all of these research areas are interactions between macromolecules and ligands. Interactions between the components of a cell will remain the focus of structural biology for many years to come and represent a real change in what is expected from a structural investigation. In the early days of X-ray crystallography, it was sufficient to determine the structures of the components. Initially every structure of a protein or nucleic acid was considered a major advance with little regard to the ligands or macromolecular interactions involved. However, every protein, nucleic acid, oligosaccharide, and small molecule ligand interacts with something else in the cellular system. Consequently, structure determination today goes hand in hand with biochemical and cellular studies that examine the hypotheses that arise from the structures themselves. This is because the focus has moved away from methodological development back towards understanding biological phenomena. This progress has been accompanied by an increase in the size and complexity of the biological systems that can be investigated.

The traditional approach in macromolecular structure has been to divide the problem into the smallest pieces that yield useful information and are amenable to study and then to construct a conceptual model of the original larger entity from the pieces. As techniques for determining the structures of large complexes have improved the size of the structures that can be studied has steadily increased so that less division is required. This trend is likely to continue. The challenge with complexes such as the nuclear pore complex [1] or kinetochores [2] is to isolate stable subassemblies that will crystallize in a form that yields useful structural information. Great progress has been made, but larger complexes that will ultimately lead to a complete model are still required. The next frontier in many areas will be to define the transitory interactions between molecules.

Most of the structures of complexes that have been determined thus far represent stable complexes (dissociation constants in the low micromolar or nanomolar range), but many interactions in biology are much weaker, transitory, or modulated by posttranslational modification or small molecule ligands. This is



particularly true when interactions involve an ensemble of weaker interactions such as those associated with the cytoskeleton. These studies will necessarily interface with results from electron microscopy that can provide a big picture of a macromolecular assembly. Enhanced use of molecular modeling will eventually become a vital tool in these studies, because, even with large complexes, interactions between a comparatively small number of side chains or functional groups can profoundly influence the behavior of a biological system. Most interactions in biology are dominated by hydrogen bonds and hydrophobic interactions. Hence high resolution structures of components will continue to be essential, but these will have to be incorporated into a larger model.

### ***12.1.2 Macromolecular Crystallography: X-Rays***

Conventional structural determination will almost certainly become increasingly routine. The major developments in this area will be dominated by robotic protein preparation, crystal growth and handling, automated data collection, and structural determination. This approach has been pioneered by the efforts in structural genomics, but is rapidly becoming the standard mode of operation for data recorded with synchrotron radiation. These techniques allow non-expert users to incorporate X-ray structural studies in their research protocols.

The most challenging technical problems in X-ray crystallography lie with massive macromolecular complexes, transitory interactions between molecules, and problems that yield vanishingly small crystals. At the frontiers of difficult structures, considerable advances are expected, driven by current developments in detector technology (pixel array detectors) coupled with the ability to record high quality data from exceedingly small crystals (1–5  $\mu\text{m}$ ). As a consequence, considerably less material is needed for a complex structural study than was once deemed necessary (micrograms to milligrams). Increasing emphasis will be placed on determining the structures of large macromolecular complexes, recognizing that protein:protein and protein:nucleic acid interactions dominate much of cell biology. The crystals of most of these complexes will not diffract to high resolution and will thus require new approaches to determining low resolution structures. Development of suitable metrics for assessing the reliable information content of these structures will be critical for the outside reader or user of this structural data.

Another area that will see rapid growth is the crystallographic study of integral membrane proteins. These have lagged behind soluble cytosolic and extracellular proteins because they are difficult to prepare and crystallize. Even when they do crystallize, most crystals of membrane proteins do not diffract well. The improvements in detector and crystallization technology are expected to have a profound impact in this area. Structural studies of membrane proteins will also be strongly influenced by developments in low resolution structural determination.

Synchrotron radiation has revolutionized X-ray structural determination, but even though high resolution data can now be recorded in a few minutes with pixel

array detectors, radiation damage is still a major problem. Recent developments in free-electron lasers that deliver ultrashort flashes in the femtosecond range of radiation have the potential to overcome this challenge [3]. With the use of ultrashort pulses of X-rays, the data can be recorded before the crystal has a chance to disintegrate or suffer radiation damage. This technology also creates an opportunity to examine even smaller crystals (less than 1  $\mu\text{m}$ ) and will facilitate study of macromolecules that are difficult to crystallize. This is a highly challenging approach since it requires combining scattering data from millions of diffraction experiments; however, improvements in automated data collection and sample handling are expected to simplify this approach for important structural problems.

### ***12.1.3 Small Angle Scattering: X-Rays***

As is the case for macromolecular crystallography, the results from small angle scattering will increasingly be utilized by investigators who are not experts in the field and thus will require improvements in automation and validation to ensure high quality routine data collection and appropriate interpretation of the results [4]. A large part of the effort to increase the use of small angle scattering will be associated with continued development of algorithms needed for *ab initio* modeling of the scattering data and interfacing the results with those derived from other biophysical techniques such as NMR and crystallography. In-house facilities have shown dramatic improvements in recent years and have significantly increased the number of users, however, synchrotron radiation will continue to play a major role because of the improved signal to noise and speed of data collection. A standard set of validation tools and protocols for depositing and reporting the results from small angle scattering studies will be needed to optimize the investment in this technique.

### ***12.1.4 Neutron Scattering Methods***

Neutrons provide an enormously powerful alternative to X-rays because of the greater scattering power of hydrogen and deuterium relative to other elements in biological molecules. The high scattering power of these elements makes possible contrast variation in scattering studies and the localization of hydrogen atoms in X-ray structures. In contrast, hydrogen atoms are not observed in X-ray studies except at ultra-high resolution. The only restriction on the routine usage of neutron scattering is limited access to neutron sources and the length of time required for adequate data collection. Nuclear reactors have been the mainstay of neutron sources throughout the world, but more recently spallation sources have been coming online. These accelerator-driven sources provide beams of pulsed neutrons that are considerably more intense than those available from other sources. It can be expected that these sources will encourage greater use of neutrons in the biophysical studies of macromolecules.

## 12.2 Mass Spectrometry

Although one of the “youngest” analytical techniques in the experimental arsenal of biophysics, mass spectrometry (MS) has already established itself as an indispensable tool, providing answers to challenging problems that cannot be addressed using other approaches. The list of targets suitable for MS analysis continues to expand, with many applications that seemed ground-breaking only a few years ago now becoming routine and commonplace. As the entire field of biophysics continues to advance, MS is expanding its scope of inquiry to include such challenging targets as membrane proteins, large macromolecular assemblies, and many others. For MS, as for other areas of biophysics, the greatest challenge is to break away from the reductionist paradigm and embrace the complexity of living systems.

### *12.2.1 Characterization of Conformation and Dynamics of Membrane Proteins by MS*

Although membrane proteins constitute about one-third of the entire proteome, the three-dimensional structures of only 357 unique membrane proteins were available as of September, 2012. The architecture and dynamics of membrane proteins are defined by a wide range of intermolecular forces, including interactions with the hydrophobic interior of the membrane, its polar solvent interface region, as well as internal and external water molecules. As a result, membrane proteins generally have very poor solubility characteristics, making any experimental study of the architecture, dynamics, and interactions of these macromolecules extremely difficult. Traditionally, solubilization and isolation of membrane proteins relied on detergents, but many earlier attempts to characterize detergent-solubilized membrane proteins by MS had very little success because of the suppressive effect of detergents [5]. While various techniques that remove detergents prior to MS analysis remain the most popular strategy for dealing with this problem, such a dramatic change in the environment of the protein inevitably leads to the loss of higher order structure. Fortunately, small amounts of detergents can be tolerated by MS at least in some cases, allowing direct ESI MS analyses of non-covalently bound membrane protein assemblies to be carried out after reconstituting them in a minimum amount of detergent [6]. A similar approach was used recently to study very large non-covalent assemblies of transmembrane proteins [7].

Despite initial successes in using detergents for direct MS characterization of membrane proteins, one must be aware of some potential pitfalls, the most serious of which is the denaturing action of many (if not all) detergents. An ideal membrane mimetic would not only form a bilayer-based structure, but also reflect the physical properties of the specific biological membrane. Several MS-based experimental approaches are currently under investigation as potential probes of the structure and behavior of membrane proteins with bilayer-based membrane mimics. These

include limited proteolysis to identify membrane-bound protein segments, chemical probes to obtain topological information on various protein segments, and hydrogen–deuterium exchange to provide information on interfacial positioning and stability of transmembrane polypeptides in lipid bilayers. Another recently introduced bilayer-based membrane-mimicking system is a nanodisc where the bilayer structures are maintained by membrane scaffold proteins modeled after apolipoprotein A1. However, the best environment to study the behavior of membrane proteins is indisputably the specific biological membrane itself. Although characterization of various properties of membrane-bound proteins within the context of their native environment using MS was a technical impossibility until very recently, several examples of such studies have been published in the past few years [8, 9].

## **12.2.2 Mass Spectrometry Above 1 MDa**

### **12.2.2.1 Characterization of Large Macromolecular Assemblies**

Large protein assemblies play crucial roles in a variety of cellular functions. For example, each cellular protein emerges from a large assembly upon its birth (ribosome), enters another large assembly at the end of its life (proteasome), and interacts with a number of other macromolecular assemblies throughout its lifetime. While the ability of electrospray ionization mass spectrometry (ESI MS) to detect and characterize relatively modest non-covalent assemblies of proteins and other biopolymers (e.g., protein/DNA complexes) was recognized over 20 years ago and has been used actively since, large macromolecular assemblies representing complete self-contained units of biological machinery (such as ribosomes and proteasomes) remained out of reach of MS analysis for a much longer period of time.

The situation began to change in the past decade as a result of pioneering work of Robinson [10] and Heck [11], who demonstrated that careful control of ionization conditions and use of mass analyzers with extended  $m/z$  range may allow very large non-covalent complexes to be preserved in the gas phase, and meaningful structural information to be extracted for protein assemblies whose masses exceed several MDa. Although still far from being a routine method of analysis of large macromolecular complexes, the so-called native mass spectrometry is now capable of dealing with complex objects ranging from proteasomes and ribosomes to intact viral capsids.

#### **12.2.2.2 MS of Highly Heterogeneous Proteins**

Despite the dramatic expansion of the mass limit of macromolecules for which meaningful information can be provided by MS, the bar remained disappointingly low until recently for MS analysis of several classes of proteins. These include extensively glycosylated proteins and protein–polymer conjugates, which

frequently exhibit remarkable degrees of structural heterogeneity. Heterogeneity poses a formidable challenge to MS-based studies of higher order structure, dynamics, and interactions of such proteins, frequently making the mundane task of mass measurement an extremely challenging undertaking. Among several recent developments in this field, a particularly promising approach combines reduction of complexity of the protein ion ensemble (by mass selecting a narrow fraction of the entire ionic population) and gas phase chemistry (charge reduction via electron capture or electron transfer) [12].

Another MS technique that holds great promise vis-à-vis dealing with macromolecular complexity is ion mobility (IM) MS [13]. While the majority of current applications of this technique exploit its ability to provide information on the physical size of macromolecular ions in the gas phase, the potential utility of IM MS to provide an additional separation stage prior to MS detection, thereby reducing complexity of heterogeneous systems, is frequently overlooked. Nevertheless, the ability of IM MS to separate various isoforms of biopolymers has been acknowledged and has already been used to facilitate MS characterization of covalent structure of large glycoproteins [14] and protein-polymer conjugates [15].

### 12.2.2.3 Mass Spectrometry *In Vivo*

A very important aspect of macromolecular interactions *in vivo* is their extreme complexity due to the large number of participating players. While most biophysical studies have traditionally used the so-called reductionist approach by focusing attention only on the minimal number of players deemed absolutely essential for a particular process or interaction, the limitations of this approach are now becoming commonly acknowledged. Emergence of the new paradigm that embraces, rather than downplays, the complexity of biological processes has been catalyzed by the completion of genome sequencing for several organisms, which highlighted the enormous repertoire of biomolecules making up living cells.

One approach to dealing with the complexity of real-living systems that enjoyed great popularity in the past decade, is functional proteomics [16–22]. Above and beyond proteomic approaches that provide a global picture of biomolecular interactions in living systems, a number of groups are beginning to invest significant effort in expanding the existing experimental strategies to study biomolecules in their native environment. These include the possibilities for investigation of protein structure and interactions in living cells provided by chemical cross-linking with MS detection [23], or chemical labeling and footprinting methods [24]. Efficient delivery of cross-linking and/or labeling reagents to the cell without disrupting its normal functioning or indeed killing it remains a formidable challenge. This obstacle places a significant limitation on the number of reagents that can be used in such *in vivo* measurements. One particularly attractive approach to overcoming this problem would tap into the arsenal of the emerging field of synthetic biology by reprogramming the genetic code of the cell, forcing it to produce and incorporate into proteins amino acids with reactive side chains that can be used as *in situ* chemical probes [25].

The past two decades witnessed many triumphs of MS in various subfields of biophysics and structural biology, and it is certain that this technique will remain a valuable contributor in these fields, catalyzing their progress in the years to come and bringing about new exciting discoveries. Despite reaching a respectable age, biological MS remains very dynamic and constantly adapts to the ever changing landscape in the life sciences, always remaining at the forefront and ready to deal with the most challenging problems.

## **12.3 The Future of Biophysical Analysis in Therapeutic Protein Development**

The development of therapeutic proteins is an endeavor that includes extensive use of biophysical techniques, as has been described in numerous publications (see, for example [26]). As is the case for all proteins, proteins being developed and used for therapeutics are complex macromolecules that require appropriate primary, secondary, and tertiary structure to maintain their function and stability, as discussed in Chap. 2. The ultimate goal of therapeutic development is the creation of a molecule that is safe and efficacious, and that will maintain its structural integrity during manufacturing, storage (usually two years, often in solution, and under variable conditions), and administration. Different biophysical tools are employed during the different stages of development of this important class of drugs, depending on the amount of material and time available, and the goal of the analysis.

The protein therapeutic development lifecycle includes several steps, beginning with the identification of a biological target. After the target has been chosen, the molecule with the greatest chance of succeeding as a drug and with the desired biological activity must be selected from multiple candidates with different primary sequences. Following the choice of candidate, process and formulation development, and characterization are the next steps, with selection of delivery device and route of administration coming next. During all of these steps, the integrity of the protein, in terms of its secondary, tertiary, and quaternary structure needs to be maintained. The last step in this process is clinical trials and then, if successful, commercialization. During these later stages of development, the focus is on product consistency and lot release assays, exploration of different delivery devices and therapeutic indications, comparability assessments, and support for product and process failure investigations.

Biophysical tools are used at all of these stages in the therapeutic protein lifecycle. Currently characterization is done by removing an aliquot of the sample and analyzing specific properties with different techniques, and then using heuristics to combine the results. This can be time-consuming and involves multiple aliquots and a fair amount of material. The desired future state for biophysical assessment of protein therapeutics would include the ability to do multiple analyses on the same sample at all stages of development. This would increase the reliability of the results because different attributes could be directly compared, and also enable the testing

**Table 12.1** The goals and challenges of the “biophysics of the future of therapeutic protein development”

Goal/challenge	Current	Desirable
Analysis at high/low concentration	Many biophysical techniques require dilution to 0.5–1 mg/mL range, others require concentration to >10 mg/mL	At actual formulation concentration
High throughput	Many techniques are labor-intensive and low throughput	Automation, high throughput data collection and analysis
Noninvasive	Requires removing sample from device (vial or syringe)	In situ analysis
Online biophysics for process control	Discrete sampling, off-line and often time-consuming analysis	Online sampling and analysis during fermentation and purification, the ability to make changes based on result obtained on the fly

of more samples to better understand the variability of the methods. The vision of the future for the application of biophysics during protein development also includes being able to perform these tests on actual process samples and to obtain results in real-time so that decisions can be made based on the identity, conformation of the protein, and the state of aggregation. Automation and/or use of easy-to-operate instrumentation for these techniques in a manufacturing environment is another important goal for which to strive. Different phases of drug product development have different specific needs as well that could result in the evolution of different instrumentation and applications in the future. This issue is discussed below and briefly summarized in Table 12.1.

During the selection of the unique protein that will become the product candidate, in addition to biological activity, the stability of the candidates under consideration to the conditions used for manufacturing and storage is assessed. Characteristics to be considered include stability to low pH, agitation, mixing of the air–liquid interface, and temperature. The protein therapeutic also needs to withstand storage in solution at 4–8 °C for two years, often at protein concentrations above 100 mg/mL [27]. Screening for this type of stability usually involves predictive assays that rely on subjecting the protein to harsher conditions than it would encounter normally, in order to predict what may happen with time under milder conditions. This requires an understanding of potential pathways of degradation, in order to ensure that the response of the protein to the conditions used are truly predictive of long-term stability during the actual process. After stressing the material, the impact of the conditions on the integrity of the protein, with particular emphasis on protein aggregation and irreversible unfolding of the native three dimensional structures, is assessed. Assays with minimal material requirements and high throughput are especially valuable at these early stages. Qualitative results that allow comparison of the relative degree of change so that candidates can be categorized as passing or failing are an acceptable output.

The ability to assess multiple different protein characteristics on a single sample after each stress, rather than having to remove aliquots followed by sample manipulation in order to be compatible with the different analyses, would be hugely



valuable at this stage. Primary attributes that should be assessed are conformational and colloidal stability, the propensity of the protein to aggregate, and chemical modification of the amino acid residues in the primary structure. The ability to measure, either directly or indirectly, the primary, secondary, tertiary, and quaternary structure of a protein, and the size of any aggregated species generated, all in a high throughput format, is the ultimate goal. The more candidates that can be assessed, the greater the chance of identifying one that has the desired properties, and so the availability of automated methods is also important. In the future one can envision a robotic system that subjects samples to different stresses such as elevated temperature, extremes of pH and ionic strength, mechanical shaking or stirring, exposure to light, etc., and then runs the multi-well plates through sequential biophysical analyses, ultimately providing a relative ranking of the candidates based on a multivariate analysis of the matrix of data generated. It is worth noting that in some cases in addition to the traditional biophysical techniques (such as MS, different types of spectroscopy) other methods, such as chromatography, can often be used as part of this assessment. For example, ion exchange chromatography can detect changes in chemical modification, hydrophobic interaction chromatography can be used to detect changes in conformation, and size exclusion chromatography can follow loss of monomer, or formation of smaller oligomers such as dimers and tetramers [28].

An important aspect of this early stage of development is the feedback between protein engineering, modeling, and the results of the predictive assays. There is an iterative process as the correlation between the predicted behavior, the actual behavior as the protein moves through process development, and the structure of the modeled protein becomes available. Collecting these data into usable databases allows constant improvement in the sequence-based predictive algorithms, such that more and more of the potential “hot spots” for modification or self-association can be eliminated before the protein is ever included in the panel of potential candidates to be screened.

The focus changes to developing the production process and formulation to be used for the commercial product once the specific molecule that will be developed as a therapeutic has been chosen. At this stage, material availability is no longer rate limiting, and more rigorous techniques that compare the higher order structure of the actual material obtained during the different processing steps can be used to ensure that the final product was not irreversibly damaged by the conditions being used for its manufacture. The ability to get real-time, high resolution information on the primary, secondary, and tertiary structure, and especially of the aggregation state, of samples as they are generated by the cells, and passed through the purification process, would allow decisions about sample collection to be made based on the quality of the material as it was being processed. This requires online instruments that are robust enough to withstand the conditions of a protein manufacturing plant, and are also rapid enough to provide results in time to be used to make process conditions. Online light scattering analysis to assess aggregation; Raman spectroscopy to assess the secondary and tertiary structure of the protein; mass spectrometry to determine primary structure including amino acid sequence, carbohydrate content, and chemical modification; and morphological analysis to assess types of aggregate are some of the potential process analytical technologies that are currently being explored.



During formulation development, the stability of the target protein is assessed in different buffer compositions, pH, storage conditions, and delivery devices. These studies typically involve the generation of many samples that must be analyzed in order to arrive at the optimal formulation conditions, and thus many of the principles that apply during candidate selection apply here as well and some of the same assays can be used. The primary difference is that at this point in the development lifecycle the amount of material is no longer rate limiting and so formats other than the 96 (or more) well plates can be considered. However, an instrument that uses robotics to stress and test multiple samples for several attributes simultaneously is still the goal. Special attention should be paid to the aggregation state and the integrity of the primary sequence of the protein. Ideally the analyses would occur under the actual solution and storage conditions that would be used, including protein concentration. The majority of the protein therapeutics under development will be administered at high concentration, and so the ability to determine these properties without dilution is an important consideration.

As the product moves into production, the emphasis switches from developing and optimizing conditions to maintaining process/product control; biophysical techniques to follow the protein higher order structure are important elements of comparability studies, and are required for obtaining licensure of the drug. In this case the methods must be shown to be fit for the purpose and the sensitivity of the assays to detect changes in the product must be determined. Another important aspect of preclinical and clinical development is the monitoring of stability samples, stored both under accelerated and recommended conditions, for comparability. Biophysical techniques are also used as tools to help ensure that changes in device, concentration, and formulation made as different indications or patient populations are added do not affect the conformation of the biotherapeutic. Techniques that can give reproducible and accurate results, and where the readout is understood, are most commonly used at this stage of development, rather than the high throughput tests that were employed in the beginning of the product development lifecycle. These analyses must be sensitive to changes in the protein conformation that can occur if the protein is exposed to slightly different process or storage conditions, as demonstrated by samples exposed to conditions outside the normal parameters. At this stage future directions lie in the ability to carry out multiple biophysical tests on the same sample in the commercial formulation, removed directly from the commercial delivery device. This capability would allow for testing of a statistically relevant number of samples, and direct comparison of the results. One difficulty with the current tools available for biophysical characterization of proteins is that most of these lack the sensitivity necessary to detect changes of less than 5 %. They also provide information on the average of the molecular population. Thus even when a difference is detected, it is not possible to determine whether 6 % of the population has lost all signals in that assay, or 100 % of the population has lost 6 % of the signal. Evolution of single molecule methods to the point where they are applicable for quick and reproducible analyses with very little variability would be a huge step forward in our ability to interrogate samples and truly understand if they are comparable or not. The ability to apply high resolution methods such as NMR and MS

to gain better understanding of protein higher order structure down to a single residue is being explored as one avenue to obtain this type of information. The ability to track and characterize minor species in the structural ensemble that is present at any given time in a protein solution would also contribute to this. Finally, proteins are not static species, but are truly dynamic and can sample multiple folding structures as part of the natural thermodynamic equilibrium of the states possible in solution. Techniques to provide quick assessments of the dynamics of any given protein solution would also be helpful for this stage of development.

Finally, during commercial production batches occasionally fail the various lot release assays; biophysical techniques can be used to help identify the root cause and contribute to the safety assessment of the different lots of protein produced under supposedly equivalent conditions. In this case very often a single sample is being tested, with a single visible aggregate being studied, and so the methods must have the sensitivity to detect and analyze a very small amount of protein and provide a positive identification of the material if possible. For this application ideal future biophysical tools would include analysis by mass spectrometry for molecule identification and determination of any chemical modification, as well as analysis of the conformation of the protein, and the aggregation state. This analysis should occur *in situ* in the glass vial, syringe, or other device used to administer the drug to the patient, and all the analyses must be performed on the same particle or other species that resulted in the lot release failure. While throughput is important, the ability to obtain very reliable results from such a small sample set is far more important than throughput at this stage.

As illustrated in Table 12.1, and from the discussion above, there are many gaps between the current state of protein biophysical characterization during biotherapeutic development and the desired future state. While challenging, much progress has been made in recent years. The evolution of computational and material sciences is resulting in miniaturization of instrumentation to the point where the “lab on a microchip” will become feasible. The development of high throughput, automated, instruments that assess more than one attribute on these chips, coupled with sophisticated statistical calculations and multivariate analysis of the information does not seem outside the realm of possibility in the relatively near future.

## 12.4 Conclusions

This chapter has provided perspectives on future directions in three major areas of molecular biophysics, as examples of what the future holds. While many advances will be specific to a particular field, there are several overarching themes that are common to the three topics discussed here as well as many other areas of biology. Throughout biophysics, the focus is moving from isolated components to entire systems. At the same time single molecule analyses will increasingly enable us to visualize and characterize minority species against the background of the entire molecular population, including transitory states. The evolution of high throughput

methods will result in an increase in throughput and a decrease in the amount of material required. Increasing use of automation will make biophysical approaches accessible to a wider group of users, and application to a larger variety of systems. Massive databases will allow comparison of results across different samples, systems, and even laboratories, while increasingly powerful computational approaches will enable large systems to be modeled at high resolution. Finally, the emerging field of synthetic biology will enable biophysics to extend beyond natural systems to novel synthetic systems.

## References

1. Bilokapic S, Schwartz TU (2012) 3D ultrastructure of the nuclear pore complex. *Curr Opin Cell Biol* 24:86–91
2. Corbett KD, Harrison SC (2012) Molecular architecture of the yeast monopin complex. *Cell Rep* 1:583–589
3. Boutet S, Lomb L, Williams GJ, Barends TR, Aquila A, Doak RB, Weierstall U, DePonte DP, Steinbrener J, Shoeman RL, Messerschmidt M, Barty A, White TA, Kassemeyer S, Kirian RA, Seibert MM, Montanez PA, Kenney C, Herbst R, Hart P, Pines J, Haller G, Gruner SM, Philipp HT, Tate MW, Hromalik M, Koerner LJ, van Bakel N, Morse J, Ghonsalves W, Arnlund D, Bogan MJ, Coleman C, Fromme R, Hampton CY, Hunter MS, Johansson LC, Katona G, Kupitz C, Liang M, Martin AV, Nass K, Redecke L, Stellato F, Timneanu N, Wang D, Zatsepin NA, Schafer D, Defever J, Neutze R, Fromme P, Spence JC, Chapman HN, Schlichting I (2012) High-resolution protein structure determination by serial femtosecond crystallography. *Science* 337:362–364
4. Petoukhov MV, Svergun DI (2013) Applications of small-angle X-ray scattering to biomacromolecular solutions. *Int J Biochem Cell Biol* 45(2):429–437
5. Annesley TM (2003) Ion suppression in mass spectrometry. *Clin Chem* 49:1041–1044
6. Lenggqvist J, Svensson R, Evergren E, Morgenstern R, Griffiths WJ (2004) Observation of an intact non-covalent homotrimer of detergent-solubilised rat microsomal glutathione transferase 1 by electrospray mass spectrometry. *J Biol Chem* 279(14):13311–13316, M310958200
7. Barrera NP, Di Bartolo N, Booth PJ, Robinson CV (2008) Micelles protect membrane complexes from solution to vacuum. *Science* 321:243–246
8. Pan Y, Stocks BB, Brown L, Konermann L (2009) Structural characterization of an integral membrane protein in its natural lipid environment by oxidative methionine labeling and mass spectrometry. *Anal Chem* 81:28–35
9. Wen JZ, Zhang H, Gross ML, Blankenship RE (2009) Membrane orientation of the FMO antenna protein from *Chlorobaculum tepidum* as determined by mass spectrometry-based footprinting. *Proc Natl Acad Sci U S A* 106:6134–6139
10. Sobott F, McCammon MG, Hernandez H, Robinson CV (2005) The flight of macromolecular complexes in a mass spectrometer. *Philos Trans A Math Phys Eng Sci* 363:379–389, discussion 389–391
11. Heck AJR (2008) Native mass spectrometry: a bridge between interactomics and structural biology. *Nat Methods* 5:927–933
12. Abzalimov RR, Kaltashov IA (2010) Electrospray ionization mass spectrometry of highly heterogeneous protein systems: protein ion charge state assignment via incomplete charge reduction. *Anal Chem* 82:7523–7526
13. Bohrer BC, Mererbloom SI, Koeniger SL, Hilderbrand AE, Clemmer DE (2008) Biomolecule analysis by ion mobility spectrometry. *Annu Rev Anal Chem* 1:293–327

14. Damen C, Chen W, Chakraborty A, van Oosterhout M, Mazzeo J, Gebler J, Schellens J, Rosing H, Beijnen J (2009) Electrospray ionization quadrupole ion-mobility time-of-flight mass spectrometry as a tool to distinguish the lot-to-lot heterogeneity in N-glycosylation profile of the therapeutic monoclonal antibody trastuzumab. *J Am Soc Mass Spectrom* 20:2021–2033
15. Bagal D, Zhang H, Schnier PD (2008) Gas-phase proton-transfer chemistry coupled with TOF mass spectrometry and ion mobility-MS for the facile analysis of poly(ethylene glycols) and PEGylated polypeptide conjugates. *Anal Chem* 80:2408–2418
16. Collins MO, Choudhary JS (2008) Mapping multiprotein complexes by affinity purification and mass spectrometry. *Curr Opin Biotechnol* 19:324–330
17. Monti M, Cozzolino M, Cozzolino F, Vitiello G, Tedesco R, Flagiello A, Pucci P (2009) Puzzle of protein complexes in vivo: a present and future challenge for functional proteomics. *Expert Rev Proteomics* 6:159–169
18. Terentiev AA, Moldogazieva NT, Shaitan KV (2009) Dynamic proteomics in modeling of the living cell. Protein–protein interactions. *Biochemistry (Mosc)* 74:1586–1607
19. Malik R, Dulla K, Nigg EA, Korner R (2010) From proteome lists to biological impact-tools and strategies for the analysis of large MS data sets. *Proteomics* 10:1270–1283
20. Zhou M, Robinson CV (2010) When proteomics meets structural biology. *Trends Biochem Sci* 35:522–529
21. Gavin AC, Maeda K, Kuhner S (2011) Recent advances in charting protein–protein interaction: mass spectrometry-based approaches. *Curr Opin Biotechnol* 22:42–49
22. Sardiù ME, Washburn MP (2011) Building protein–protein interaction networks with proteomics and informatics tools. *J Biol Chem* 286:23645–23651
23. Sinz A (2010) Investigation of protein–protein interactions in living cells by chemical cross-linking and mass spectrometry. *Anal Bioanal Chem* 397:3433–3440
24. Zhu Y, Guo TN, Park JE, Li X, Meng W, Datta A, Bern M, Lim SK, Sze SK (2009) Elucidating in vivo structural dynamics in integral membrane protein by hydroxyl radical footprinting. *Mol Cell Proteomics* 8:1999–2010
25. Xie J, Schultz PG (2006) A chemical toolkit for proteins—an expanded genetic code. *Nat Rev Mol Cell Biol* 7:775–782
26. Narhi L (2012) In: Narhi L (ed) (2013) Biophysical characterization during protein therapeutic development. Springer
27. Mahler H-C, Friess W, Grauschopf U, Kiese S (2009) Protein aggregation: pathways, induction factors and analysis. *J Pharm Sci* 98:2909–2934
28. Chen S, Lau H, Brodsky Y, Kleemann GR, Latypov RF (2010) The use of native cation-exchange chromatography to study aggregation and phase separation of monoclonal antibodies. *Protein Sci* 19:1191–1204

# Index

## A

- A<sub>1</sub>A<sub>0</sub>-ATP synthase, 315
- A-ATPase synthase, 314, 315, 317–318
- A<sub>1</sub>-ATPase synthase, 317–318
- Absorbance spectra, 196
  - amino acids, 36
  - chromophores, 39
  - proteins, 39
- Actin
  - atomic structure, 343
  - ATP binding, 354
  - conformational changes, 349
  - fiber, 11
  - fluorescently labeled actin filament, 351
  - G-actin structures, 343
  - in vitro* actin gliding velocity, 351
  - and myosin, 10
  - non-muscle myosin motility, 352
- Actin binding site, 345, 353
- Actin-myosin interaction, 351
- Active unwinding. *See* DNA unwinding mechanism
- Activity silencing, 317
- Actomyosin
  - force production, 349
  - mechanical cycles, 346
  - mechanochemical cycle, 347
- ADC. *See* Analog-to-digital conversion (ADC)
- Adenosine diphosphate (ADP)
  - actin coupling, 354
  - ADP.BeF<sub>3</sub>, 346
  - ADP.VO<sub>4</sub>, 346
  - bacterial plasma/inner mitochondrial membrane, 316
  - equilibrium mass action ratio, 325
  - and inorganic phosphate (P<sub>i</sub>), 327, 328, 346, 347
  - Adenosine-5'-diphosphate.aluminum-fluoride (ADP.AlF<sub>3</sub>), 346
  - Adenosine-5'-diphosphate.beryllium-fluoride (ADP.BeF<sub>3</sub>), 346
  - Adenosine-5'-diphosphate.vanadate (ADP.VO<sub>4</sub>), 346
  - Adenosine-5'-triphosphate (ATP)
    - ATPase cycle, 351
    - hydrolytic cycle, 342
  - Adenosine triphosphate (ATP)
    - enzymes, 273
    - hydrolysis-driven proton pump, 316
    - process, ion gradient-driven, 325
    - protein translocation, 266
    - proton gradient, 329
  - Adenylyl-imidodiphosphate (AMPPNP), 346
  - ADP. *See* Adenosine diphosphate (ADP)
  - AFM. *See* Atomic force microscopy (AFM)
  - A<sub>0</sub>-ion channel, 315, 318
  - Alignment tensor, 138
  - Allison, D.P., 261
  - Allosteric activation, 342
  - Allosteric regulation, 342
  - Allostery, 342, 354
  - Alzheimer's disease, 27, 101
  - Amide bands, 64, 66
  - Amide exchange. *See* Hydrogen-deuterium exchange
  - AMPPNP. *See* Adenylyl-imidodiphosphate (AMPPNP)
  - Amyloid, 27
  - Amyloid fibrils, 101
  - Analog-to-digital conversion (ADC), 154, 158
  - Analytical ultracentrifugation, 343
  - Angular momentum, spin, 164–165
  - Anomalous scattering methods, 97

Araki, A., 61  
 Archaeal ATPase, 315  
 Aromatic amino acids, 35–36, 40  
 Asbury, W., 99  
 Ashkin, A., 266  
 Assembly, 342, 345  
 Atomic force microscopy (AFM)  
   advantages, 260  
   description, 260  
   imaging modes, 262  
   principles, 260–261  
   single biomolecules, 262–263  
   SMFS, 263–266  
 ATP. *See* Adenosine triphosphate (ATP)  
 ATPases  
   actomyosin cycle, 351  
   allosteric regulation, 342  
   rotary motor (*see* Rotary motor ATPase)  
 ATP binding site, 345  
 ATP hydrolysis by myosin, 346–348  
 ATP synthase  
   chloroplast, 315  
   *E. coli*, 320–321

**B**

Back door hypothesis, 349  
 Back-exchange, 239, 240  
 Bacterial V-ATPase  
   modeling studies, 330  
   single molecule rotation experiments, 329  
 Bacteriophage T7  
   ATP/GTP unwinding, 298  
   enzymological studies, 293  
   replicative helicase, 307  
 Baenziger, J.E., 67  
 Bagshaw, C.R., 346, 348  
 Bagshaw–Trentham model, 348  
 Bandwidth, 115–117  
 Barth, A., 66  
 Belfort, G., 68  
 Bernard, C., 3  
 $\beta$ -sheet, 349  
 Betterton, M.D., 303, 305  
 Biemann, K., 220  
 Biological macromolecules, 11–12  
 Biological motility, 342  
 Biological motor system, 342  
 Biomolecular machines, 315  
 Biomolecular structure, 114, 216  
 Biophysics  
   computation role, 10–11  
   description, 2–3

electron–electron spin–spin interactions,  
   203–211  
 hemoglobin three-dimensional structure, 6–7  
 hyperfine coupling and spin-density  
   distributions, 200–203  
 molecular biophysics, 4  
 NMR, 166  
 proteins, atomic resolution, 6  
 rotational catalysis, 326–327  
 spin-orbit coupling and g-value anisotropy,  
   198–200  
 Bíró, N.A., 342  
 Boltzmann distribution, 119  
 Bonhoeffer, K.F., 236  
 Boyer, P.D., 326  
 Brownian ratchet, 330–332, 352  
 Burley, R.W., 236  
 Bustamante, C., 267

## C

$^{13}\text{C}$ , 123–124, 126, 130  
 $\text{Ca}^{2+}$ , 342, 353  
 CAD. *See* Collision-induced dissociation (CID)  
 Calmodulin family, 343, 353  
 CAN experiment, 160  
 Cardiac muscle, 345, 353  
 Carr–Purcell–Meiboom–Gill experiment  
   (CPMG), 151  
 CBCA(CO)NH experiment, 131, 159  
 CC-COSY experiment, 160  
 CCD. *See* Charge-coupled device (CCD)  
 CC-TOCSY experiment, 160  
 CD. *See* Circular dichroism (CD)  
 Cell biology, 2, 14, 59, 270, 281, 342, 368  
 Cell division, 352–353  
 Cell migration, 352–353  
 Cellular protrusions, 352–353  
 Central stalk  
   lipid vesicle, 323  
   and stator stalk, 318  
   synthesis/hydrolysis, 320  
 Chaperone, 266  
 Chaperonins, 280–281  
 Charge-coupled device (CCD), 272, 277  
 Charge state distribution  
   determination, protein mass, 216  
   protein compactness, solution, 234–236  
 Chattopadhyay, A., 58  
 Chemical cross-linking  
   DNA higher order structure, 247  
   MS detection, 372  
   proteins, 243–245

- Chemical energy, 342
- Chemical labeling
- chemical and nonselective (oxidative), 246
  - FPOP, 247
  - selective modification, 245
- Chemical shift
- and nuclear shielding, 121–123
  - paramagnetic effects, 123–124
  - perturbation and line width changes, 147–148
- Chemiosmotic hypothesis, 315
- Chittur, K.K., 65
- Chromophore
- aromatic amino acid, 39
  - CD spectra, 46
  - peptide, 35
- CID. *See* Collision-induced dissociation (CID)
- Circular dichroism (CD)
- conformational changes, proteins, 46–47
  - DNA, 47–48
  - protein and DNA, 50–51
  - protein binding, 49
  - quantitative comparison, 48
  - secondary structure, 43–44
  - SRCD, 50
  - tertiary structure, 45
  - theory, 42–43
  - VCD, 50
- Coherence (in NMR), 124
- Coherence transfer
- J-coupling, 124
  - NMR, 124
- Coiled coil, 321, 323, 344
- Collision-activated dissociation (CAD). *See* Collision-induced dissociation (CID)
- Collision-induced dissociation (CID), 219
- Computational model fitting, 300–302
- CON experiment, 160
- Conformation
- aromatic side chains, 49
  - changes, proteins, 46
  - DNA, 47
  - FRET, 58
  - proteins and nucleic acid, 36
  - therapeutic proteins, 65
- Conformational change, 349
- Conformational diseases, 249
- Conjugate peak refinement (CPR), 350
- Connexin, 262–263
- Conserved loop, 348
- Contact shift, 123
- Contractile apparatus, 350
- Contractile properties, 342
- Contrast transfer function (CTF), 279
- Converter, 345, 348
- Correlated spectroscopy (COSY)
- experiment, 126
- Correlation time, 144, 150
- Coupling, dipolar
- NOE (*see* Nuclear overhauser effects (NOE))
  - residual (RDC) (*see* Residual dipolar couplings (RDC))
- Coupling, scalar, 124
- CPR. *See* Conjugate peak refinement (CPR)
- Crick, F., 4, 5, 19, 99, 101
- Cross- $\beta$ , 101
- Crossbridge, 343, 345
- Cross-correlated relaxation enhanced
- polarization transfer (CRINEPT) experiment, 144, 160
- Cross-linking. *See* Chemical cross-linking
- Cross-polarization, 139, 141–142
- Cryo-electron microscopy (cryo-EM)
- actomyosin rigor complex, 348–349
  - A/V-type ATPase, 323
  - biological macromolecules, 275
  - and enzyme decoration, 323
  - rotary ATPases, 315
- Cryo-EM. *See* Cryo-electron microscopy (cryo-EM)
- Crystallography
- ATPase sectors, rotor rings and stator stalks, 318–321
  - near-atomic resolution structure, 315
- Crystals
- distribution, electrons, 92
  - three-dimensional diffraction grating, 93
- Crystal structure, 344, 345
- CTF. *See* Contrast transfer function (CTF)
- CW EPR spectra, 186
- Cytoskeletal transporter, 353
- Cytoskeleton, 367–368
- D**
- D'Antonio, J., 69
- da Vinci, Leonardo, 3
- DEER. *See* Double electron electron resonance (DEER)
- Delbrück, M., 4–7
- Dempsey, C.E., 237
- Deoxyribonucleic acid (DNA)
- helical structure, 19
  - and proteins, 21
  - and RNA, 18

- Deuteration (of macromolecules for NMR), 156
  - Deuterium-neutron scattering, 107–109
  - Dichroism, circular, 8
  - Differentiation, 353
  - Diffraction, 277
  - Diffusion (NMR measurement of), 146
  - Digitization, NMR signal, 131
  - Dimerization, 352, 353
  - Dipolar coupling, 190, 197, 203
  - Dipolar coupling and nuclear Overhauser effects, 133–137
  - Dipolar relaxation, 149
  - Dipole, nuclear spin, 124
  - Dissociation constant ( $K_d$ ), 297
  - Distribution
    - charge state (*see* Charge state distribution)
    - isotopic, 219, 239
  - Disulfide bond
    - aromatic amino acid chromophores, 39
    - circular dichroic spectroscopy, 8
    - PTM, 221
    - sequence coverage, 240
  - Disulfide bridge. *See* Disulfide bond
  - DLS. *See* Dynamic light scattering (DLS)
  - DNA-based motor proteins, 352
  - DNA diffraction, 99, 104
  - DNA polymerase, 260, 308–309
  - DNA replication. *See* Replication
  - DNA unwinding
    - active *vs.* passive mechanism, 303–305
    - computational model, 300–302
    - polymerase (*see* DNA polymerase)
    - primase (*see* Primase)
    - processivity, 302
    - rate ( $K_u$ )
      - average base pair, 302
      - ensemble methods, 293
      - and  $K_d$ , 302
      - T7 helicase, 308
  - DNA unwinding mechanism
    - active, 303–305
    - passive, 303–305
  - Docking, 343
  - Domain
    - actin monomer, 343
    - sequence information, 352
    - tails, myosins, 353
  - Double electron electron resonance (DEER), 190
  - Double-quantum filtered (DQF) COSY experiment, 126
  - Drag force, 354
  - Drug development, 373, 374
  - Duty ratio (duty cycle), 354
  - Dynamic information, NMR
    - chemical shift perturbation and line width changes, 147–148
    - crystallization, 145
    - diffusion measurements, 146
    - EXSY and *zz*-exchange spectroscopy, 149
    - H/D exchange, 147
    - heteronuclear relaxation, 149–152
    - macromolecular motions, 145
    - solid state  $^2\text{H}$  line shape analysis, 152
  - Dynamic light scattering (DLS)
    - cytochrome, 79–80
    - hydrodynamic radius, 78–79
    - protein concentrations, 80
  - Dynamic range (NMR), 158
  - Dynein, 11
- E**
- ECD. *See* Electron capture dissociation (ECD)
  - Effector binding domain, 353
  - Eisenberg, D., 101
  - Elastase, 108, 109
  - Elastic energy coupling, 330
  - ELC. *See* Essential light chain (ELC)
  - Electrochemical potential, 315–316
  - Electron capture dissociation (ECD), 220
  - Electron density distribution, 93
  - Electron density equation, 104, 105
  - Electron–electron spin–spin interactions
    - high spin metal center systems, 208–211
    - light-induced radical pairs, 204–206
    - molecular triplet states, 206–207
    - site-directed spin labeling, 203
  - Electron micrograph, 343
  - Electron microscopy (EM)
    - molecular machines, 315
    - projection images, 3D reconstructions, 322–324
    - single-molecule methods, 258
    - structure and stoichiometry analysis, 314
  - Electron-nuclear double resonance (ENDOR), 190
  - Electron paramagnetic resonance (EPR)
    - biophysics (*see* Biophysics)
    - bound electrons, 177
    - characteristic lineshapes
      - rapid tumbling regime, 192–194
      - rigid limit regime, 195–198
    - experimental techniques (*see* Experimental methods)
    - field modulation detection, 178, 179
    - interaction energy, 177
    - magnetization, 179–180



- muscle fibers, 345
  - physical principles, Zeeman interaction, 177
  - Electron spin-echo envelope modulation (ESEEM), 189, 190
  - Electrophoresis, 343
  - Electrospray ionization (ESI)
    - charge state distribution, 216
    - convoluted process, 216
    - direct measurements, 232–234
    - non-covalent interactions, 232–234
    - positive ion mode, 216–217
    - spectra, intact proteins, 216
  - EM. *See* Electron microscopy (EM)
  - Endocytosis, 337
  - ENDOR. *See* Electron-nuclear double resonance (ENDOR)
  - Energetics, 350
  - Energy coupling
    - F-ATPase, 327
    - proton channel, 322
    - and rotational catalysis, 330
  - Energy transduction, 349
  - Ensemble unwinding assays
    - assembly, helicase, 295–296
    - DNA substrate, 294, 295
    - fluorescence
      - DNA strand separation, 294
      - stopped-flow assay, 295
    - radiometric, 294
    - steady state vs. pre-steady state kinetics, 294
  - Enthalpy
    - and entropy, 24
    - free energy, 26–27
    - products and reactants, 24
    - temperature, 26
  - Entropy
    - and enthalpy, 24
    - negative change, 24
  - Enzymatic cycle, 348, 351
  - Enzyme efficiency, 317, 327
  - Enzymes
    - chemical mechanisms, 264
    - electron transfer reactions, 200
    - metabolism, 11–12
    - molecular motors., 342
    - synchronization, 294
  - EPR. *See* Electron paramagnetic resonance (EPR)
  - Equilibrium constant, 24–25
  - ESEEM. *See* Electron spin-echo envelope modulation (ESEEM)
  - ESI. *See* Electrospray ionization (ESI)
  - Essential light chain (ELC), 343
  - Eukaryotic cell, 314
  - Exchange, chemical, 147
  - Exchange spectroscopy (EXSY), 149
  - Excited state
    - fluorophore, 51
    - and ground, 35
    - molecules, 34
  - EX1 exchange regime, 238, 242
  - EX2 exchange regime, 238
  - Exocytosis, 260
  - Experimental methods
    - field modulation lock-in detection, 186
    - magnetic field and microwave frequency, 181
    - pulsed EPR, 186–190
    - relaxation, 183–185
    - resonator design, 182–183
    - sensitivity and consequences, 181–182
    - transient EPR, 190–188
  - External force, 342, 352
  - External load, 351
  - Extinction coefficient, 39, 40
  - Extrinsic fluorescence, 56–57
- F**
- Fabian, H., 67
  - F-actin. *See* Filamentous actin (F-actin)
  - Faraday constant, 316
  - Fast photochemical oxidation of proteins (FPOP), 247
  - F-ATPase
    - animal mitochondria, 315
    - atomic resolution X-ray structures, 321
    - ATP synthesis, 316
    - binding change mechanism, 326
    - crystal structure, 319
    - function, bacteria, 314
  - F<sub>1</sub>-ATPase
    - catalytic mechanism, 327
    - crystallographic structure, 322
    - fluorescence anisotropy relaxation measurements, 327
    - mitochondria-rich animal tissues, 318
  - Fenn, J.B., 216
  - Fenn, W.O., 350, 351
  - Fermi, G., 6
  - F<sub>1</sub>F<sub>0</sub>-ATP synthase
    - detergent-solubilized membranes, 323
    - rotary ATPases, 316

- Fiber diffraction
  - experimental arrangement, 99, 100
  - fibrous biological materials, 99
  - highly ordered gels, 102
  - molecular dynamics and energy minimization, 101
  - molecular transitions, 103
  - natural Syrian hamster, 101, 102
  - structure, TMV, 102, 103
- FID. *See* Free-induction decay (FID)
- Filament assembly, 345, 353
- Filamentous actin (F-actin), 343, 346
- Filamentous viruses, 100, 102
- FIONA. *See* Fluorescence imaging with one nanometer accuracy (FIONA)
- Florin, E.-L., 263
- Fluorescence
  - microscopy, 59–60
  - quenching, 56
  - spectroscopy
    - description, 51–52
    - extrinsic, 56–57
    - FRET, 58–59
    - intrinsic, 53–54
    - molecule, 52
    - protein conformation, 54–55
    - quenching, 56
    - red edge excitation, 58
    - solid-state, 60–62
    - time-resolved fluorescence spectroscopy, 53
- Fluorescence imaging with one nanometer accuracy (FIONA), 273, 352
- Fluorescently-labeled nucleotide, 352
- Fluorescent probe, 345
- Fluorophore, 270–271
- Folding. *See* Protein folding
- Force
  - manipulation techniques, 342
  - powerstroke, 348
  - production, 349–350
- Force-clamp, 264–265, 268
- Force-feedback, 268
- Force-generating step, 343, 350
- Force generation
  - kinetic pathway, 348
  - and motility, 350–352
- Force manipulation, 342, 350
- Force production, 349, 350
- Force-velocity relationship, 350
- Förster/Fluorescence resonance energy transfer (FRET)
  - dipole–dipole coupling, 52
  - nanometer distance, 310
  - optical spectroscopic methods, 58–59
  - ring-shaped replicative helicases, 309
  - single-molecule, 273
  - and smFRET, 329
  - subunit rotation, 328
- Fourier transform (FT)
  - cyclotron frequencies, 227
  - electron density distribution, 93
  - image processing, 279
  - scattering curve, 105–106
- Fourier transform infrared (FTIR)
  - amide, 64–65
  - clinical diagnostics, 65
  - data analysis, 68–69
  - difference spectroscopy, 66
  - H/D exchange, 66–67
  - IR spectroscopy, 64
  - peptide backbone, 63
  - protein folding and stability, 67–68
  - protein secondary structure analysis, 65
  - proteins, lipids and nucleic acids, 64, 65
  - tertiary structure, 66
- Fourier transform ion cyclotron resonance MS (FT ICR MS)
  - broadband excitation and detection, 225, 226
  - electrostatic and magnetic fields, 225
  - high-resolution mass analysis, 227
  - ion fragmentation techniques, 227
  - mass analyzer, 225
  - orthogonal ion fragmentation techniques, 227
  - ultra-high mass resolution and accuracy, 226
  - unsynchronized motion, 226
- Fourier transform MS (FT MS). *See* Fourier transform ion cyclotron resonance MS (FT ICR MS)
- FPOP. *See* Fast photochemical oxidation of proteins (FPOP)
- F<sub>0</sub>-proton channel, 326
- Fragment ion. *See* Ion
- Franklin, R.E., 4, 5, 99
- Free-electron lasers, 369
- Free energy, 315–316
- Free-induction decay (FID), 116
- French, D.L., 67
- FRET. *See* Förster/Fluorescence resonance energy transfer (FRET)
- FT ICR MS. *See* Fourier transform ion cyclotron resonance MS (FT ICR MS)

**G**

G-actin. *See* Globular actin (G-actin)  
Gas constant, 25  
Geeves, M.A., 349  
Gfit, 301  
Gibbs free energy, 24  
Gliding, 351  
Globular actin (G-actin), 343  
Glycogen, 18  
Glycolipids, 18, 20  
Glycoproteins, 18, 19  
Glycosylated proteins, 371  
Gold nanorods, 329–330  
Griebenow, K., 65  
GTP-dependent signaling system, 342  
Guanosine-5'-triphosphate (GTP), 342  
Guinier, A., 104, 105  
Guinier approximation, 104

**H**

<sup>1</sup>H, 114–115, 122  
Half channel  
    accessibility experiments, 331  
    proton pathway, 323  
    *T. thermophilus* ATPase, 331  
Hanson, J., 343  
Hare, D.R., 162  
Hartmann-Hahn condition, 126, 131, 141  
Harvey, W., 3  
H<sup>+</sup>-ATPase, 317  
HCCH-TOCSY experiment, 126, 131,  
    144, 156, 159  
H/D exchange. *See* Hydrogen-deuterium  
    (H/D) exchange  
HDX. *See* Hydrogen-deuterium exchange  
    (HDX)  
Heat, 24, 26  
Heavy chain, 343–345  
Heavy chain fragment, 345  
Heavy meromyosin (HMM), 343–346  
Heck, A.J.R., 371  
He, F., 38  
Helical biopolymers, 99  
Helicases, 13  
Hemi channel, 331  
Hemoglobin, 23  
Hershey, A., 6, 7  
Heteronuclear relaxation, 149–152  
Heteronuclear single-quantum coherence  
    (HSQC) experiment  
    NOESY experiment, 134  
    polarization transfer, 131

## Hexameric helicases

dsDNA translocation, 292  
translocation, ssDNA, 292

## Higher order structure

DNA, 247  
and dynamics, RNA, 248

## High throughput automation, 377–378

## Hillenkamp, F., 218

## Hirschfeld, T., 270

## HNCACB experiment, 129, 142, 160

## HNCA experiment, 129, 130

## HN(CO)CA experiment, 129, 131, 160

## Hodgkin, A., 4

## Hodgkin, D.C., 4, 5

## Holmes, K.C., 349

## Hookean spring, 266–267

## Horizontal gene transfer, 314

## Huxley, A.F., 4, 343

## Huxley, H.E., 343

## Hvidt, A., 236

## Hydrogen bonds, 21, 23

## Hydrogen-deuterium exchange (HDX)

backbone amide hydrogen atoms, 237

conformational dynamics, 239, 240

dynamic structure analysis, 66–67

evolution, deuterium content, 242

exchange-incompetent state of the  
protein, 238

hydrogen bonding network, 236

intrinsic exchange, 237

measurements, 238–239

NMR, 147

protein higher order structure, 239, 240

receptor binding interface, 241

spatial resolution, 239

top-down approach, measurements,  
242–243

types, reactions, 236

Hydrogen exchange. *See* Hydrogen-deuterium  
exchange (HDX)

## Hydrolysis

ATP, 346

products (*see* Hydrolysis products)

## Hydrolysis products, 342, 346, 347, 349

## Hydrolysis step, 347

## Hydrophobic bonds, 23, 27

## Hydrophobic interaction

chromatography, 368, 375

## Hyperfine coupling

biological samples experiments, 201

Fermi contact term, 201

interaction, organic cofactors, 200

partially resolved splitting, 199, 202

Hyperfine coupling (*cont.*)

- photosynthetic reaction centers, 201
- solution spectrum, nitroxide radical, 194
- spin-density distributions, 200–203
- valence electrons, 201

**I**

Imaging

- AFM, 262
- molecular motors, 260

Inner membrane, 316, 321

In-phase anti-phase (IPAP) experiment, 161

Instrumental analysis, 215

Instrumentation

- electronics of NMR, 154
- macromolecular NMR spectroscopy, 152
- solid-state NMR probes, 153–154
- solution-state NMR probes, 153

Intact muscle, 350

Integral membrane proteins, 368

Intracellular transport, 23

Intrinsic exchange rate

- amide hydrogen atoms, 239
- types, labile hydrogen atoms, 237

Intrinsic fluorescence, 53–54

Intrinsic Trp fluorescence, 346

*In vitro*

- actin gliding velocity, 351
- and *in vivo*, 345
- motility assay, 351

*In vivo*, 345, 351

**Ion**

- charge state distribution, 234–236
- ESI MS, 216–217
- fragment
  - electron-based techniques, 231
  - sequence coverage,
    - macromolecular ions, 227
- MALDI, 217–218
- molecular, 216–218
- multiply charged, 216

**Ion channel**

- catalytic sites, 326
- F-ATPase, 323
- proteolipid subunits, 317

Ion exchange chromatography, 375

Ion gradient, 316, 325, 326

**Ionization**

- applications, 216
- matrix and analyte molecules, 218
- sequence information, 229

Ionization source, 229

Ion mobility (IM) MS, 372

Ion motive force (IMF), 316

**Ion trap MS**

- FT ICR MS, 225, 226
- mass analyzer, 225
- quadrupole and triple quadrupole, 222–224

**IQ motif**, 353

**Isometric force**, 351

**Isotope**

- abundance, 221, 228
- distribution, 218–219

**Isotope exchange**, 346

**Isotope labeling**

- description, 155
- 25 kDa molecular mass, 156
- proteins, 156

**J**

**J-coupling**. *See* Coupling, scalar

**J-coupling and coherence transfer**

- coherence transfer, 127
- Hartmann-Hahn matching, 126
- nuclear spins, 124
- one bond couplings, 126
- TOCSY, 126, 128
- TROSY-HSQC, 124–125

Julicher, F., 303, 305

**K**

Kalonia, D.S., 60

Kamerzell, T.J., 67, 68

Karas, M., 218

Kelly, S.M., 44

Kendrew, J., 6

Keratin (wool) diffraction, 99, 100

Kim, J., 59

Kinesin, 11

- motor, 268
- and myosin, 272

**Kinetic pathway selection**, 348

**Kinetic resolution**, 346–350

**Kinetics**

- pre-steady state, 294
- steady state, 294
- and thermodynamics, 24–25
- trace
  - estimation,  $L_m$ , 299
  - helicase-DNA complex, 297–299

**Kinetic step size**, 300

**Kinetic study**, 342, 346

**Kinetic transition**, 350

**Kinetochores**, 367

Klewpatinod, M., 49

Klibanov, A.M., 65

Kratky Plot, 104, 105

**L**

Lab on a microchip, 377  
Lakowicz, J.R., 58  
Lambert-Beer law, 38, 40  
Larmor frequency, 114, 116  
Laser beam, 266–267  
Laser induced liquid bead ion desorption (LILBID), 324  
Latypov, R.F., 55  
Leeuwenhoek, A., 3, 4  
Length clamp, 263–265  
Length-jump experiments, 350  
Lever  
    movement, 345  
    priming, 349  
    swing (*see* Lever swing)  
Lever arm hypothesis, 351  
Lever length, 351  
Lever movement, 345, 348, 349  
Lever orientation, 345, 347  
Lever priming, 348, 349  
Lever swing, 346, 347, 349  
Levin, M.K., 302  
Light absorbance  
    biological macromolecules, 38  
    chromophores, 41  
    concentration determination, 40–41  
    detection, UV region, 39–40, 42  
    nucleic acids, 39  
    protein spectrum, 38  
    structural determination, 41, 42  
Light chain of meromyosin, 343–345, 353  
Light-induced radical pairs  
    antiphase doublet split, 204  
    energy level diagram and spectra, 204, 205  
    out-of-phase echo modulation experiment, 205, 206  
    polarization pattern, 204  
    population distribution and dynamic properties, 204  
    W-band spectra, 204, 205  
Light scattering  
    applications, 80–81  
    DLS, 76, 78–80  
    electromagnetic radiation, 36  
    QELS, 76  
    Raleigh ratio, 37  
    static light scattering, 77–78  
    techniques, 81  
Light spectroscopy  
    amino acids electronic transitions, 35–36  
    description, 33  
    electron, 34  
    Jablonski diagram, 34–35

    Planck relation, 34  
    transition dipole moment, 35  
    tryptophan, 36  
LILBID. *See* Laser induced liquid bead ion desorption (LILBID)  
Limited proteolysis, 343  
Linderstrom-Lang, K., 236  
Lineshape analysis, 152  
Lipid bilayer, 316, 321, 329  
Lipid membrane, 321, 332  
Lipids, 18, 20, 23  
Liposome, 329  
Liquid chromatography (LC)-MS  
    protein sequence information, 228  
    proteolytic fragments, 240  
Load, 350–351, 353  
Load-bearing myosin, 354  
Load-dependent kinetics, 351  
Loop 1, 345, 349  
Loop 2, 345  
Low-angle scattering, 103  
Low-angle X-ray diffraction, 343  
Lower 50 kDa subdomain (L50), 345, 348  
Lucius, A.L., 300, 302  
Ludtke, S.J., 280  
Lumry-Eyring framework, 28  
Luria, S., 6, 7  
Lymn, R.W., 346–348, 354  
Lymn-Taylor model, 347, 348  
Lysozyme, 93, 96

**M**

Macromolecular assembly  
    biological, 22–23  
    gas phase, 232  
    hydrogen bonds, 23  
Macromolecular crystallography  
    anomalous scattering techniques, 97  
    biochemical research, 92  
    crystallography biology, 99  
    electron density map, 94  
    graphical applications, 97  
    isomorphous replacement, 97  
    myoglobin and hemoglobin, 98  
    Ramachandran plot, hen egg white lysozyme, 96  
    resolution, 95  
    stereochemical restraints, 95  
    structural determination, 94  
    three-dimensional diffraction grating, 93  
    X-ray crystallographic study, 92, 93  
Macromolecular interactions, 275  
Magic-angle spinning (MAS), 139, 141

- MALDI. *See* Matrix-assisted laser desorption/ionization (MALDI)
- MALDI matrix, 218
- Mäntele, W., 66
- MAS. *See* Magic-angle spinning (MAS)
- Mass
- analyzers (*see* Mass analyzers)
  - average
    - atomic masses, stable isotopes, 218
    - kinetic energy, ions, 232
  - measurements, 218–219
  - monoisotopic, 219
  - most abundant, 219, 221
  - spectrometry (*see* Mass spectrometry (MS))
- Mass analyzers
- FT ICR MS, 225–227
  - quadrupole, triple quadrupole and ion trap, 222–224
  - TOF MS and hybrid quadrupole, 224–225
- Mass resolution, 219, 222, 224
- Mass spectrometry (MS)
- architecture and dynamics, biological molecules, 249
  - characterization, macromolecular assemblies, 371
  - covalent structure, polypeptides and proteins, 227–231
  - heterogeneous proteins, 371–372
  - higher order structure, biopolymers, 247–248
  - hydrogen/deuterium exchange MS, 236–243
  - in vivo*, 372–373
  - membrane proteins, 370–371
  - structural information, 324–325
  - tandem, 219–221
- Mass-to-charge ratio ( $m/z$ ), 216, 218
- Matrix-assisted laser desorption/ionization (MALDI)
- biopolymer ions, 218
  - UV light-absorbing small organic molecules, 218
- Mean residue ellipticity, 43
- Mechanical energy, 342
- Mechanical manipulation, 342, 350
- Mechanical work, 343
- Mechanobiochemistry, 342
- Mechanochemical cycle, 347, 349, 354
- Mechanoenzyme, 350
- Membrane complexes, 367
- Membrane potential, 316
- Membrane proteins
- classical biochemical methods, 324
  - structure, 258
- Membrane trafficking, 353
- Metabolites, 18
- Metalloproteins
- Helicobacterium modesticaldum*, 210
  - Kramer's doublet, 208–209
  - powder spectrum features, 209
  - X-band EPR spectrum,
    - horse myoglobin, 211
  - Zeeman splitting, 208
  - zero-field splitting, 208
- Méthot, N., 67
- Microscopy, 351–353
- Microtubules, 367
- Middaugh, C.R., 67, 68
- Milligan, R.A., 354
- Mitchell, P., 315
- Mitochondria
- biochemical experiments, 322
  - macrolide oligomycin, 314–315
  - multi-site catalysis, 315
- Models, use of, 12
- Molecular biophysics
- atomic-level structural methods, 8–9
  - carbohydrates, 18, 20
  - cell, 18
  - circular dichroic spectroscopy, 8
  - description, 7
  - DNA and RNA, 18, 19
  - fluorescence spectroscopy, 8
  - mass spectrometry, 9
  - proteins, 18, 19
  - single molecule methods, 9–10
  - and structural biology, 215
  - three dimensional structure, DNA, 19, 21
- Molecular dynamics, 350
- Molecular envelope
- scattering profile, 105
  - scattering signal, 104
- Molecular forces, 351
- Molecular genetics, 342, 348
- Molecular machines
- bovine mitochondrial F1 ATPase, 12, 13
  - DnaB hexameric helicase, 12–13
- Molecular modeling, 368
- Molecular motor, 272, 315, 342
- Molecular property, 352–354
- Molecular replacement, 97, 98
- Molecular structure
- neutron crystallography, 108
  - nucleic acids, 5
  - and supramolecular, 343–346
- Molecular triplet states, 197, 206–207
- Molecular tweezers, 10
- Molten globule, 27
- Momentum transfer vector, 104

- Motility, 342, 350–352  
Motor activity, 352  
Motor domain (MD), 345, 347  
Motor enzyme. *See* Rotary motor ATPase  
Motor proteins  
    double-stranded (ds) unwinding, 291  
    step size and stepping rate, 300  
Motor-track systems, 354  
Movement of myosin lever, 348  
MS. *See* Mass spectrometry (MS)  
MS/MS. *See* Mass spectrometry, tandem  
Muller, D.J., 263  
Multiple isomorphous replacement, 97  
Muscle  
    fibers, 350–351  
    seminal discoveries, 342  
Muscle contraction, 343, 350, 353  
Muscle fiber, 351  
Muscle myosin 2, 345, 353  
Mutagenesis, 348  
Myofibril, 343  
Myosin  
    actin fiber drives muscle contraction, 11  
    active site, 348, 349  
    holoenzyme, 343–344  
    isoform, 349, 351–353  
    molecular motors, 266  
    molecular tweezers, 10  
    superfamily, 353  
Myosin 1, 352  
Myosin 2, 344–345, 349, 353  
Myosin 5, 349, 353, 354  
Myosin 6, 353  
Myosin 10, 353  
  
**N**  
<sup>15</sup>N, 122, 123–124, 130  
Nano-ESI. *See* Nanospray ionization  
Nanomachine, 258  
Nanometer, 260, 261  
Nanonewton, 260  
Nanoscale, 257  
Nanospray ionization, 215  
Narhi, L.O., 67  
Native mass spectrometry, 324–325  
Naumann, D., 67  
NCACX experiment, 142  
NCA experiment, 142  
NCOCX experiment, 142  
NCO experiment, 142  
Neck of myosin, 345, 351, 353, 354  
Negative stain, 323, 325  
Neutron crystallography, 108–109  
Neutron diffraction, 107, 108  
Neutron scattering  
    and diffraction methods, 107, 108  
    and X-ray  
        automated structural determination, 367  
        data collection, 366  
        diffraction methods, 367  
        macromolecular crystallography,  
            368–369  
        methods, 369  
        small angle, 369  
        structural biology, 367–368  
Niedergerke, R., 343  
NMR. *See* Nuclear magnetic resonance (NMR)  
NOESY experiment  
    acireductone dioxygenase, 134  
    HSQC, 135  
Non-muscle cell, 345  
Non-muscle myosin 2, 353, 354  
Normalized spatial discrepancy (NSD), 107  
Normal mode analysis (NMA), 350  
NSD. *See* Normalized spatial discrepancy  
    (NSD)  
NTP hydrolysis  
    biochemical and structural, 292  
    double-stranded (ds) unwinding, 291  
Nuclear magnetic resonance (NMR)  
    data processing and assignment software,  
        162–163  
    description, 114  
    excitation, transitions  
        carrier frequency, 115  
        coherent ensemble, 116, 118  
        Larmor frequency, 116  
        pulse length and excitation bandwidth,  
            116, 117  
        pulse phase, 116  
        radiofrequency, 115  
    isotope labeling, 155–157  
    nuclear spin, 114  
    nucleic acids, 160–161  
    residual dipolar coupling and diffusion  
        measurements, 161–162  
    resonance frequencies, 114–115  
    sample requirements, solution, 154–155  
    solution state, 160  
    solvent suppression, 158–159  
    spin–lattice (T<sub>1</sub>) relaxation, 118–119  
    structural and dynamic analysis, 163–165  
    structural information, 9–10  
    structural information  
        chemical shift and nuclear shielding,  
            121–123  
        D-couplings, 141–142

Nuclear magnetic resonance (NMR) (*cont.*)

- dipolar coupling and nuclear overhauser effects, 133–137
  - gyromagnetic ratios, 121
  - HNCA pulse sequence, 130
  - isotopes, 121
  - macromolecules and membrane-bound proteins, 143–145
  - paramagnetic effects, chemical shift, 123–124
  - polarization transfer, 131
  - resonance assignments, 142
  - solid-state, 139
  - valine spin system, 126–129
  - type-selective, residue-selective and segmental labeling, 157
- Nuclear overhauser effects (NOE)
- signal intensity, 134
  - transfer of polarization, 203
- Nuclear pore complexes, 367
- Nucleic acid-based molecular motors, 342
- Nucleotide affinity, 349
- Nucleotide analog, 345–346
- Nucleotide binding, 317, 319
- Nucleotide binding site, 345, 348, 353
- Nucleotide exchange factor, 342
- Nylon beads, 327, 330

**O**

- Oberhauser, A.F., 265
- $^{18}\text{O}$  exchange, 326
- Ohgushi, M., 27
- Okten, Z., 274
- Oligomycin, 315
- Optical spectroscopy
- CD, 42–51
  - fluorescence, 51–63
  - FTIR (*see* Fourier transform infrared (FTIR))
  - light
    - absorbance, 38–42
    - scattering, 36–37
    - spectroscopy, 33–36
  - Raman spectroscopy, 69–76
- Optical trap, 351
- Optical tweezers
- biological applications, 268–269
  - DNA handle, 268
  - molecular motors, 266
  - operation principles, 266–267
  - single-molecule, 268
- Orbitrap MS, 225

## Organic radicals

- Q-band spectrometers, 181
- slow relaxing systems, 184
- spin-orbit coupling, 199, 200

**P**

- $^{31}\text{P}$ , 121, 132–133, 153, 160
- Pace, C.N., 40
- Pair density distribution function (PDDF), 104, 105
- Particle tracking, 350
- Partner binding domain, 353
- Passive unwinding. *See* DNA unwinding mechanism
- Pauling, L., 6, 99
- PDDF. *See* Pair density distribution function (PDDF)
- PELDOR. *See* Pulsed electron double resonance (PELDOR)
- Penefsky, H.S., 326
- Pepsin, 239
- Peptide
- Biemann's nomenclature, 219, 220
  - covalent structure
    - ESI mass spectrum, 229, 230
    - fragmentation, MALDI MS, 229, 230
    - glycopeptides, 231
    - MS/MS methods, 231
    - oligonucleotide sequencing, 229, 231
    - polypeptide sequencing, 227–229
    - PTM, 229
  - ionization technique, 216
  - isotopic distributions, 219
- Peripheral stalk, 317
- Periplasm, 331, 332
- Perutz, M.F., 4–6
- PFGs. *See* Pulsed field gradients (PFGs)
- Phase problem
- molecular replacement, 97
  - neutron diffraction, 108
  - X-ray crystallography, 94
- pH gradient, 329, 332
- Phosphate (Pi), 346, 349
- Phosphorylation, 353
- Photodetector, 261, 267
- Physiological function, 352–354
- Piconewton, 260, 269
- $\text{P}_i$  release from myosin, 349, 354
- PISEMA experiment, 158
- Pixel array detectors, 368
- Plasma membrane, 314, 316



- P-loop, 348, 349
  - Polarization, spin
    - chlorophyll triplet state spectra, 207
    - EPR spectra, 192
    - transfer, 141
  - Polypeptide, 264
  - Polysaccharides, 18, 20
  - Posttranslational modification (PTM), 229
  - Powerstroke
    - force-generating step, 343
    - up-to-down movement, 348
  - Prestrelski, S.J., 65
  - Primase, 307–308
  - Priming, 346, 348–350
  - Probe, NMR
    - cryogenically-cooled, 153
    - magic angle spinning (for solid-state NMR), 139, 141
  - Processivity
    - ATP binding, 347
    - myosin 5 molecules, 354
    - nucleotide-induced actomyosin, 349
  - Protein
    - NMR spectroscopy, 321–322
    - thylakoid lumen, 316
  - Protein aggregation
    - DLS, 78
    - MS analysis, 249
    - stages, 234
  - Protein conformation, 46, 49, 50, 54
  - Protein Data Bank (PDB)
    - molecular replacement, 97
    - software/applications, 92
    - structural analysis, 92
    - X-ray structure, 96
  - Protein folding
    - energetics, 26–27
    - molecular mechanisms, 264
    - optical tweezers, 269
    - time-resolved fluorescence spectroscopy, 53
  - Protein pharmaceuticals, 27–28
  - Proteins
    - chemical cross-linking
      - heterobifunctional cross-linkers, 243
      - monofunctional (or zero-length) cross-linkers, 243
    - MS HDX biochemical technique, 243
    - multi-protein complex, 244
    - tools, bioinformatics, 245
    - and covalent structure, polypeptides, 227–231
    - HDX, 236–238
    - ionic charge state distribution, 234–236
  - Protein stability, 58
  - Protein therapeutics
    - biophysical techniques, 373
    - commercial production, 377
    - formulation development, 376
    - instrumentation and applications, 374
    - lifecycle, stages, 373
    - online light scattering analysis, 375
    - primary attributes, 375
    - production process and formulation, 375
    - protein characteristics, 374
    - Raman spectroscopy, 375
    - statistical calculations and multivariate analysis, 377
  - Proteobacteria, 314
  - Proteolipid ring
    - atomic resolution detail, 318
    - proton channel, 322
    - SDS-resistant, 320
  - Proteomics, 372
  - Proto-eukaryote, 314
  - Proton channel, 322, 326
  - Proton concentration gradient, 342
  - Proton gradient, 316, 329
  - Proton motive force, 316
  - Proton pump
    - eukaryotic V-ATPase, 317
    - sodium ions, 316
  - Proximity map(s), 243
  - Pseudocontact shifts, 124
  - PTM. *See* Posttranslational modification (PTM)
  - Pulsed electron double resonance (PELDOR), 190
  - Pulsed EPR
    - electronic spin–spin coupling, 190
    - ENDOR, 190
    - ESEEM, 189, 190
    - magnetic resonance experiments, 186
    - relaxation, 189
    - spin-echo methods, 188
    - types, 188
  - Pulsed field gradients (PFGs), 131–132
  - Pulse, radio frequency (RF)
    - rotor-synchronized (in SSNMR), 141
    - selective, 141
  - Pyrene fluorescence, 348, 349
- Q**
- QELS. *See* Quasi elastic light scattering (QELS)
  - Quadrupole ion trap MS. *See* Ion trap MS

- Quadrupole MS  
   ion trapping devices, 223  
   mass filter, 222, 223  
   mass spectrometers, 222  
   MS/MS experiments, 222  
   precursor ion scans, 222  
 Quadrupole, nuclear spin, 115, 152  
 Quasi elastic light scattering (QELS), 76  
 Quenched flow  
   Ensemble DNA unwinding assays, 295  
   guanosines, 296  
   polyacrylamide gel electrophoresis, 296  
   ssDNA trap, 299  
 Quenched-flow, 346
- R**
- Radio frequency-driven recoupling (RFDR)  
   experiment, 142  
 Radon, J., 278  
 Ramachander, R., 60  
 Ramachandran plot, 96, 101  
 Raman deconvolution, 74  
 Raman microscopy, 74–75  
 Raman spectroscopy  
   Cys, 71  
   deconvolution, 74  
   DNA, 72  
   His, 71  
   intensity and frequency, 69  
   microscopy, 74–75  
   peptide bond, 70  
   protein conformation, 72  
   protein dynamics, 73–74  
   technologies, 75–76  
   Trp, 71  
   Tyr, 70  
 Rate constant, 25, 26, 274  
 Rate-limiting step, 346, 348  
 Rath, P., 67  
 RAVE. *See* Regulator of H<sup>+</sup>–ATPases  
   of vacuolar and endosomal  
   membranes (RAVE)  
 Rayleigh criterion, 272, 276  
 Rayment, I., 345  
 RDC. *See* Residual dipolar couplings (RDC)  
 Reactive sulfhydryl groups (SH1 and SH2), 345  
 Recombinant protein, 348  
 Recovery, 347  
 REDOR experiment, 142  
 Regulation, 342, 345, 353  
 Regulator of H<sup>+</sup>–ATPases of vacuolar  
   and endosomal membranes  
   (RAVE), 317  
 Regulatory light chain (RLC), 343  
 Relaxation, nuclear spin, 119  
 Relay loop, 348  
 Replication  
   unwinding assay (*see* Unwinding assay)  
 Residual dipolar couplings (RDC)  
   characterizations, 138  
   D-coupling, 137  
   macromolecules, 138  
   orienting media, 138  
   solid-state NMR, 137  
 Resolution  
   definition, 95  
   mass (*see* Mass resolution)  
 Reversibility, 346, 347  
 Reversible disassembly  
   (or dissociation), 317  
 Reversible reaction, 27  
 $R_{\text{factors}}$ , 95  
 $R_{\text{free}}$ , 95, 96  
 Ribonucleic acid (RNA)  
   building blocks, 19  
   and DNA, 18  
   three-dimensional structures, 21  
 Ribosome, 12  
   catalytic activity, 343  
   catalytic residue, 348  
 Right handed coiled coil, 321, 323  
 Rigor-like state, 346  
 Rigor state, 346  
 Ring current, 122, 165  
 $R_{\text{merge}}$ , 95, 96  
 Robinson, C.V., 371  
 Robotic systems, 375  
 Rod, 343–344  
 Rotary (molecular) motor, 315  
 Rotary motor ATPase  
   cryo electron microscopy maps, 332  
   family, 314–315  
   function, 315–317  
   mechanism, catalysis, 325–332  
   structure, 317–325  
 Rotating frame NOE spectroscopy (ROESY)  
   experiment, 136  
 Rotational catalysis  
   biophysics, 326–327  
   and elastic energy coupling, 330  
 Rotor  
   atomic resolution X-ray structures, 321  
   timescale of catalysis, 326  
   X-ray crystallography, 318–321  
 Rubredoxin, 108, 109  
 Rulers, molecular, 8, 10  
 $R_{\text{work}}$ , 95, 96

**S**

- Sako, Y., 61
- Sarcomeric myosin 2, 345
- Sawtooth pattern, length-clamp mode, 264, 265
- SAXS. *See* Small angle X-ray scattering (SAXS)
- Scattering
  - cross section, 109
  - lengths, 107, 108
- Schrödinger, E., 4, 7
- SEC. *See* Size exclusion chromatography (SEC)
- Sensory function, 353
- Sequence, amino acid, 229, 231
- Sequence analysis, 344
- Serine proteases-mechanism, 108, 109
- Sethuraman, A., 68
- Sharma, S., 68
- Sharma, V.K., 60
- Shielding, nuclear and chemical shift, 121–123
- Shih, W.M., 58
- Shrödinger, E., 4
- Single molecule (SM)
  - AFM, 329
  - A/V-ATPase sector, 329
  - experimental setup, 327, 328
  - $F_1F_0$ -ATP synthase, 327
  - FRET, 329–330
- Single molecule fluorescence methods
  - biological applications, 273–274
  - description, 270
  - emitted fluorescence, 270
  - experimental setups, 270–271
  - FRET, 272
  - principles, 270
  - “super-resolution,” 273
- Single molecule fluorescence resonance energy transfer (FRET) spectroscopy
  - Escherichia coli* Rep, 273
  - Tetrahymena ribozyme, 274
- Single-molecule force spectroscopy (SMFS)
  - apparatus and control electronics, 264–265
  - avidin, 266
  - description, 263–264
- Single molecule Förster resonance energy transfer (smFRET), 329
- Single molecule methods
  - AFM (*see* Atomic force microscopy (AFM))
  - cryo-EM, 275–281
  - description, 258
  - features, 258, 259
  - forces range, 258, 260
  - molecular tweezers, 10
  - optical tweezers, 266–269
  - single-molecule fluorescence methods, 270–274
- Single-molecule motility, 351–354
- Single molecule observation of F-ATPase, 327–329
- Single molecule unwinding assays
  - FRET (*see* Fluorescence resonance energy transfer (FRET))
  - magnetic tweezers
    - piconewton forces, 309
    - single molecule methods, 309
    - T7 helicase, 308
  - optical trap, 309
- Single-particle cryo-electron microscopy
  - biomolecules, 277–278
  - electron microscope, 275–276
  - image processing, 279–280
  - Rayleigh criterion, 277
  - techniques, 280–281
  - X-ray crystallography, 275
- Single strand binding (SSB) protein
  - E. coli*, 305
  - interaction energy, 307
  - replisome, 305, 306
- Single strand DNA (ssDNA) and dsDNA, 292
  - gel-based assay, 298
  - strand exclusion model, 292, 293
  - translocation
    - description, 303
    - dTTP concentrations, 305, 307
    - helicase’s speed, 309
    - NTP binding and hydrolysis, 303
- Size exclusion chromatography (SEC), 60, 62, 375
- Skeletal muscle, 345, 346, 354
- Sliding filament model, 343
- Sliding velocity, 351
- SM. *See* Single molecule (SM)
- Small angle neutron scattering, 109–110
- Small-angle X-ray scattering (SAXS)
  - experimental requirements, 103
  - Guinier approximation, 104
  - Kratky plot, 104, 105
  - low-resolution three-dimensional models, 106
  - neutron low-angle scattering, 103
  - neutron small-angle scattering, 109
  - NSD, 107
  - PDDF, 104
  - quality, structural models, 107
  - scattered radiation, 92
  - structural determination, RNA, 106

- smFRET. *See* Single molecule Förster resonance energy transfer (smFRET)
- Smooth muscle, 345, 353, 354
- Solid-state fluorescence  
intrinsic fluorescence, 60, 61  
proteins, 60  
SEC, 60, 62
- Solid-state NMR (SSNMR), 139
- Sosa, L.D.V., 68
- Spallation neutron sources, 369
- Spectral density, 149, 150
- Spectroscopic probes, 345, 348
- Spectroscopy  
absorption, 8  
fluorescent, 8  
mechanochemical cycle, 346
- Spin–lattice relaxation, 119
- Spin locking, 126, 152
- Spin-orbit coupling  
metal centers, iron proteins, 200, 202  
orbital angular momentum., 198  
organic cofactor radicals  
photosystem I (PS I), 199  
Q-band EPR spectrum, 200, 201
- Spin-spin relaxation  
*D*-modulated interaction, 133  
heteronuclear relaxation, 149–152  
large molecules, 150
- Spliceosomes, 367
- Spontaneous reaction, 24, 26
- SRCD. *See* Synchrotron radiation circular dichroism (SRCD)
- SSB protein. *See* Single strand binding (SSB) protein
- SSNMR. *See* Solid-state NMR (SSNMR)
- Stacking interactions, 23
- Static light scattering  
applications, 80–81  
and DLS, 76
- Stator stalk  
F-ATPase, 321  
statistical image analysis, 323  
V-ATPase, 325  
X-ray crystallography, 318–321
- Stepping model of DNA unwinding. *See* DNA unwinding
- Stereochemistry of models, 96
- Stigler, J., 269
- Stopped flow  
KinTek, 295  
quenched-flow instruments, 296
- Strand exclusion model of unwinding  
hexameric helicases, 292, 293  
translocation, 292
- Structural biology, 248, 249
- Structural genomics, 368
- Structural state, 346–350
- Structure  
factor amplitude, 93–94  
molecular and supramolecular, myosin, 343–346  
myosin head, 348  
refinement, 95, 97  
secondary  
nucleic acid, 74  
protein, 65  
tertiary  
*de novo* characterization, 144  
protein folding and function, 60
- Structure-function relationship, 342
- Subfragment 1 (S1), 343
- Subfragment 2 (S2), 343
- Sulfhydryl groups, 270
- Supramolecular assembly, 342
- Sweeney, H.L., 354
- Swinging crossbridge theory, 345
- Swinging lever hypothesis, 351
- Switch-1, 348, 349
- Switch-2, 348, 349
- Synchrotron, 368, 369
- Synchrotron radiation  
photon-counting devices, 100  
scattering techniques, 97  
X-ray beams, 100
- Synchrotron radiation circular dichroism (SRCD), 50
- Synthetic biology, 372, 378
- Szent-Györgyi, A.G., 342, 350
- T**
- Tail, 343, 353
- Tanaka, K., 218
- Taylor, E.W., 346–348, 354
- Tension, 350, 351
- Thakkar, S.V., 58
- Therapeutic protein development.  
*See* Protein therapeutics
- Therapeutics, 14
- Thermal neutrons, 107
- Thermodynamic coupling, 349
- Thermodynamics  
coupling, 349  
and kinetic principles, 24–25
- Thick filament, 343, 347
- Thin filament, 343
- Time-of-flight (TOF) MS  
ESI mass spectrum, tRNATHr, 229  
and hybrid quadrupole, 224–225

- Time-resolved fluorescence anisotropy decay, 344
- Time resolved X-ray crystallography, 98
- TIRF. *See* Total internal reflection fluorescence microscopy
- Titin, 263
- TMV. *See* Tobacco mosaic virus (TMV)
- Tobacco mosaic virus (TMV), 102, 103
- TOF MS. *See* Time-of-flight (TOF) MS
- Total internal reflectance microscopy (TIRFM), 10
- Total internal reflection fluorescence microscopy (TIRF), 352
- evanescent wave, 270–271
- immobilized molecules, 273
- Totally correlated spectroscopy (TOCSY) experiment
- advantages, 126
- and NOESY experiment, 134, 135
- Track, myosin molecules, 352–354
- Transducer, 349
- Transferrin (Tf), 241
- Transient EPR, 190–192
- Transient kinetics, 346
- Translocation, 352, 354
- Transmembrane, 315, 320, 326
- Transverse relaxation optimized spectroscopy (TROSY) selection, 124, 125, 144, 159, 161
- T1 relaxation. *See* Spin–lattice relaxation
- T2 relaxation. *See* Spin–spin relaxation
- Trentham, D.R., 346, 348
- Tropomyosin, 353
- Troponin, 353
- Tryptophan (Trp), 346
- Tubulin, 342
- U**
- Umbrella method, 350
- Unconventional myosins, 352, 353
- Unwinding assay
- ensemble (*see* Ensemble unwinding assays)
- gel-based, 296–297
- kinetic trace (*see* Kinetics)
- real time, 296
- Upper 50 kDa subdomain (U50), 345
- UV absorbance, 42
- V**
- Vacuolar ATPase (V-ATPase)
- endomembrane system of all eukaryotic cells b, 314
- proton pump, 317
- single molecule rotation experiments, 329
- V-ATPase. *See* Vacuolar ATPase (V-ATPase)
- V1-ATPase, 324, 325
- VCD. *See* Vibrational circular dichroism (VCD)
- Vibrational circular dichroism (VCD), 50
- Virus
- and bacteria, 266
- icosahedral, 281
- Visscher, K., 269
- V<sub>o</sub>-proton channel, 322
- V<sub>1</sub>V<sub>o</sub>H<sup>+</sup>-ATPase, 109
- W**
- Wada, A., 27
- Walker, J.E., 326
- Wallace, B.A., 44
- WATERGATE solvent suppression, 159
- Watson, J.D., 4, 5, 19, 99
- Weber, A., 342
- Wen, Z., 75
- Wilkins, M., 4, 5
- Wong, S.S., 243
- Wyatt, P.J., 82
- X**
- X-ray crystallography
- atomic resolution, 318
- catalytic and proteolipid domains, 318, 319
- mitochondria-rich animal tissues, 318
- transmembrane segments, 320
- X-ray diffraction
- fiber, 99–103
- noncrystalline materials, 99
- X-ray scattering
- neutron (*see* Neutron scattering)
- theory, 91–92
- Y**
- Yu, S., 67
- Z**
- Zeeman splitting
- Boltzmann population difference, 130
- molecular triplet states, 206–207
- nondegenerate spin states, 114, 115
- non-Kramer's systems, 183
- Zscherp, C., 66